OECD LOFT-T-3810-U1
Volume 1

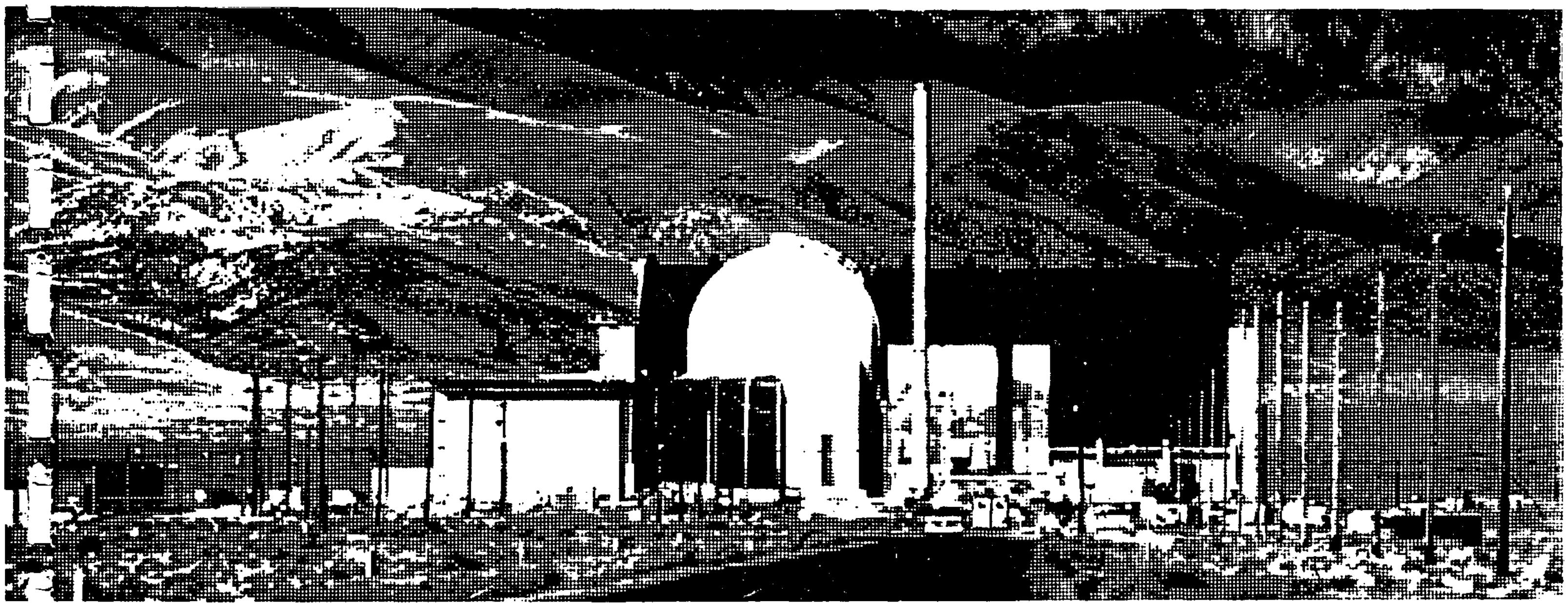

OECD LOFT Project

Postirradiation Examination Data and Analyses for OECD LOFT Fission Product Experiment LP-FP-2

Volume 1

December 1989

NOTICE

This report is for the benefit of OECD LOFT participants and their designees only

This report has been prepared pursuant to the "Agreement on an OECD Project of the LOFT Experimental Programme." It is the policy of the Management Board that the information contained in this report be used only for the benefit of the participants and the participants' designees. The contents of this report should not be disclosed to others or reproduced wholly or partially unless authorized in accordance with the laws, regulations, policies, or written permission of the appropriate project participant.

Prepared by EG&G Idaho, Inc.
under the direction of the U.S. Department of Energy,
Idaho National Engineering Laboratory.

OECD LOFT-T-3810
VOLUME 1

POSTIRRADIATION EXAMINATION DATA AND ANALYSES FOR OECD LOFT FISSION PRODUCT EXPERIMENT LP-FP-2
VOLUME 1

Steven M. Jensen
Douglas W. Akers
Bruce A. Pregger

December 1989

Idaho National Engineering Laboratory
EG&G Idaho, Inc.
Idaho Falls, Idaho 83415

ABSTRACT

The LP-FP-2 experiment was conducted on July 9, 1985, in the Loss of Fluid Test (LOFT) facility located at the Idaho National Engineering Laboratory (INEL). The primary purpose of this experiment was to provide information on the release, transport, and deposition of fission products and aerosols during a severe core damage event performed in a large scale nuclear reactor facility. Postirradiation nondestructive and destructive examinations of the fuel bundle provided information to assist in achieving this objective, as well as providing information on the material behavior and interactions that occurred within the fuel bundle during this severe core damage experiment. This was a large-scale integral test, incorporating an 11x11 array of fuel rods, control rods, and instrumentation tubes, with an active core length of 1.68 m. Peak temperatures in the fuel bundle exceeded 2100 K for approximately 4.5 min, with localized peak temperatures exceeding the melting point of the UO_2 fuel (3120 K). Large amounts of zircaloy oxidation and material relocation occurred during the experiment. The transient phase was terminated by a rapid reflood of cooling water, which resulted in significant oxidation and hydrogen generation. Zircaloy oxidation during the reflood period caused a rapid temperature excursion to occur in the upper two-thirds of the fuel bundle. This report presents the data and analysis from the postirradiation examinations of the LP-FP-2 fuel bundle.

EXECUTIVE SUMMARY

The LP-FP-2 experiment was conducted on July 9, 1985, in the Loss of Fluid Test (LOFT) facility located at the Idaho National Engineering Laboratory (INEL). The primary objective of the LP-FP-2 experiment was to provide information on the release, transport, and deposition of fission products and aerosols during a severe core damage event performed in a large-scale nuclear reactor facility. Following the successful completion of the experiment, it was decided to perform postirradiation examinations of the fuel bundle to provide additional information to assist in determining the factors that may have influenced the thermal-hydraulic and fission product behavior. These postirradiation examinations also expanded the scope of this experiment to include material behavior and interactions occurring within a fuel bundle during a severe core accident. This report presents the results obtained from the postirradiation examinations of the LP-FP-2 fuel bundle.

The LP-FP-2 experiment was the second fission product release and transport experiment and the eighth and last experiment conducted in the LOFT facility under the auspices of the Organization for Economic Cooperation and Development (OECD). This was an internationally sponsored[a] program to investigate conditions that may occur during a severe core damage accident in a pressurized water reactor. This experiment was the largest integral test of its kind ever conducted, incorporating an 11x11 array of 100 fuel rods, 11 control rods, and 10 instrumented and empty guide tubes. The active core length was 1.68 m, and the fuel bundle burnup was 430 MWd/tU prior to the initiation of the test. During the experiment, the peak temperatures exceeded the goal of 2100 K for approximately 4.5 min, with localized peak temperatures exceeding the melting point of the UO_2 fuel (3120 K).

---

[a] Sponsors of the program included Austria, the Federal Republic of Germany, Finland, Italy, Japan, Spain, Sweden, Switzerland, the United Kingdom, and the United States (U. S. Department of Energy, U. S. Nuclear Regulatory Commission, and the Energy Power Research Institute)

Both nondestructive and destructive examinations of the LP-FP-2 fuel module were performed. The nondestructive examinations included visual examinations of the exterior surface of the fuel bundle, gross and isotopic gamma scans of the overall fuel bundle, and neutron radiographs at two perpendicular orientations through the fuel bundle. The destructive examinations entailed sectioning the fuel module to provide 21 transverse cross-sectional surfaces for metallographic examination. Small core bore samples obtained in specific areas from these metallographic samples were selected for scanning electron microscope/wavelength dispersive spectroscopic examination, as well as radiochemical analyses for fission product retention.

The postirradiation examinations revealed that the relocation of material within the fuel module resulted in the formation of distinctive regions that were very similar to those observed in smaller-scale severe fuel damage experiments, as well as in the TMI-2 accident. Near the bottom of the fuel module was an accumulation of relocated metallic melt material and fuel debris. The metallic melts consisted of low melting eutectic phases, primarily composed of silver and zirconium, with iron, chromium, and nickel also present. This was the first material to relocate during the experiment, occurring after the control rods failed and released (Ag,In,Cd) in the form of aerosols and melts. The silver was able to interact with the zircaloy cladding and cause it to liquefy at temperatures well below its melting point of 2030 K. The zirconium in the resulting Ag-Zr melt was subsequently able to interact with the stainless steel cladding on the control rods and the Inconel spacer grids, causing these components to also liquefy below their melting point (1720-1730 K).

In the central portion of the fuel bundle was a large blockage of previously molten $(U,Zr)O_2$. This material formed as a result of interactions between molten zircaloy and the UO_2 fuel, along with oxidation of the resulting (U,Zr,O) by steam passing through the bundle. This material relocated later in the test than did the metallic melt material in the lower blockage region, with significant amounts relocating and oxidizing during reflood when large quantities of steam were available for zircaloy oxidation. Temperatures exceeded fuel melting (>3120 K) in the center of this blockage region, with the molten liquid phase contained within a crust of solidified $(U,Zr)O_2$. Thermocouple data suggest that temperatures remained hot in the central portion of this melt region for a few hundred seconds following reflood. This is very similar to the behavior that occurred in the TMI-2 accident.

In the upper portion of the fuel bundle was a debris bed, which was primarily composed of fuel pellets without any intact zircaloy cladding to restrain them. Small amounts of ceramic melt material between the fuel pellets held this debris bed together. This debris bed rested on top of intact rod stubs, which protruded from the $(U,Zr)O_2$ blockage region. The formation of similar debris beds has also been observed in smaller scale severe fuel damage experiments and in the TMI-2 accident.

Extensive melting and oxidation of the stainless steel upper tie plate in the upper end box of the fuel module occurred. Fuel fragments and molten materials relocated upward from the fuel module and deposited in this region, interacting with the upper tie plate. Thermocouple data indicate that the only time in the experiment when temperatures exceeded 1000 K at this location, and in which this melting and oxidation could have occurred, was during the reflood period. The LP-FP-2 fuel module was reflooded from the bottom up over a period of about 13 s, but the thermocouple data from several locations throughout the bundle indicated that temperatures actually increased after the onset of reflood. This indicates that the large amount of steam (~5 kg/s) that passed through the fuel bundle during the reflood period resulted in extensive zircaloy oxidation and generated large amounts of heat. This large steam mass flow rate was also responsible for relocating fuel fragments and molten materials to the upper tie plate during this period.

Of the five Inconel spacer grids in LP-FP-2, only the bottom one remained completely intact; and the next highest one was only partially intact. The three uppermost spacer grids were completely liquefied during the experiment. Material interactions observed at the partially intact second spacer grid indicated that Zr-Ni eutectic interactions resulted in liquefaction of the spacer grids below the 1725-K melting point of the Inconel 718 spacer grid. Relocating material accumulated on both of the remaining spacer grids, which indicates that the spacer grids tended to impede material relocation until they ultimately failed. The greatest flow blockages found in LP-FP-2, 78-86% of the available flow area, were located through, or just above, the remaining spacer grids.

Integration of the as-fabricated and posttest open flow measurement data indicates an 11% reduction in the open flow volume. This corresponds to a 15% volume expansion in the material within the fuel bundle due to porosity entrapped in the various melt regions.

Approximately 70% (10 kg) of the available (Ag,In,Cd) control rod material alloy was released to the bundle either as an aerosol or as a molten liquid. The lack of zircaloy in the upper portion of the bundle and the accumulation of Ag-Zr metallic material in the lower portion of the bundle indicate that much of the silver interacted with unoxidized zircaloy cladding and liquefied it at temperatures above 1400 K. The stripping of much of the zircaloy cladding in the upper portion of the bundle also contributed to the formation of the fuel pellet debris bed in this region.

Cladding ballooning and rupture occurred throughout the central portion of the fuel bundle, resulting in rod-to-rod contact and fusion of the oxidized cladding remnants. Throughout this region, only a fully oxidized outer shell of the original zircaloy cladding was still intact. The unoxidized inner surface of the zircaloy had melted and relocated.

Fuel grain boundary separation occurred throughout the higher-temperature portions of the fuel bundle. Pore migration, fission gas diffusion, and grain boundary coalescence contributed to this phenomenon; but the separation was enhanced in fuel adjacent to metallic melts. This suggests that reduction of the fuel near these metallic melts resulted in the formation of hypostochiometric UO_2 and liquid metallic uranium on these grain boundaries. The liquid phase would tend to weaken the grain boundaries and cause grain boundary separation. Fuel fragmentation and powdering were also observed throughout the highly damaged regions of the fuel bundle. This evolved as a result of the factors that caused grain boundary separation, but was also probably enhanced as a result of thermal shock at reflood.

Fuel liquefaction occurred as a result of interactions between molten zircaloy and the fuel at temperatures above approximately 2200 K. Interactions between some fuel pellets and molten iron-oxides also resulted in the liquefaction of some fuel and the formation of foamy fuel structures with large amounts of porosity. Porous fuel structures indicative of temperatures near fuel melting were observed in the high-temperature regions of the bundle, where molten $(U,Zr)O_2$ surrounded the fuel pellets. In the core of this high-temperature region, the fuel pellets were completely gone, indicating temperatures in excess of the 3120-K melting point of UO_2.

Measurements from the metallographic cross sections indicated that approximately 15% of the fuel and approximately 63% of the zircaloy cladding and inner liner had liquefied. Most of the liquefied zircaloy and fuel were contained in the high-temperature ceramic melt region. Material balances based on density measurements and elemental analysis of core bore samples accounted for all the fuel and zircaloy in the fuel bundle within the uncertainties in the measurements. The good agreement in these material balances provided a consistency check on the material distribution measurements.

The best estimate of the amount of hydrogen generated as a result of zircaloy oxidation was 862 g, with conservative lower and upper limits of 575 and 1064 g, respectively. The nominal value corresponds to 49% of the zircaloy in the cladding and inner liner. An additional 163 ± 83 g of hydrogen are estimated to have been generated from oxidation of stainless steel and Inconel components in the fuel bundle, bringing the total to 1025 g of hydrogen, with lower and upper limits of 655 and 1310 g. These values are in very good agreement with the 1024 ± 364 g estimated from grab samples taken from the blowdown suppression tank and estimates of the amount of hydrogen in the primary coolant system. Those estimates included

205±11 g in the blowdown suppression tank and 819±364 g in the primary coolant system. The amount in the blowdown suppression tank is indicative of the amount of hydrogen generated during the transient phase and the amount in the primary coolant system is indicative of the amount released upon reflood, because the blowdown suppression tank was isolated just prior to reflood.

An alternate method of calculating the hydrogen generation from the postirradiation examination data indicated that 836 g of hydrogen were generated from zircaloy oxidation (with conservative lower and upper limits of 546 and 1204 g), which is in good agreement with the 862 g previously calculated. This alternate method also provided information on the distribution of material from which the hydrogen was generated. This analysis indicated that nominally 181 g of hydrogen were generated as a result of oxidation of the intact cladding shells and the material in the lower blockage region and hence can be assumed to have been generated during the transient. This is also in good agreement with the 205±11 g of hydrogen found in the blowdown suppression tank. Some of the zirconium oxidation in the molten regions in the upper portions of the fuel bundle probably occurred during the transient; however, a great deal of zircaloy oxidation must have occurred during reflood, when large amounts of steam and water were available. Steam mass flow rates through the fuel bundle during the transient were inadequate to account for all the oxidation observed posttest, and the rapid temperature increases measured by thermocouples during the reflood period could only have been caused by extensive zircaloy oxidation.

Large uncertainties are associated with independent estimates of the hydrogen analyses because of very conservative lower and upper limits. However, two different methods of calculating the zircaloy oxidation from the postirradiation examination data are in very good agreement; and the total amount of hydrogen is also in very good agreement with an independent analyses based upon measurements from the blowdown suppression tank and the primary coolant system. The partitioning of the hydrogen generated in various materials is also in agreement with the partitioning between the blowdown suppression tank (transient phase) and the primary coolant system (reflood phase). The good agreement between these three independent calculations provides a greater degree of confidence in the data than the separate estimates would imply.

The as-fabricated fuel grain size was 14 μm, and most of the intact fuel at the end of the experiment had this same grain size. Grain growth was observed in the center of some fuel pellets in the high-temperature portion of the fuel bundle, with an average grain size of 27 μm and a 2-sigma standard deviation of 17 μm. The relatively large as-fabricated grain size of 14 μm was one factor which contributed to small fission product gas releases in this experiment.

Cesium was generally retained within intact and fragmented fuel pellets. Iodine was retained in the intact fuel pellets; however, significant losses were apparent in fragmented fuel at temperatures of approximately 2200 to 2600 K. Significant losses of both cesium and iodine were measured in foamy fuel/partially liquefied fuel.

The ceramic melt samples indicate significant loss of cesium and iodine in all cases, ranging from essentially complete release to less than 50% retention. However, variations between samples suggest that the melt relocated incoherently and that several factors affected the fission product release (temperature, time at temperature, and the surrounding material, i.e., lower-temperature crusts surrounding high-temperature regions). These large variations precluded the estimate of retained bundle inventories.

The results from these postirradiation examinations provide additional insight into the factors which influenced the thermal-hydraulic and fission product behavior in the LP-FP-2 experiment, as well as providing data on material behavior occurring during a severe core accident. The data from the LP-FP-2 experiment provide a valuable link between smaller-scale experiments and the TMI-2 accident.

ACKNOWLEDGMENTS

The authors wish to acknowledge the assistance of several persons whose efforts significantly contributed to this project. These include: Terry Arrington, for his engineering assistance during the bundle sectioning operations and in particular for his lead in modifying the sectioning saw; Dean Mandiloff and Derril Sparks, for their engineering assistance in the hot cell operations; Gordon Rigby, for the outstanding work he performed in several phases of the hot cell operations, and in particular for his commitment to accurately performing very tedious measurements that were necessary to determine the material redistributions in LP-FP-2; "Moose" Lindstrom, for his assistance in the development of some of the specialized hot cell equipment and for the fine quality of the metallographic examinations; Todd Morris, for his work in core boring the SEM and RFP samples; Patricia Stephens, for developing the multitude of photographs; Kevin Streeper, Kevin Lundquist, Gene Cook, Steve Porter, Ilene Walstrom, and Steve McClaskey, for their dedication and professionalism in operating the hot cell equipment and assisting in the resolution of problems that arose; Craig Nielsen, for his assistance in the hot cell operations; J. Blair Briggs, James Bazley, and Helmut Worle, for performing the criticality and safety analyses for the safe handling of LP-FP-2 in the hot cells; N. Kim Rogers, for his assistance in project engineering; Don Deddens, for coordinating and performing much of the graphics work in this report; Nadine Wade for editing this report; Mike Vaughn and Dwight Taylor, for their work at ANL-W in developing the hardware and procedures necessary to perform neutron radiography of LP-FP-2; Richard Hobbins and Jack Hartwell, for their review and comments on this report; José Esteban of the Junta de Energia Nuclear, Spain, for his overall assistance in the OECD LOFT Program; and Michael Carboneau, for his technical capabilities in the analysis of the LP-FP-2 experimental data and his persistence in convincing many unbelieving souls along the road to enlightenment.

CONTENTS

POSTIRRADIATION EXAMINATION DATA AND ANALYSES FOR OECD LOFT FISSION PRODUCT EXPERIMENT LP-FP-2

1. INTRODUCTION

The LP-FP-2 experiment was conducted on July 9, 1985, in the Loss of Fluid Test (LOFT) facility located at the Idaho National Engineering Laboratory (INEL). LP-FP-2 was designed to provide information on the release, transport, and deposition of fission products and aerosols during a severe core damage event performed in a large-scale nuclear reactor facility. This was the second fission product release and transport experiment and the eighth and last experiment conducted in the LOFT facility under the auspices of the Organization for Economic Cooperation and Development (OECD).

Probabilistic risk assessment studies[1] have shown that the interfacing system loss-of-coolant accident (LOCA), a hypothetical event first postulated in the Reactor Safety Study[2] and labeled the V-sequence, represents a significant contribution to the risk associated with pressurized water reactor operation. Consequently, this risk-dominant accident sequence was selected as the thermal-hydraulic event in which fission product release, transport, and deposition would be measured in the LP-FP-2 experiment. The specific interfacing systems LOCA associated with the V-sequence accident scenario is a pipe break in the low-pressure injection system (LPIS), also referred to as the residual heat removal system. This system typically serves two functions in a commercial pressurized water reactor: (a) it provides emergency coolant injection for core recovery during intermediate- and large-break LOCAs and (b) it provides for decay heat removal during normal shutdown. The LPIS represents a potential pathway for release of primary coolant from the reactor vessel.

As detailed in Section 1.1, the original experiment objectives were concerned with the thermal-hydraulic conditions in the test and fission product behavior after release from the fuel bundle. These data were to be used to help develop and evaluate computer codes attempting to model fission product release, transport, and deposition following this type of severe core accident. There were initially no plans to perform postirradiation examinations of the fuel bundle itself. However, following the successful completion of the LP-FP-2 experiment, it became apparent that very valuable and useful information could be obtained from postirradiation examinations of the fuel bundle. These additional data would provide information on conditions within the bundle to assist in determining the factors that influenced the thermal hydraulic behavior and observed fission product releases. In addition to providing data in these areas, these postirradiation examinations also expanded the scope of this experiment to include material behavior and interactions occurring within a fuel assembly during a severe core accident. Due to the size of the LP-FP-2 fuel assembly, this provided an important link between smaller-scale severe fuel damage experiments[3,4,5,6] and the Three Mile Island accident.[7]

A multitude of data was obtained during the experiment and from analyses of sample data obtained after the experiment. These data include, but were not limited to, information from thermocouples, aerosol and steam sampling systems, hydrogen monitors, gamma spectrometers, deposition devices, and grab samples from the primary coolant system. All this, plus additional related data, has been previously reported.[8,9,10] This report documents the data and analytical results from the nondestructive and destructive postirradiation examinations of the LP-FP-2 fuel bundle. The nondestructive examinations of the bundle, which included visual examinations, gross and isotopic gamma scans of the fuel bundle, and neutron radiography, are reported in Section 2.0. The qualitative results from the destructive examinations are described in Section 3.0. This includes photographs and generalized descriptions of all the metallographic cross sections in Section 3.1, with descriptions of the behavior of specific materials in Section 3.2. In Section 4.0, the results from the quantitative data analysis are presented. This includes data on material distributions throughout the fuel bundle in Section 4.1; estimation of the amount of zircaloy oxidation and associated hydrogen generation in Section 4.2; estimation of bundle temperatures based upon metallographic observations in Section 4.3; fuel grain size measurements in Section 4.4; and the radiochemical and elemental analyses of retained fission product samples from various locations throughout the fuel bundle is provided in Section 4.5. Section 5.0 presents a postulated bundle scenario of the major events, and Section 6.0 summarizes the results and conclusions from these postirradiation examinations.

A description of the hot cell equipment that had to be designed and built to handle the LP-FP-2 fuel module for these postirradiation examinations is provided in Appendix A, and a description of the sequence of fuel bundle handling operations is provided in Appendix B. This information is useful for understanding the conditions to which the fuel module was exposed. Appendix C presents a detailed description of the fuel bundle gamma scans, and Appendix D presents photographs of the longitudinal surfaces of the metallographic samples. Appendix E includes all the results from the SEM/WDS examinations. This includes backscattered electron images, secondary electron images, elemental distribution dot maps, energy dispersive spectra, and wavelength dispersive quantitative elemental analysis. Appendix F presents the cross-sectional measurement data used to determine the distribution of materials throughout the fuel bundle. Appendix G provides a set of pertinent phase diagrams to assist in understanding material interactions which occurred in the LP-FP-2 experiment. Appendix H provides tables of the elemental and isotopic data from the radiochemical analyses of the retained fission product samples.

1.1 Experiment Objectives

The governing objective for the LP-FP-2 experiment was to:

Obtain fission product release, transport, and deposition data during the early phases of a risk-dominant reactor transient to establish a benchmark data base for:

1. Assessing the understanding of the physical phenomena controlling reactor system fission product behavior.

2. Assessing the capability of computer models to predict reactor system fission product release and transport.

To support this objective, the following two thermal-hydraulic and four fission product objectives were defined:

Thermal-Hydraulic Objectives:

1. Provide LPIS interfacing system LOCA thermal-hydraulic conditions from the initiation of the LPIS pipe break through the early phases of severe core damage.

2. Provide transient fuel rod temperatures in the center fuel assembly in excess of 2100 K (above the 2030-K melting point of zircaloy) with aerosol generation from the (Ag,In,Cd) control rods.

Fission Product Objectives:

1. Determine the fraction of the volatile fission products (Cs, I, Te, Xe, Kr) and aerosols released to and from the upper plenum region.

2. Determine the fraction of volatile fission products and aerosols transported out of the primary coolant system.

3. Determine the retention of volatile fission products on representative primary coolant system surfaces in the plenum and piping.

4. Determine the general mass balance of volatile fission products in the fuel, primary coolant system, and blowdown tank.

1.2 Experiment Description

This section provides a summary of pertinent test parameters and the irradiation history of the LP-FP-2 fuel bundle. Additional information can be found in the references.[8,11,12]

1.2.1 Fuel Bundle Parameters

The LP-FP-2 fuel bundle was constructed as an 11x11 array of fuel rods, control rods, instrument tubes, and empty guide tubes, with low-density ZrO_2 insulating material surrounding the array. A cross-sectional view showing the locations of all these rods is presented in Figure 1. A summary of the fuel bundle characteristics is presented in Table 1. Some of the fuel rods and guide tubes had thermocouples, as shown in Figure 2. The fuel rod thermocouples measured fuel and cladding temperatures at 0.25, 0.69, 1.07, and 1.68 m (10, 27, 42, and 66 in.) above the bottom of the instrumented fuel rods. Fuel rods with thermocouples only at the 0.25-m elevation and fuel rods with thermocouples at both the 0.25- and 0.69-m elevations had their thermocouple leads routed out the bottom of the fuel rod, while the other instrumented fuel rods had their leads routed out the top of the fuel rods. This affected the internal construction of the fuel rods, as well as affecting the axial positioning of these rods in the fuel bundle, as shown in Figure 3. These differences are apparent in some of the metallographic cross sections. All axial locations in this report are referenced from the bottom of the instrumented fuel rods, which was 0.1 m above the bottom of the fuel bundle. This is the same reference system as was used to describe the thermocouple locations, and this system has been used in previous reports describing the LP-FP-2 experiment.[9,10]

The as-fabricated fuel bundle cross section was 21.4 x 21.4 cm. The length of the fuel module to the top of the upper end box was 2.0 m, and the entire length of the fuel module and upper support structure was approximately 6.8 m.

1.2.2 Power History

The LP-FP-2 experiment consisted of four distinct phases: (a) fuel preconditioning, (b) pretransient, (c) transient, and (d) posttransient.

The purpose of the fuel preconditioning phase, in conjunction with the pretransient phase, was to subject the center fuel module fuel rods to a

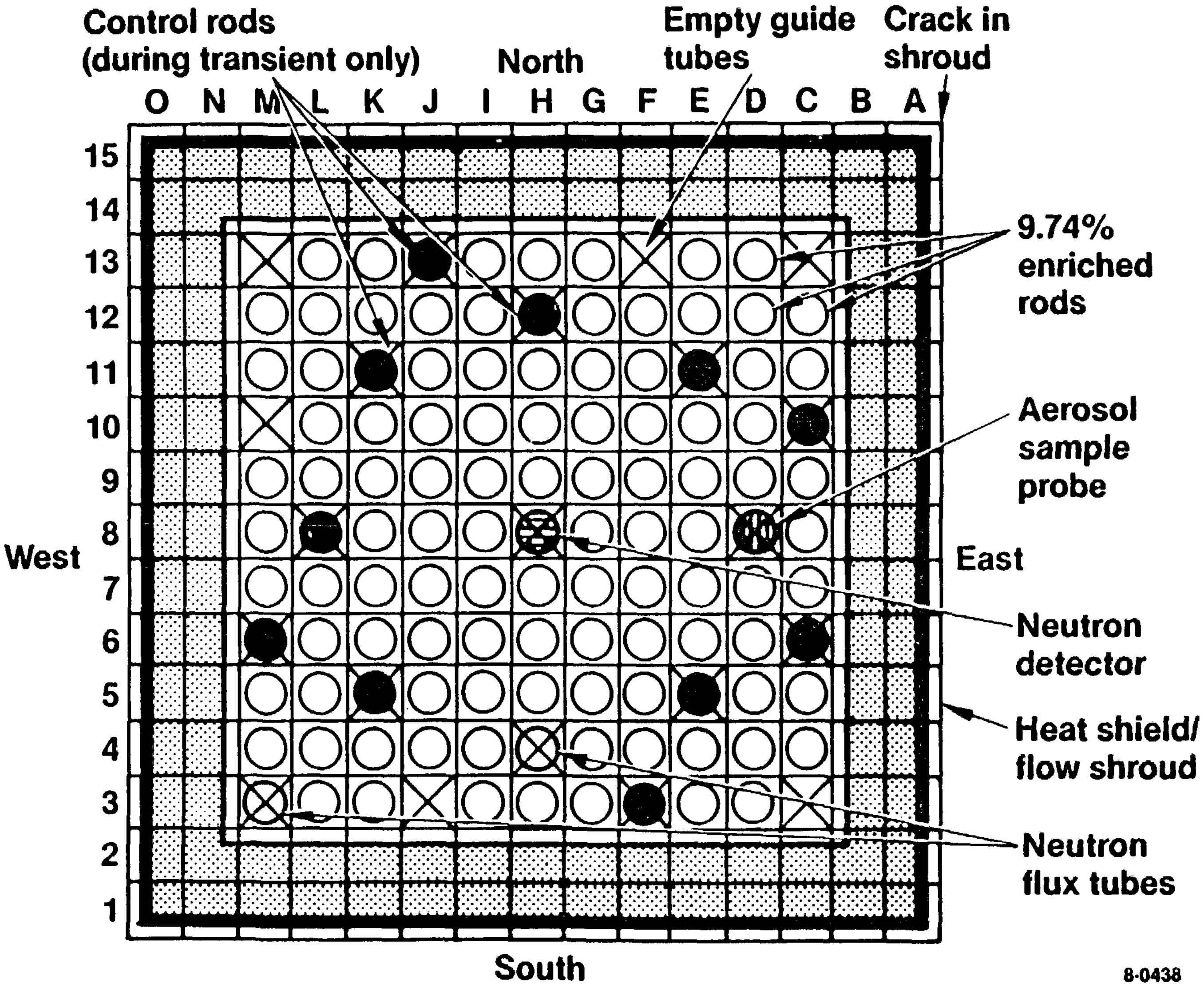

Figure 1. Cross section through LP-FP-2 fuel bundle showing rod locations and orientations.

TABLE 1. LP-FP-2 TEST DESIGN PARAMETERS

Fuel Rods	
Number of fuel rods	100
Outer diameter	10.72 mm (0.42 in.)
Cladding thickness	0.62 mm (0.024 in.)
Length	1.8 m (70.4 in.)
Cladding material	Zr-4
Fill gas	He (2.4 MPa; 350 psi)
Fuel pellet	Sintered UO_2
Enrichment	9.74 wt% ^{235}U
Fuel Density	94.7±0.4%TD
Control Rods	
Number of control rods	11
Outer diameter	11.23 mm (0.44 in.)
Cladding thickness	0.51 mm (0.02 in.)
Cladding material	304 SS
Neutron absorber	80 wt% Ag, 15 wt% In, 5 wt% Cd
Guide Tubes	
Number of guide tubes	6 empty, 15 on nonfueled rods
Outer diameter	13.84 mm (0.55 in.)
Inner diameter	12.98 mm (0.51 in.)
Material	Zr-4
Spacer Grids	
Material	Inconel 718
Shroud	
Wall material	Zr-4
Outer wall thickness	3.18 mm (0.125 in.)
Inner wall thickness	1.52 mm (0.060 in.)
Insulation	Solid ZrO_2 (~20%TD)
Insulation thickness	22.35 mm (0.88 in.)

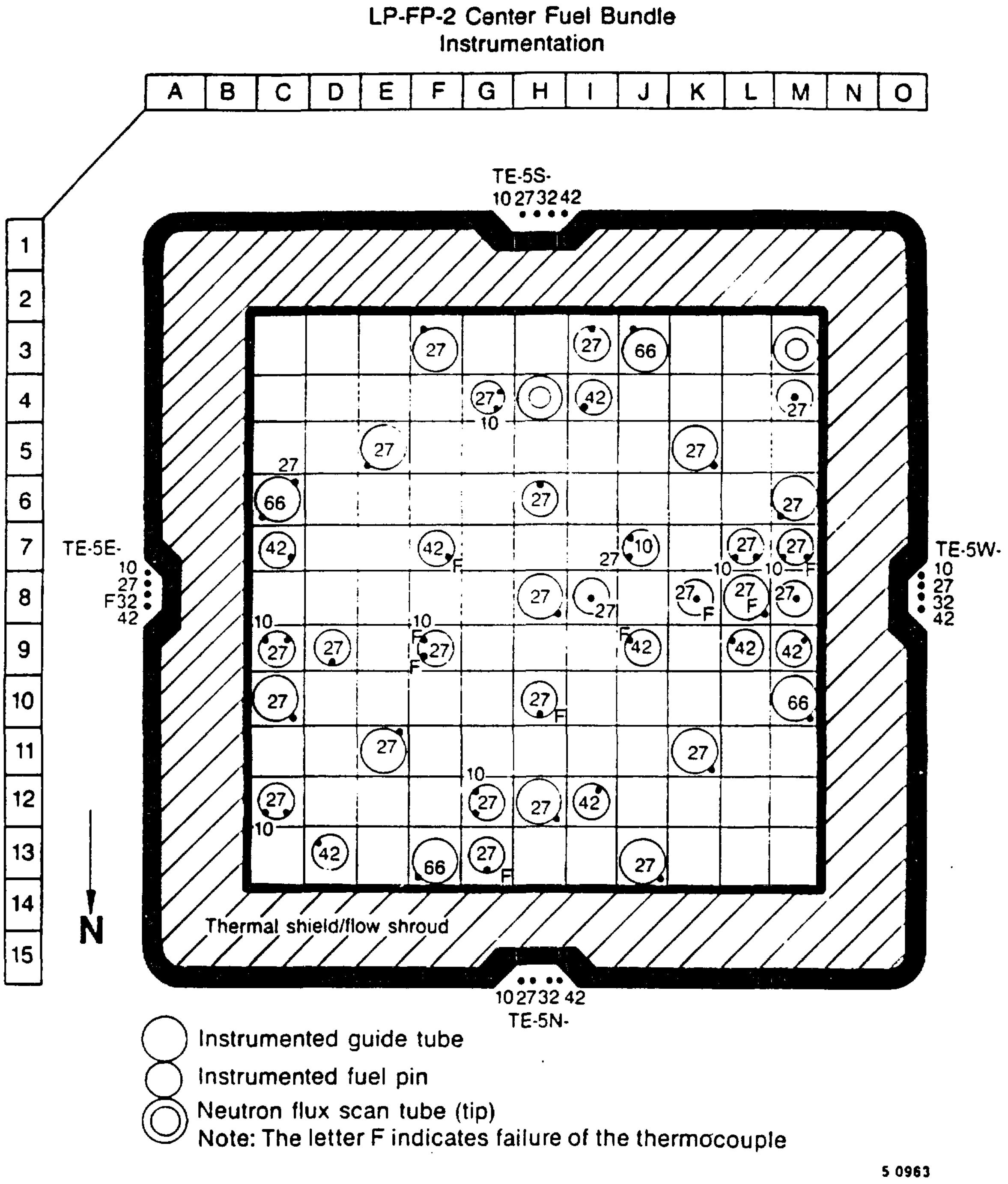

Figure 2. Thermocouple locations in LP-FP-2 fuel module.

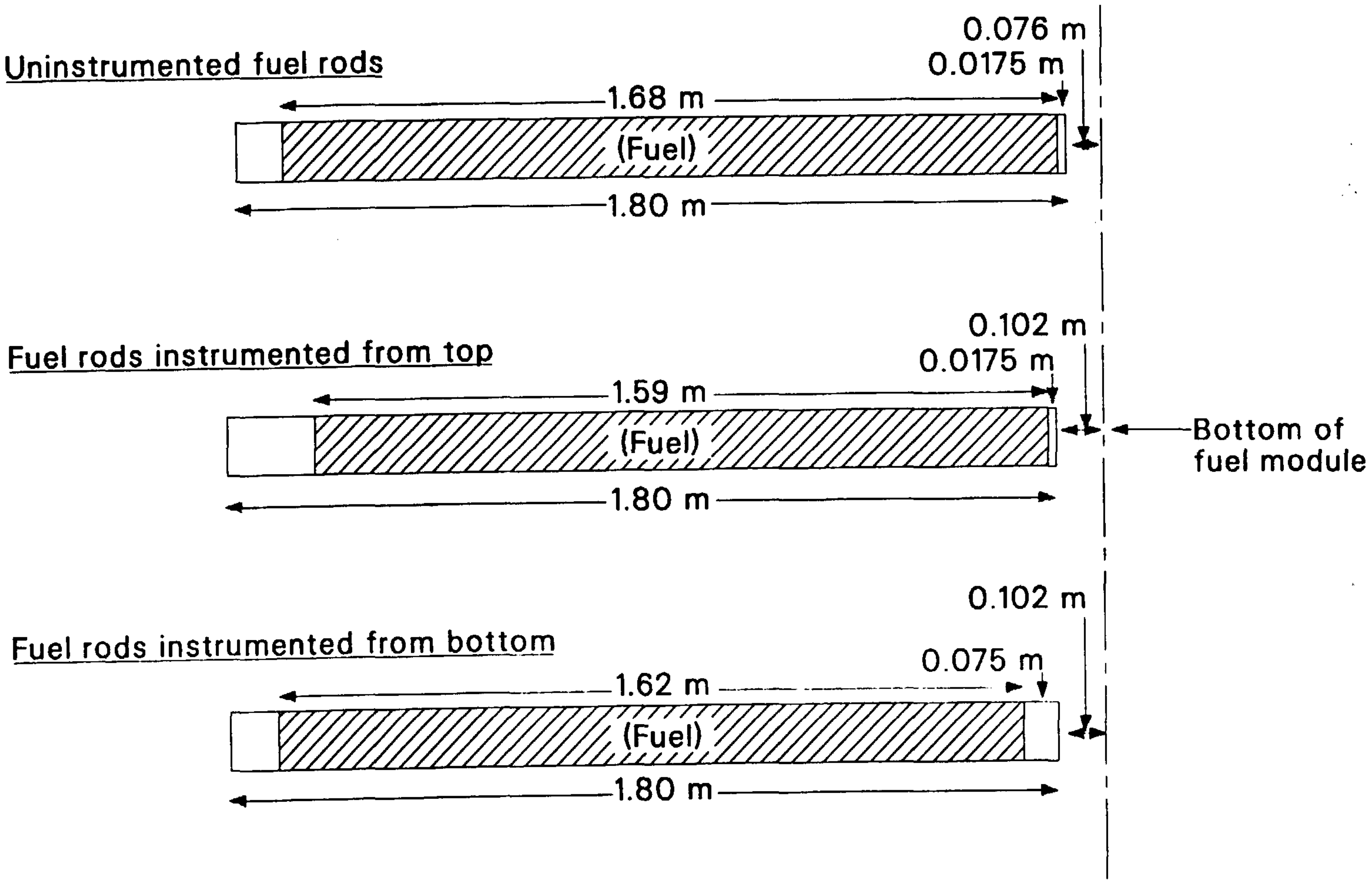

Figure 3. Axial orientations of instrumented and uninstrumented fuel rods. S51 SMJ-989-01

minimum burnup of 325 MWd/tU. This was achieved by operating the LOFT reactor at a thermal power of 32 MW for ~84 h, shutting down for ~75 h, and then operating at 26.5 MW for a period of 80 h. The burnup that the center fuel module received during this initial preirradiation period is calculated to be 346 MWd/tU.

The pretransient phase consisted of a reactor shutdown interval of about 96 h, followed by a power operation interval. The purpose of the final irradiation period was to finish the planned burnup of the center fuel module and establish an inventory of short-lived fission products. The initial condition requirements included a core decay heat of between 675 kW and 695 kW at 200 s following the reactor scram and also the establishment of typical pressure, temperature, and flow conditions that would simulate a commercial PWR. This phase of the experiment immediately followed the termination of the preconditioning phase and ended with the initiation of the transient phase (reactor scram). The pretransient included the operation of the LOFT reactor at an average thermal power of 31 MW for ~26 h, followed by an additional 15 h of irradiation at approximately 26.5 MW. The estimated burnup on the center fuel module following this irradiation was 84 MWd/tU. Consequently, the total burnup on the center fuel module prior to test initiation was 430 MWd/tU.

The actual burnup on the center fuel module was much higher than originally planned. This occurred because the experiment was initially planned to be run on July 3, 1985, with a burnup of 346 MWd/tU; however, the center fuel module control rods would not fall during this first attempt and the experiment had to be aborted. It was later discovered that high flow conditions in the core caused this condition, and tripping the primary coolant pumps early into the transient would allow the control rods to fall. The experiment was successfully run six days later on July 9, 1985. A serendipitous result of the extended down time and extra irradiation was the achievement of a higher Cs-to-I ratio than originally predicted (e.g., 4.0 vs. 2.9).

The transient phase started with a reactor scram and ended when the simulated LPIS line was closed. The transient was terminated when the external temperature on the center fuel module shroud reached 1517 K, at which time reflood of the reactor vessel was initiated. The maximum measured temperature during the experiment exceeded 2400 K, and the time at temperature (time with cladding temperatures in excess of 2100 K) was ~4.5 min.

The final, or posttransient, phase of the experiment consisted of a time interval of 44 days during which the redistribution of fission products in the gas and liquid volumes in the blowdown suppression tank and the leaching of fission products from the damaged core in the central fuel module were measured.

A complete description of the experiment procedures and the fission product detection system, along with the resulting thermal-hydraulic and fission product data, has been previously reported.[9,10]

1.3 Objectives of the Postirradiation Examination Program

Formal approval to perform postirradiation examinations of the LP-FP-2 fuel module was provided by the OECD LOFT Management Board in June 1986. However, the following objectives for the program were established by the OECD LOFT Program Review Group in April 1986:

To provide data on:

1. The final distribution of fuel and control rod materials;

2. The posttest metallurgical and chemical form of materials;

3. The maximum temperatures achieved as a function of position in the fuel bundle; and

4. The fission product distribution in both fueled and nonfueled materials.

The final distribution of fuel and control materials was determined from the neutron radiographs and metallographic cross sections. The final analyses included data on the extent of flow blockages and the material relocation behavior of all the material within the fuel bundle, not just the fuel and control material. Axial distributions, integral volumes of intact and molten materials, and mass quantities of uranium and zirconium in specific types of materials were calculated.

Data on the posttest metallurgical and chemical form of materials were provided from metallographic and Scanning Electron Microscope/Energy Dispersive and Wavelength Dispersive X-ray Spectroscopic (SEM/EDS/WDS) examinations. These included data on material interactions and phase formations, zircaloy oxidation and hydriding, fuel fragmentation, and grain size.

Temperature estimates were determined from the metallographic examinations. These estimates were based upon the observation of molten materials and microstructures that can only occur above certain temperatures. These indicators provide the only data on peak temperatures that occurred after the fuel and cladding thermocouples shunted and became inoperable.

The fission product distribution in fueled and nonfueled materials was determined from radiochemical analyses of core bore samples obtained from the various materials present in the bundle. These included intact fuel pellets, fuel in the process of undergoing various microstructural changes, ceramic melts, and various metallic melts. Within these categories, samples were obtained to investigate differences in fission product retention as a function of axial and radial location where possible, as well as variations caused by localized conditions (such as in a melt near a former control rod position).

1.4 Scope of the Postirradiation Examination Program

The extent of the postirradiation examinations conducted on the LP-FP-2 fuel module was predetermined and authorized by the OECD LOFT Program Review Group under the auspices of the OECD LOFT Management Board. Changes to the workscope were made during the course of the program, including the deletion of some examinations and changes in the number of metallographic, SEM/WDS, and retained fission product samples; however these changes always were made with the approval of the OECD LOFT Program Review Group and Management Board. Decisions on such matters as the final sectioning locations and which of the cross sections to metallographically examine also had to be approved by the Program Review Group in advance. The final extent of the postirradiation examinations is summarized below.

- Neutron radiography was performed over the entire fueled region at two perpendicular orientations.
- Nineteen cross sections were cut through the fuel bundle for examination.
- The 19 cross sections were quartered to provide 76 samples. The full cross sections had to be quartered to be of a manageable size for polishing and examination on the metallograph.
- Both transverse sides of eight of the quartered samples were examined, raising the total to 84 sample surfaces polished and photographed. These eight surfaces were from two elevations, so data are available from 21 cross-sectional elevations through the fuel bundle.
- Detailed metallographic examinations were performed on 42 of the 84 sample surfaces.
- Thirty SEM/WDS samples from the metallographic samples were examined.

- Thirty core bores from the metallographic samples were obtained for retained fission product analyses. Elemental analysis and density measurements were also performed on these samples.

2. NONDESTRUCTIVE POSTIRRADIATION EXAMINATION DATA

The nondestructive postirradiation examinations consisted of visual examinations of the exterior of the fuel module, gross and isotopic gamma scans of the bundle, and neutron radiography at two perpendicular orientations. The results from each of these examinations are presented in the following subsections.

2.1 Visual Examinations

The LP-FP-2 fuel module was vertically lifted out of its underwater storage location in the Test Area North (TAN) water pit on January 20, 1986, for visual examinations of the exterior surfaces. These examinations revealed some discoloration of the zircaloy shroud in the fueled region of the bundle, as a result of heatup during the experiment, and that a portion of the shroud in the northeast corner had broken off, allowing some of the ZrO_2 insulation to fall out. The discoloration and missing portion of shroud are shown in Figure 4, and details of the cracked region of the shroud are shown in Figure 5. It is not clear whether the cracked and broken shroud occurred while the fuel module was in the reactor or whether it occurred sometime after the test when the module was being removed from the reactor and transferred to its storage location in the TAN water pit.

Visual examinations also revealed ceramic debris in the upper end box, which had relocated upward from the fuel module. Photographs of this debris are shown in Figure 6. Radiochemical analyses and SEM/WDS examinations of this debris material later identified it as fuel and melt particles.

Examinations of the bottom side of the lower tie plate did not show any previously molten material, which indicated that material did not relocate out the bottom of the fuel module. Following these visual examinations, the fuel module was returned to its storage canister in the TAN water pit.

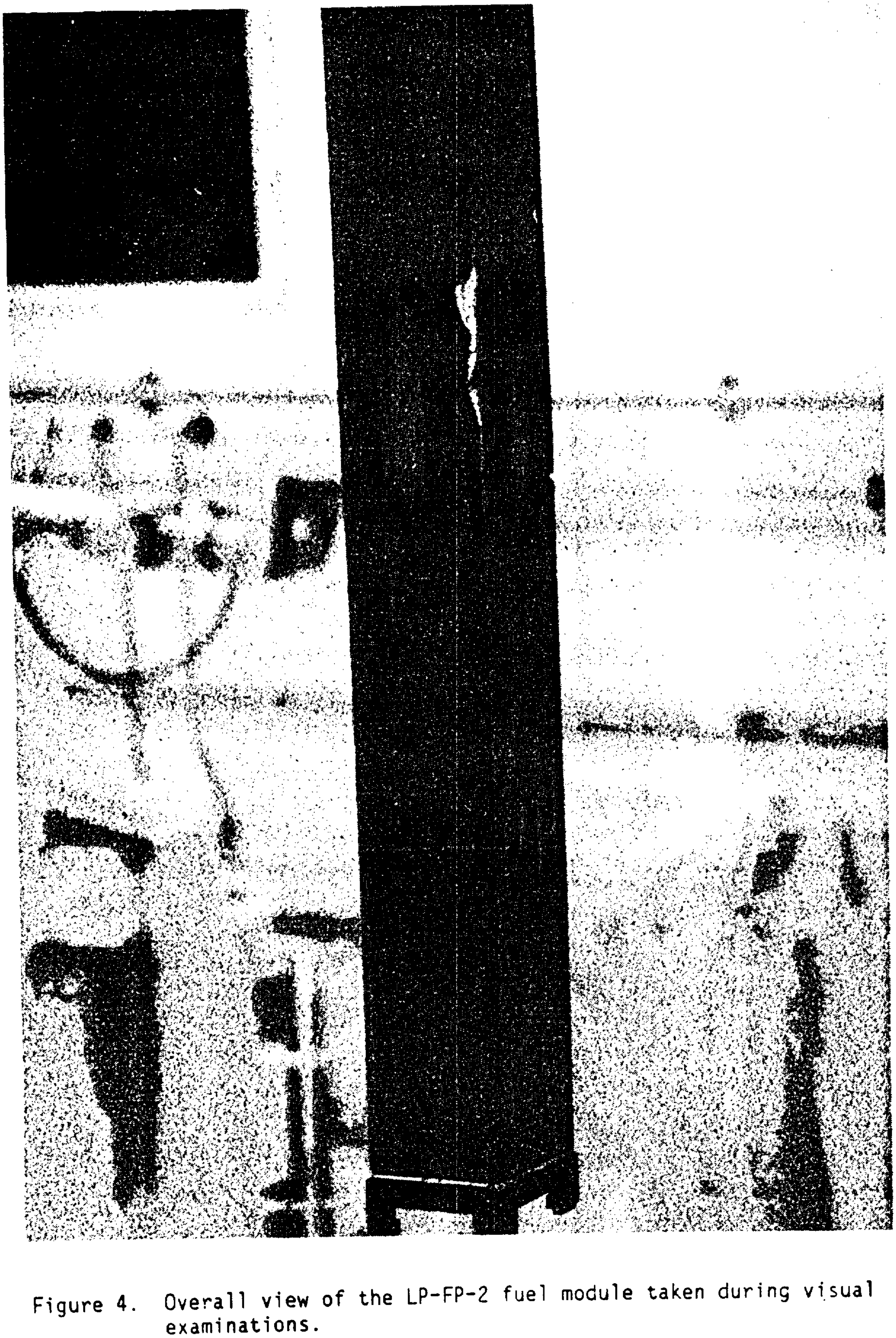

Figure 4. Overall view of the LP-FP-2 fuel module taken during visual examinations.

Figure 5. Close-up view of cracked region in the LP-FP-2 shroud.

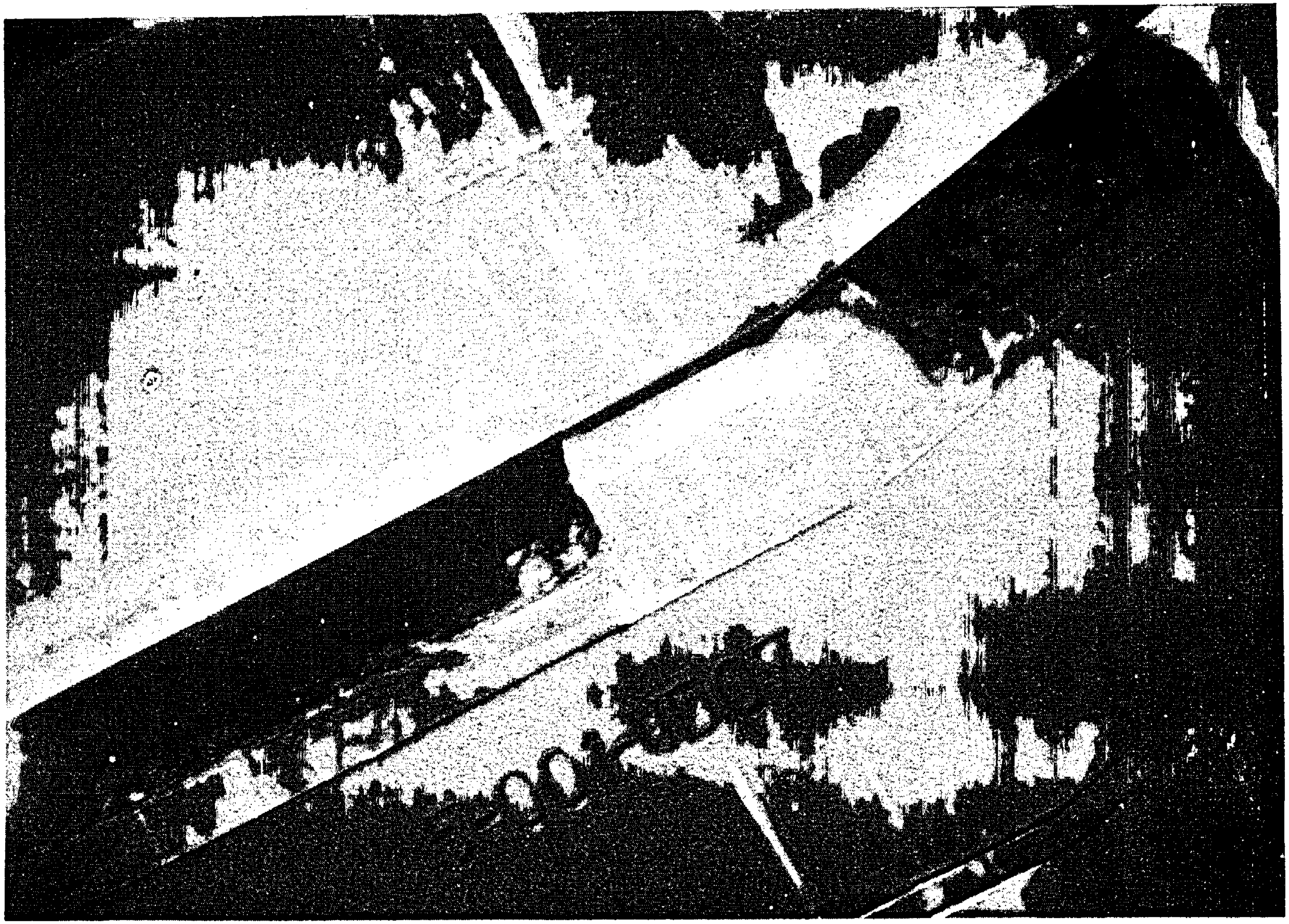

Figure 6. Close-up view of relocated debris in the LP-FP-2 upper end box.

2.2 Gross and Isotopic Gamma Scans of the Fuel Module

Details of the gross and isotopic gamma scans of the LP-FP-2 fuel module have been previously reported;[9] however, the results are reproduced in Appendix C. These examinations were conducted in September 1986 to provide some early insights into the posttest internal condition of the fuel module. As such, many of the conclusions and observations from these examinations were supported by subsequent examinations or the reasons for observed behavior are now better understood. The fuel module was always in the vertical position from the time it was removed from the reactor through the completion of the gamma scans; consequently, these gamma scans indicate material redistribution before the module was ever placed in a horizontal position. The fuel module had to be horizontal for handling in the TAN hot cell and for shipment to Argonne National Laboratory-West (ANL-W) for neutron radiography. Results from these gamma scans are consistent with the material distribution in the neutron radiographs, which indicate that there was very little movement of loose material as a result of these rotations. Consequently, the neutron radiographs accurately reflect the posttest condition of the bundle.

The principal results of these examinations were:

- There had been material relocation within the fuel module, with significant amounts of material no longer present on the eastern side of the upper portion of the bundle. This was later verified by the neutron radiographs and metallographic cross sections.

- the bottom spacer grid was intact, and very little material relocated to this region. There had been material relocation into the region near the second spacer grid. Both of these observations were later verified by metallographic examination.

- the isotopic gamma scans indicated that silver was present in the lower portion of the fuel module. Metallography later showed that the control rods were intact in this region, and in addition there had been relocation of silver-bearing materials to this region.

- There was no evidence that any Te-129m was transported out of the assembly; however, there were relatively high concentrations in the upper portion of the fueled region, which suggested that some tellurium may have volatilized and deposited in the upper portion of the fuel module.

- The isotopic scans indicated that ruthenium and cerium had been transported into the upper plenum region, probably as particulate fuel debris. Radiochemical and SEM/WDS examinations of samples from this region later verified this.

- Only a small fraction of the total fission product bundle inventory was deposited in the upper plenum region of the fuel module.

2.3 Neutron Radiography

Neutron radiography of the LP-FP-2 fuel module was performed at ANL-W in September 1987 at two perpendicular orientations over the entire fuel bundle and a portion of the upper support structure. The composites of these radiographs are shown in Figures 7 and 8. The zero reference refers to the bottom of the instrumented fuel rods, as described in Section 1.2.1. The north and east orientations can be referenced to Figure 1 and refer to that face which the neutron beam first intercepted on its passage through the module. The east face is therefore on the left side of the north-face view. The remaining portion of the upper support structure, which was not cut off in preparing the module for shipment to ANL-W, can be seen near the top of the radiographs. The object attached to the upper support structure is a lift attachment, which was used to handle the fuel module after the upper support structure was cut off, as described in Appendices A and B.

The ZrO_2 insulation layers between the zircaloy shroud and inner liner are visible in these radiographs, as well as the end boxes and control rod spider assembly. In the upper portion of the assembly, it is apparent that the inner liner was gone and the ZrO_2 insulation was free to relocate. Along the length of the fuel module were regions in which previously molten material penetrated into the insulation region, and it can be seen that these molten materials came very close to reaching the shroud in some places. The debris that was observed in the upper end box region during the visual examinations is also apparent. In the upper portion of the fuel module on the eastern side (the left side of the north view), it can be seen that there was significant relocation of material out of this region. This substantiates the results from the gross gamma scans taken earlier, which indicated that this condition existed before the fuel module was ever laid horizontal. There is no indication of any material having relocated below the bottom spacer grid of the fuel module, which agrees with observations made during the visual examinations.

Several distinct regions were identified from these neutron radiographs, and a description of each of these is provided in the following subsections.

2.3.1 Region 1 (<0.1 m)

This region encompasses the bottom spacer grid and below. The spacer grid and intact rod array are visible in the radiographs, and there are no significant amounts of relocated material.

2.3.2 Region 2 (~0.1-0.23 m)

The rod array is no longer readily discernible, which indicates that material relocated into this region from above and filled the flow channels between the rods. Subsequent metallographic examinations showed that the relocated material consisted of an agglomeration of previously molten metallic materials, fuel, and debris that had accumulated above the bottom spacer grid. The previously molten metallic materials were primarily Ag-Zr eutectic melts, with Fe, Cr, Ni and other elements mixed in. The accumulation of this material at the bottom of the fuel module indicates that this was the first material to relocate during the test.

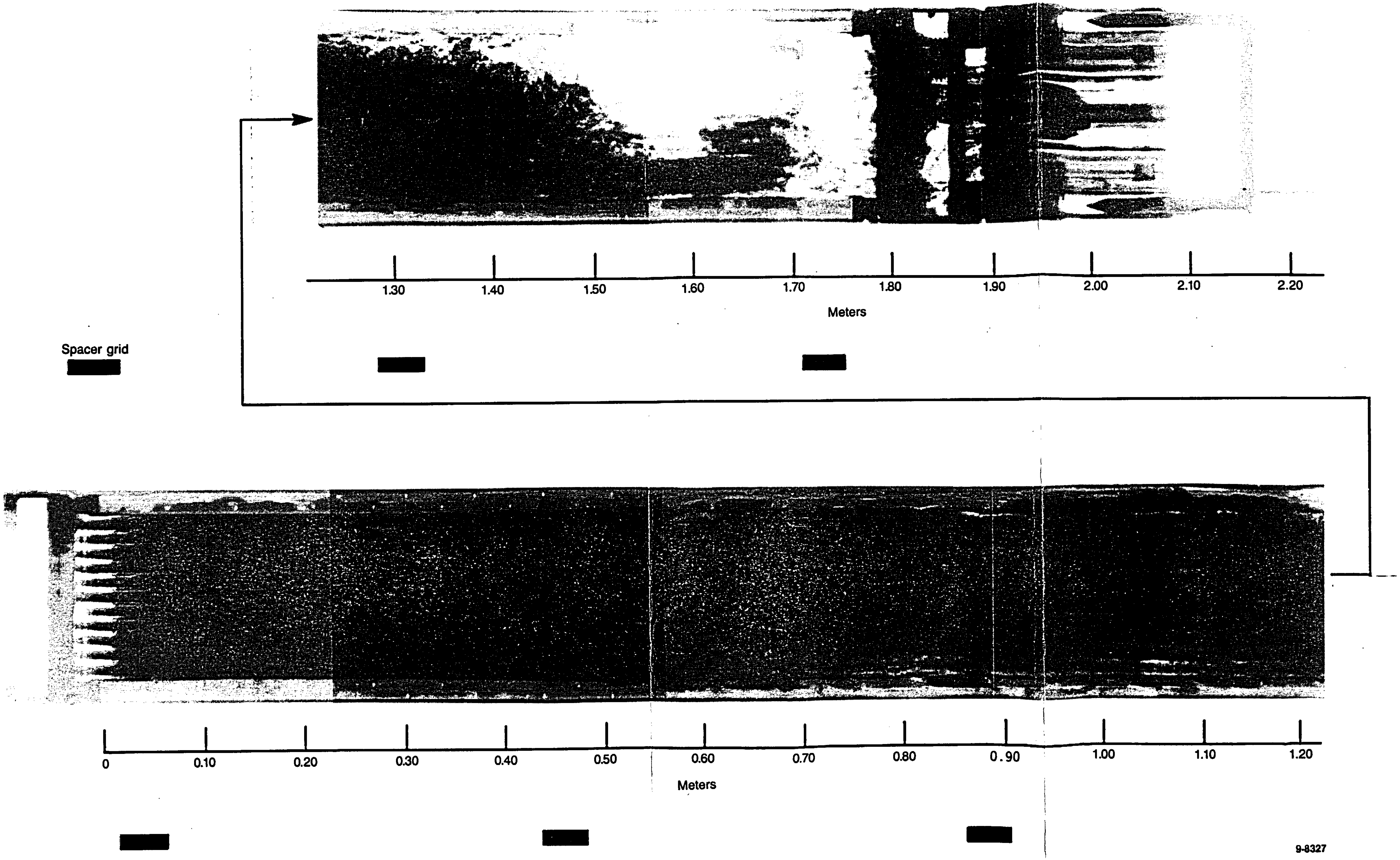

Figure 7. Neutron radiograph of the LP-FP-2 fuel module (north view). Elevations referenced from bottom of instrumented fuel rods.

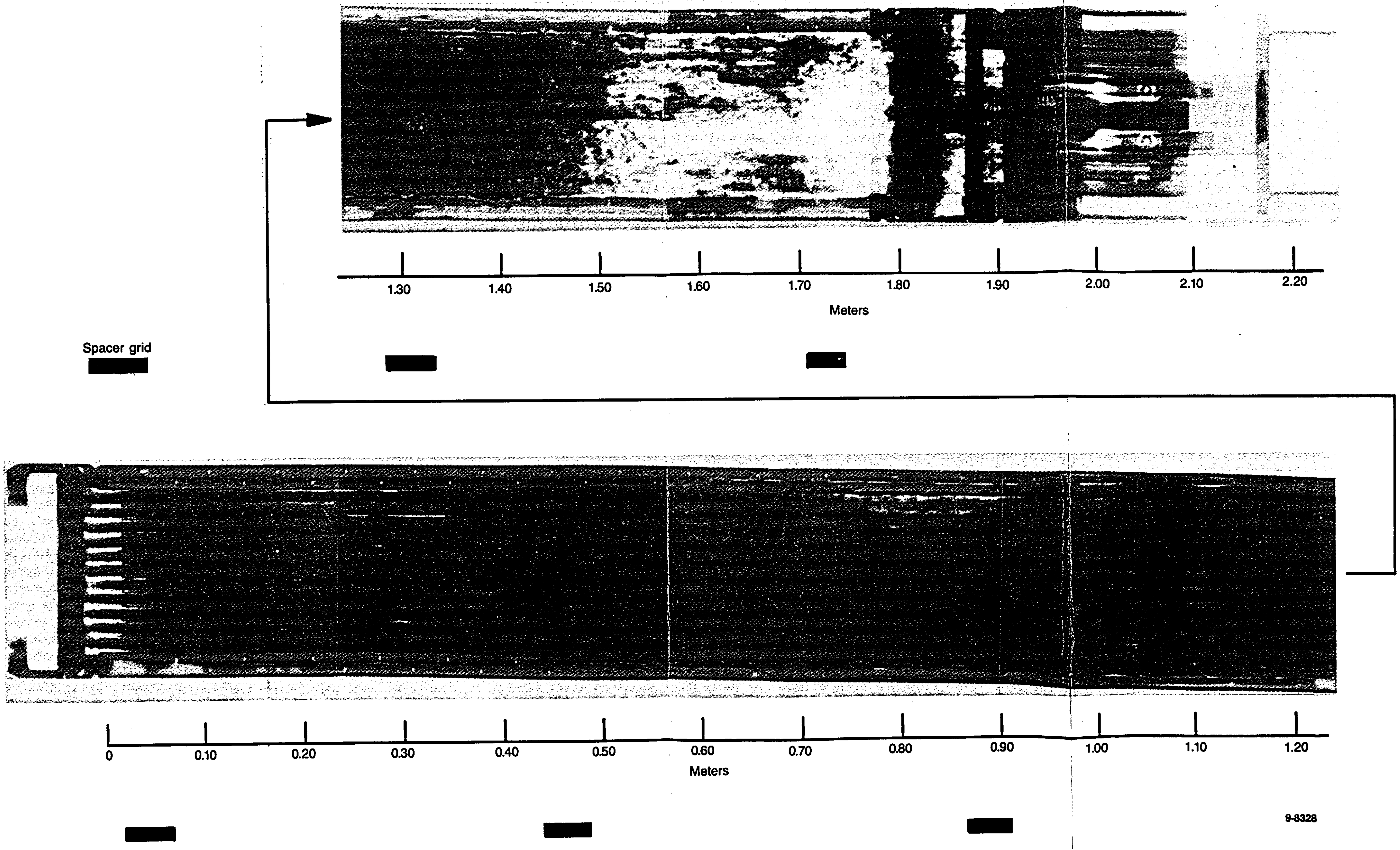

Figure 8. Neutron radiograph of the LP-FP-2 fuel module (east view). Elevations referenced from bottom of instrumented fuel rods.

2.3.3 Region 3 (~0.23-0.44 m)

In this region, the rod array can once again be observed, although it is apparent that there is some relocated material present in the flow channels. Subsequent metallographic examinations confirmed these findings and showed an intact rod array with significantly less relocated material in the flow channels than was observed in the lower blockage region.

2.3.4 Region 4 (~0.44-0.85 m)

Significant portions of the rod array are obscured throughout this region, and it is apparent that material relocated from above to fill many of the flow channels. Subsequent metallographic examinations showed previously molten $(U,Zr)O_2$ filling much of the flow area between the fuel rods. This upper blockage region was situated above the second spacer grid, just as the lower blockage was situated above the bottom spacer grid. This suggests that the spacer grids tended to impede material relocation. Previously molten material can also be observed penetrating into the insulation region throughout this upper blockage region. Subsequent examinations revealed that the zircaloy inner liner had melted and was no longer present throughout this region.

2.3.5 Region 5 (~0.85-1.15 m)

Throughout this region, the rod array is once again apparent, although there is material partially blocking the flow channels. Subsequent metallographic examinations showed extensive cladding ballooning and rupture in this region, with relocated ceramic melts surrounding some of the fuel rods and partially obstructing the flow channels. The zircaloy inner liner was missing throughout this region, and previously molten materials penetrated into the insulation.

2.3.6 Region 6 (~1.15-1.70 m)

In this region, the rod array is generally not apparent from the radiographs, except on the western side of the module near the very top of the fueled region. A lot of material was missing on the eastern side of the fuel module, including the loss of much of the insulation. The lack of material in this region of the fuel bundle is consistent with results from the gamma scans. Subsequent metallographic examinations showed that the material in this region consisted primarily of a rubble bed of fuel pellets without any cladding, with ceramic melts surrounding the fuel fragments.

3. DESTRUCTIVE POSTIRRADIATION EXAMINATION DATA

This section provides a qualitative description and analyses of the metallographic results. Section 3.1 provides a general description of each of the metallographic cross sections. This provides information on some of the pertinent features that were observed, as well as explaining, where appropriate, how the posttest handling of the fuel bundle affected the appearance of these cross sections. In Section 3.2, the description and analyses are categorized into specific topics (zircaloy, fuel, control material, etc.), to discuss how each of these materials behaved throughout the entire fuel module.

3.1 General Description of Metallographic Cross Sections

The axial locations of each of the cross sections are shown in Table 2. The orientation of the samples in the photographs is such that they can be directly compared to Figure 1. The #1 samples are in the northwest quadrant, the #2 samples are in the northeast quadrant, the #3 samples are in the southwest quadrant, and the #4 samples are in the southeast quadrant.

3.1.1 Cross Section A (0.003 m; Figures 9-13)

This cross section was through the intact rod region below the bottom spacer grid. It intercepted the fueled region on the noninstrumented fuel rods, but the fueled region on the instrumented fuel rods was above this axial elevation. The thermocouple wires can be seen in the instrumented rods routed from the bottom, whereas the instrumented fuel rods routed through the top do not show the thermocouple wires and their cross sectional areas are smaller. This section was also through the stainless steel lower end caps of the control rods, instead of the (Ag,In,Cd) alloy; and variations from rod to rod are either caused by material fallout after sectioning (when the bundle was filled with epoxy it could not get within the intact portions of these rods) or because the final sample had a slight tilt to it when it was polished. Variations in the appearance of fuel

TABLE 2. AXIAL LOCATIONS OF METALLOGRAPHIC CROSS SECTIONS

Cross Section	Elevation (m)
A	0.003
B	0.03
C	0.12
D	0.22
E	0.27
F	0.36
G (bottom face)	0.43
G (top face)	0.46
H	0.48
I	0.66
J	0.77
K	0.88
L	0.96
M	1.04
N	1.14
O	1.20
P	1.30
Q	1.45
R	1.68
S (bottom face)	1.80
S (top face)	1.83

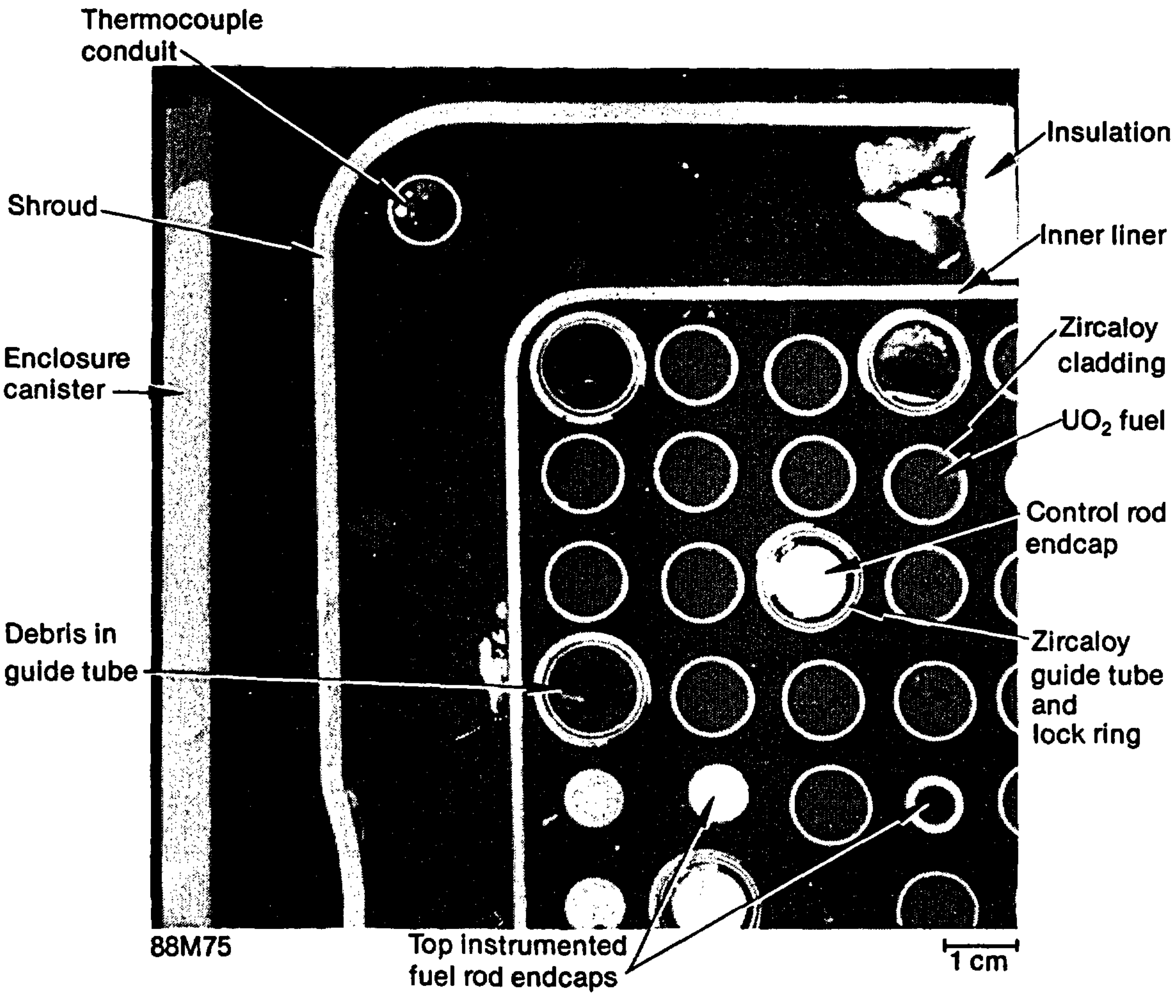

A1

Figure 9. Metallographic cross section A1 at 0.003 m above the bottom of the instrumented fuel rods.

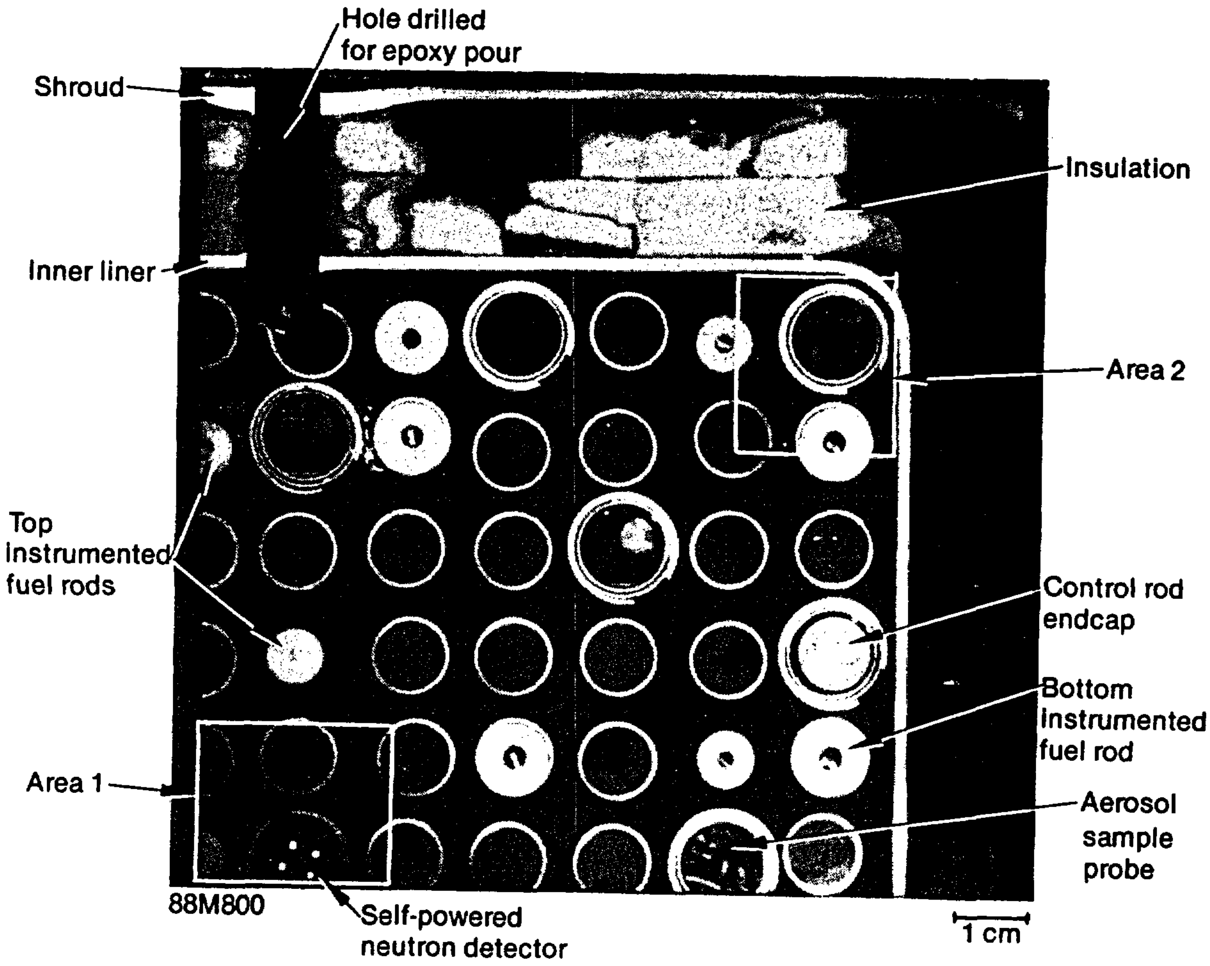

A2

Figure 10. Metallographic cross section A2 at 0.003 m above the bottom of the instrumented fuel rods.

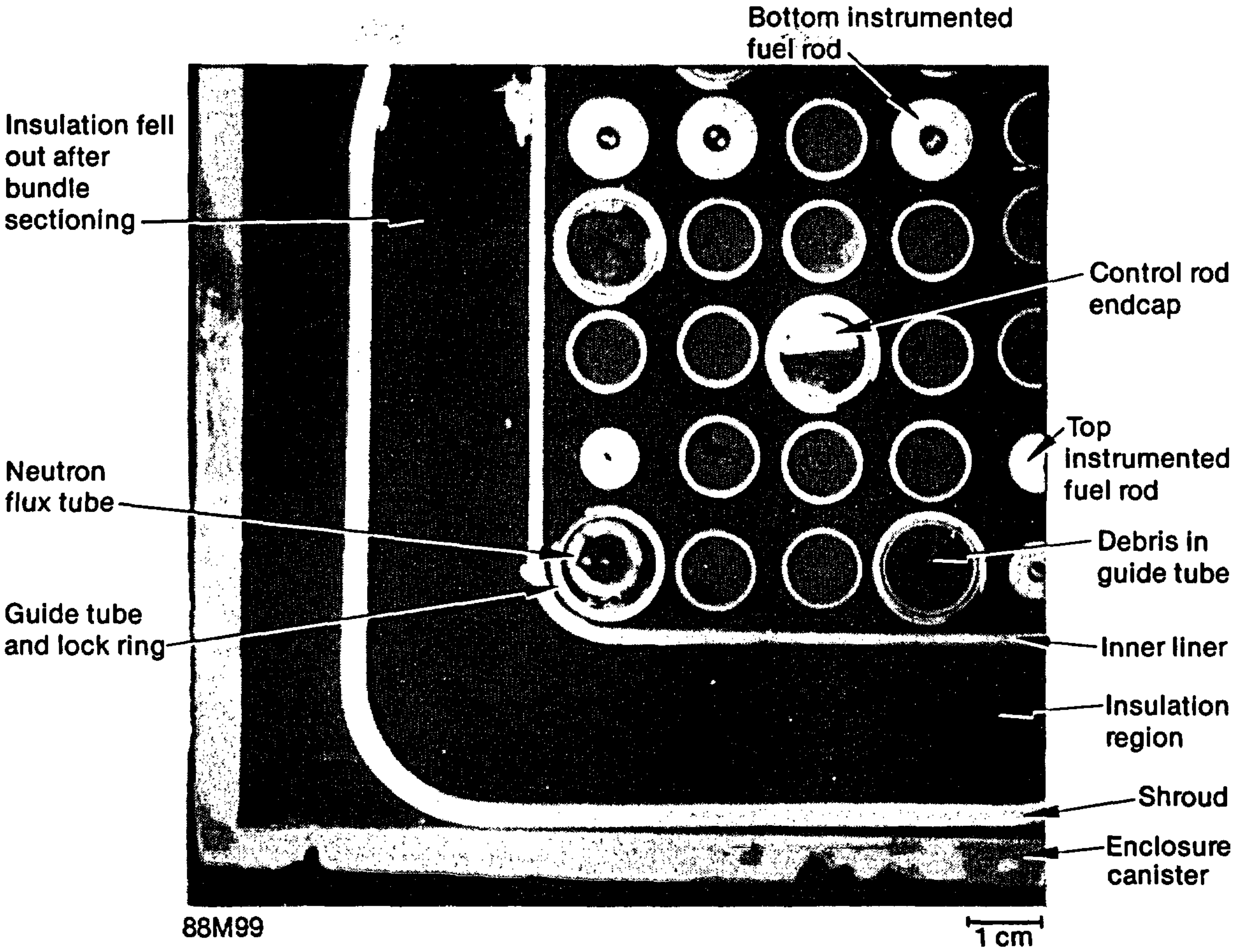

A3

Figure 11. Metallographic cross section A3 at 0.003 m above the bottom of the instrumented fuel rods.

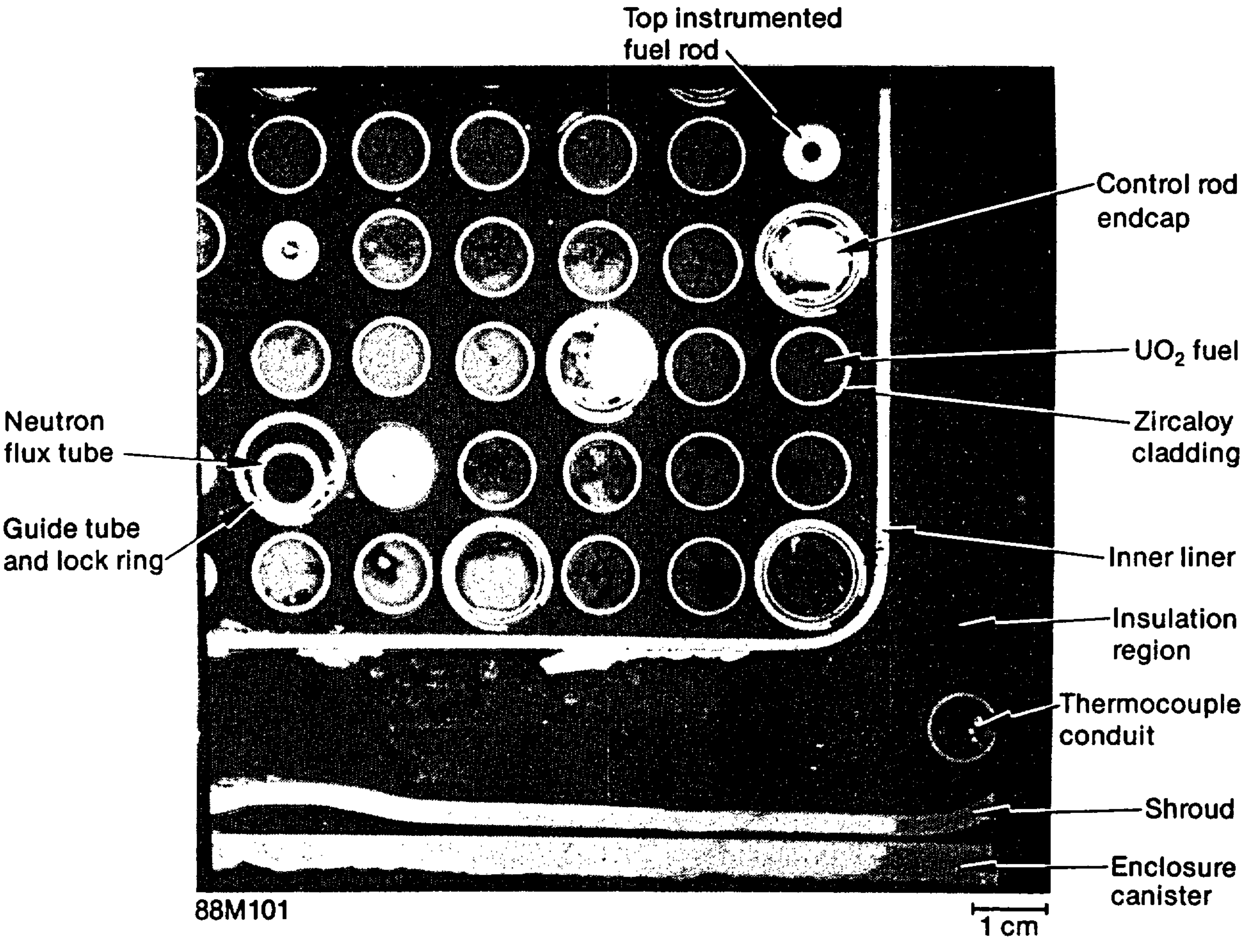

A4

Figure 12. Metallographic cross section A4 at 0.003 m above the bottom of the instrumented fuel rods.

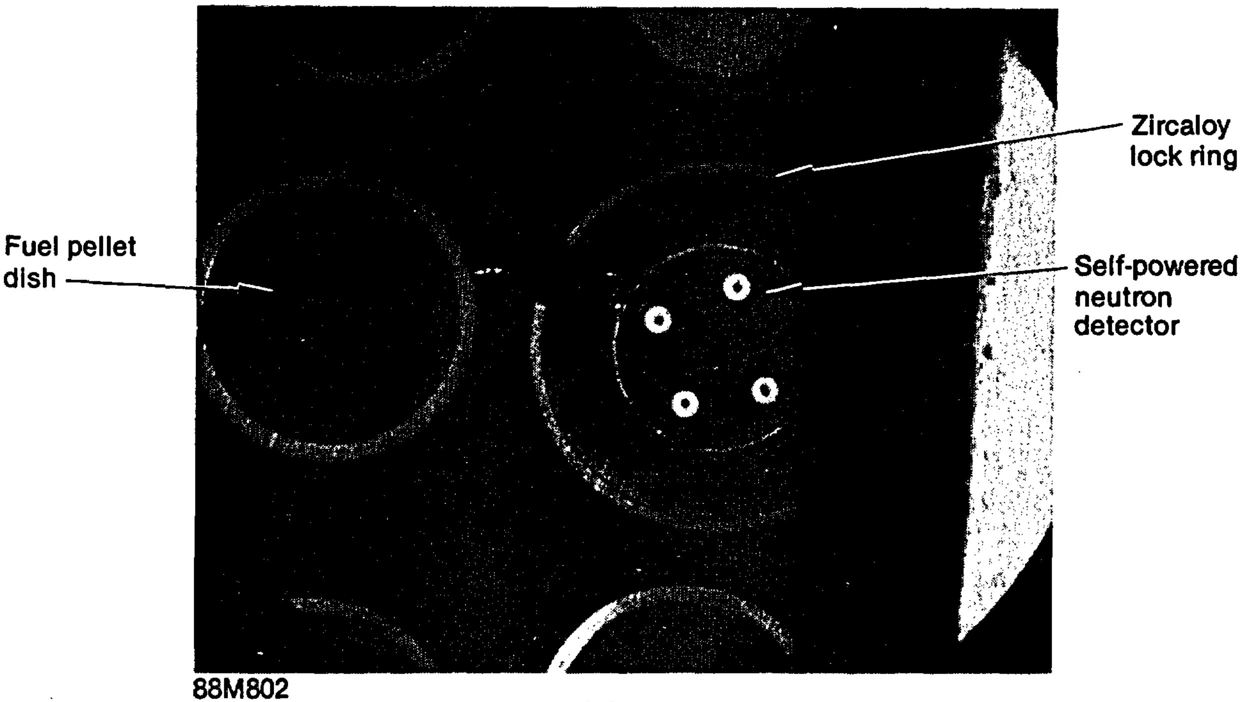

A2 Area 1

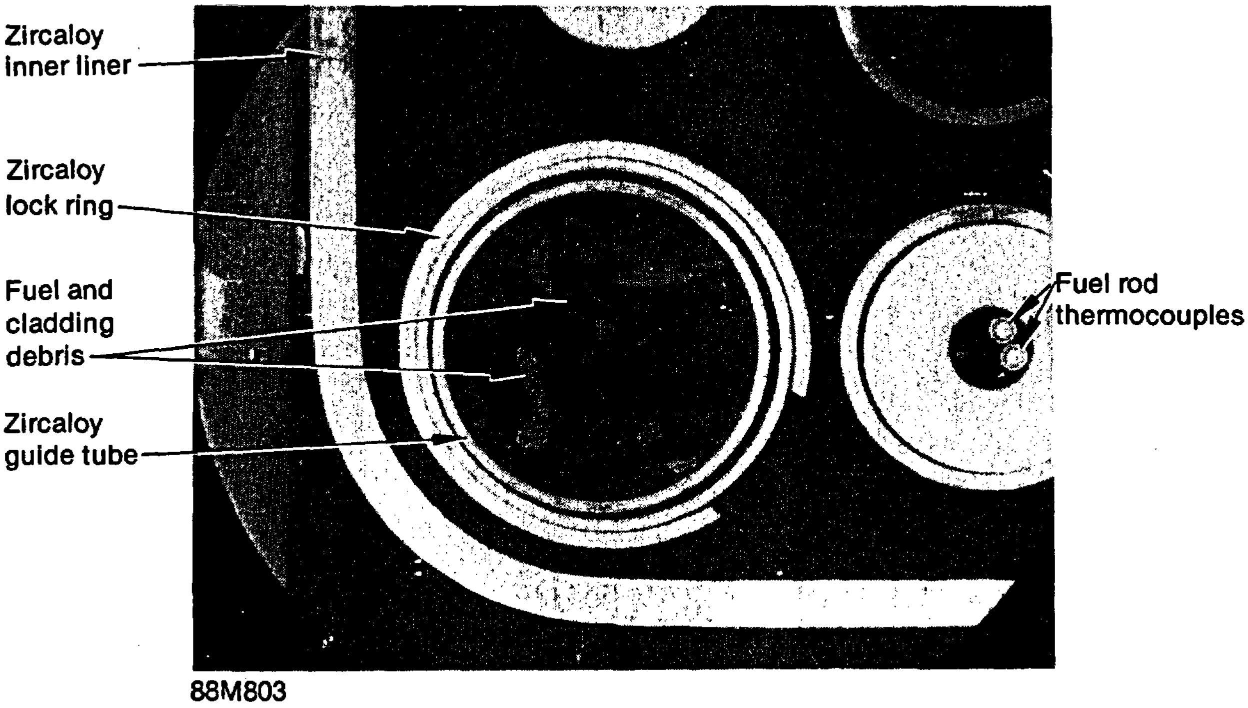

A2 Area 2

Figure 13. Details of the A2 metallographic cross section at 0.003 m.

pellets are due to material fallout during the sectioning operation and sectioning through the dished portion of the fuel rods. Debris that has fallen down from above can be observed resting in the bottom of the empty guide tubes. The insulation that appears to be missing was actually intact until it was lost during the bundle sectioning operation. It can be seen in the neutron radiographs. One of the holes drilled into the fuel module to allow epoxy to be poured into the bundle can be seen through the insulation region in Figure 10.

3.1.2 Cross Section B (0.03 m; Figures 14-18)

This cross section was through the bottom spacer grid. It cut through the fueled region of all the fuel rods except those that were instrumented from the bottom. The thermocouple leads can be seen in the bottom instrumented fuel rods. The (Ag,In,Cd) alloy is present at this elevation in the control rods. The stainless steel cladding containing the control material was surrounded by a zircaloy guide tube and an additional zircaloy lock ring. The purpose of these lock rings was to support the spacer grid, and they extended just above and below the spacer grids. Some relocated debris can be observed in some of the empty guide tubes, and some droplets of metallic melt solidified at this spacer grid location. All the fuel, insulation, and shroud material can be assumed to have been intact prior to sectioning these samples, because the inner liner and fuel rod cladding were completely intact.

3.1.3 Cross Section C (0.12 m; Figures 19-22)

Burrs on the bottom of the cut slab resulted in difficulties in removing this sample from the work table, as described in Appendices A and B. Consequently, almost all of the insulation was lost; and the inner liner and epoxied material within the inner liner were free to move in relation to the shroud. This accounts for the unequal spacing between the inner liner and shroud on samples from this cross section. This cross section had a ring of relocated material, which in three dimensions had an egg-like structure, surrounding the intact rod array in the center of the fuel

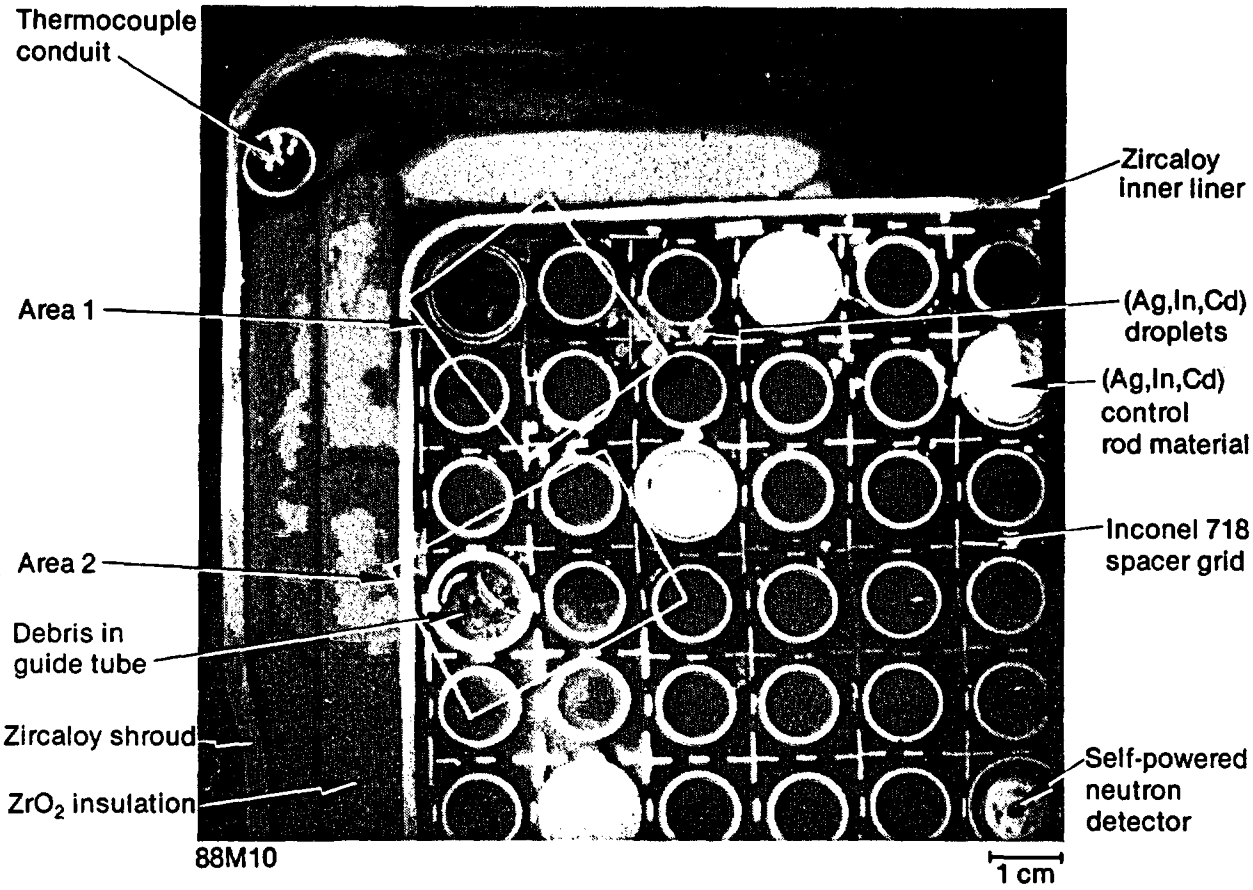

B1

Figure 14. Metallographic cross section B1 at 0.03 m above the bottom of the instrumented fuel rods.

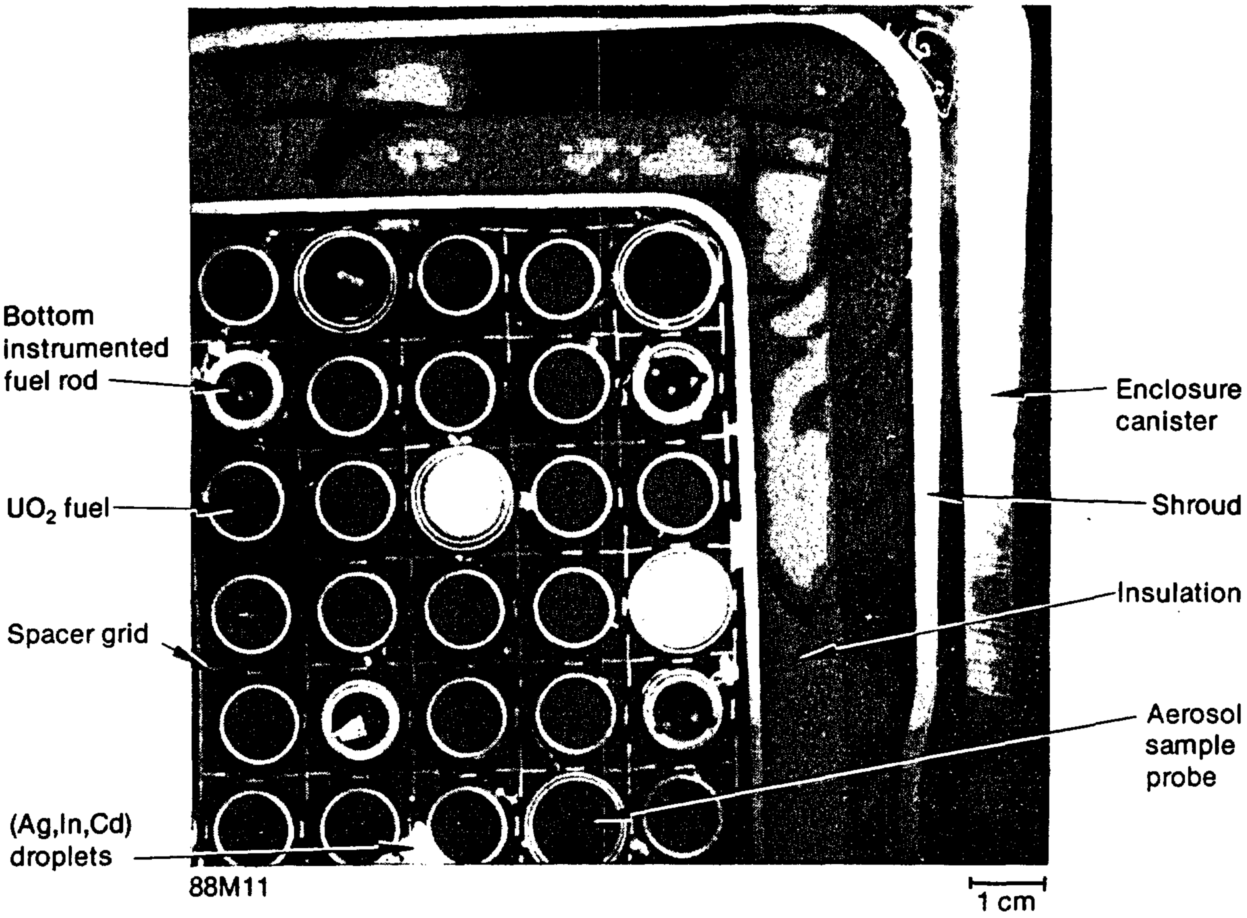

B2

Figure 15. Metallographic cross section B2 at 0.03 m above the bottom of the instrumented fuel rods.

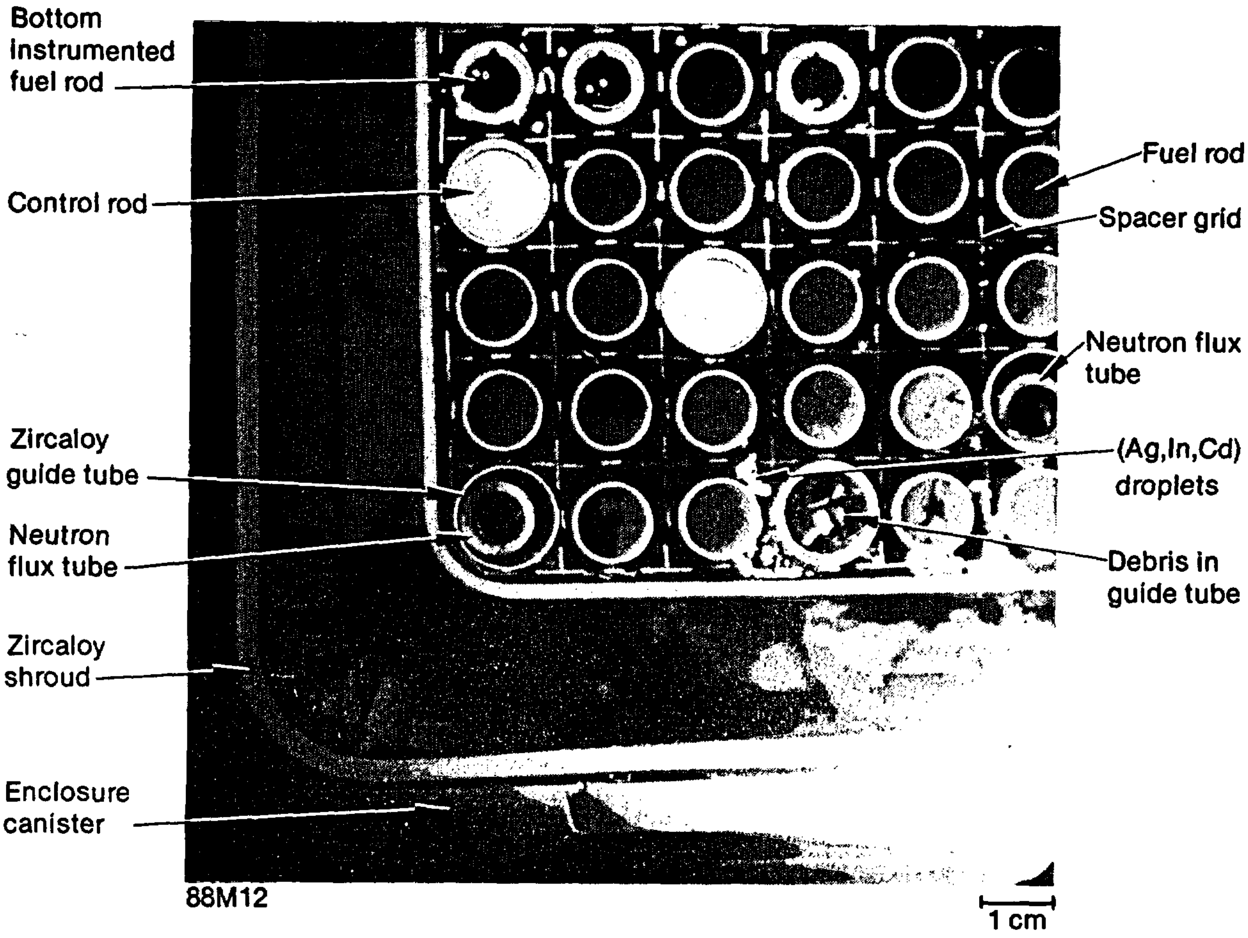

B3

Figure 16. Metallographic cross section B3 at 0.03 m above the bottom of the instrumented fuel rods.

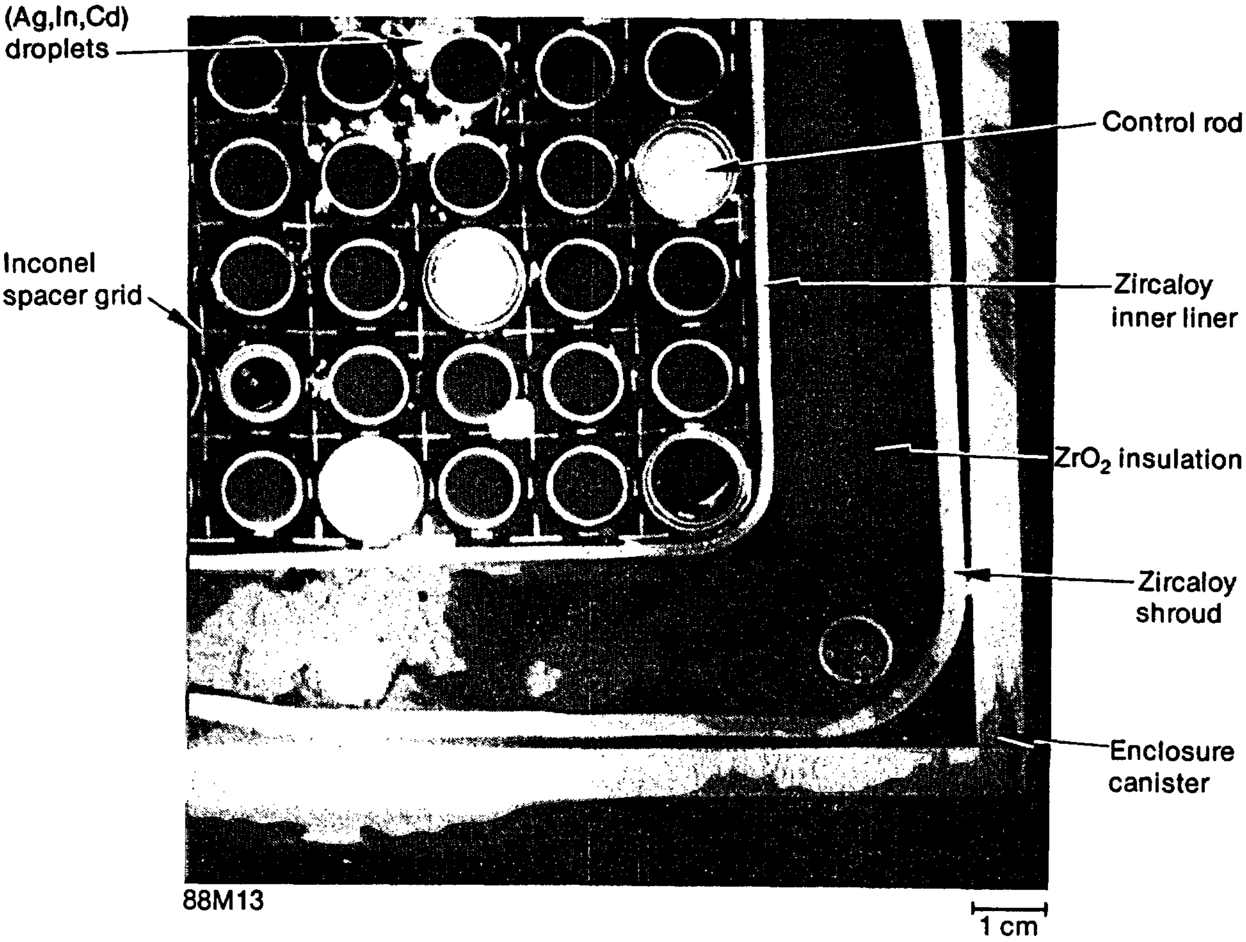

B4

Figure 17. Metallographic cross section B4 at 0.03 m above the bottom of the instrumented fuel rods.

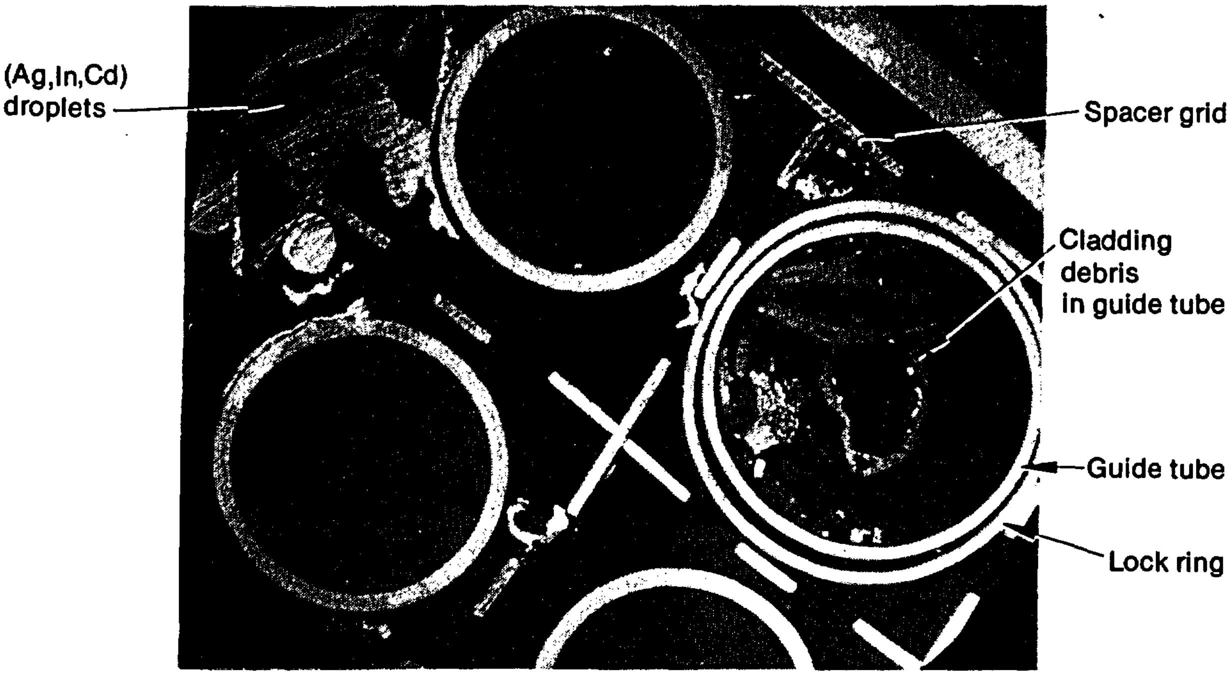

88M14

B1 Area 1

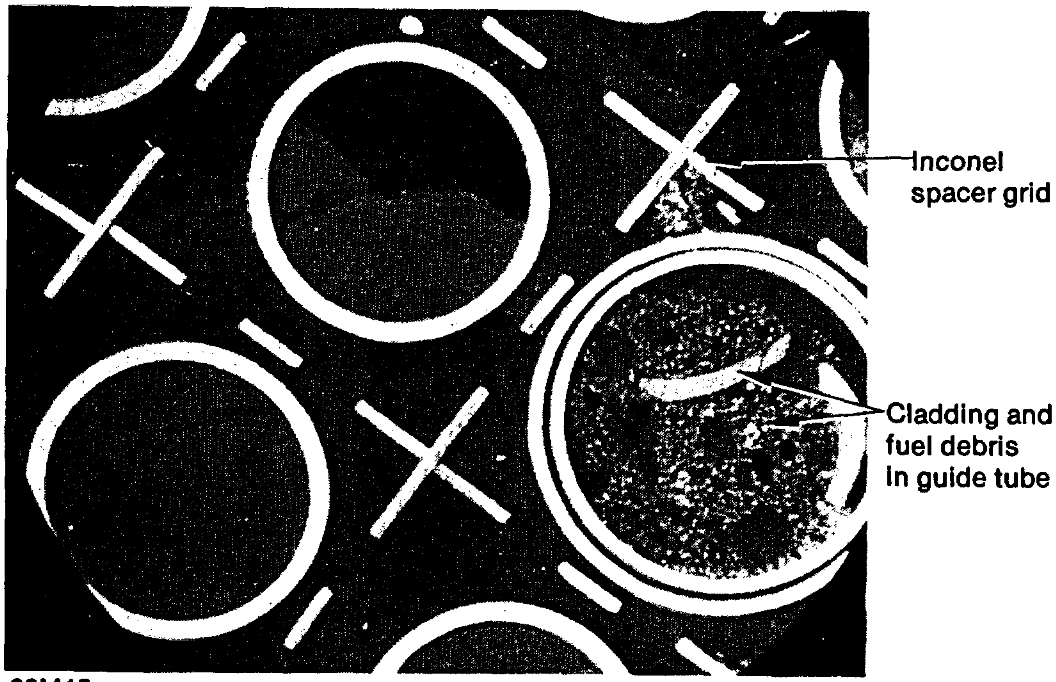

88M15

B1 Area 2

Figure 18. Details of the B1 metallographic cross section at 0.03 m.

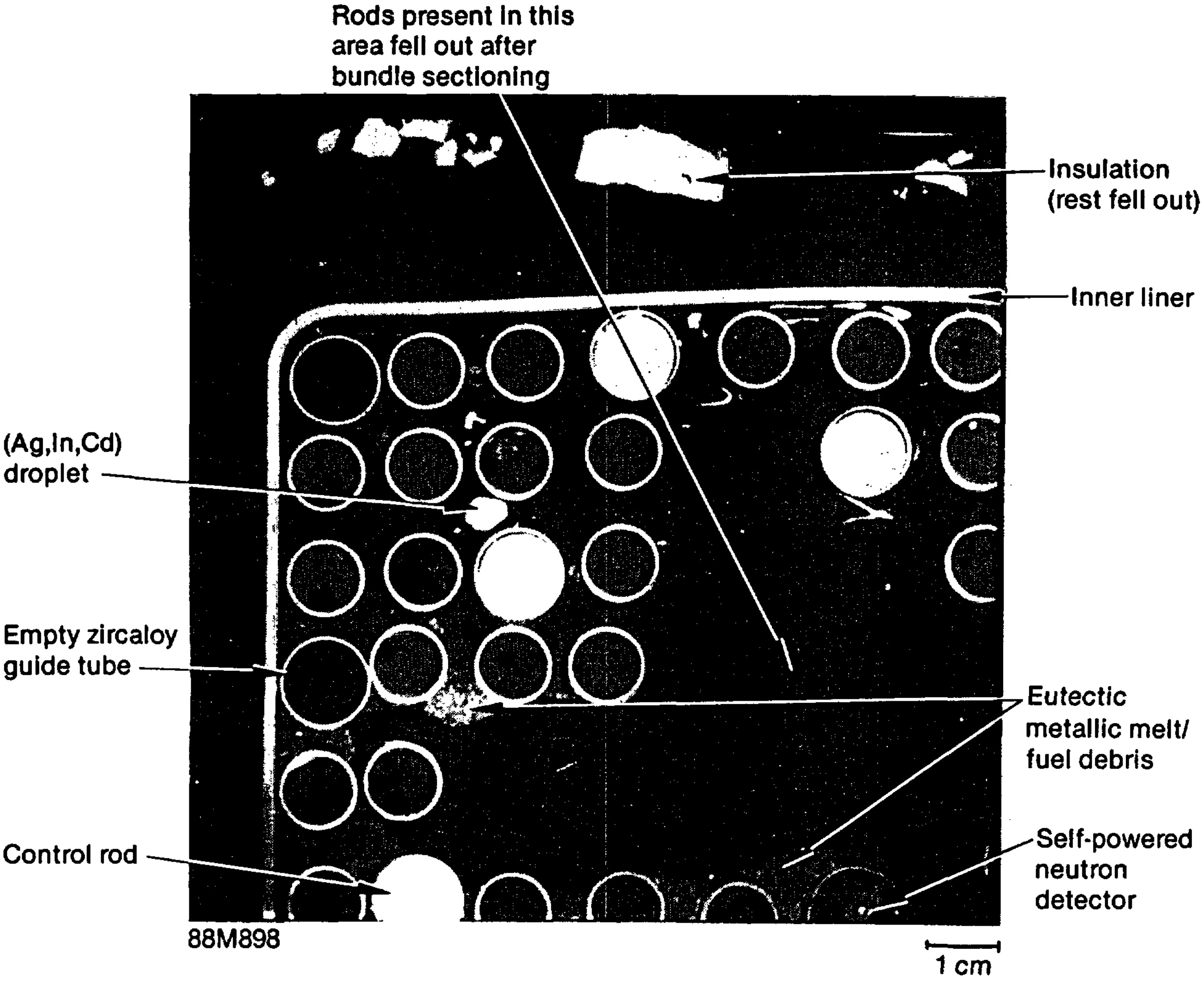

C1

Figure 19. Metallographic cross section C1 at 0.12m above the bottom of the instrumented fuel rods.

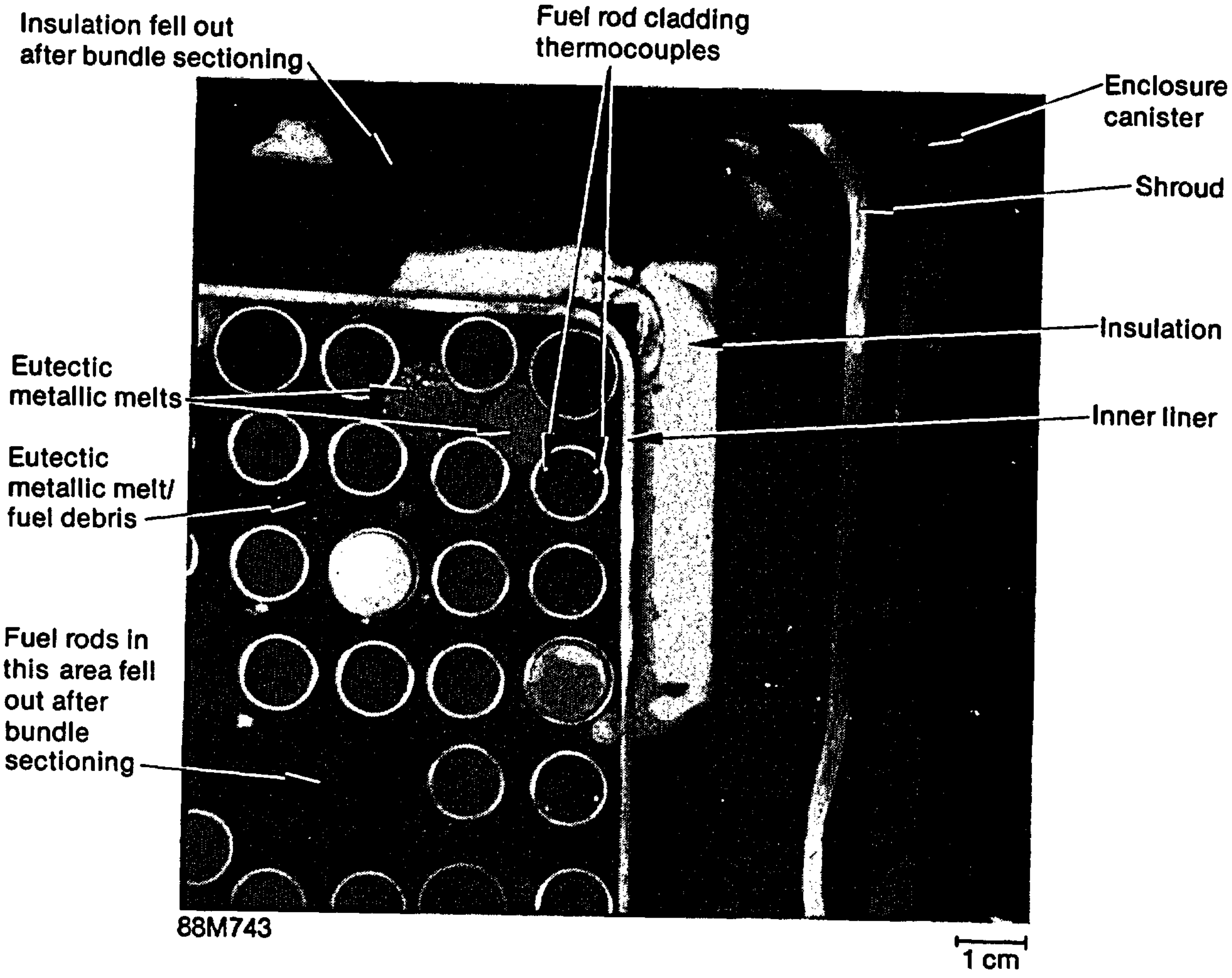

C2

Figure 20. Metallographic cross section C2 at 0.12m above the bottom of the instrumented fuel rods.

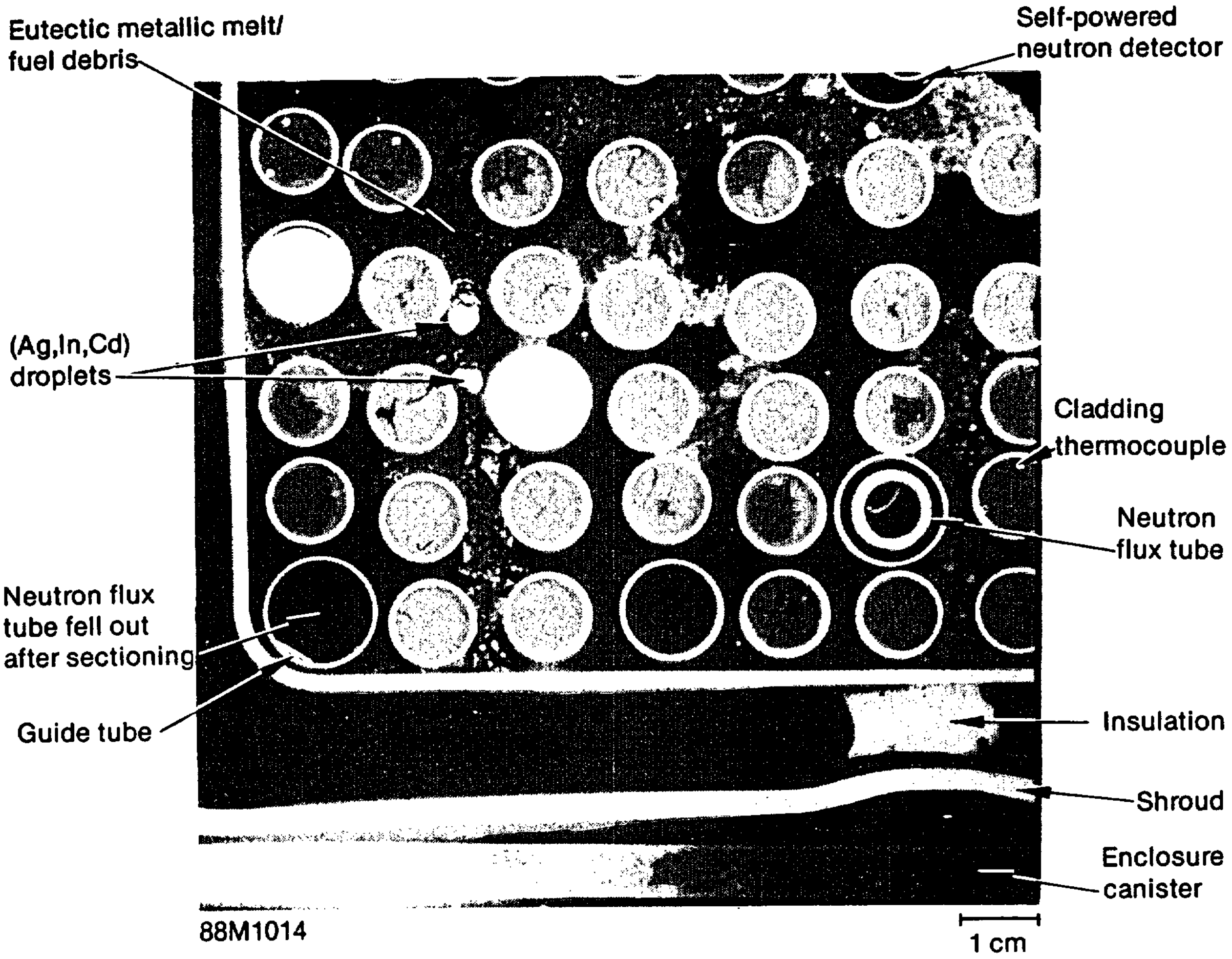

C3

Figure 21. Metallographic cross section C3 at 0.12m above the bottom of the instrumented fuel rods.

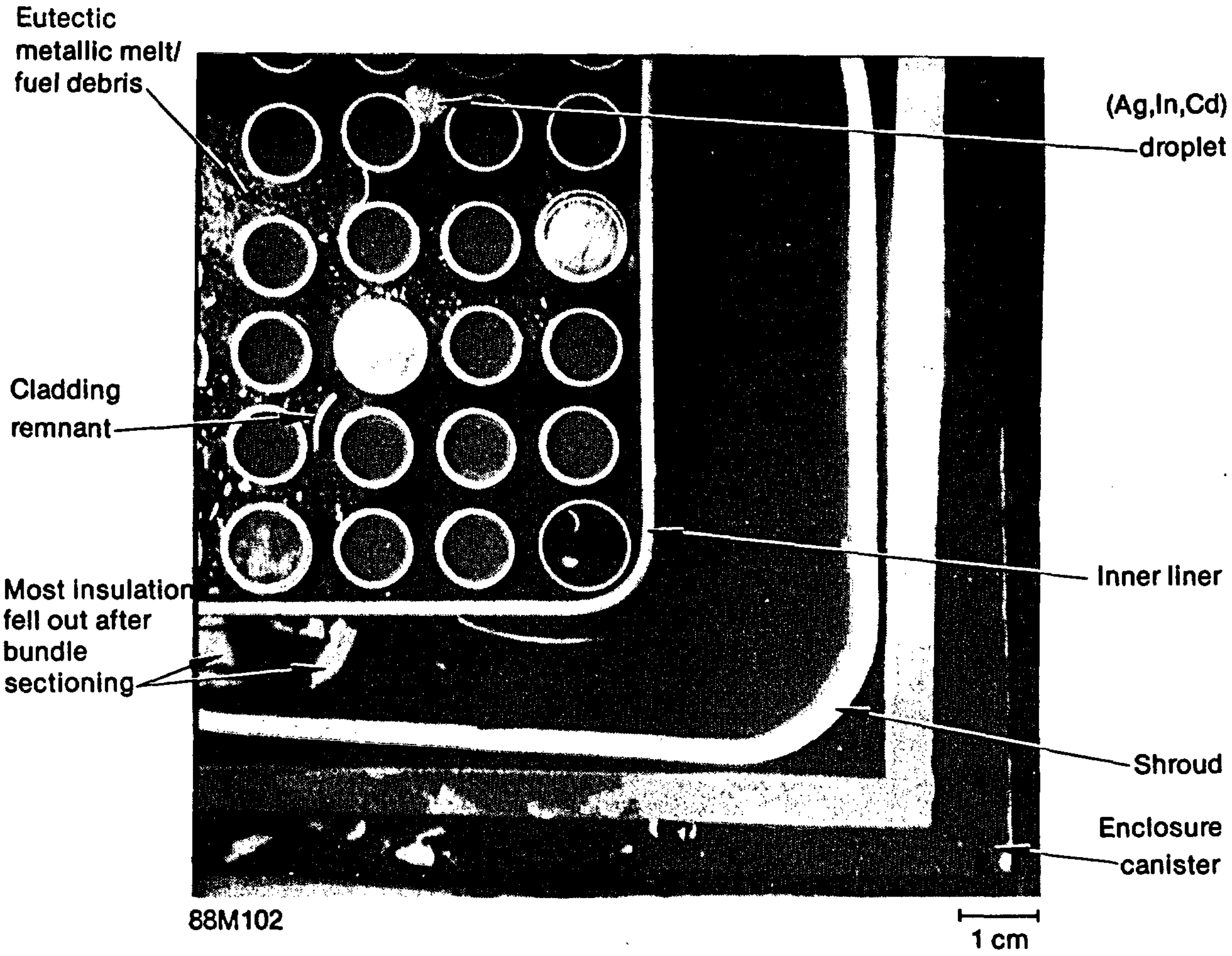

Figure 22. Metallographic cross section C4 at 0.012m above the bottom of the instrumented fuel rods.

bundle. This relocated material sealed off the central rods from the rest of the fuel module and prevented epoxy from entering this region. Consequently, the rods in this central region were not held in place and were able to fall out after this cross section was cut. This accounts for the missing rods in Figures 19 and 20. The neutron flux tube contained within the guide tube in the corner position of Figure 21 was also unsupported and lost during sample handling. The relocated material that formed this lower blockage region was primarily composed of (Ag,Zr) eutectic metallic melts and fuel debris, which were the first materials to relocate during the experiment. There were also some droplets of (Ag,In,Cd) and pieces of oxidized cladding debris scattered throughout these samples.

As described in more detail in Section 4.1, assuming that steam flow was excluded from the egg-shaped cavity region in this lower blockage, the flow blockage measurements indicate that this cross section had the greatest flow impedance in the test, corresponding to 86% of the area within the inner liner. However, before this cavity was enclosed, steam flow resulted in small oxide layers on the zircaloy cladding near the center of the fuel assembly. This was the lowest axial extent that any oxidized zircaloy was observed, and its location within the cavity indicates the lower extent of oxidation prior to complete relocation of the material in the lower blockage.

3.1.4 Cross Section D (0.22 m; Figures 23-30)

This cross section was located near the 0.25-m (10-in.) thermocouple location, and its appearance is very similar to the C cross section. Some rods within the egg-shaped blockage were unsupported and fell out after bundle sectioning, as did much of the ZrO_2 insulation. The relocated blockage material was again primarily composed of eutectic metallic melt materials and fuel debris, but there were more large pieces of solidified metallic melts contained within the blockage at this elevation than at the C elevation. Metallic melts flowing down the outer surface of the inner liner in the corner of sample D2 resulted in localized melting of the inner liner. The circular void regions in some of the fuel pellets are the result

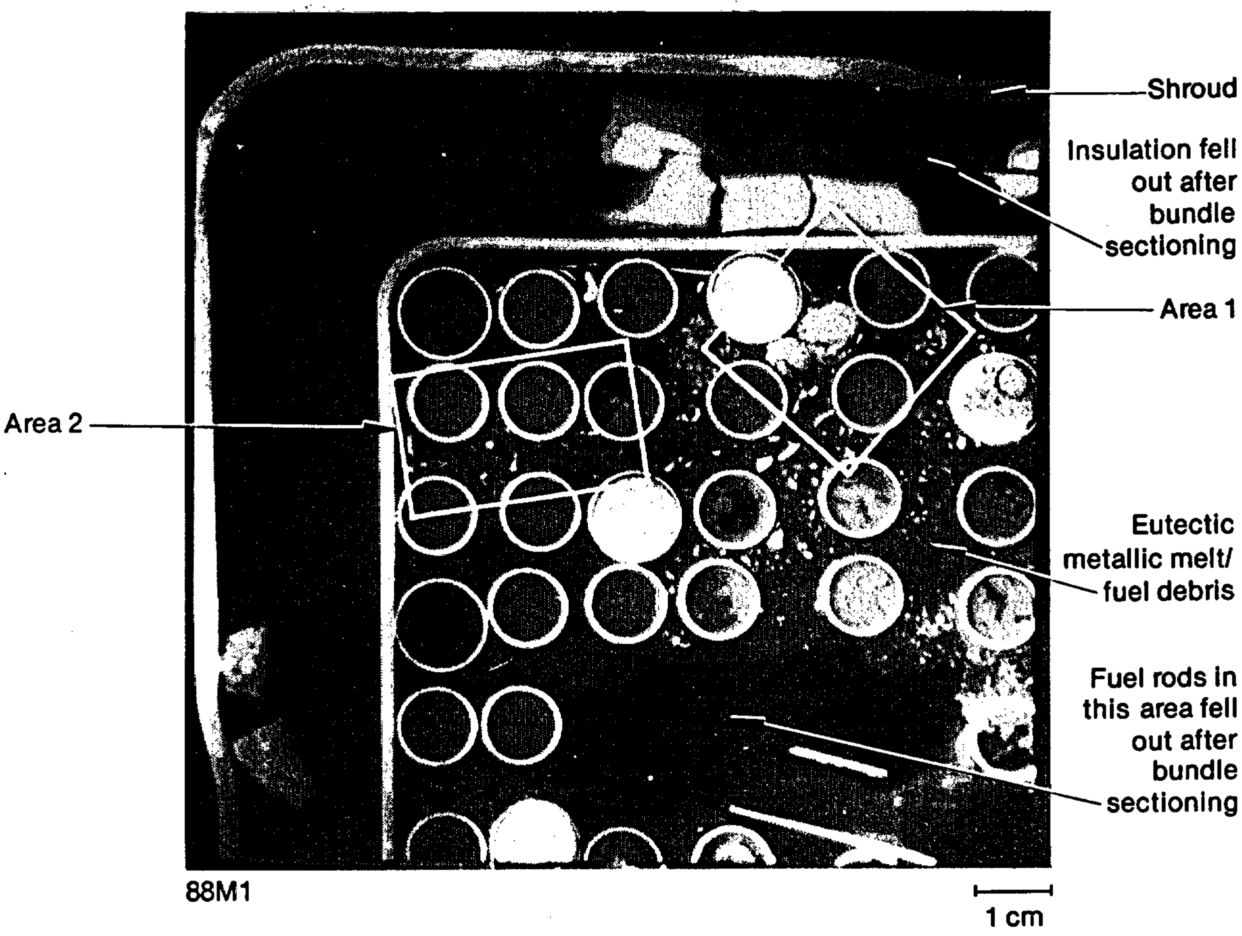

D1

Figure 23. Metallographic cross section D1 at 0.22m above the bottom of the instrumented fuel rods.

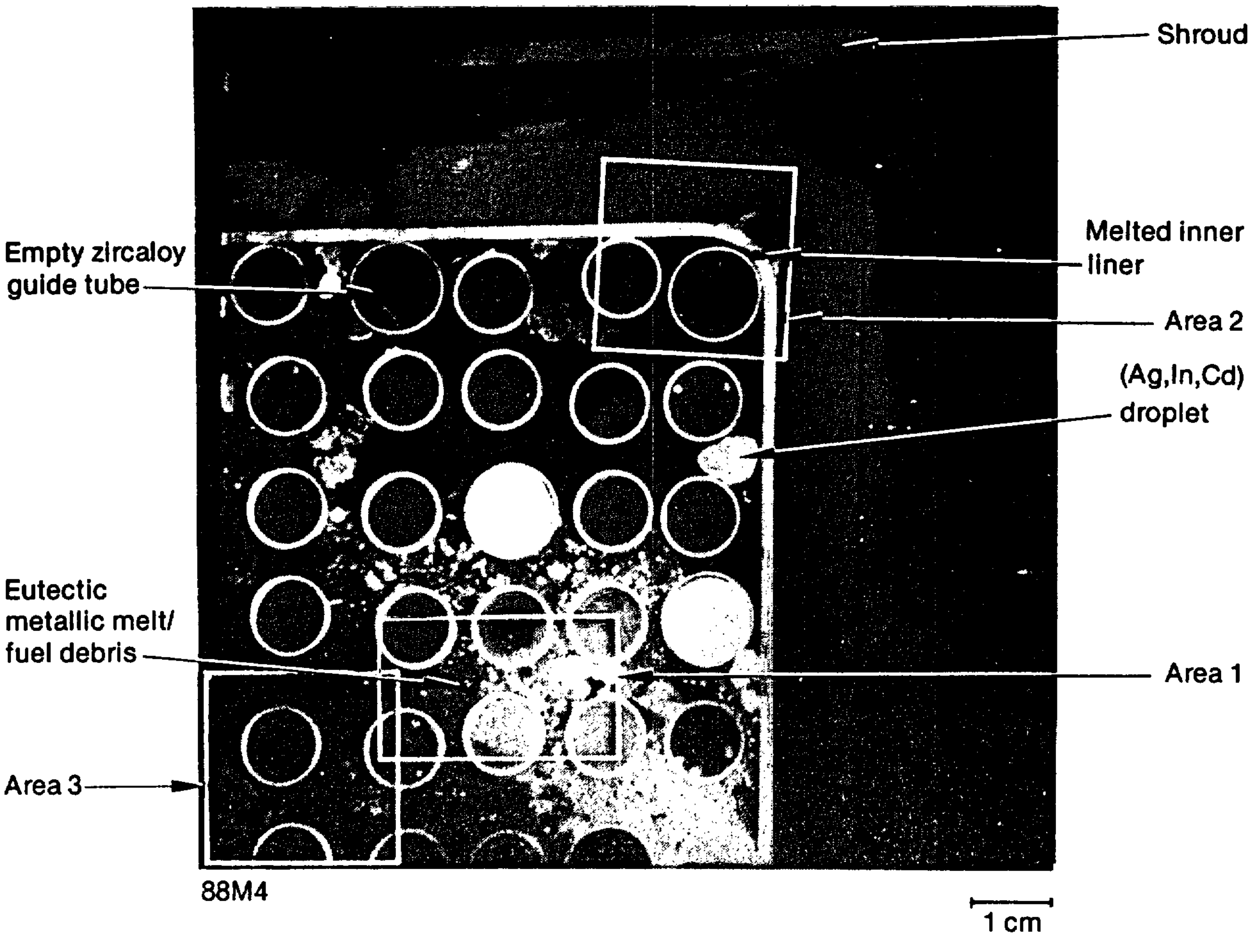

D2

Figure 24. Metallographic cross section D2 at 0.22m above the bottom of the instrumented fuel rods.

D3

Figure 25. Metallographic cross section D3 at 0.22m above the bottom of the instrumented fuel rods.

D4

Figure 26. Metallographic cross section D4 at 0.22m above the bottom of the instrumented fuel rods.

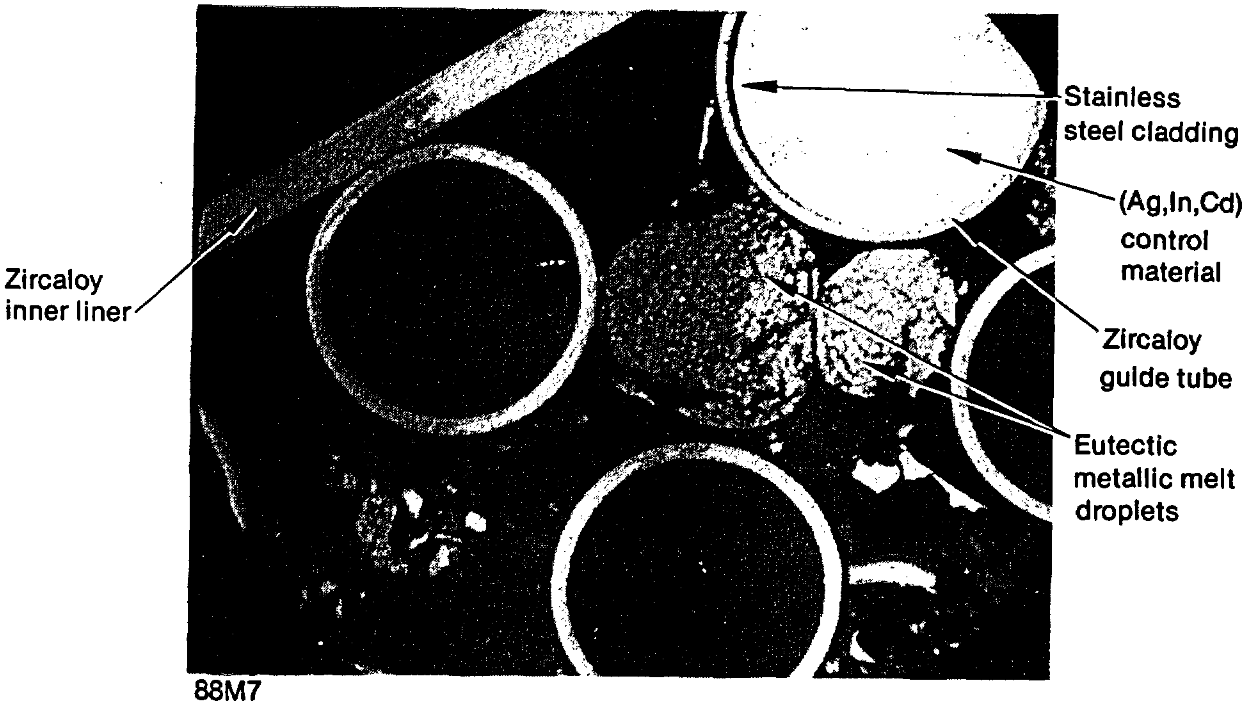

88M7

D1 Area 1

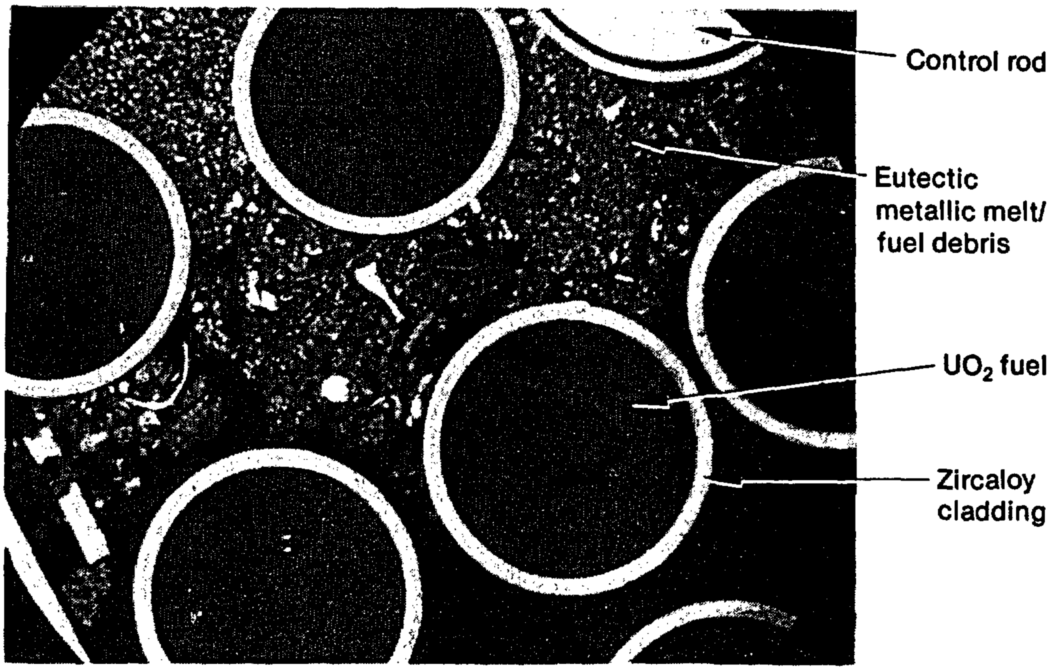

88M8

D1 Area 2

Figure 27. Details of metallographic cross section D1 at 0.22 m.

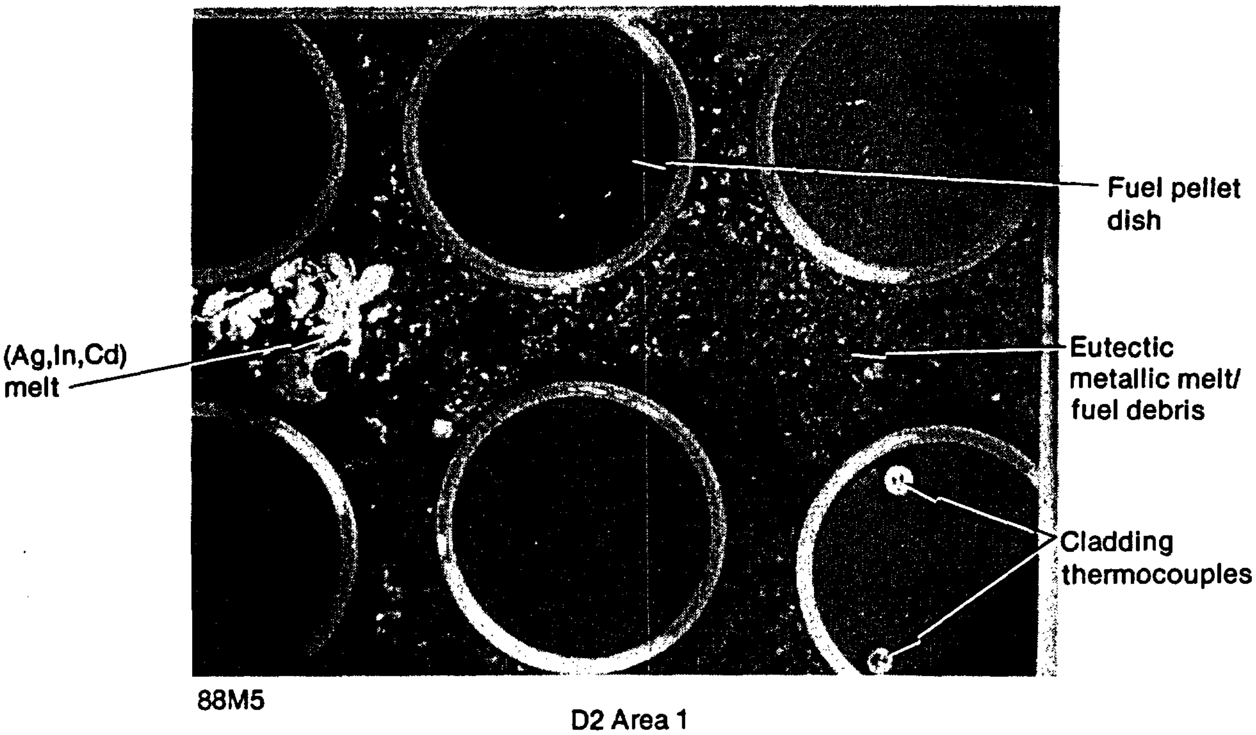

D2 Area 1

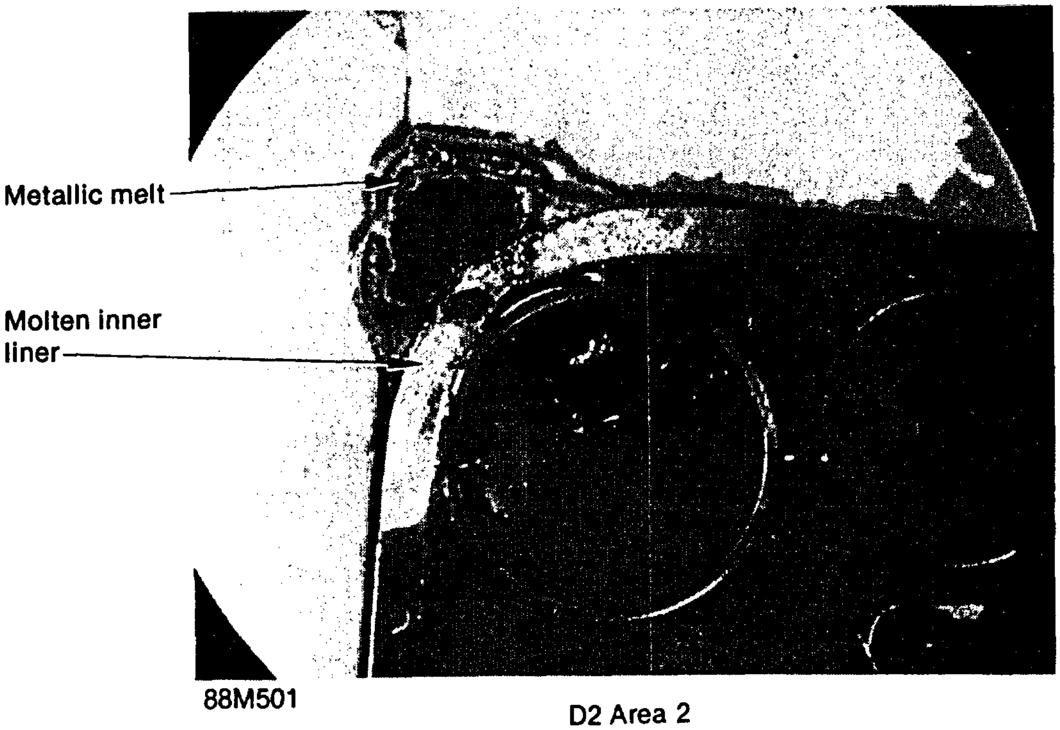

D2 Area 2

Figure 28. Details of metallographic cross section D2 at 0.22 m.

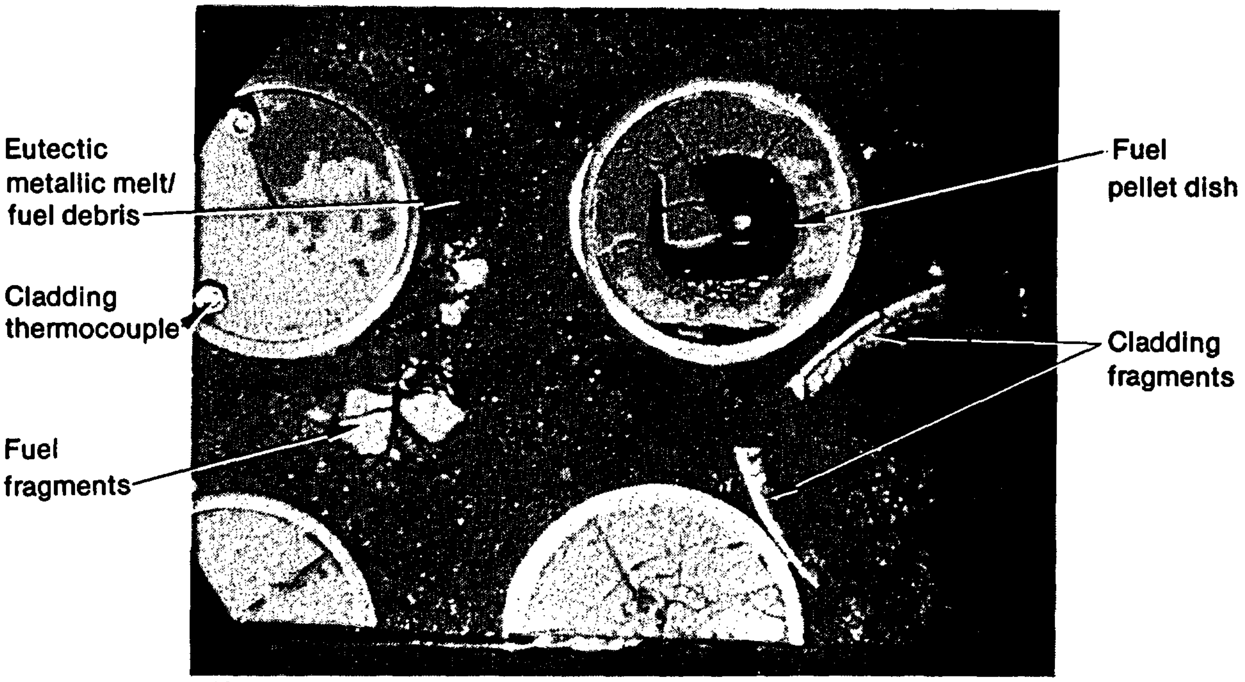

D2 Area 3

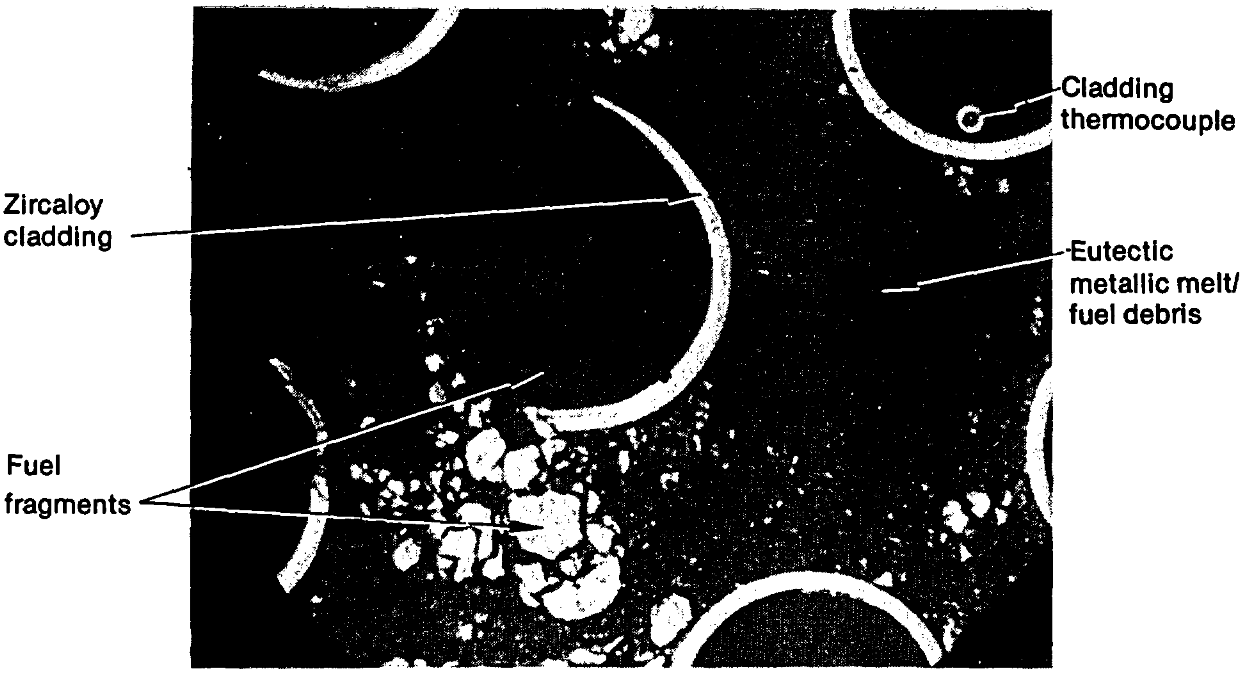

D3 Area 1

Figure 29. Details of metallographic cross sections D2 and D3 at 0.22 m.

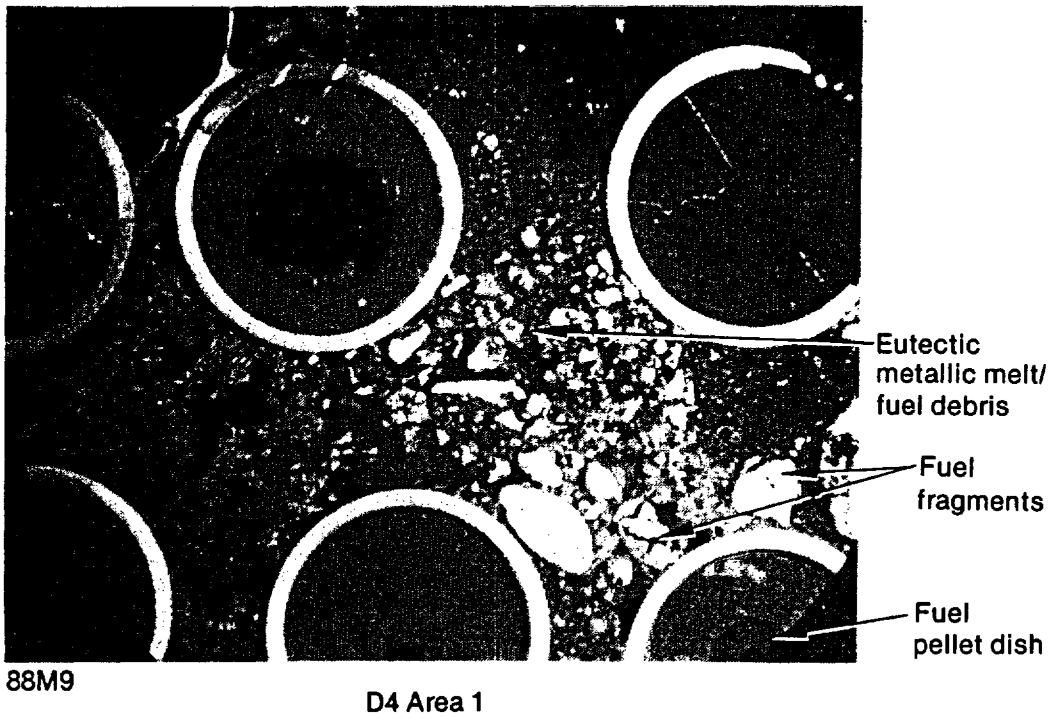

Figure 30. Details of metallographic cross sections D4 at 0.22 m.

of sectioning through the dished end of these pellets. As described in Appendices A and B, the asymmetries in some of the dished ends is probably due to warpage of the saw blade during this cut, which produced a slightly curved surface, in conjunction with material which fell out and wedged under the sample when it was laid in the sample tray prior to vacuum-impregnation with epoxy. Both of these factors would result in polishing a sample surface that was not exactly perpendicular to the bundle axis. This is also the reason that part of the insulation and shroud regions on sample D2 were not completely polished; those portions of the sample were lower than the rest of the sample.

3.1.5 Cross Section E (0.27 m; Figures 31-35)

This cross section was through the solid upper portion of the egg-shaped lower blockage region. The epoxy was able to completely penetrate everywhere at this elevation; and, as a result, there was no loss of material. The relocated blockage material was still primarily composed of eutectic metallic melt materials and fuel debris, but it also contained relatively large pieces of previously molten metallic materials and fuel fragments. The self-powered-neutron-detector (SPND) was no longer intact at this elevation or above. Localized melting of the inner liner in the corner of sample E2 was more severe than was observed lower down on sample D2. All the insulation and fuel were intact prior to sectioning.

3.1.6 Cross Section F (0.36 m; Figures 36-41)

The fuel bundle rod array was intact at this elevation, and there were only small amounts of relocated material compared to regions above and below this elevation. This relocated material is similar to the metallic melts and fuel debris observed in the lower blockage region. The inner liner was intact except for localized melting in the corner of sample F2, and all the insulation was present prior to sectioning. All the fuel rods were intact except for two near the center of the assembly. As described in Section 3.2.2, all the control rods were also intact at this elevation; however the (Ag,In,Cd) alloy in the interior control rods was molten, indicating temperatures in excess of 1073 K.

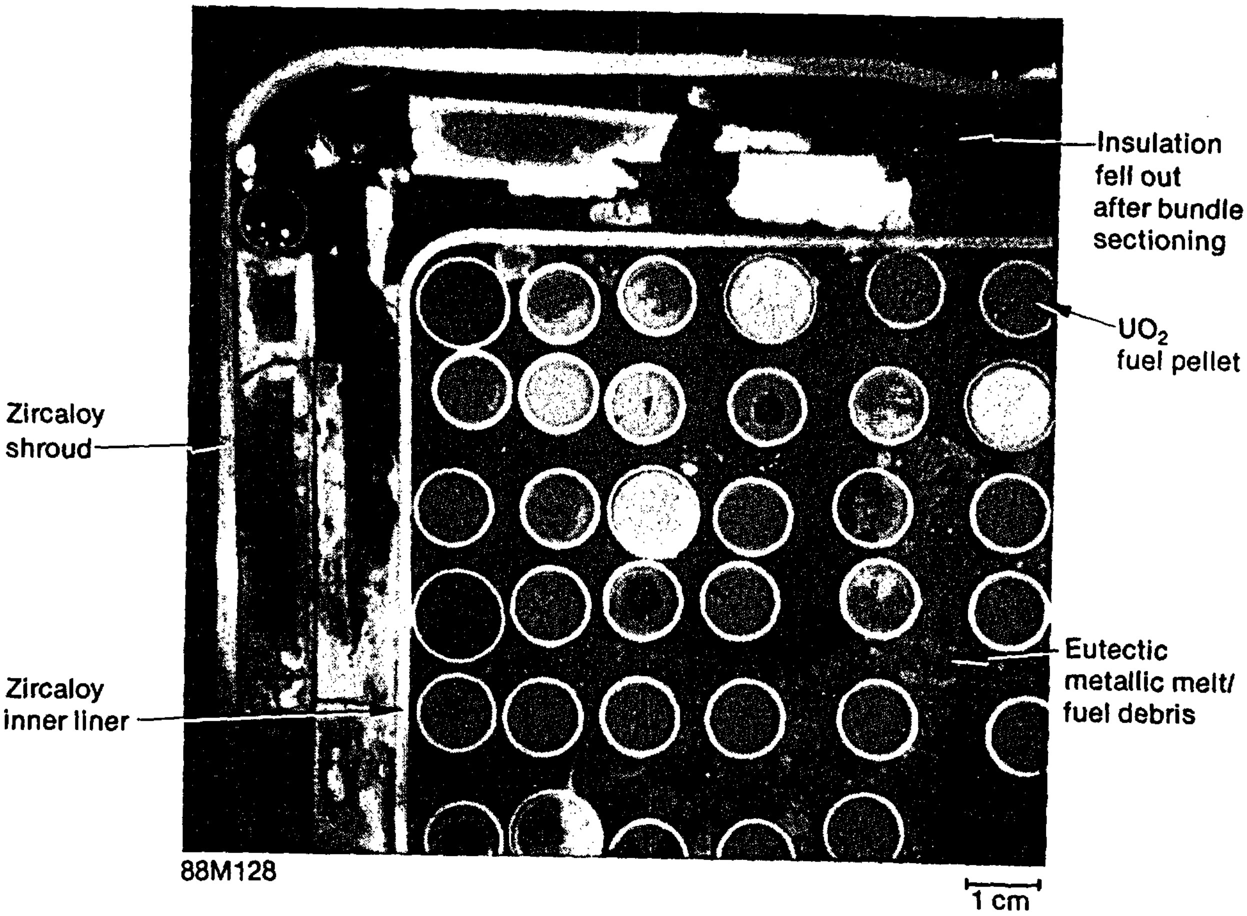

E1

Figure 31. Metallographic cross section E1 at 0.27 m above the bottom of the instrumented fuel rods.

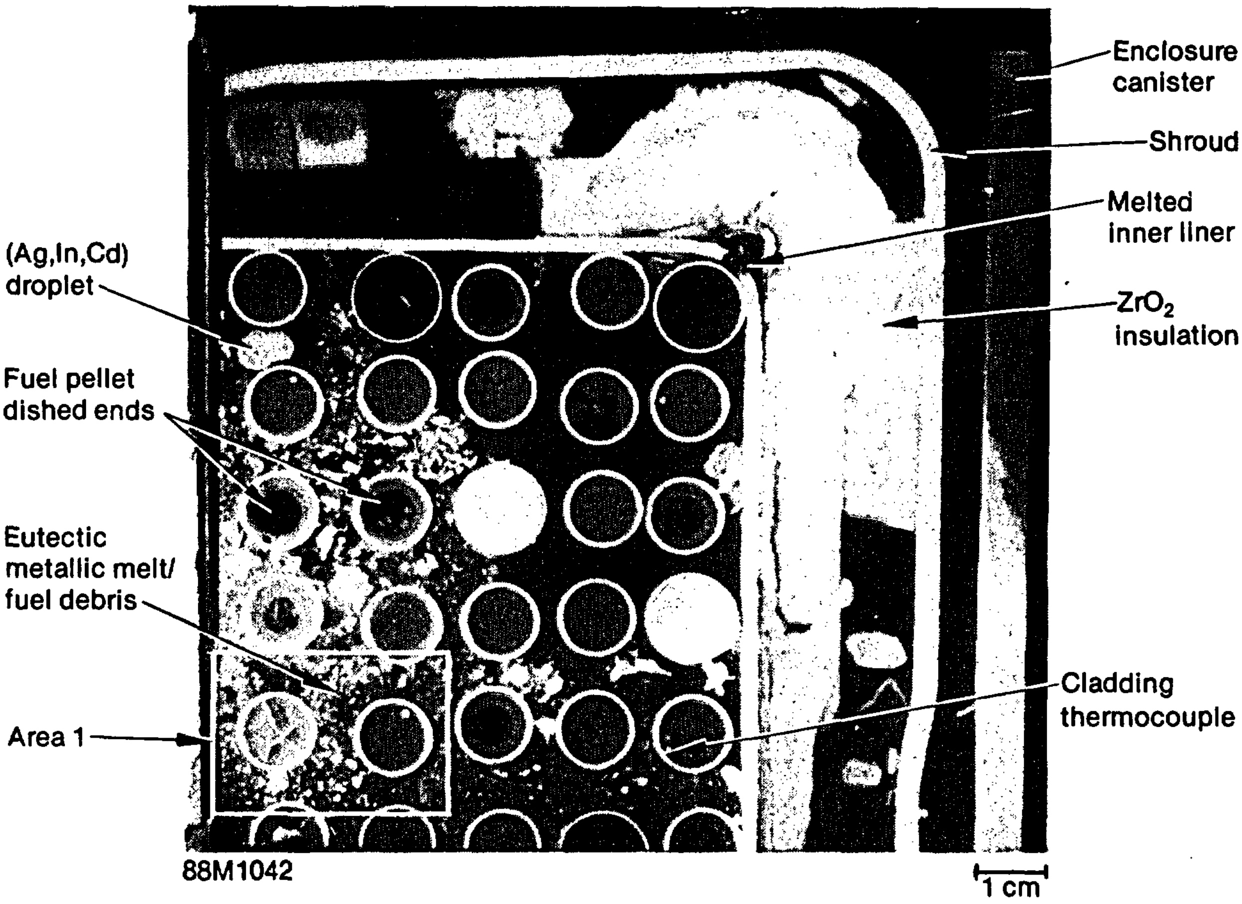

E2

Figure 32. Metallographic cross section E2 at 0.27 m above the bottom of the instrumented fuel rods.

E3

Figure 33. Metallographic cross section E3 at 0.27 m above the bottom of the instrumented fuel rods.

E4

Figure 34. Metallographic cross section E4 at 0.27 m above the bottom of the instrumented fuel rods.

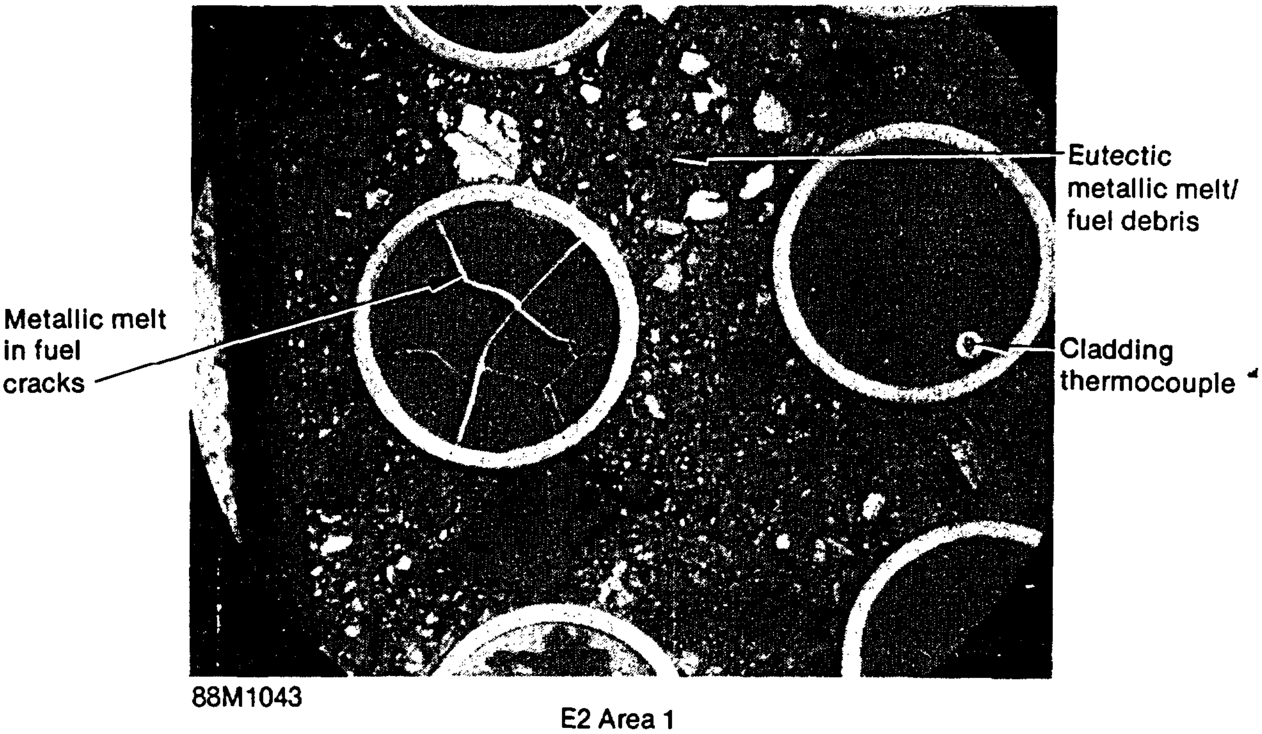

E2 Area 1

Figure 35. Details of metallographic cross section E2 at 0.27 m.

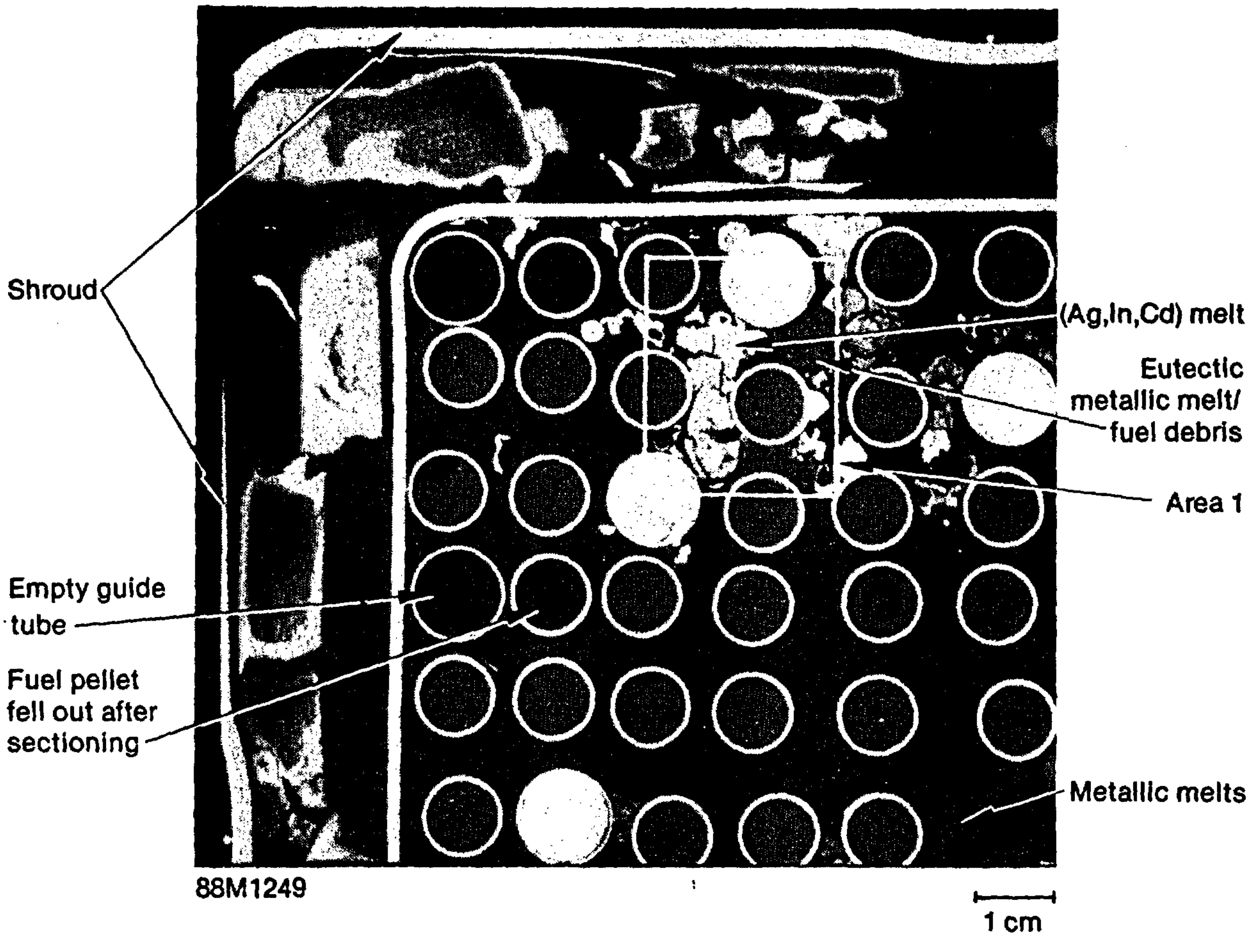

F1

Figure 36. Metallographic cross section F1 at 0.36 m above the bottom of the instrumented fuel rods.

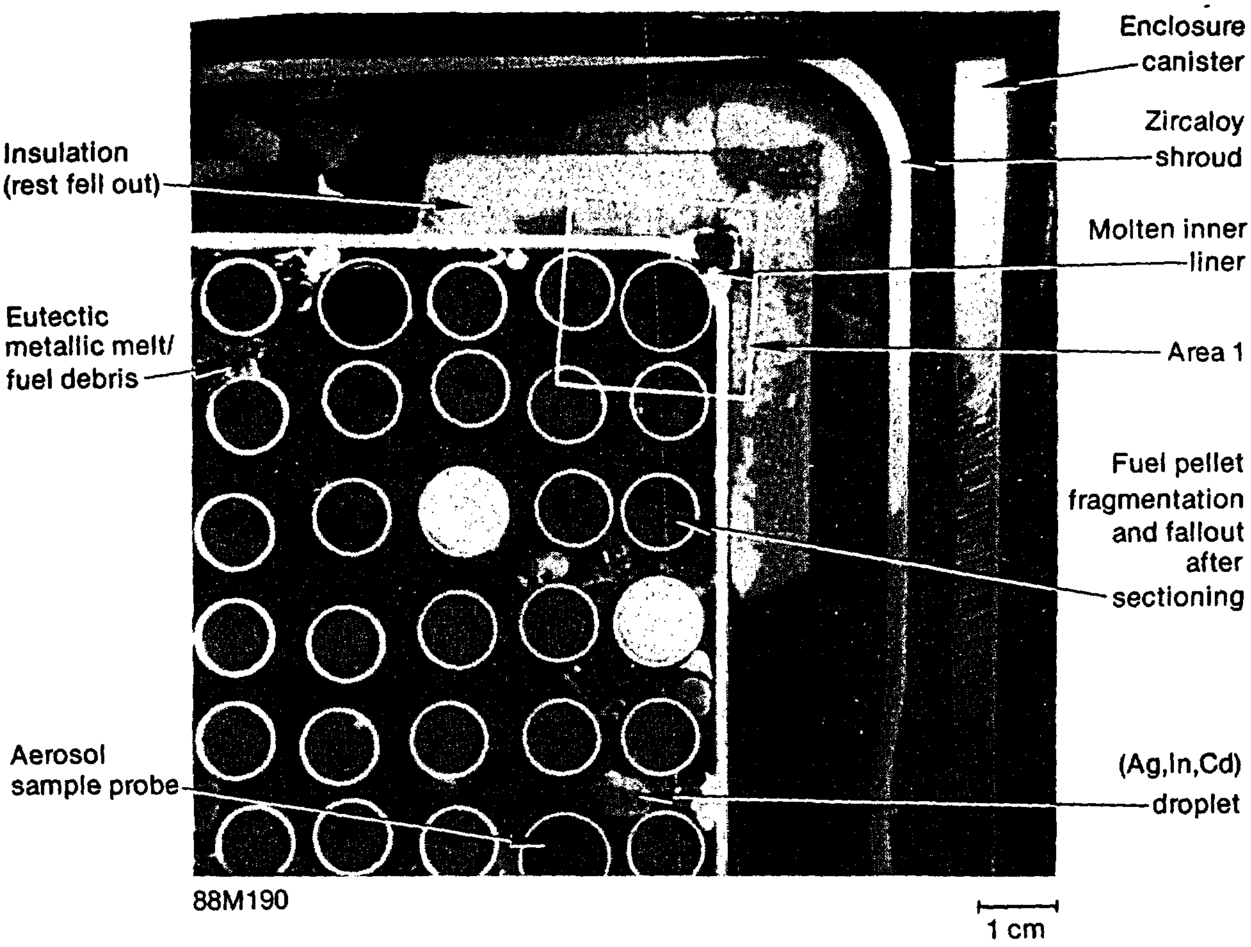

F2

Figure 37. Metallographic cross section F2 at 0.36 m above the bottom of the instrumented fuel rods.

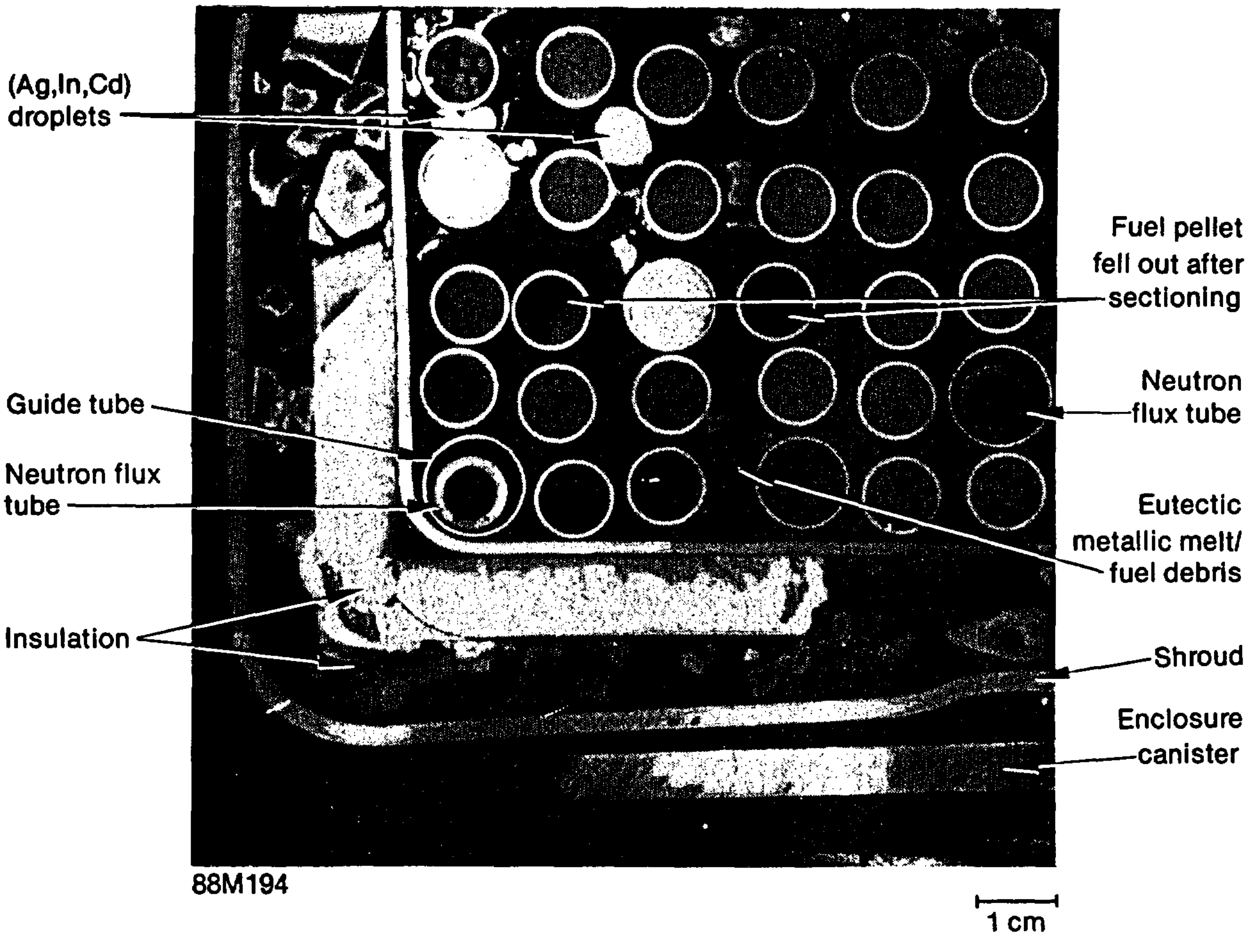

F3

Figure 38. Metallographic cross section F3 at 0.36 m above the bottom of the instrumented fuel rods.

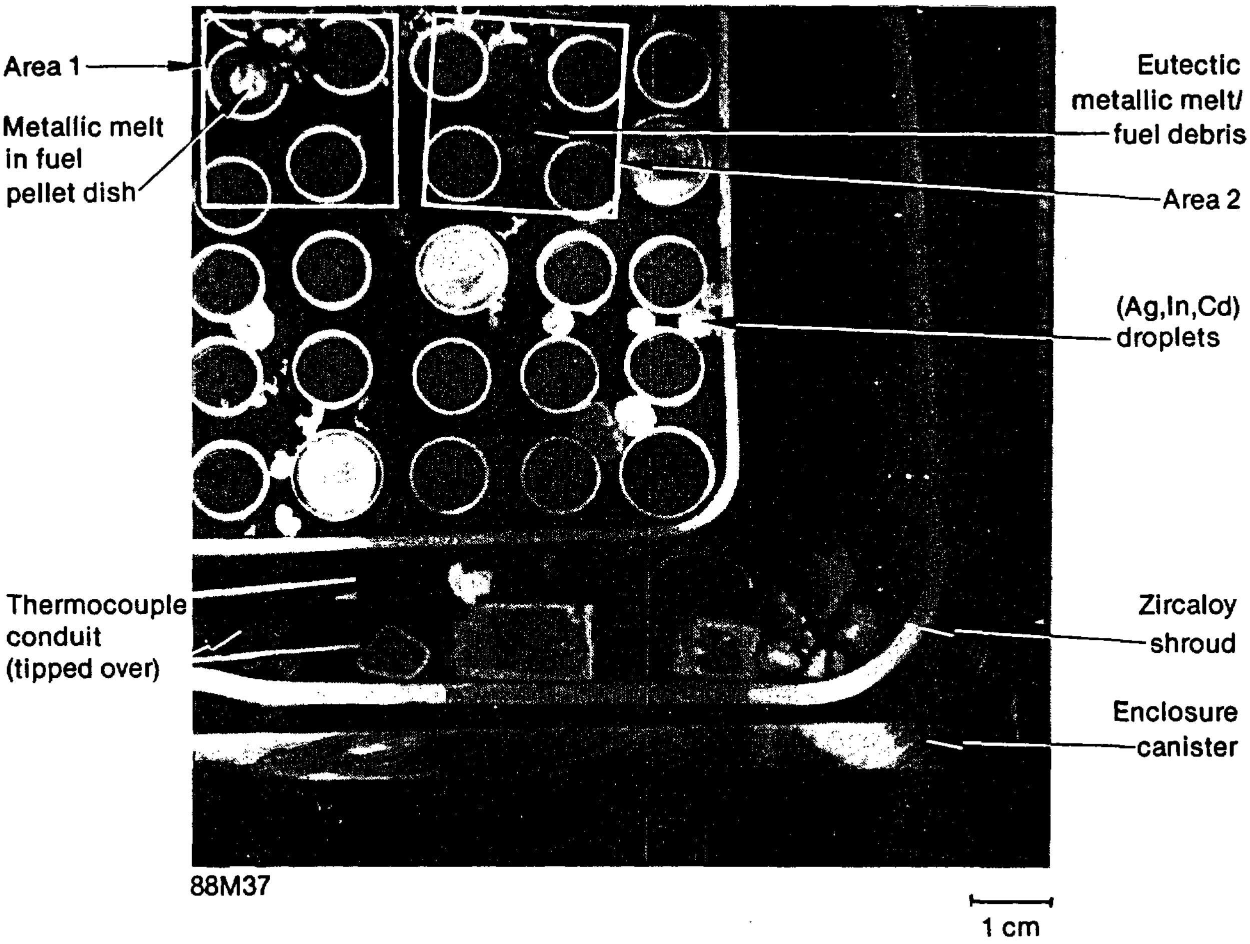

F4

Figure 39. Metallographic cross section F4 at 0.36 m above the bottom of the instrumented fuel rods.

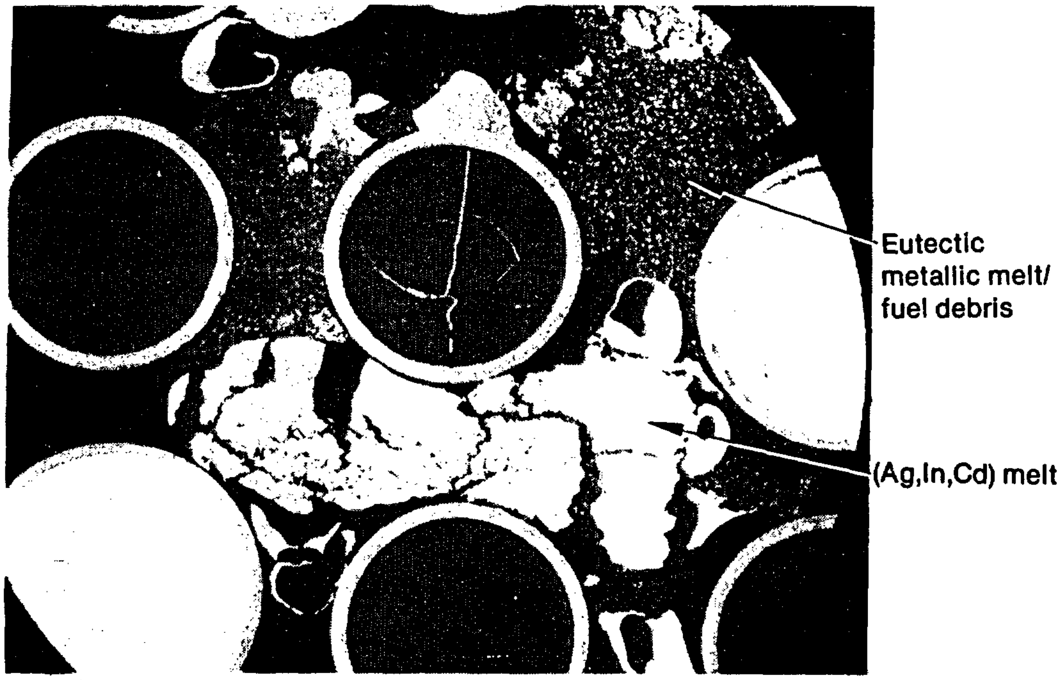

F1 Area 1

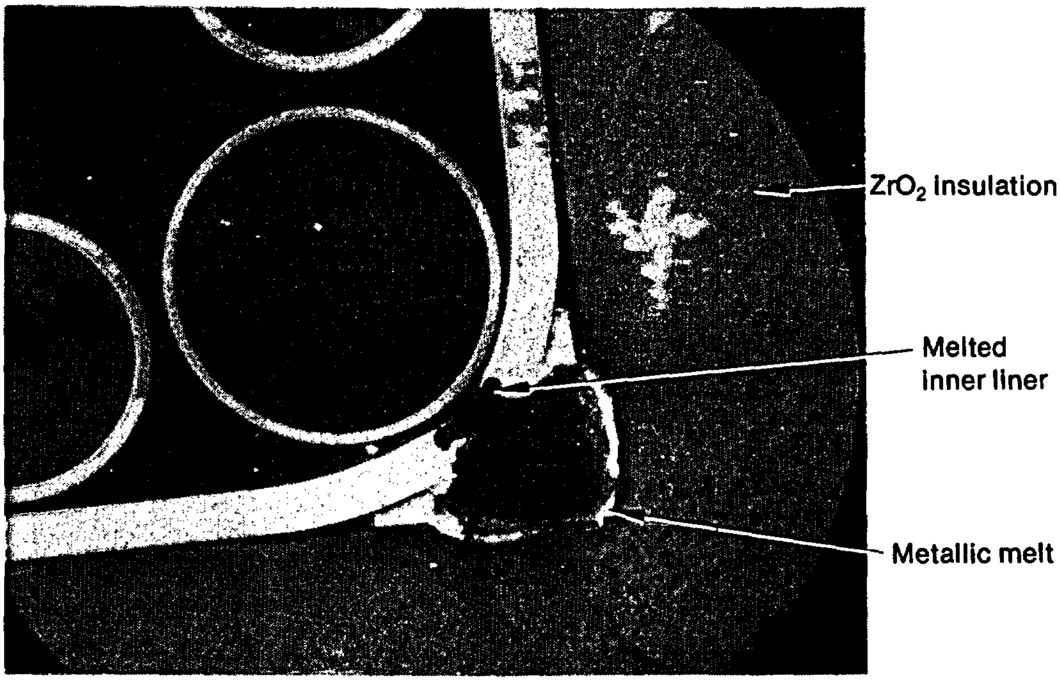

F2 Area 1

Figure 40. Details of metallographic cross sections F1 and F2 at 0.36 m.

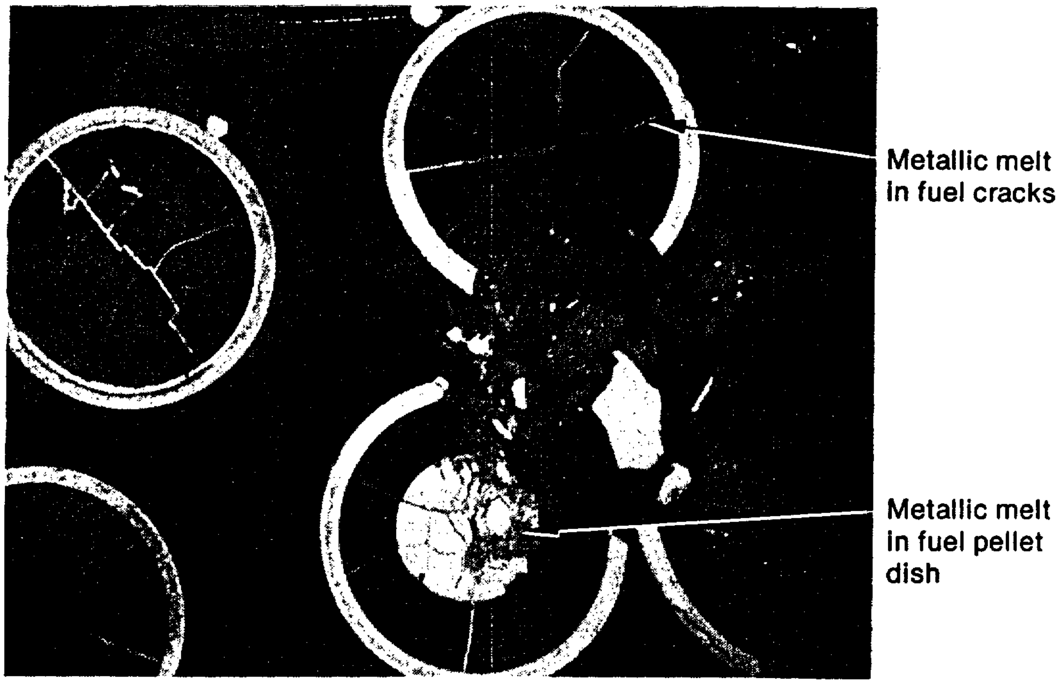

88M26

F4 Area 1

88M27

F4 Area 2

Figure 41. Details of metallographic cross section F4 at 0.36 m.

3.1.7 Cross Section G(bottom) (0.43 m; Figures 42-49)

This cross section was obtained just below the second spacer grid and was the bottom surface of sample G. All the other sample surfaces (except S bottom) were of the top side of their respective samples. Consequently, the orientation of the rods in sample G(bottom) is a mirror image of the other samples. This is most easily seen by comparing the locations of the control rods with those in Figure 1.

More relocated material accumulated at this elevation than at the F elevation. This relocated material is similar to that observed in the lower blockage region. Only very small amounts of the ceramic melt material observed higher in the bundle were present at this elevation. Several fuel rods near the central portion of the assembly had disintegrated. The zircaloy lock rings surrounding the guide tubes were generally intact, but the guide tubes surrounding the control rods had liquefied in some instances. As described in Section 3.2.2, attack of the stainless steel control rod cladding by zirconium-bearing melts also occurred at this elevation. Droplets of metallic melts were present, and the inner liner was still intact except for a localized region in the corner of sample G2 (bottom). All the insulation was present prior to sectioning.

3.1.8 Cross Section G(top) (0.46 m; Figures 50-58)

This cross section was through the second spacer grid; and, as described in Section 4.1, this cross section had the greatest mass accumulation in the bundle, corresponding to 78% of the area within the inner liner. A lot of relocated previously molten material solidified at this spacer grid location. Most of this material is similar to the eutectic metallic melt and fuel debris observed in the lower blockage region; however, there was some ceramic melt near the central portion of the assembly on sample G2. These relocated materials caused liquefaction of the cladding and spacer grid materials in some places (particularly in the northeast quadrant) and fuel fragmentation and powdering. The zircaloy lock rings and guide tubes surrounding the control rods were either completely

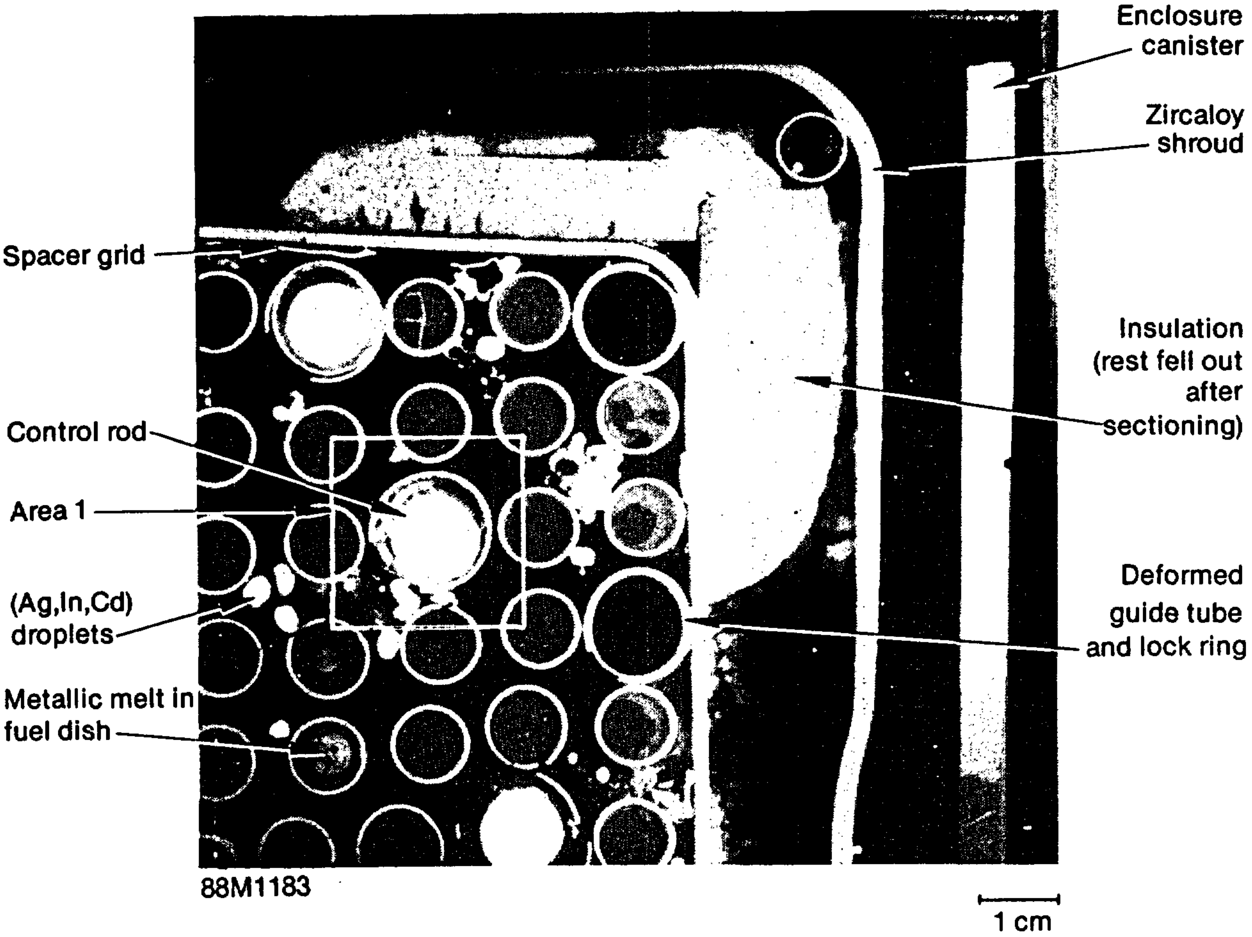

G1 bottom

Figure 42. Metallographic cross section G1 (bottom) at 0.43 m above the bottom of the instrumented fuel rods.

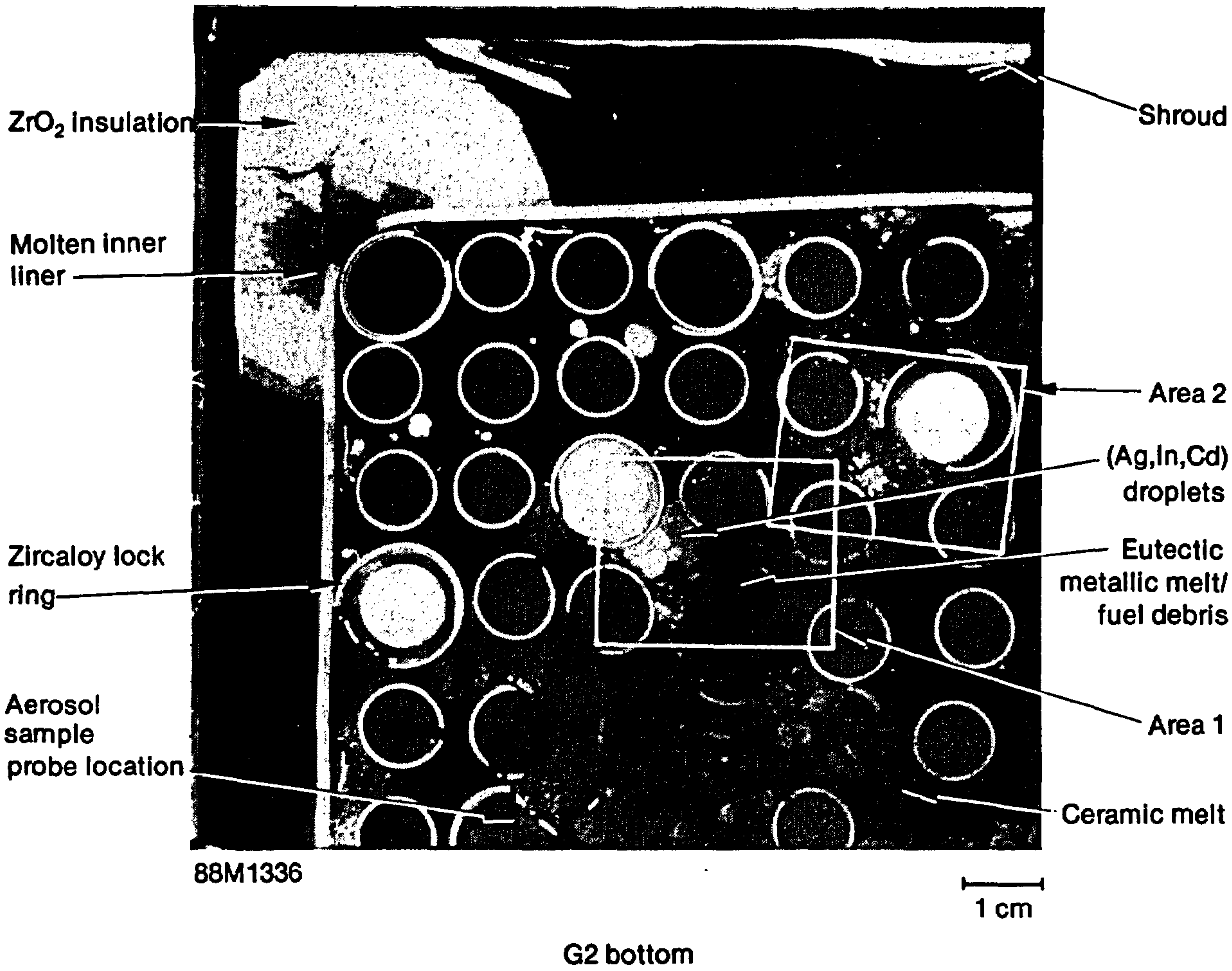

Figure 43. Metallographic cross section G2 (bottom) at 0.43 m above the bottom of the instrumented fuel rods.

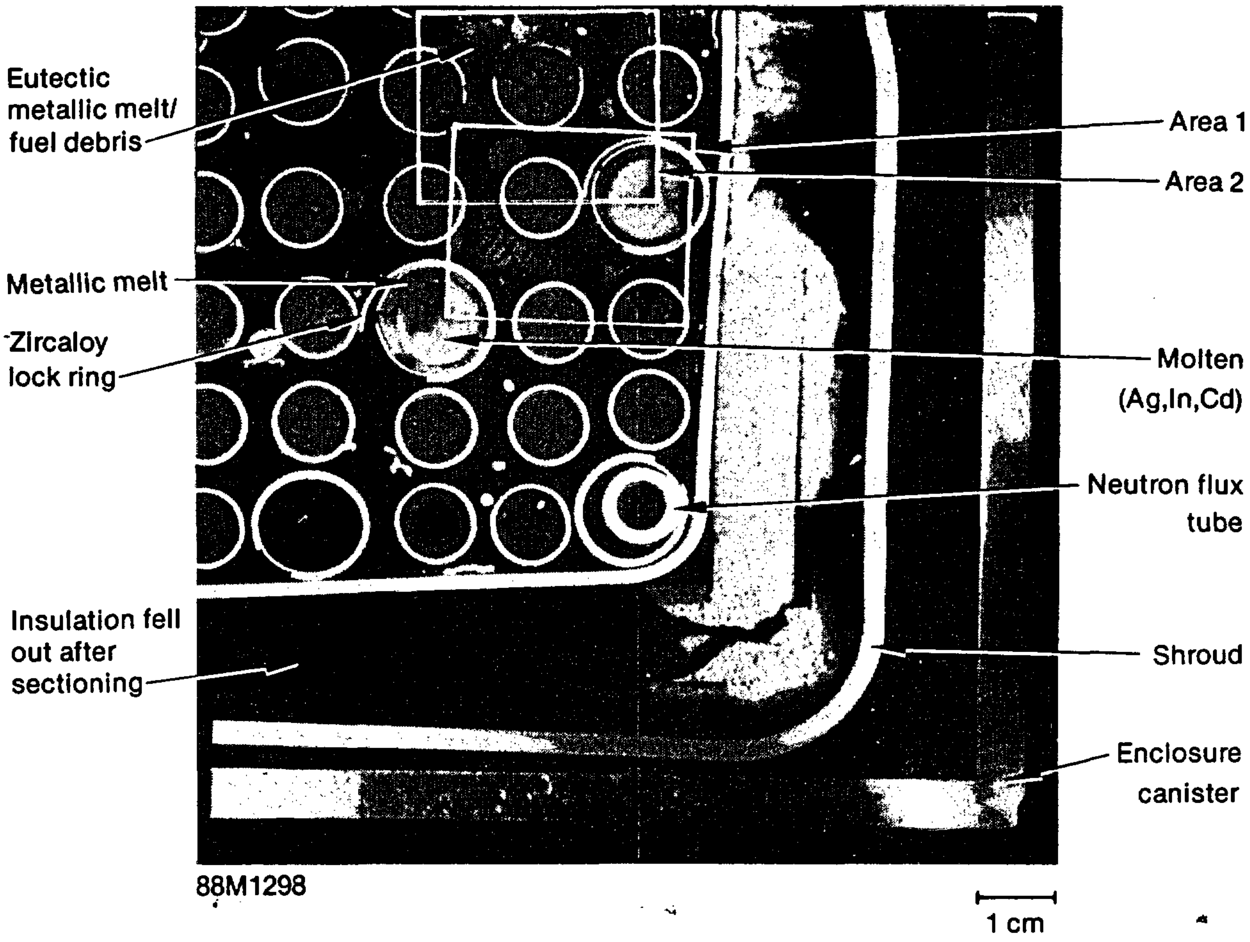

G3 bottom

Figure 44. Metallographic cross section G3 (bottom) at 0.43 m above the bottom of the instrumented fuel rods.

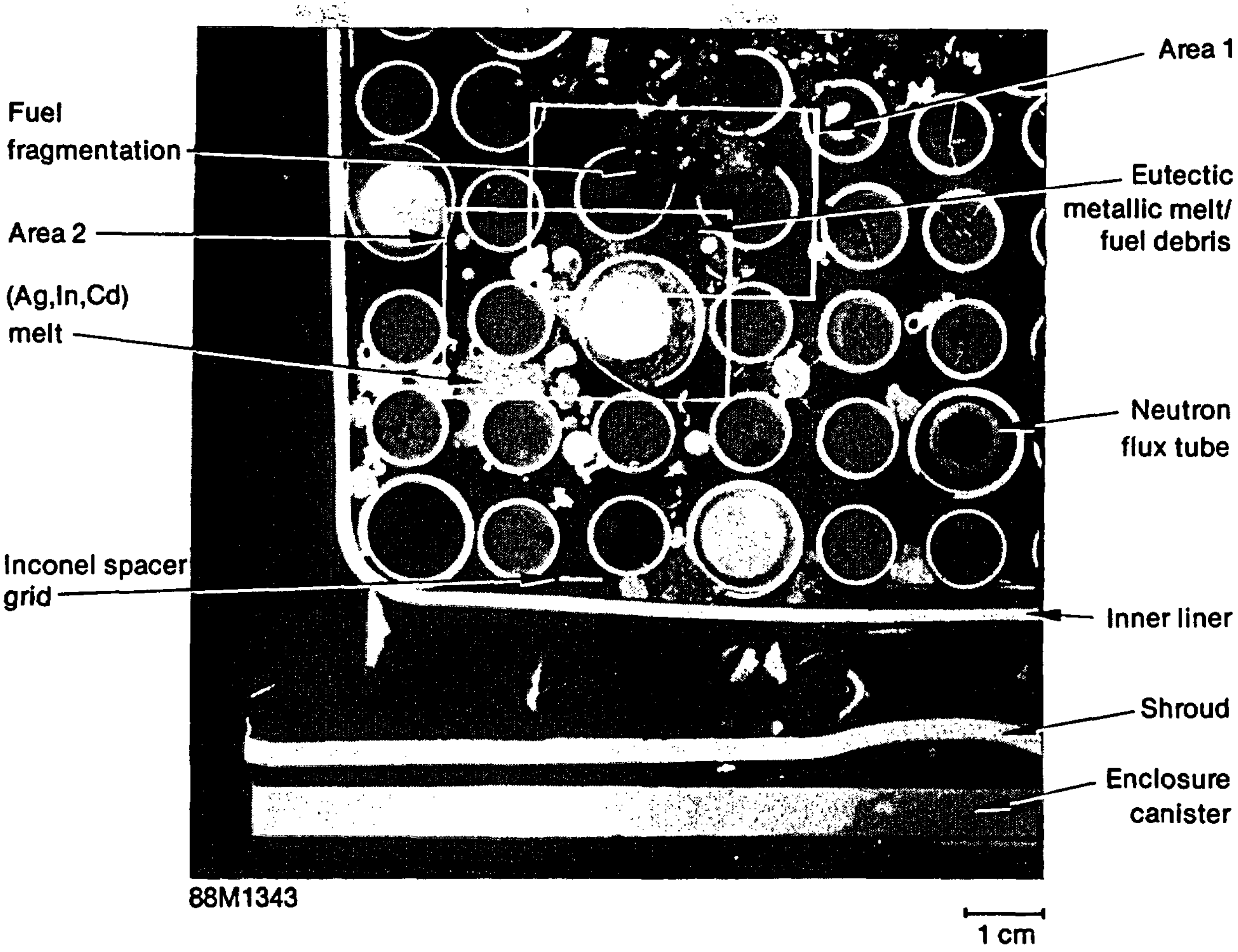

G4 bottom

Figure 45. Metallographic cross section G4 (bottom) at 0.43 m above the bottom of the instrumented fuel rods.

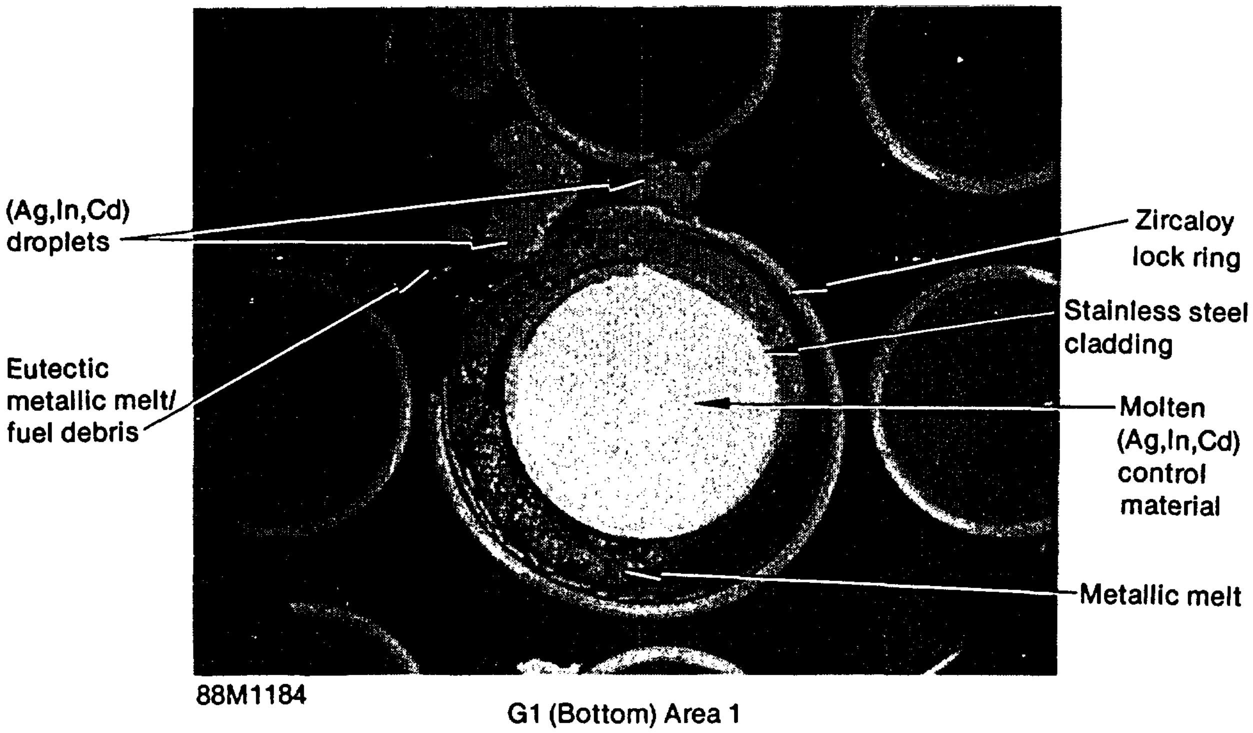

Figure 46. Details of metallographic cross section G1 (bottom) at 0.43 m.

88M1337

G2 (Bottom) Area 1

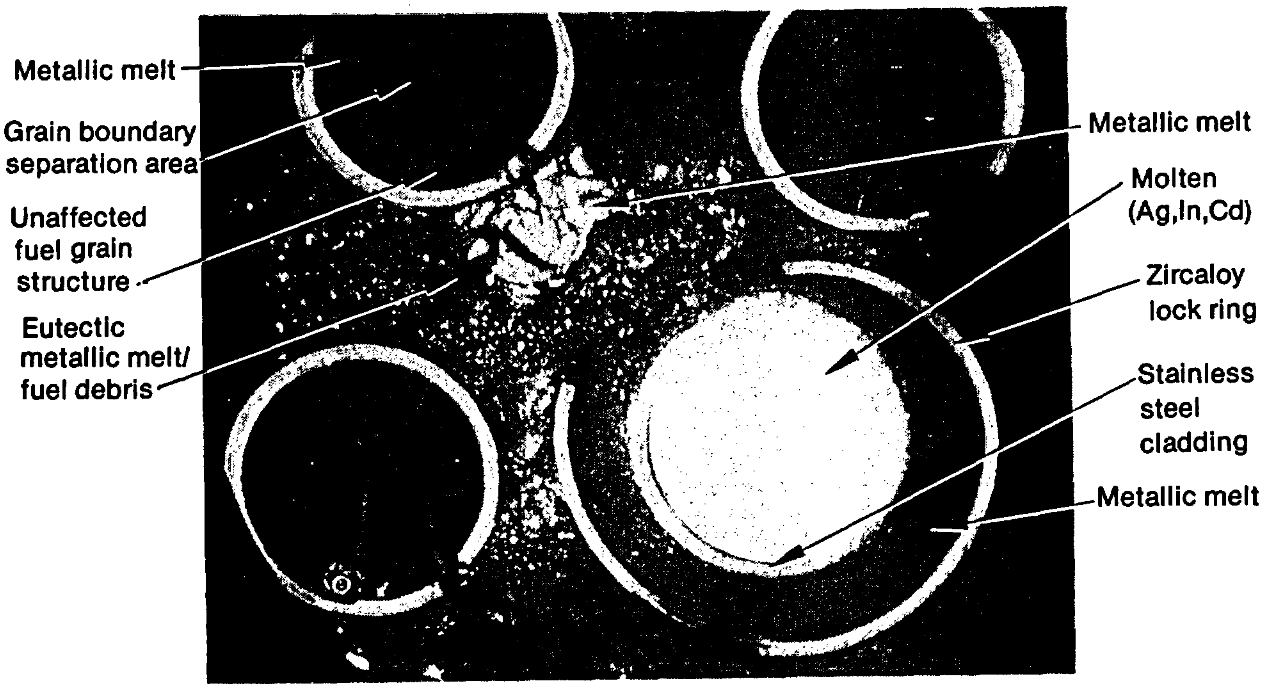

88M1338

G2 (Bottom) Area 2

Figure 47. Details of metallographic cross section G2 (bottom) at 0.43 m.

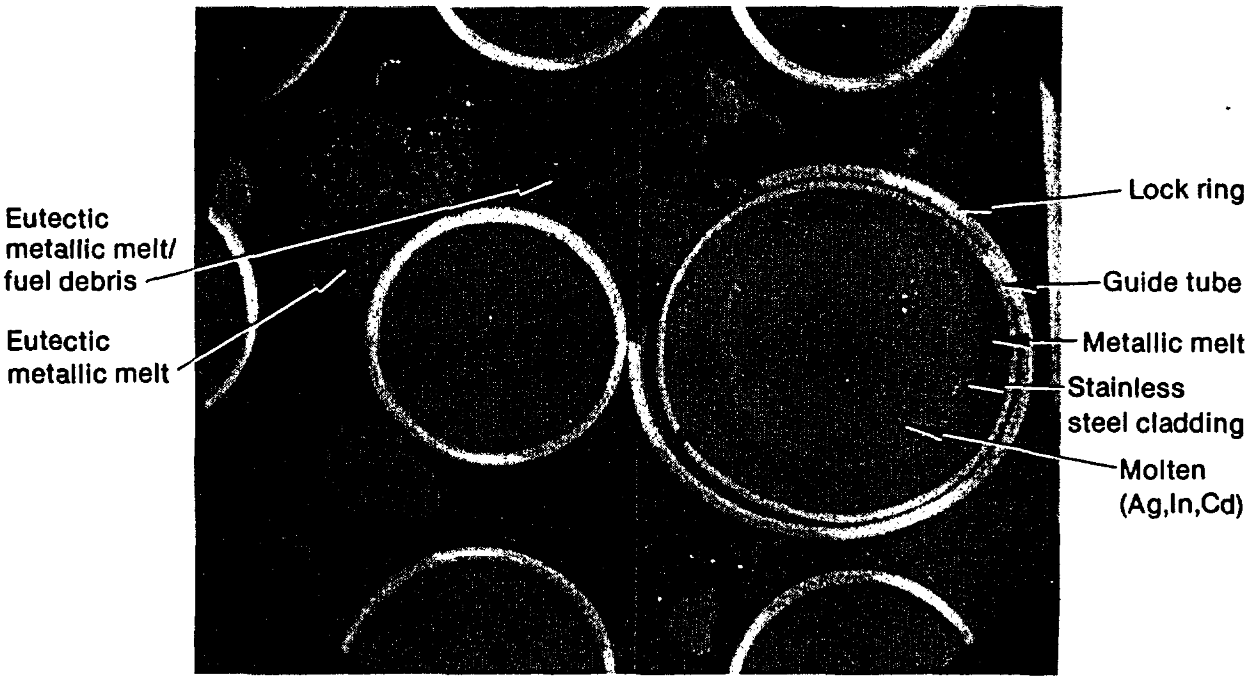

G3 (Bottom) Area 1

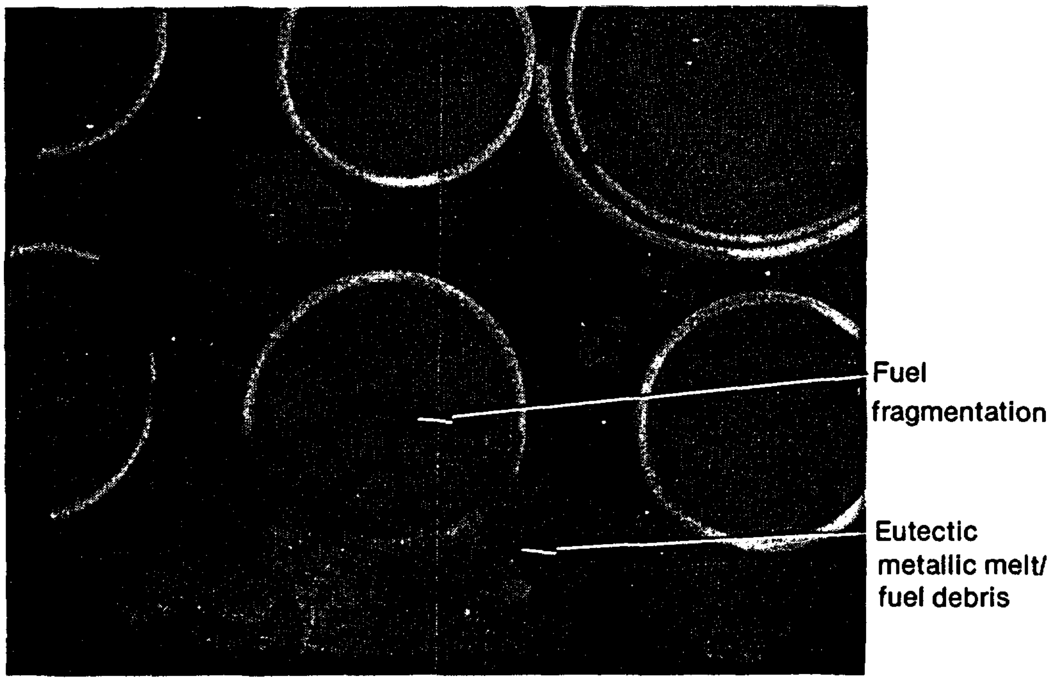

G3 (Bottom) Area 2

Figure 48. Details of metallographic cross section G3 (bottom) at 0.43 m.

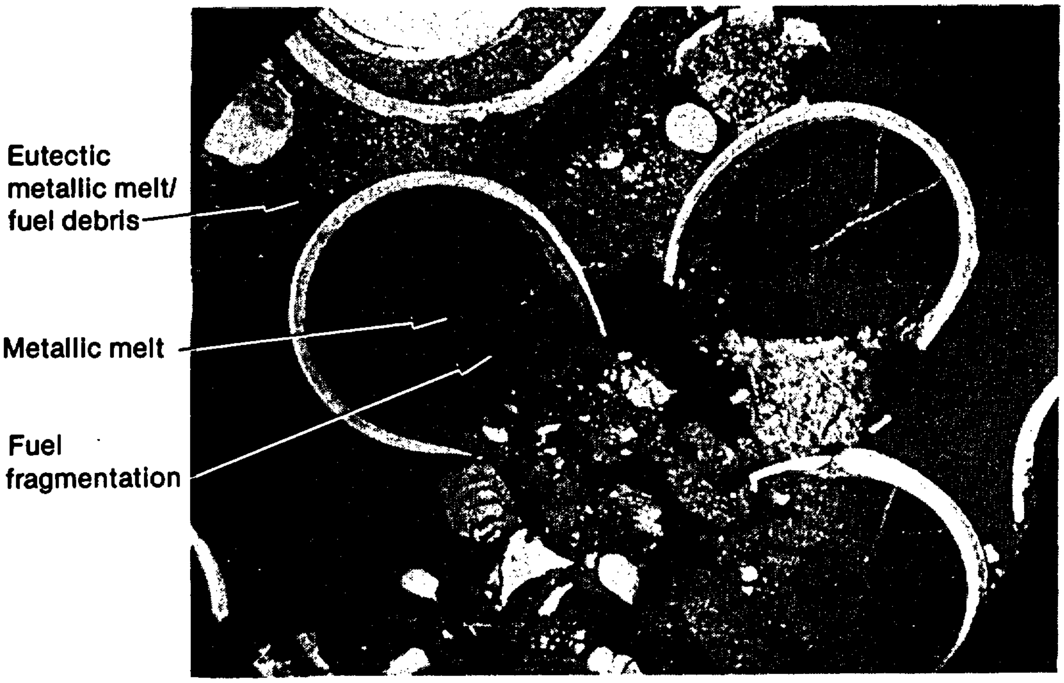

G4 (Bottom) Area 1

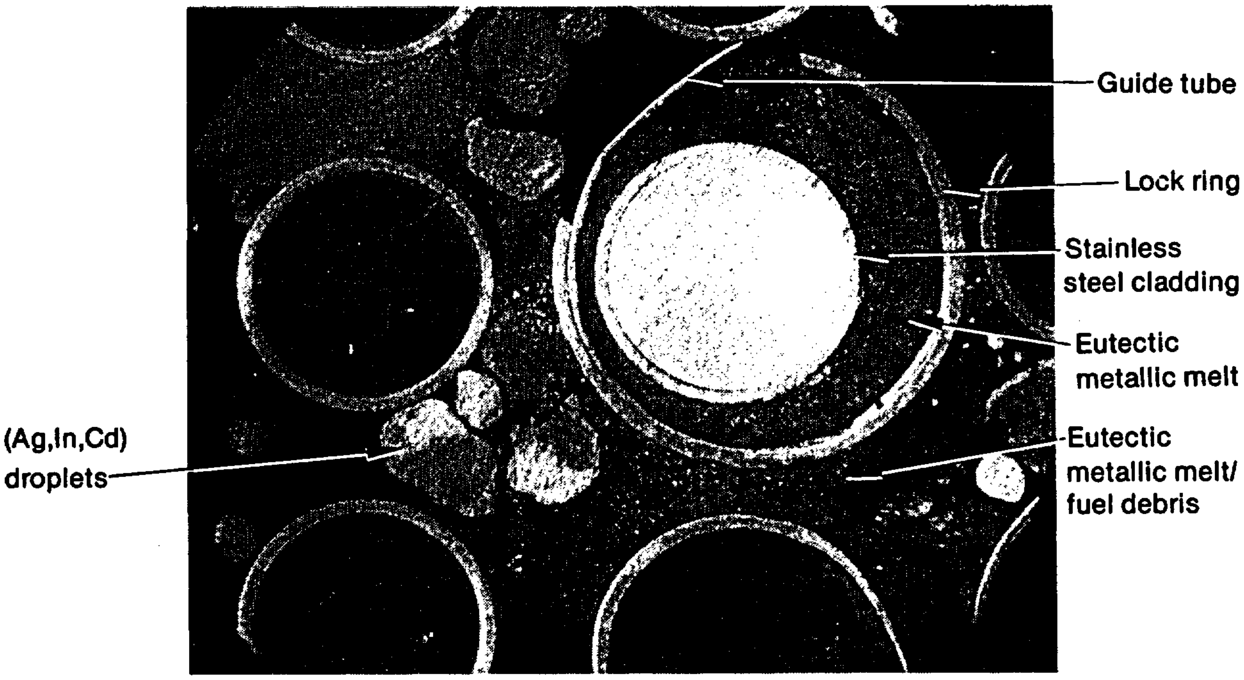

G4 (Bottom) Area 2

Figure 49. Details of metallographic cross section G4 (bottom) at 0.43 m.

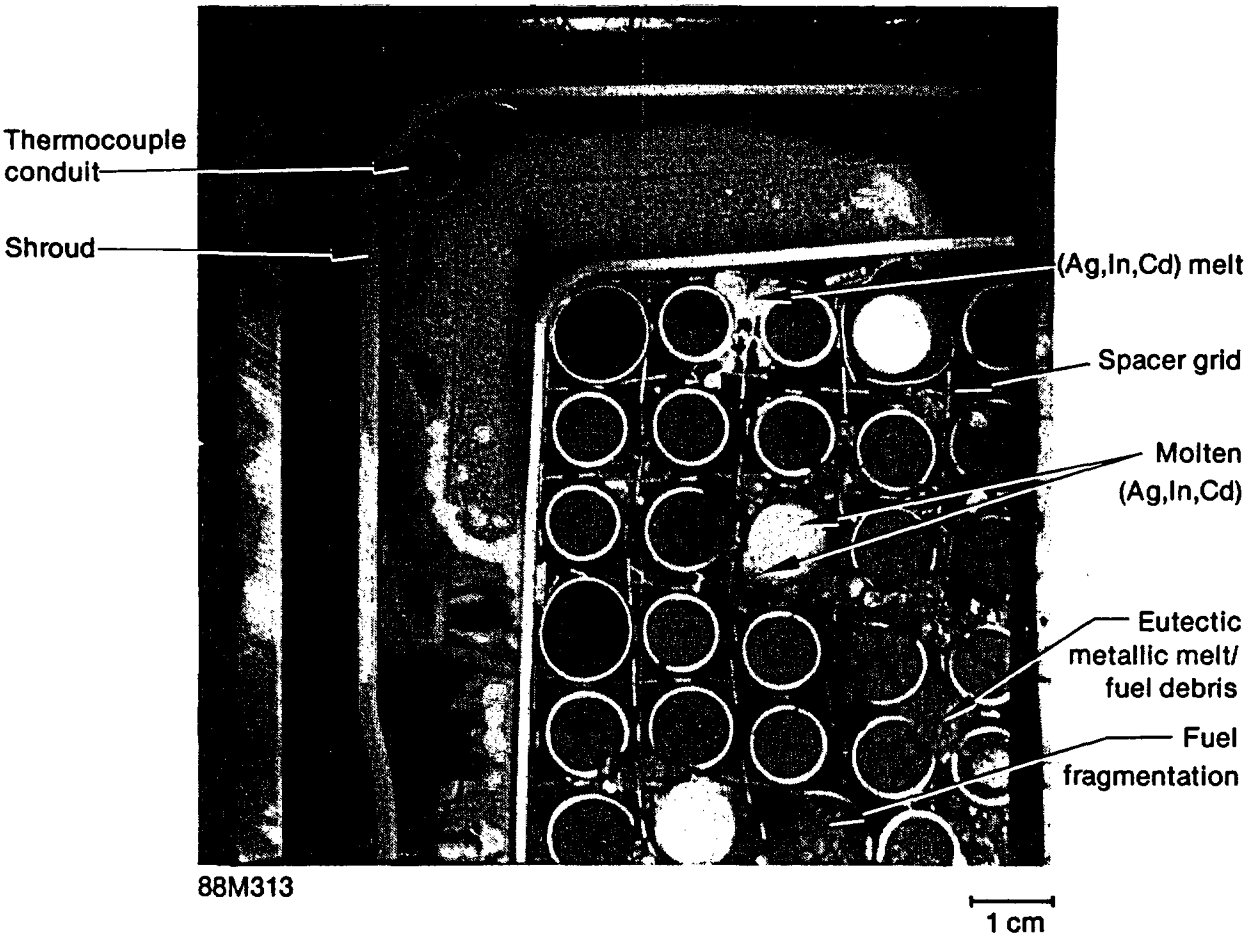

G1

Figure 50. Metallographic cross section G1 at 0.46 m above the bottom of the instrumented fuel rods.

G2

Figure 51. Metallographic cross section G2 at 0.46 m above the bottom of the instrumented fuel rods.

G3

Figure 52. Metallographic cross section G3 at 0.46 m above the bottom of the instrumented fuel rods.

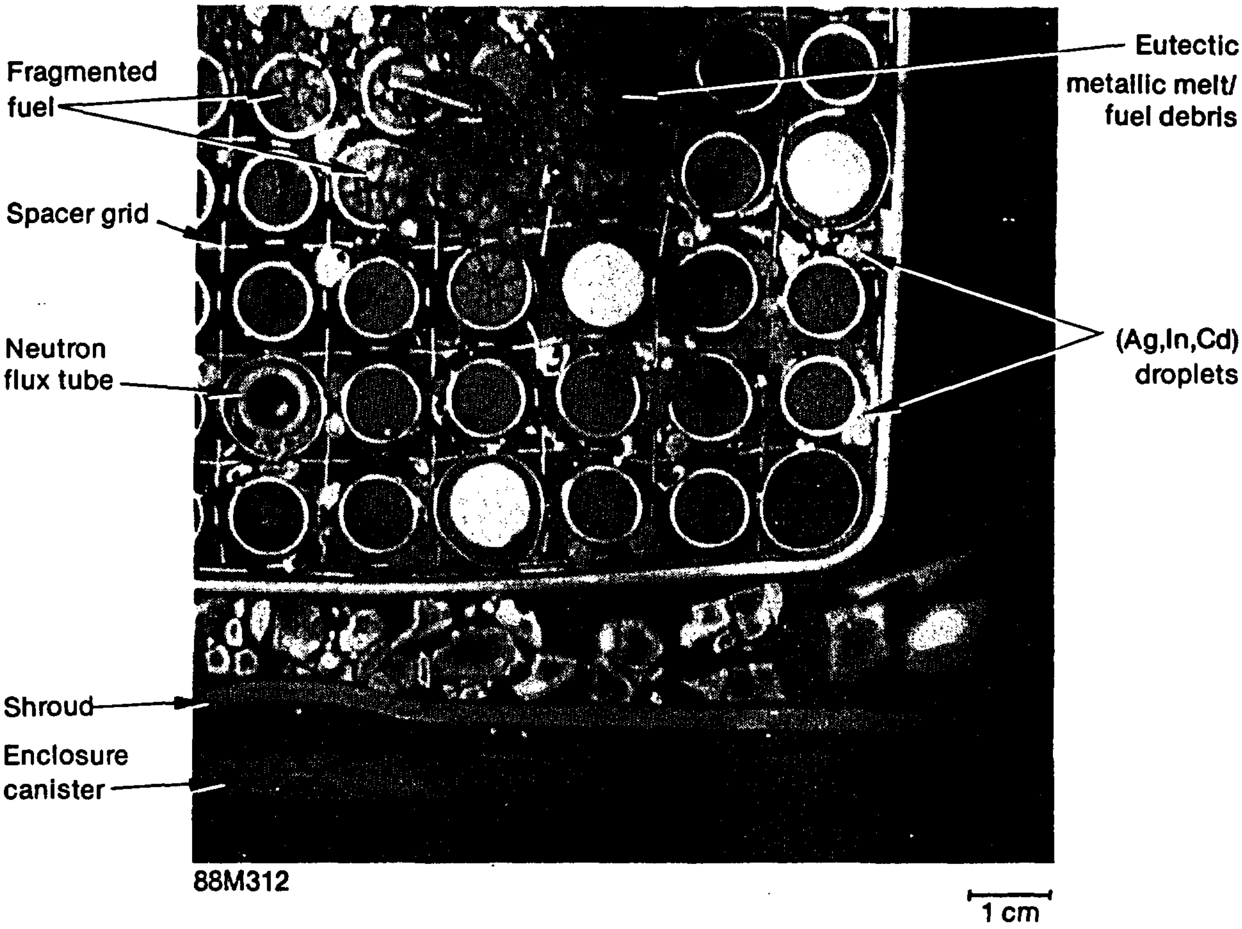

G4

Figure 53. Metallographic cross section G4 at 0.46 m above the bottom of the instrumented fuel rods.

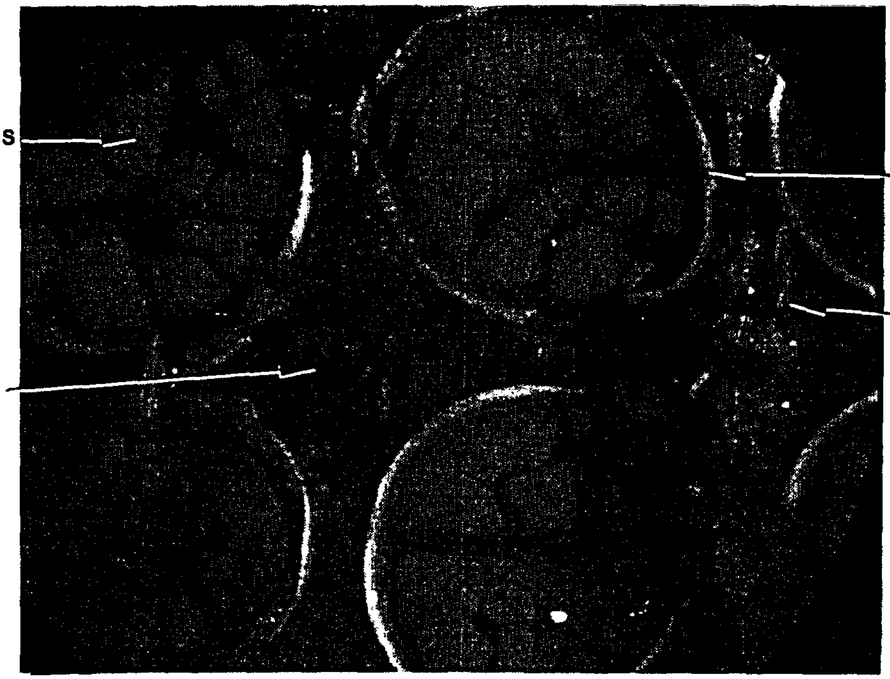

G2 Area 1

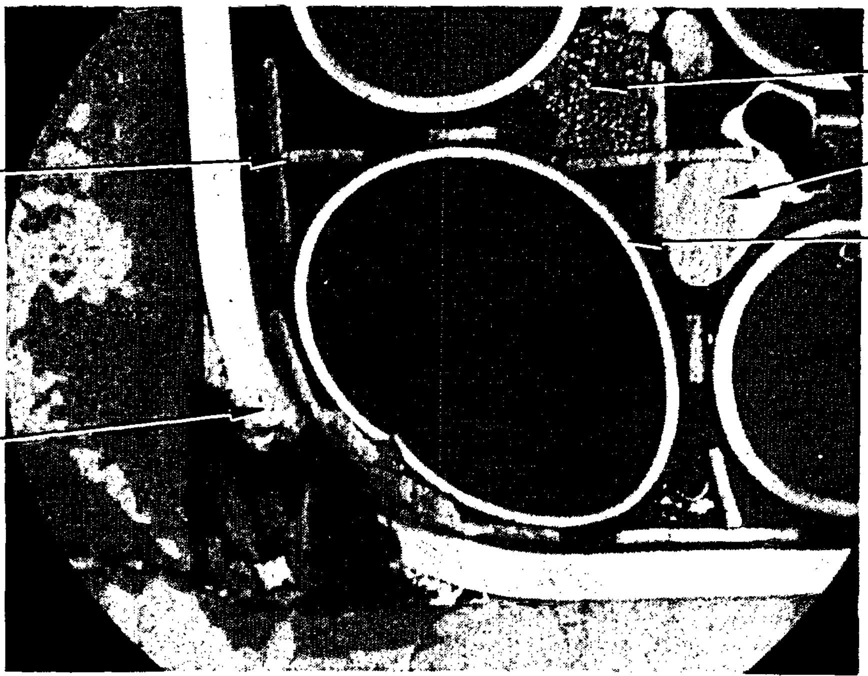

G2 Area 2

Figure 54. Details of metallographic cross section G2 at 0.46 m.

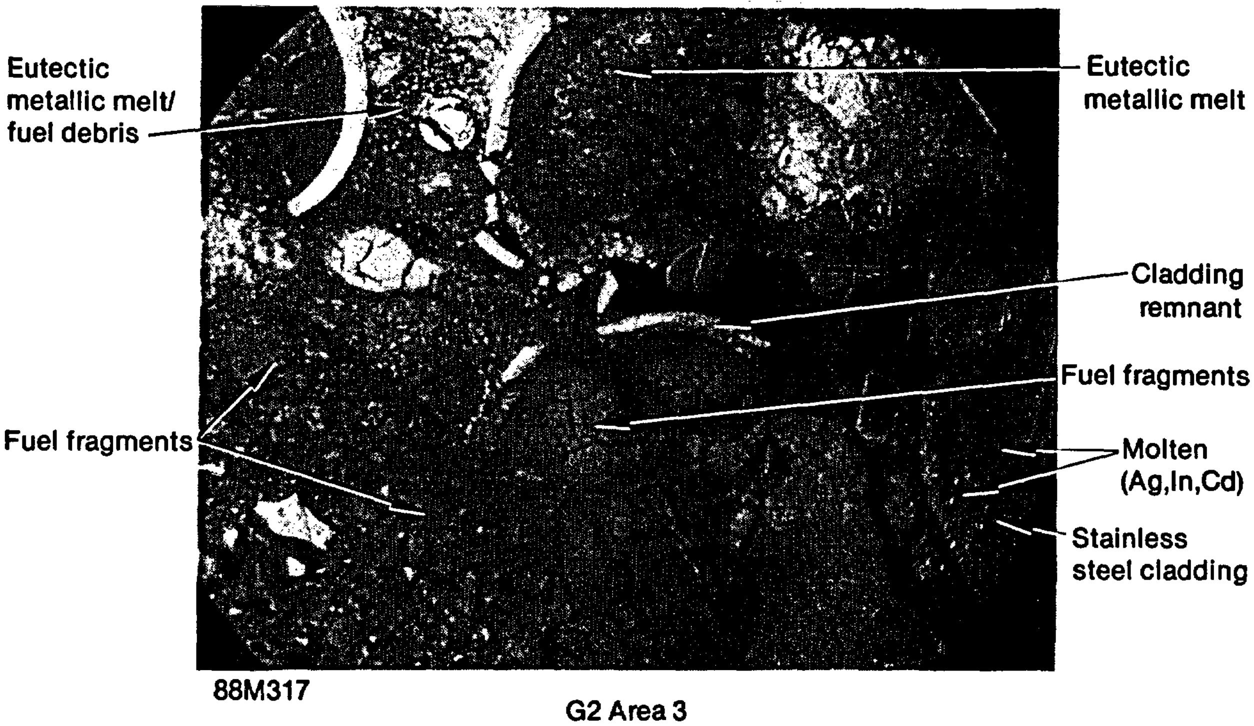

G2 Area 3

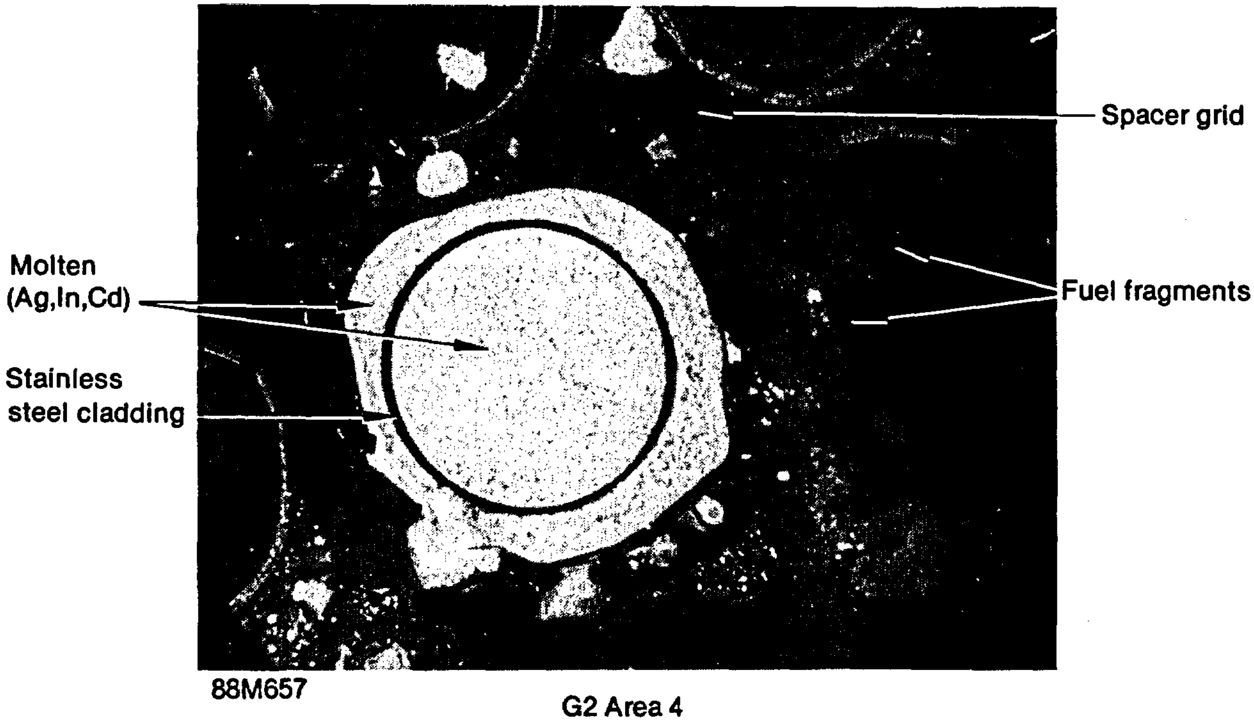

G2 Area 4

Figure 55. Details of metallographic cross section G2 at 0.46 m.

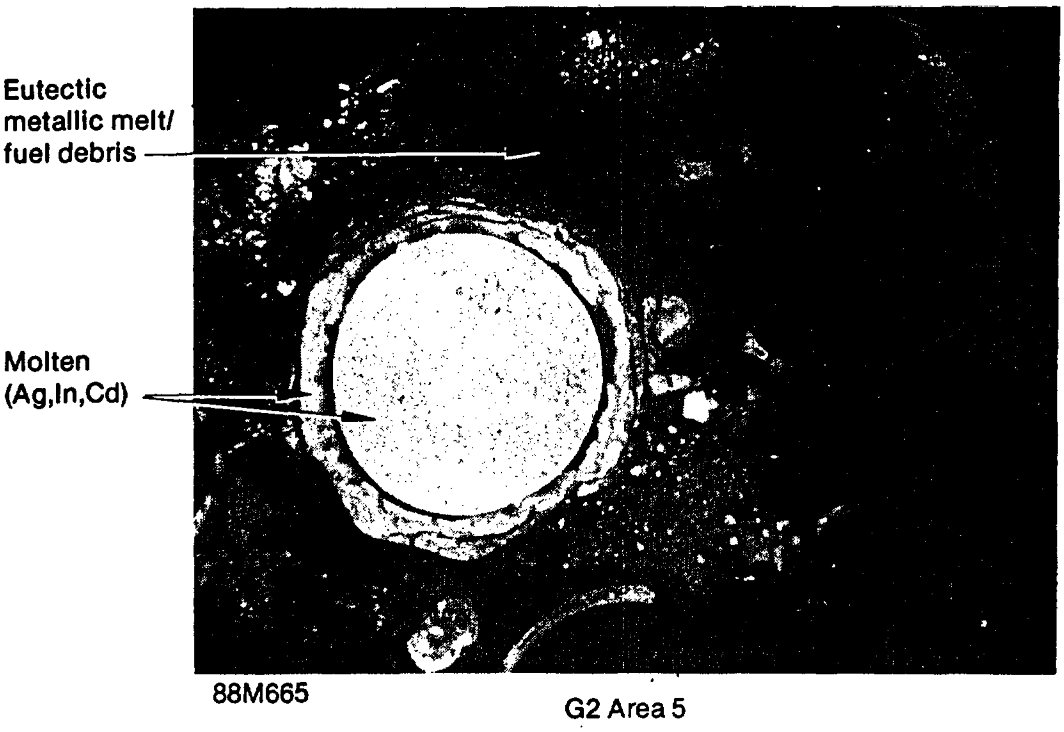

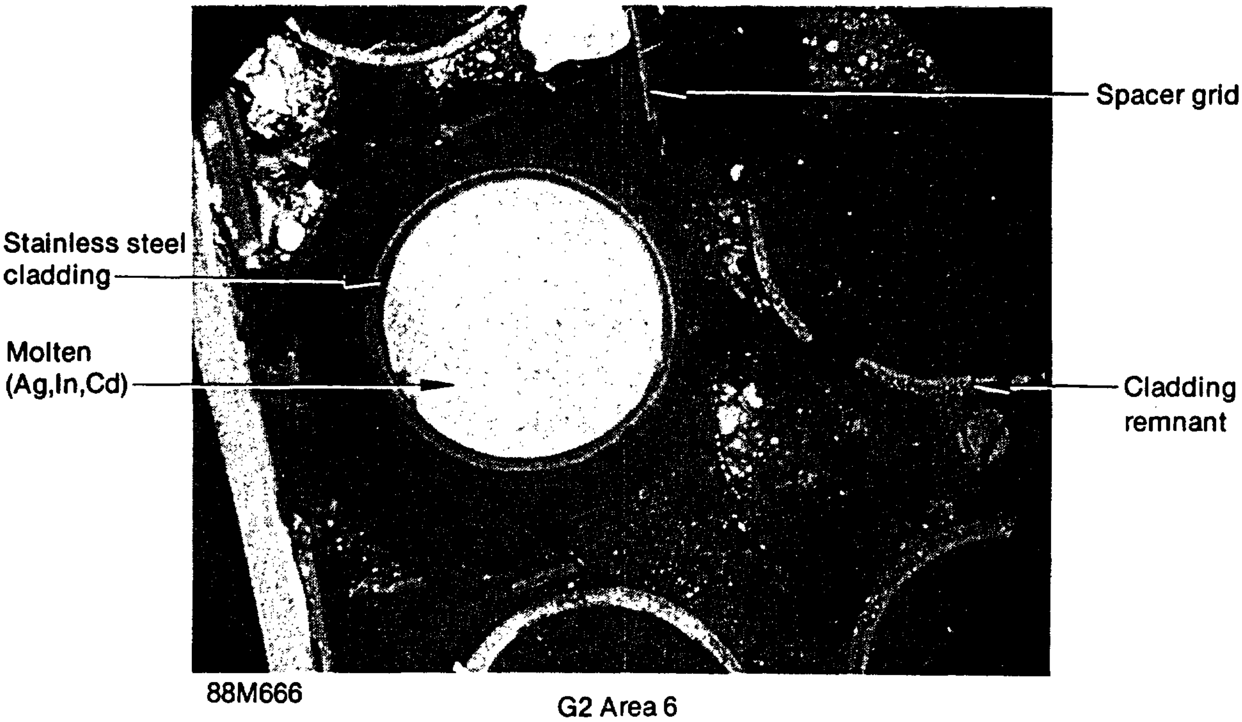

Figure 56. Details of metallographic cross section G2 at 0.46 m.

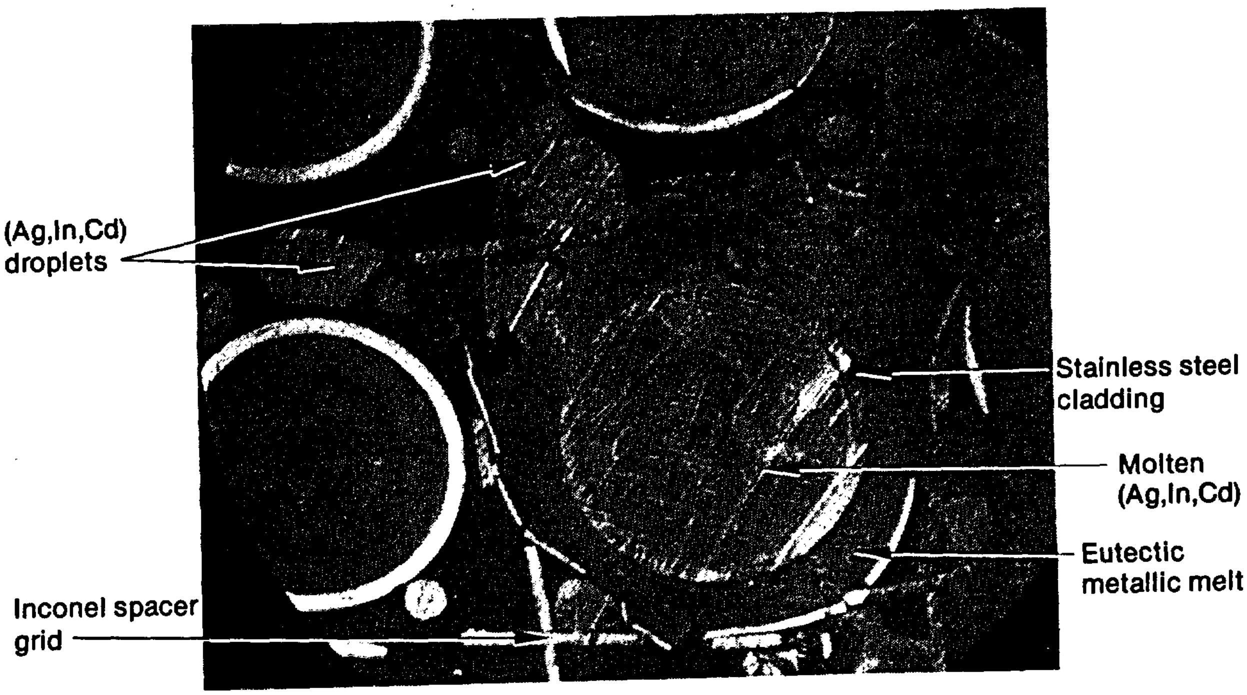

88M261 G3 Area 1

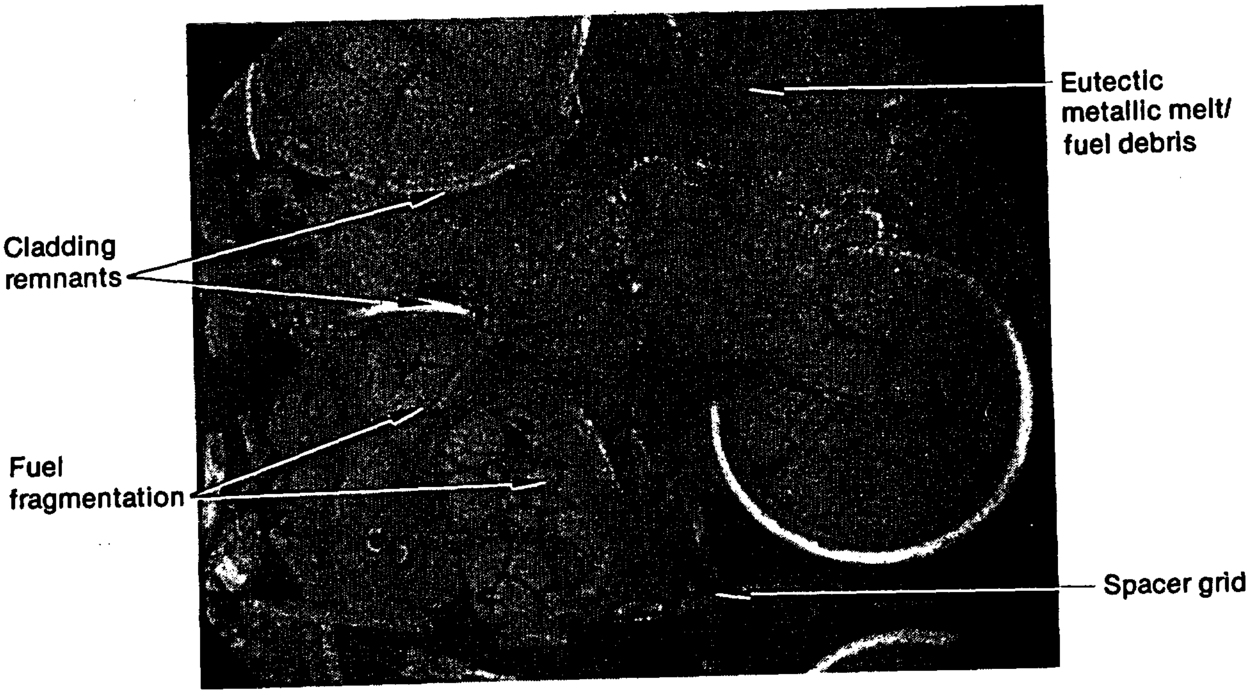

88M262 G3 Area 2

Figure 57. Details of metallographic cross section G3 at 0.46 m.

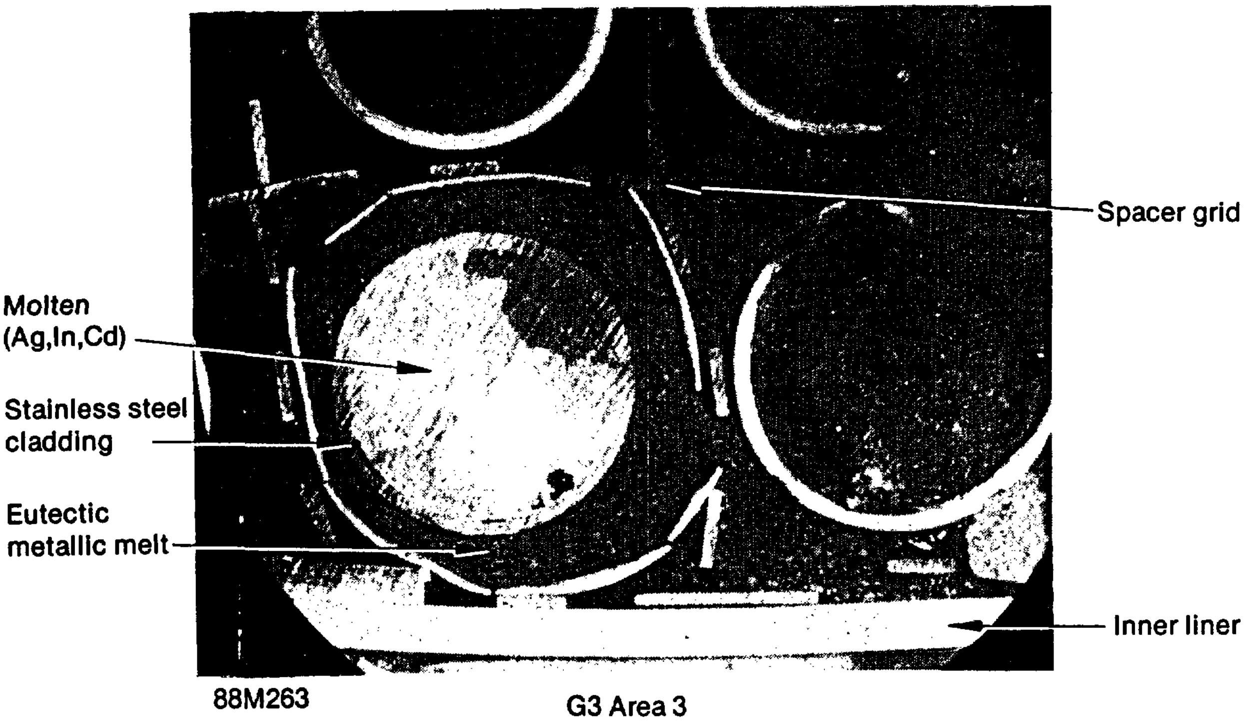

Figure 58. Details of metallographic cross section G3 at 0.46 m.

liquefied or in the process of being attacked by silver-bearing melts. The (Ag,In,Cd) alloy was molten in all the control rods at this elevation, but it was still contained within the remaining stainless steel cladding. The inner liner was still intact except for localized melting in the corner of sample G2, and all the insulation was intact prior to sectioning. Deformation of the spacer grids, lock rings, guide tubes, and fuel rod cladding is apparent.

3.1.9 Cross Section H (0.58 m; Figures 59-66)

At and above this cross section, all the control rods have failed; and the (Ag,In,Cd) alloy was free to relocate and interact with other materials. The inner liner has liquefied and is gone in several places. This allowed molten materials to penetrate into the low-density ZrO_2 insulation region. The majority of the relocated blockage material was ceramic $(U,Zr)O_2$ instead of the metallic melts observed on lower elevations. Fuel fragmentation and powdering is readily apparent, and significant amounts of the zircaloy fuel rod cladding were either completely gone, as a result of contact with the ceramic melts, or only an outer shell of ZrO_2 remains. Only in the lesser-damaged corner regions was unoxidized zircaloy cladding found, although this zircaloy did have an oxide layer on the outer surface. The greatest amount of damage was once again in the northeast quadrant.

3.1.10 Cross Section I (0.66 m; Figures 67-86)

This cross section was located near the 0.69-m (27-in.) thermocouple elevation. It was through a large $(U,Zr)O_2$ ceramic melt, which surrounds the fuel rod array. At and above this elevation, essentially all the remaining zircaloy was fully oxidized. (The only exception was a small amount in the corner of sample Q2.) In most instances, an outer shell of fully oxidized cladding surrounded the fuel pellets; but the inner surface of the zircaloy cladding had melted and relocated downward. Cladding ballooning and rod-to-rod contact were apparent on some of the fuel rods. The inner zircaloy liner was gone, and molten materials were able to

H1

Figure 59. Metallographic cross section H1 at 0.58 m above the bottom of the instrumented fuel rods.

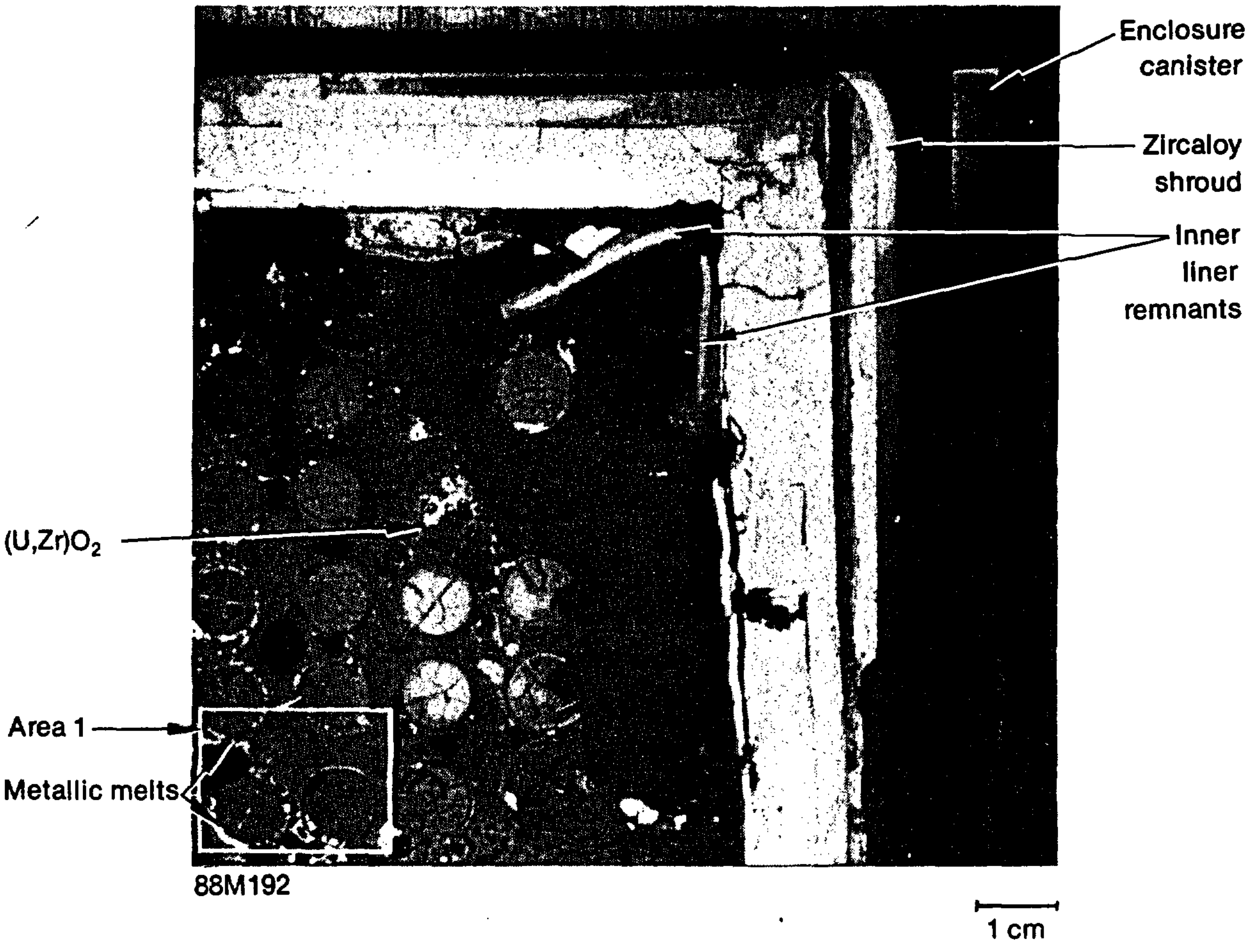

H2

Figure 60. Metallographic cross section H2 at 0.58 m above the bottom of the instrumented fuel rods.

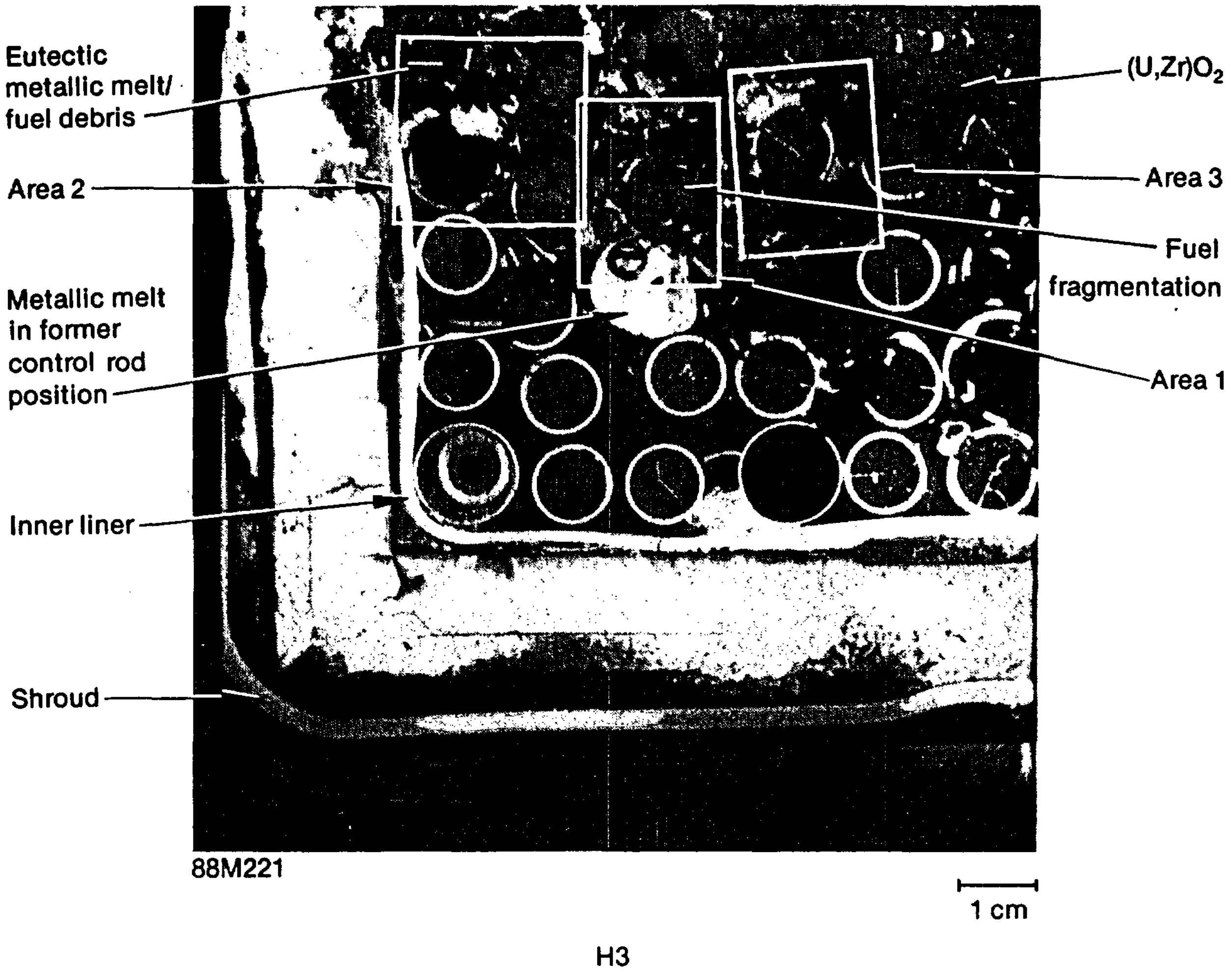

Figure 61. Metallographic cross section H3 at 0.58 m above the bottom of the instrumented fuel rods.

H4

Figure 62. Metallographic cross section H4 at 0.58 m above the bottom of the instrumented fuel rods.

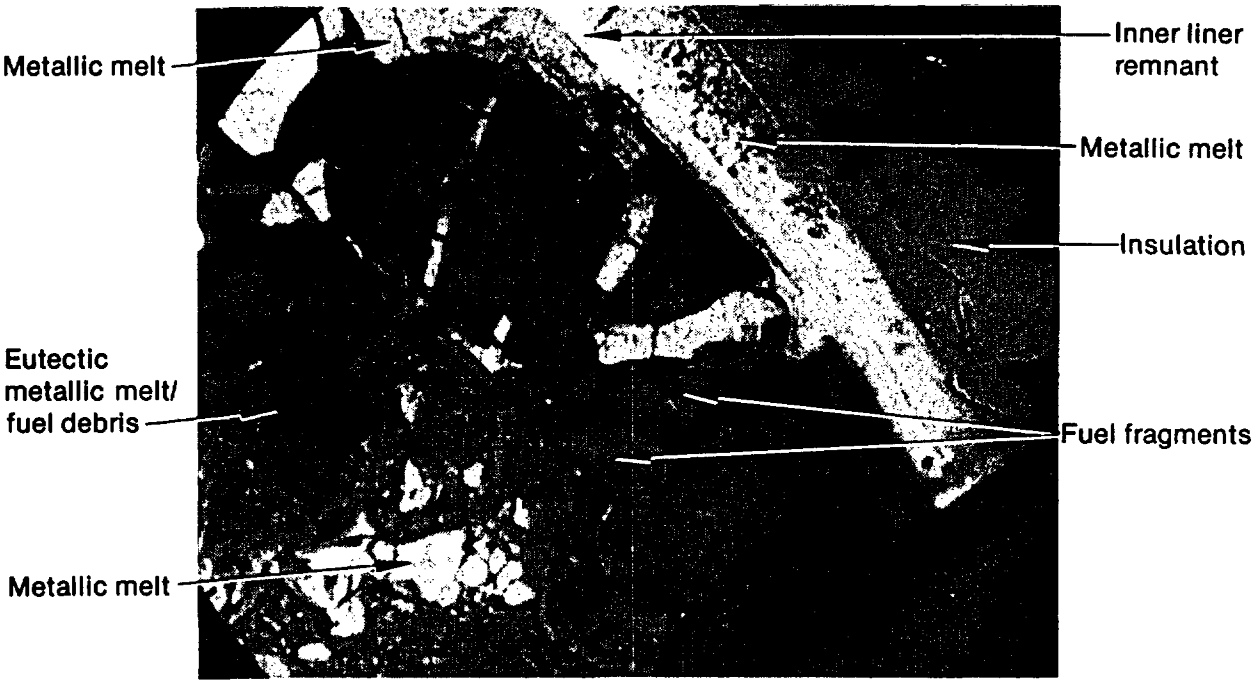

H1 Area 1

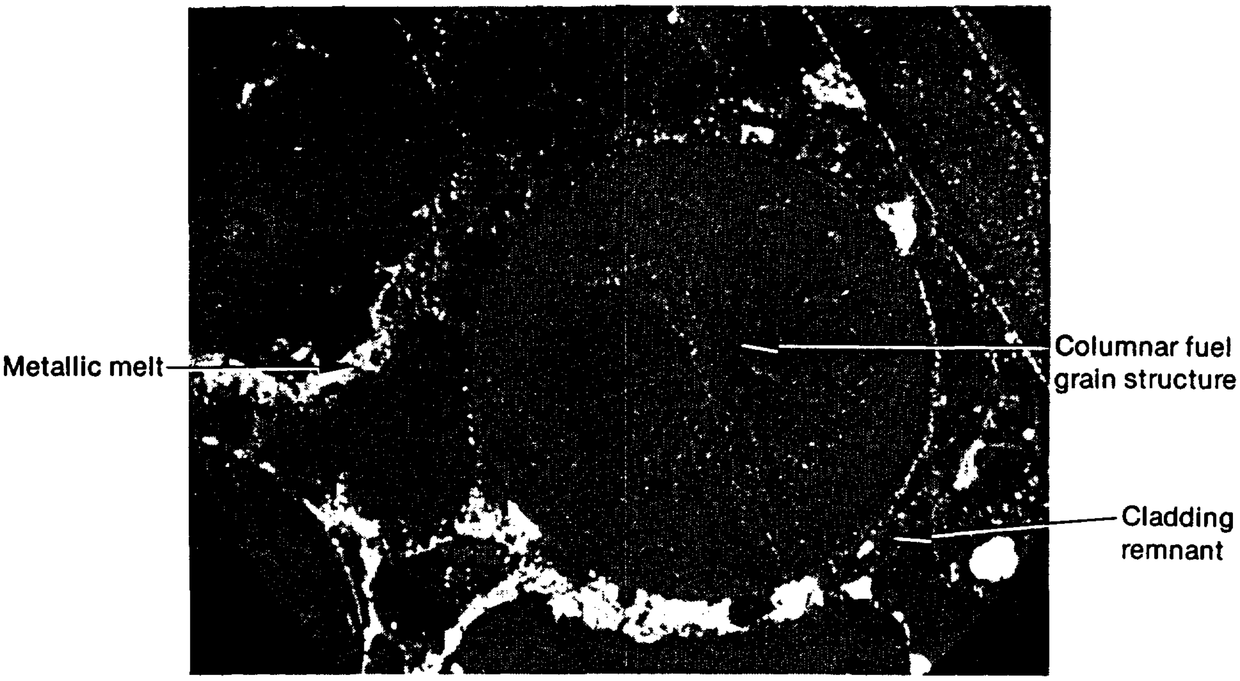

H1 Area 2

Figure 63. Details of metallographic cross section H1 at 0.58 m.

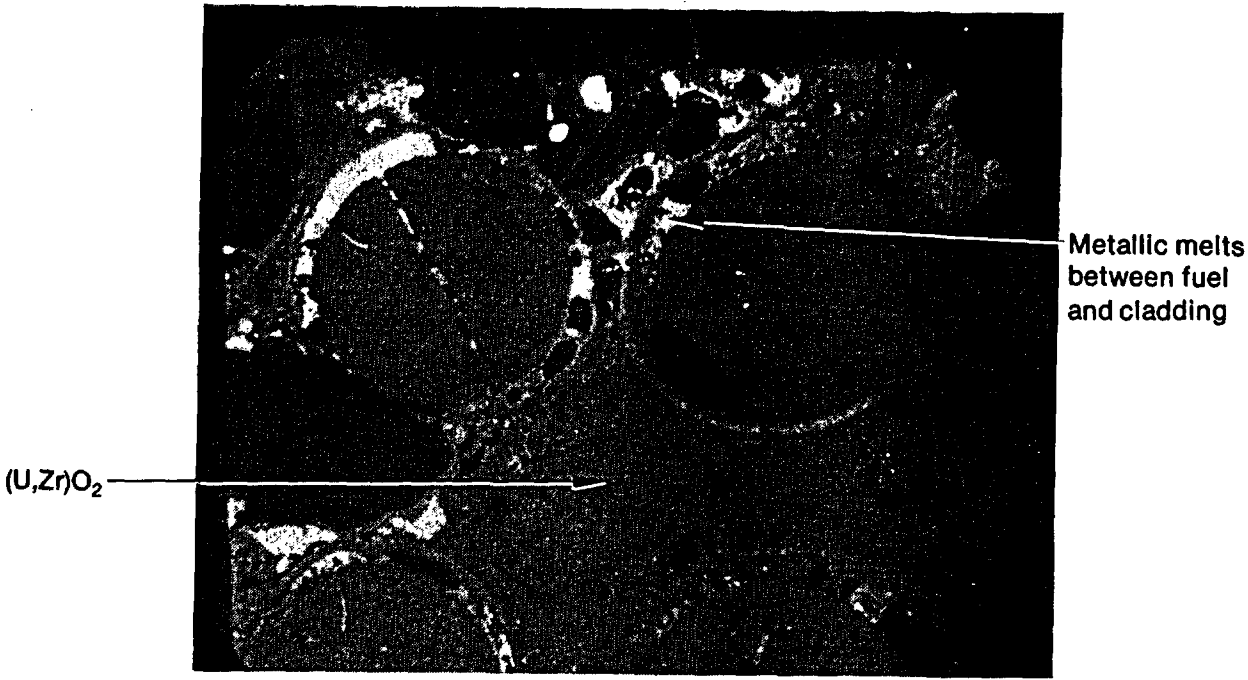

88M193 H2 Area 1

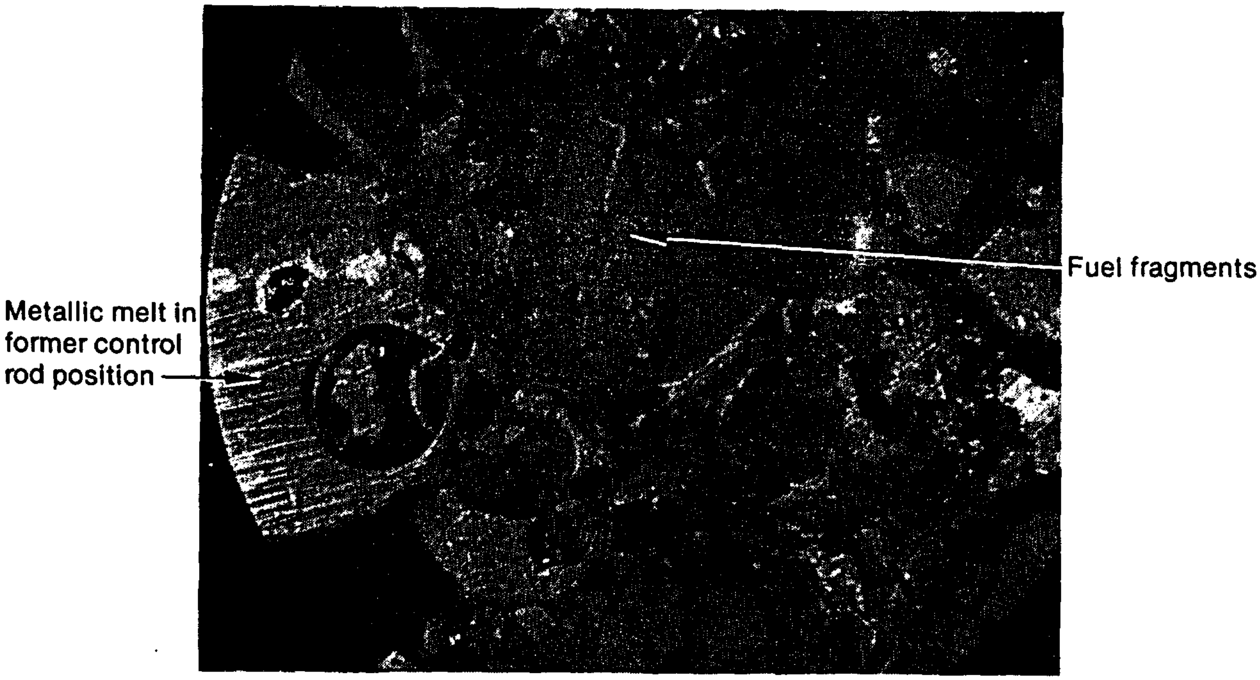

88M225 H3 Area 1

Figure 64. Details of metallographic cross section H2 and H3 at 0.58 m.

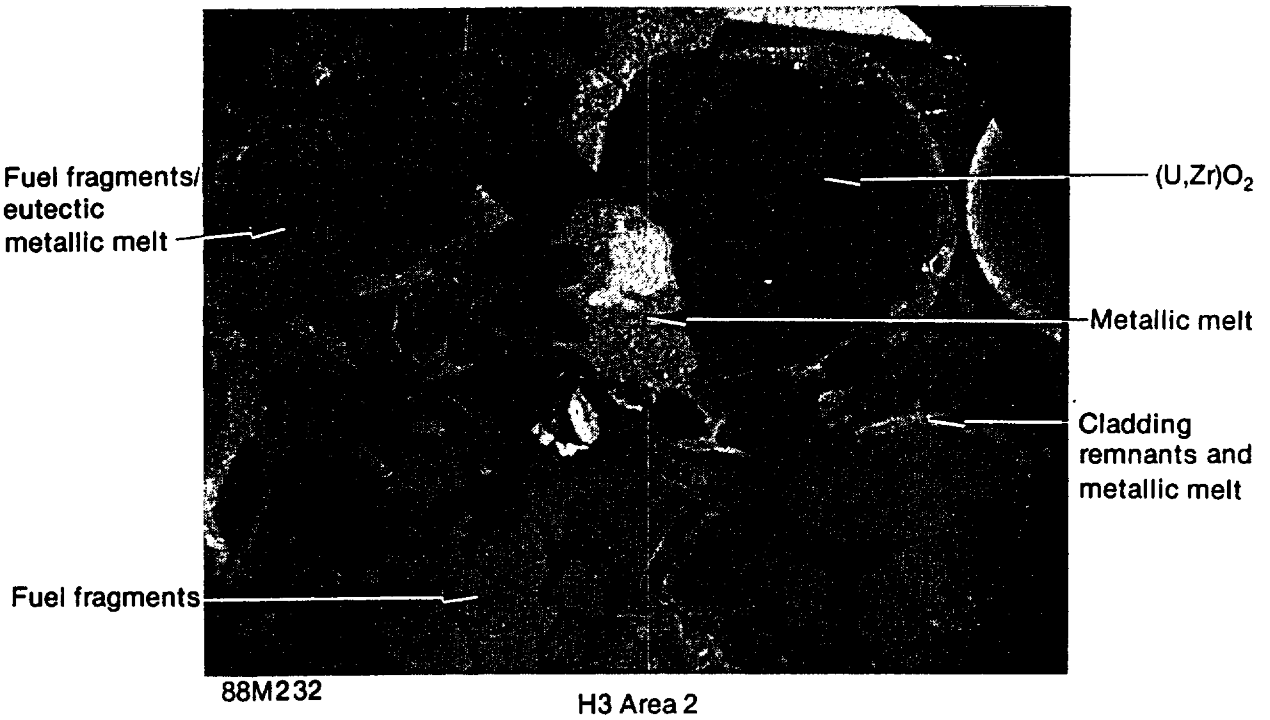

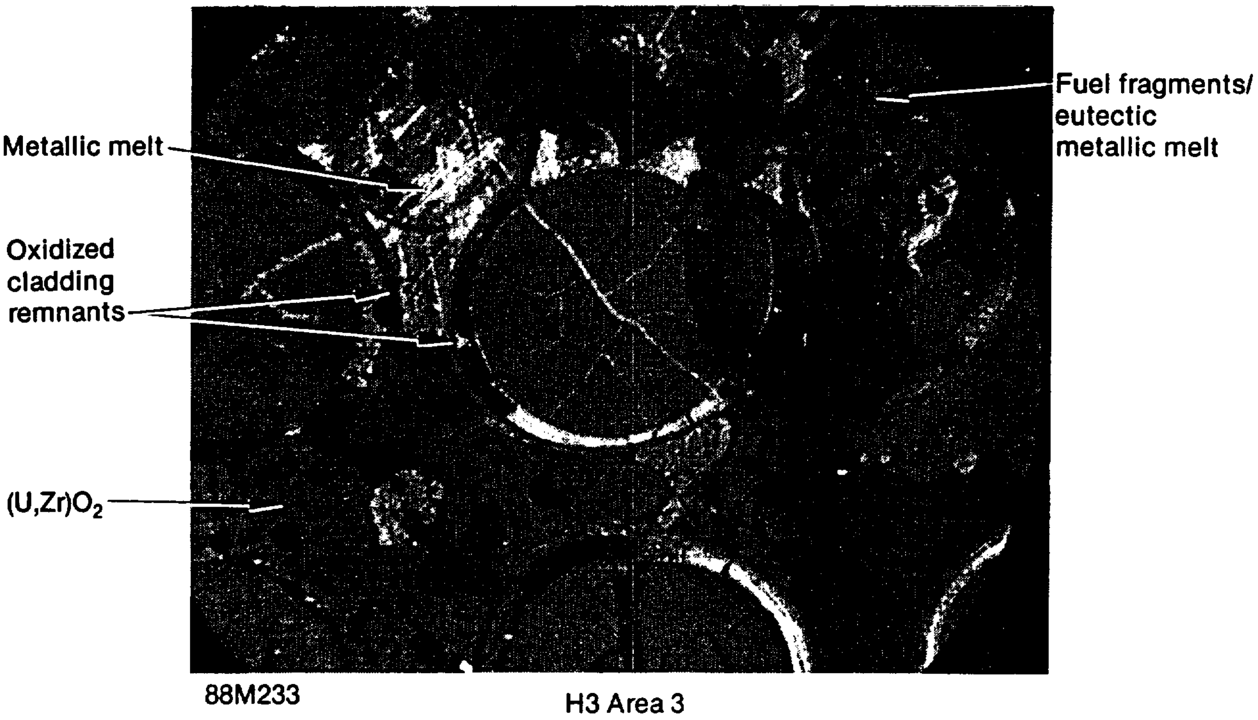

Figure 65. Details of metallographic cross section H3 at 0.58 m.

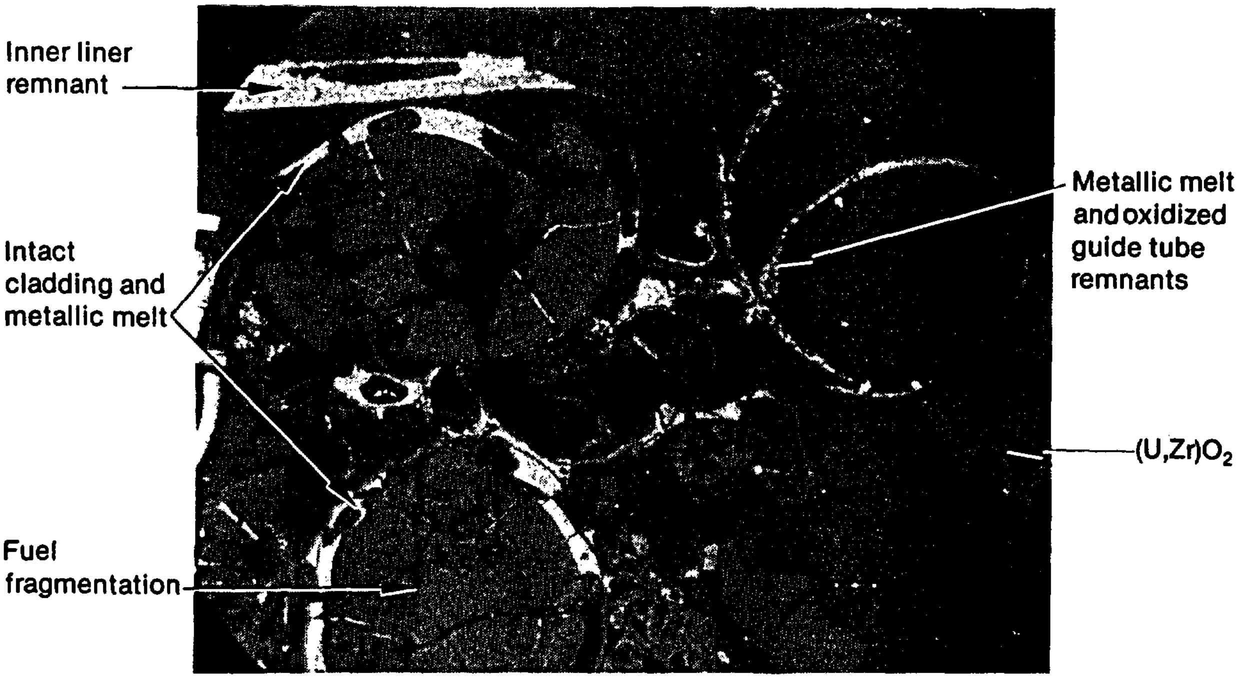

88M1039 H4 Area 1

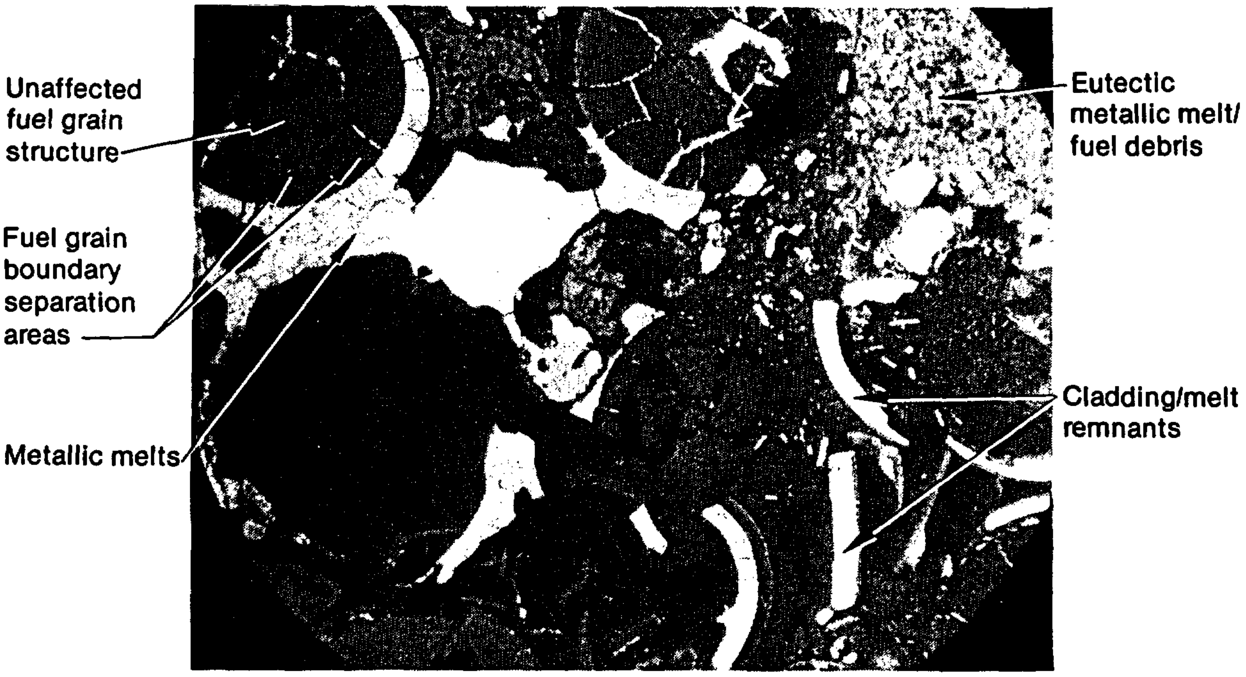

88M1040 H4 Area 2

Figure 66. Details of metallographic cross section H4 at 0.58 m.

I1

Figure 67. Metallographic cross section I1 at 0.66 m above the bottom of the instrumented fuel rods.

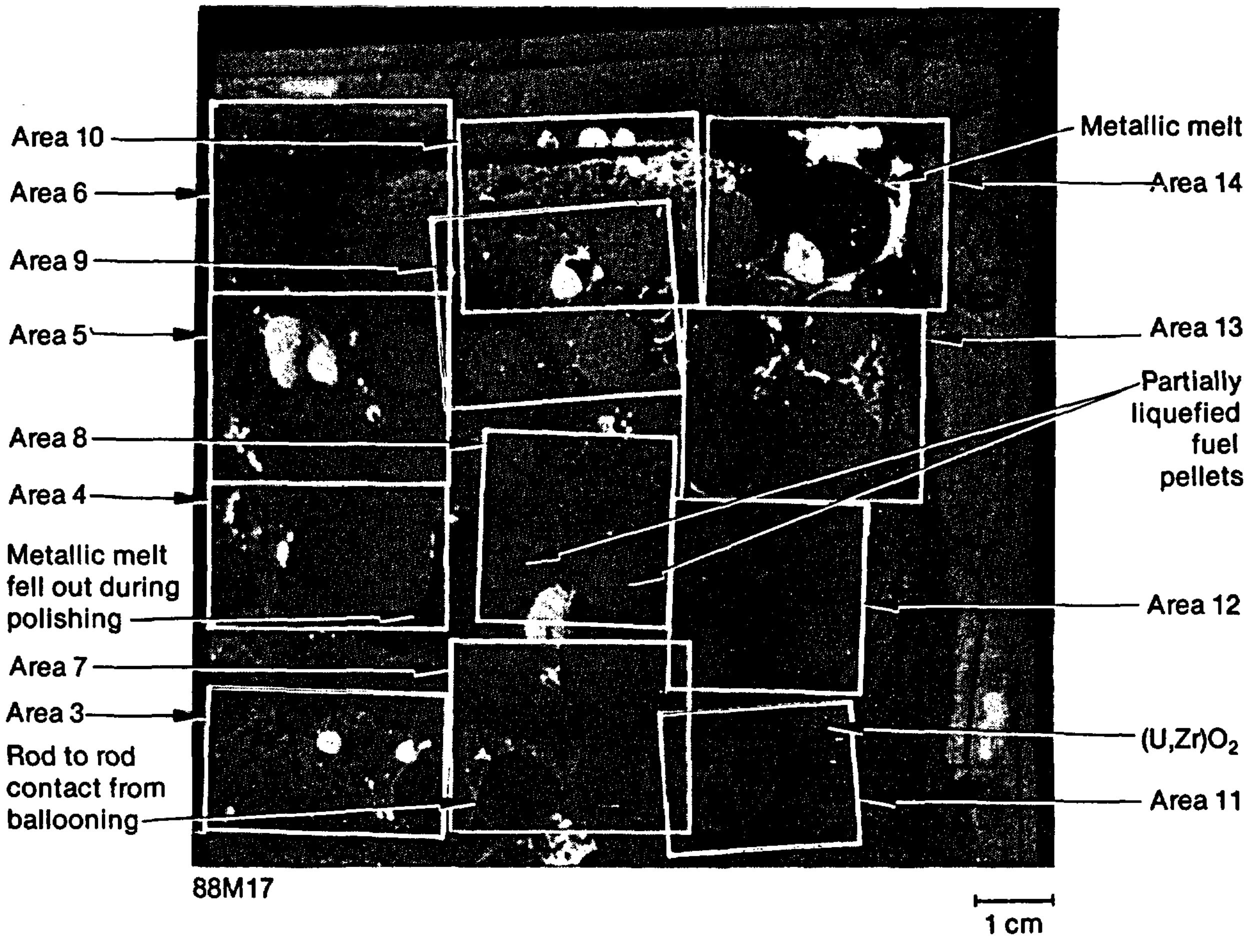

I2

Figure 68. Metallographic cross section I2 at 0.66 m above the bottom of the instrumented fuel rods.

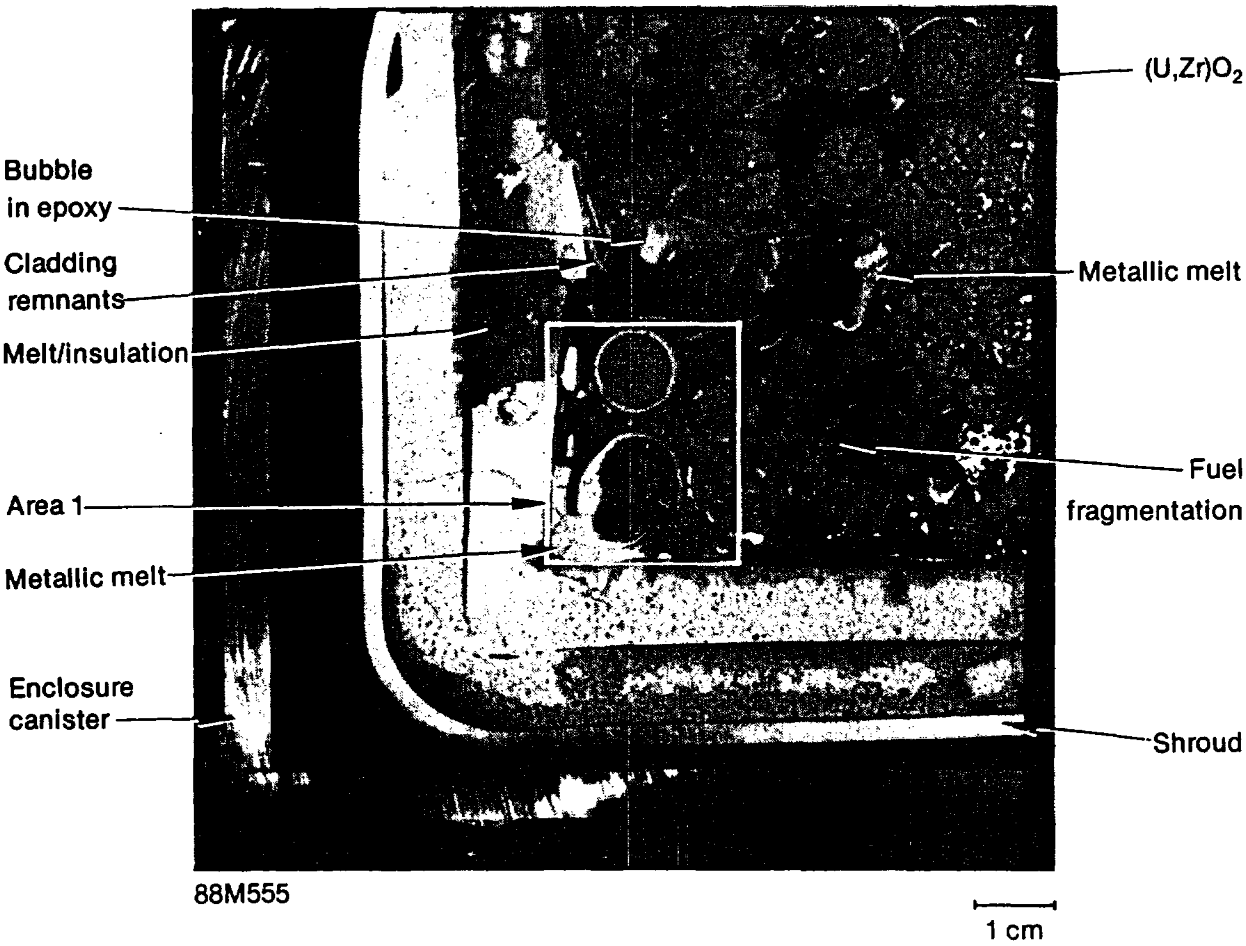

I3

Figure 69. Metallographic cross section I3 at 0.66 m above the bottom of the instrumented fuel rods.

I4

Figure 70. Metallographic cross section I4 at 0.66 m above the bottom of the instrumented fuel rods.

I1 Area 1

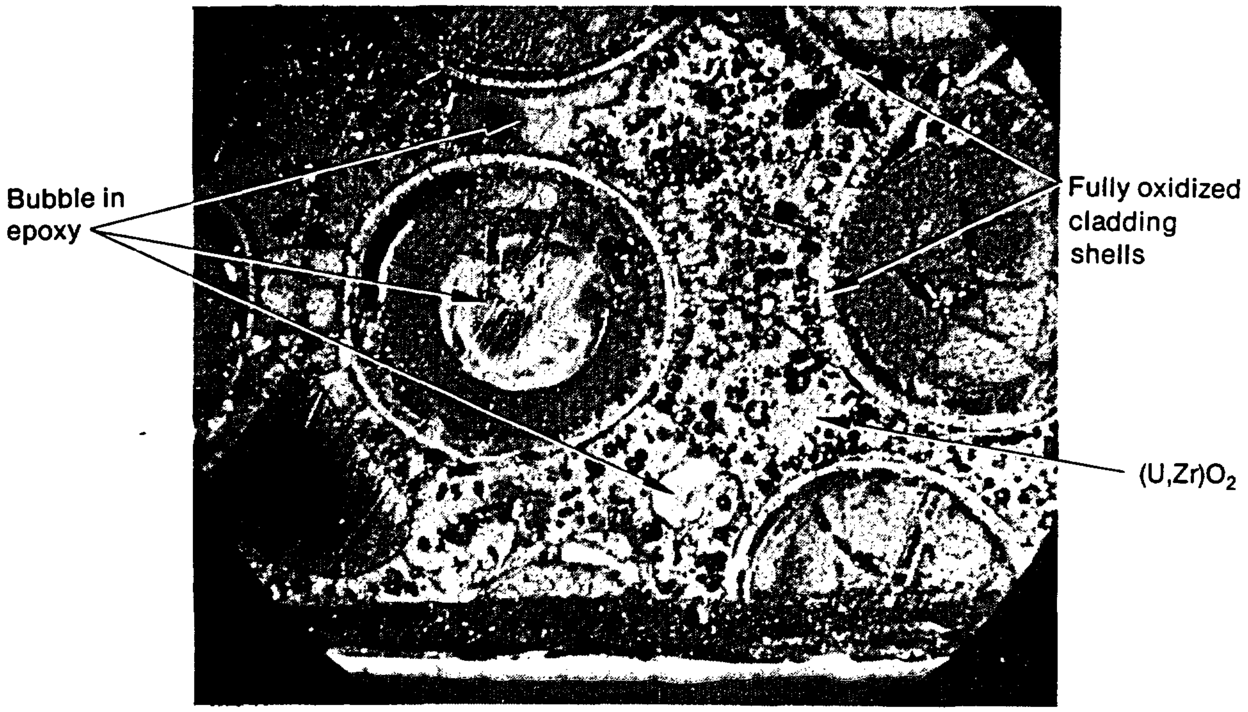

I1 Area 2

Figure 71. Details of metallographic cross section I1 at 0.66 m.

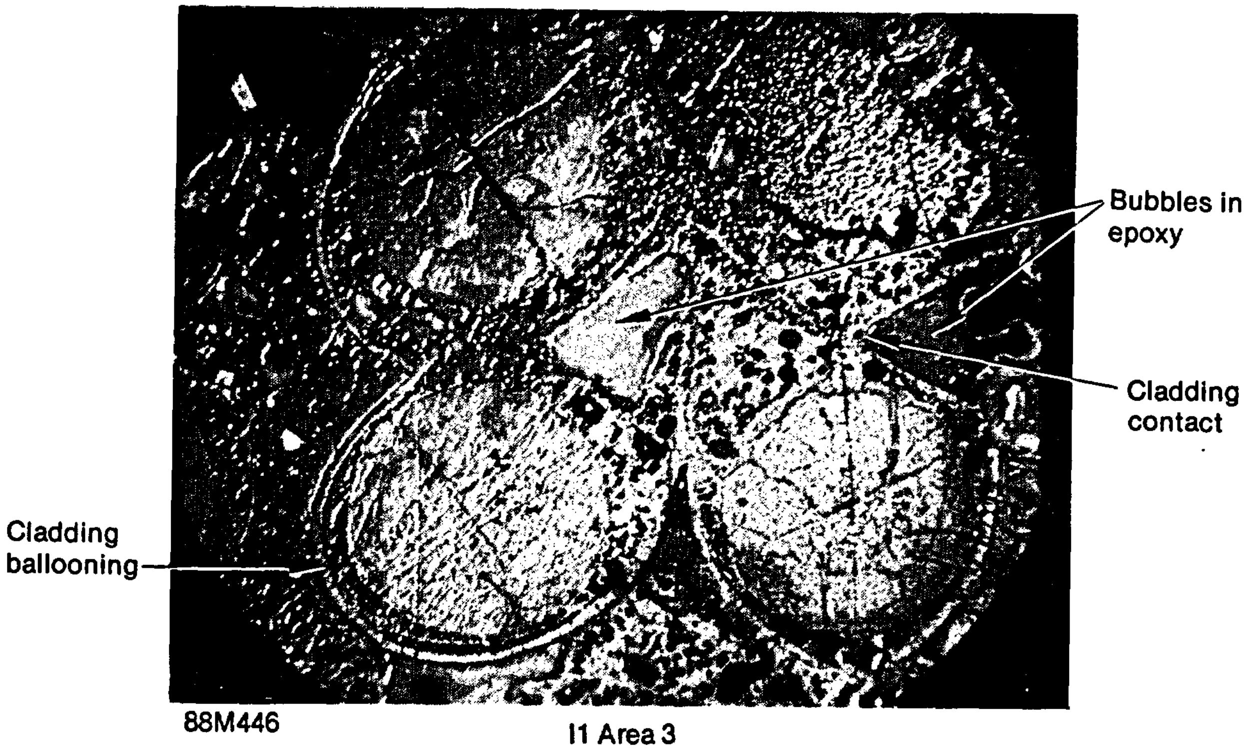

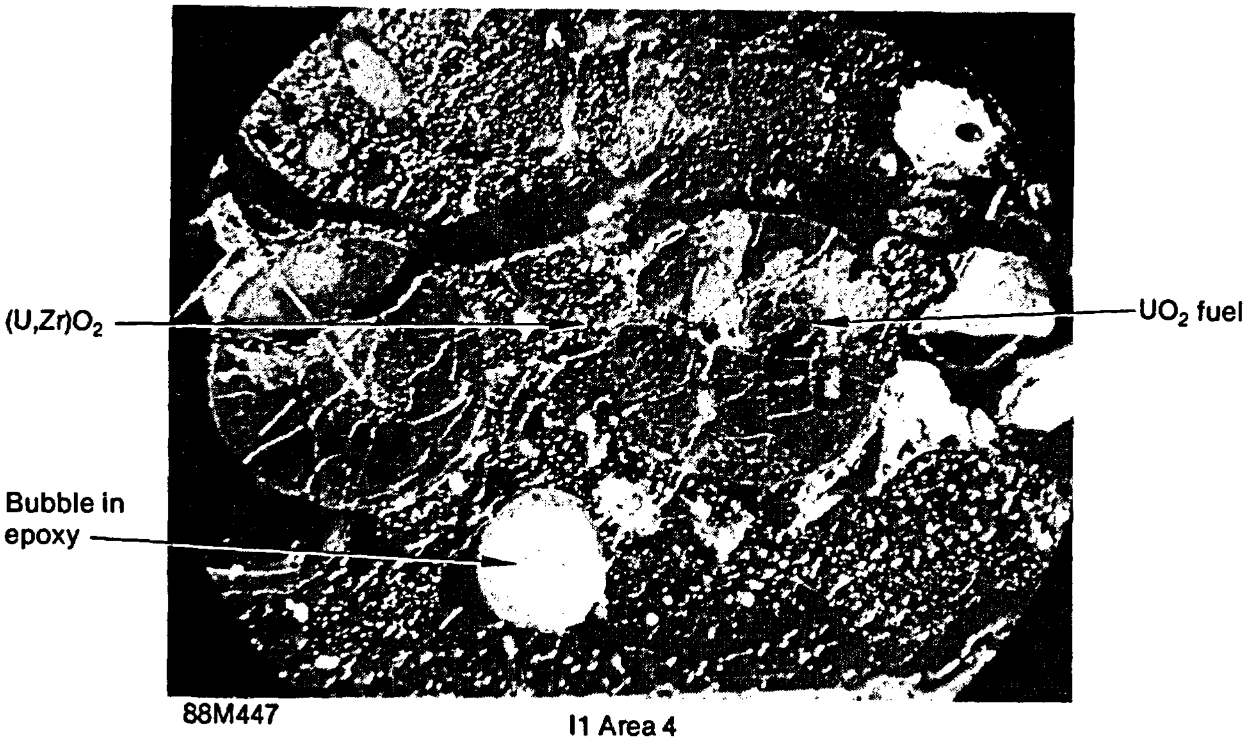

Figure 72. Details of metallographic cross section I1 at 0.66 m.

88M448 I1 Area 5

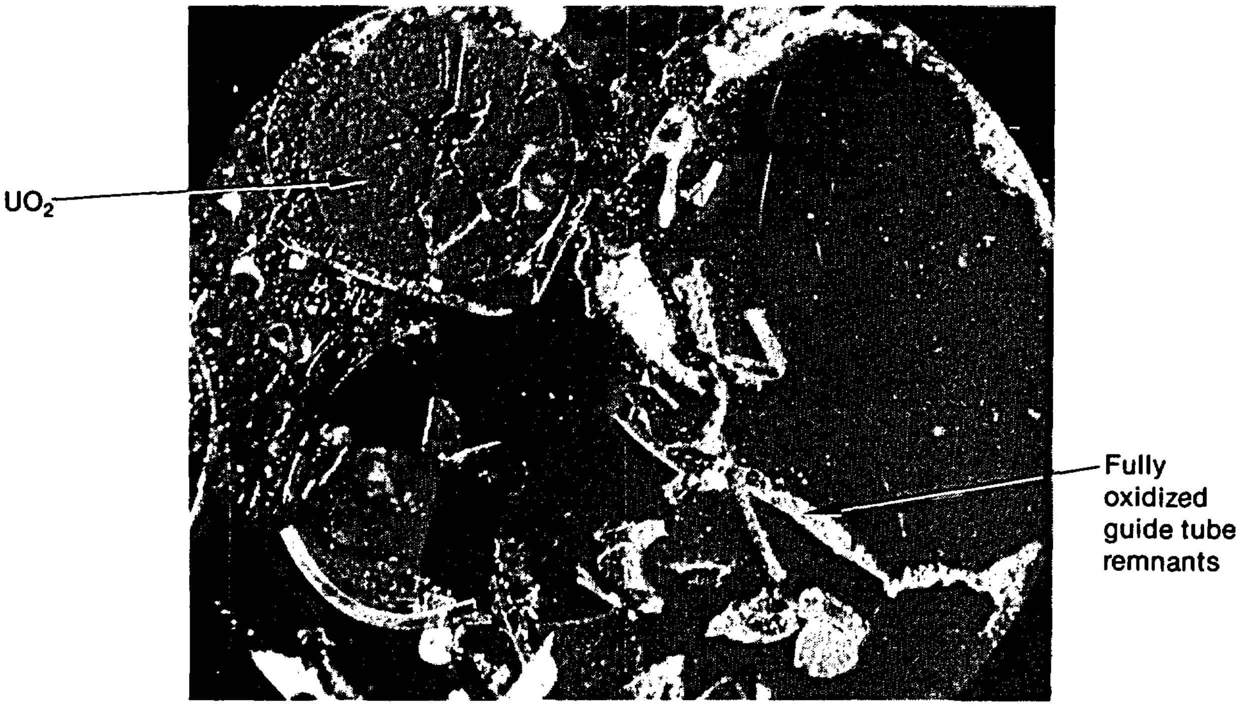

88M449 I1 Area 6

Figure 73. Details of metallographic cross section I1 at 0.66 m.

88M450 I1 Area 7

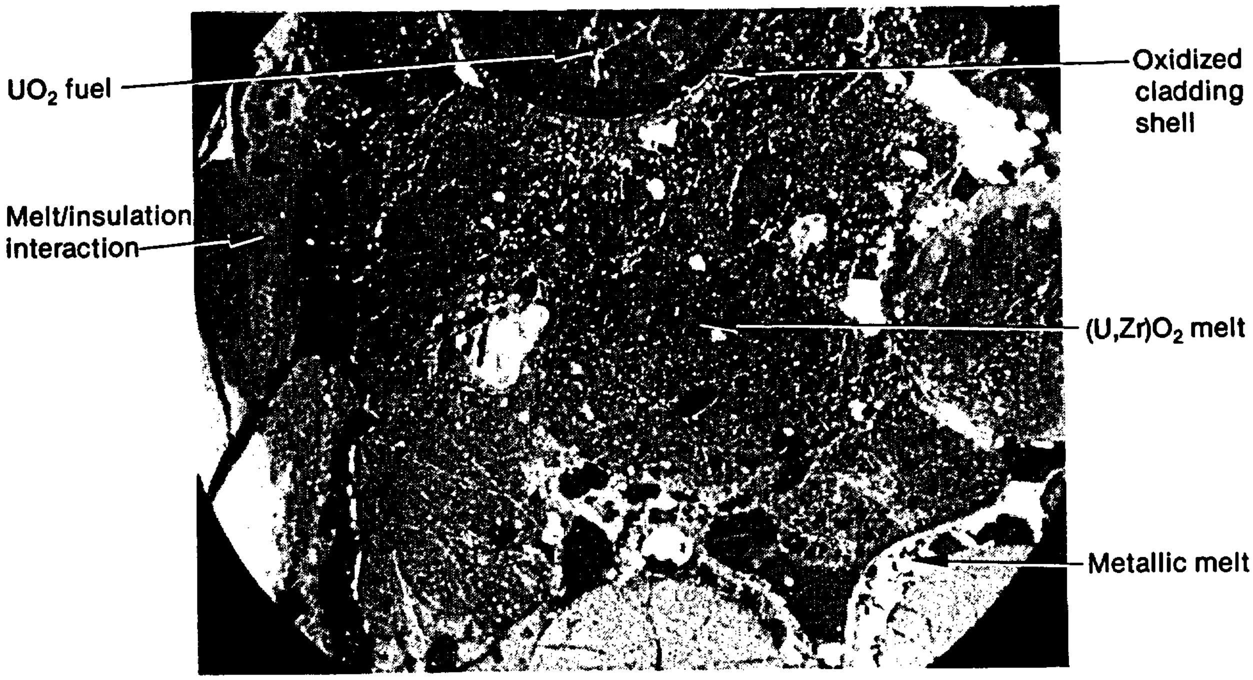

88M451 I1 Area 8

Figure 74. Details of metallographic cross section I1 at 0.66 m.

88M 452 I1 Area 9

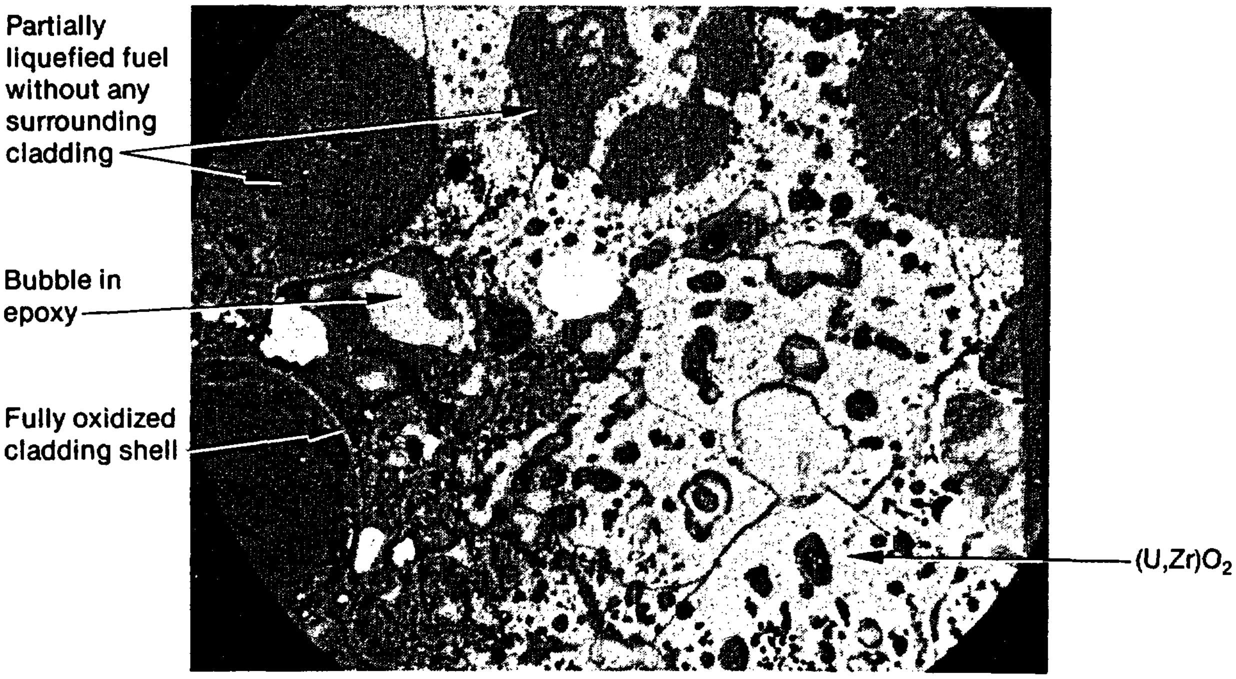

88M420 I2 Area 3

Figure 75. Details of metallographic cross section I1 and I2 at 0.66 m.

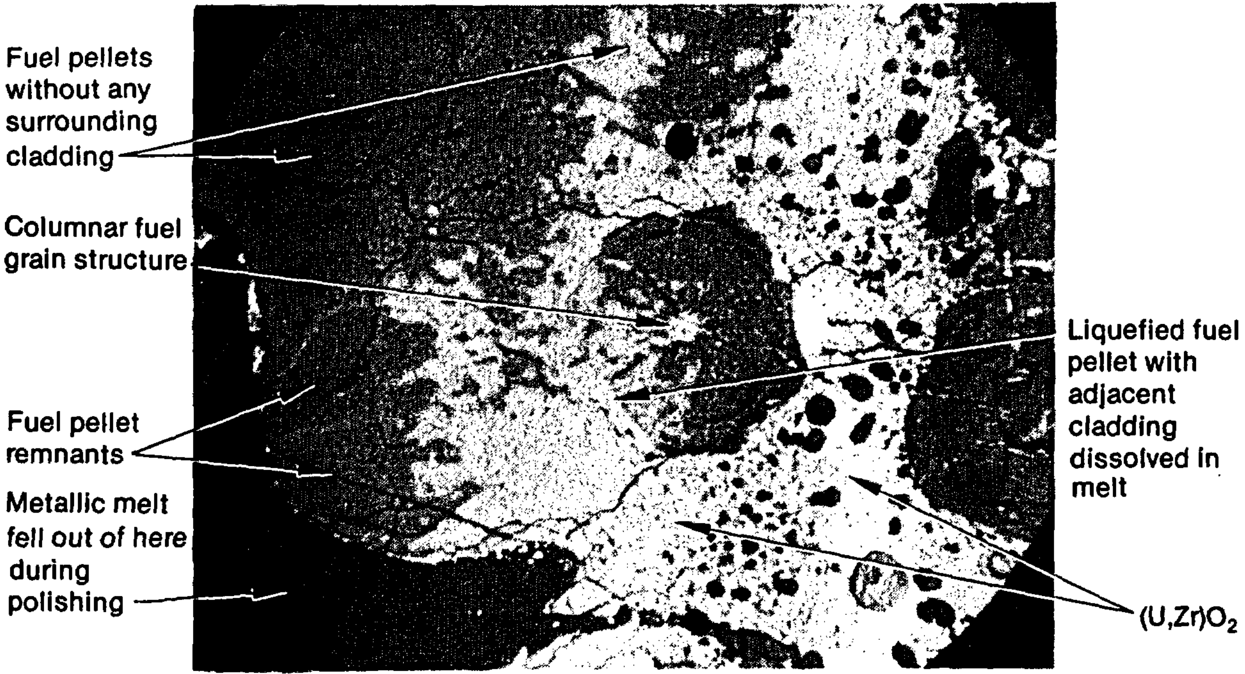

I2 Area 4

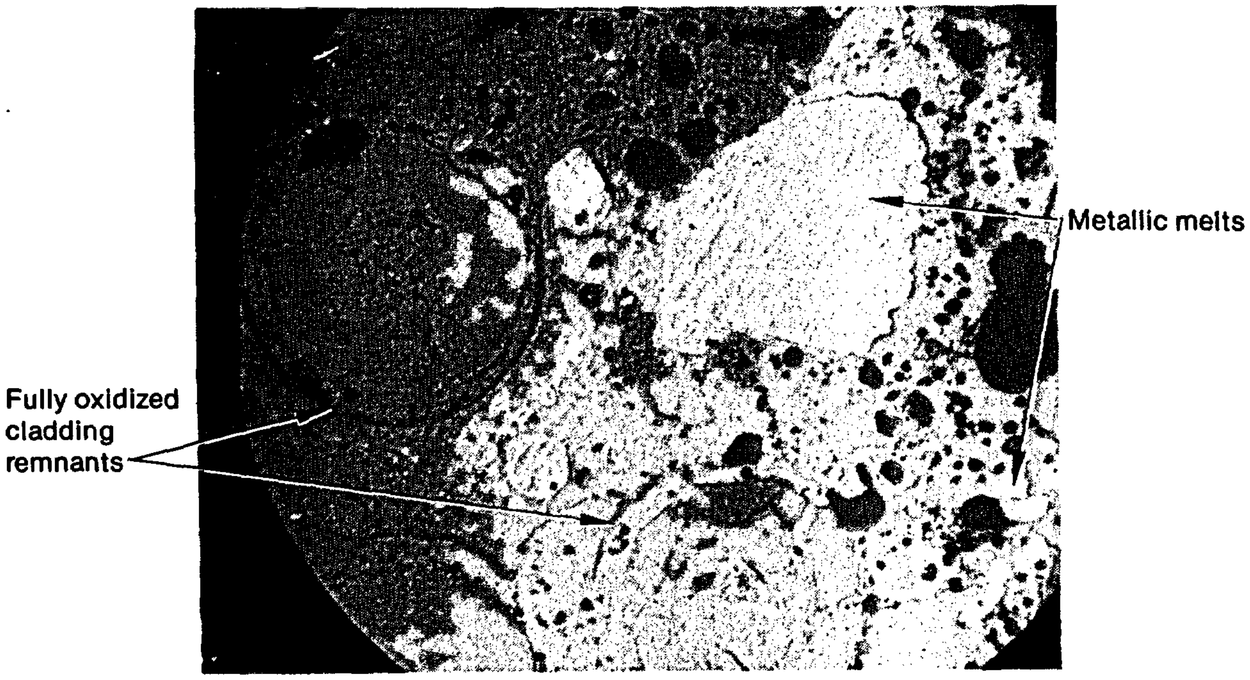

I2 Area 5

Figure 76. Details of metallographic cross section I2 at 0.66 m.

I2 Area 6

I2 Area 7

Figure 77. Details of metallographic cross section I2 at 0.66 m.

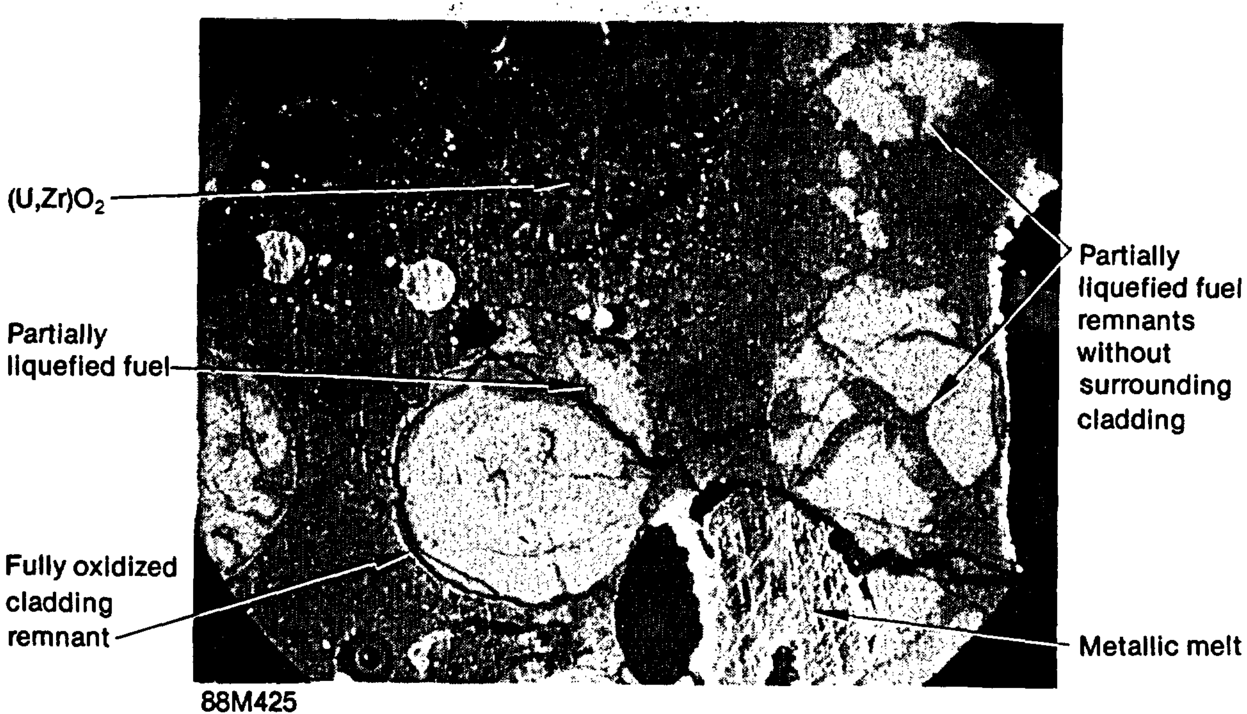

I2 Area 8

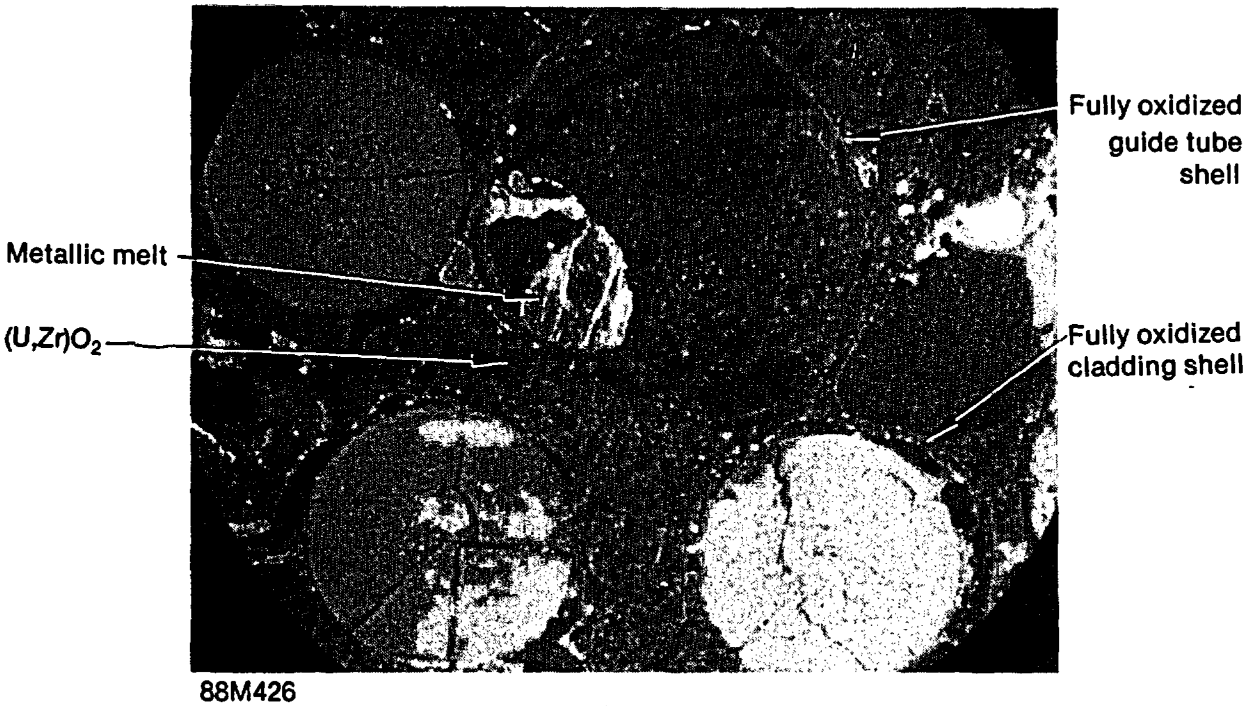

I2 Area 9

Figure 78. Details of metallographic cross section I2 at 0.66 m.

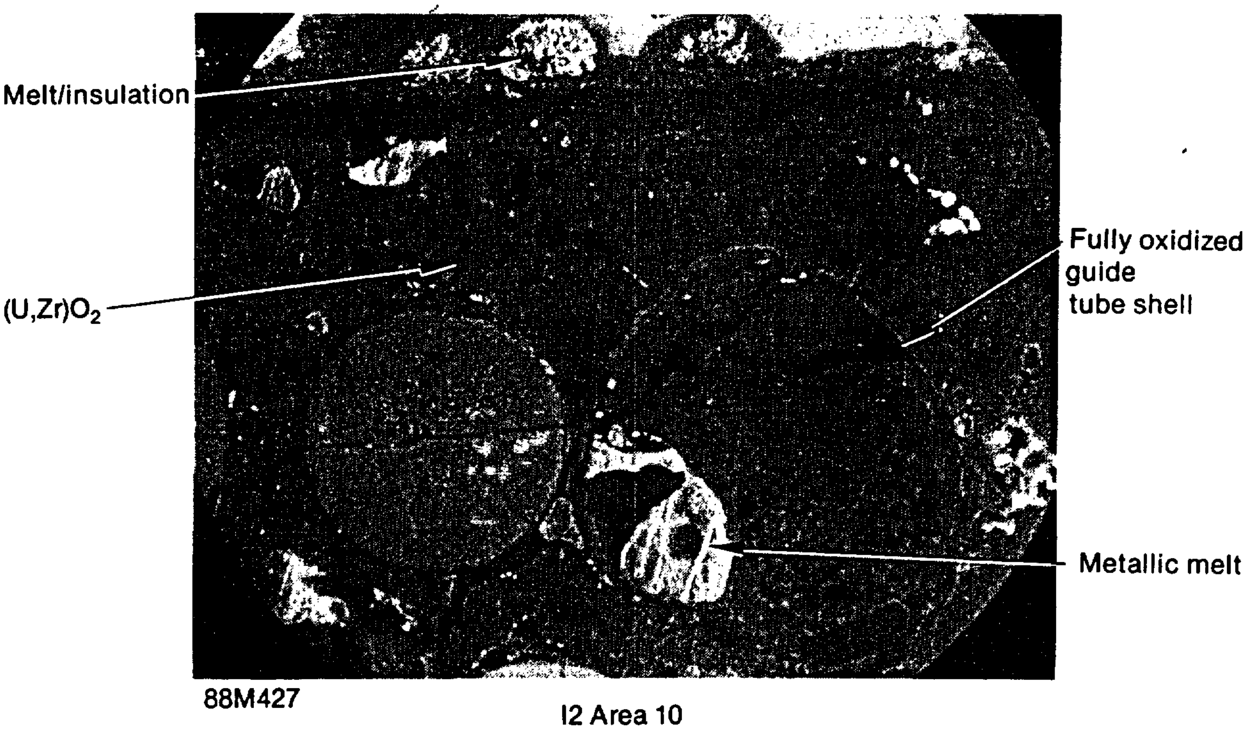

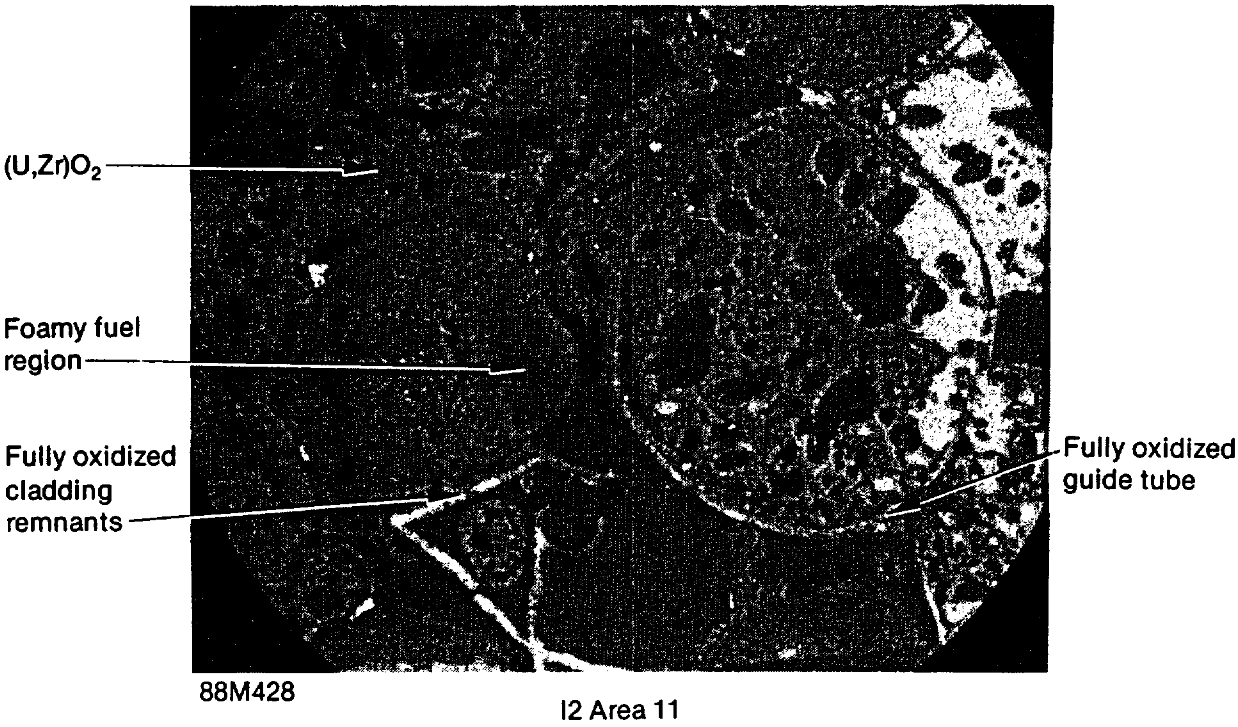

Figure 79. Details of metallographic cross section I2 at 0.66 m.

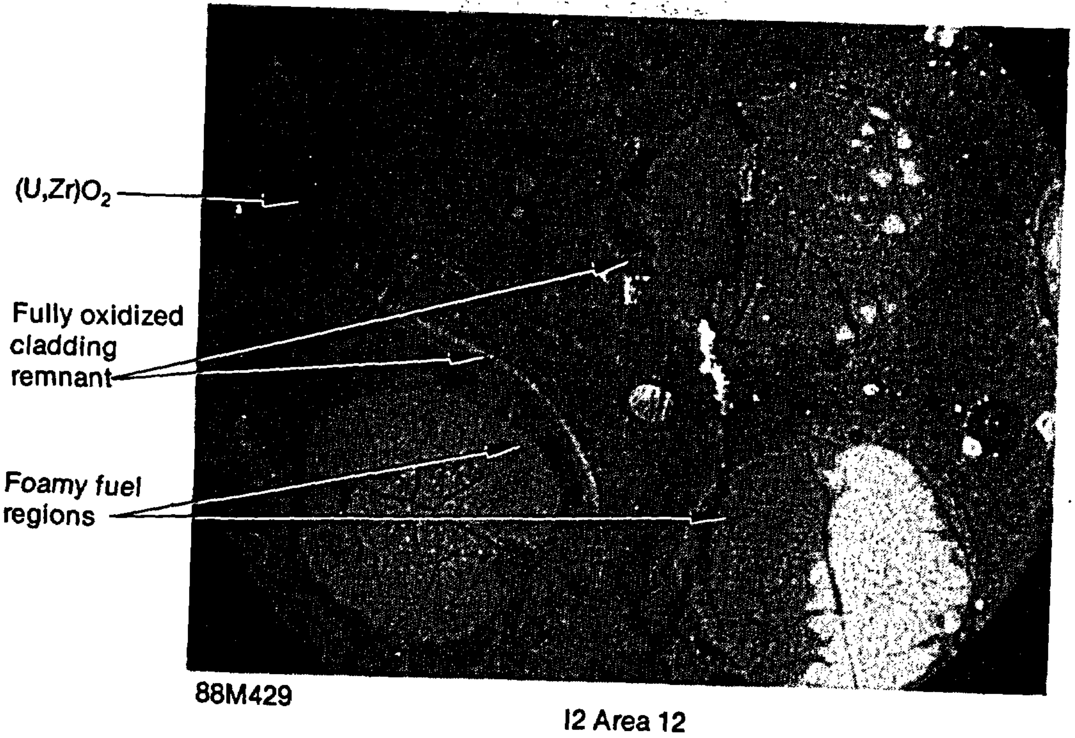

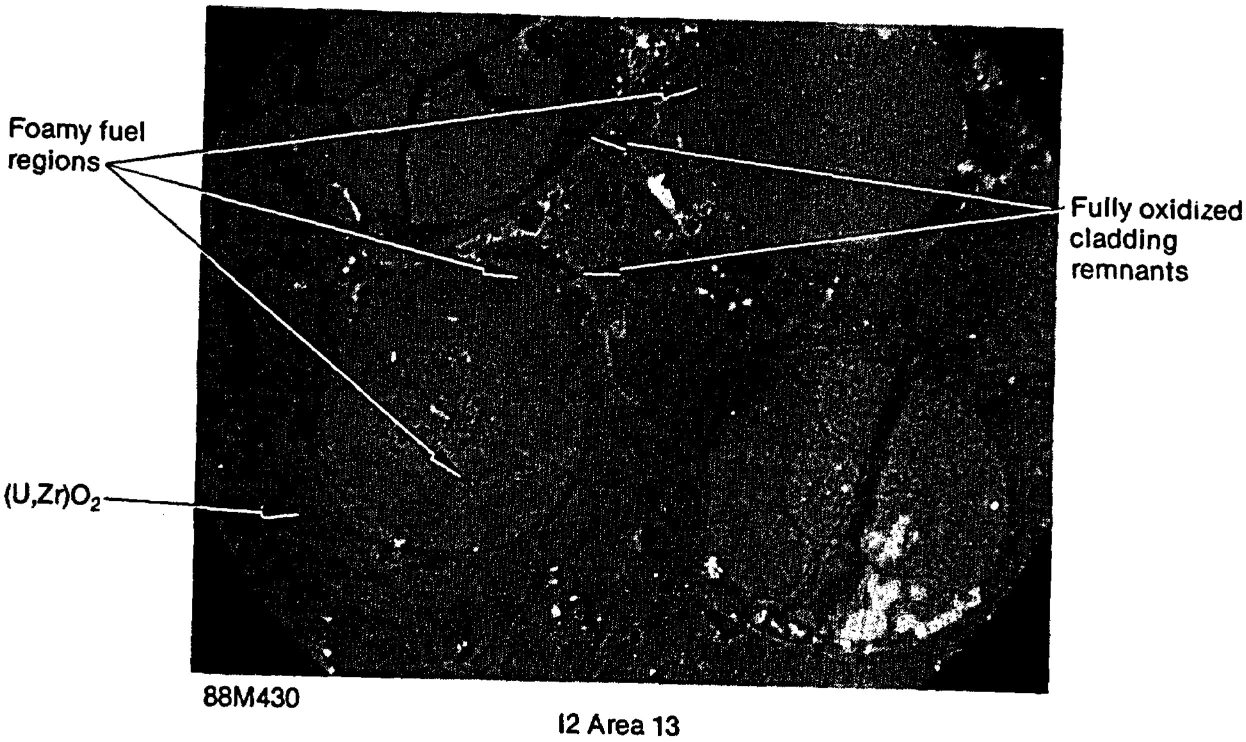

Figure 80. Details of metallographic cross section I2 at 0.66 m.

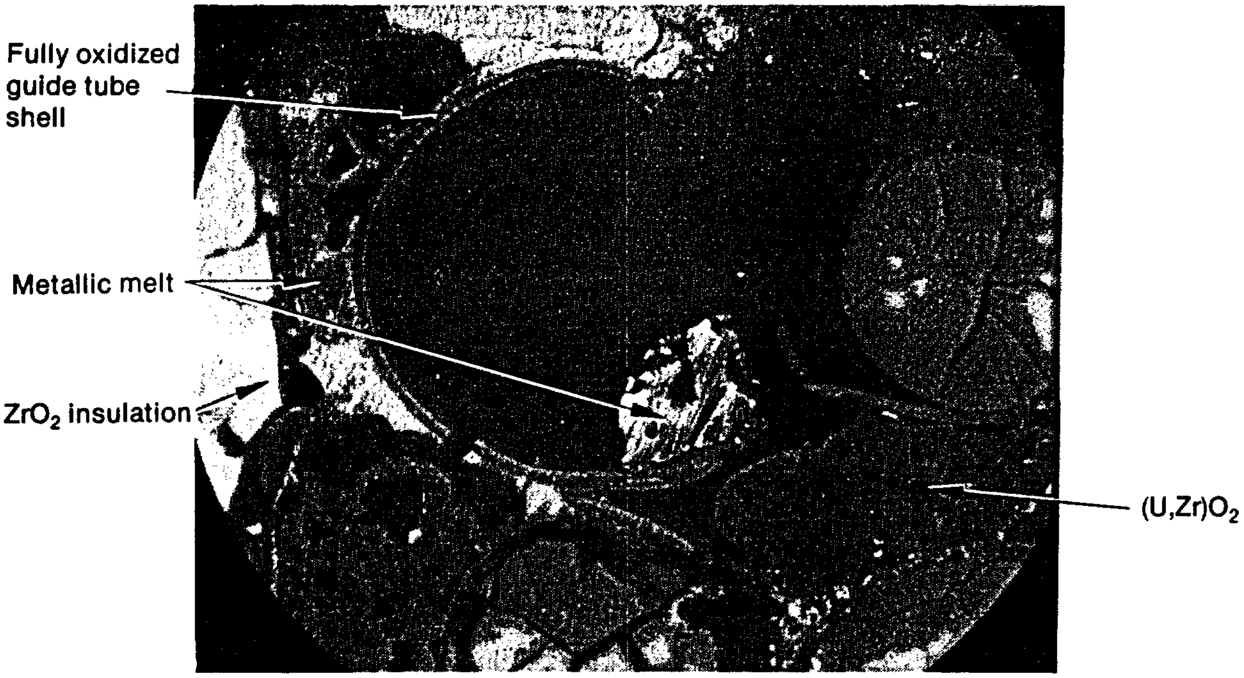

88M431 I2 Area 14

88M556 I3 Area 1

Figure 81. Details of metallographic cross section I2 and I3 at 0.66 m.

88M491 I4 Area 1

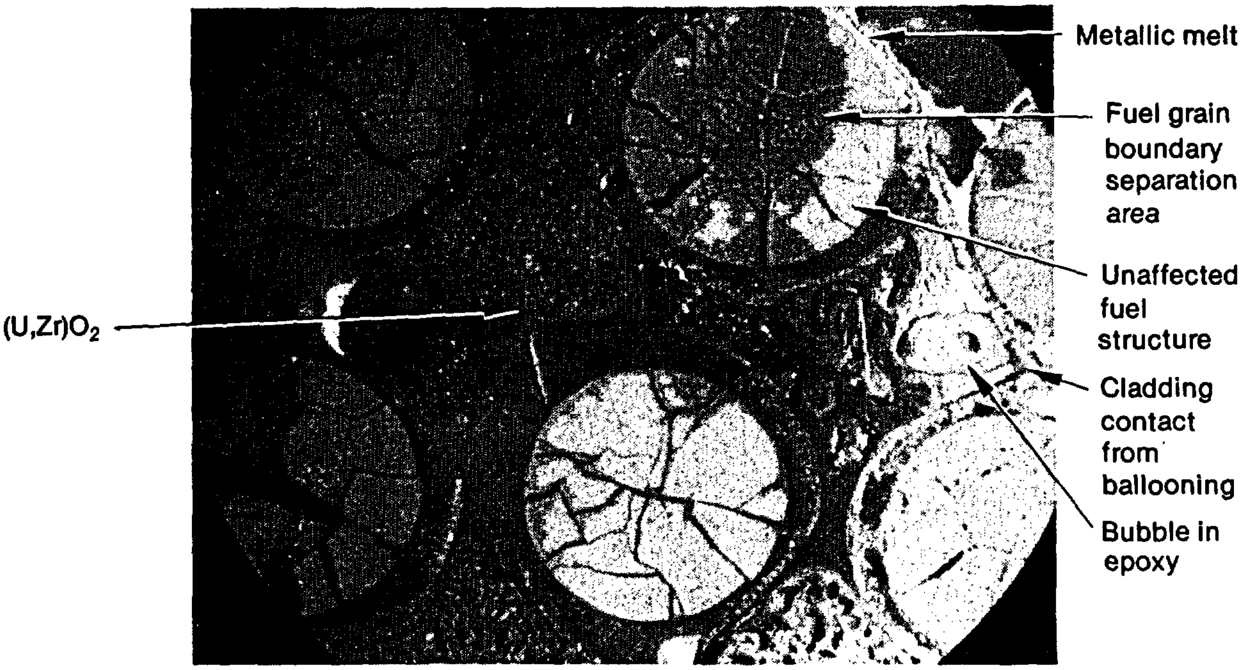

88M492 I4 Area 2

Figure 82. Details of metallographic cross section I4 at 0.66 m.

88M493 I4 Area 3

88M494 I4 Area 4

Figure 83. Details of metallographic cross section I4 at 0.66 m.

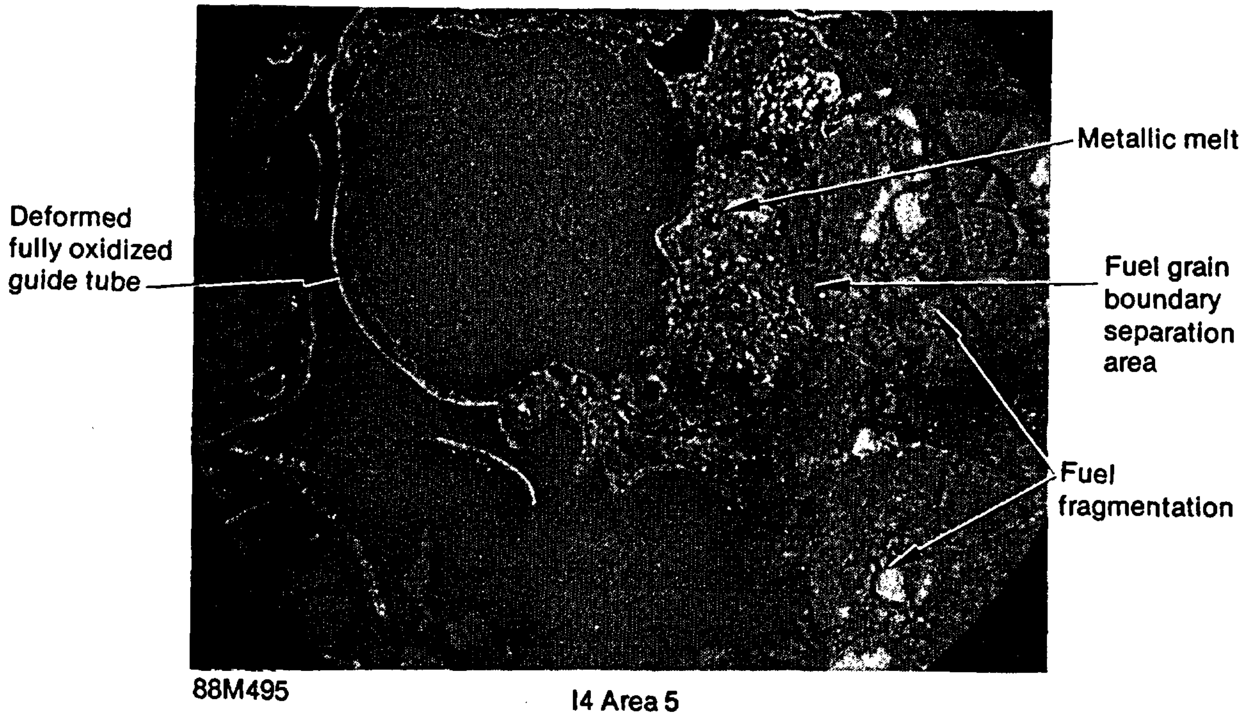

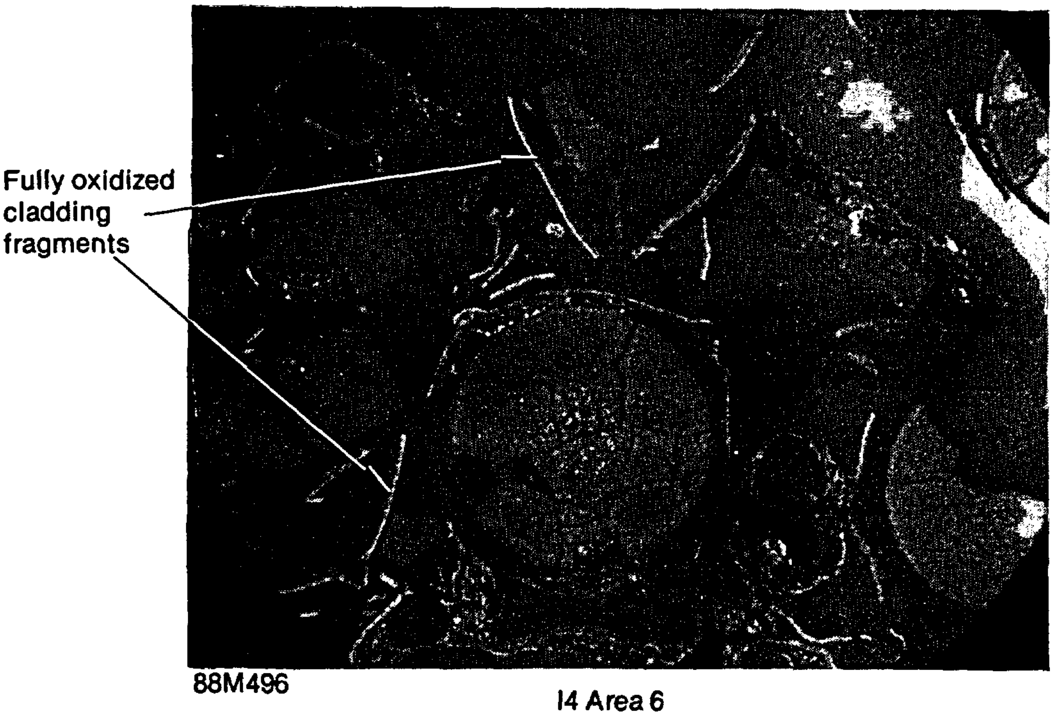

Figure 84. Details of metallographic cross section I4 at 0.66 m.

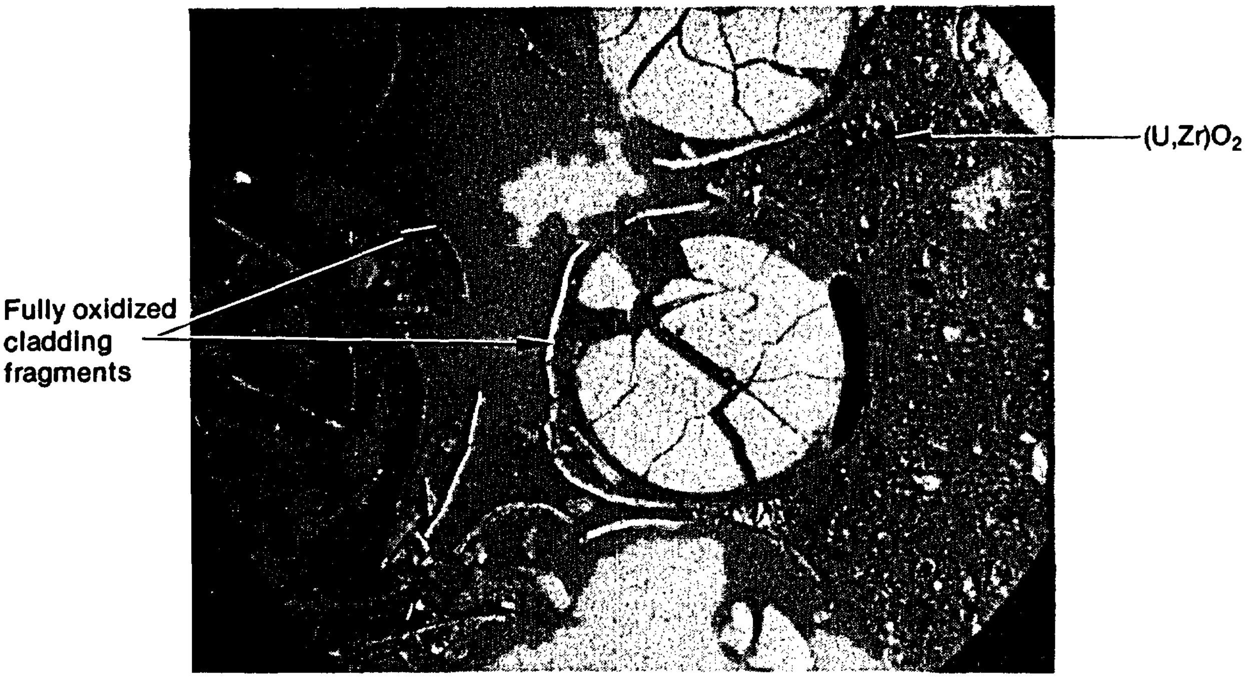

88M497 I4 Area 7

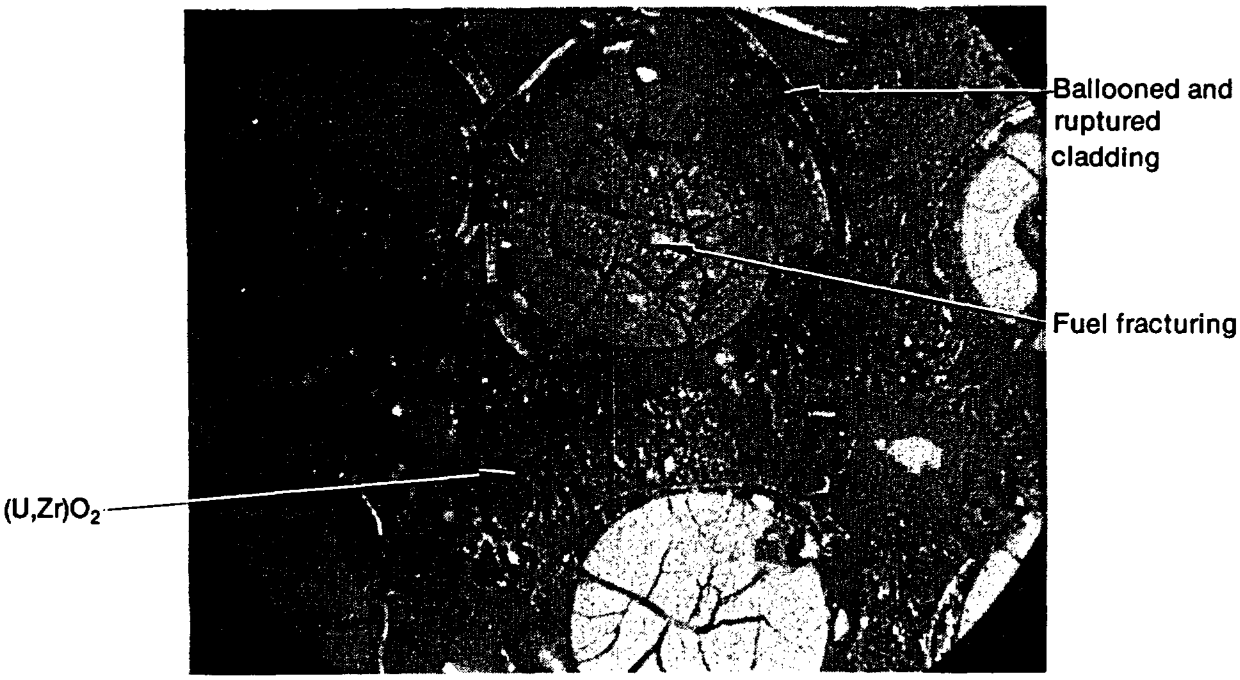

88M498 I4 Area 8

Figure 85. Details of metallographic cross section I4 at 0.66 m.

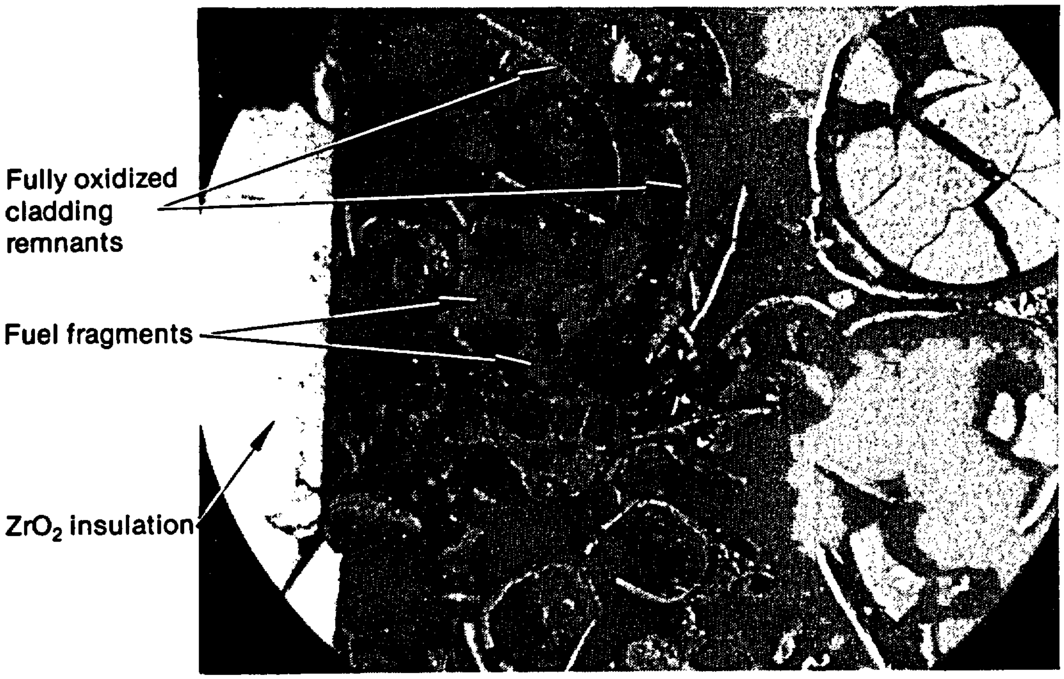

88M499 I4 Area 9

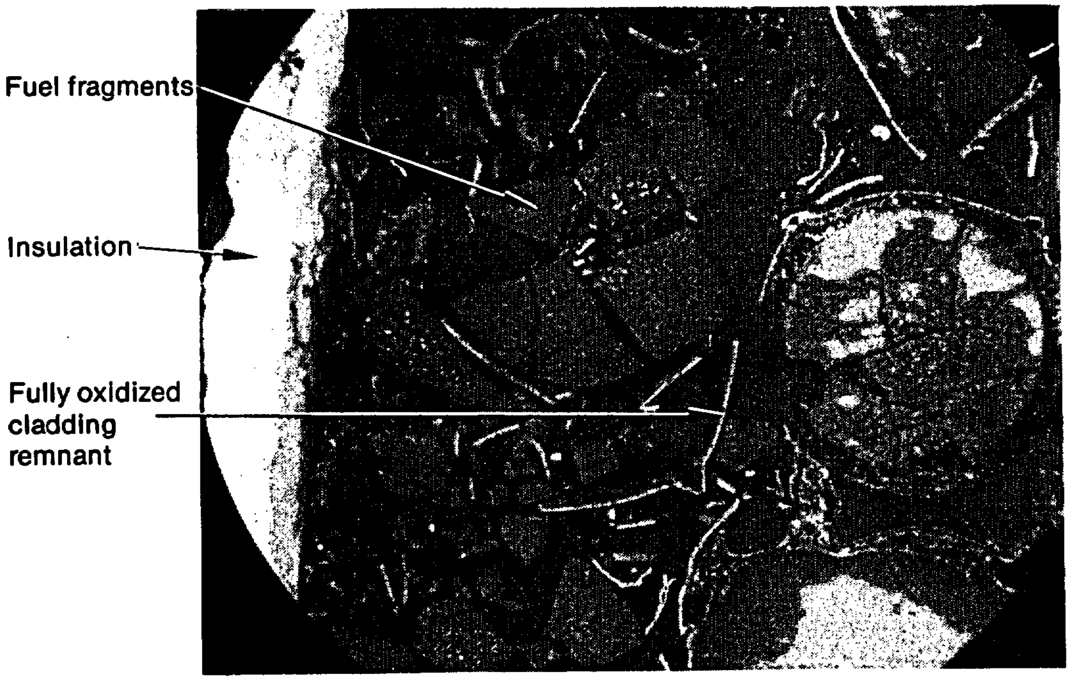

88M500 I4 Area 10

Figure 86. Details of metallographic cross section I4 at 0.66 m.

penetrate into the ZrO_2 insulation. Fuel pellet and cladding fracturing was more apparent in peripheral and corner locations, where they were not restrained by surrounding melts and where they were exposed to water during reflood. The extent of the metallic melts was very limited compared to the amount of ceramic melt present, and these metallic melts were generally limited to localized areas or droplets. (Some air bubbles which were entrapped in the epoxy sometimes resemble metallic droplets. The bubbles can be distinguished by their blurry, featureless characteristics, as compared to the sharp, bright, metallic melts.) The northeast corner once again had the greatest amount of damage, and it had the largest amount of relocated ceramic melt. The majority of the ceramic melt had extensive closed porosity, as a result of steam and fission gasses being trapped in the melt; however, there was a ceramic melt region in the northeast quadrant that did not contain any significant porosity. The L-shaped dark region contained within the nonporous melt region previously contained a metallic melt that fell out during sample preparation. This metallic melt may have contained Al_2O_3 from the spacers at the top of the fuel column, since elemental analysis of a core bore sample from the nonporous ceramic melt region showed large amounts of aluminum.

3.1.11 Cross Section J (0.77 m; Figures 87-93)

This cross section was through the middle of the ceramic melt blockage region. Extensive amounts of ceramic $(U,Zr)O_2$ melt surrounded the fuel rod array. In Figure 88 is an area in which fuel no longer remained, surrounded by fuel pellets without any oxidized cladding shells surrounding them. As described in more detail in Section 4.3.3, this suggests that temperatures in the core of the upper blockage region reached fuel melting (>3120 K), with temperatures of $2960 \text{ K} < T < 3120 \text{ K}$ in the regions where the oxidized cladding melted. Towards the periphery of the ceramic melt, temperatures were less than the 2960 K required to melt the ZrO_2 oxidized cladding shells.

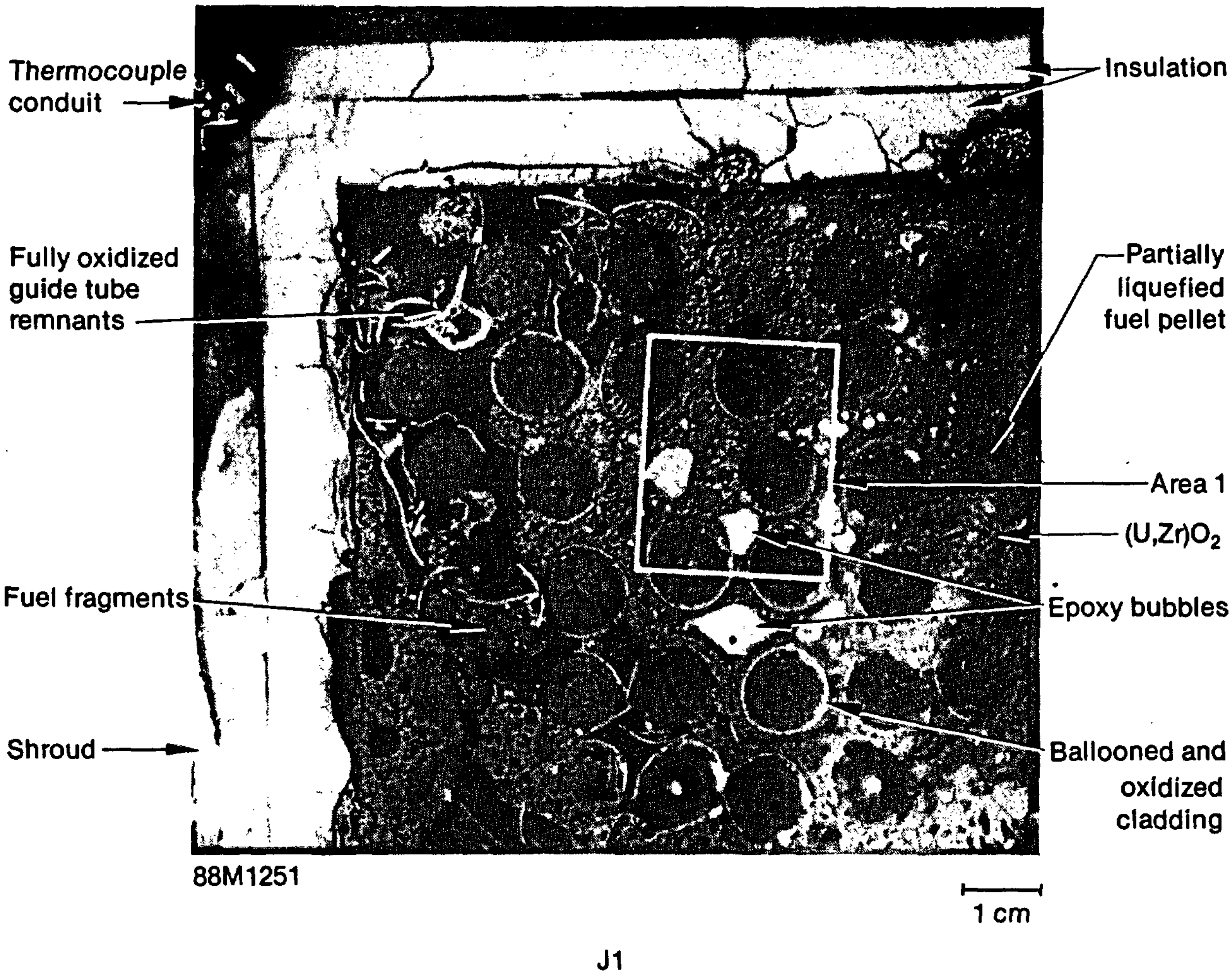

Figure 87. Metallographic cross section J1 at 0.77 m above the bottom of the instrumented fuel rods.

Figure 88. Metallographic cross section J2 at 0.77 m above the bottom of the instrumented fuel rods.

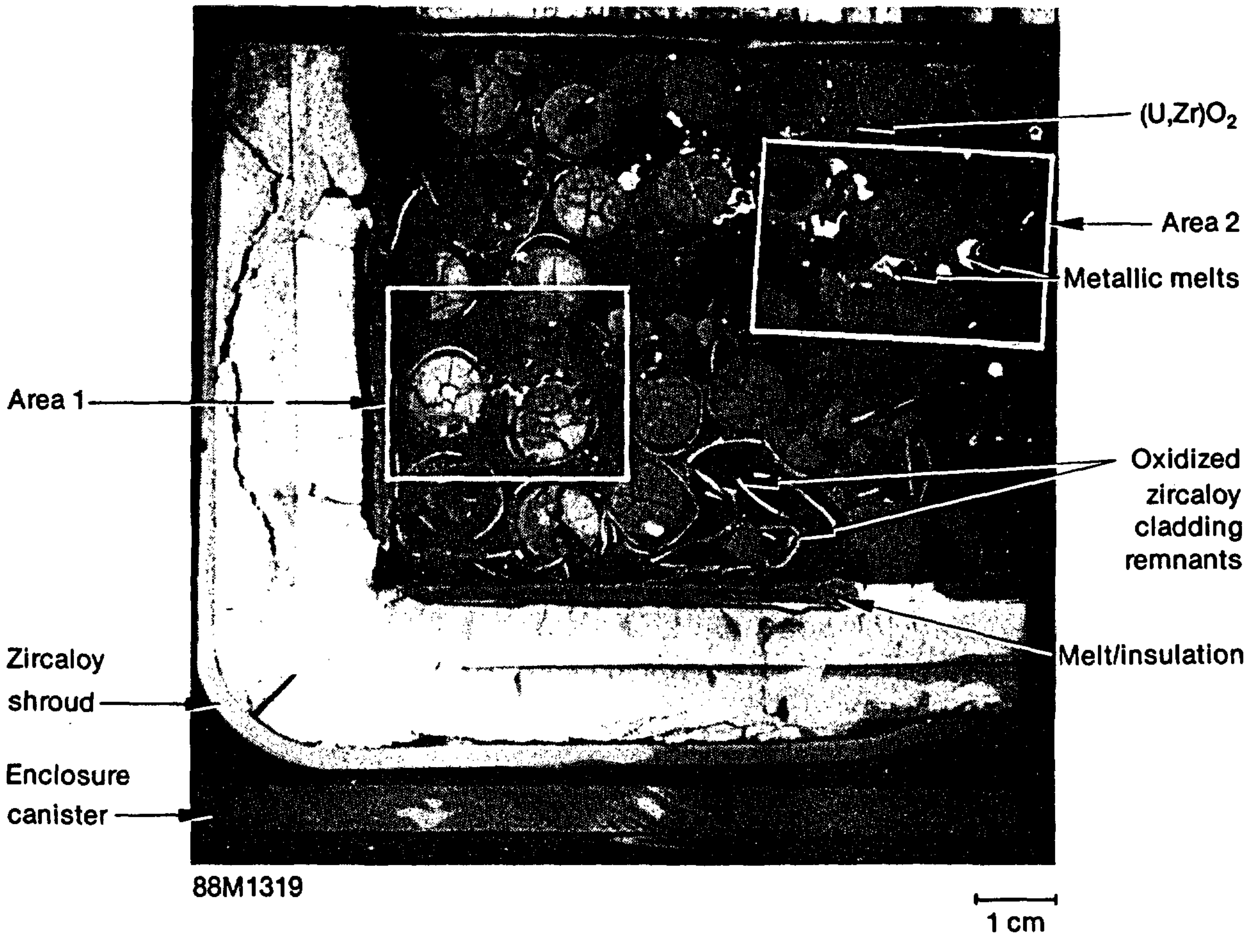

J3

Figure 89. Metallographic cross section J3 at 0.77 m above the bottom of the instrumented fuel rods.

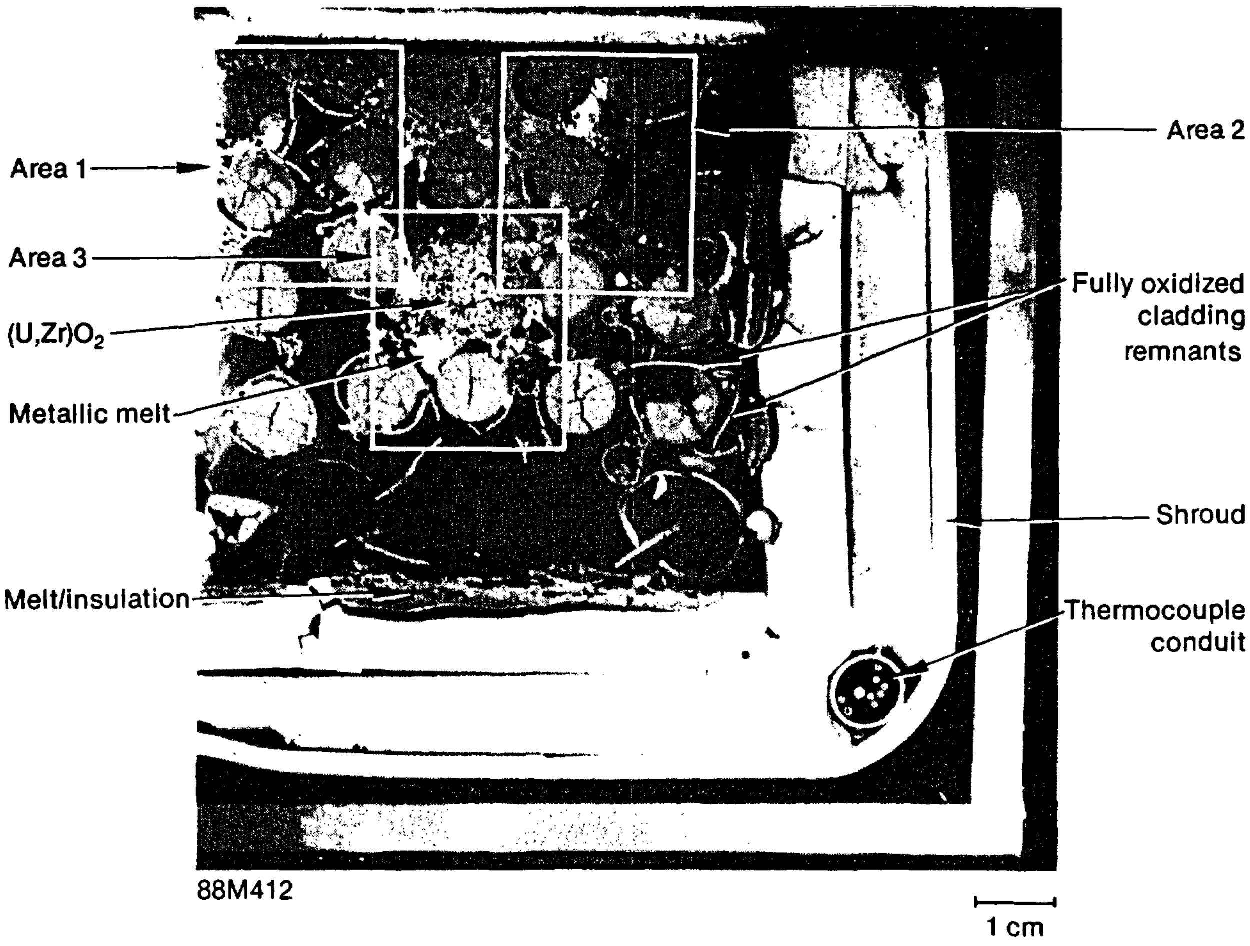

J4

Figure 90. Metallographic cross section J4 at 0.77 m above the bottom of the instrumented fuel rods.

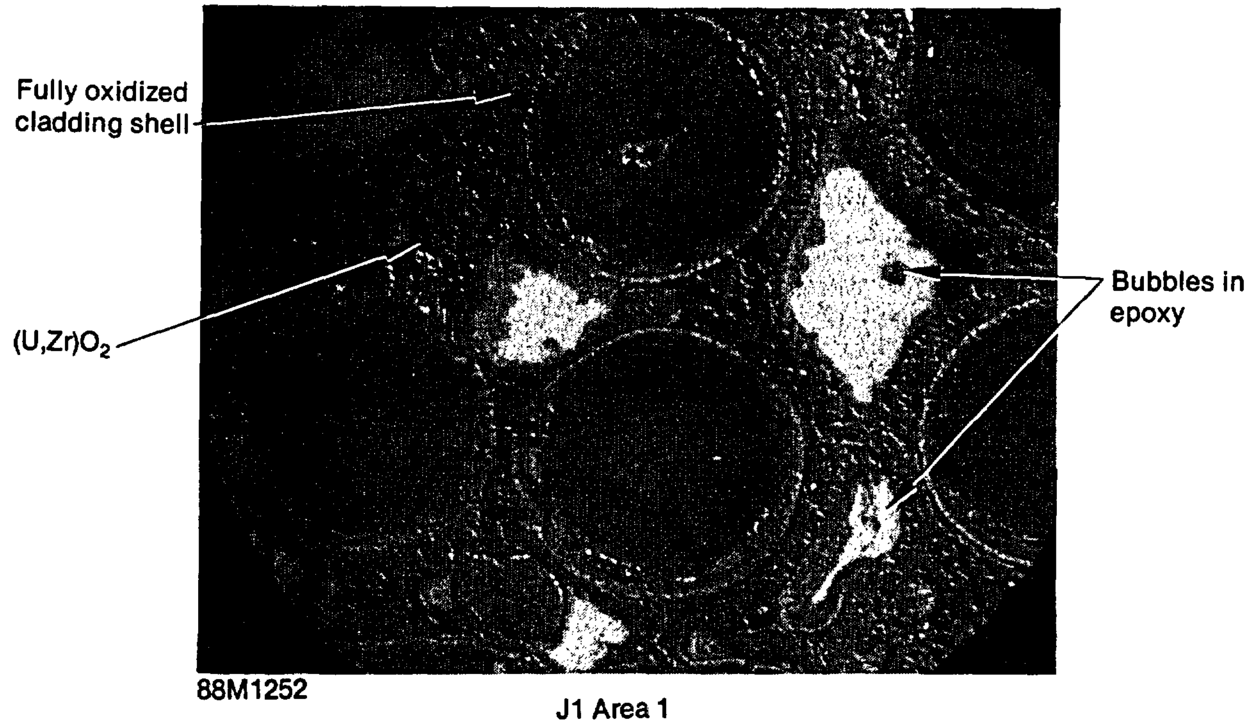

J1 Area 1

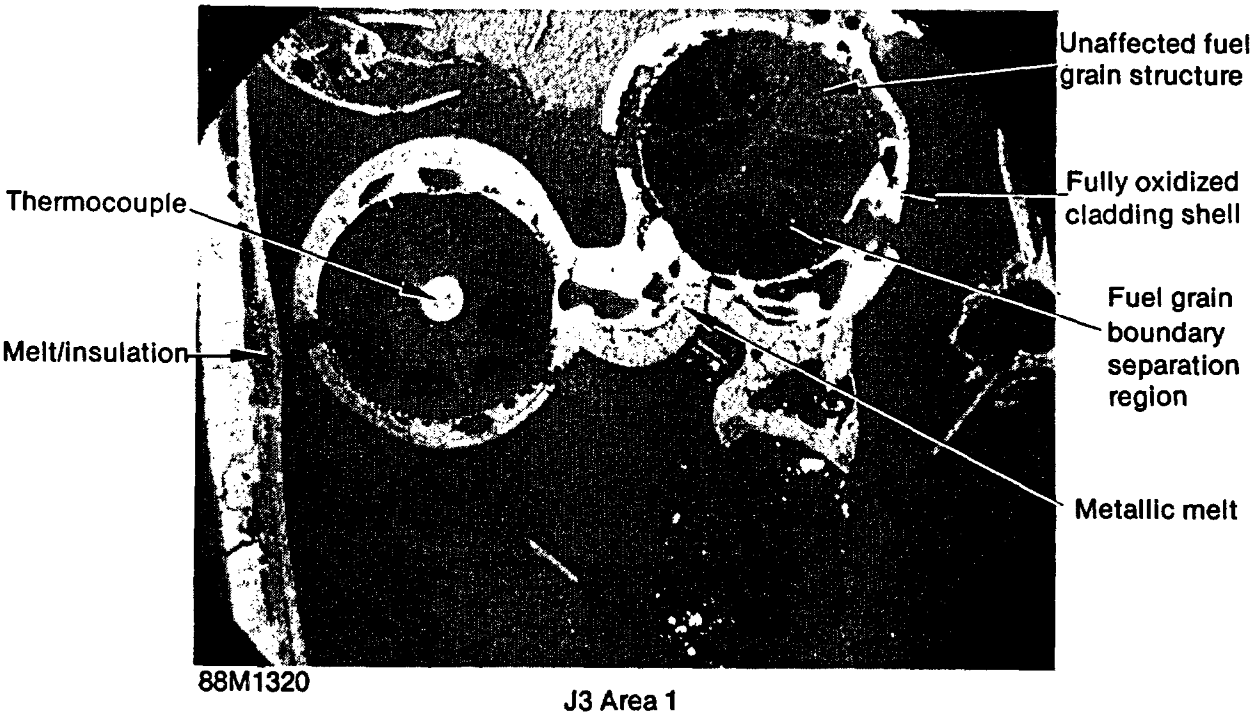

J3 Area 1

Figure 91. Details of metallographic cross sections J1 and J3 at 0.77 m.

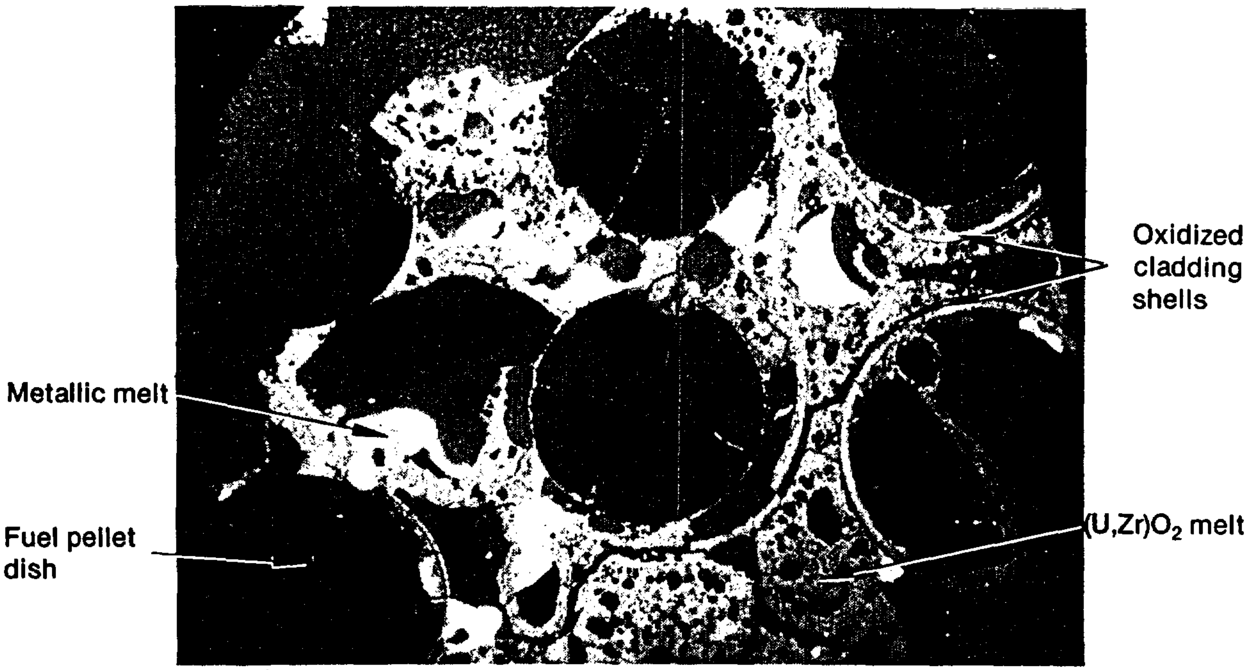

J3 Area 2

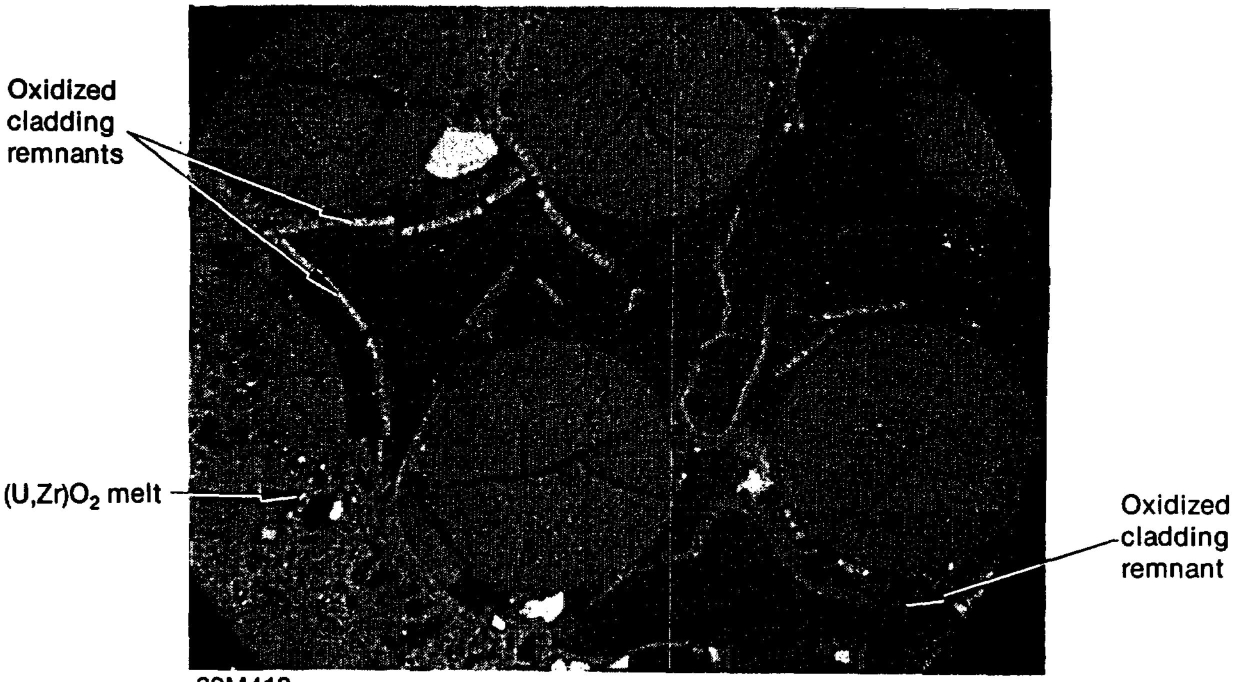

J4 Area 1

Figure 92. Details of metallographic cross sections J3 and J4 at 0.77 m.

88M414

J4 Area 2

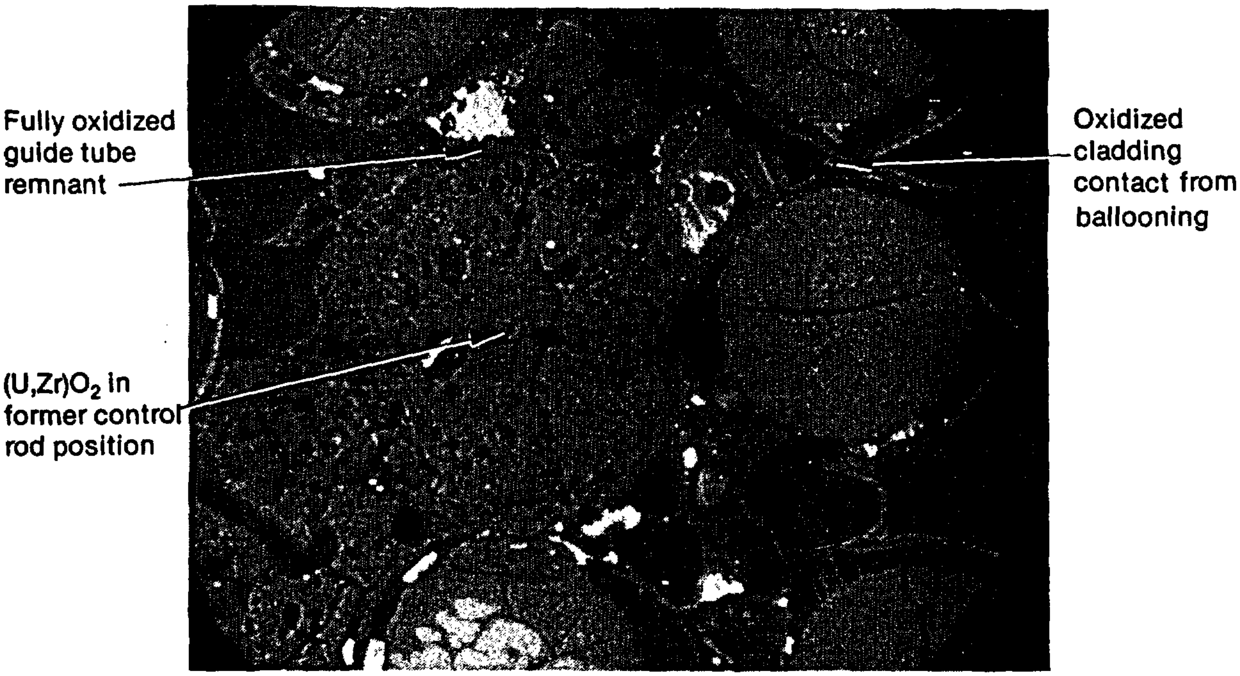

88M415

J4 Area 3

Figure 93. Details of metallographic cross section J4 at 0.77 m.

Dark and light regions within the ceramic melt were caused by uneven light conditions and polishing of these large samples. Therefore, the different shades in the melt regions do not represent compositional differences in the ceramic melt. However, different shades within a single fuel pellet do indicate differences in fuel behavior in general. Dark regions observed within a fuel pellet were caused by areas of grain boundary separation, or regions of foamy fuel, which reflected the light differently than the unaffected fuel regions (see Figure 89, for example). However, shade differences between different fuel pellets do not necessarily indicate differences in fuel behavior, because of the same polishing and lighting problems noted in conjunction with the ceramic melt regions. (Note the difference in shades between fuel pellets in Figures 87 and 88.)

Cladding ballooning and rod-to-rod contact were present; and, in areas where the cladding was not surrounded by melts, it fragmented and portions relocated. The fuel centerline thermocouples that were routed upward are visible in several of the fuel pellets. Several air bubbles were trapped within the epoxy at this elevation.

3.1.12 Cross Section K (0.88 m; Figures 94-102)

This cross section was through the upper portion of the large ceramic melt region, where the third spacer grid was originally located. There was a large agglomeration of metallic melt in Figure 94, which was associated with an atypical cracking pattern in the fuel pellets it surrounded. Significant fuel liquefaction occurred in some of the centrally located fuel pellets surrounded by the ceramic melt, as indicated by their smaller and irregularly shaped cross sections. All the zircaloy cladding was gone on several of the centrally located fuel rods, while the fully oxidized outer shells remained on other rods. As detailed in Section 4.3.3, these observations suggest that temperatures were in excess of 2960 K in the central melt regions where the ZrO_2 oxidized cladding shells no longer remain. SEM/WDS examinations of one fuel pellet in Figure 95 (K2-S32), which was surrounded by the ceramic melt, showed a porous structure indicative of temperatures near fuel melting.

K1

Figure 94. Metallographic cross section K1 at 0.83 m above the bottom of the instrumented fuel rods.

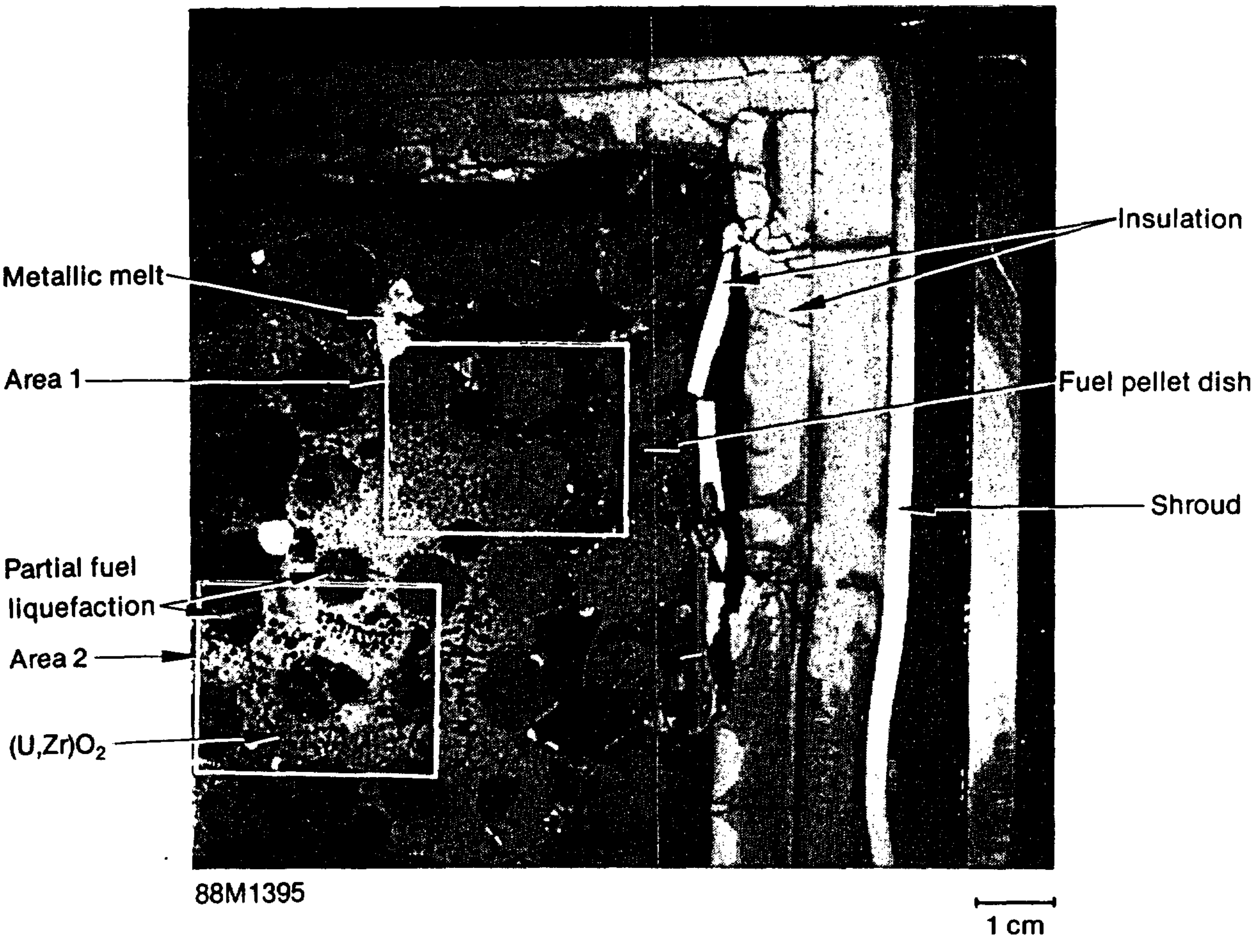

K2

Figure 95. Metallographic cross section K2 at 0.88 m above the bottom of the instrumented fuel rods.

K3

Figure 96. Metallographic cross section K3 at 0.88 m above the bottom of the instrumented fuel rods.

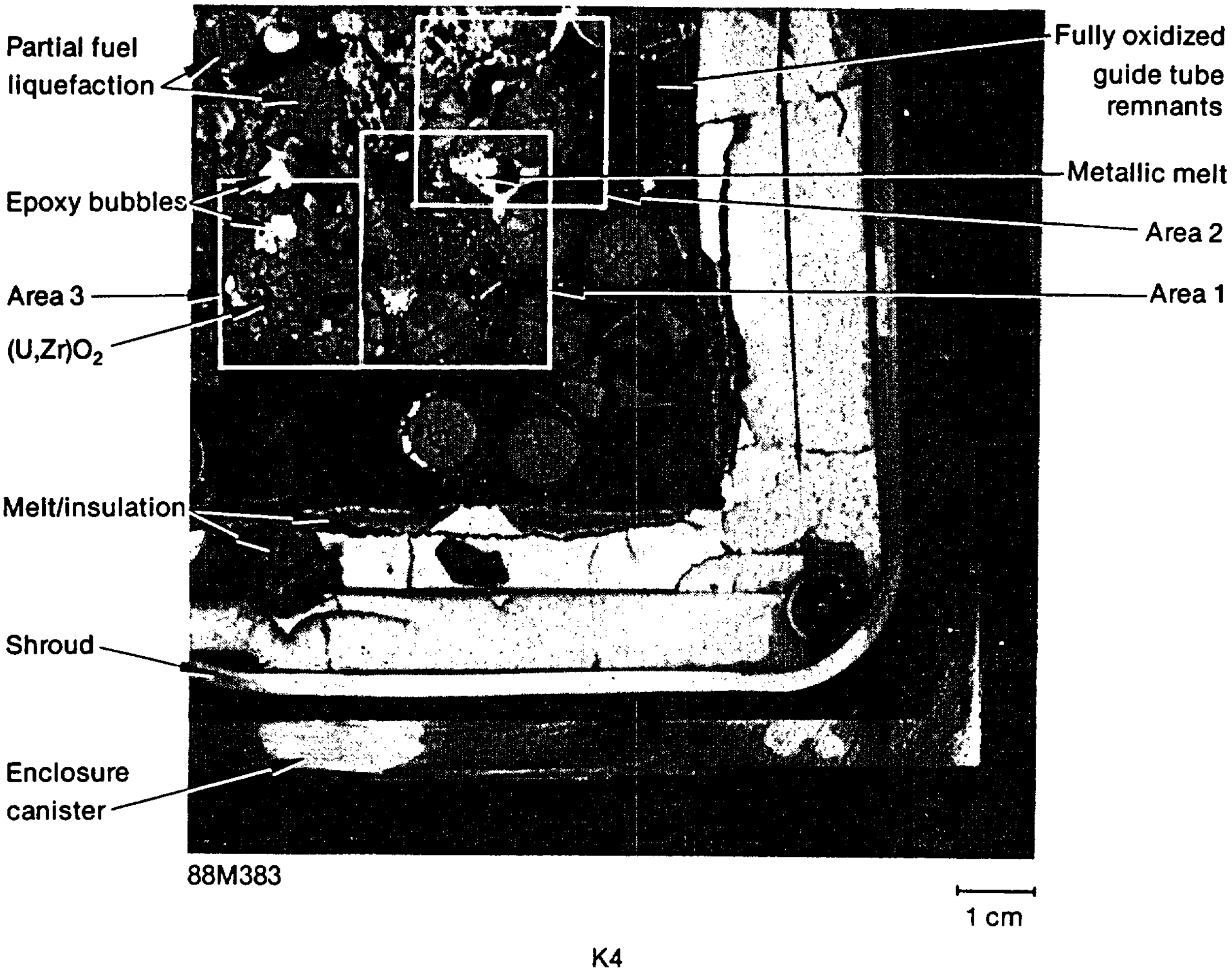

Figure 97. Metallographic cross section K4 at 0.88 m above the bottom of the instrumented fuel rods.

88M437

K1 Area 1

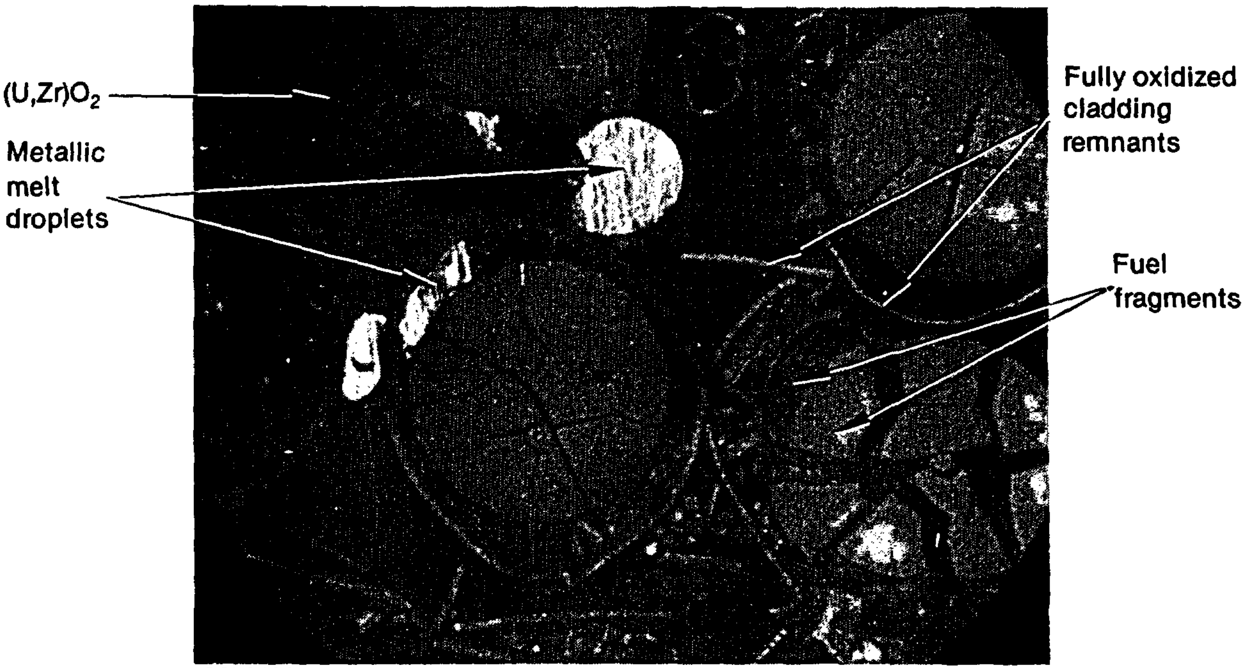

88M438

K1 Area 2

Figure 98. Details of metallographic cross section K1 at 0.88 m.

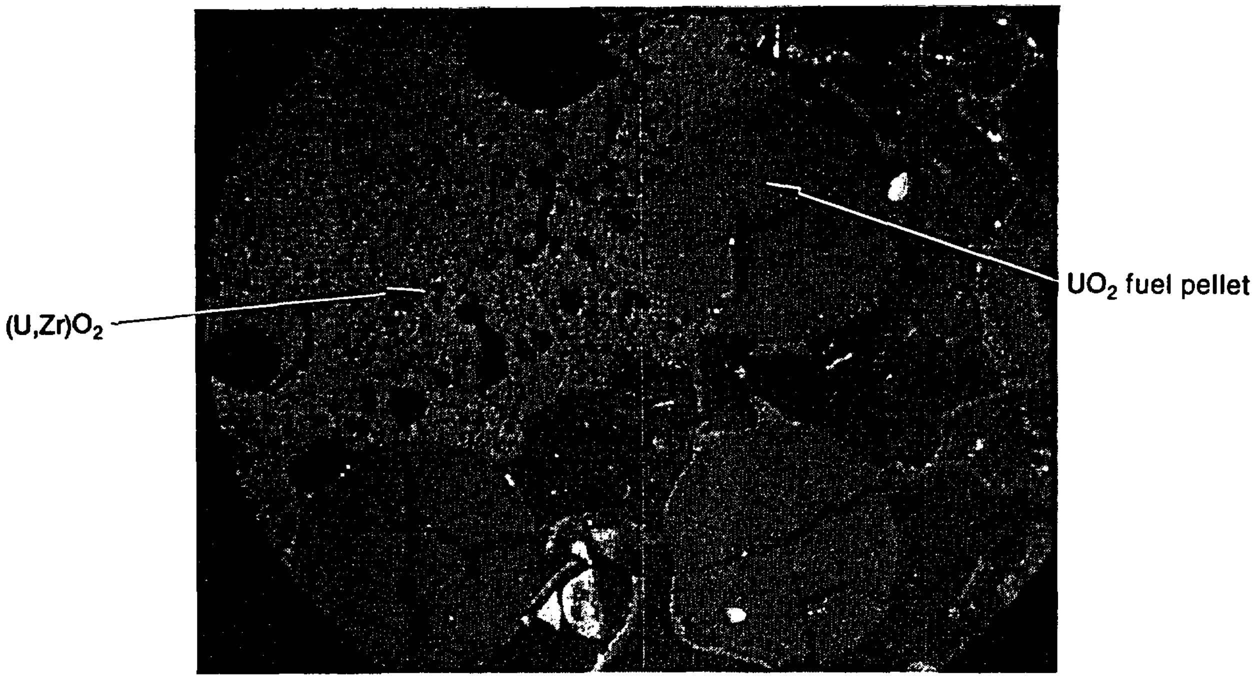

88M1396

K2 Area 1

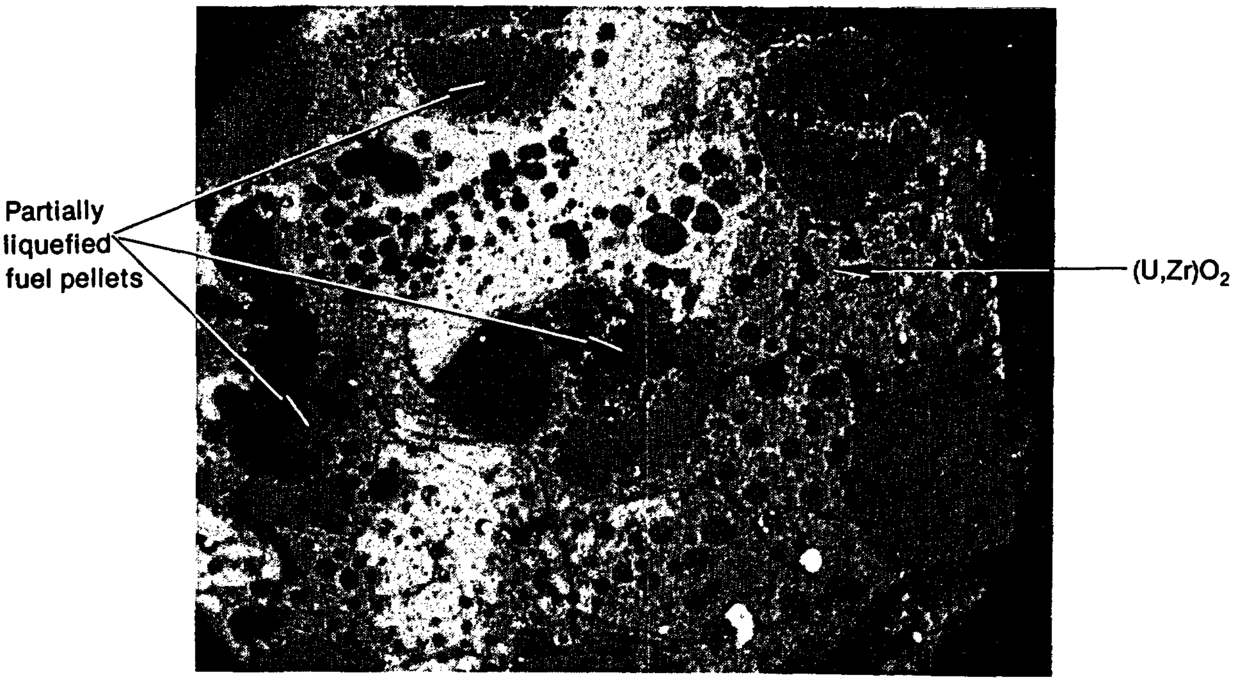

88M1401

K2 Area 2

Figure 99. Details of metallographic cross section K2 at 0.88 m.

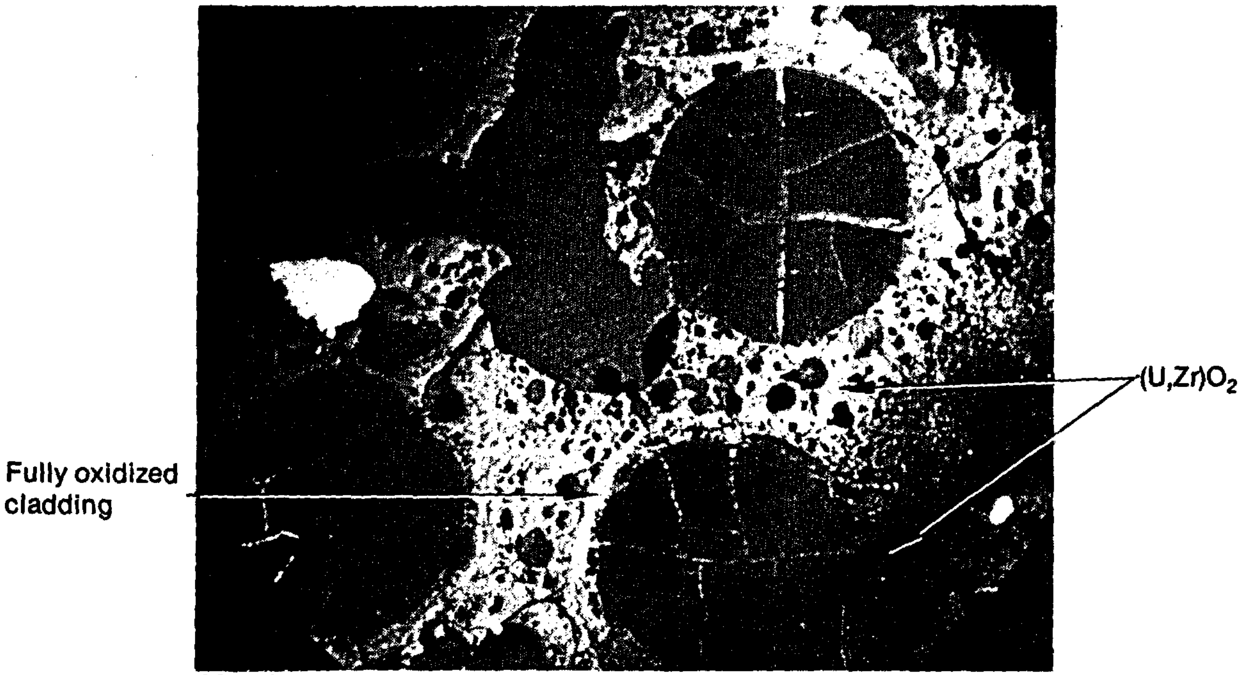

88M32

K3 Area 1

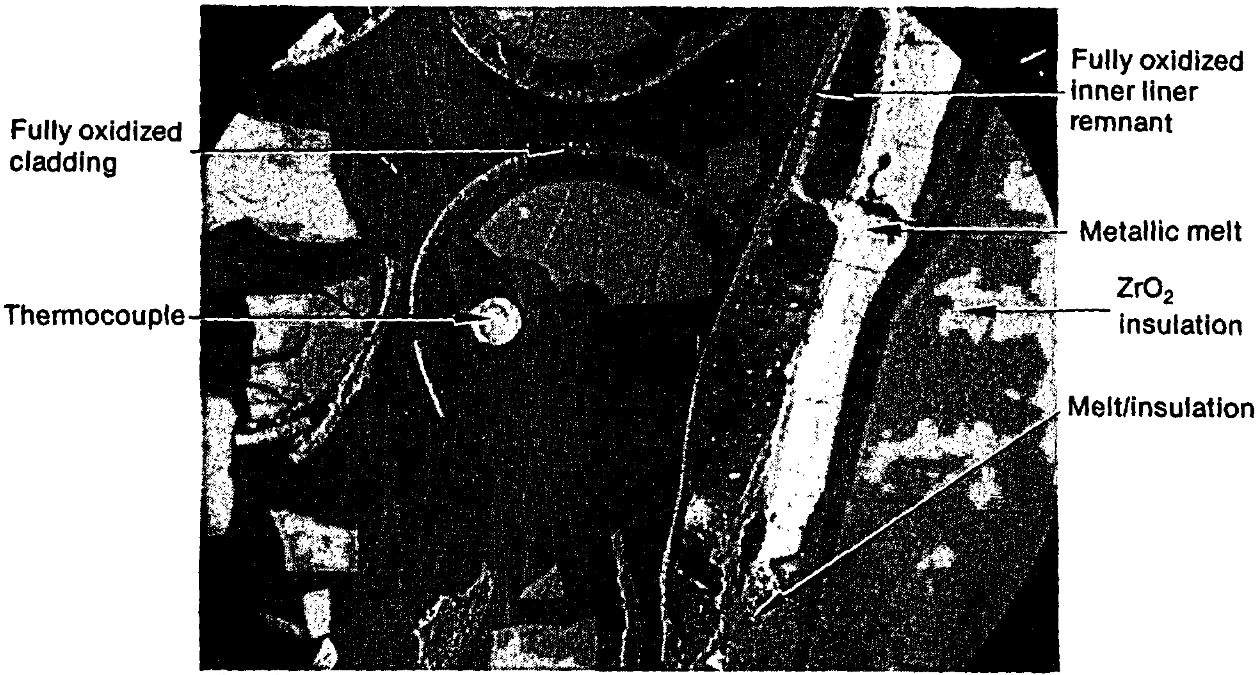

88M33

K3 Area 2

Figure 100. Details of metallographic cross section K3 at 0.88 m.

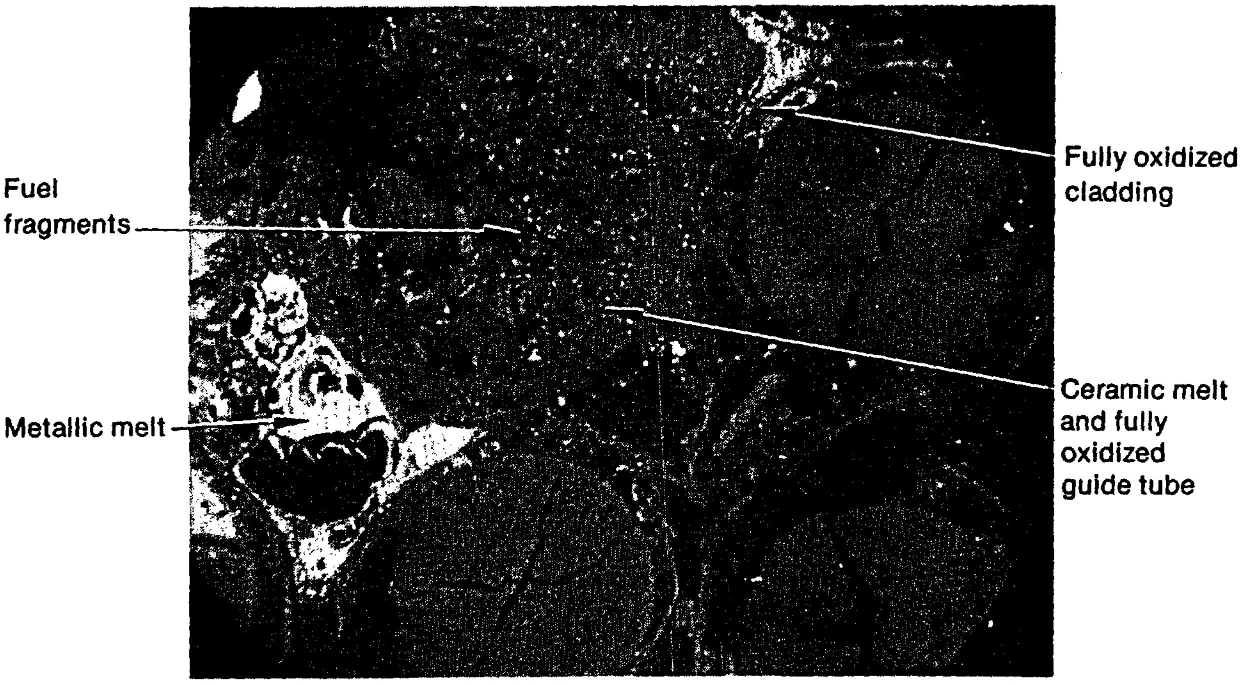

K4 Area 1

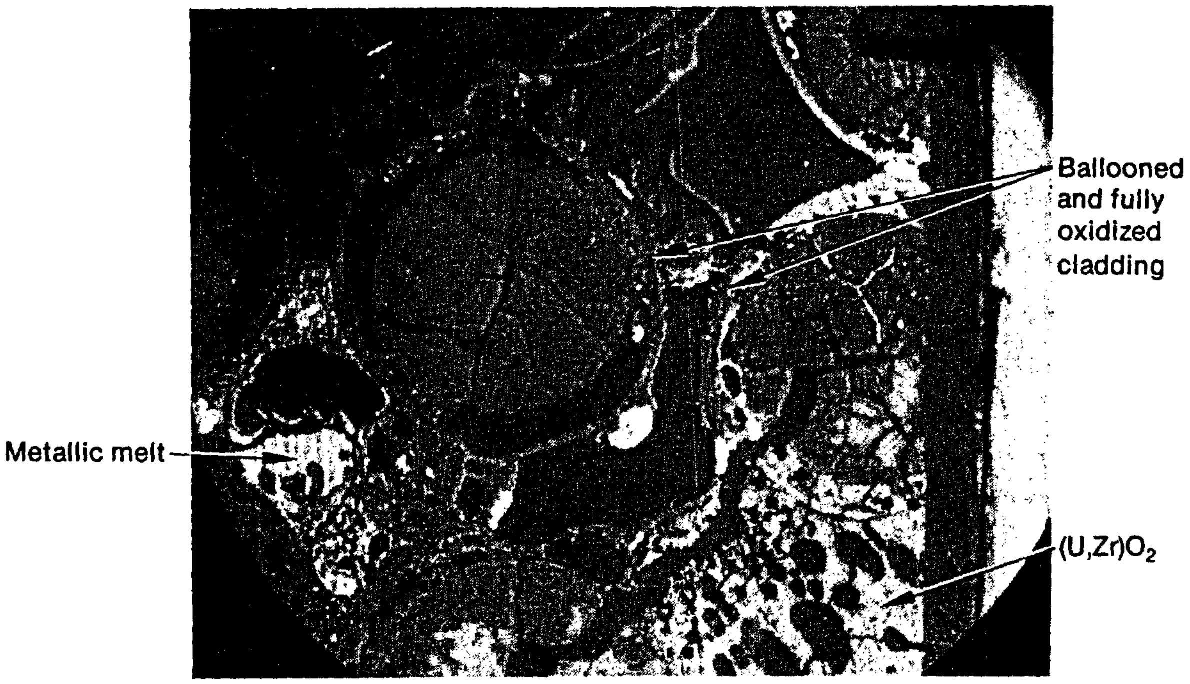

K4 Area 2

Figure 101. Details of metallographic cross section K4 at 0.88 m.

K4 Area 3

Figure 102. Details of metallographic cross section K4 at 0.88 m.

Cladding ballooning, deformation, and fragmentation is apparent on many of the fuel rods. Oxidized cladding on many of the corner and peripheral fuel rods probably fragmented and relocated downward. Melts were apparent between the fuel and outer cladding shell in some instances. Some air bubbles were also present in the epoxy.

3.1.13 Cross Section L (0.96 m; Figures 103-111)

Extensive cladding ballooning and fragmentation occurred at this elevation. Small, irregularly shaped, fuel pellet cross sections suggest that fuel liquefaction occurred on some of the centrally located rods, whereas other fuel pellets were unaffected. Fuel pellet cracking and fragmentation was commonly observed. The inner liner was essentially completely gone, and melts (primarily the molten inner liner) penetrated into the low-density ZrO_2 insulation. The insulation fragmented, and pieces relocated downward.

3.1.14 Cross Section M (1.04 m; Figures 112-119)

This cross section was located near the 1.07-m (42-in.) thermocouple elevation. Many of the features observed on the L cross section were also observed at this elevation. Extensive cladding ballooning, rod-to-rod contact, and cladding fragmentation occurred at this elevation. There was less previously molten material present at this elevation than was present at lower elevations, and much of the molten material was limited to the region between a fuel pellet and the oxidized cladding shell surrounding that fuel pellet. Some of the fuel pellets partially liquefied, some were fragmented, some had regions of grain boundary separation or areas of foamy fuel, and others were completely unaffected. The inner liner was gone, and melt penetrated into much of the insulation. Some of the insulation fragmented and relocated downward. Air bubbles in the epoxy were present in several areas.

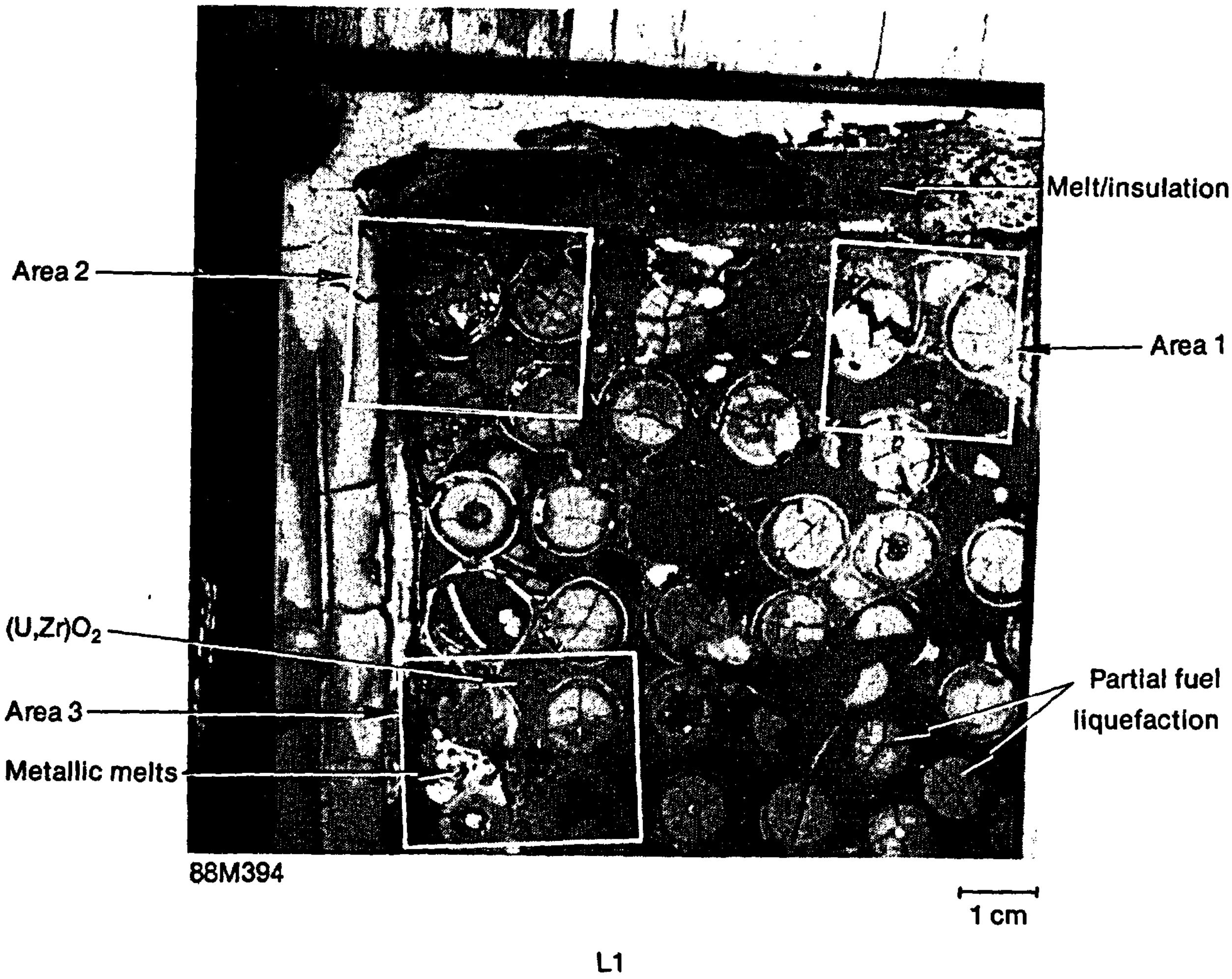

Figure 103. Metallographic cross section L1 at 0.96 m above the bottom of the instrumented fuel rods.

L2

Figure 104. Metallographic cross section L2 at 0.96 m above the bottom of the instrumented fuel rods.

L3

Figure 105. Metallographic cross section L3 at 0.96 m above the bottom of the instrumented fuel rods.

L4

Figure 106. Metallographic cross section L4 at 0.96 m above the bottom of the instrumented fuel rods.

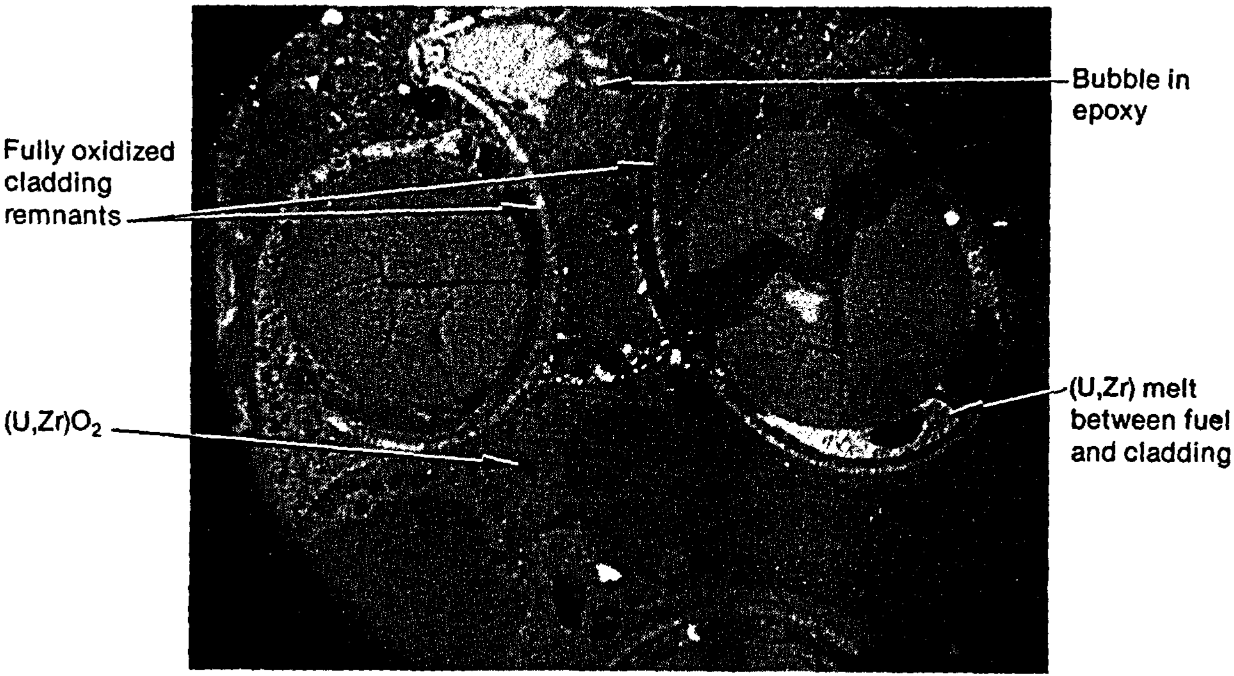

88M 395

L1 Area 1

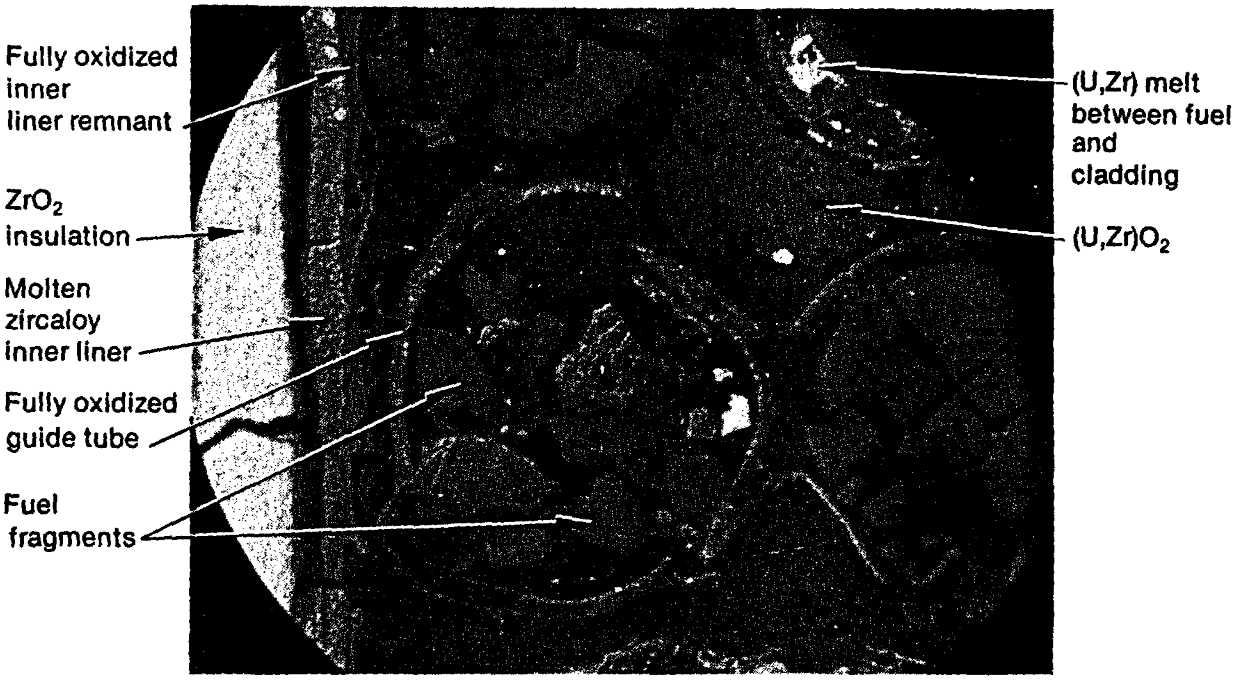

88M396

L1 Area 2

Figure 107. Details of metallographic cross section L1 at 0.96 m.

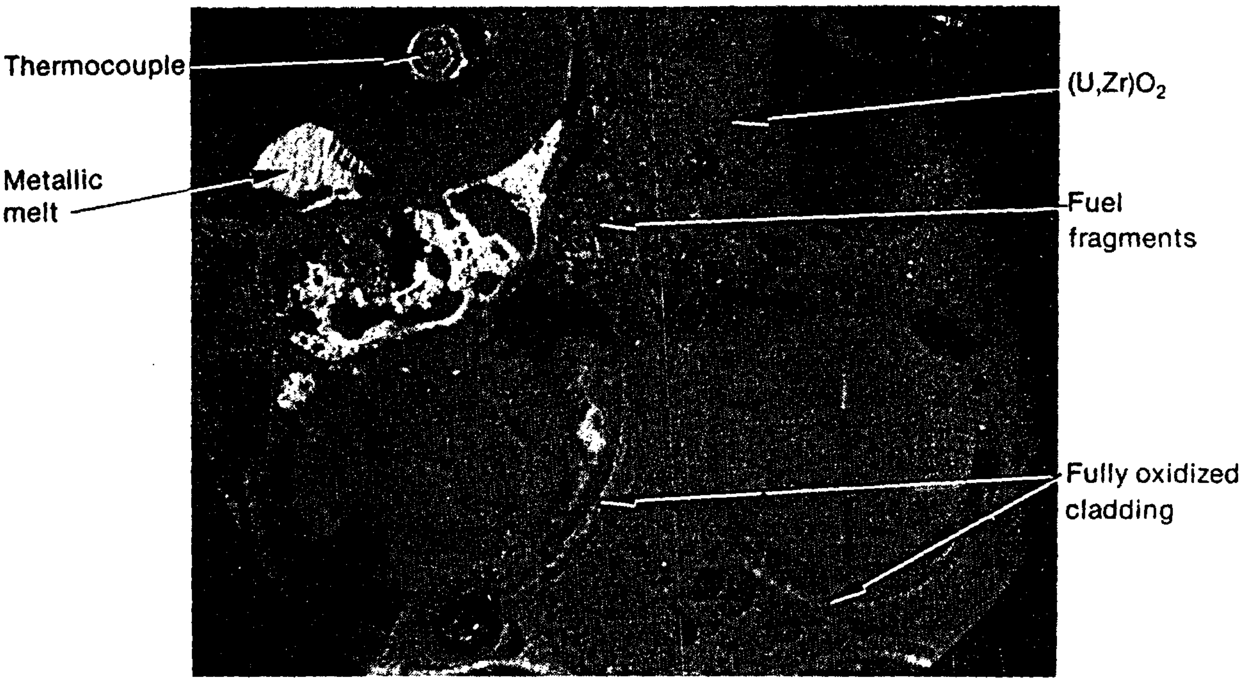

88M397

L1 Area 3

88M745

L2 Area 1

Figure 108. Details of metallographic cross section L1 and L2 at 0.96 m.

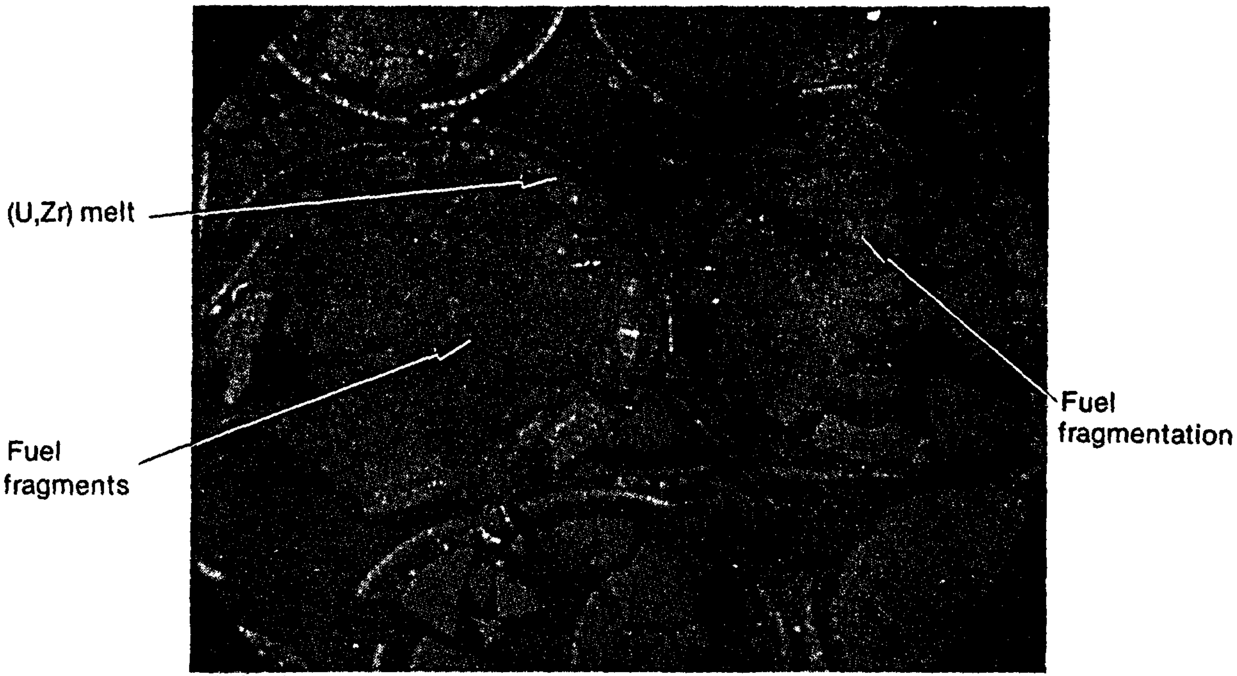

88M746

L2 Area 2

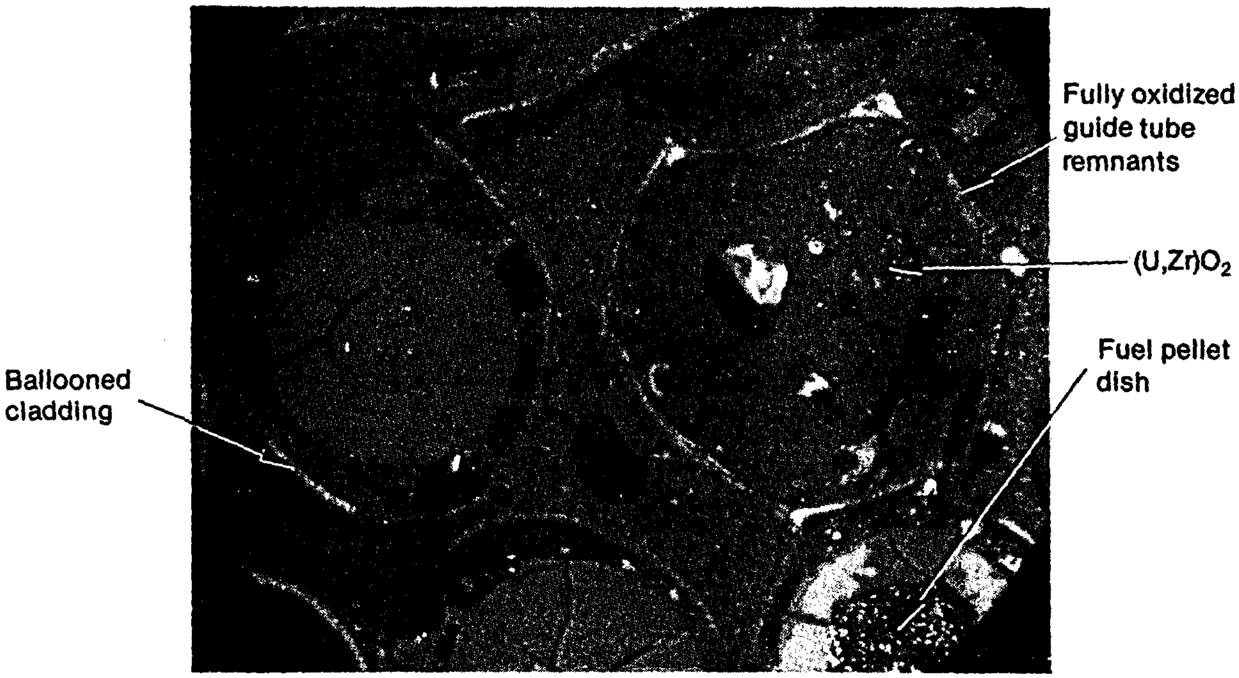

88M747

L2 Area 3

Figure 109. Details of metallographic cross section L2 at 0.96 m.

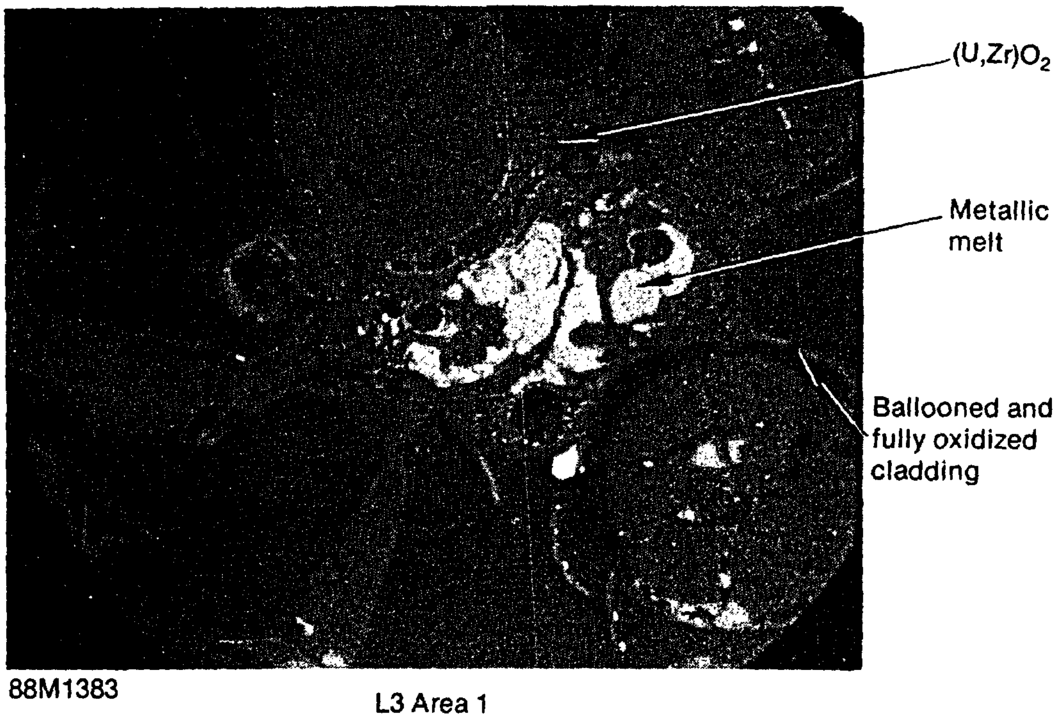

Figure 110. Details of metallographic cross section L3 at 0.96 m.

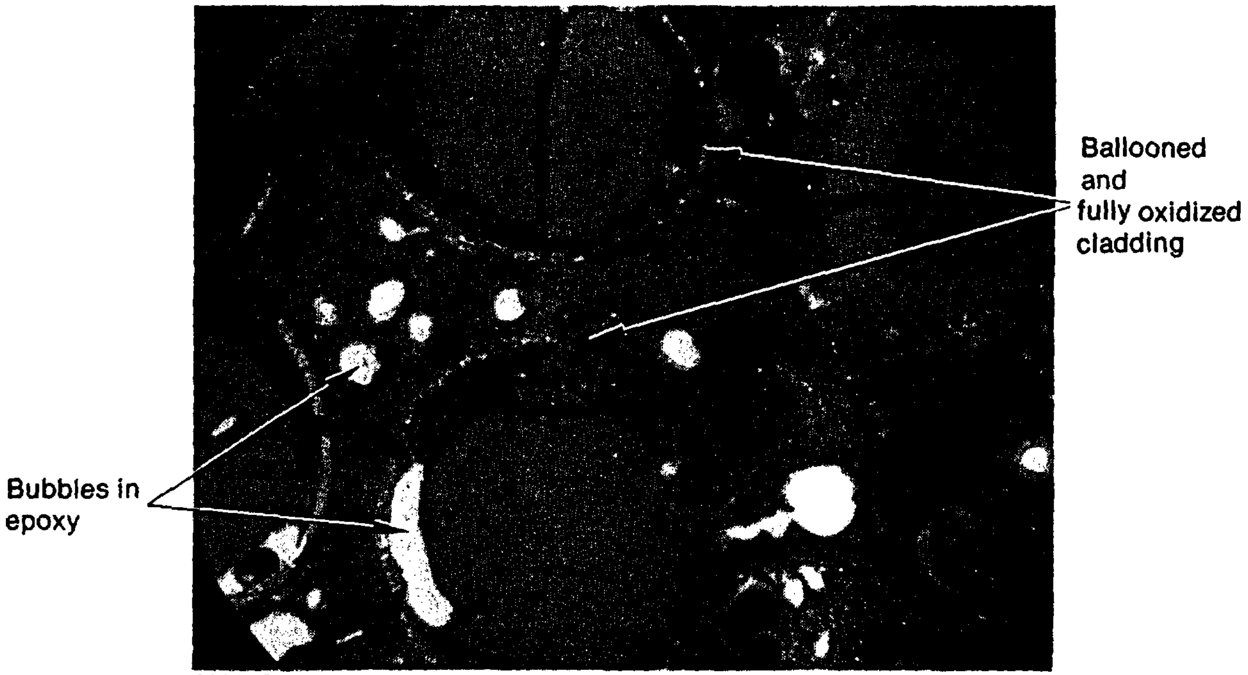

88M461

L4 Area 1

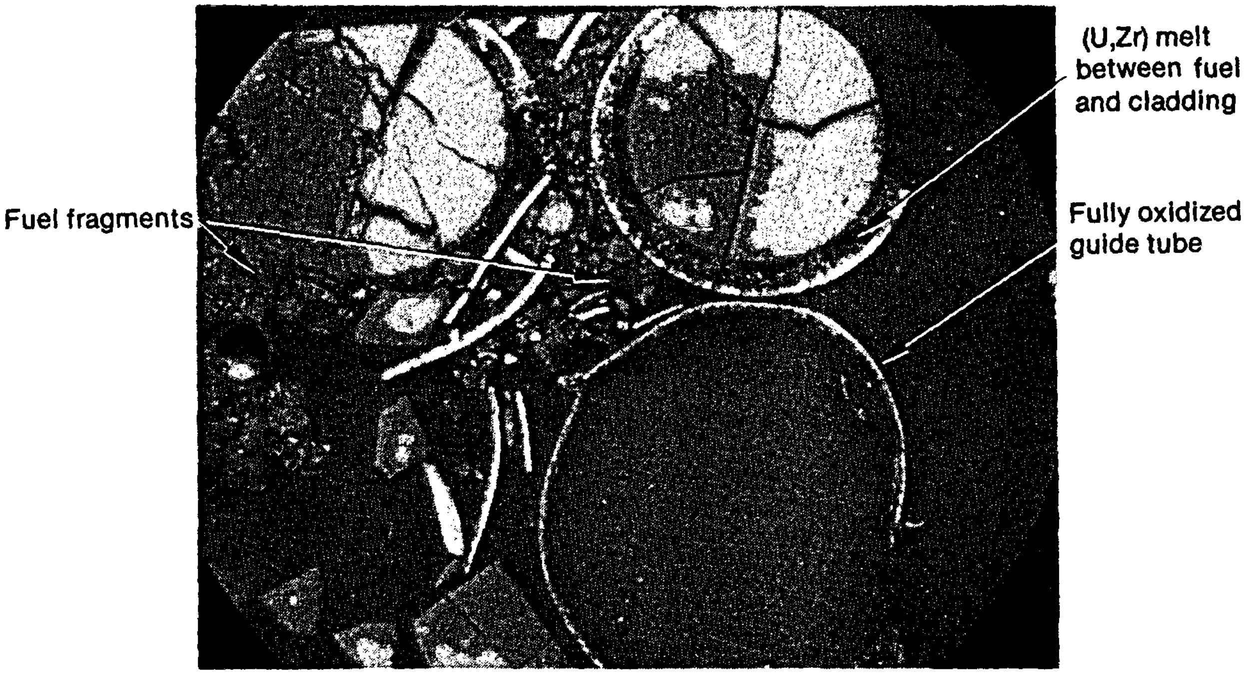

88M462

L4 Area 2

Figure 111. Details of metallographic cross section L4 at 0.96 m.

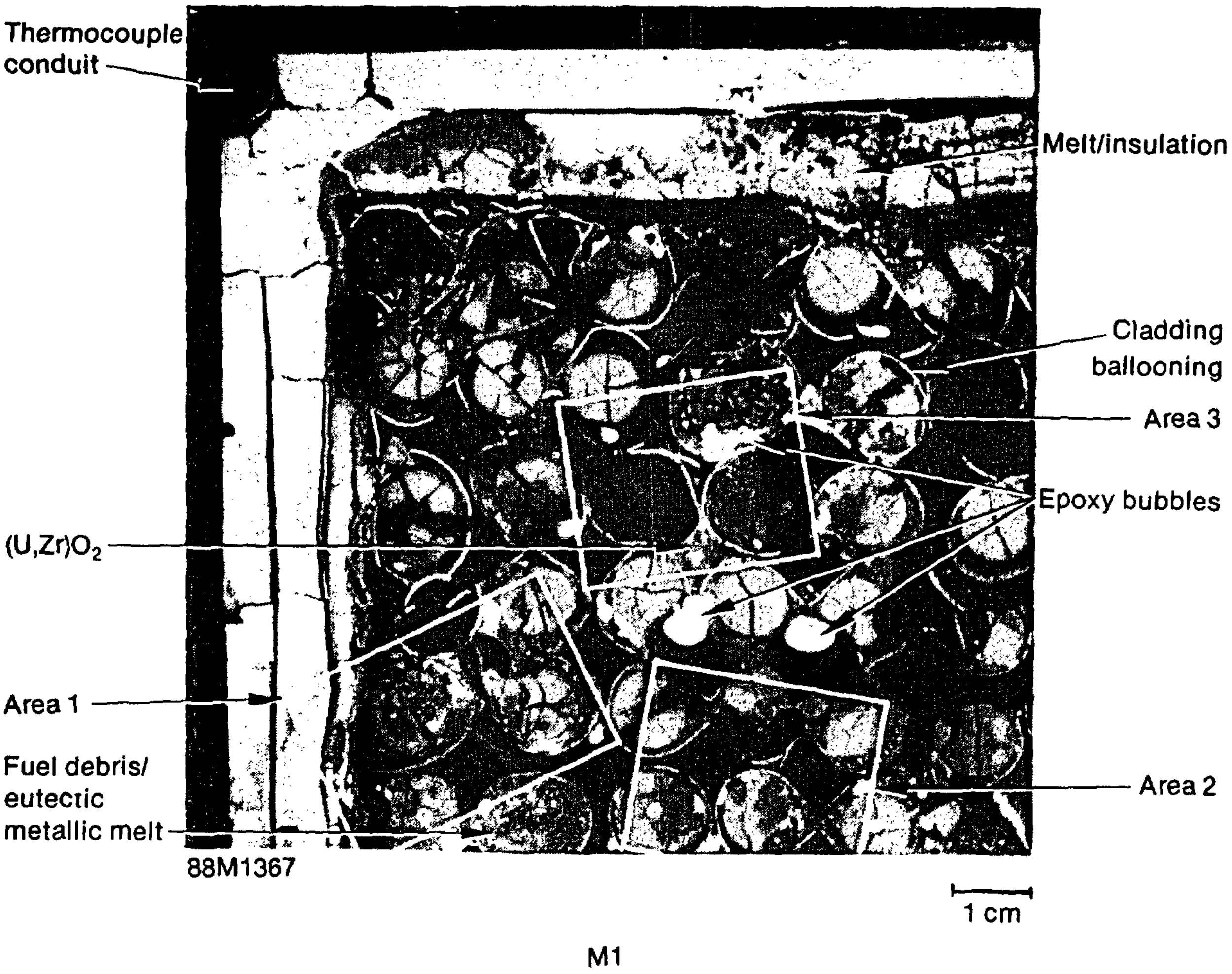

Figure 112. Metallographic cross section M1 at 1.04 m above the bottom of the instrumented fuel rods.

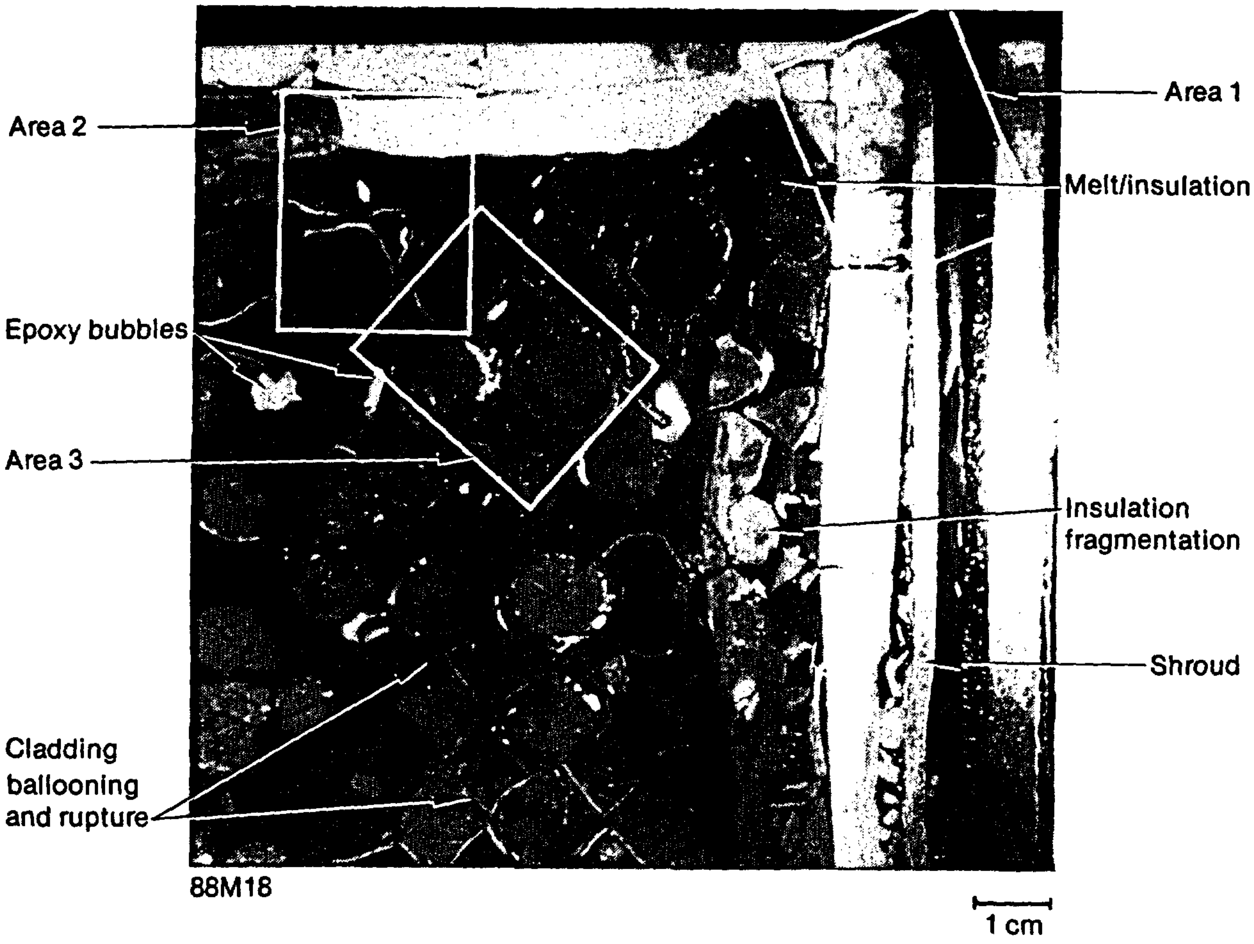

M2

Figure 113. Metallographic cross section M2 at 1.04 m above the bottom of the instrumented fuel rods.

M3

Figure 114. Metallographic cross section M3 at 1.04 m above the bottom of the instrumented fuel rods.

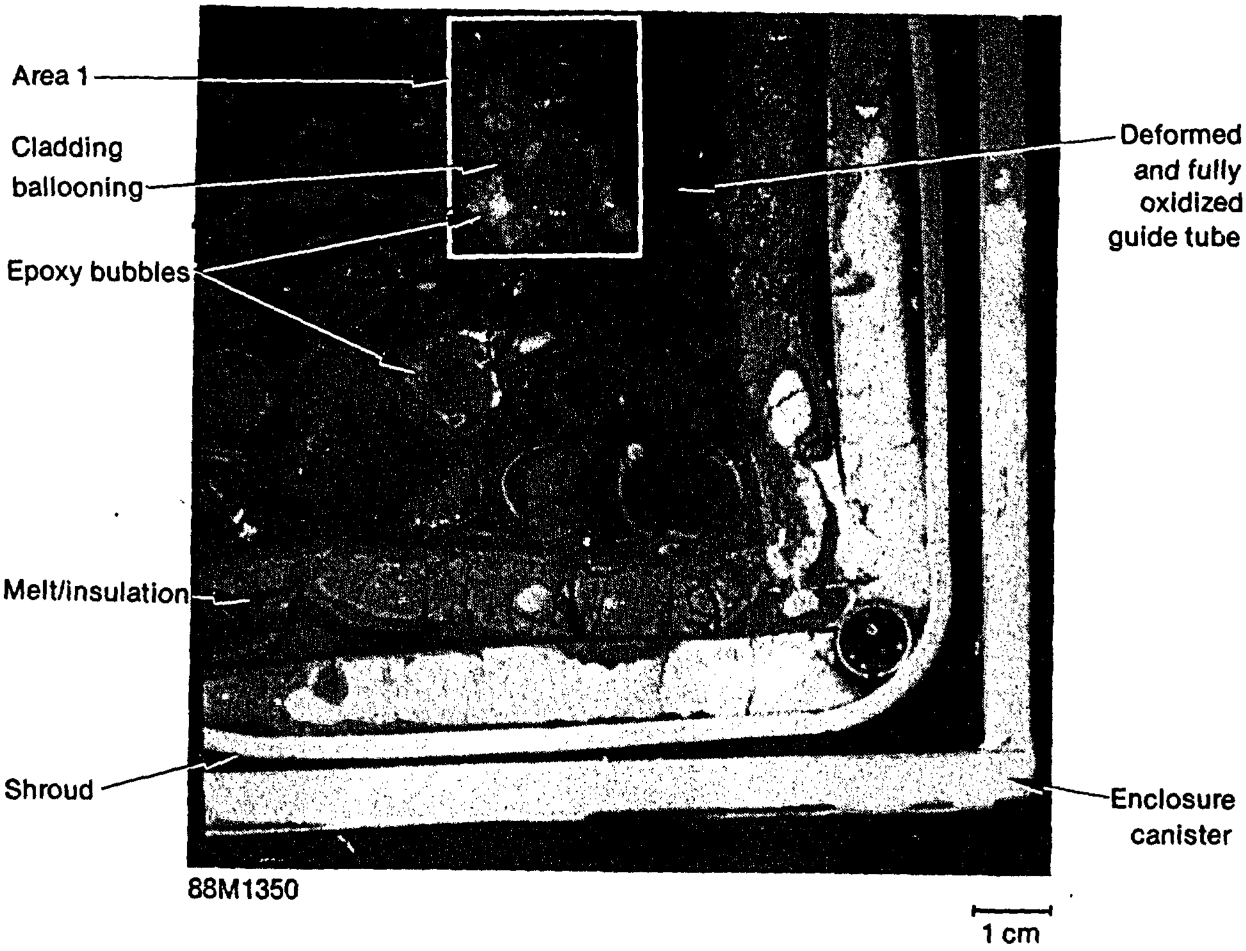

M4

Figure 115. Metallographic cross section M4 at 1.04 m above the bottom of the instrumented fuel rods.

88M1379

M1 Area 1

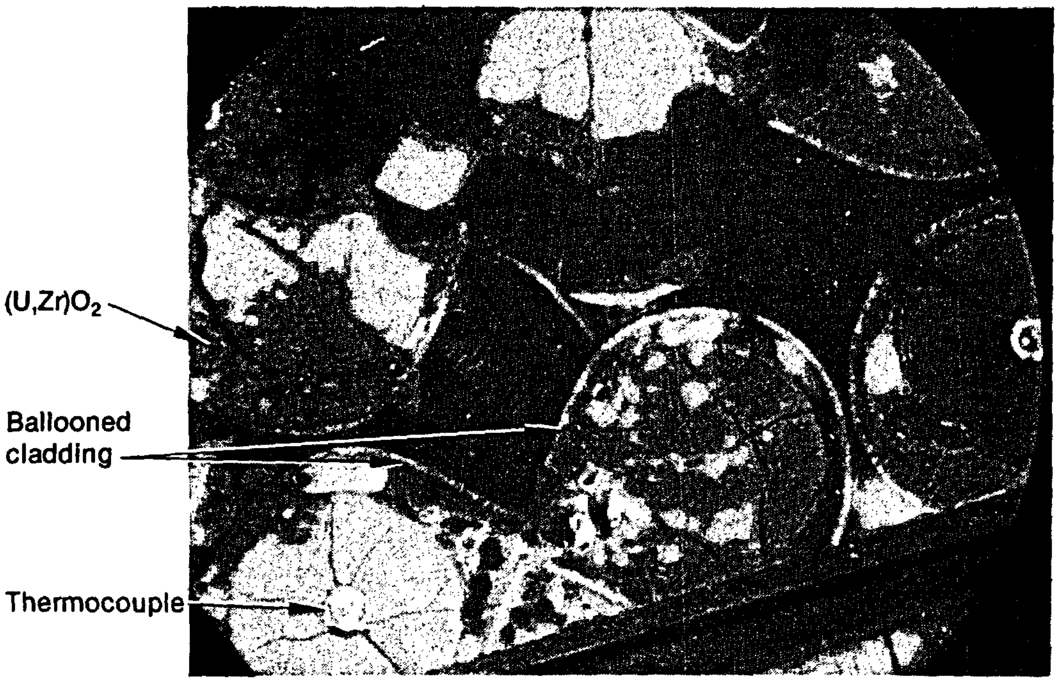

88M1380

M1 Area 2

Figure 116. Details of metallographic cross section M1 at 1.04 m.

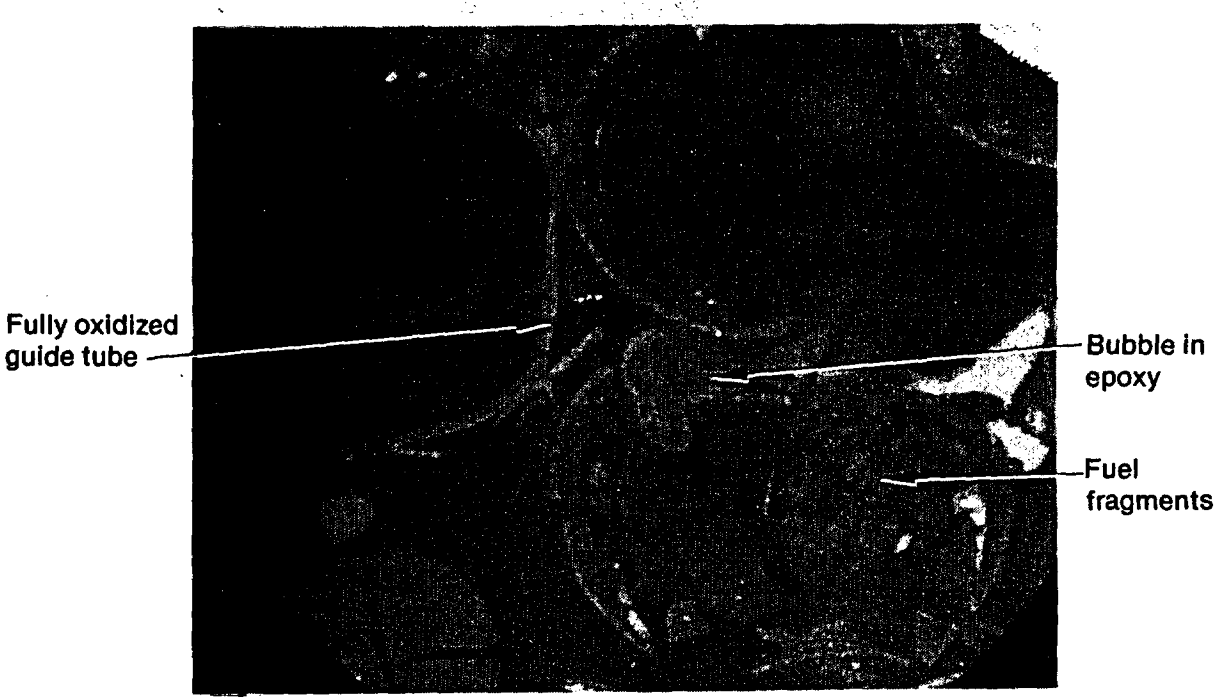

M1 Area 3

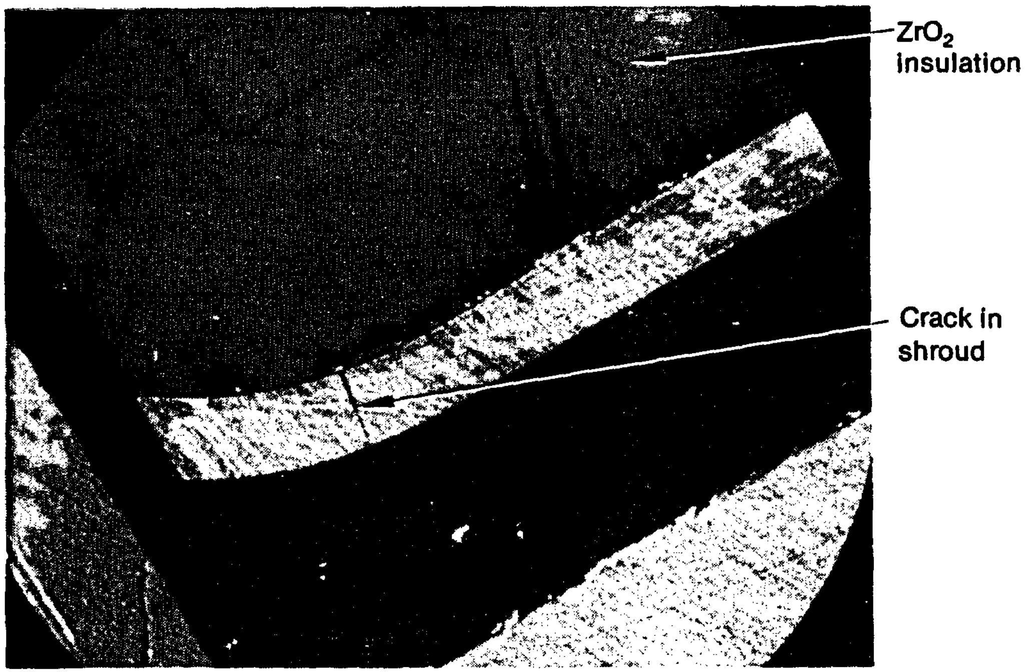

M2 Area 1

Figure 117. Details of metallographic cross section M1 and M2 at 1.04 m.

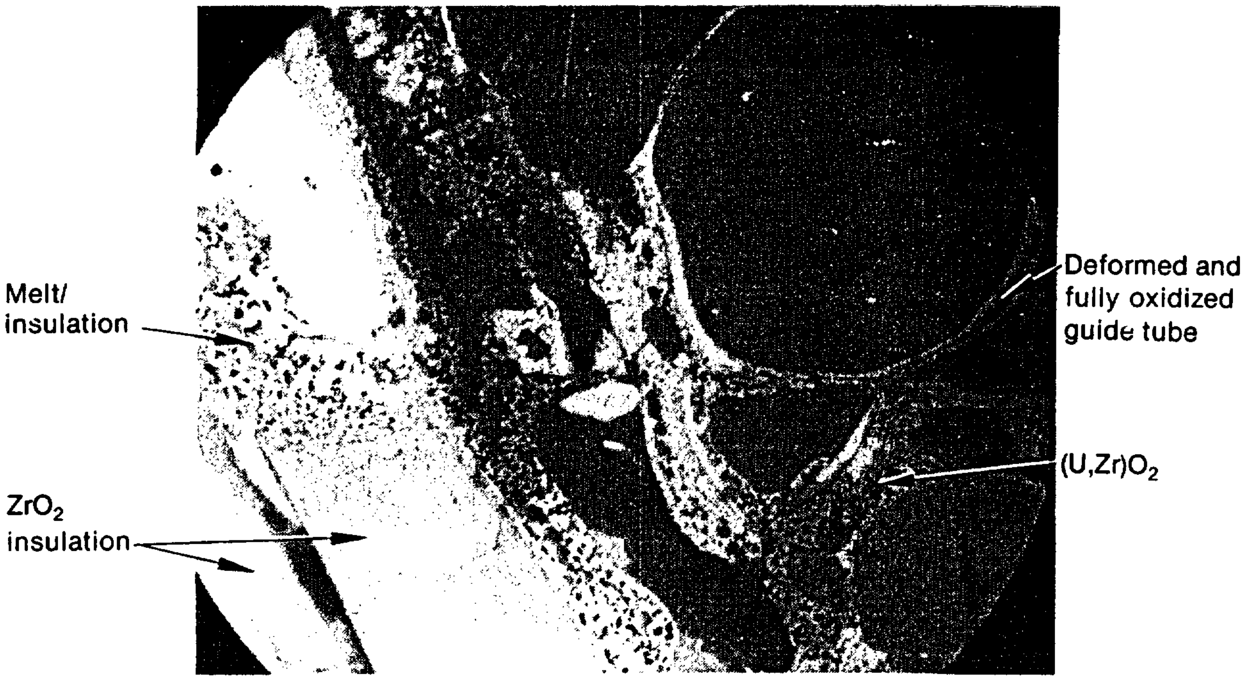

M2 Area 2

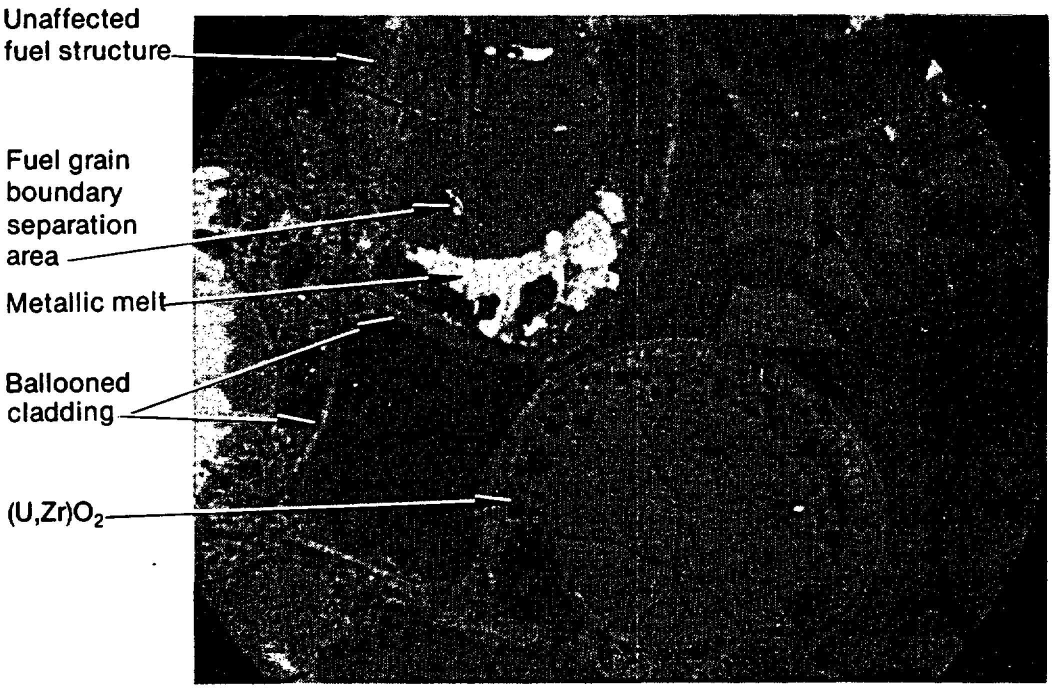

M2 Area 3

Figure 118. Details of metallographic cross section M2 at 1.04 m.

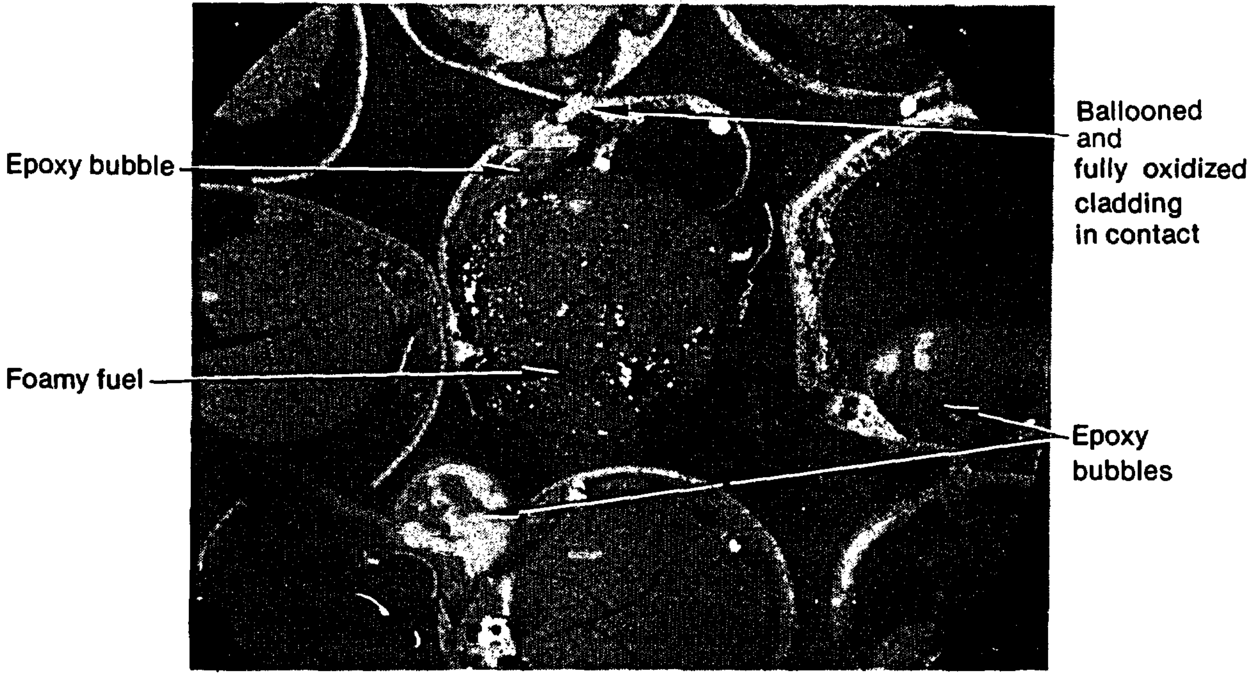

88M1353

M3 Area 1

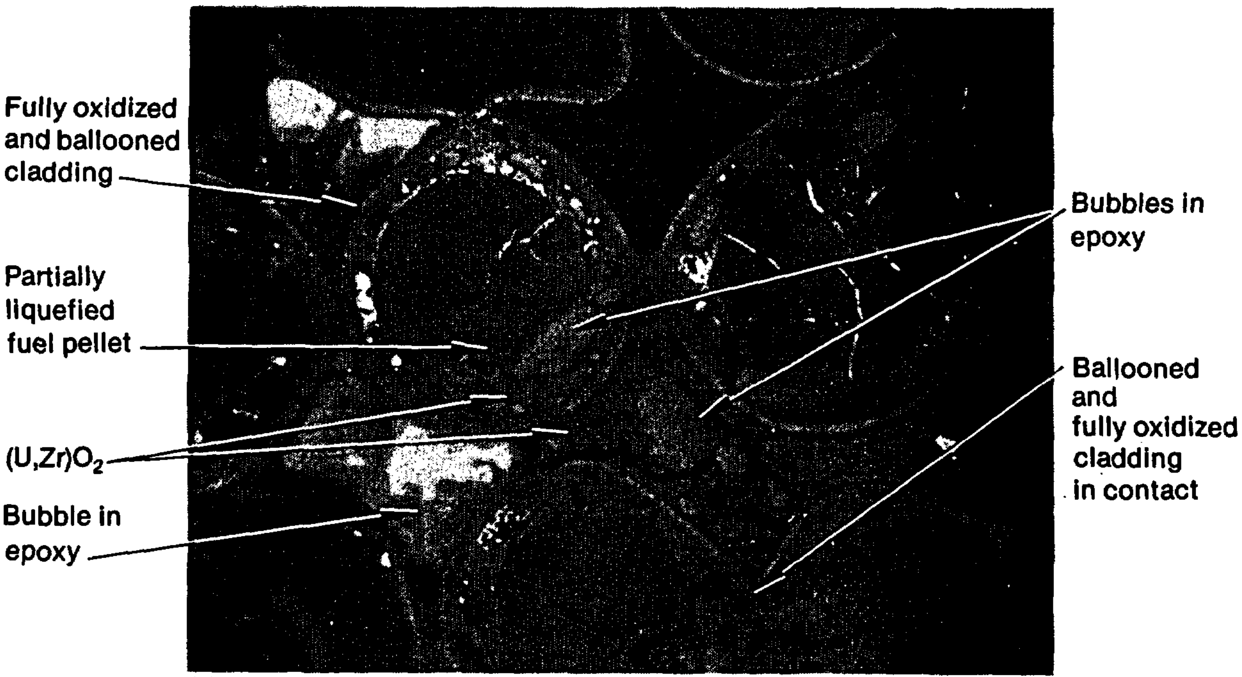

88M1351

M4 Area 1

Figure 119. Details of metallographic cross section M3 and M4 at 1.04 m.

3.1.15 Cross-Section N (1.14 m; Figures 120-126)

This cross section was through the uppermost portion of the upper rod-like array region visible on the neutron radiographs. Most of the fuel pellets no longer had any cladding surrounding them, and some of the fuel pellets had fallen over and started to form a debris bed. This debris bed becomes more evident at higher elevations. The remaining cladding was generally limited to the corner locations and consisted of ballooned and deformed oxidized outer shells. Deformation of the guide tubes is also apparent. The inner liner was completely gone, allowing melt penetration into the insulation and fragmentation and relocation of the insulation. Various extents of fuel damage were present, ranging from liquefaction to unaffected regions. Only small amounts of localized metallic melts were present. The insulation missing in the corner of sample N2 was due to loss of this material through a cracked and missing portion of the shroud in this area. This missing portion of the shroud was observed during visual examinations of the fuel module (see Section 2.1), and it extended upwards for approximately 0.2 m above this elevation.

3.1.16 Cross Section O (1.20 m; Figures 127-133)

All the cladding was gone at this elevation except in some of the corner locations. The fuel pellet stacks had fallen over and formed a rubble bed. Ceramic melts surrounded many of the fuel pellets. Fuel liquefaction is indicated by the smaller size of some of the pellet cross sections and their irregular shape. Fuel pellet cracking and fragmentation is also apparent; and there were areas of agglomerated material, consisting largely of fuel grains and eutectic metallic melts similar to the material in the lower blockage. These areas of agglomerated materials contained microscopic porosity similar to that found in the lower blockage, but they can be distinguished from the melt regions by their lack of large voids. There were only a few localized areas of metallic melts. The inner liner was completely gone, and melt penetration into the insulation occurred. The insulation fragmented and relocated, and the insulation missing in the exterior corner of sample O2 was lost through the missing portion of the shroud.

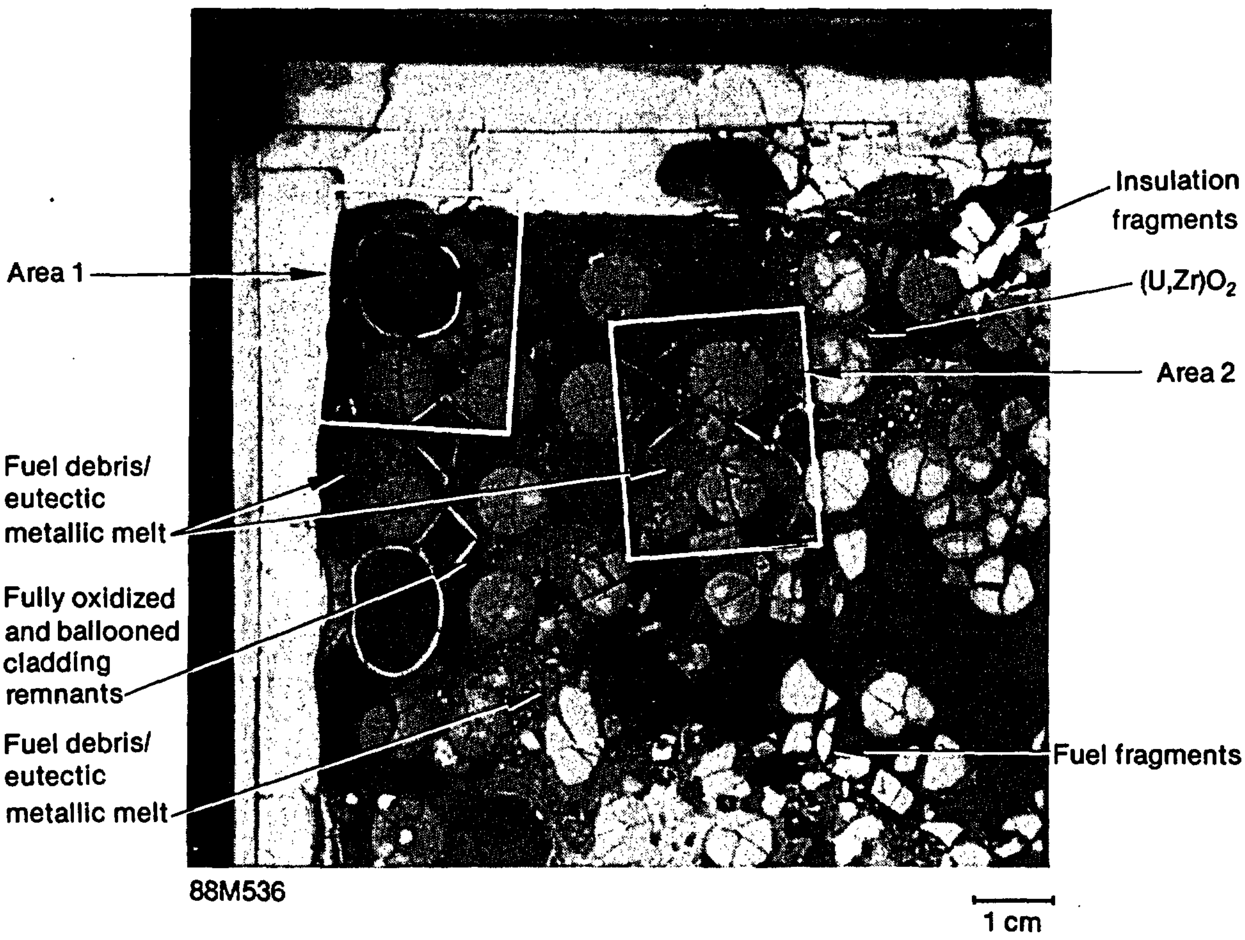

N1

Figure 120. Metallographic cross section N1 at 1.14 m above the bottom of the instrumented fuel rods.

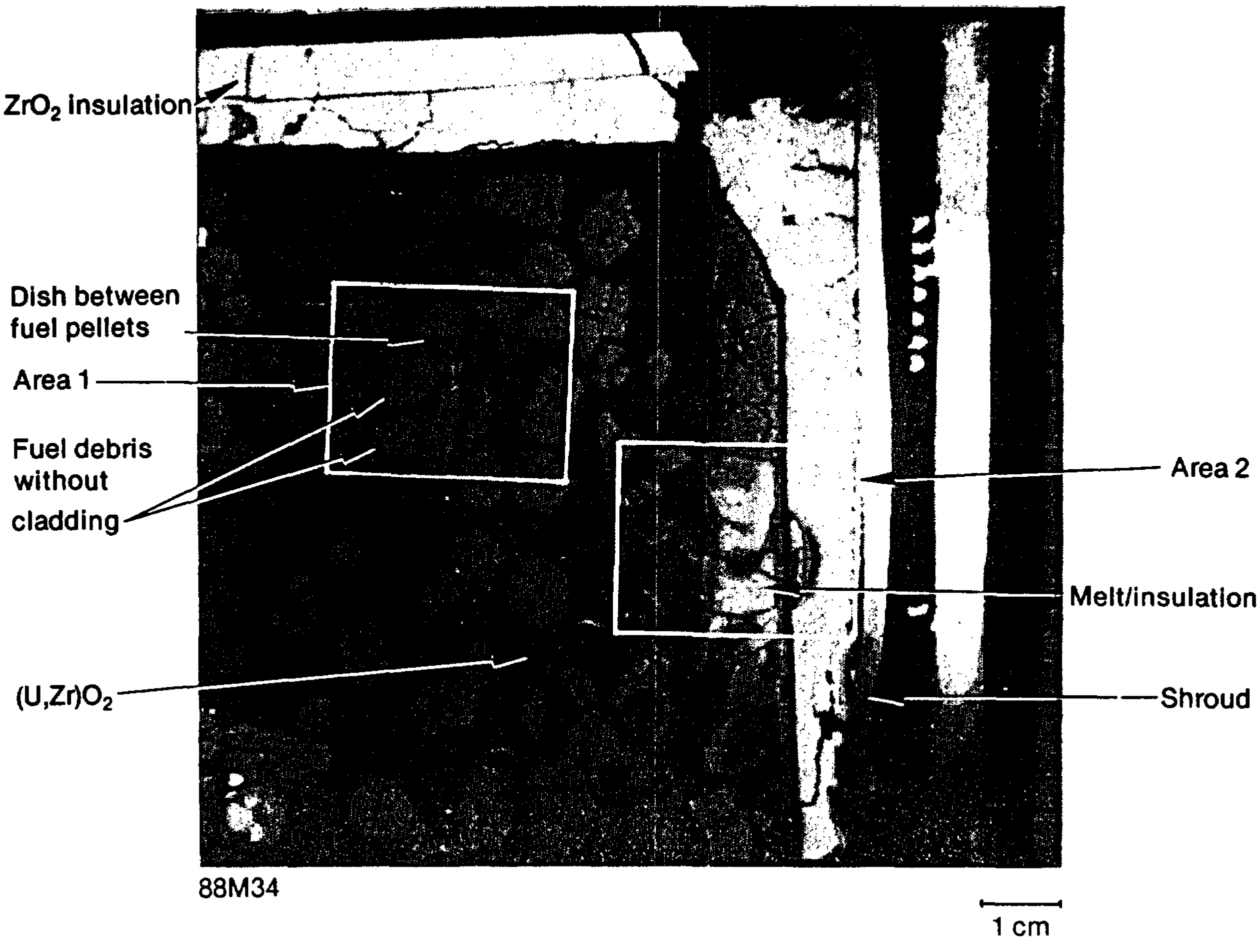

N2

Figure 121. Metallographic cross section N2 at 1.14 m above the bottom of the instrumented fuel rods.

N3

Figure 122. Metallographic cross section N3 at 1.14 m above the bottom of the instrumented fuel rods.

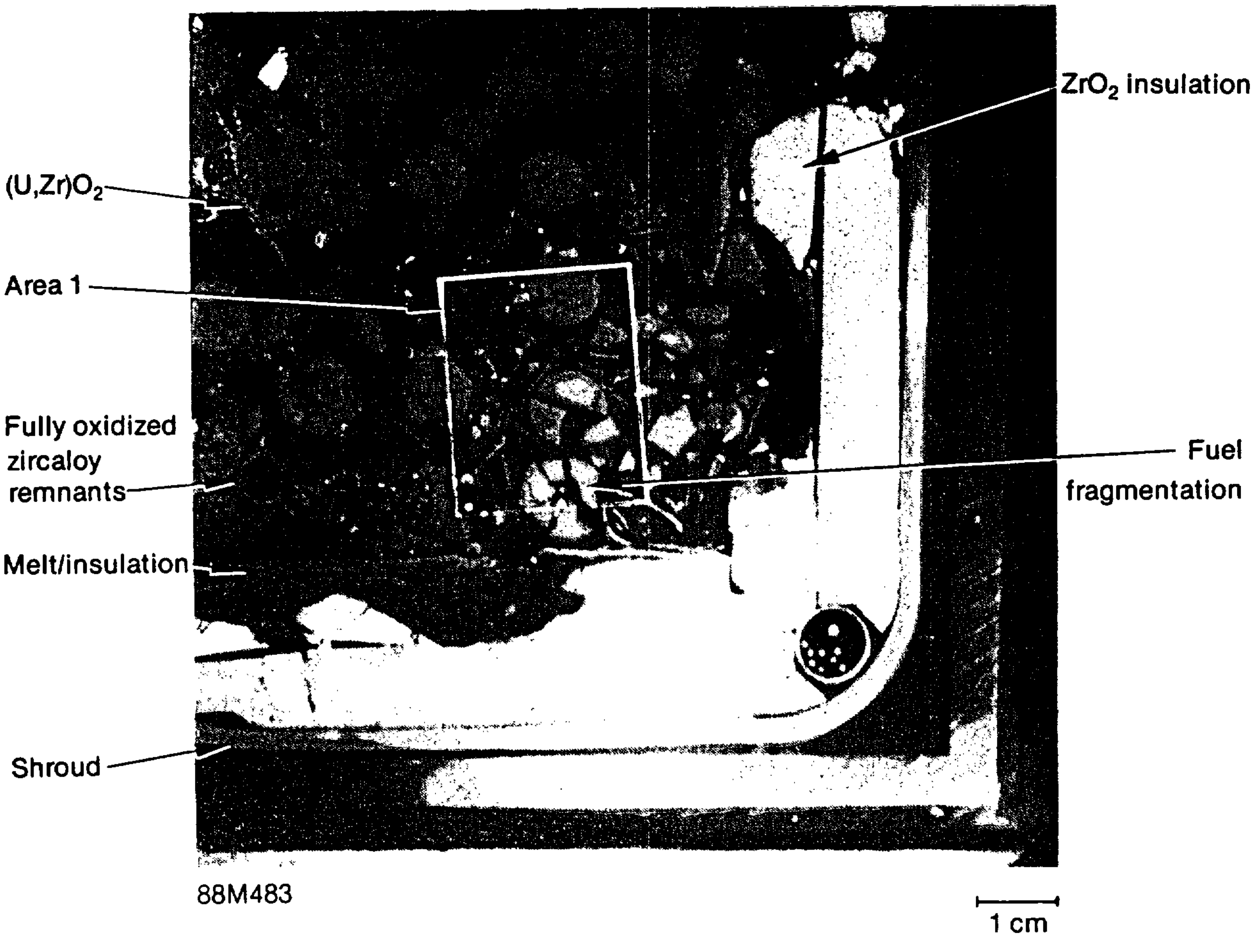

N4

Figure 123. Metallographic cross section N4 at 1.14 m above the bottom of the instrumented fuel rods.

N1 Area 1

N1 Area 2

Figure 124. Details of metallographic cross section N1 at 1.14 m.

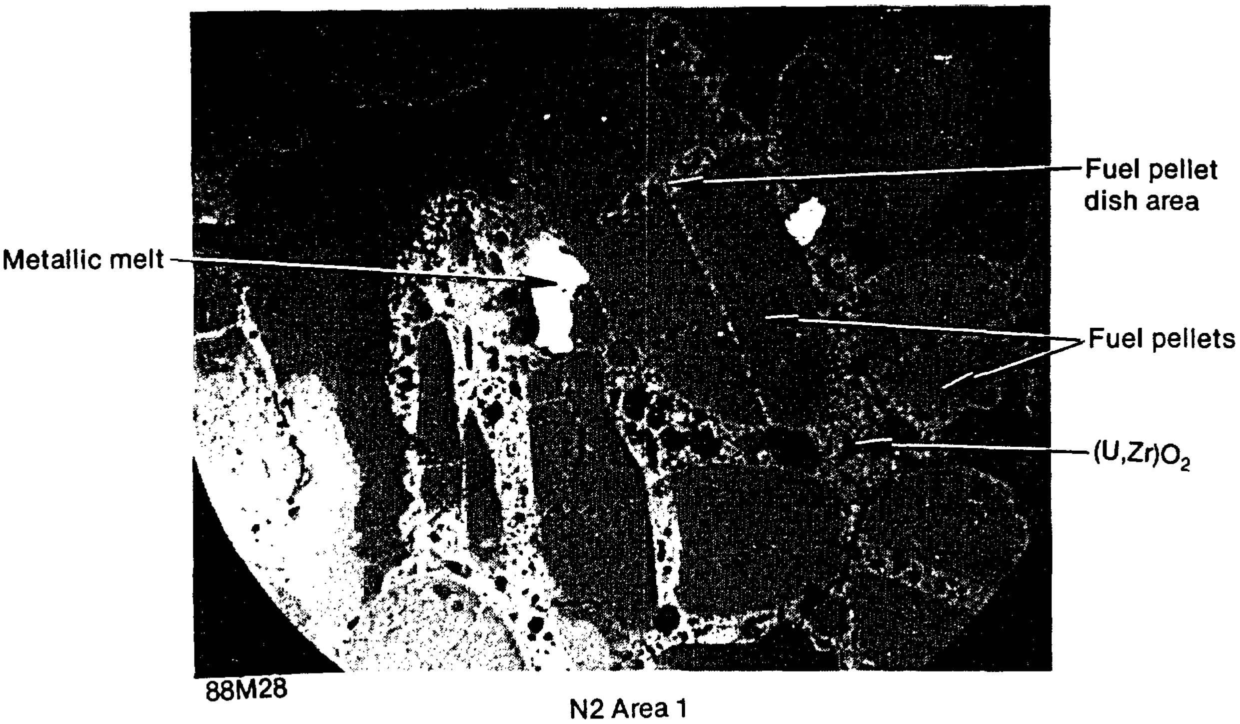

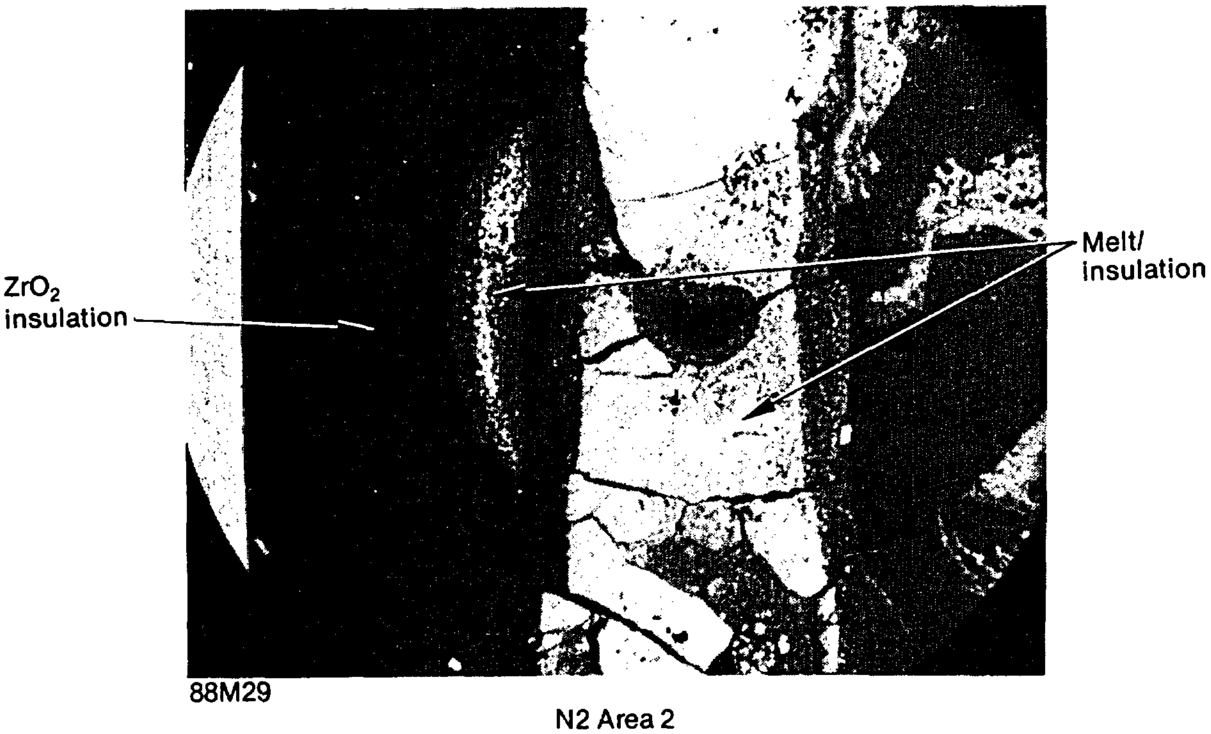

Figure 125. Details of metallographic cross section N2 at 1.14 m.

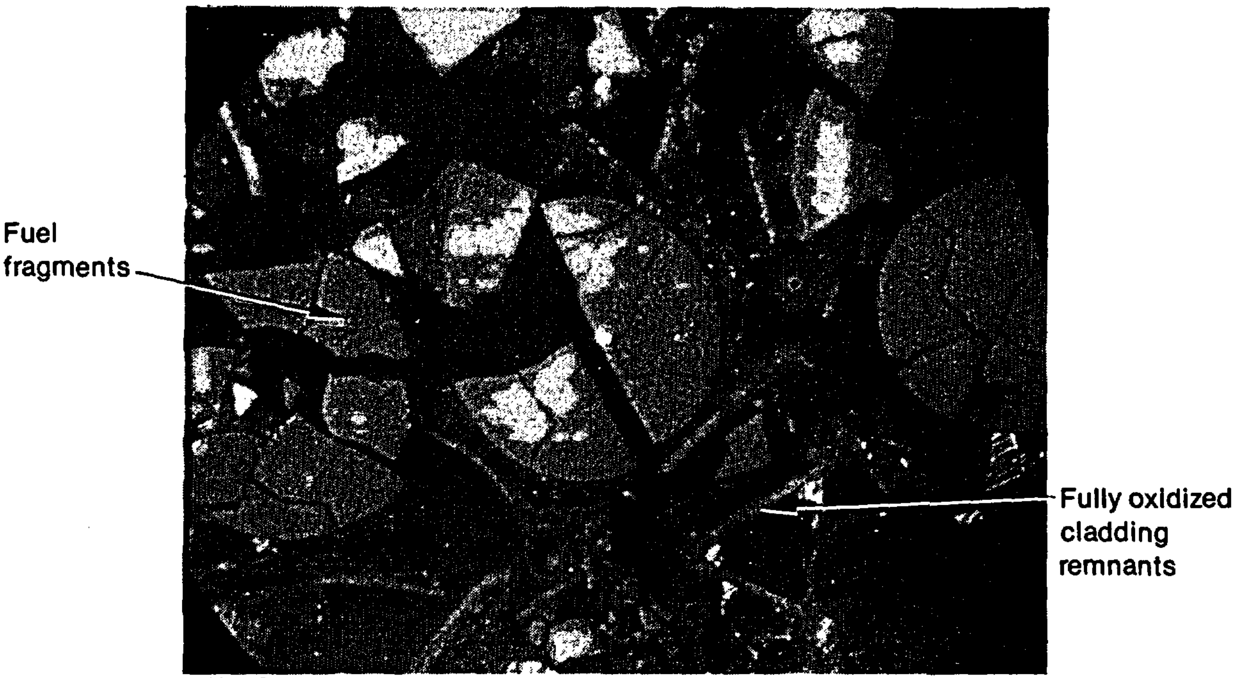

N4 Area 1

Figure 126. Details of metallographic cross section N4 at 1.14 m.

O1

Figure 127. Metallographic cross section O1 at 1.20 m above the bottom of the instrumented fuel rods.

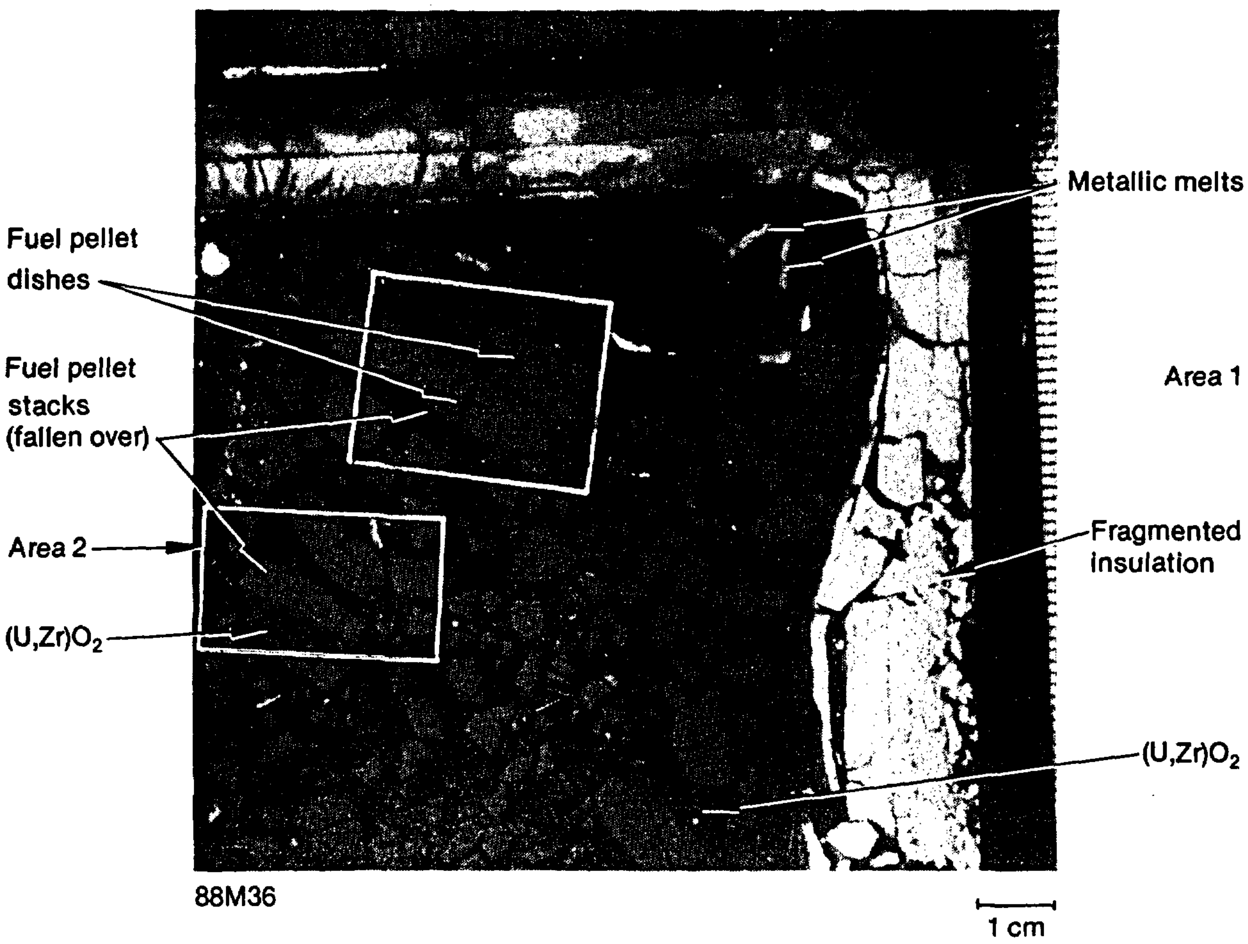

O2

Figure 128. Metallographic cross section O2 at 1.20 m above the bottom of the instrumented fuel rods.

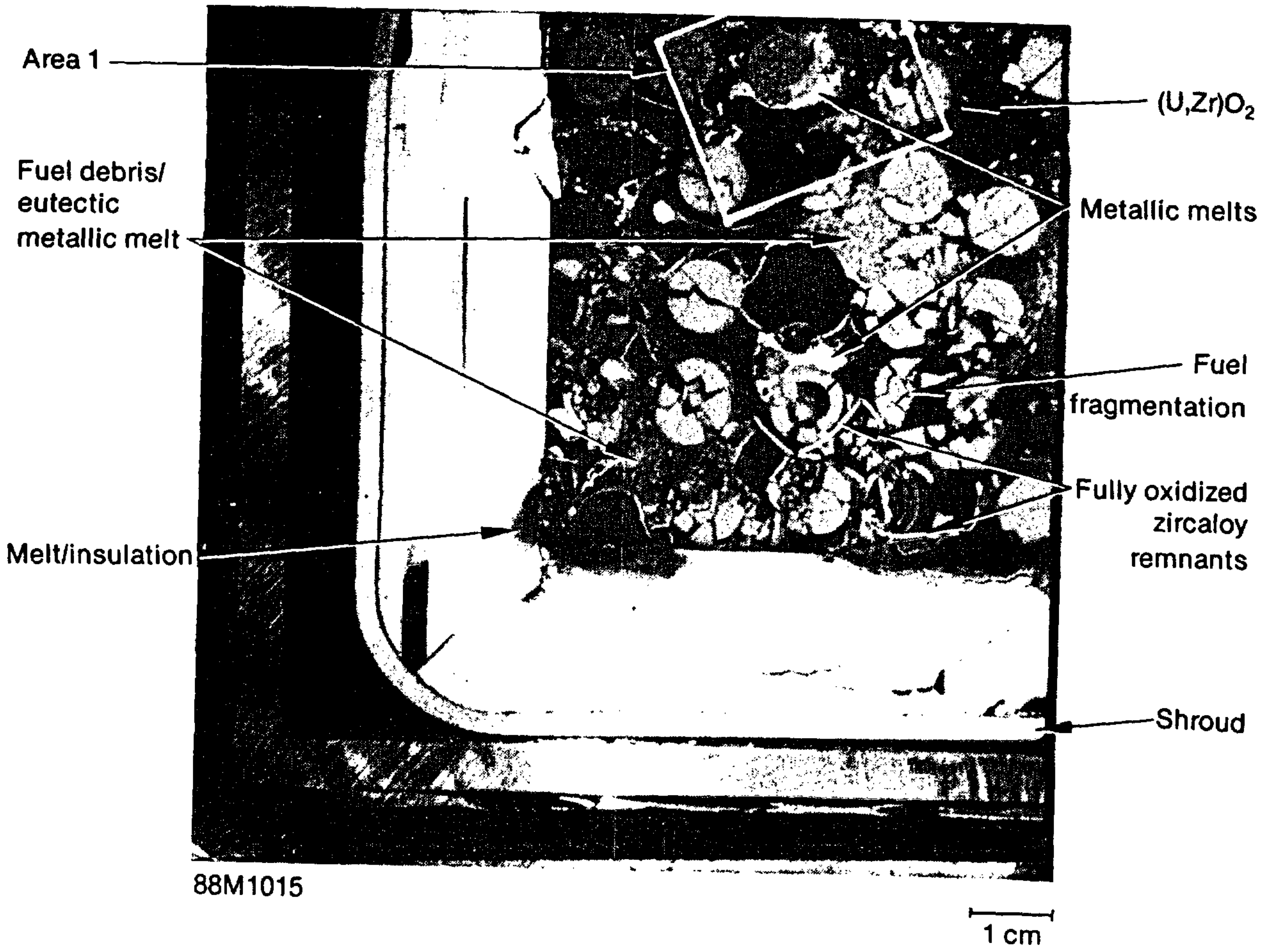

O3

Figure 129. Metallographic cross section 03 at 1.20 m above the bottom of the instrumented fuel rods.

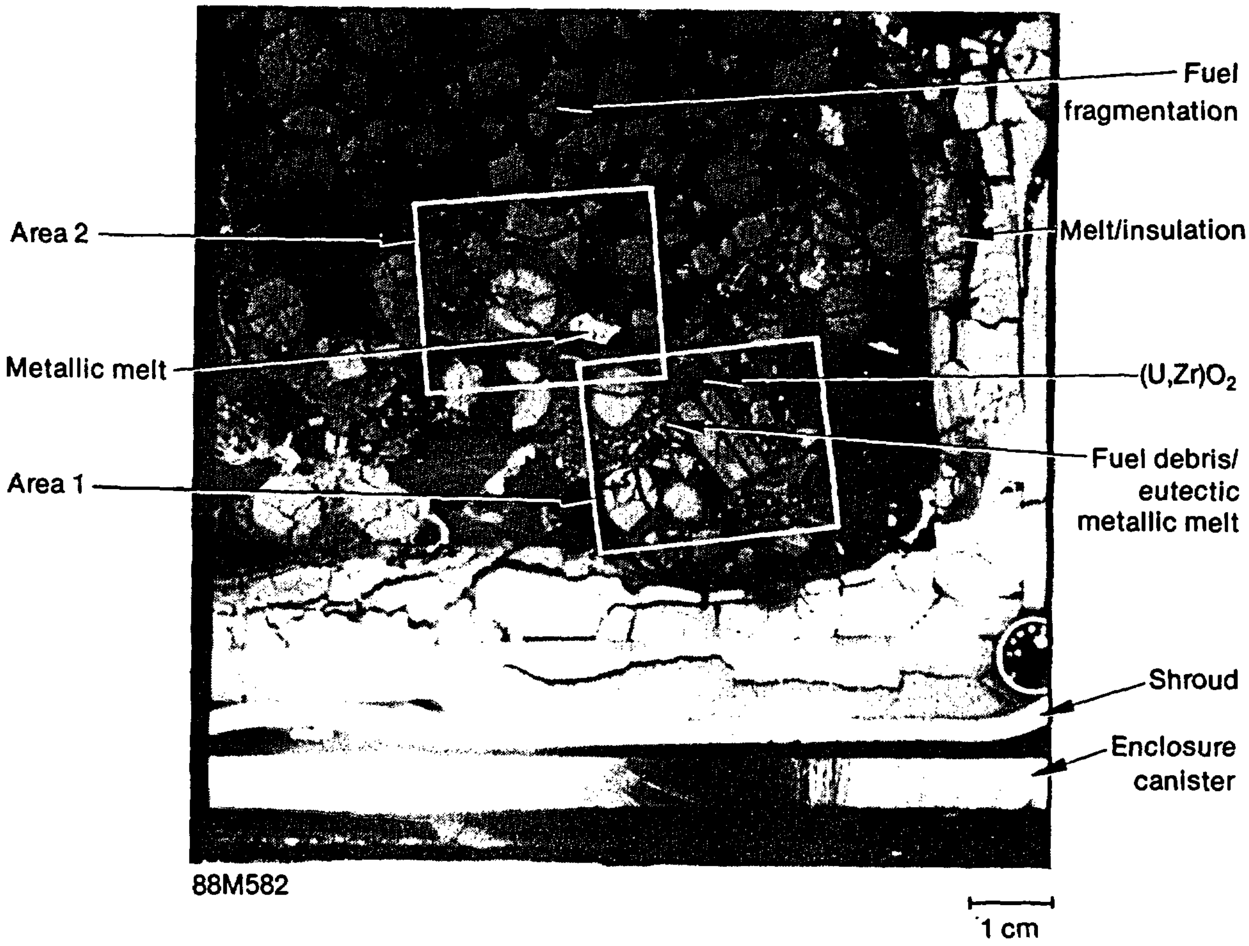

O4

Figure 130. Metallographic cross section O4 at 1.20 m above the bottom of the instrumented fuel rods.

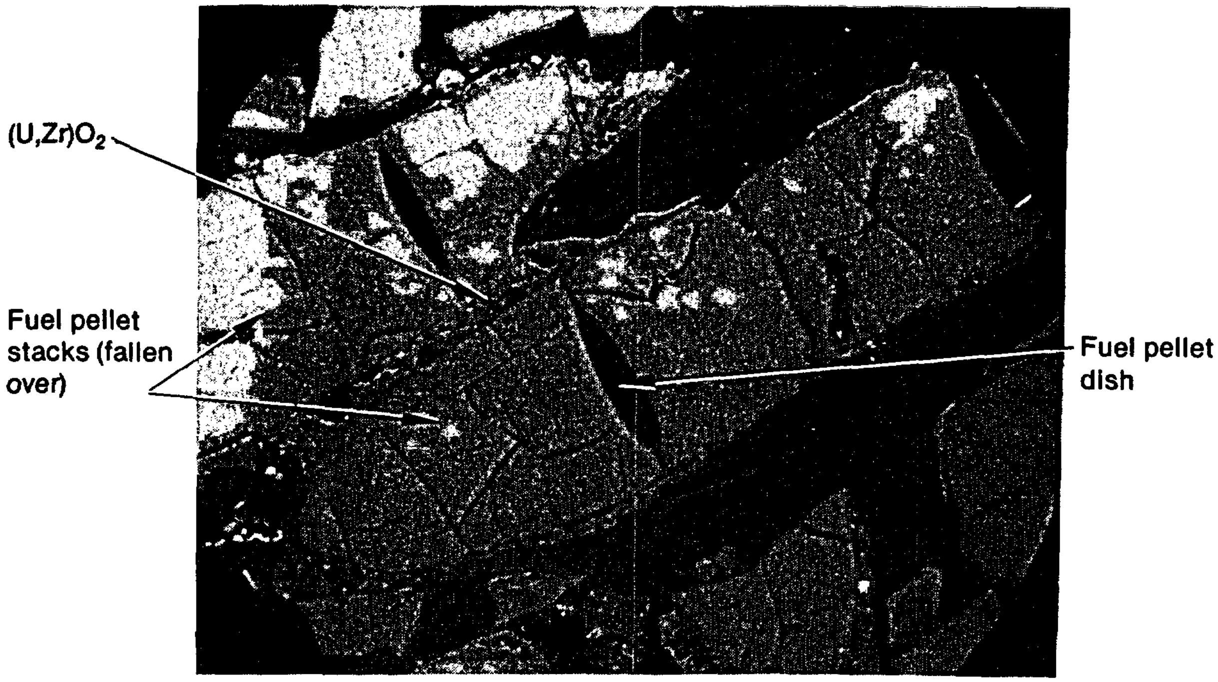

88M30

O2 Area 1

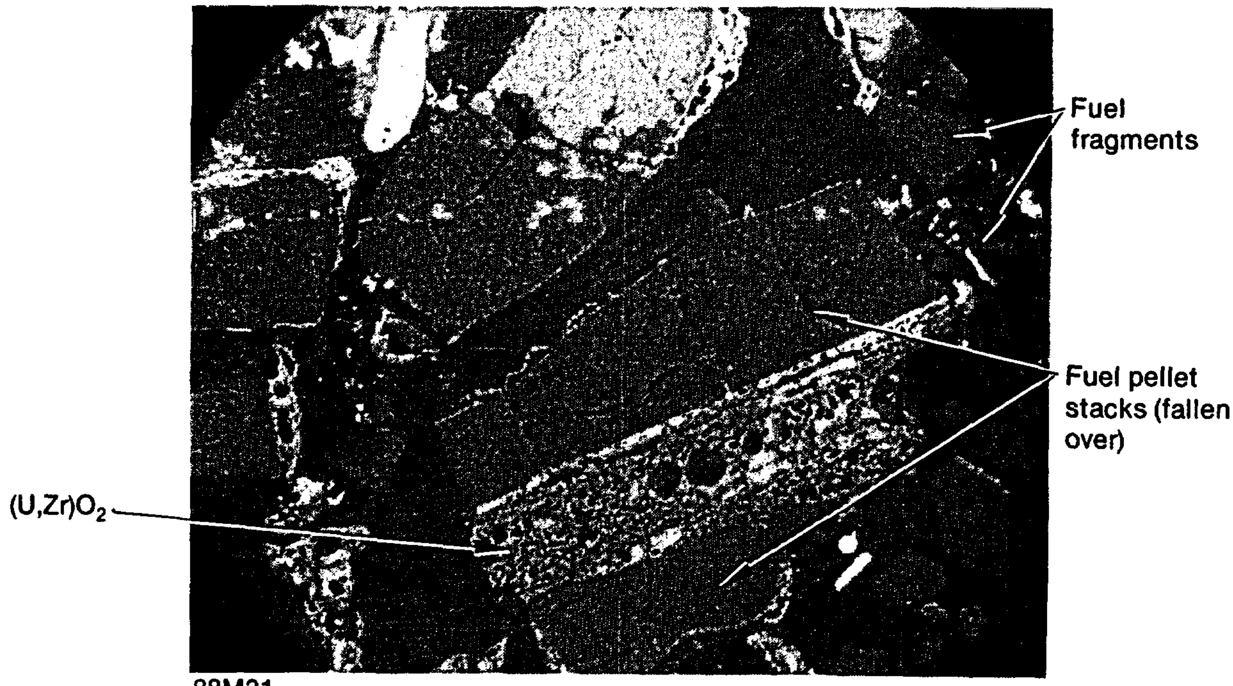

88M31

O2 Area 2

Figure 131. Details of metallographic cross section 02 at 1.20 m.

03 Area 1

Figure 132. Details of metallographic cross section 03 at 1.20 m.

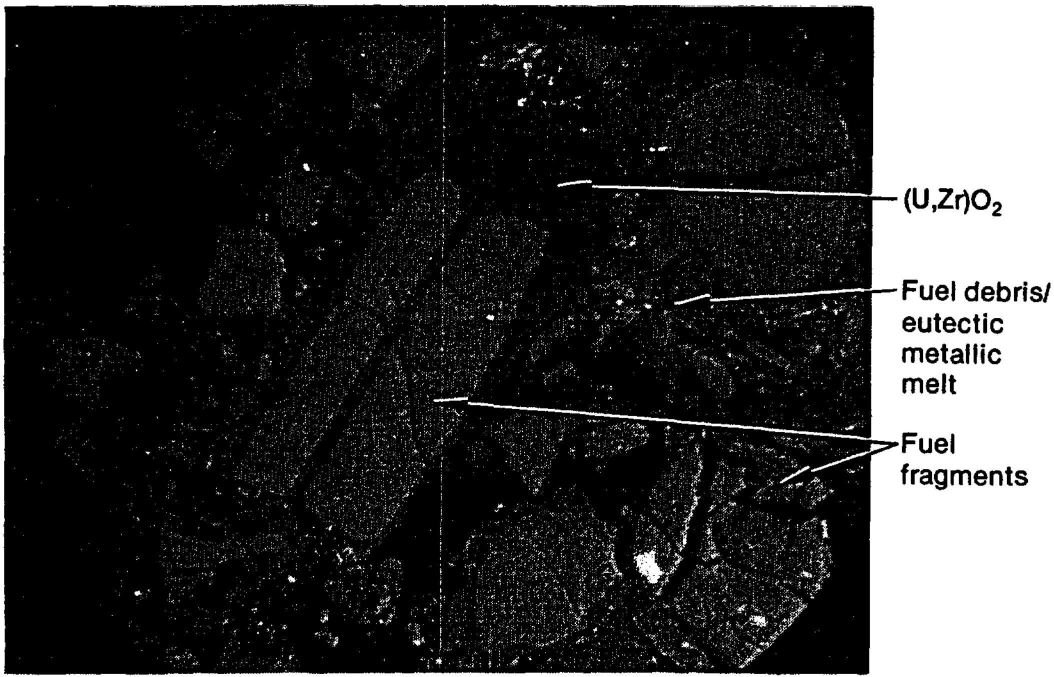

O4 Area 1

O4 Area 2

Figure 133. Details of metallographic cross section O4 at 1.20 m.

3.1.17 Cross Section P (1.30 m; Figures 134-137)

This cross section was very similar to the O cross section. The only cladding still present at this elevation was in the corner of sample P3. The inner liner was completely gone except for a small piece in the corner of P3, and the insulation was free to fall out in several places. (The bright white material in the corner of sample P1 is insulation and should not be confused with metallic melts.) The insulation that remains was generally free from melt penetration. Fuel liquefaction and fragmentation is apparent on some pellets, but most of the remaining fuel appears unaffected. One exception is an area of grain boundary separation adjacent to a localized metallic melt on sample P3. There were also areas of agglomerated material at this cross section, which consisted largely of fuel grains and eutectic melts similar to the material in the lower blockage region.

3.1.18 Cross Section Q (1.45 m; Figures 138-143)

This cross section was through the debris bed and was similar to the O and P cross sections. There was a small section of inner liner in the corner of sample Q3, but a lot of the insulation had fallen down into the fuel bundle. As on cross sections just below this, there was minimal melt penetration into the remaining insulation. A relatively large amount of metallic melts was concentrated in the corner of sample Q3, and in this corner there was even one fuel rod with cladding remaining that was not fully oxidized. This cladding, and the section of inner liner adjacent to it, were the only pieces of zircaloy that were not fully oxidized above the I cross section (neglecting the shroud).

3.1.19 Cross Section R (1.68 m; Figures 144-149)

This was the topmost cross section taken through the fueled region of the bundle. It corresponds very nearly to the elevation of the 1.68-m (66-in.) thermocouple location. All the cladding was completely gone at this elevation, and all the fuel pellets that remained were supported by

P1

Figure 134. Metallographic cross section P1 at 1.30 m above the bottom of the instrumented fuel rods.

P2

Figure 135. Metallographic cross section P2 at 1.30 m above the bottom of the instrumented fuel rods.

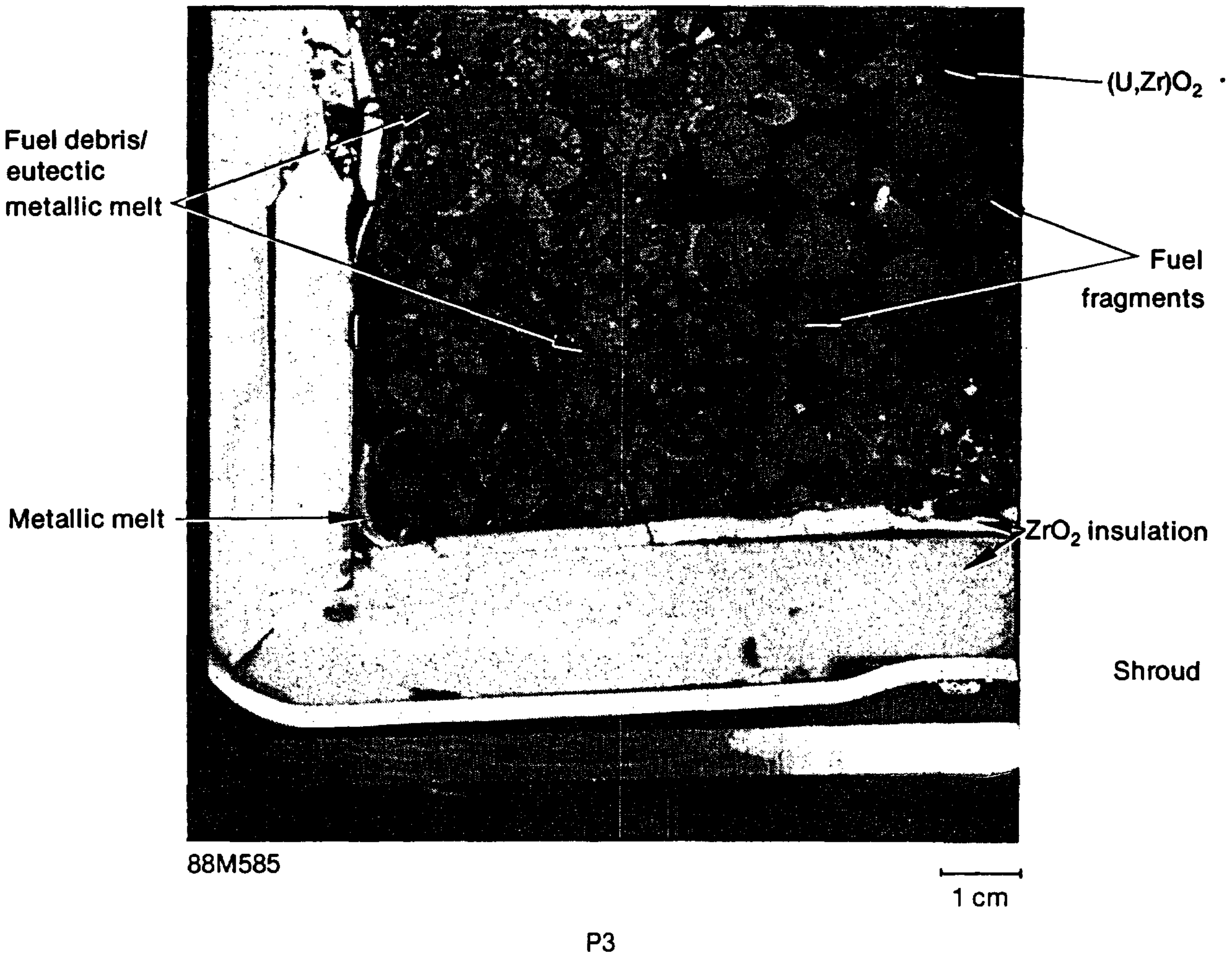

Figure 136. Metallographic cross section P3 at 1.30 m above the bottom of the instrumented fuel rods.

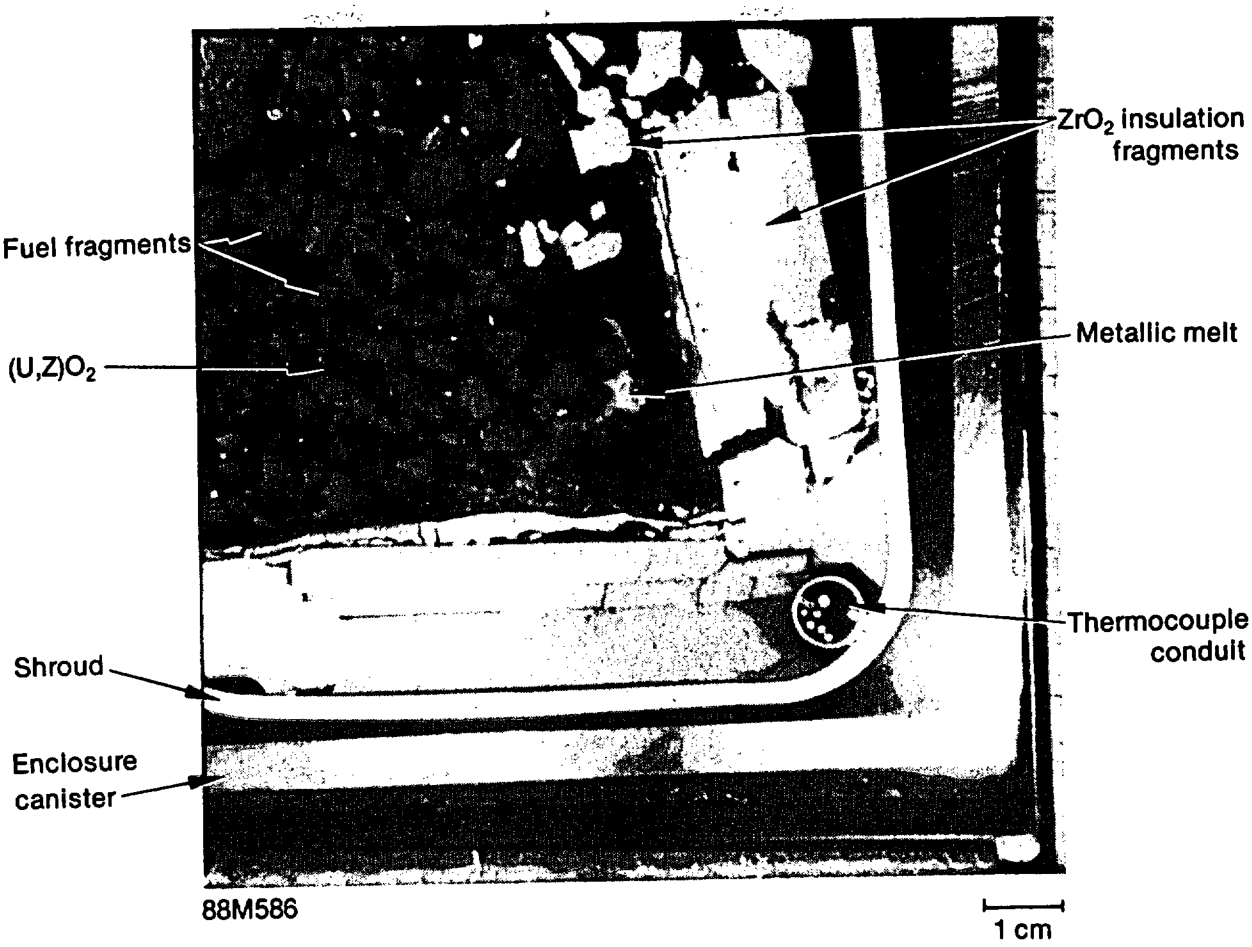

P4

Figure 137. Metallographic cross section P4 at 1.30 m above the bottom of the instrumented fuel rods.

Q1

Figure 138. Metallographic cross section Q1 at 1.45 m above the bottom of the instrumented fuel rods.

Q2

Figure 139. Metallographic cross section Q2 at 1.45 m above the bottom of the instrumented fuel rods.

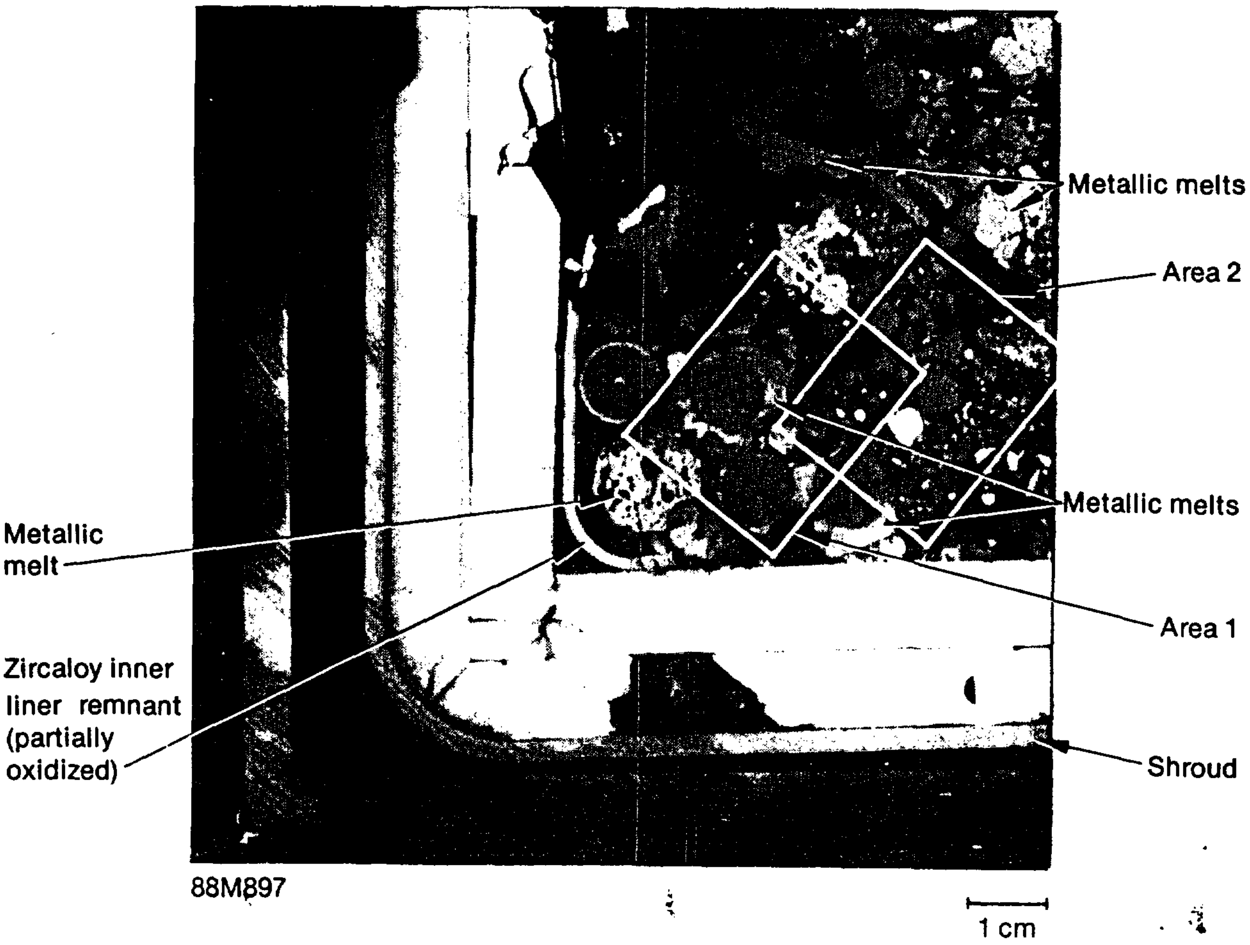

Q3

Figure 140. Metallographic cross section Q3 at 1.45 m above the bottom of the instrumented fuel rods.

Q4

Figure 141. Metallographic cross section Q4 at 1.45 m above the bottom of the instrumented fuel rods.

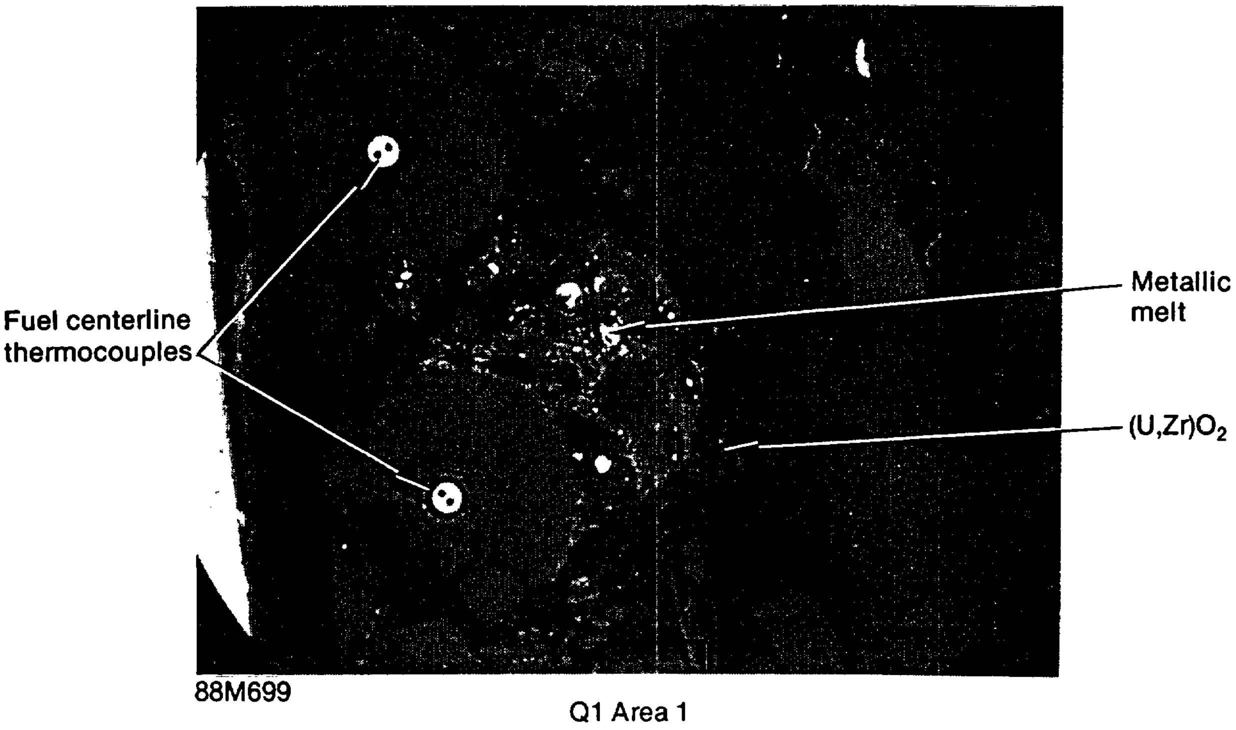

Figure 142. Details of metallographic cross section Q1 at 1.45 m.

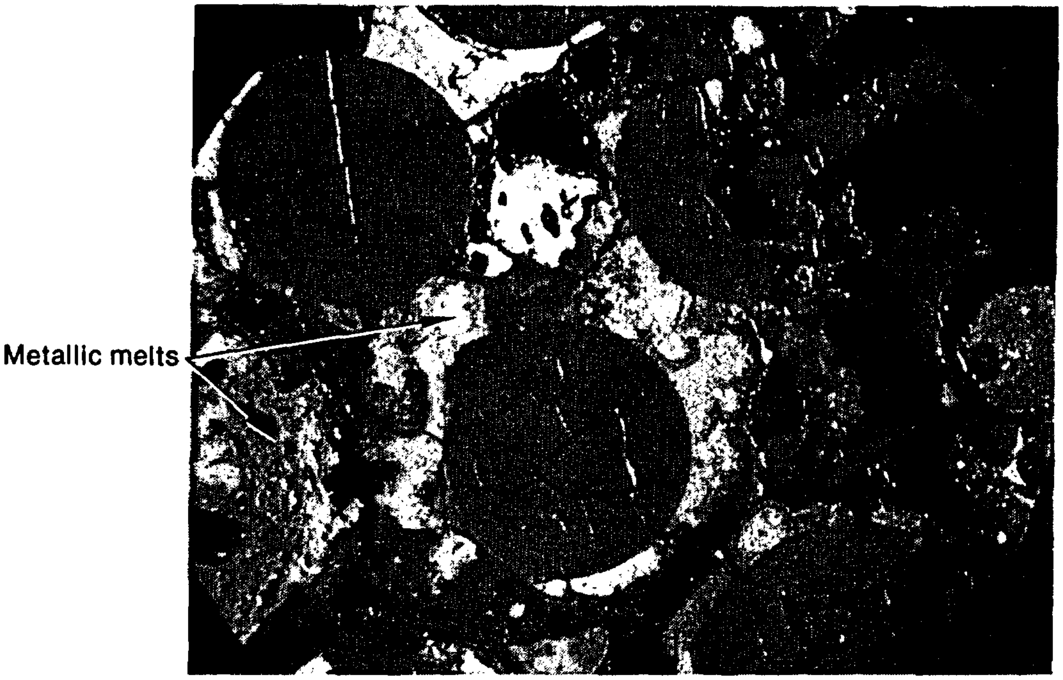

Q3 Area 1

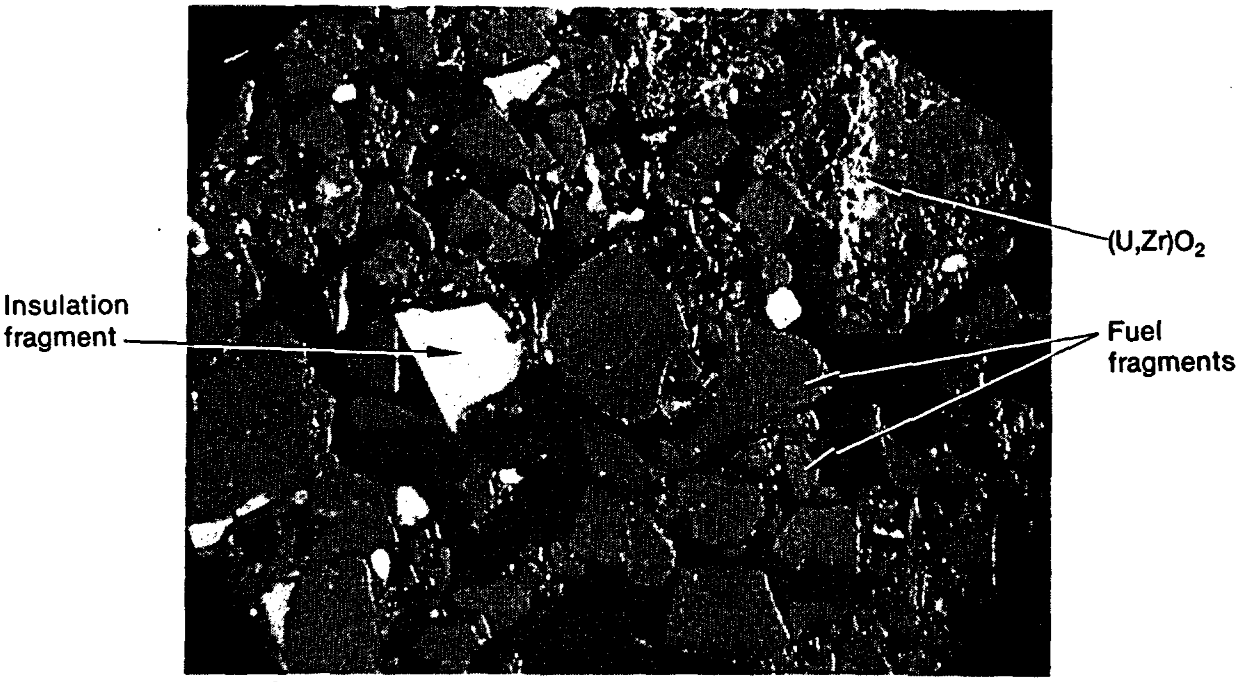

Q3 Area 2

Figure 143. Details of metallographic cross section Q3 at 1.45 m.

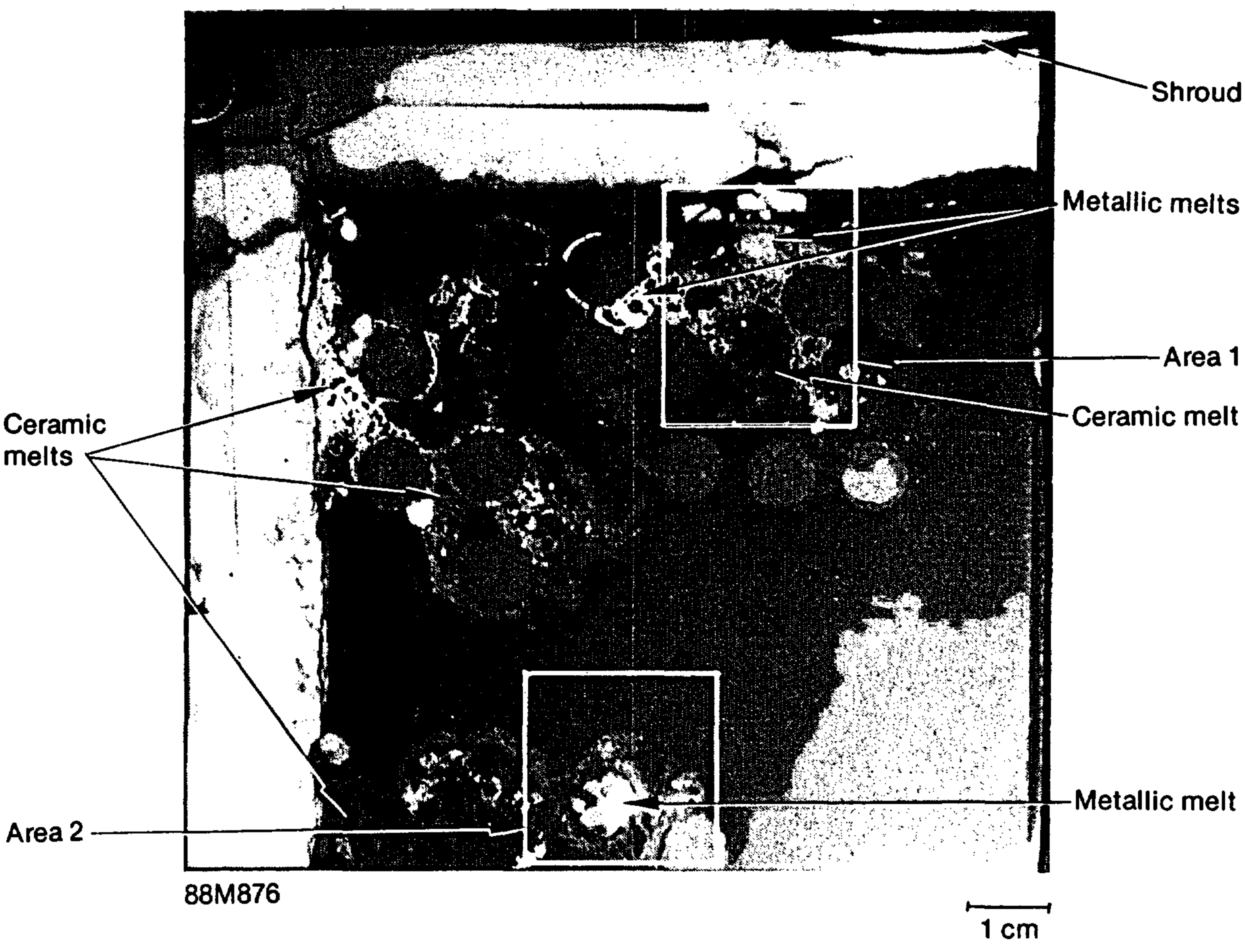

R1

Figure 144. Metallographic cross section R1 at 1.68 m above the bottom of the instrumented fuel rods.

R2

Figure 145. Metallographic cross section R2 at 1.68 m above the bottom of the instrumented fuel rods.

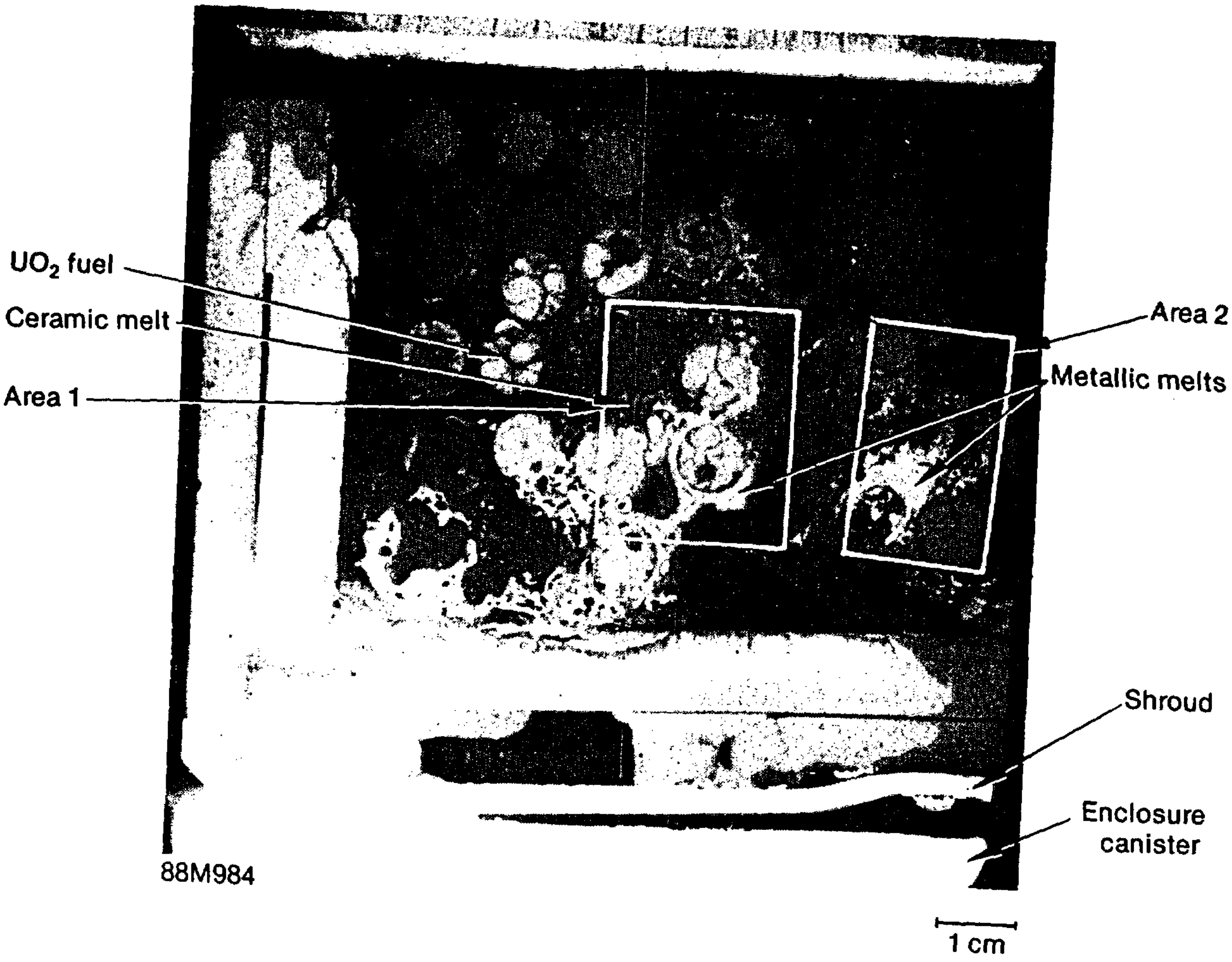

Figure 146. Metallographic cross section R3 at 1.68 m above the bottom of the instrumented fuel rods.

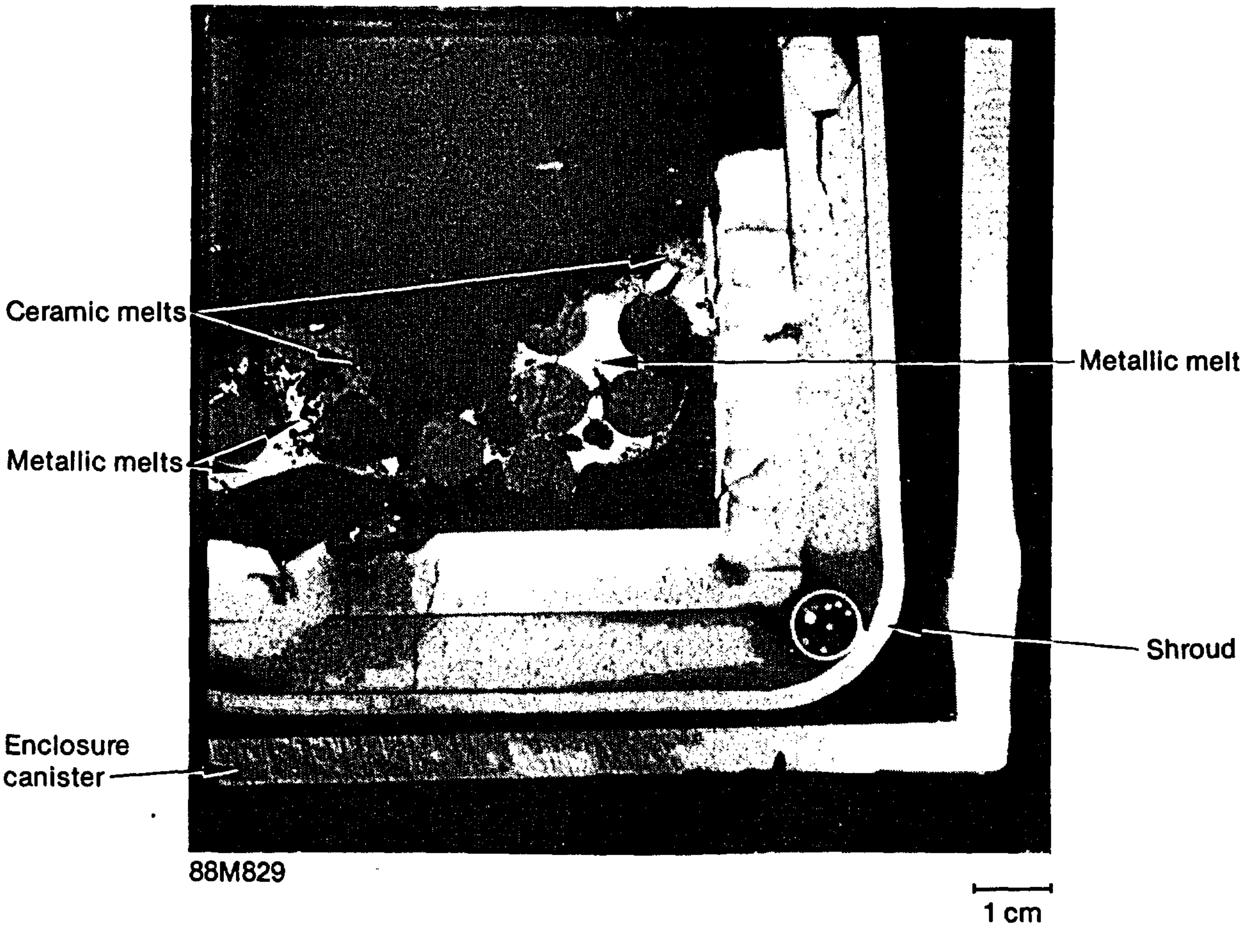

R4

Figure 147. Metallographic cross section R4 at 1.68 m above the bottom of the instrumented fuel rods.

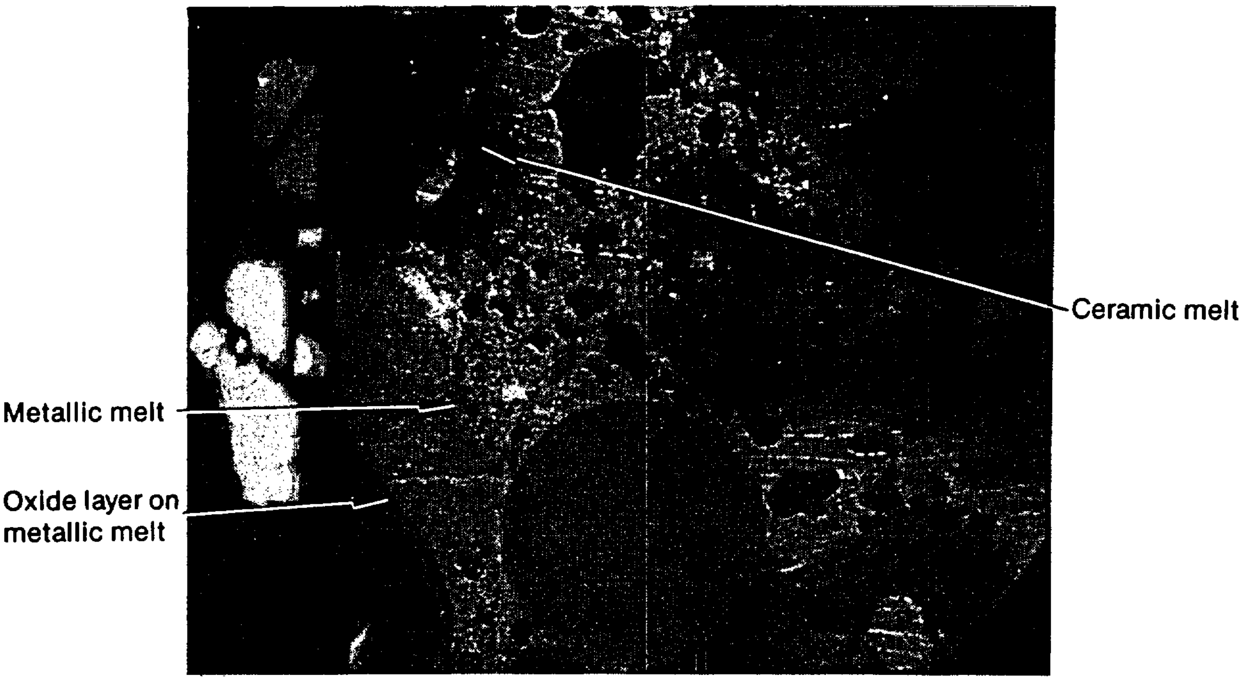

88M877

R1 Area 1

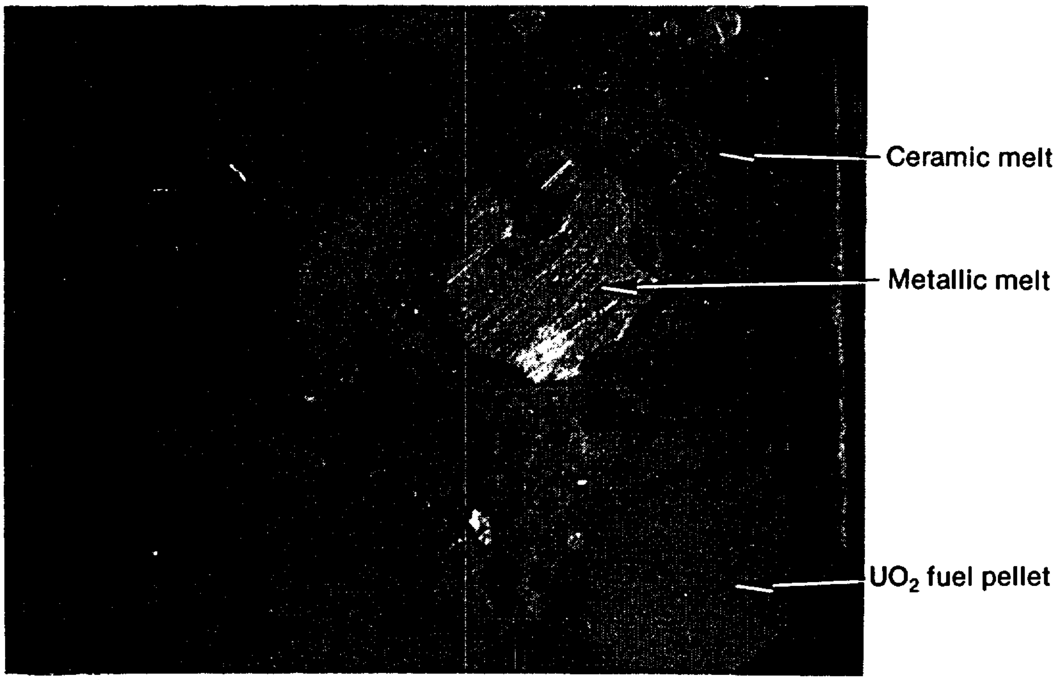

88M878

R1 Area 2

Figure 148. Details of metallographic cross section R1 at 1.68 m.

88M1185

R3 Area 1

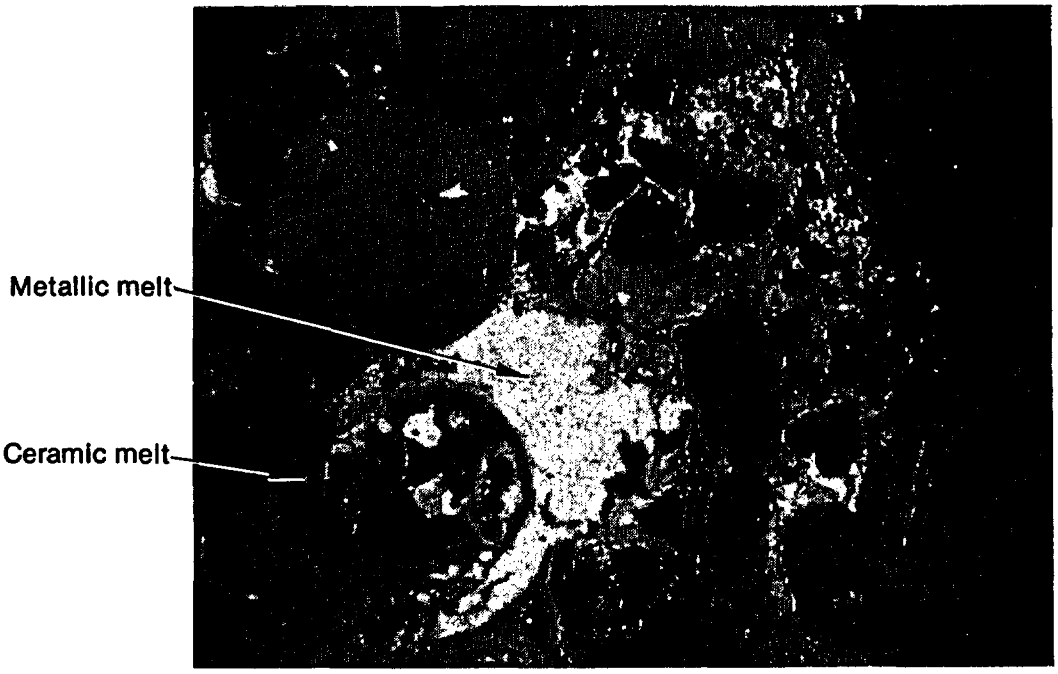

88M1186

R3 Area 2

Figure 149. Details of metallographic cross section R3 at 1.68 m.

previously molten materials that flowed down the exterior surface of the fuel pellets. The rubble bed of fuel pellets present at lower elevations was not present at this elevation. The previously molten materials consisted of both metallic and ceramic phases. Much of these ceramic and metallic melts were probably relocated material from the upper end box.

3.1.20 Cross Section S(bottom) (1.80 m; Figures 150-156)

This cross section was through the stainless steel upper tie plate in the upper end box of the fuel module. Portions of the upper tie plate were intact around the periphery of the cross section; however, the central portion of the upper tie plate had liquefied and portions of the melt had oxidized. SEM/WDS examinations of samples from this metallographic cross section indicated the presence of relocated fuel and control rod materials (Ag and In). Zirconium was also present, but it may have come from the guide tubes that passed through the upper tie plate or it may have relocated like the fuel and control materials did. Molten interactions occurred between these relocated materials, the stainless steel upper tie plate, and the zircaloy guide tubes. These examinations also confirmed that the dark molten material observed metallographically was oxidized.

As described in Section 4.3.4, data from four thermocouples on the bottom surface of the upper tie plate indicated temperatures were <1000 K during the entire transient. All four of these thermocouples showed a temperature excursion during the reflood period, which resulted in temperatures in excess of the melting point of the stainless steel (~1700 K). Exact times and temperatures are uncertain due to failure of the thermocouples during this temperature excursion. There are no interactions that would account for the damage to the upper tie plate when temperatures were <1000 K, which indicates that the melting and oxidation of the upper tie plate had to have occurred during reflood.

3.1.21 Cross Section S(top) (1.83 m; Figures 157-163)

This cross section was just above the upper tie plate, and it was selected to examine the debris noticed in this region during visual

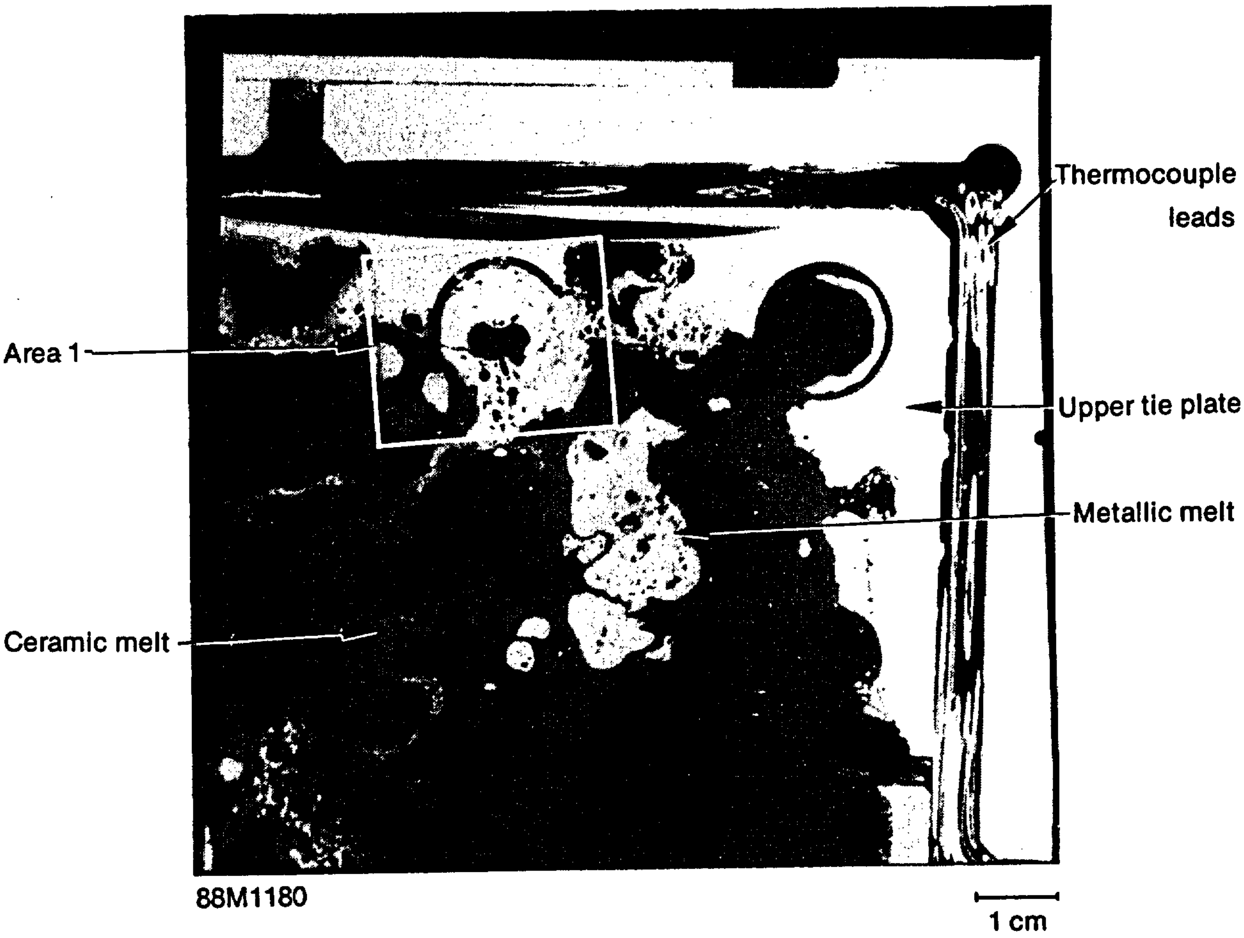

S1 bottom

Figure 150. Metallographic cross section S1 (bottom) at 1.80 m above the bottom of the instrumented fuel rods.

S2 bottom

Figure 151. Metallographic cross section S2 (bottom) at 1.80 m above the bottom of the instrumented fuel rods.

S3 bottom

Figure 152. Metallographic cross section S3 (bottom) at 1.80 m above the bottom of the instrumented fuel rods.

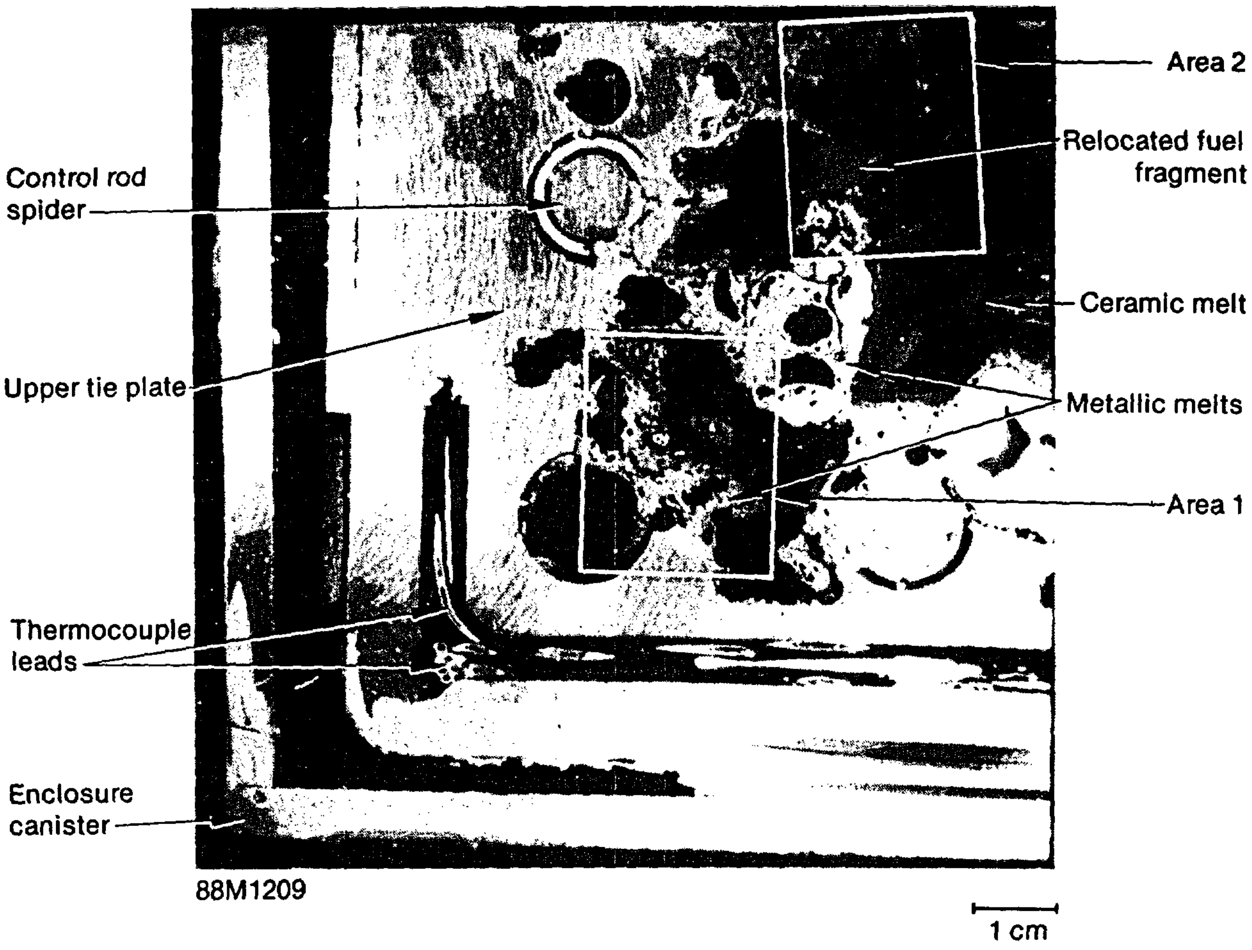

S4 bottom

Figure 153. Metallographic cross section S4 (bottom) at 1.80 m above the bottom of the instrumented fuel rods.

S1 (Bottom) Area 1

S2 (Bottom) Area 1

Figure 154. Details of metallographic cross section S1 (bottom) and S2 (bottom) at 1.80 m.

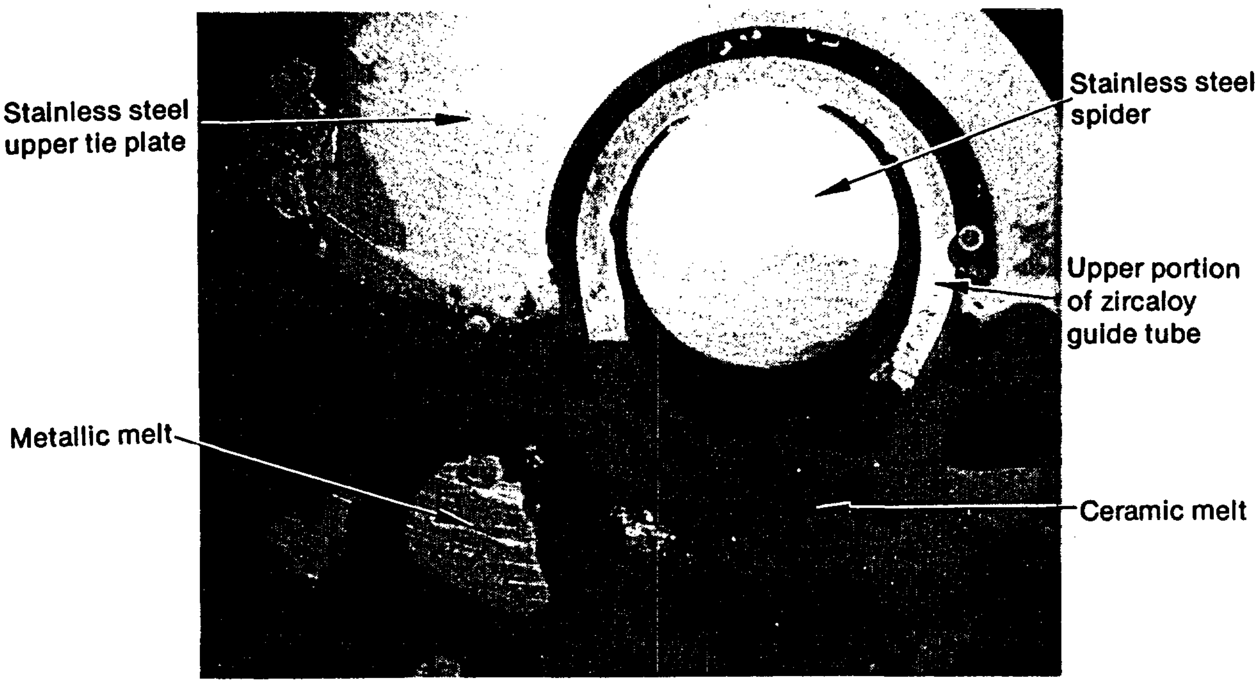

88M1109

S3 (Bottom) Area 1

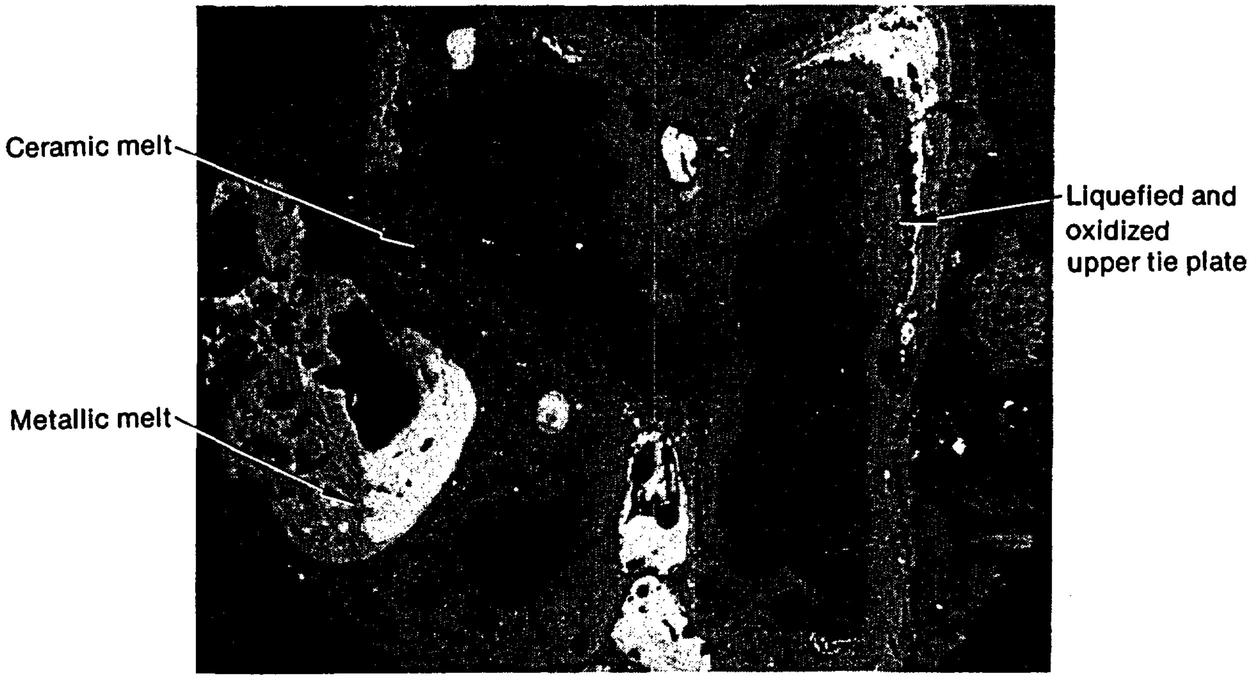

88M1110

S3 (Bottom) Area 2

Figure 155. Details of metallographic cross section S3 (bottom) at 1.80 m.

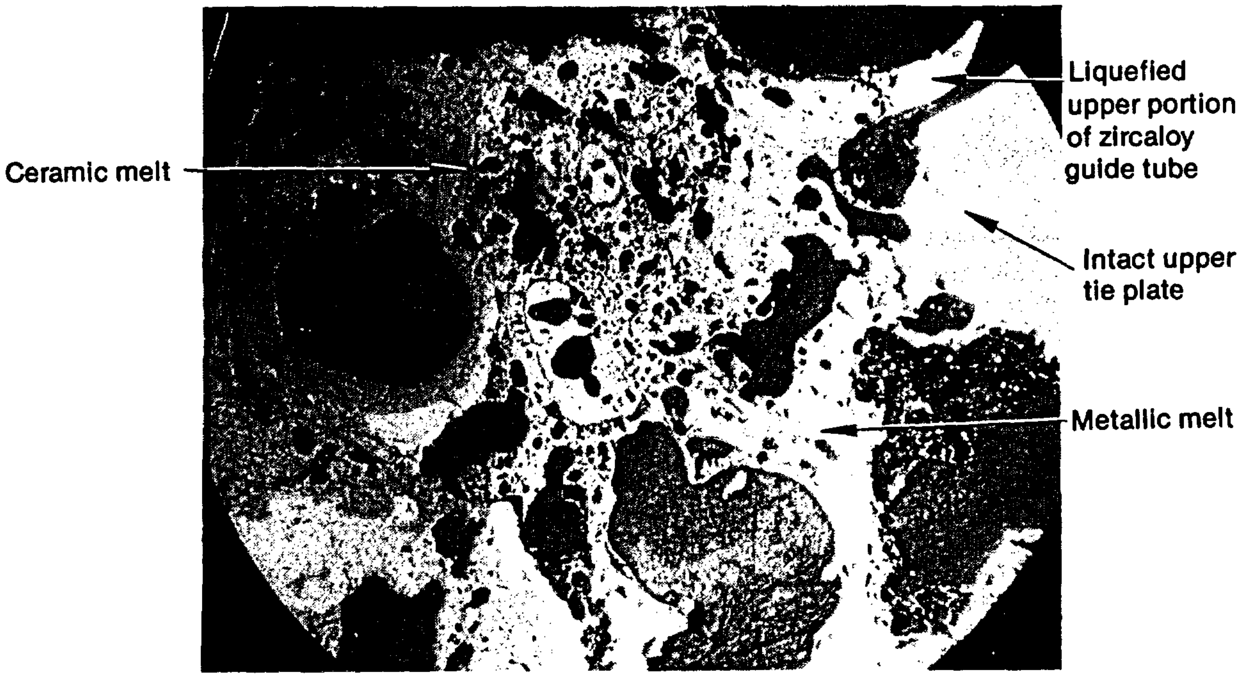

88M1211

S4 (Bottom) Area 1

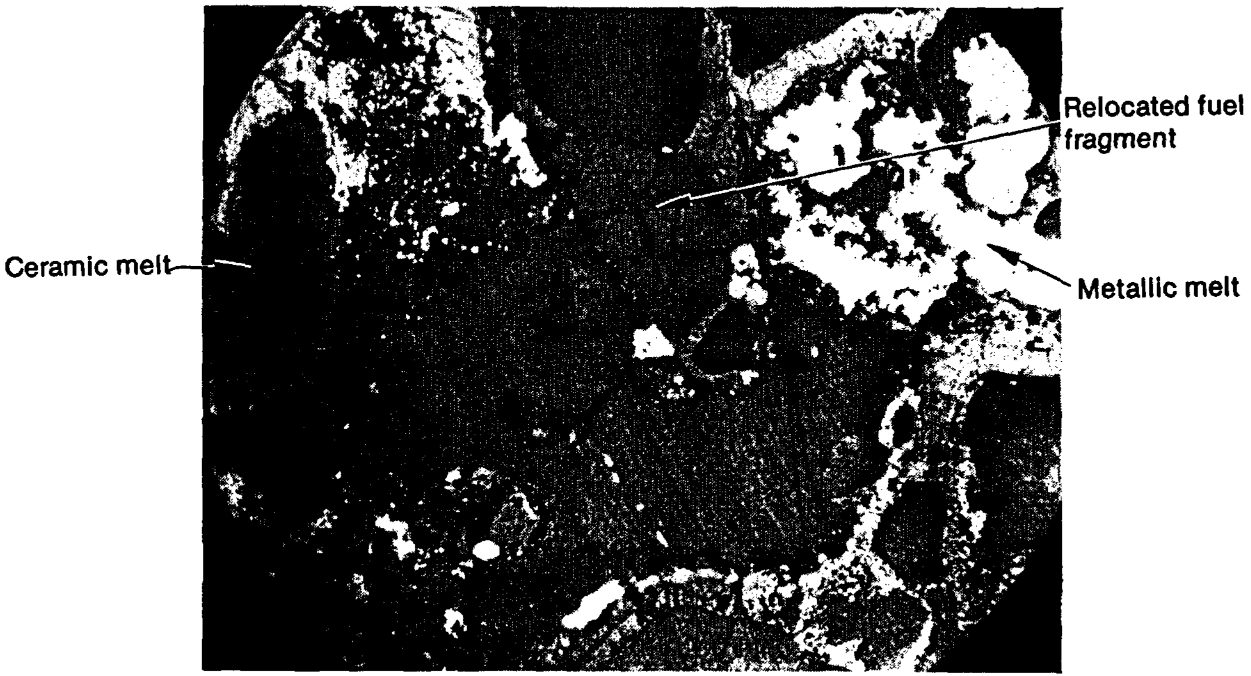

88M1210

S4 (Bottom) Area 2

Figure 156. Details of metallographic cross section S4 (bottom) at 1.80 m.

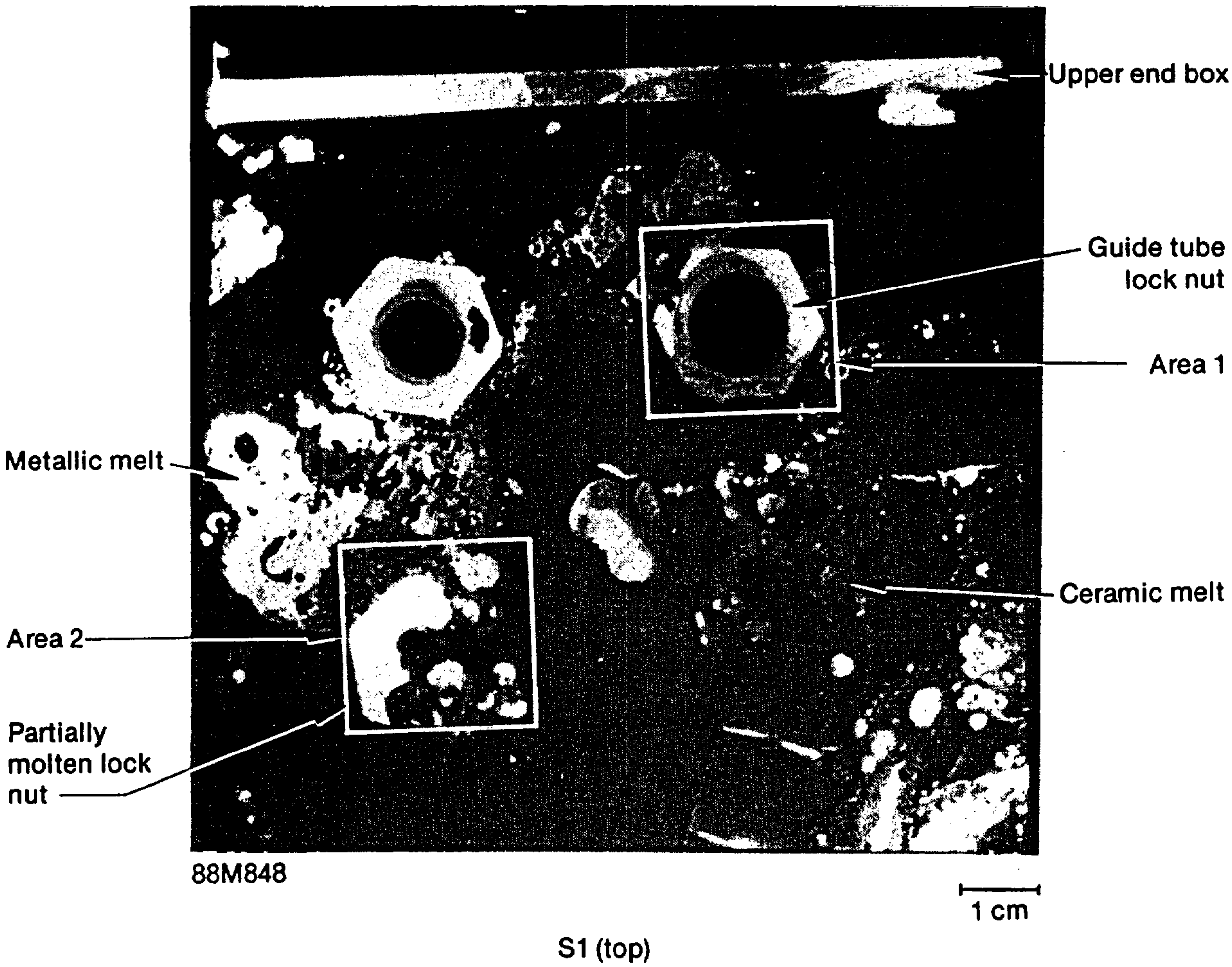

Figure 157 Metallographic cross section S1 at 1.83 m above the bottom of the instrumented fuel rods.

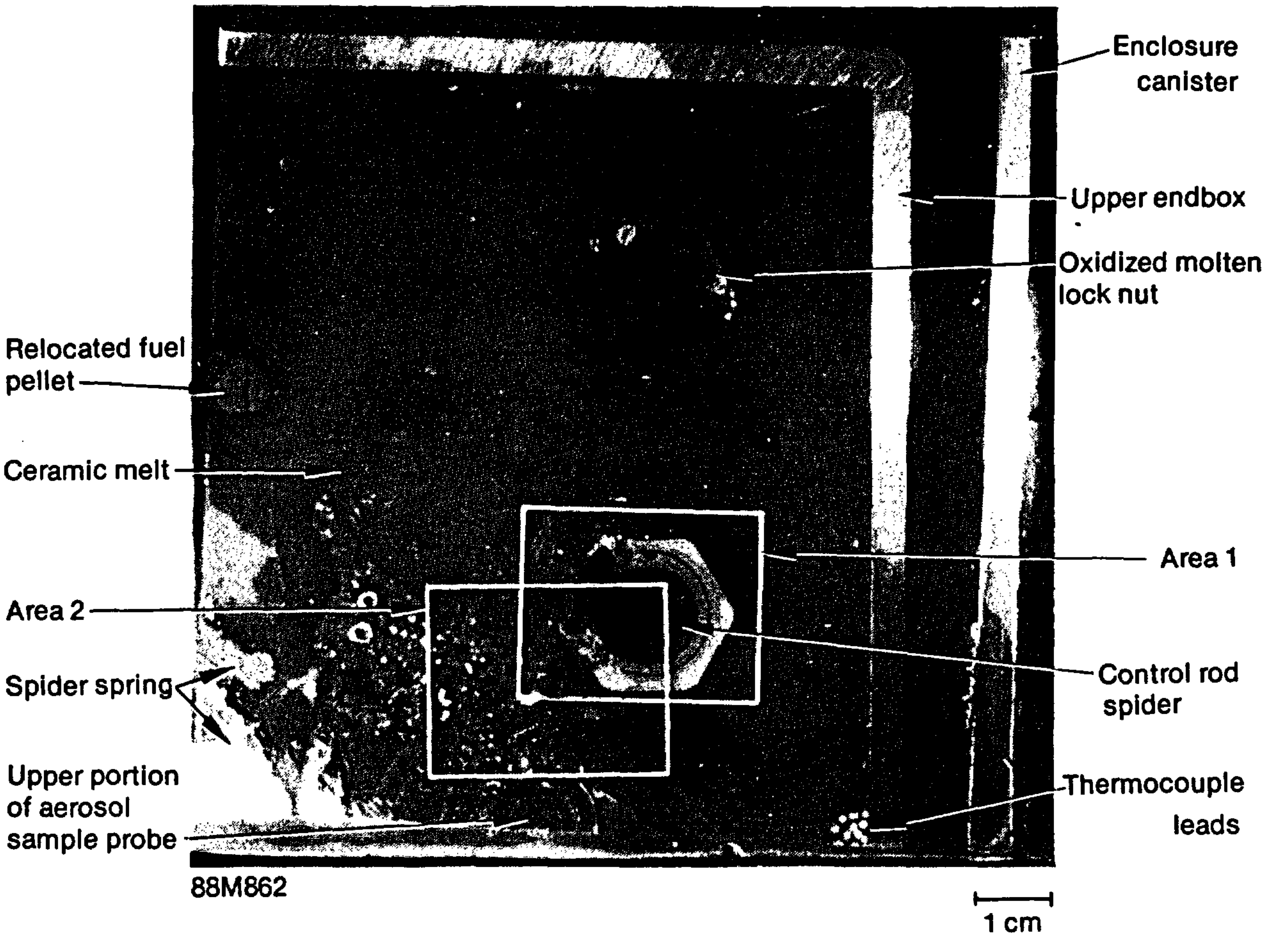

S2 (top)

Figure 158. Metallographic cross section S2 at 1.83 m above the bottom of the instrumented fuel rods.

S3 (top)

Figure 159. Metallographic cross section S3 at 1.83 m above the bottom of the instrumented fuel rods.

S4 (top)

Figure 160. Metallographic cross section S4 at 1.83 m above the bottom of the instrumented fuel rods.

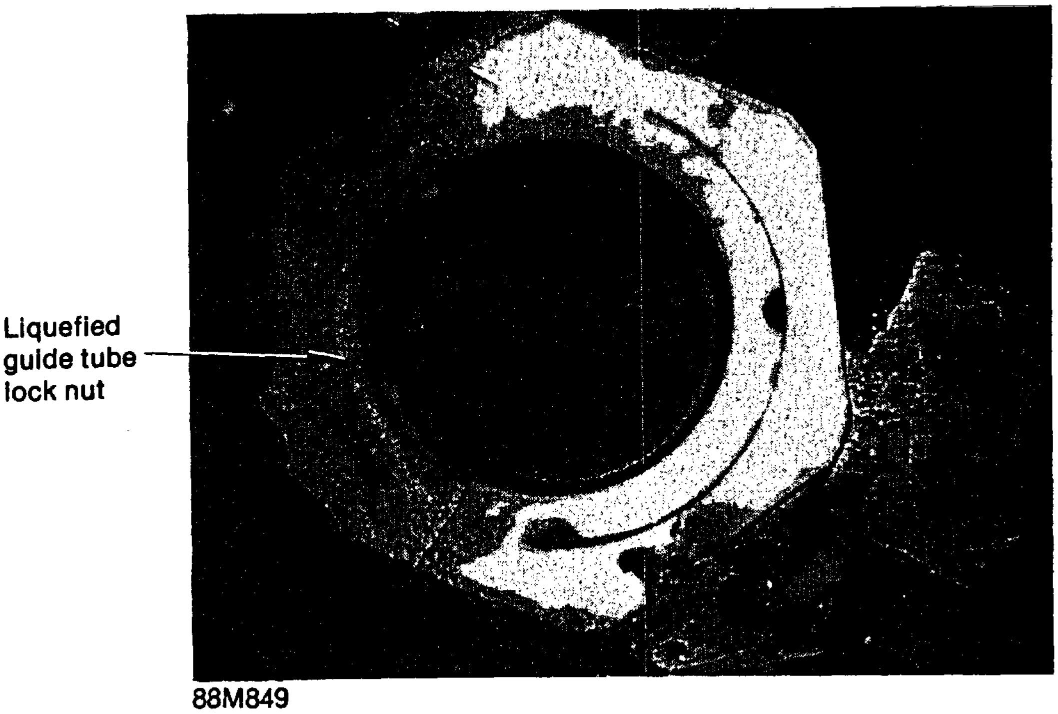

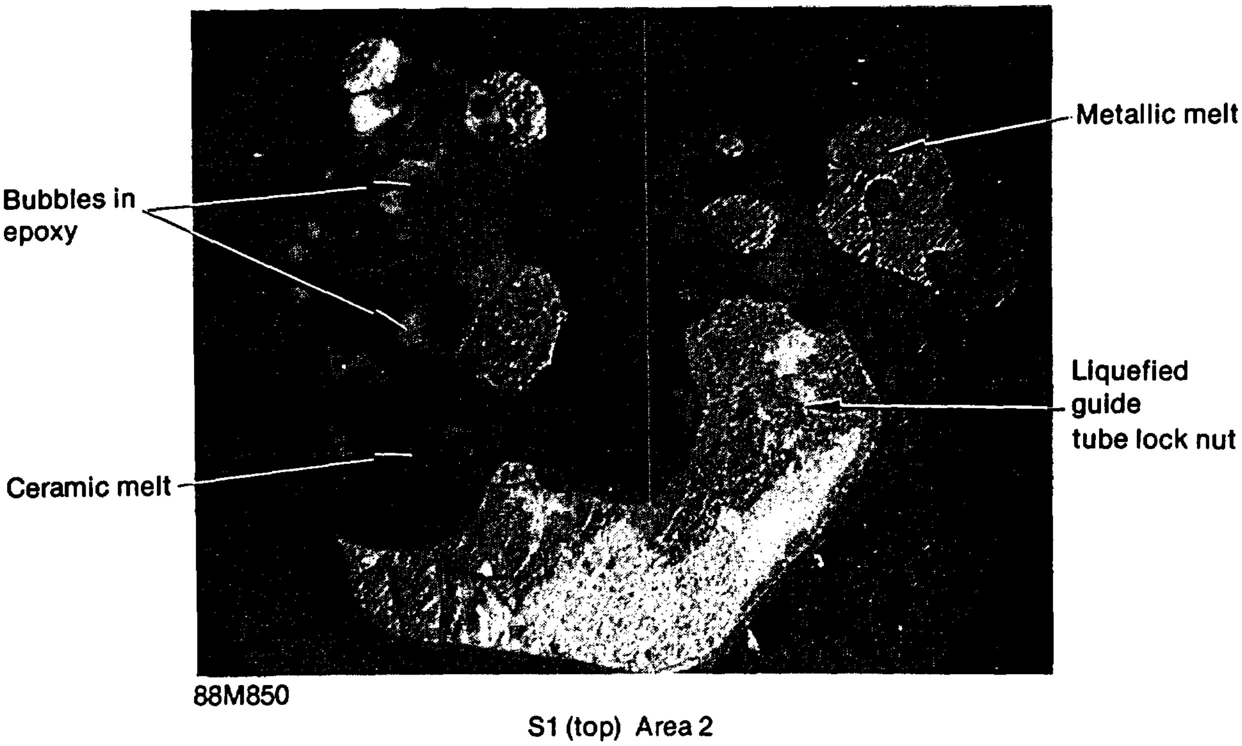

Figure 161. Details of metallographic cross section S1 at 1.83 m.

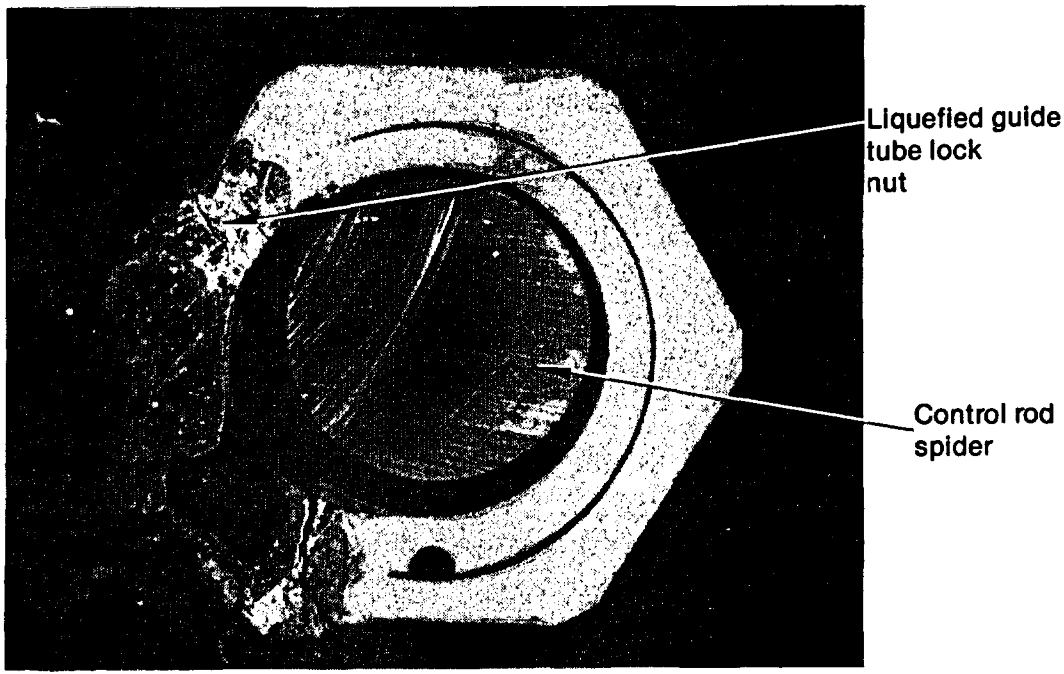

S2 (top) Area 1

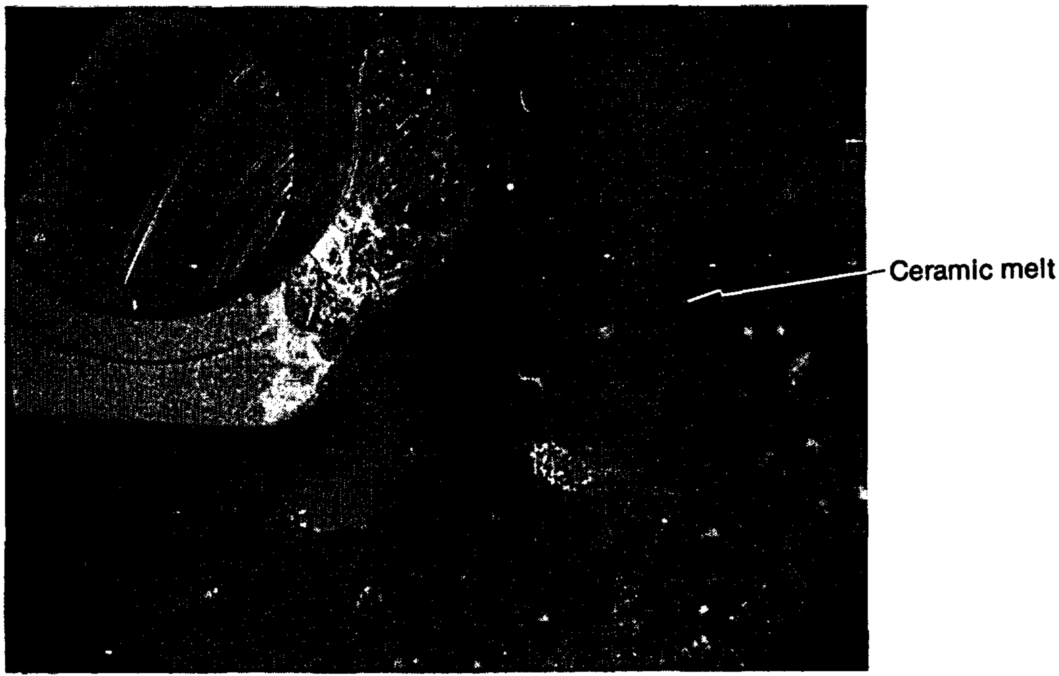

S2 (top) Area 2

Figure 162. Details of metallographic cross section S2 at 1.83 m.

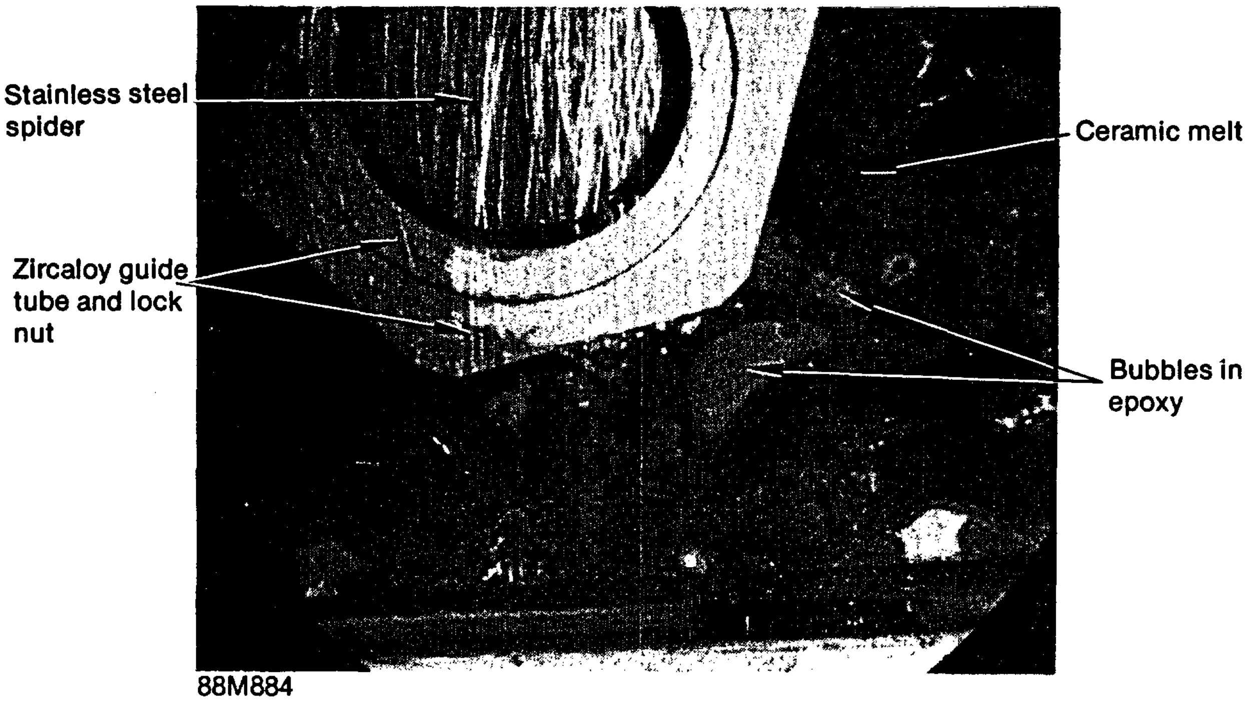

S4 (top) Area 1

Figure 163. Details of metallographic cross section S4 at 1.83 m.

examinations and in the neutron radiographs. Partially molten guide tube lock nuts are visible, along with a variety of previously molten metallic and ceramic phases. SEM/WDS and radiochemical analyses samples from this region confirmed that fuel material had relocated to this area. This material had to have relocated to this position during the reflood period when the steam mass flow rates increased to ~5 kg/s. Steam mass flow rates were only ~13 g/s during the high-temperature portion of the transient.

3.2 Behavior of Specific Materials

3.2.1 Spacer Grid Behavior

Five Inconel 718 spacer grids were used in the LP-FP-2 fuel module. The axial locations of these spacer grids are shown on the neutron radiographs in Figures 7 and 8. Following the completion of the experiment, only the bottom spacer grid was still completely intact. The second highest spacer grid (0.44-0.49 m) was partially intact. The other three spacer grids had completely liquefied. Relocating material accumulated at the second spacer grid, which suggests that the spacer grids served as traps for relocating material until they ultimately failed. Both of the large blockage regions were located just above the two remaining spacer grids.

The bottom spacer grid can be seen in the photographs of the B cross section (Figures 14 through 18). Only minor amounts of molten (Ag,In,Cd) droplets relocated to this elevation, and no interactions occurred between these droplets and the spacer grid. This is attributed to the relatively low heat content of the droplets and the large heat sink provided by the spacer grid.

The second spacer grid can be seen in the photographs of the G(top) cross sections in Figures 50 through 58. The most extensive damage to the spacer grid was in the G2 quadrant. The majority of the relocated material at this elevation is composed of eutectic metallic melt and fuel debris, similar to the material composing the lower blockage.

Examples of typical interactions between the spacer grids and molten materials are provided in Figures 164 through 168. SEM/WDS examinations of these types of interactions were performed on samples G1-S19 and G2-S20 and are discussed in detail in Appendix E. The results from these examinations provide information on the damage progression involved in liquefaction of the spacer grids. This progression involved the formation of an intergranular metallic phase within the intact spacer grid, which was composed of zirconium and niobium. The subsequent liquefaction of the spacer grid is apparently rapid enough that, other than the intergranular Zr-Nb phase, no elemental diffusion is observed beyond the spacer grid/melt interface. One indicator that the Widmanstatten structure region was previously molten and was not just a result of solid state diffusion of elements into the spacer grid was the formation of a ZrO_2 layer on its outer surface. Similar oxide layers were observed on molten droplets of (Ag,In,Cd), as described in Section 3.2.2. In other areas, a dendritic structure is observed (Figures 165,166A). The change from the Widmanstatten structure to the dendritic structure may be caused by differences in composition and/or cooling rates. Figure 168 shows one example of this transition in morphology.

The SEM/WDS examinations of sample G1-S19 (Area 1) indicated that the intergranular phase, which can be seen in Figures 165 and 166B at the interface between the unaffected spacer grid and the molten regions, was composed of zirconium and niobium. The zirconium contained in the melt penetrated along the grain boundaries and combined with the niobium in the spacer grid. As shown in the Zr-Nb phase diagram in Appendix G, this metallic phase would be solid below 2013 K, so this intergranular phase does not result in liquefaction of the Inconel spacer grid. Results from G1-S19 (Area 1) also indicated that in the previously molten region adjacent to the intergranular attack in Figures 166B and 167 was a complex mixture of zircaloy components (Zr,Sn), interacting with the Inconel components (Ni,Fe,Cr,Nb,Mo,Ti), with indium and small amounts of silver from the control rods also mixed in. Results from G2-S20 (Area 1) indicated that the dendritic melt phase was composed of the same elements as in the region of Widmanstatten structure and that the melt observed in Figure 164, adjacent

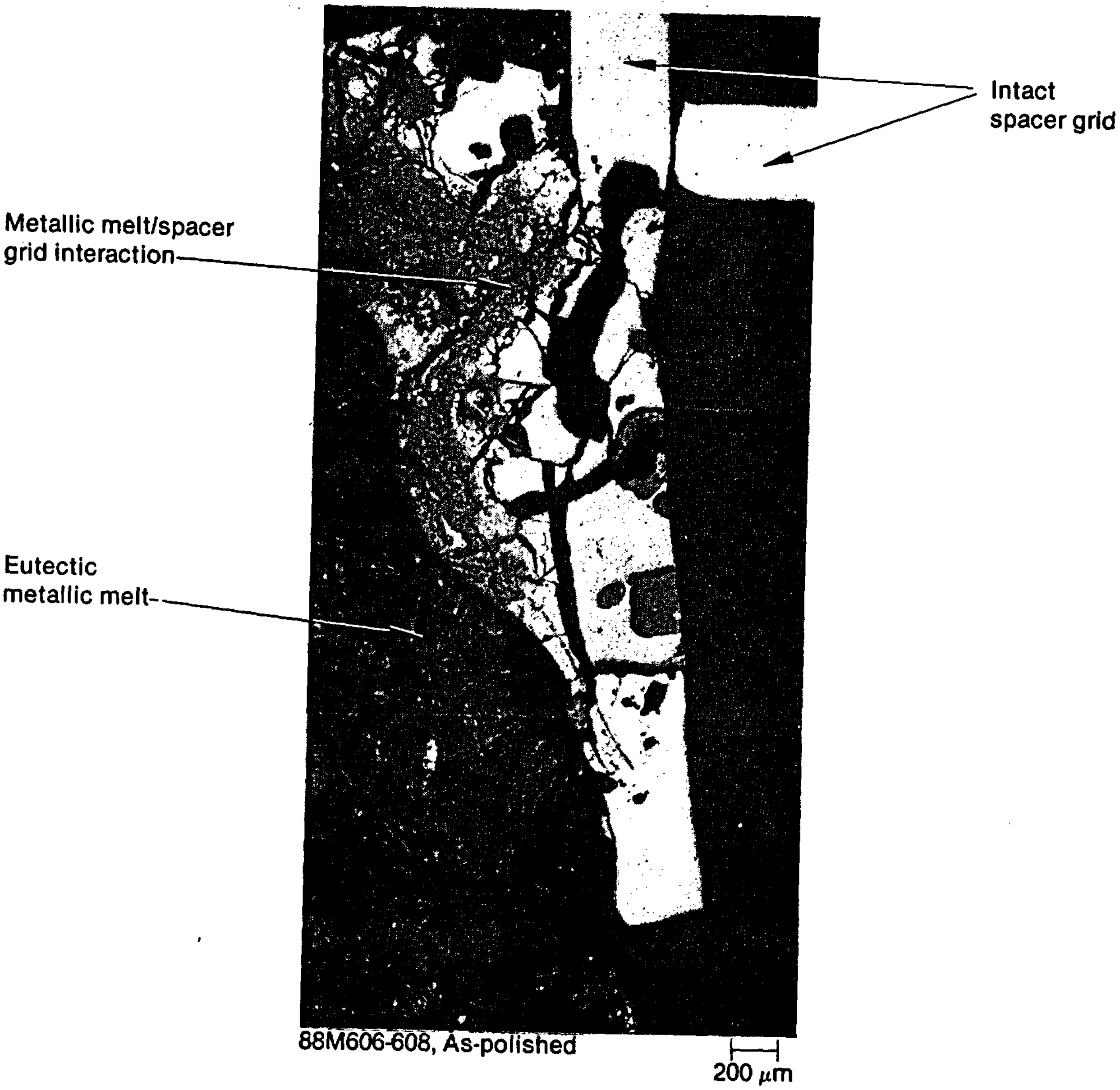

Figure 164. Metallic melt interacting with Inconel spacer grid at 0.46 m.

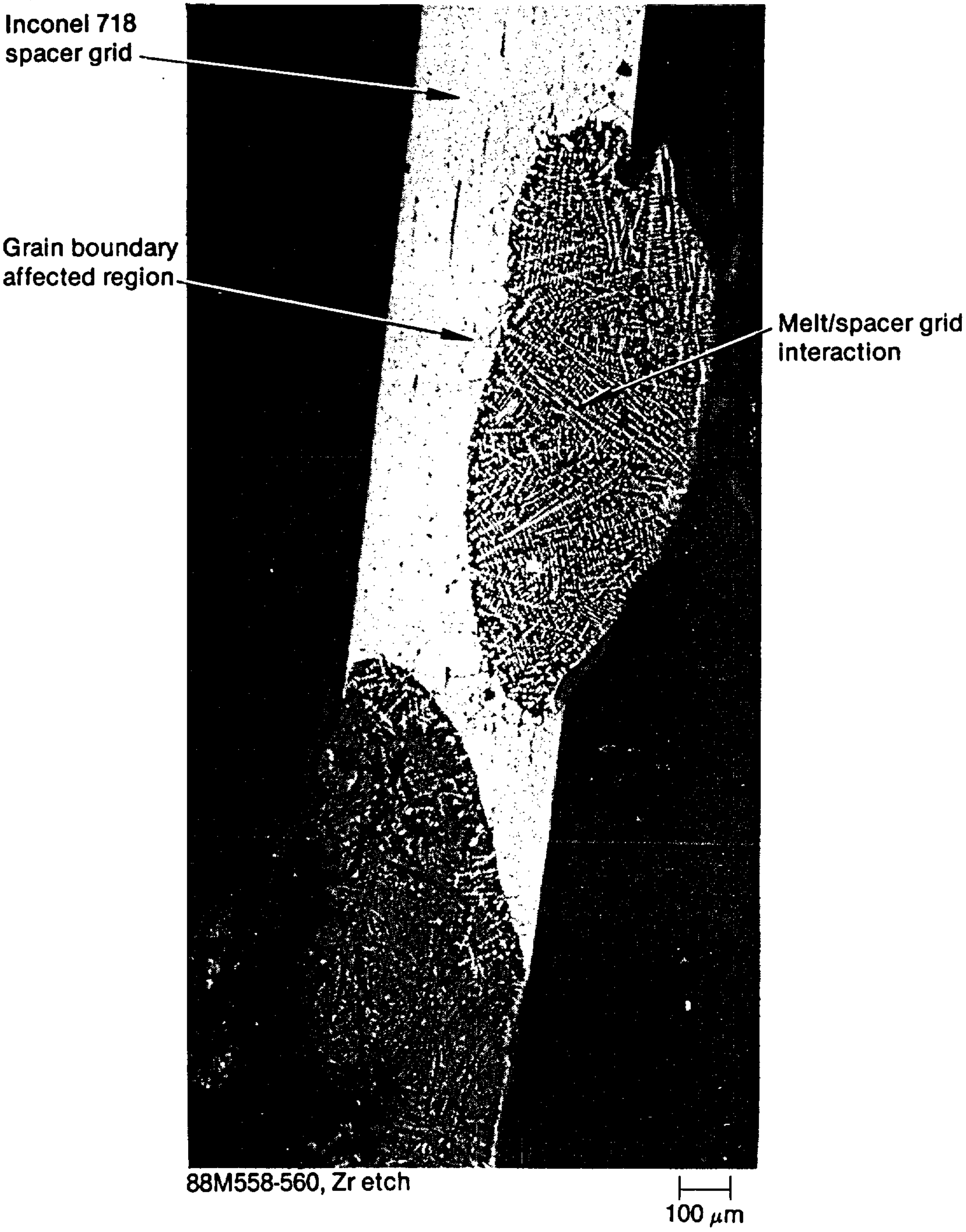

Figure 165. Dendritic metallic melt interacting with Inconel spacer grid at 0.46 m.

(A) Dendritic structure of melt interacting with spacer grid.

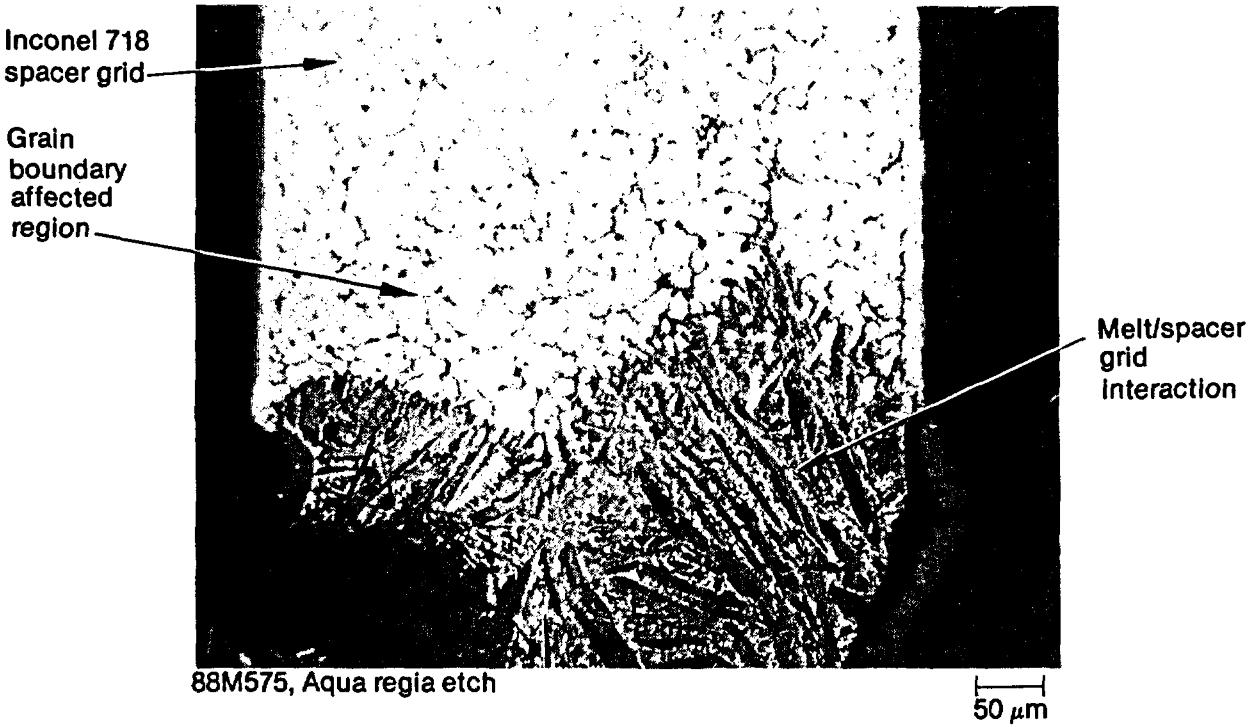

(B) Melt/spacer grid interactions

Figure 166. Details of metallic melt/spacer grid interactions at 0.46 m.

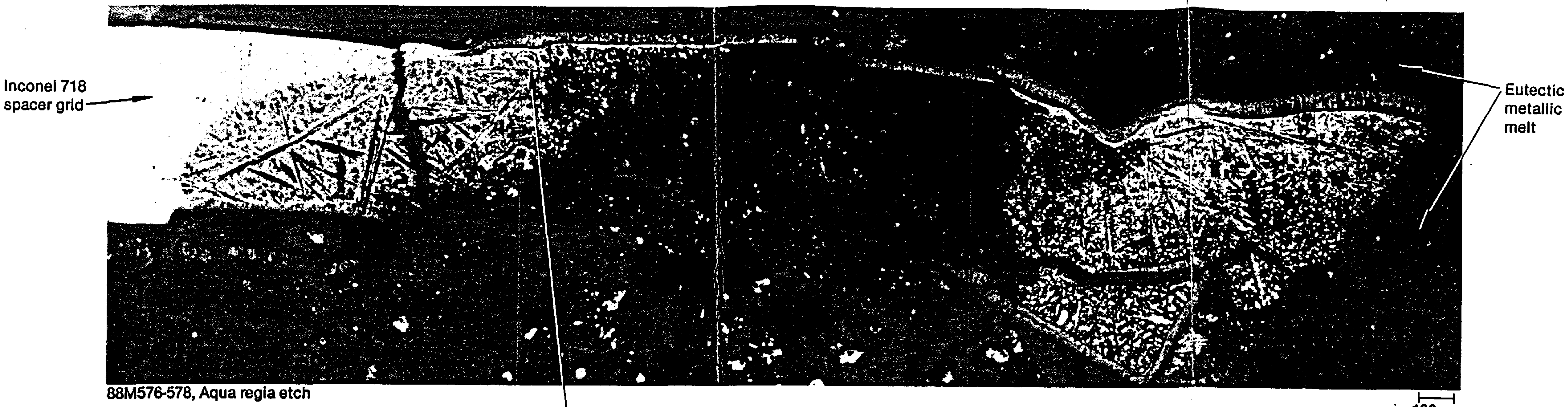

(A) Melt interactions with Inconel spacer grid

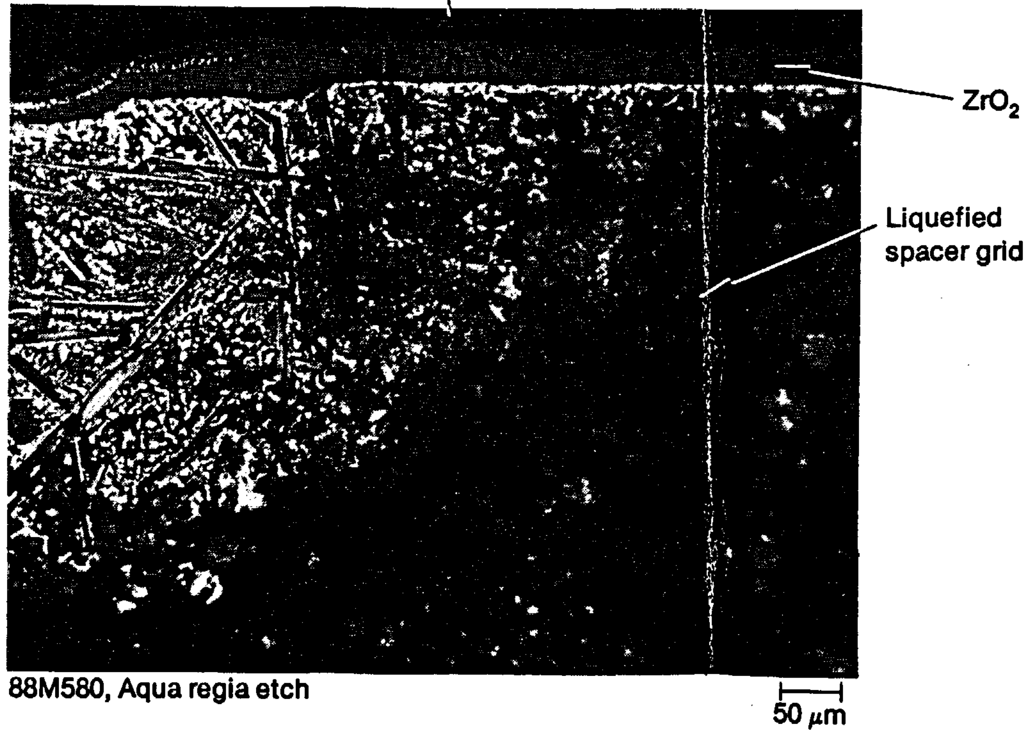

(B) Detail of melt/spacer grid interaction

Figure 167. Melt interactions with spacer grid at 0.46 m.

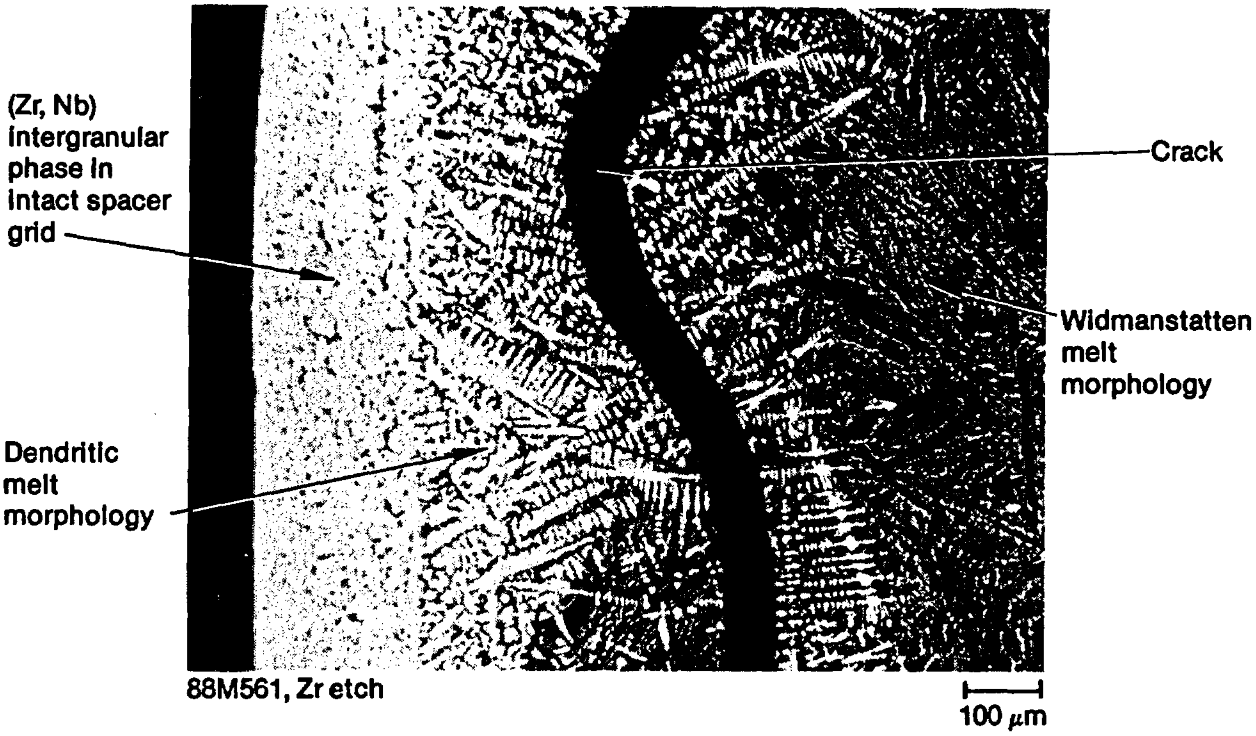

Figure 168. Damage gradient in metallic melt/spacer grid interactions at 0.46 m.

to the spacer grid, was also composed of these same elements, except for the presence of greater amounts of (Ag,In,Cd) alloy. The various morphologies observed metallographically may be attributed to compositional differences in the melt before it came in contact with the Inconel spacer grid and differences in temperatures and cooling rates.

As shown in Appendix G, the formation of eutectic melt phases between Zr,Ni and Zr,Fe could result in liquid phases as low as 1220-1233 K for Zr-rich mixtures of these elements. A series of eutectic melts can also form between Zr and Ni over wide compositional ranges at temperatures between 1233 and 1443 K, as shown in the Ni-Zr phase diagram. Since the majority of Inconel 718 is nickel (~50 wt%), the Ni-Zr phase diagram suggests that extensive liquefaction of the spacer grids can be expected at temperatures between 1400-1500 K, well below the 1720-K melting point of Inconel 718. This type of behavior is certainly consistent with the SEM/WDS examinations of G1-S19 and G2-S20, which show that zirconium is interacting with the elemental components in the Inconel to form eutectic and multiphase compounds.

Zirconium, nickel, and iron would seem to be the primary components involved in the liquefaction process, based upon their relative abundance and the possible interactions indicated by the binary phase diagrams. However, other secondary interactions are also probably occurring. For instance, the indium in the molten control material may also have affected the spacer grid liquefaction behavior, due to interactions with the nickel. Figure G-11 in Appendix G shows eutectic interactions on the nickel-rich side of the Ni-In phase diagram at 1183 K. However, due to the relatively small amount of indium in the experiment, these interactions are probably negligible when trying to model this phenomenon.

The zirconium required to cause liquefaction of the spacer grids could have come from two sources. The first possibility is solid-state diffusion from the zircaloy guide tubes that were in contact with the spacer grids. The second possibility is from relocating melt material. The zirconium in the melt may have resulted from aerosol or molten (Ag,In,Cd) interactions with the zircaloy. The presence of Ag-Zr eutectic melts in the lower blockage region indicates that this type of interaction was responsible for early material relocation. Another possibility is that the molten zirconium was released from the cladding inner surface, upon failure of the ZrO_2 oxide shell containing the molten pool. It is likely that all three of these possibilities contributed to the liquefaction of the spacer grids at some point during the experiment.

3.2.2 Control Rod Behavior

As shown in the photographs of the G(top) cross sections (Figures 50-58), all the (Ag,In,Cd) was still contained in all eleven control rods at the second spacer grid elevation (0.46 m). However, at the next cross section (0.58 m), all the stainless steel cladding on the control rods had liquefied, allowing all the molten (Ag,In,Cd) above this elevation to be released to the fuel bundle. This release may have been in the form of an aerosol spray when the cladding initially failed at some point, but after this initial failure the molten (Ag,In,Cd) would have candled down the outer surface of the control rod cladding. As described in Section 4.1, 70% (~10 kg) of the (Ag,In,Cd) in the fuel bundle was released and available to interact with other bundle constituents. All the (Ag,In,Cd) at and below the E elevation (0.27 m) remained as a solid throughout the experiment, which indicates temperatures below 1073 K. Examples of intact and molten control material are shown in Figure 169; the molten material can be identified by its dendritic structure. At the F elevation (0.36 m), all the (Ag,In,Cd) was molten on sample F1 and on the interior control rods of sample F4; however, it was still intact on the exterior control rods of sample F4. Samples F2 and F3 were not metallographically examined. These data indicate that (Ag,In,Cd) temperatures were near the 1073-K melting point at this elevation. On the G(bottom) and G(top) cross sections (0.43-0.46 m), all the (Ag,In,Cd) alloy was molten; but essentially all of it was still contained within the stainless steel cladding. Figure 170 shows molten control material flowing through a breach in the stainless steel cladding at what must be the upper extent of intact cladding on sample G2(top). Liquefaction of the outer stainless steel surface as a result of

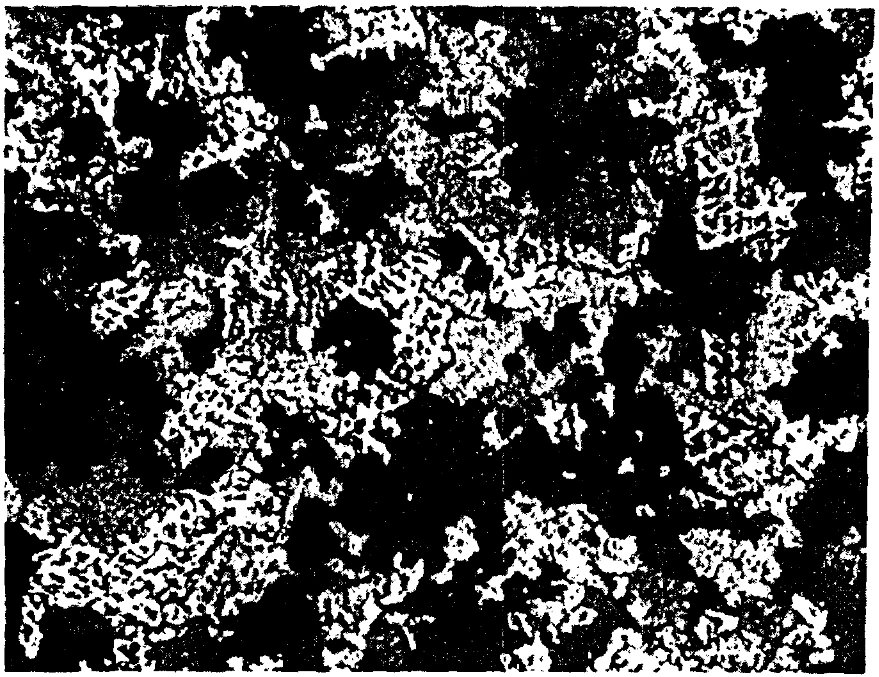

88M535, Zr etch

100 μm

(A) Molten (Ag,In,Cd) control material

88M98, Zr etch

100 μm

(B) As-fabricated (Ag,In,Cd) control material

Figure 169. Structures of molten and as-fabricated (Ag,In,Cd) control material.

Figure 170. Molten droplet of (Ag,In,Cd) escaping through failed stainless steel cladding at 0.46 m.

Zr,Fe and Zr,Ni eutectic interactions was apparent at both of the G cross sections. The stainless steel cladding on the control rods was completely unaffected by any melt interactions at lower elevations. Droplets of molten (Ag,In,Cd) were located throughout the fuel bundle below the second spacer grid. Above this elevation, the metallic melts tended to have significant concentrations of other elements (Fe,Cr,Ni,Zr,U) and were multiphase.

Figure 43 of the G2(bottom) cross section shows a series of (Ag,In,Cd) droplets that have flowed down the exterior of a control rod and solidified. This molten material was present between the stainless steel cladding and the zircaloy lock ring. The zircaloy guide tube was completely gone. (The lock ring and guide tube can be differentiated based upon their thicknesses.) This area is shown in detail in Figure 171, and SEM/WDS sample G2-S16A was examined to provide compositional data on the material in this area. The results from these SEM/WDS examinations are discussed in detail in Appendix E, but a summary of the pertinent results is provided below.

Figure 171 shows that an oxide layer formed on the some of the surfaces between the droplets. This oxide layer is not present on adjacent surfaces of the melt droplets. SEM/WDS examinations of sample G2-S16A indicated that this layer was composed of ZrO_2. Similar formations of ZrO_2 oxide layers on the surface of melts were observed in other instances. A typical examples is provided in Figure 167.

Material interactions between the molten control material and the zircaloy lock ring are also apparent in Figure 171. Elemental dot maps of this interaction area are shown for SEM/WDS sample G2-S16A Area 4 in Appendix E. These SEM/WDS examinations showed a Ag-Zr melt phase on the outer surface of the intact zircaloy lock ring. This area is similar to the melt phase adjacent to the intact zircaloy lock ring in Figure 171. However, the areas on the surfaces of the lock ring that appear to have a needlelike dark phase in Figure 171 only showed zirconium to be present. This is in contrast to examinations of similar appearing zircaloy, described in Section 3.2.3 on the zircaloy behavior, which indicated diffusion of

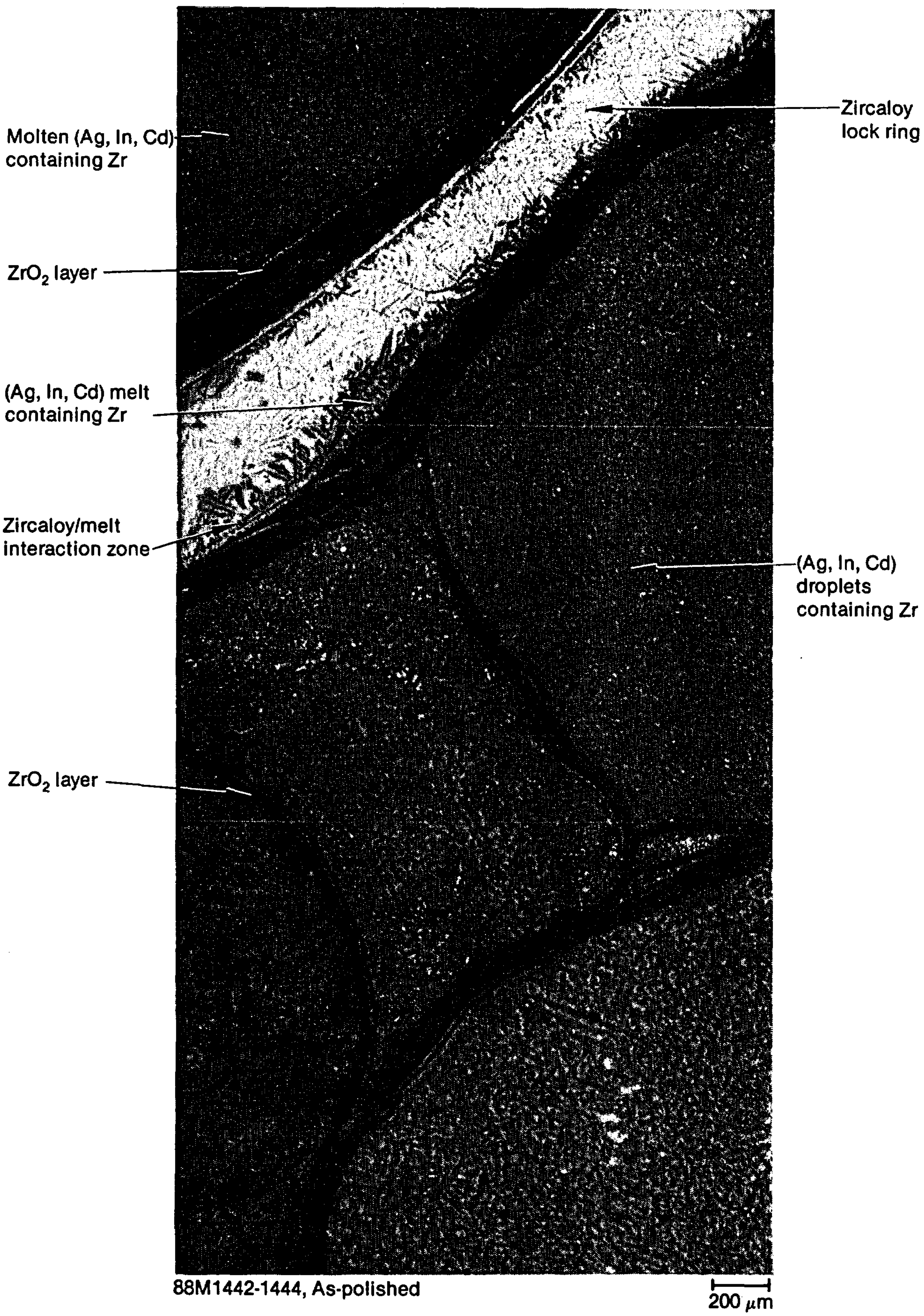

Figure 171. Control material droplets interacting with zircaloy lock ring at 0.43 m.

silver and other elements into these regions. It is not clear why such differences exist.

The various interactions between molten control material, stainless steel, and zircaloy are exemplified in Figure 172. This figure shows molten (Ag,In,Cd) contained within its stainless steel cladding and molten control material which relocated from above and subsequently interacted with zircaloy and stainless steel. The molten control material interacted with the zircaloy guide tube to the extent that only its former location is identifiable. The resulting zirconium containing melt was then able to interact with the stainless steel cladding and form eutectic or low-melting-point intermetallic Zr,Ni phases. This interaction zone can be seen on the outer surface of the stainless steel cladding in Figures 172 and 173. SEM/WDS examinations of sample G2-S16B from the same region as Figure 173 showed the formation of a Zr-Ni intermetallic phase in this type of region. This low-melting phase surrounded small portions of the stainless steel cladding and ultimately resulted in liquefaction of the cladding. In contrast to the effect the relocating melts had on zircaloy and stainless steel, the molten (Ag,In,Cd) contained within the stainless steel cladding did not interact with the stainless steel at all.

Another example of stainless steel interacting with molten material is shown in Figure 174 and, in more detail, in Figure 175. SEM/WDS sample G2-S15 was examined to provide data on the interactions occurring in this area. In this case, the melt adjacent to the stainless steel does not have the characteristic dendritic structure associated with molten control material observed in Figure 172 but instead is composed of control material and structural materials (Zr, Fe, Cr, Ni, etc.). Complex intermetallic phases were formed as a result of these interactions; and these eventually formed laminar structures, as shown in Figure 175. These laminar structures are very similar to the eutectic metallic material observed in the lower blockage region. However, the results from SEM/WDS sample G2-S15 (Areas 1 and 3) showed that, at the interface between the intact stainless steel and the melt, there was an interaction zone exactly like that observed in Figure 172. This indicates that Zr containing melts of various compositions caused

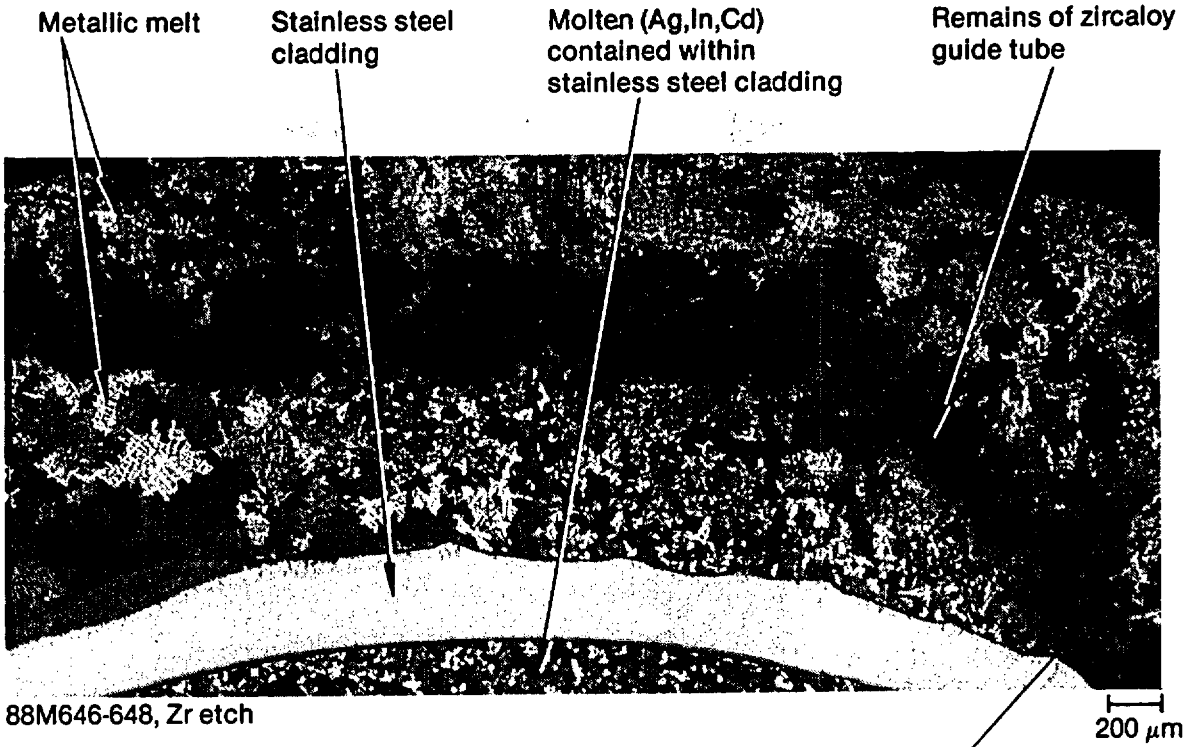

(A) Control rod/melt interactions

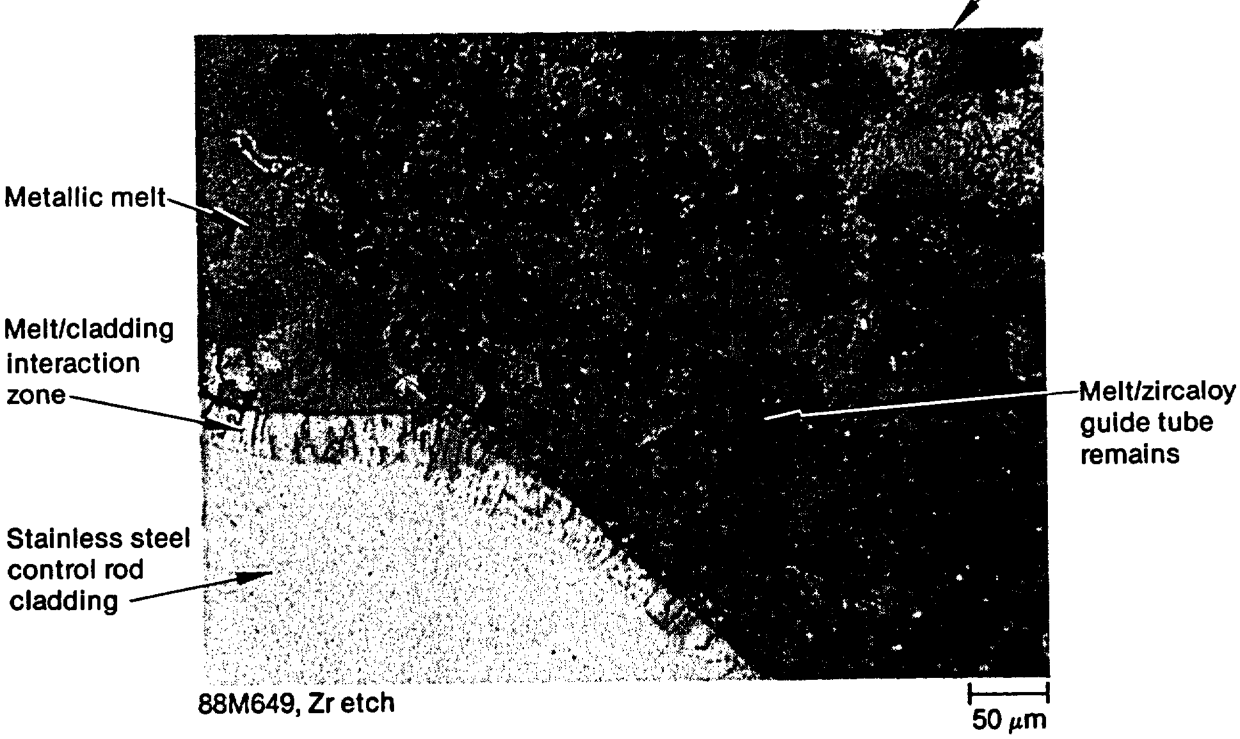

(B) Detail of (A)

Figure 172. Molten control rod material interacting with stainless steel cladding and zircaloy guide tube at 0.46 m.

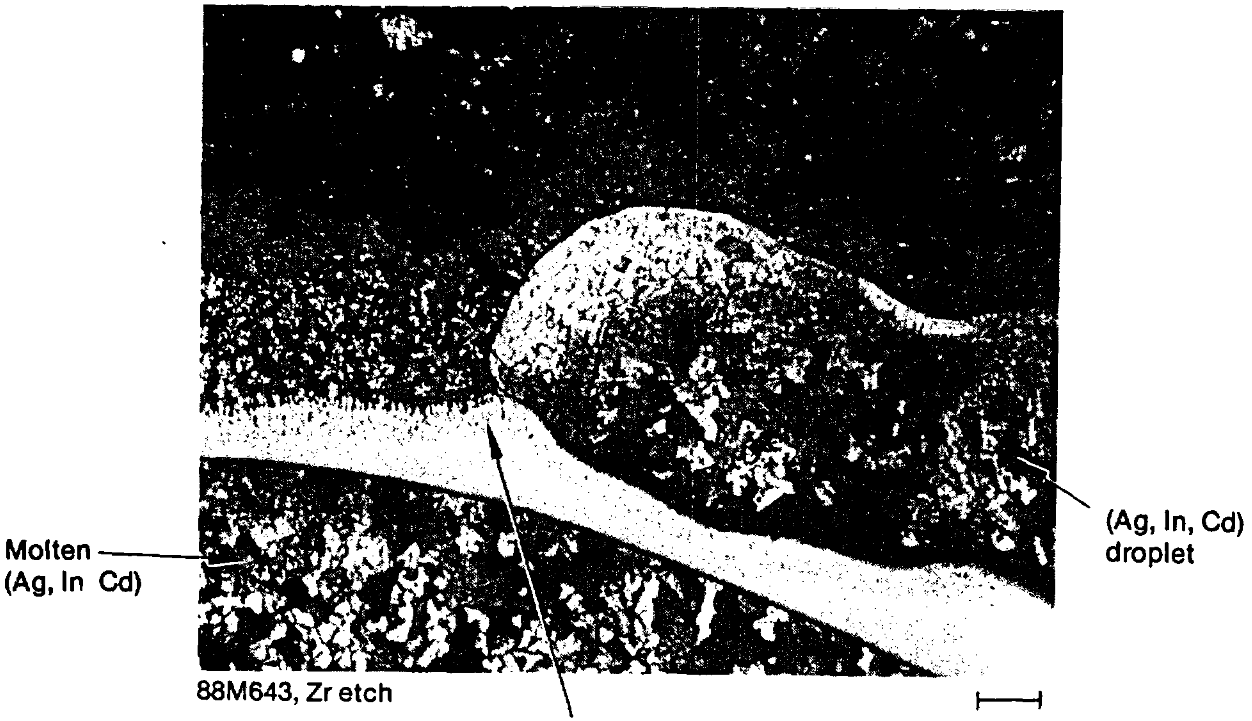

(A) Stainless steel/melt interaction

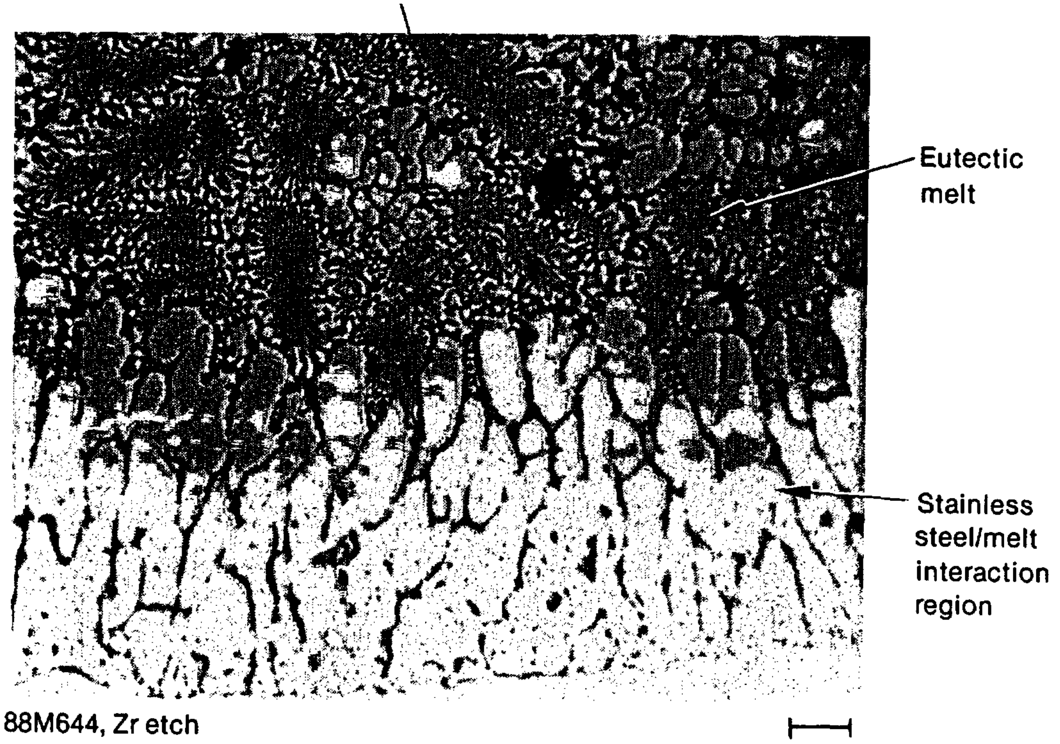

(B)— Detail of interaction zone in (A)

Figure 173. Interaction zone between metallic melt and stainless steel cladding at 0.46 m.

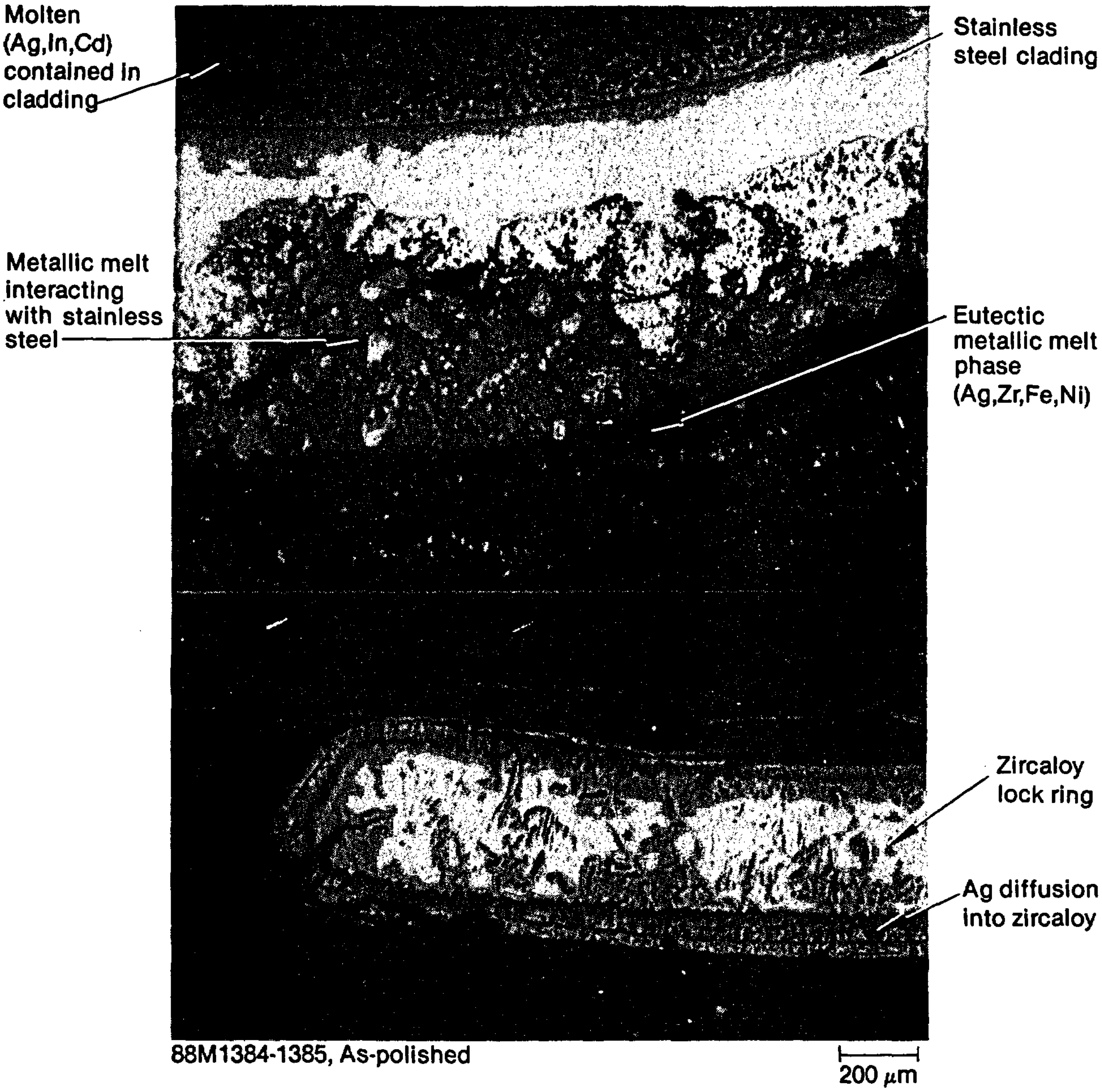

Figure 174. Interactions between metallic melts and stainless steel cladding and zircaloy lock ring at 0.43 m.

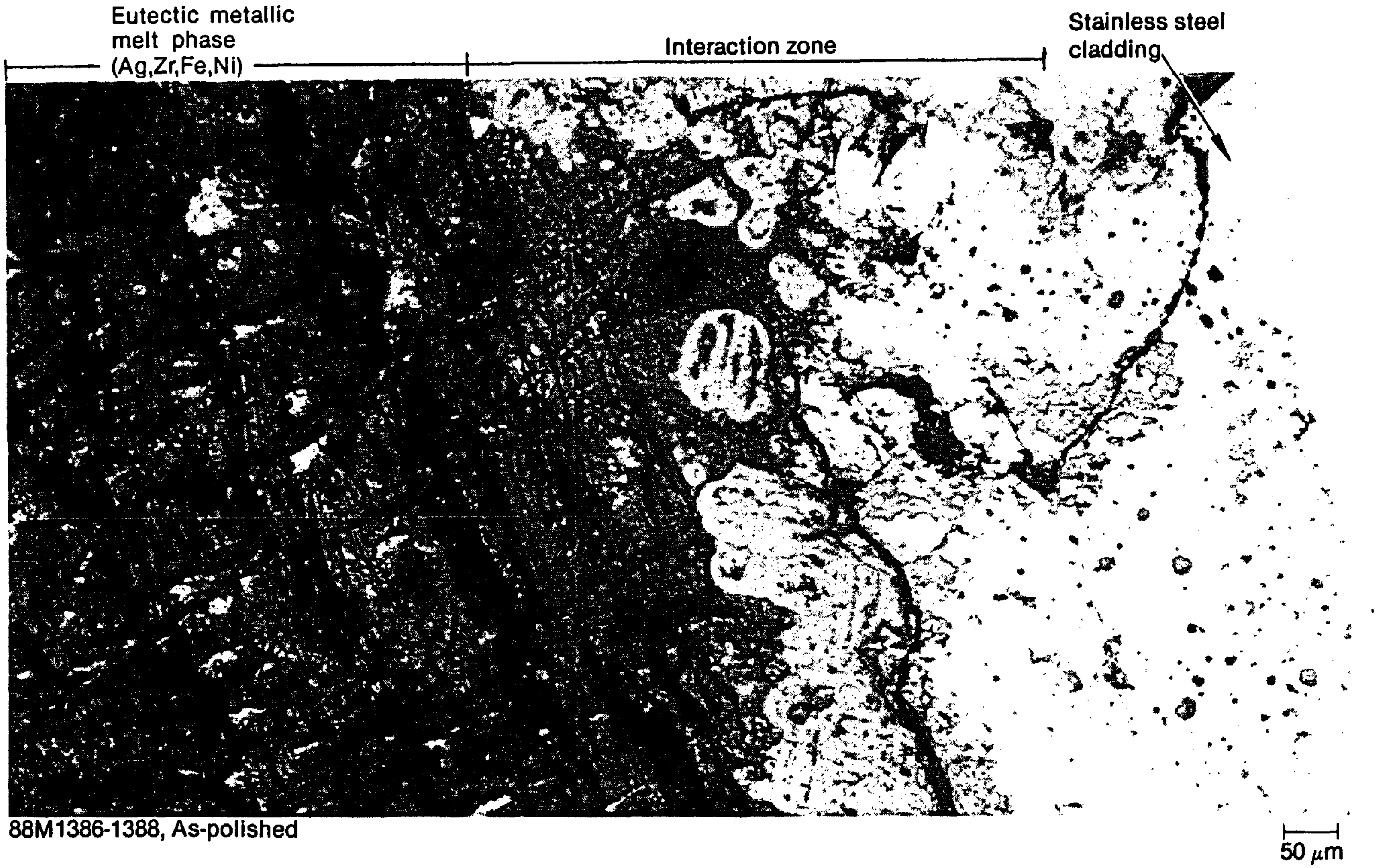

Figure 175. Details of metallic melt/stainless steel interaction zone shown in Figure 174 at 0.43 m.

liquefaction of the stainless steel cladding in the same manner, i.e., as a result of Zr-Ni interactions.

3.2.3 Zircaloy Cladding and Guide Tube Behavior

In this section, several aspects of zircaloy behavior will be qualitatively discussed. These include cladding ballooning, oxidation, structural changes, hydriding, melt interactions between the fuel and cladding, and material interactions on the cladding outer surface. The behavior of the zircaloy inner liner and shroud are discussed in Sections 3.2.4 and 3.2.5. The quantitative analysis of the zircaloy oxidation is discussed in Section 4.2.

At the bottom of the fuel assembly at the A elevation (0.003 m), all the zircaloy was in the as-fabricated condition and did not contain any zirconium hydrides. Through the bottom spacer grid at the B elevation (0.03 m), all the zircaloy was still in the as-fabricated condition, as shown in Figure 176 under polarized light conditions; but zirconium hydrides were present, as shown in Figure 177 under bright field conditions. At the C elevation (0.12 m), recrystallized zircaloy was first observed on some of the central rods and adjacent to some of the metallic melt (Figure 178). This indicates cladding temperatures in excess of 925 K. In a few isolated spots in the center of the fuel assembly, the zircaloy structure was prior-beta. These isolated spots were always adjacent to relocated melt material and indicate localized temperatures in excess of 1245 K. A small, localized ZrO_2 layer was also observed in these areas, as shown in Figure 179. In some places near the center of the fuel assembly, the relocated metallic melt was hot enough to cause cladding failure.

At the D elevation (0.22 m), all the zircaloy was recrystallized and hydrided except for isolated regions of prior-beta on some of the central rods adjacent to relocated melt material. This indicates cladding temperatures in excess of 925 K, which agrees with the thermocouple data at this elevation.[10]

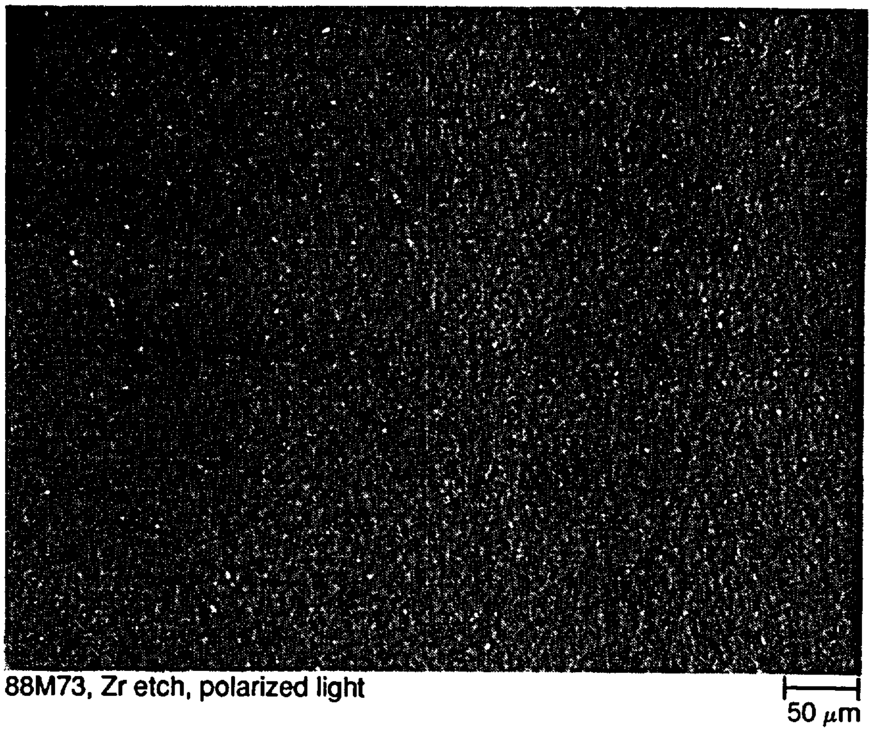

Figure 176. As-fabricated zircaloy cladding at 0.03 m.

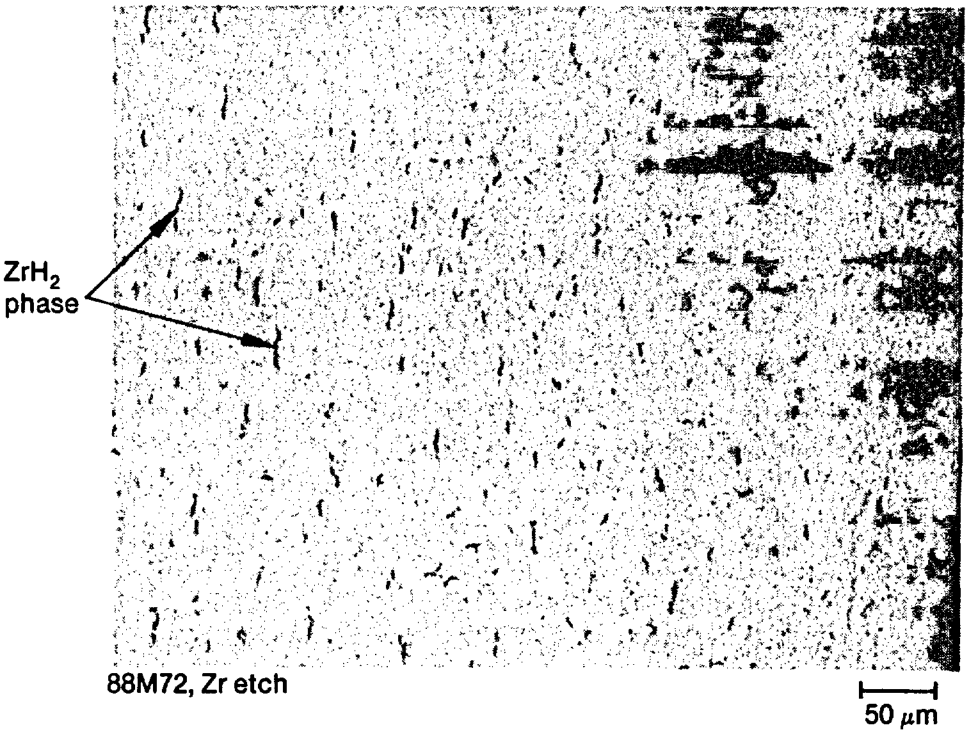

Figure 177. Zirconium hydrides in fuel rod cladding at 0.03 m.

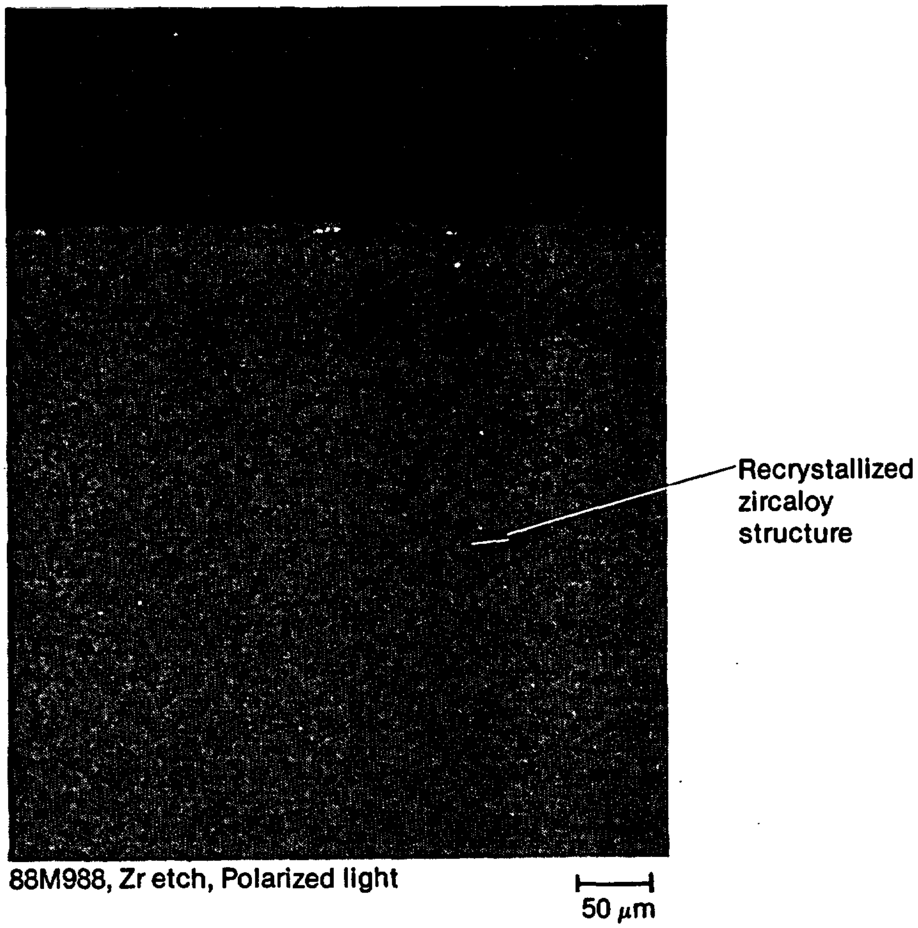

Figure 178. Recrystallized zircaloy fuel rod cladding at 0.12 m.

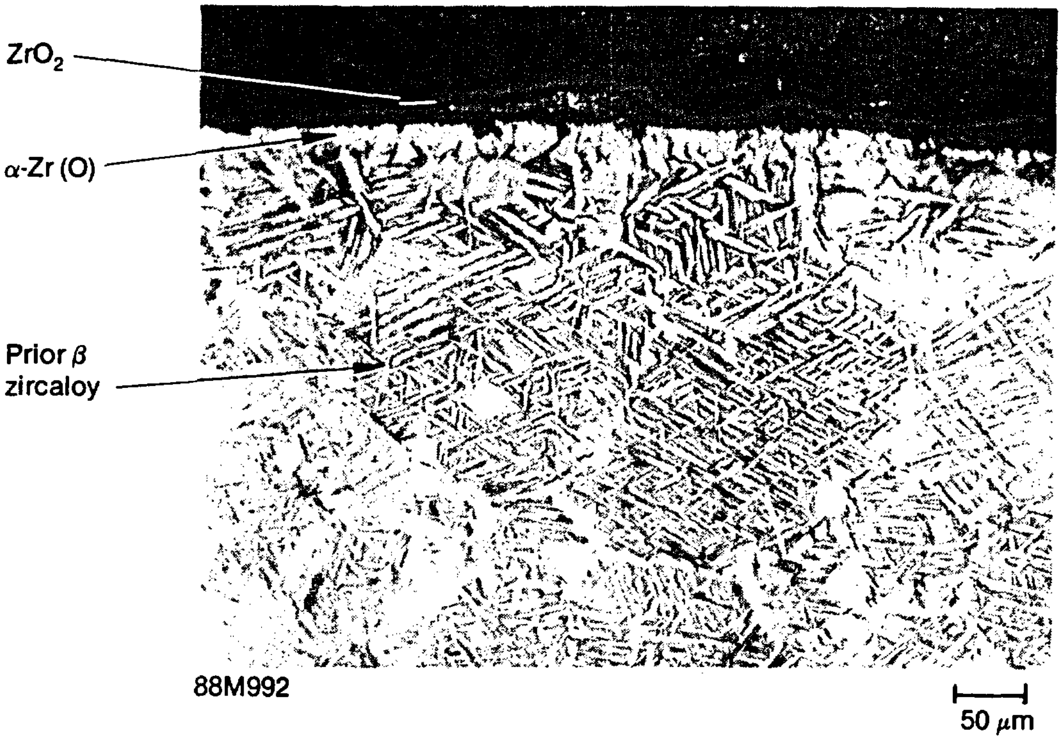

Figure 179. Structure of partially oxidized zircaloy cladding at 0.12 m.

At the E elevation (0.27 m), prior-beta zircaloy structure was present on many of the central fuel rods, with all the other fuel rod cladding having recrystallized. This indicates temperatures ranging from a minimum of approximately 925 K to somewhat above 1245 K. ZrO_2 layers on the outer cladding surface were generally limited to those fuel rods exhibiting prior-beta structure. All the recrystallized cladding had minor amounts of zirconium hydrides, as exhibited in Figure 180. (It is possible that zirconium hydrides were also in the prior-beta zircaloy, but they are difficult to distinguish in the prior-beta morphology.) Based upon comparisons with photographs of zircaloy with known zirconium hydride concentrations,[13] the concentrations of zirconium hydrides in the zircaloy in the lower regions of the LP-FP-2 fuel module were <100ppm.

At the F elevation (0.36 m), most of the fuel rod cladding was prior-beta, with recrystallized cladding limited to the exterior corner positions. Oxide layers were present on all the cladding with prior-beta structure and a few rods that were only recrystallized. This suggests minimum temperatures of approximately 1000 K for the onset of zircaloy oxidation under the conditions in this experiment.

From the G(bottom) through the H elevations (0.43-0.58 m), all the zircaloy cladding that was not oxidized had a prior-beta structure, with temperatures in excess of 1245 K. The amount of zircaloy oxidation continued to increase axially and radially in this region, and complete oxidation of all the remaining zircaloy was observed at and above the I elevation (0.66 m).

Essentially all of the zircaloy fuel rod cladding and guide tubes were intact and undeformed at and below the F elevation (0.36 m). Significant amounts of fuel rod cladding deformation and failure are first observed at the G(bottom) elevation (0.43 m), just below the second spacer grid. Deformation of guide tubes and the zircaloy lock rings surrounding the guide tubes was also apparent at this elevation. The greatest amount of damage was in the northeast quadrant and towards the center of the fuel assembly. This tendency for the greatest damage to be in the northeast quadrant was

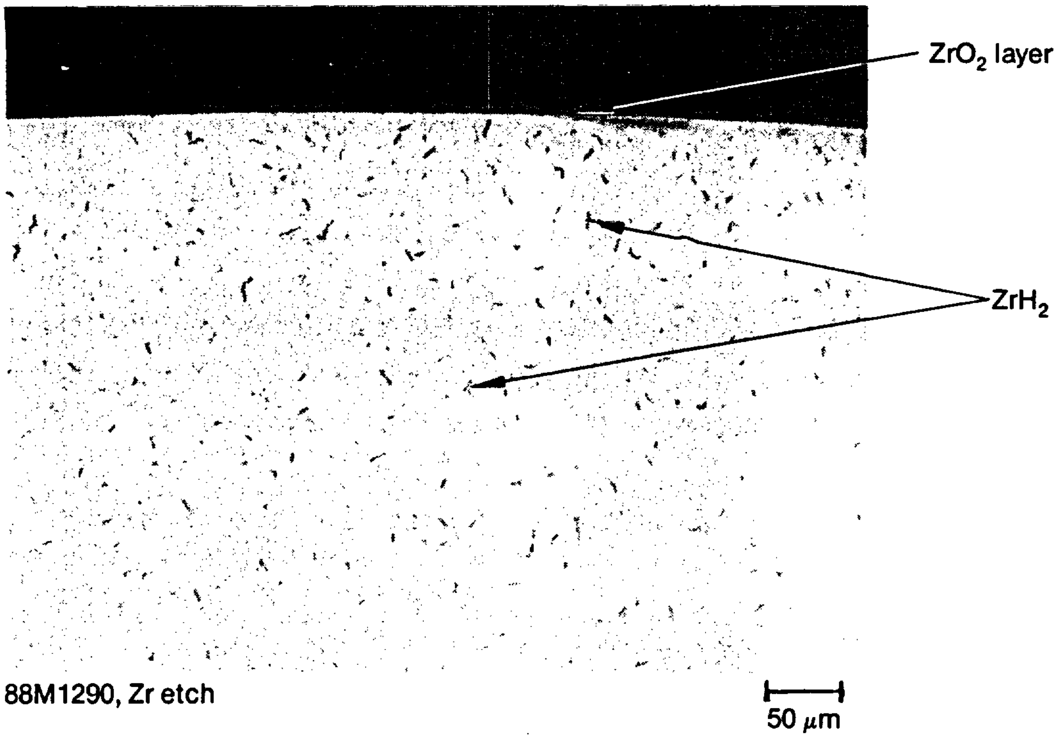

Figure 180. Zirconium hydrides in fuel rod cladding at 0.27 m.

generally true for all of the upper portion of the bundle. Cladding ballooning, deformation, and rupture were more evident at succeedingly higher elevations. Deformation of the guide tubes was also more pronounced at and above the second spacer grid. Rod-to-rod contact and fusion of the oxidized cladding occurred as low as the I elevation (0.66 m), and representative photographs of this behavior are shown in Figures 181 and 182.

The axial transition in the degree of cladding ballooning and deformation in the fuel bundle was associated with a transition in the amount of zircaloy oxidation. This suggests that the exothermic zircaloy oxidation process caused cladding temperatures to increase and resulted in enhanced ballooning and rupture in these regions in these pressurized fuel rods.

At and above the H elevation (0.58 m), oxidized zircaloy cladding shells were separated from the fuel, as shown in Figures 183 and 184. Oxide thickness measurements and measurements of the distance from the cladding outer surface to the edge of the fuel pellet confirmed that this was caused by melting of the inner surface of the cladding and that in places the cladding had ballooned away from the fuel. This phenomenon is very apparent in many of the cross-sectional photographs from the upper portion of the fuel bundle. It occurred because oxidation of the cladding outer surface formed a ZrO_2 layer, with a melting point of 2960 K, under which was a layer of partially oxidized alpha-Zr(O), which melts at approximately 2245 K. The unoxidized zircaloy on the cladding inner surface melts at 2030 K. Consequently, the oxidized cladding shells contained molten zircaloy, which was able to relocate downward through the fuel/cladding gap and cracks in the fuel until cladding failure occurred, probably as a result of internal gas pressure on the oxidized and thinned cladding. In Figures 183 and 184, an interface can sometimes be seen within the ZrO_2, as well as localized bridging between the cladding and fuel. This was probably due to molten metallic material relocating down the inner surface of the oxidized cladding shell until this melt finally solidified and oxidized.

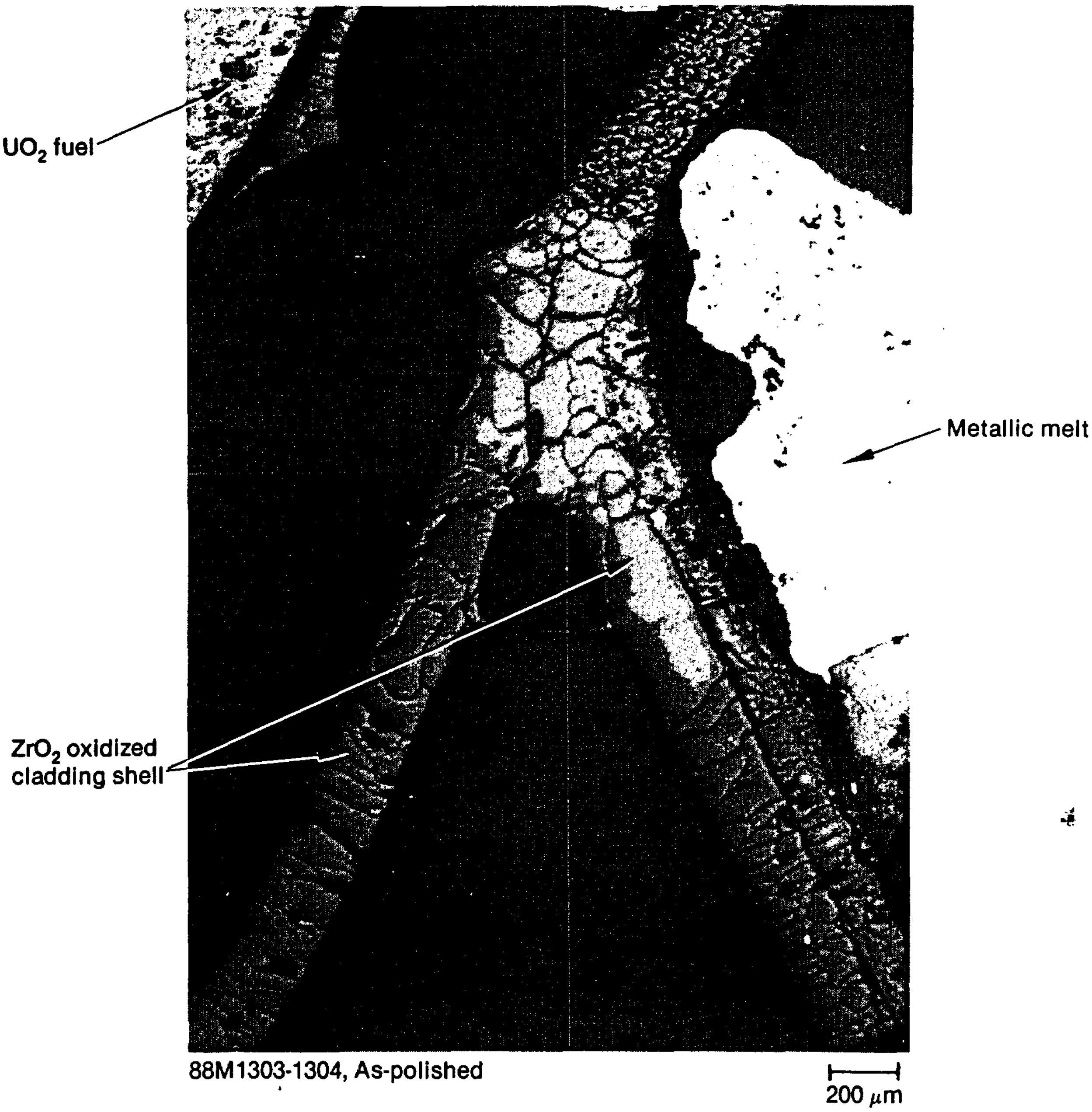

Figure 181. Contact and fusion of oxidized ballooned zircaloy cladding at 1.14 m.

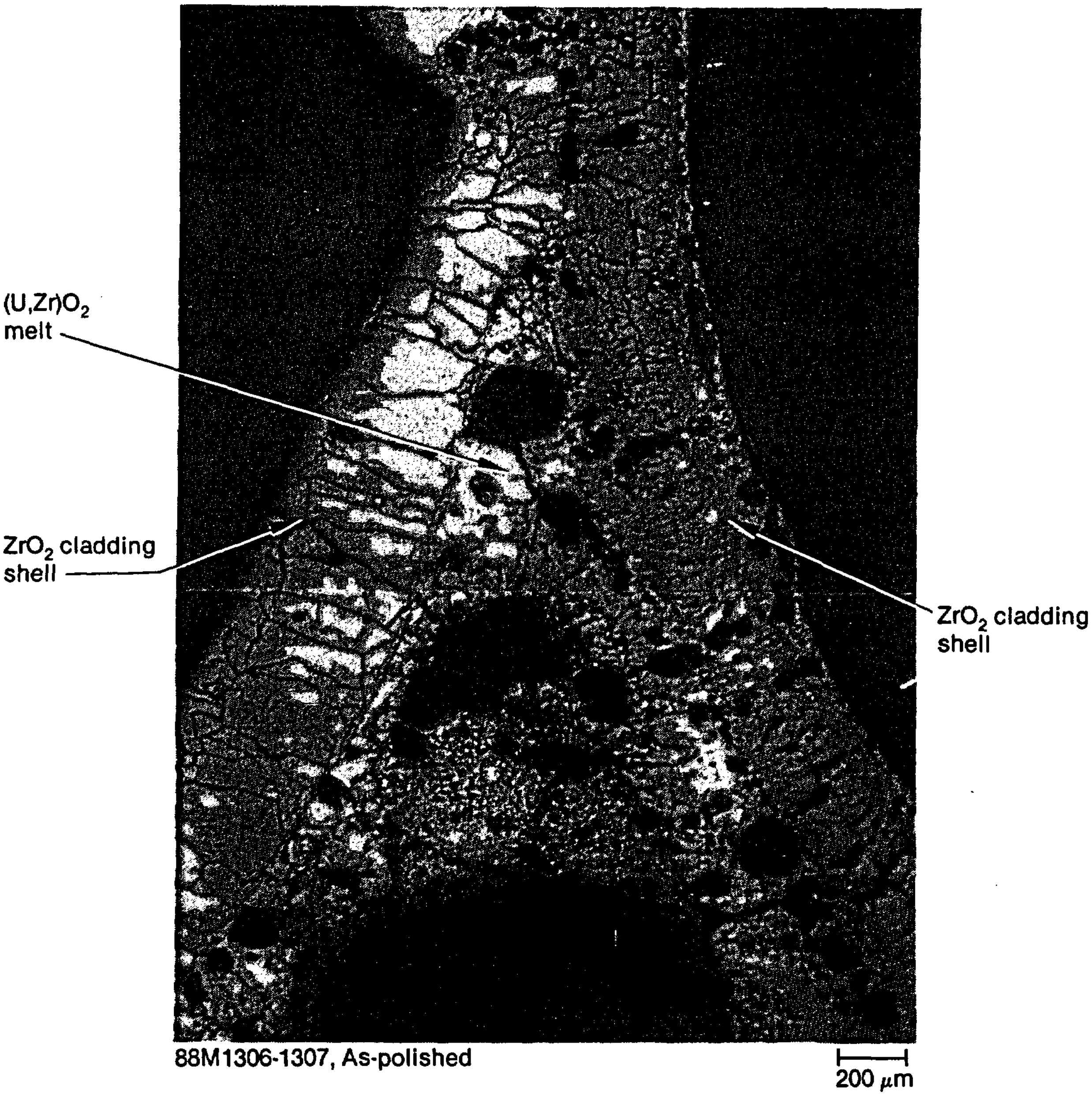

Figure 182. Cladding contact from ballooning at 1.14m.

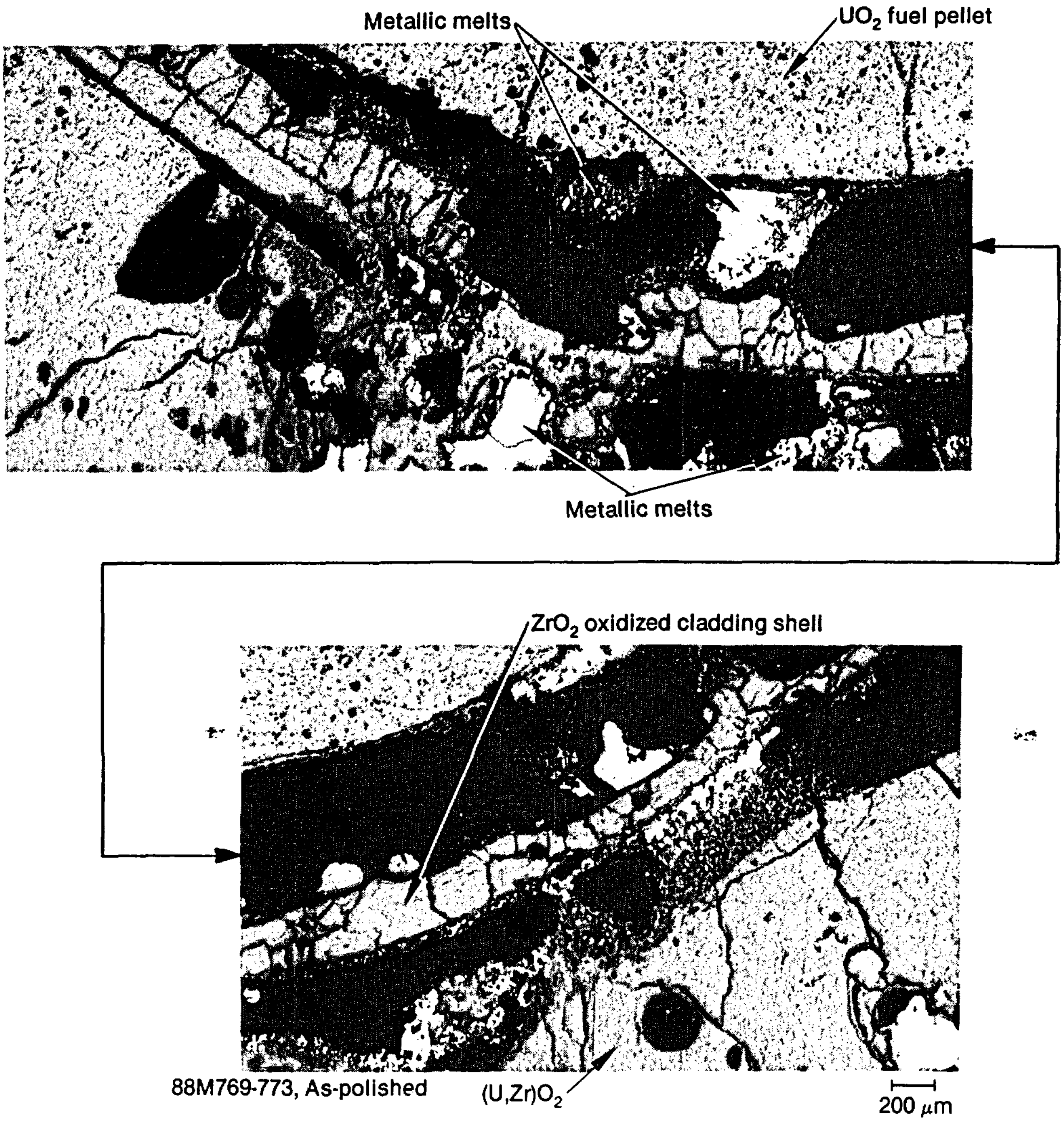

Figure 183. Melt and relocation of unoxidized zircaloy on cladding inner surface at 0.58m.

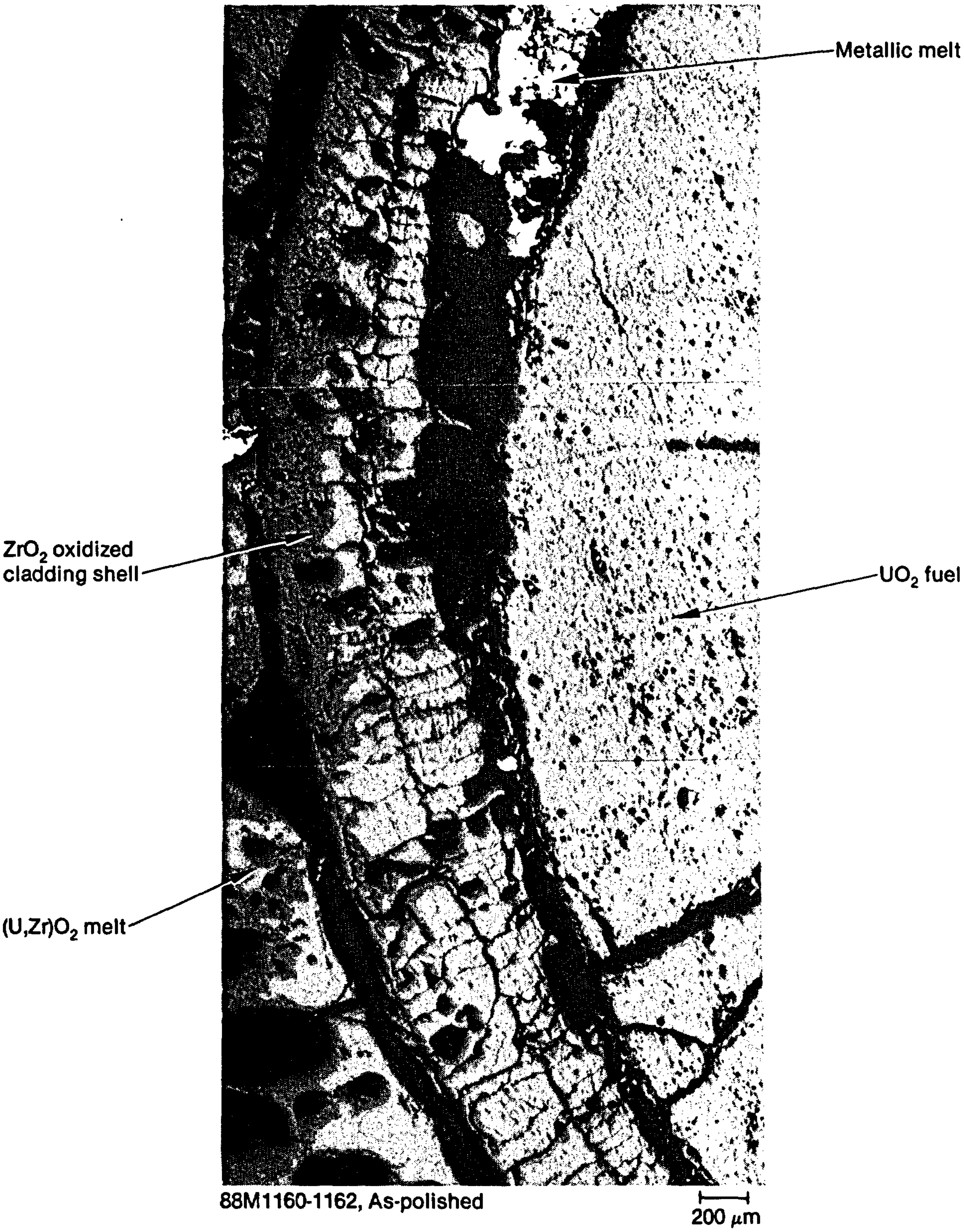

Figure 184. ZrO_2 oxide shell on cladding outer surface at 0.58 m.

Oxide thickness measurements as a function of axial and radial position are provided in Section 4.2, and these measurements provide some information on the extent of zircaloy oxidation prior to cladding failure.

Metallic melts flowed down between the fuel and cladding and interacted with both at lower elevations. The extent and type of interactions varied, and several SEM/WDS samples were examined to provide information on these interactions. The pertinent results of these examinations are summarized below, with the detailed results available in Appendix E. These interactions probably represent conditions which occurred earlier in the experiment at higher elevations, prior to release of the molten zircaloy trapped between the fuel and oxidized cladding outer shell.

SEM/WDS examinations of sample G2-S14 were conducted to examine the various interactions between melts, cladding, and fuel that are visible in Figure 185. The interactions between the metallic melt and the zircaloy cladding are discussed in this section; discussions of the interactions between the melt and the fuel are discussed in Section 3.2.9.

Figure 185 shows a metallic melt between the fuel and cladding that extended around the entire circumference of the fuel rod. On one side of the fuel rod, there was also a metallic melt contained between a small oxide layer and the prior-beta zircaloy structure in the center of the cladding. This melt layer did not extend all the way around the fuel rod. The melt layer near the cladding outer surface might be interpreted as a stain; however, backscattered electron images of sample G2-S14 confirm that this layer had the same density as the melt on the inner surface and that these densities were different from the prior-beta structure in the center of the cladding. This also suggests that the cladding in the center portion remained intact throughout the experiment. The interactions between these melts and the intact prior-beta zircaloy were characterized in Area 1 of sample G2-S14. This area examined the melt interface on the cladding inner surface; however, the interactions on the outer surface appeared very similar. These examinations indicated that the melt was composed of

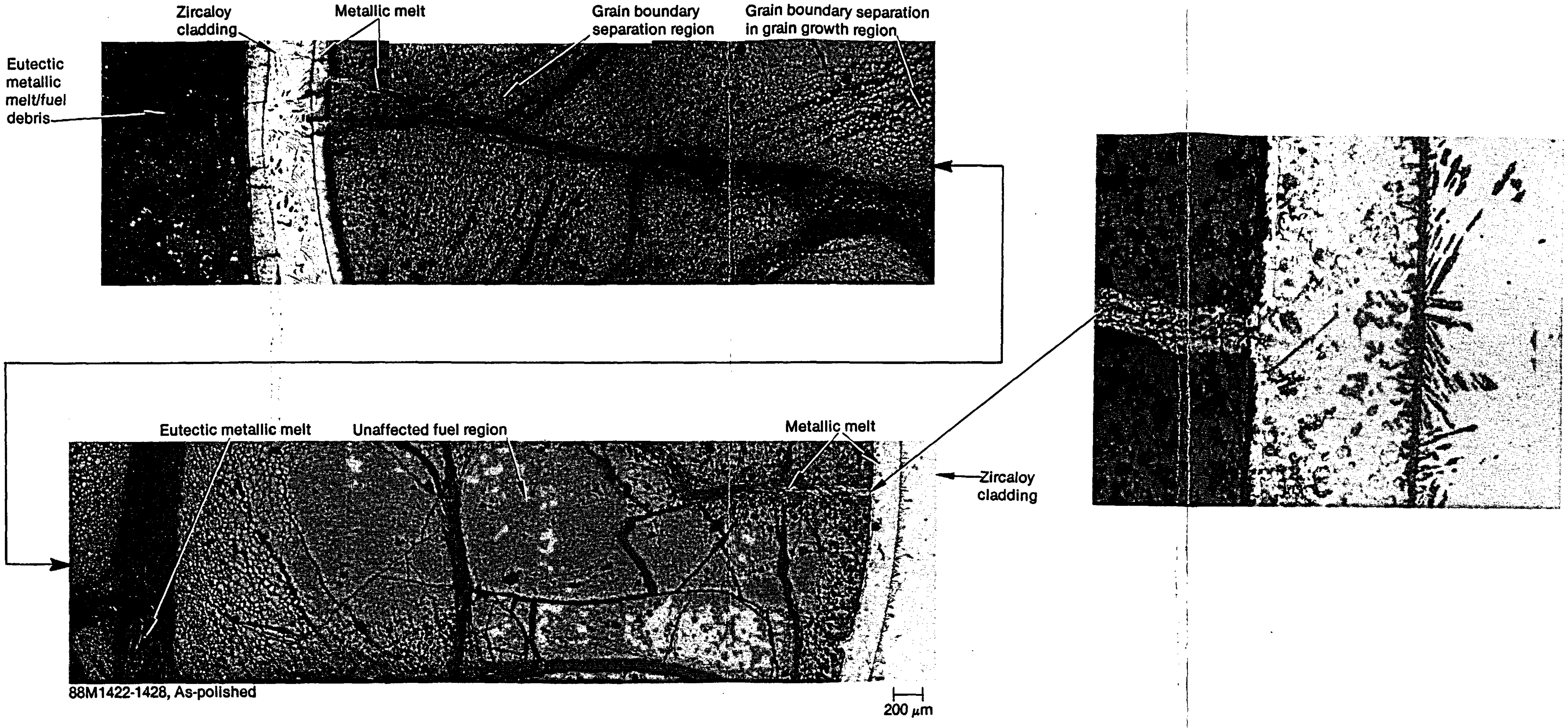

Figure 185. Metallic melt relocating down cladding inner surface and interacting with fuel at 0.43 m.

zircaloy, control material, stainless steel, and fuel components (Zr,Sn,Ag,In,Fe,Ni,Cr,U). It was apparent from the metallography that this melt had resulted in liquefaction of the zircaloy; however, the SEM/WDS results indicated that, except for Fe, there was no diffusion of these elements from the melt into the intact zircaloy. The results suggest that Ag in contact with the zircaloy dissolved the zircaloy. According to the Ag-Zr phase diagram, above approximately 1400 K the silver can dissolve up to 67 at.% Zr in the liquid phase.

Also apparent in Figure 185 are what appear to be second-phase precipitates throughout the matrix of the prior-beta zircaloy cladding on one side of the fuel rod. On the other side of the fuel rod, these precipitates are limited to the regions adjacent to the inner and outer surfaces of the intact cladding. SEM/WDS examinations of G2-S14 (Area 1) indicated that, at the boundary with the melt, these second phases were the result of Fe diffusing into the cladding. However, in the matrix of the cladding, these second-phase precipitates could not be distinguished. Only zircaloy was present, and the backscattered electron images indicated no differences in density across the intact zircaloy. Similar examinations of SEM/WDS sample G2-S15 (Area 4) indicated that in an area that appeared metallographically similar, the second phase was composed of zircaloy, stainless steel, and control material alloy. This second phase was between an intact oxide layer [ZrO_2 and alpha-Zr(O)] and intact prior-beta zircaloy. However, second-phase precipitates that were observed metallographically in the matrix of the zircaloy guide tube were indistinguishable on the SEM, just as was the case on G2-S14. The cause of these apparent discrepancies is unclear. Additional representative photographs of this phenomenon are provided in Figures 186 and 187.

SEM/WDS sample D4-S12 was selected to examine the zircaloy/metallic melt interactions observed in Figure 188 and, in more detail, in Figure 189. As described in Appendix E, these examinations indicated that the metallic melt between the fuel and zircaloy cladding was composed of Ni, Fe, Cr, Ag, In, and Zr. Similar to sample G2-S14, there was no diffusion of elements from the melt into the cladding, except for small amounts of iron.

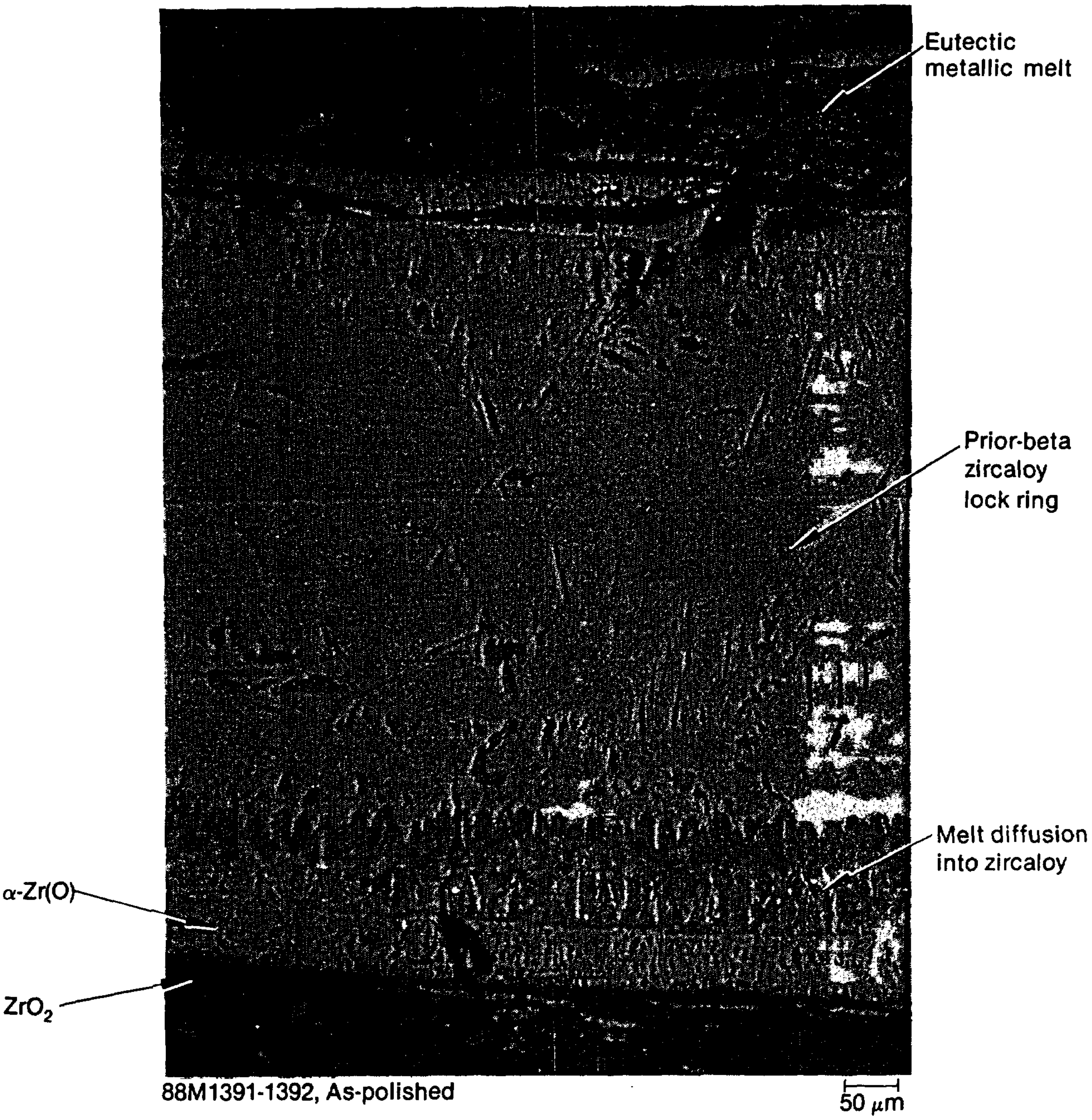

Figure 186. Melt interactions with zircaloy lock ring at 0.43 m.

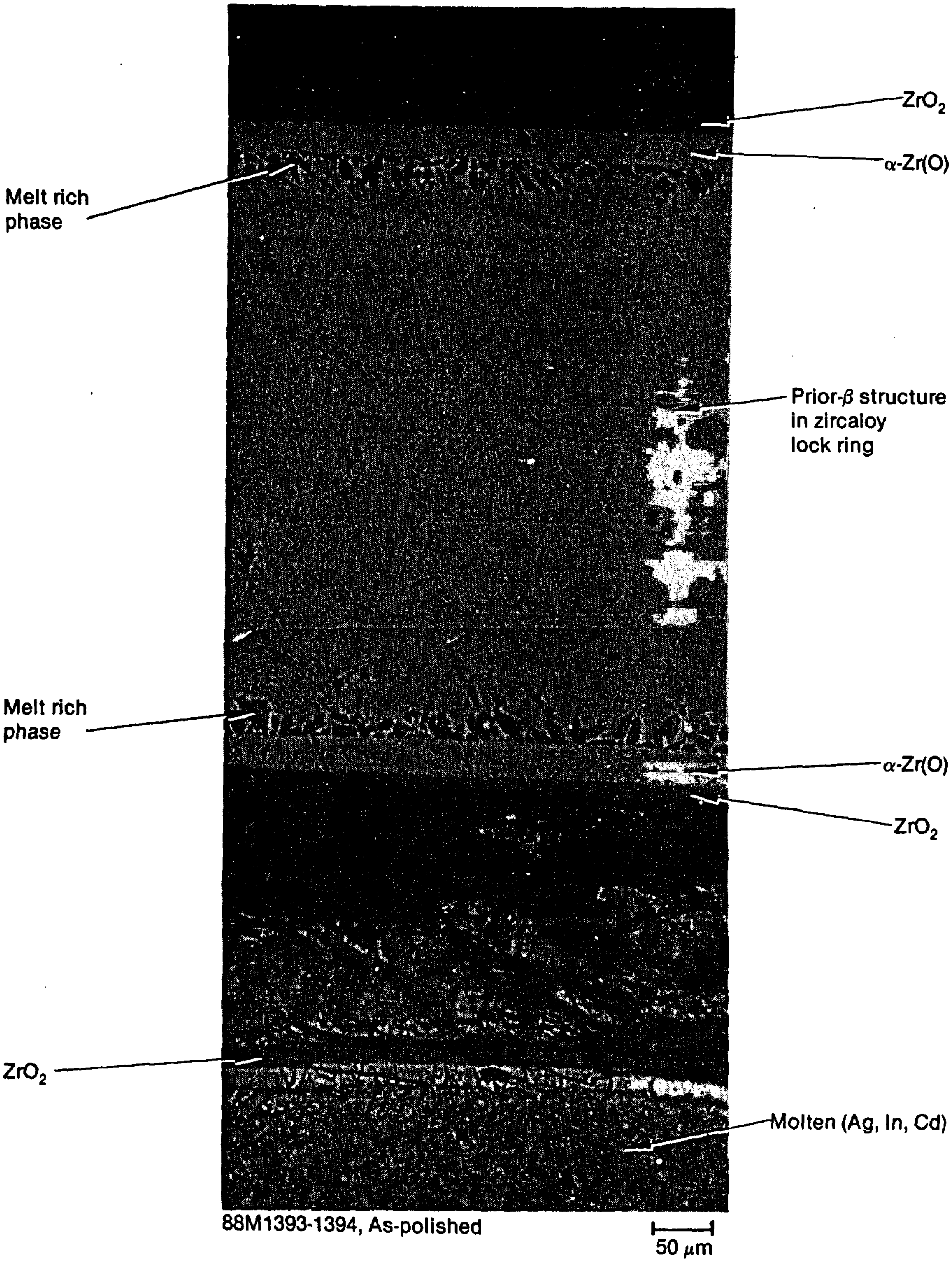

Figure 187. Melt interaction with zircaloy lock ring at 0.43 m.

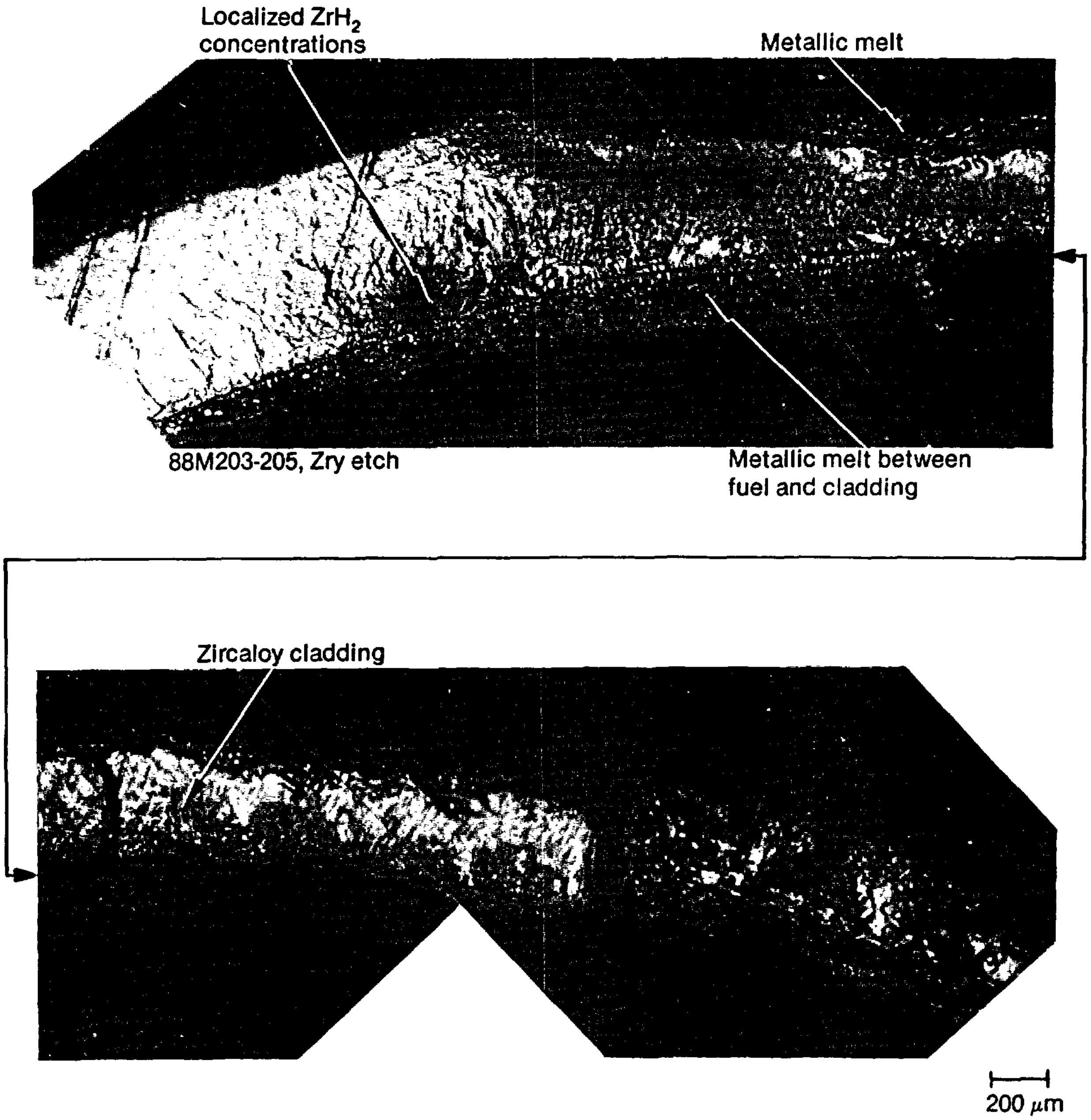

Figure 188. Metallic melt interactions with failed zircaloy fuel rod cladding at 0.22 m.

(A) Melt interaction on cladding inner surface

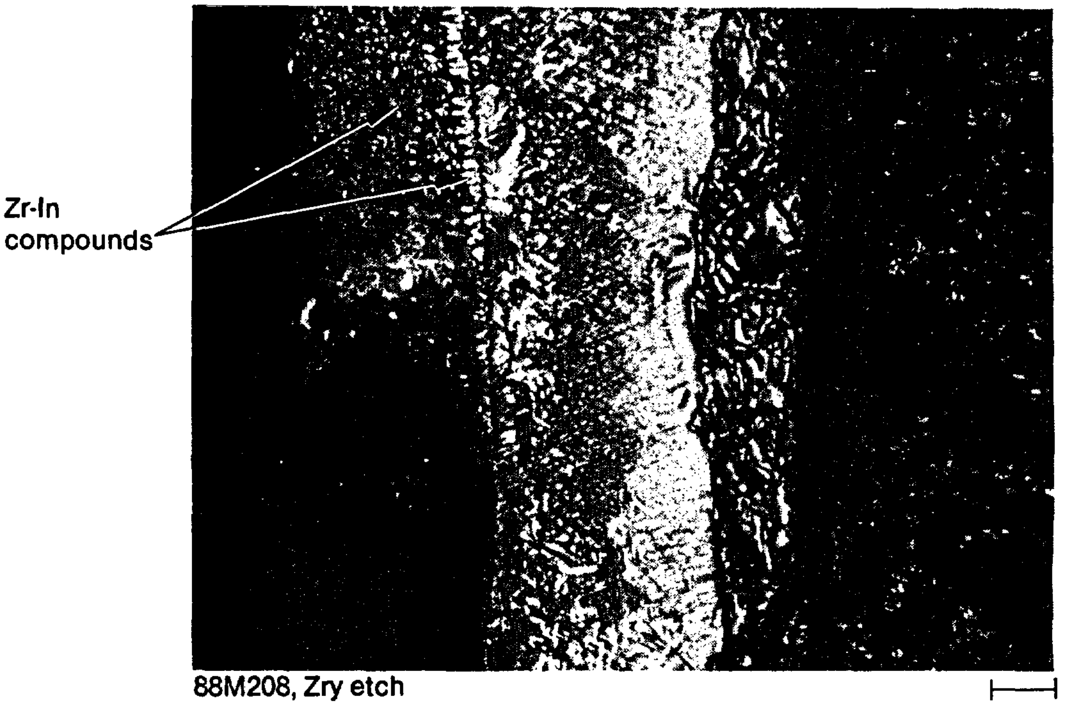

(B) Melt interactions on inner and outer cladding surfaces

Figure 189. Details of melt interactions with zircaloy cladding shown in Figure 188 at 0.22 m.

This suggests that the zircaloy was soluble in the melt, and liquefaction occurred as a result of zircaloy dissolution in the melt. As previously described, zircaloy is very soluble in silver above 1400 K. The results from these examinations also indicated the presence of Zr-In compounds in the melt, particularly along the solid/liquid interface. These Zr-In compounds are shown in Figure 189. The Zr-In phase diagram is incomplete, as shown in Figure G-16 in Appendix G, with no information on the In-rich side above about 33.7 wt.%.

SEM/WDS examinations of the melt in contact with the outer surface of the cladding in Figure 188 showed the melt to contain the same elements as the melt on the inner surface, except for the presence of uranium. Once again, there was no significant diffusion zone from the melt into the cladding.

Figure 188 also shows the presence of an unusual structure on the cladding inner surface, which is shown in more detail in Figure 190. SEM/WDS examinations of this area indicated only the presence of zircaloy, and it appears that this may have resulted from localized hydriding of the zircaloy. Hydrides are observed emanating away from the region, and the SEM/WDS examinations would not have detected hydrogen. These hydride concentrations were generally associated with metallic melts located at the end tips of cracks in the fuel.

SEM/WDS sample G2-S18 was selected to examine the zircaloy/melt interactions shown in Figure 191 and, in more detail, in Figure 192. Metallic melts were present on the cladding inner surface and between the oxide layers on the cladding outer surface and the intact prior-beta zircaloy. SEM/WDS examinations of Area 3 of G2-S18 indicated the compositions of the layers shown in Figure 192. The layer adjacent to the fuel was primarily molten zircaloy; the next outer region was rich in uranium with concentrations of Fe,Cr,Ni; the next outer region was rich in Ag, with Fe, Ni, and Cr; and the next outer region was intact prior-beta zircaloy. SEM/WDS examinations of Area 5 of G2-S18 indicated that the melt between the prior-beta zircaloy and the alpha-Zr(O) in Figure 192 was

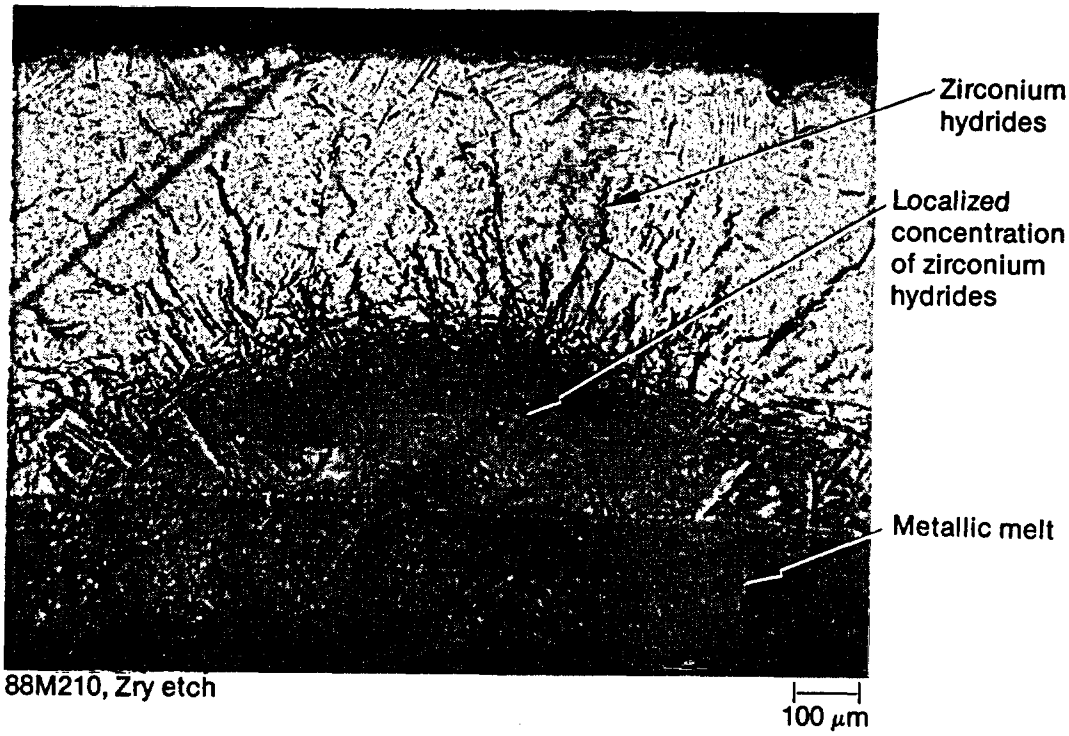

Figure 190. Localized zircaloy hydriding on cladding inner surface.

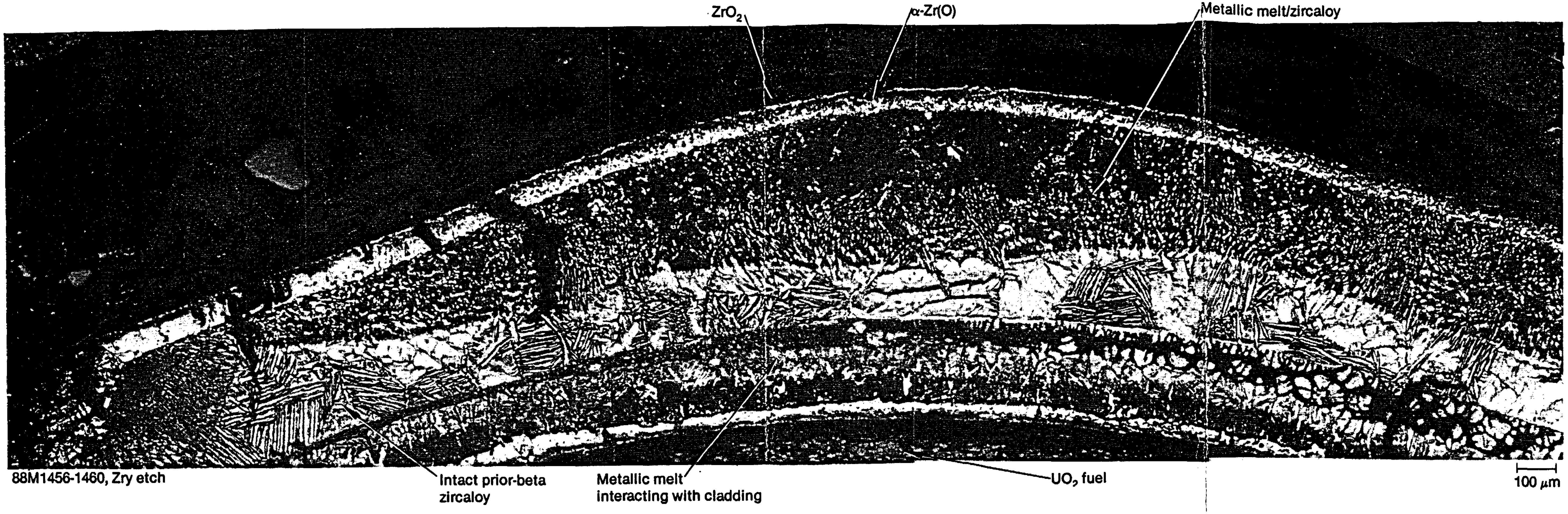

Figure 191. Metallic melt interactions with zircaloy cladding at 0.43 m.

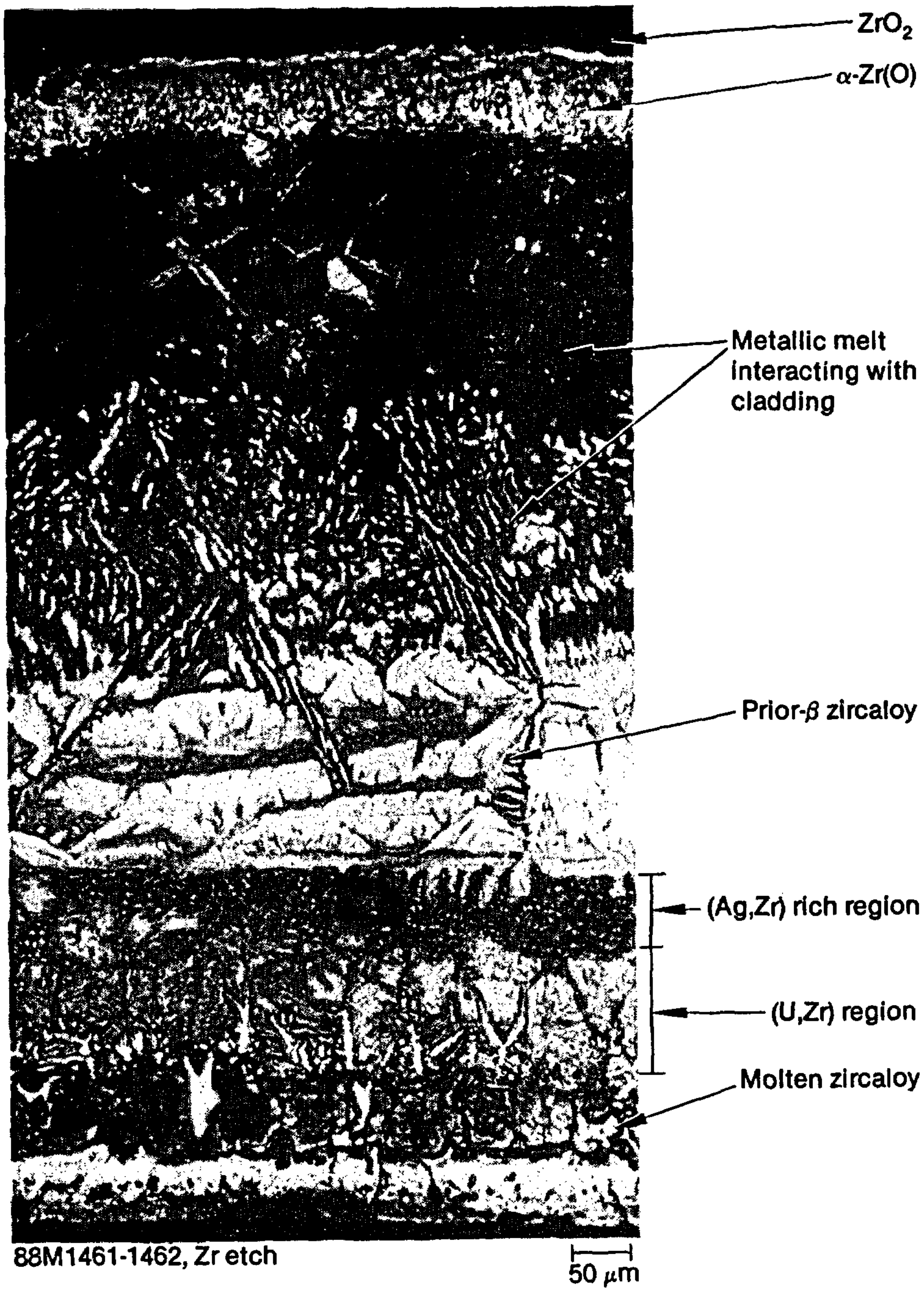

Figure 192. Details of melt interactions with zircaloy cladding shown in Figure 191 at 0.43 m.

composed of zircaloy, control material alloy, and stainless steel components. Once again, there was no significant diffusion gradient from the melt into the prior-beta intact zircaloy, except for a small amount of iron and possibly nickel.

These examinations also indicated the presence of a silver layer in contact with the outer surface of the ZrO_2 and the presence of Fe,Cr, and Ni within the ZrO_2 layer and diffusing into the alpha-Zr(O).

The presence of a metallic melt between the prior-beta and alpha-Zr(O) layers resulted in liquefaction of the unoxidized prior-beta phase, as evidenced by the uneven contour of the prior-beta boundary. It is also apparent that the metallic melt on the cladding inner surface resulted in liquefaction of the unoxidized zircaloy. This liquefaction probably resulted from the formation of Ag-Zr, Zr-Ni, or Zr-Fe low-melting eutectic phases, since temperatures were not sufficient to melt all the zircaloy. This metallic melt does not appear to have affected the alpha-Zr(O) layer, which remains fairly uniform in thickness.

Figure 193 shows the formation of a laminar, two-phase, metallic structure in the zircaloy cladding, which eventually breaks off to form the eutectic metallic melt particles observed in the lower blockage region. SEM/WDS examinations of these types of eutectic phases showed them to be composed primarily of Ag and Zr, with Fe, Cr, and Ni mixed in.

3.2.4 Zircaloy Inner Liner Behavior

The zircaloy inner liner was completely intact up through the G(top) elevation (0.46 m) except for minor melting in the corner of the northeast quadrant as low as the D elevation (0.22 m). This liquefaction was due to metallic melts relocating down the exterior of the liner. Significant liquefaction of the liner occurred at the H elevation (0.58 m), with the least damage occurring in the corners. Above this elevation, the liner was completely liquefied except in the corner of sample Q3. As shown in Figure 194 at the H elevation and in Figure 195 at the Q elevation, eutectic

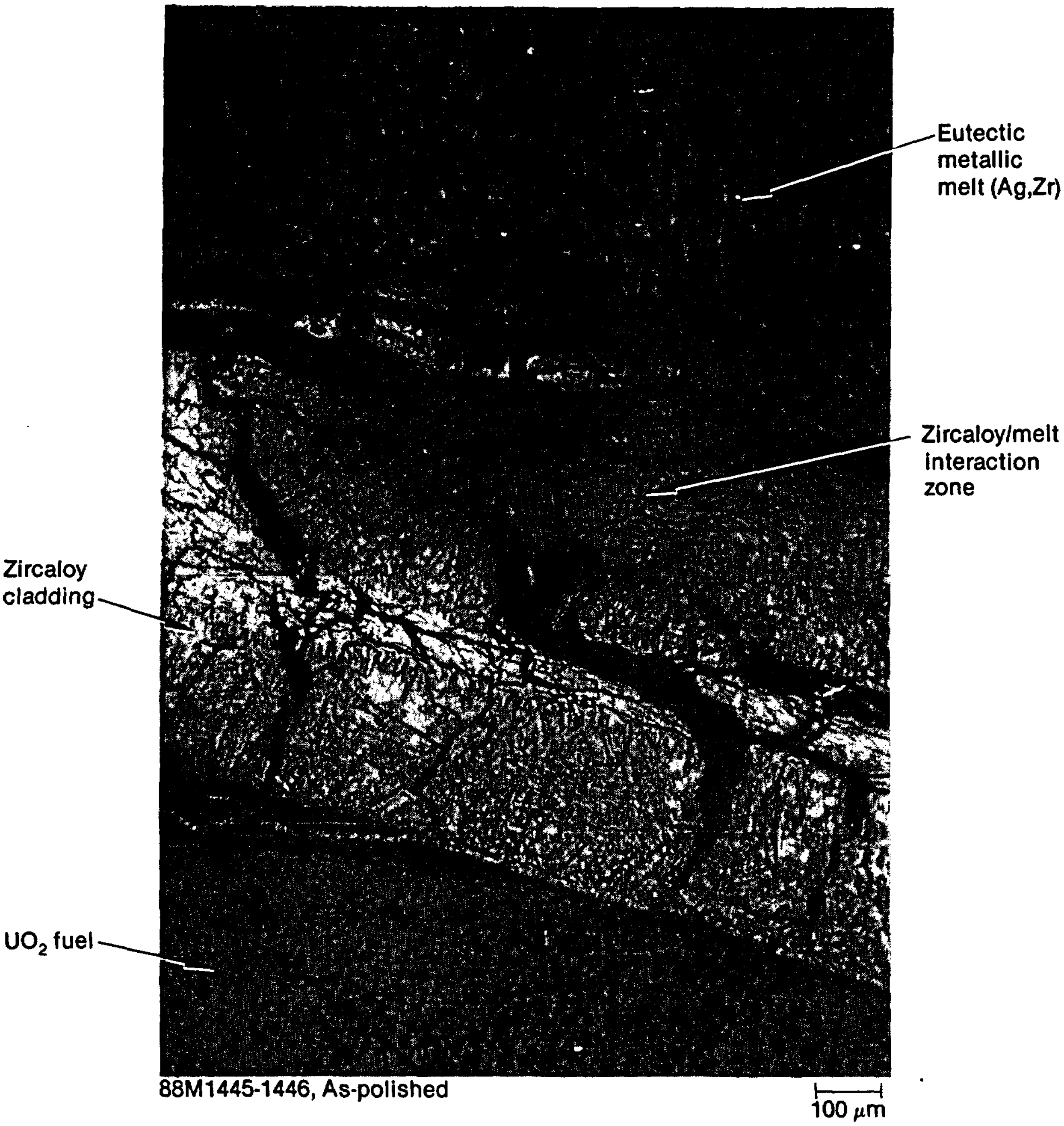

Figure 193. Formation of laminar eutectic metallic melt phase from interactions between metallic melt and zircaloy cladding at 0.43 m.

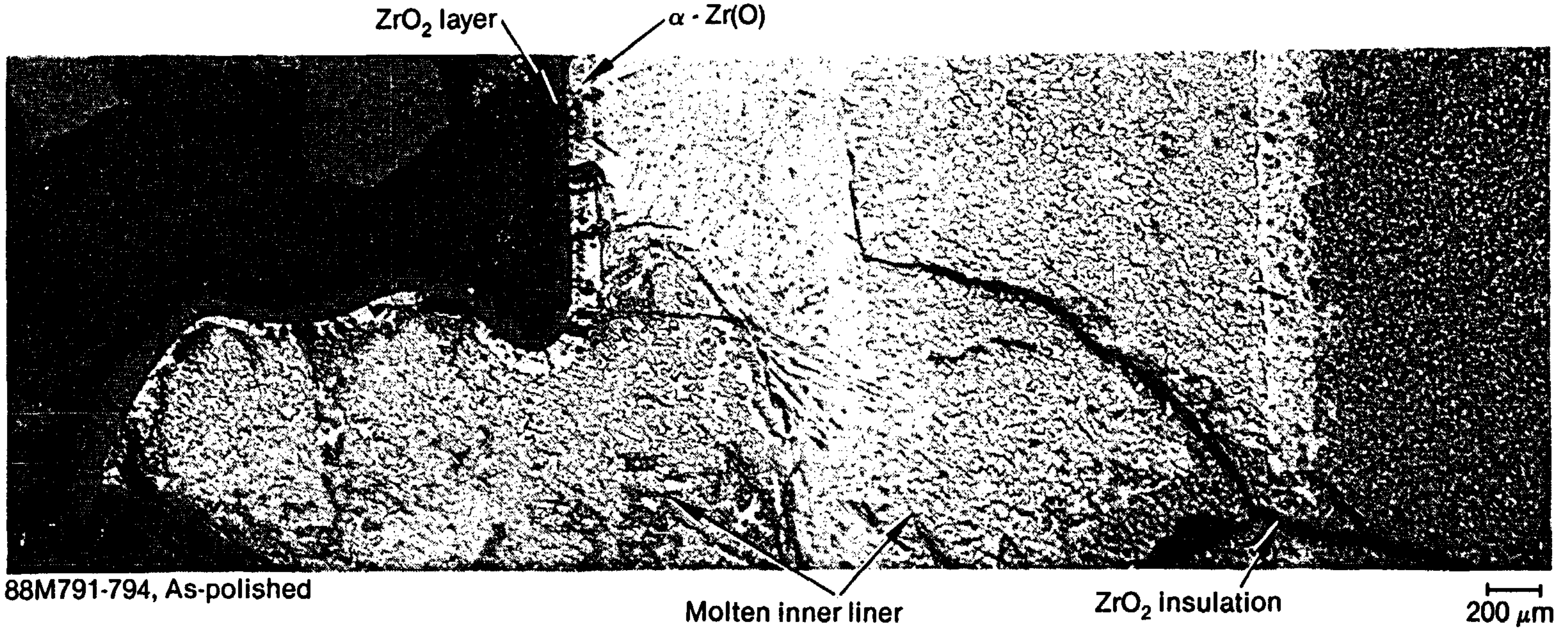

Figure 194. Molten zircaloy inner liner at 0.58 m.

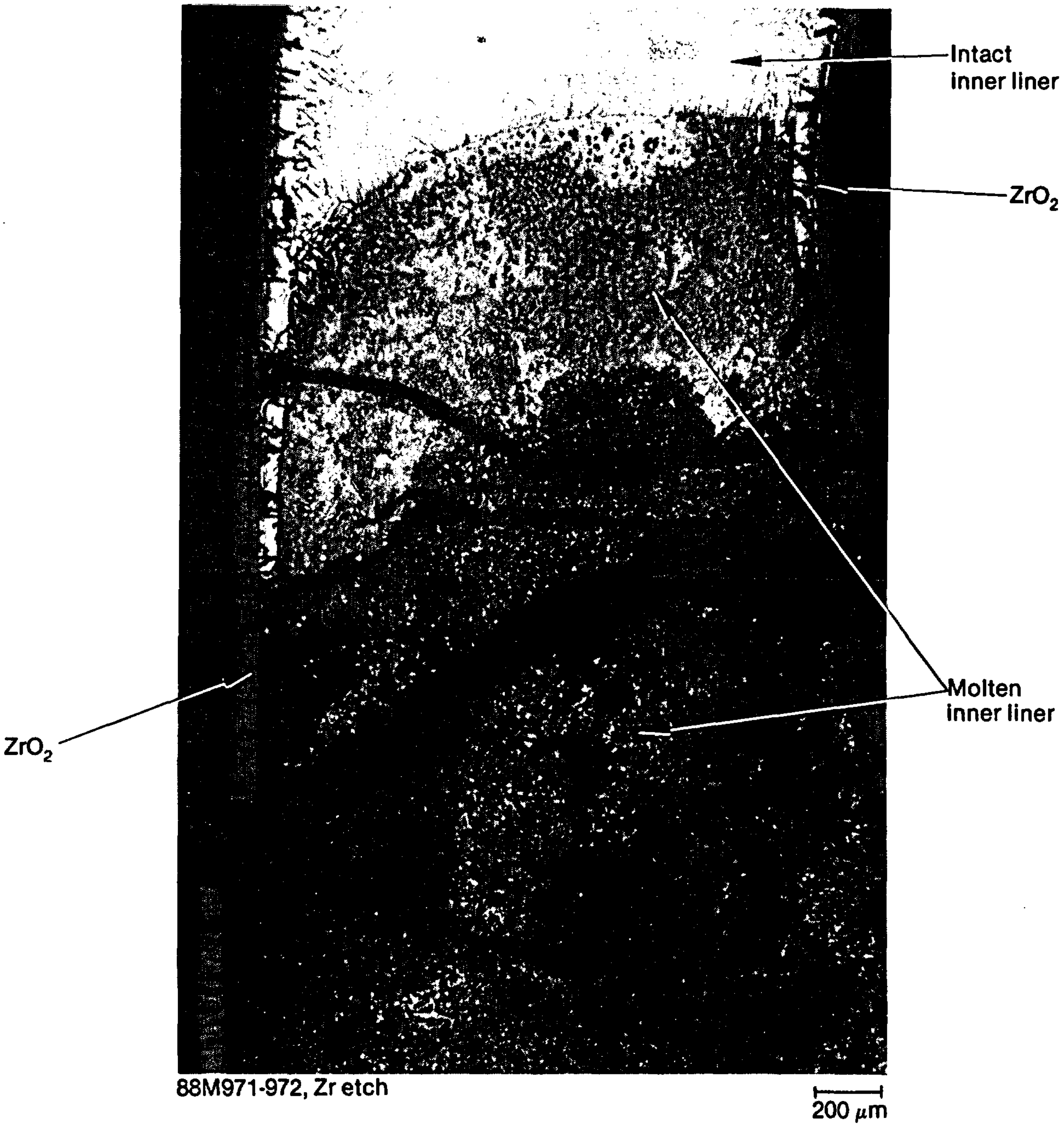

Figure 195. Molten zircaloy inner liner at 1.45 m.

melting was observed on the end tips of the intact zircaloy liner. The eutectic melts did not affect the alpha-Zr(O) or ZrO_2 layers on the liner surfaces, so temperatures were less than 2245 K; but they may have been as low as 1300-1500 K, assuming Ni-Zr or Fe-Zr eutectics.

Small amounts of zirconium hydrides were observed on the inner liner at elevations below the second spacer grid. Based upon comparisons with known standards,[13] the concentration of zirconium hydrides was <100ppm by weight. Oxidation was not observed below the G(bottom) elevation (0.43 m), and only small amounts were present between this elevation and where the liner disappeared at the H elevation (0.58 m). The microstructure of the inner liner was as-fabricated up through the D elevation (0.22 m), but areas of recrystallized zircaloy were observed on the E elevation (0.27 m). Inner liner temperatures at 0.27 m were therefore approximately 900-1000 K. At the G(bottom) elevation (0.43 m), the structure of the inner liner was prior-beta, indicating temperatures in excess of 1245 K at and above this elevation. The structure of the intact inner liner at the Q elevation (1.45 m) was also prior-beta.

3.2.5 Zircaloy Shroud Behavior

During posttest visual examinations of the fuel bundle, a small piece of one corner of the shroud was observed to be missing, as shown in Figures 4 and 5. It is not clear whether this occurred during the test or in subsequent handling of the fuel assembly. A photograph of the lower portion of this crack is shown in Figure 196. It showed a prior-beta structure, but otherwise nothing unusual. Photographs at higher elevations through the larger portion of the crack are not available because this portion of the fuel bundle was cut off during the trimming of the metallographic samples.

Minor amounts of zirconium hydriding were observed intermittently in the lower portion of the fuel bundle. The transformation to a prior-beta structure began to occur at the J elevation (0.77 m) and continued through the N elevation (1.14 m). This indicates that shroud temperatures in this region exceeded 1245 K, which agrees with peak thermocouple measurements of

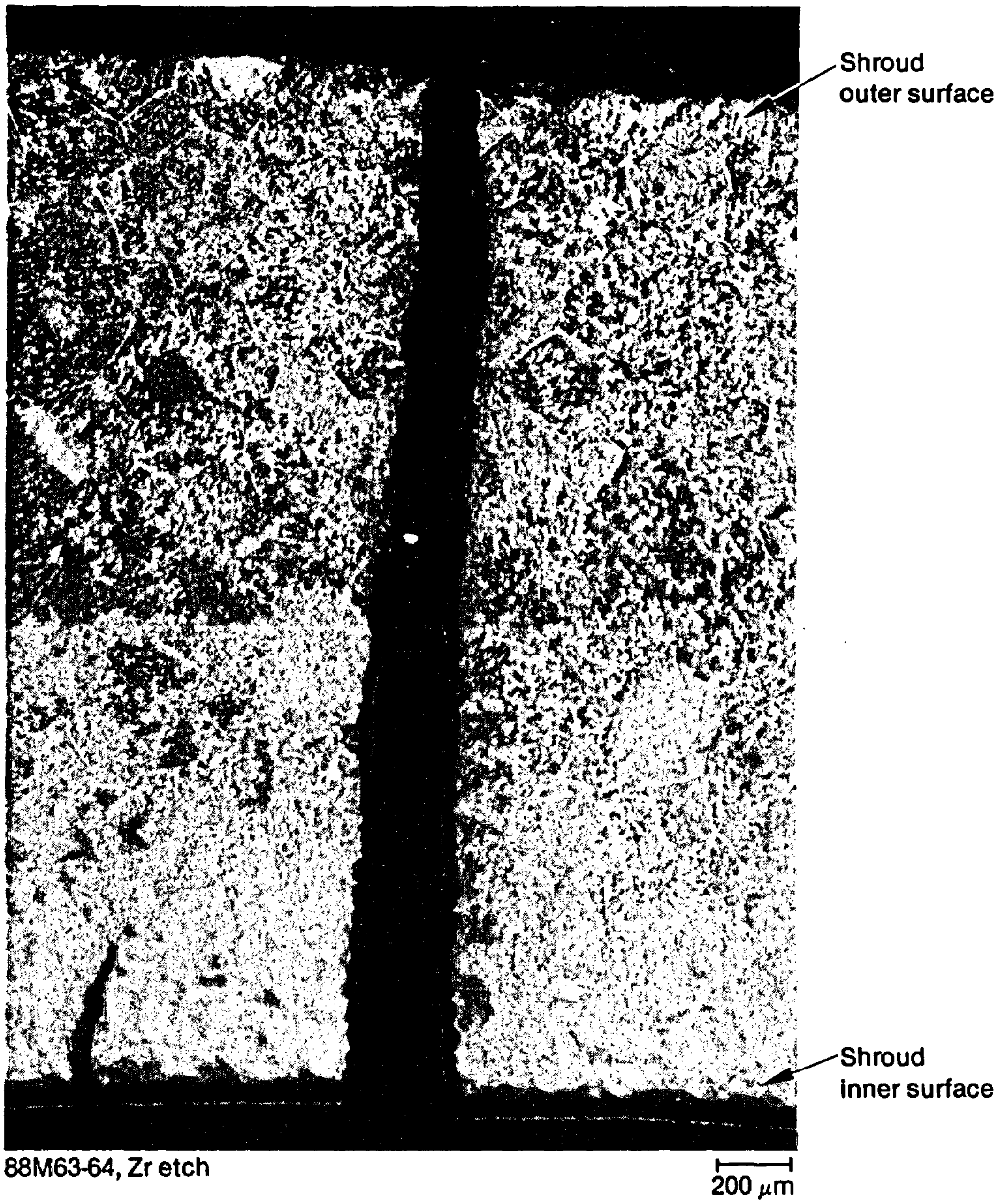

Figure 196. Crack in shroud wall at 1.04 m.

1620 K in this region.[10] Very small oxide layers were sometimes observed on the outer surface of the shroud in this region.

3.2.6 Insulation Behavior

As described in Section 3.2.4, essentially all of the liner was intact at and below the G(top) elevation (0.46 m). However, much of the insulation is missing in the photographs of these lower cross sections. This is due to fallout of the insulation during bundle sectioning operations, as described in Appendix B. The intact insulation can be seen in this lower region in the neutron radiographs shown in Figures 7 and 8.

Beginning at the H elevation (0.58 m), portions of the inner liner had liquefied and melt was able to penetrate into the low density (~20%TD) ZrO_2 insulation above this elevation. These insulation/melt regions can be seen in the photographs of the cross sections as darkened regions in the insulation region. On some of the cross sections, a thin ZrO_2 layer was present on the inner surface of the liner in the regions where the melt penetrated the insulation. This indicates that this high-melting-point oxide layer held molten unoxidized zircaloy in place and allowed it time to penetrate the insulation. In some cases, this led to crumbling and relocation of the insulation. Significant amounts of insulation, which were not affected by any melt, also broke off and tumbled into the fuel bundle in the topmost portions of the bundle. The breakup and relocation of this insulation is also apparent in the neutron radiographs and the topmost metallographic cross sections. However, as described in Section 4.1, interpolation of cross-sectional-area measurements of the insulation indicated that very little, if any, of the insulation was mixed into the melts. This suggests that the insulation may have relocated after the bundle cooled, perhaps even during handling operations following the completion of the experiment.

SEM/WDS examinations of samples K1-S31 and M3-S33 were examined to determine the composition and the oxidation state of the metallic melt that had penetrated into the insulation region. These examinations showed that in some regions the zircaloy melt, presumably from the molten inner liner, had penetrated into the insulation and fully oxidized. In other regions, the metallic melt was composed of unoxidized zirconium, stainless steel components, and control rod material. Details of these examinations are provided in Appendix E.

3.2.7 Behavior in the Lower Blockage Region

As shown in the neutron radiographs in Figures 7 and 8, the lower blockage region extended from just above the bottom spacer grid to approximately 0.30 m above the bottom of the instrumented fuel rods. It can be seen in the photographs of sections C through E (Figures 19-35). In the photographs of the C and D cross sections, a large area in the central portion of the assembly does not contain any material; and the lower blockage material completely surrounds this area. On the E cross section, the lower blockage material does not contain this open area in the central portion. This shows that the relocated material in this lower blockage region agglomerated in an egg-shaped structure. As described in Appendix B, when epoxy was poured into the fuel module prior to bundle sectioning, it did not penetrate into this central region within the lower blockage. This confirms that the relocated material formed a sealed enclosure. Because the epoxy was not able to penetrate into this central region, fuel rods which were present in this region were cut loose during bundle sectioning and fell out. This was observed during the sectioning operation; and, since the rod arrays are intact above and below the lower blockage region and considering that the relocated material was not hot enough to significantly damage the fuel rods it surrounds, it can be assumed that all the rods within this central region were in place prior to bundle sectioning. (Minor damage to some of the central rods was apparent in some instances, but this is relatively insignificant.)

The material in the lower blockage region consisted of a variety of materials but was primarily composed of eutectic metallic melt and fuel debris. An example of the variety of materials is shown in Figure 197. It shows oxidized cladding remnants, fuel particles and individual fuel grains,

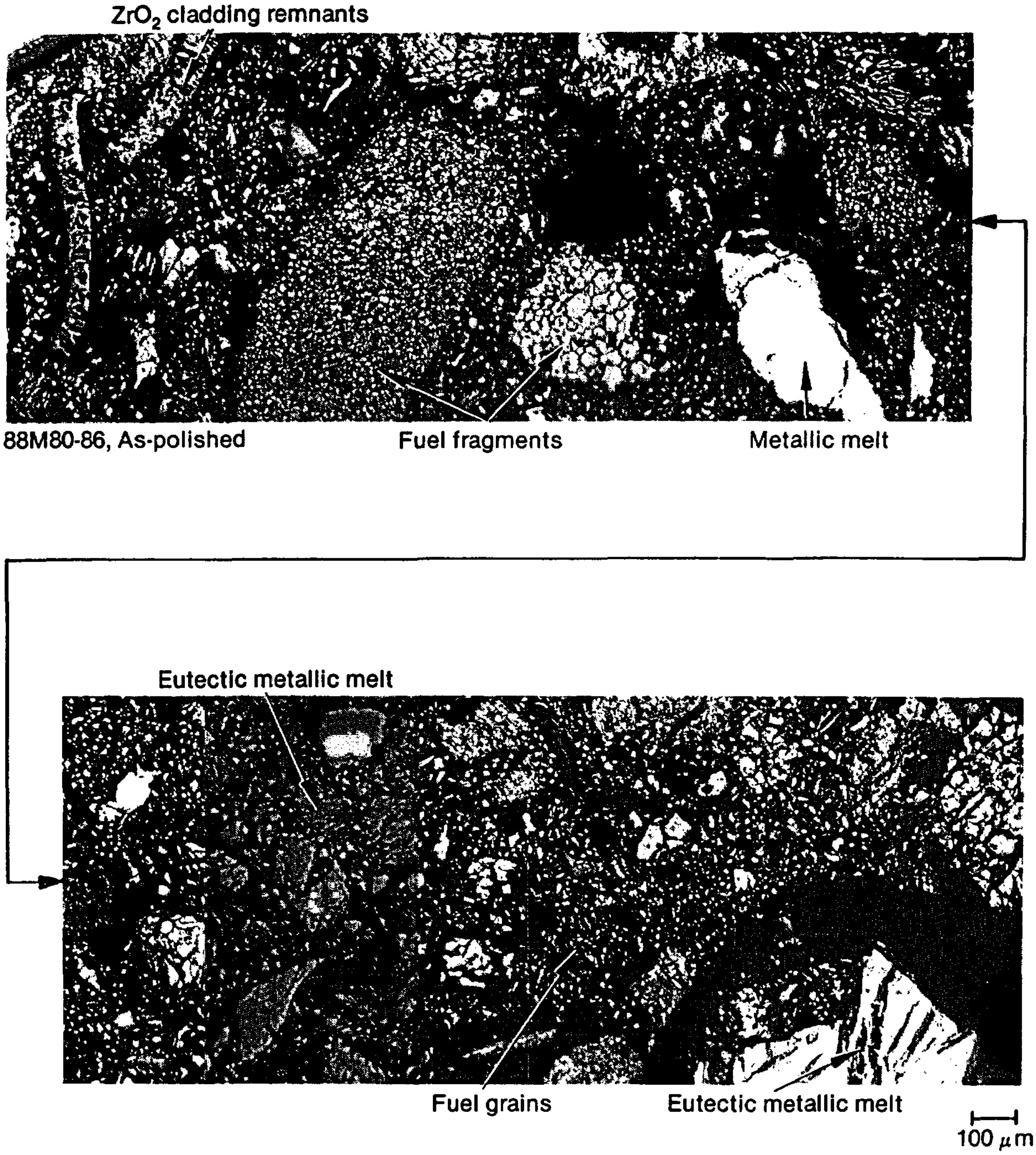

Figure 197. Assortment of debris in lower blockage region at 0.22 m.

metallic melt particles, and eutectic metallic melt particles. A significant amount of porosity also exists between these individual particles. Another example from another area within the lower blockage is shown in Figure 198. This figure shows a large amount of eutectic metallic melt, which accumulated adjacent to a fuel rod. Figure 199 shows the materials in the lower blockage in more detail.

This eutectic metallic melt material can also be seen in photographs from Sections 3.2.1, 3.2.2., and 3.2.3, which describe the liquefaction of the spacer grids, stainless steel control rod cladding, and zircaloy cladding by metallic melts. It is apparent that eutectic melting of these components relatively early in the test resulted in the relocation of these materials to form the lower blockage.

The material in the lower blockage region was very heterogeneous on a microscale. Different areas contained varying concentrations of eutectic melt material and fuel debris, as well as varying amounts of porosity. This made it very difficult to estimate the bulk composition from just the metallographic results. Consequently, it was necessary to rely upon elemental analysis and density measurements of bulk samples taken from this region to estimate the composition. This analysis is described in detail in Section 4.5. These data, in conjunction with quantitative SEM/WDS examinations of sample C2-S11, were used to estimate the amount of oxidized zirconium in this region, as described in Section 4.2. As detailed in Appendix E, the SEM/WDS results from sample C2-S11 indicated that the eutectic metallic melt material was composed of control material (Ag,In,Cd), zirconium, and stainless steel components (Fe,Ni,Cr).

3.2.8 Ceramic Melt Behavior

The upper blockage region can be seen in the neutron radiographs in Figures 7 and 8. It extended from the second spacer grid, at approximately 0.45 m, to approximately 1.0 m. The relocated material near the second spacer grid was the same type of eutectic metallic melt and fuel debris found in the lower blockage region. This relocated material can be seen in

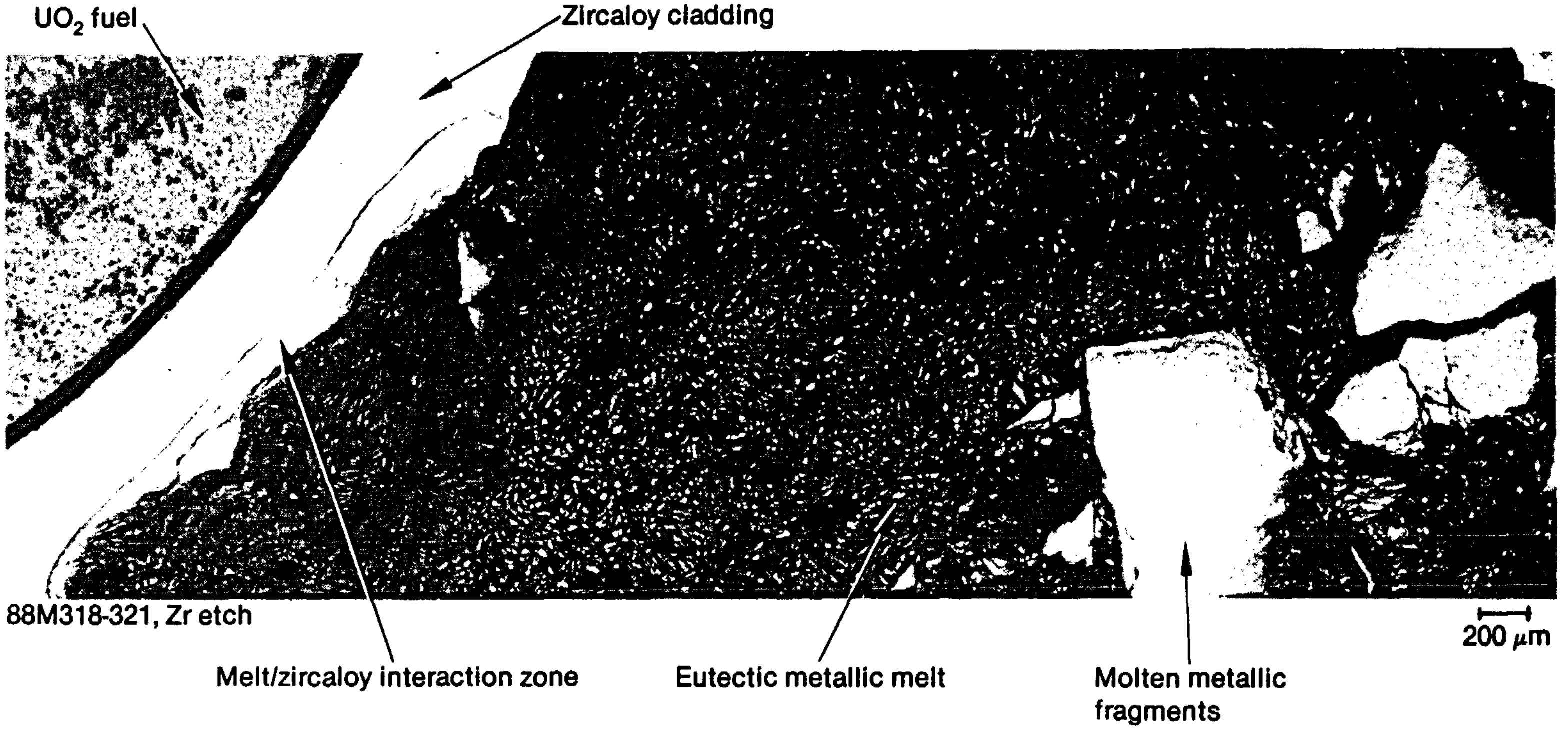

Figure 198. Laminar eutectic metallic melt material in lower blockage region at 0.22 m.

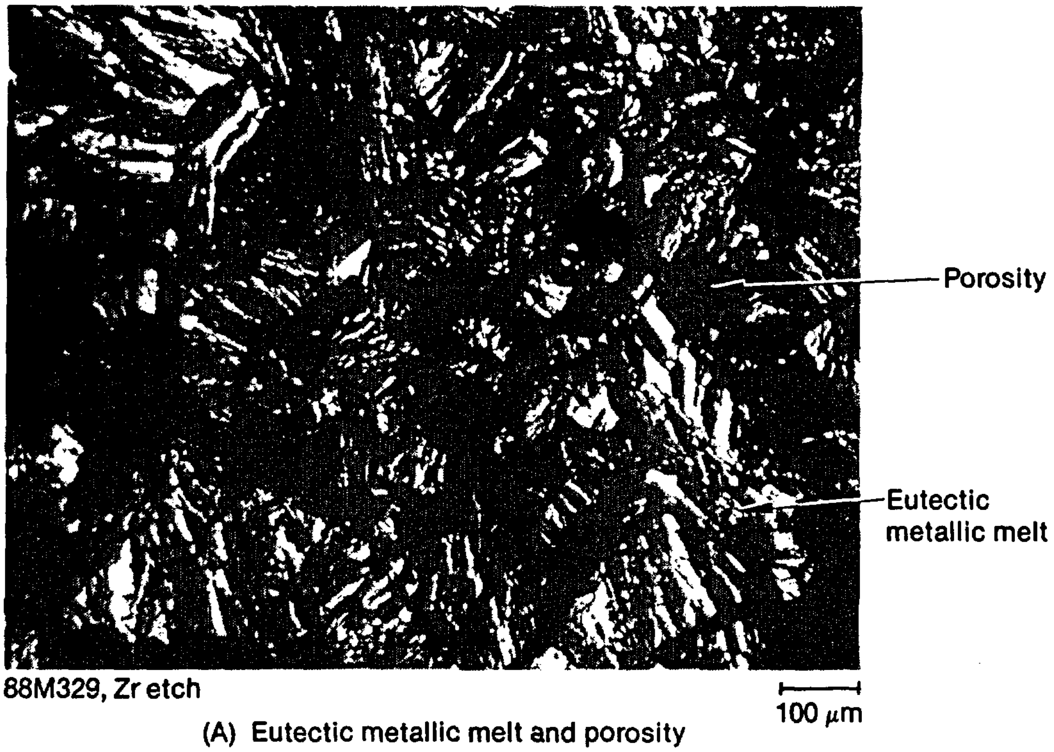

(A) Eutectic metallic melt and porosity

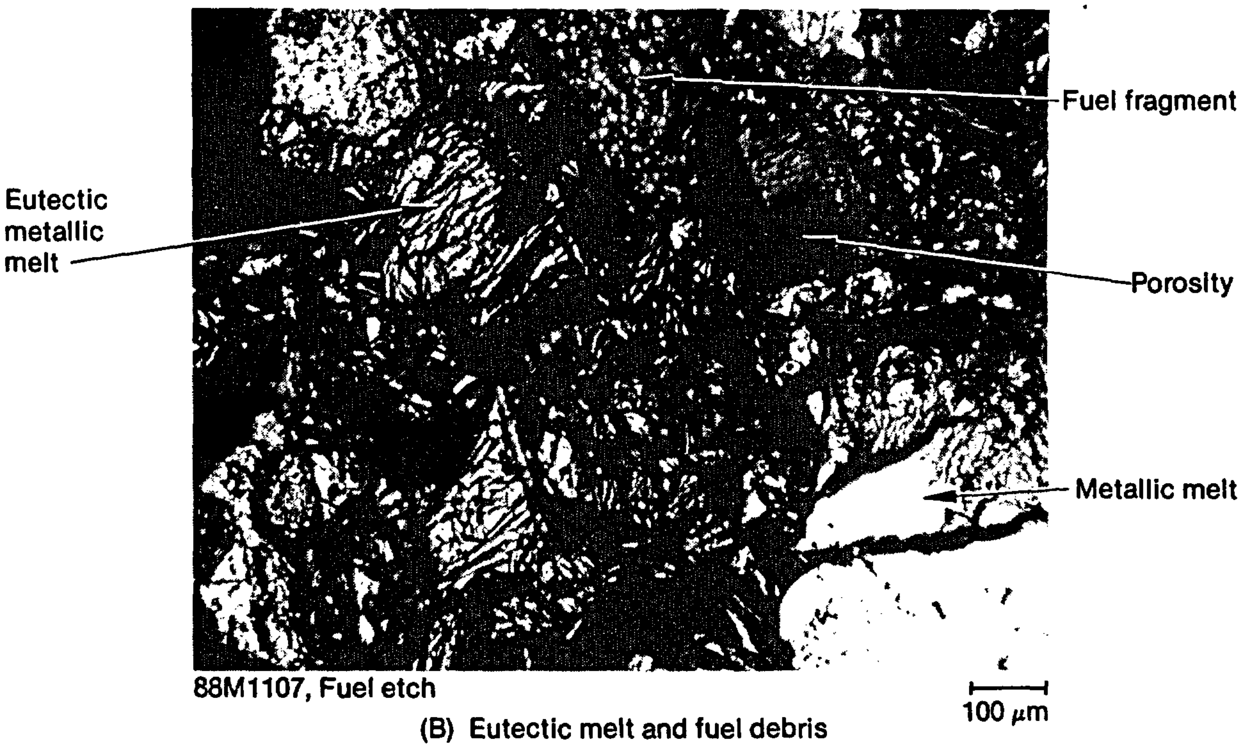

(B) Eutectic melt and fuel debris

Figure 199. Details of laminar eutectic metallic melt phase at 0.22 m.

the photographs of the G(top) and H cross sections (Figures 50-66). The photographs of the H, I, J, and K elevations (Figures 59-102) show that the relocated previously molten material in this portion of the fuel bundle (0.58-0.88 m) was a ceramic melt. Ceramic melt was also observed around individual rods above the upper blockage region. It was not observed below the second spacer grid.

Radiochemical analysis of several samples taken from the ceramic melt region (Section 4.5), as well as qualitative SEM/WDS examinations of samples I2-S1, J2-S4, and K1-S6, indicated that this melt was primarily $(U,Zr)O_2$, with smaller amounts of other bundle constituents mixed in. Quantitative SEM/WDS analysis of sample I2-S1 confirmed the composition to be $(U,Zr)O_2$. It is sometimes difficult, or even impossible, to determine for certain whether these melts were oxidized when molten or whether they were a metallic melt that later oxidized and solidified. This distinction is very important as far as determining the temperatures of the molten material. As shown in Figures G-24 and G-25 in Appendix G, (U,Zr,O) mixtures can be molten at temperatures as low as approximately 2200 K, with significantly greater amounts near 2300 K. In contrast, $(U,Zr)O_2$ mixtures are only molten above 2810 K, as shown in Figure G-14. However, metallographic observations suggest that this melt was molten as a ceramic, with temperatures in excess of 2810 K. These observations and analysis are briefly summarized below, with a more detailed account in Section 4.3.

A review of the H through K photographs (Figures 59-102) indicates that the largest areas of relocated melt are situated in the northeast quadrant, with the northwest quadrant also having significant amounts. In general, the fuel rods that were located in the central portions of these melt regions were no longer surrounded by any cladding, whereas fuel rods located near the periphery of these melt regions had oxidized cladding shells still surrounding them. Fuel pellets in the central melt regions underwent significant melting and liquefaction and were either completely dissolved in the melt or significantly reduced in size due to liquefaction of their outer surfaces. This distribution of fuel and oxidized zircaloy behavior indicates that a temperature gradient existed in this melt.

A photograph of the ceramic melt surrounding a fuel pellet and penetrating along fuel cracks is shown in Figure 200. The melt was single-phase, with small metallic ingots spread throughout. Gas bubbles were present in areas of the melt, and there was some cracking. This fuel pellet was on the boundary between a ceramic melt region, with typical amounts of gas bubbles, and a region without any large gas bubbles, as shown in Figure 201. The large gas bubbles can be seen on the side of the fuel pellet on which there are still remains of the oxidized cladding shells. In this region, the ZrO_2 cladding shells from two adjacent fuel rods came into contact and fused together. This region is shown in more detail in Figure 202. The ceramic melt surrounding this fuel pellet was hot enough to nearly completely melt these ZrO_2 shells. Metallic ingots of material within the ZrO_2 remnants can be seen. On the other side of the fuel pellet, in the region without any large gas bubbles, the oxidized cladding was completely gone. Review of Figure 201 indicates that all the oxidized cladding melted in the bubble-free region. These data provide a good indication of a temperature boundary in the ceramic melt, >2960 K on one side of the fuel pellet and very near 2960 K on the other side. Temperatures near the periphery of the melt regions were less than 2960 K where the ZrO_2 cladding shells were still intact. A more detailed discussion and analysis of estimated temperatures in this region are provided in Section 4.3.

An example of the typical morphology of the ceramic melt is shown in Figure 203. Image analyzer measurements, using these photographs, indicated an average porosity of 43%±10%.

An interesting photograph of the ceramic melt in the upper portion of the fuel bundle is provided in Figure 204. This ceramic melt was located between the two fuel pellet stacks shown in Figure 131. Different porosity distributions in the melt distinguish the former locations of the zircaloy cladding from the melt that flowed down the open space between the fuel rods.

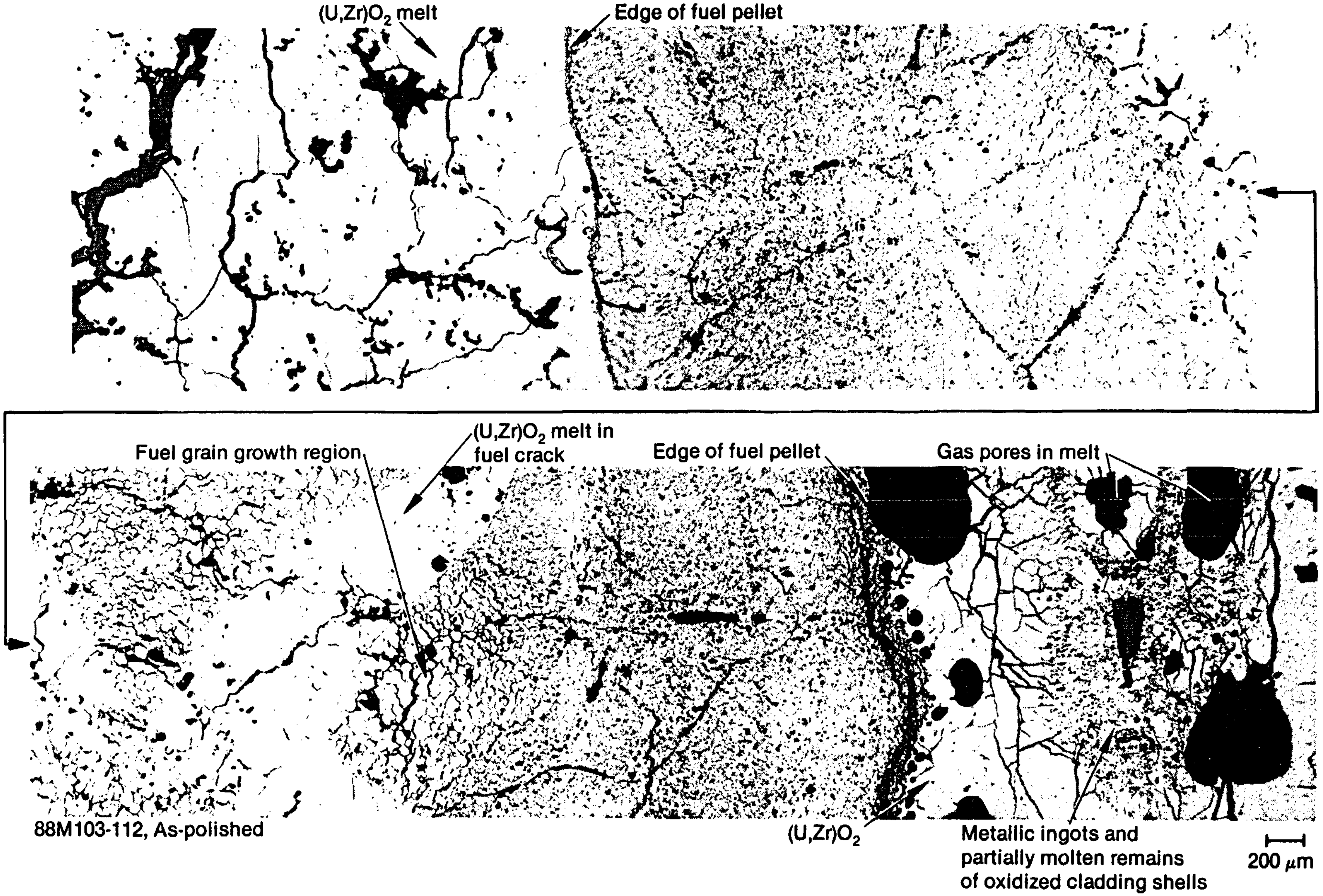

Figure 200. Interactions between (U,Zr)O$_2$ melt and fuel and oxidized cladding remnants at 0.66 m.

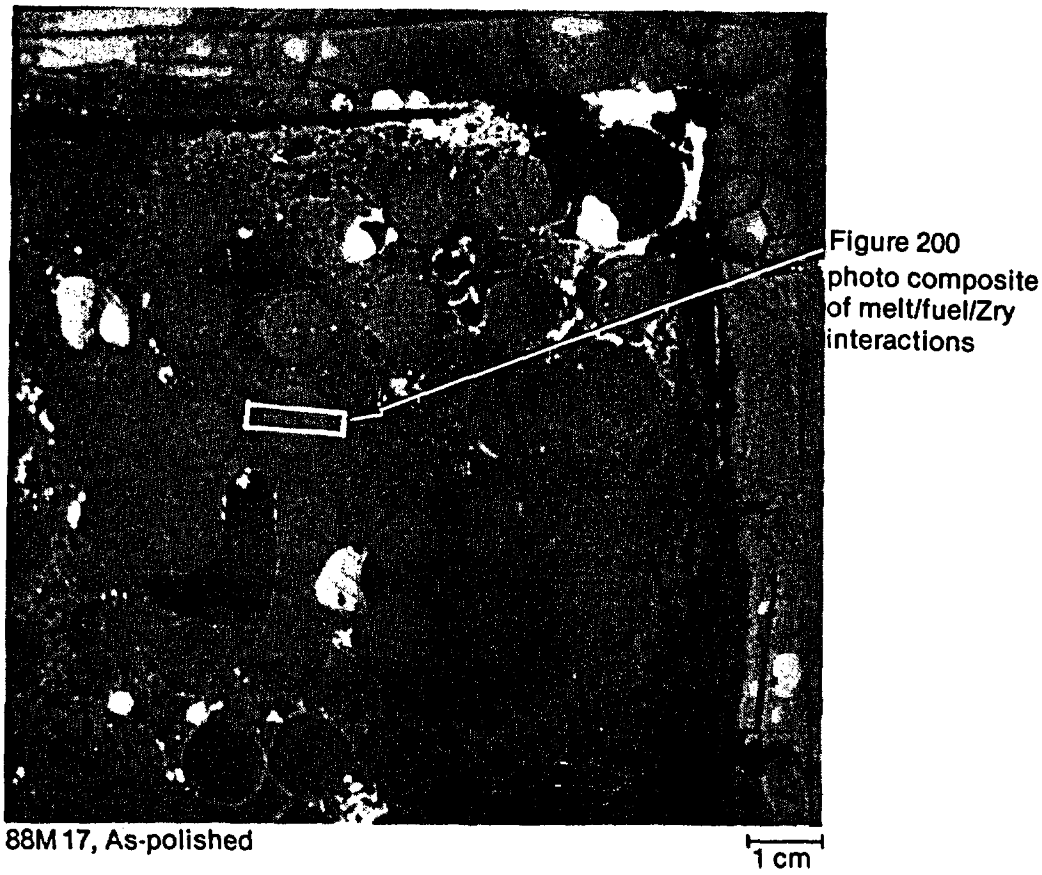

I2

Figure 201. Location of fuel pellet shown in Figure 200 at 0.66 m.

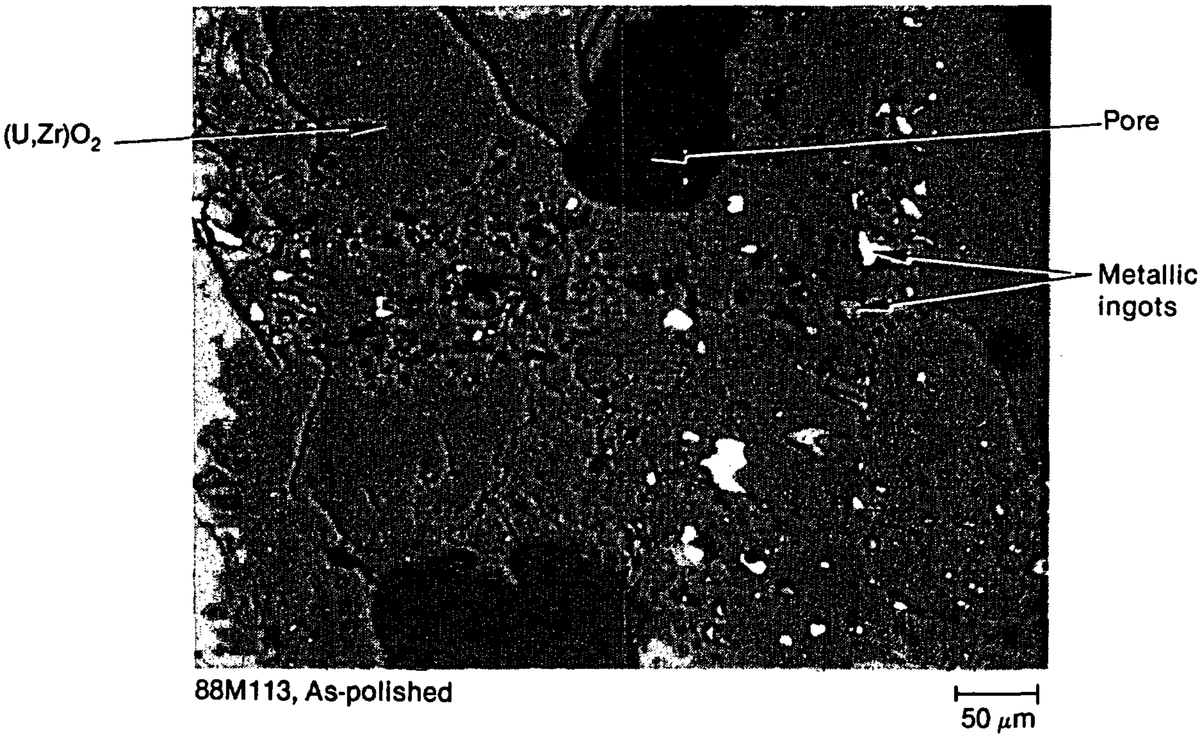

Figure 202. Detail of Figure 200 showing interaction zone between ceramic melt and oxidized cladding remnants.

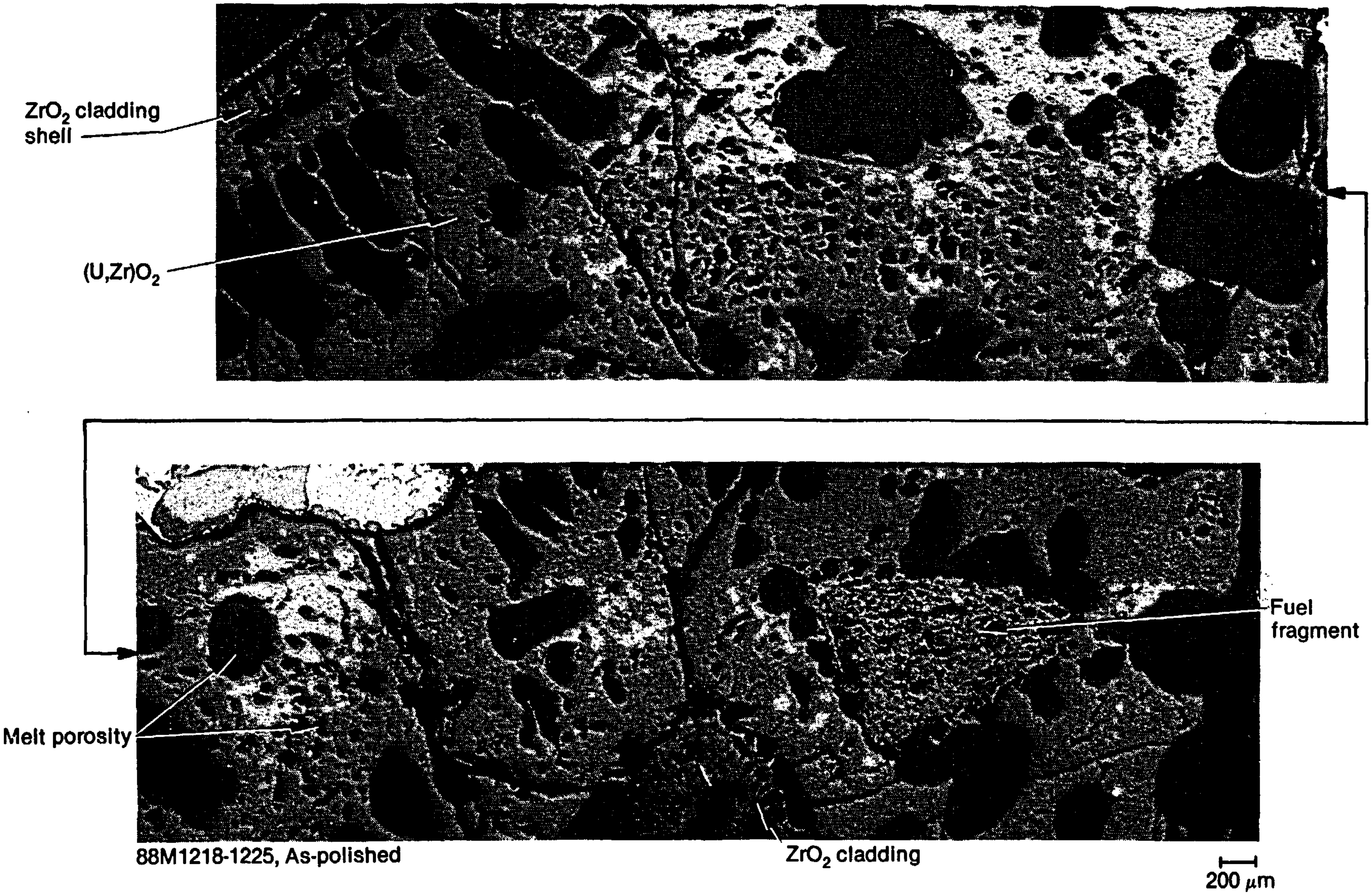

Figure 203. Porosity characterization in (U,Zr)O$_2$ melt at 0.66 m.

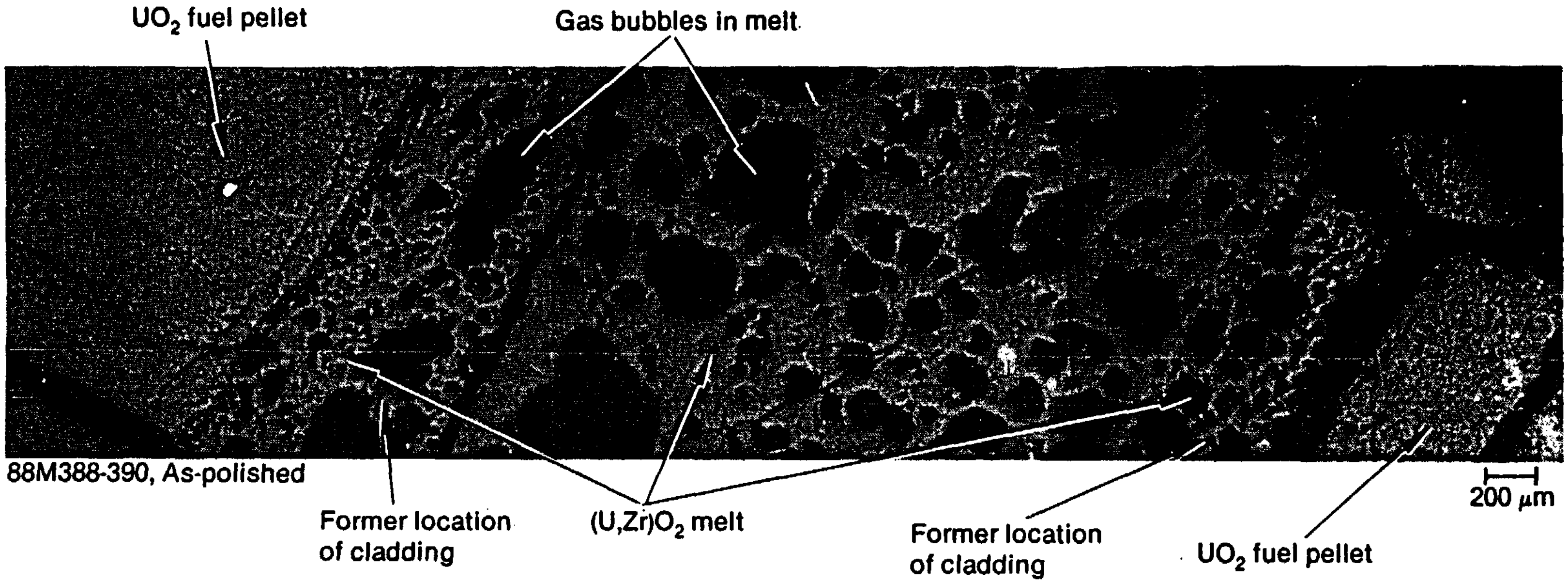

Figure 204. Ceramic melt between fuel pellets at 1.20 m.

3.2.9 Fuel Behavior

Several factors affected the behavior of the fuel in the LP-FP-2 experiment. The different aspects of fuel behavior are divided into four categories: (1) fuel restructuring, (2) fuel reduction by metallic melts, (3) fuel fragmentation and powdering, and (4) fuel liquefaction and melting. These four categories of fuel behavior are discussed in the following subsections.

3.2.9.1 Fuel Restructuring. Figures 205 and 206 show the fuel porosity and grain structure at the edge and in the center of a fuel rod located in an outer row near a corner location at the A elevation (0.003 m). Figures 207 and 208 show the corresponding fuel morphology for a fuel rod near the center of the assembly. These photographs show no difference in fuel morphology between the edge and center of the fuel assembly or within a fuel pellet. Due to the axial location of these fuel pellets in the fuel bundle, it can be assumed that no significant fuel restructuring has occurred and that this fuel morphology represents the as-fabricated fuel structure. As described in Section 4.4, the nominal grain size measured from these photographs was 14 μm. These fuel pellets were fabricated to 94.67±0.4%TD; and the resulting porosity is apparent within the fuel grains, as well as along grain boundaries. Much of this as-fabricated porosity would be filled with helium gas prior to irradiation because the fuel rods in this experiment were backfilled with helium gas to 2.4 MPa (350 psi). The fuel grain structure is shown in more detail in Figure 209 on a fuel pellet at the B elevation (0.03 m).

Higher in the fuel bundle, examples of movement of this gas-filled porosity from within the fuel grains to the grain boundaries can be observed. An example is provided in Figure 210. These photographs were taken near the edge and in the center of a fuel pellet located near the exterior corner of the fuel assembly. The photograph taken near the pellet edge shows significant amounts of porosity within the fuel grains. However the photograph of the center of the fuel pellet shows that this porosity has migrated to the grain boundaries and is no longer present within the fuel

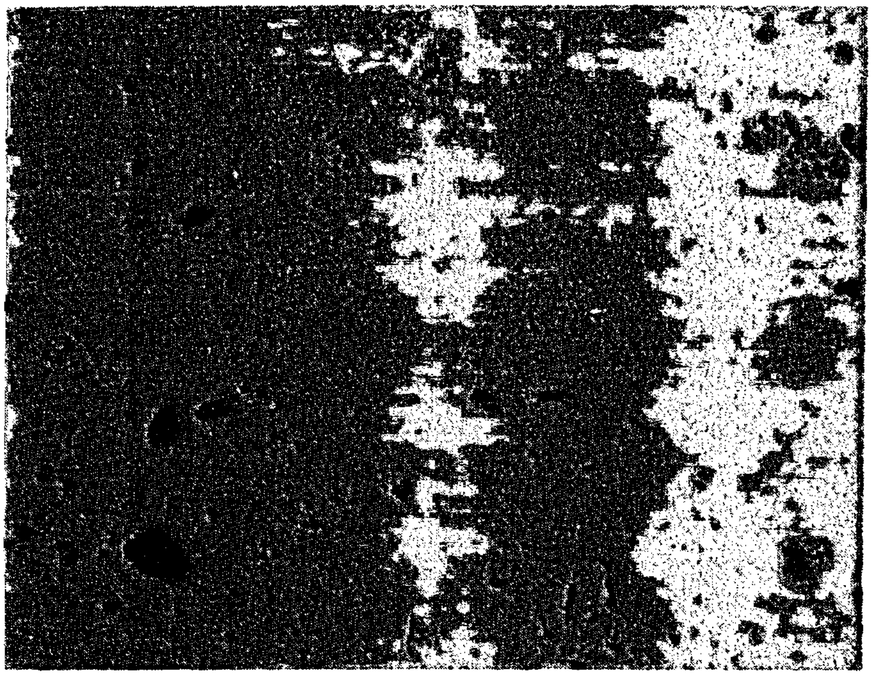

88M844, As-polished

50 μm

(A) Fuel porosity near edge of exterior fuel rod

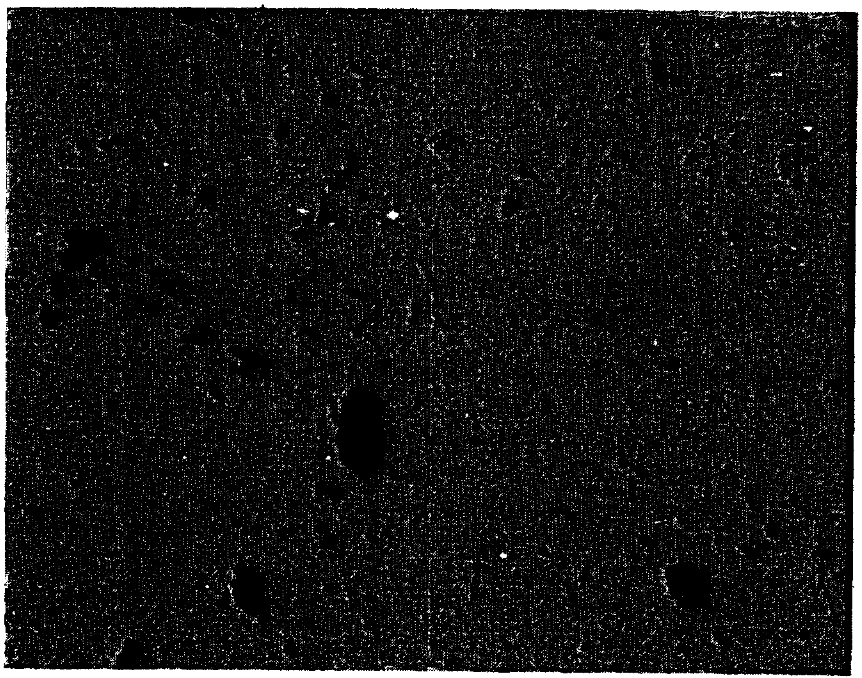

88M845, As-polished

50 μm

(B) Fuel porosity near center of exterior fuel rod

Figure 205. As-fabricated fuel pellet porosity in an exterior fuel rod at 0.003 m.

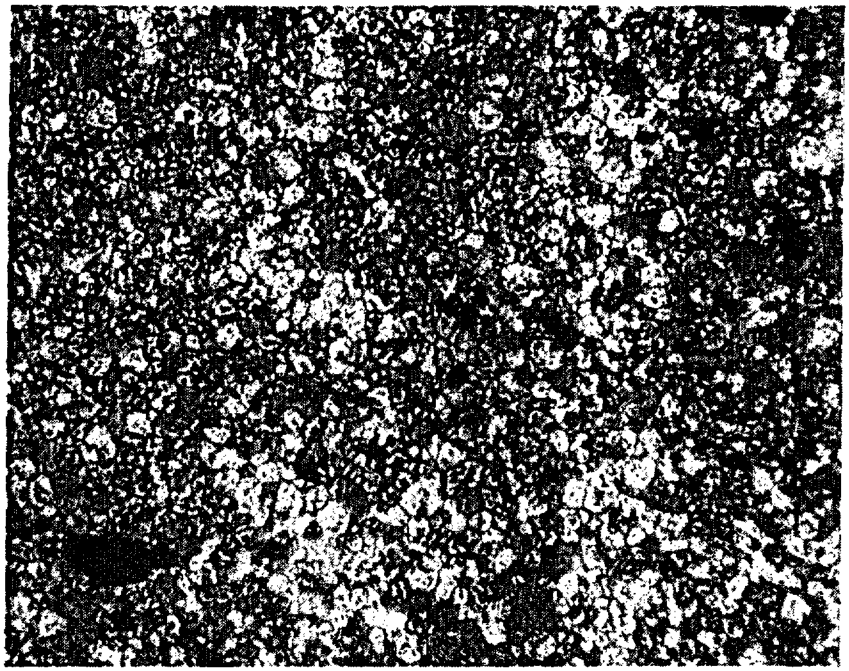

88M853, Fuel etch

50 μm

(A) Fuel grain structure near edge of exterior fuel rod

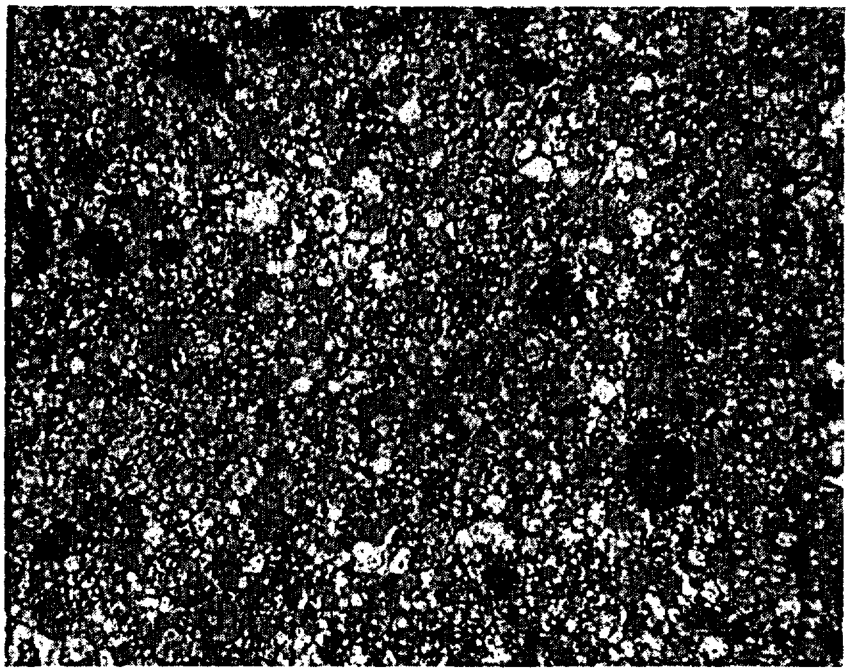

88M854, Fuel etch

50 μm

(B) Fuel grain structure near center fuel rod

Figure 206. As-fabricated fuel grain structure in an exterior fuel rod at 0.003 m.

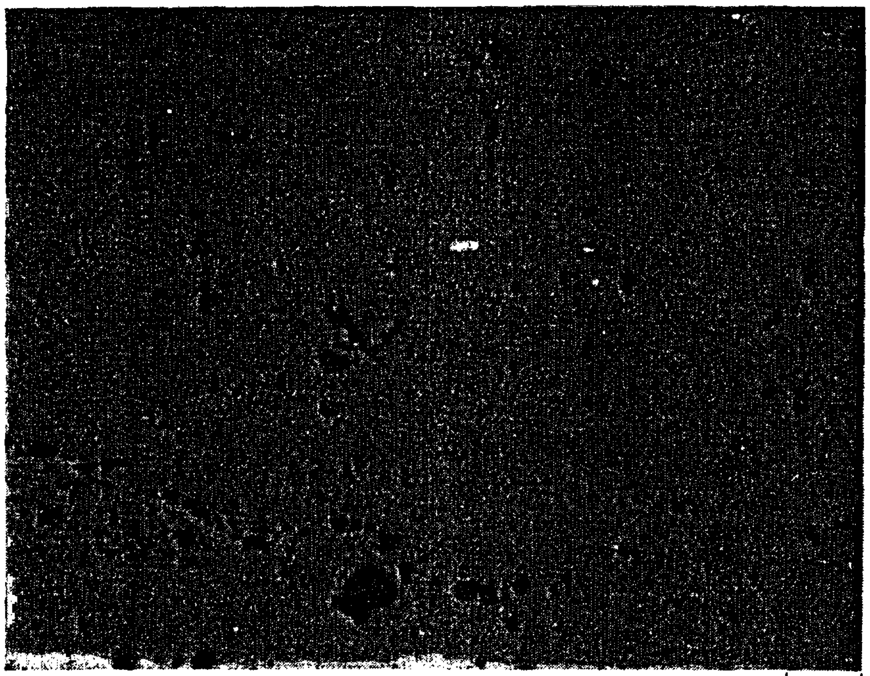

88M846, As-polished

(A) Fuel porosity near edge of interior fuel rod

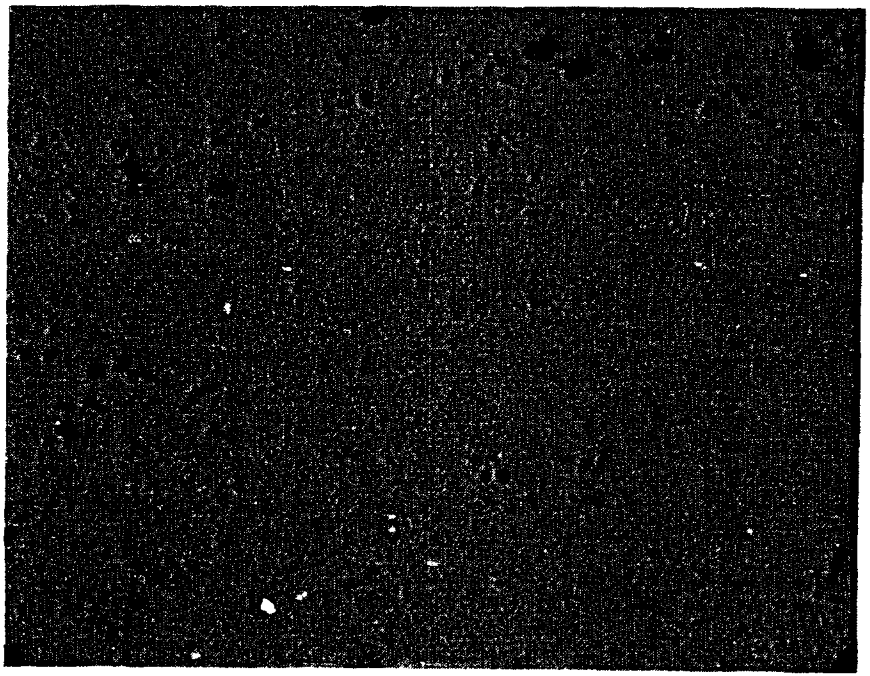

88M847, As-polished

(B) Fuel porosity near center of interior fuel rod

Figure 207. As-fabricated fuel porosity in interior fuel rod at 0.003 m.

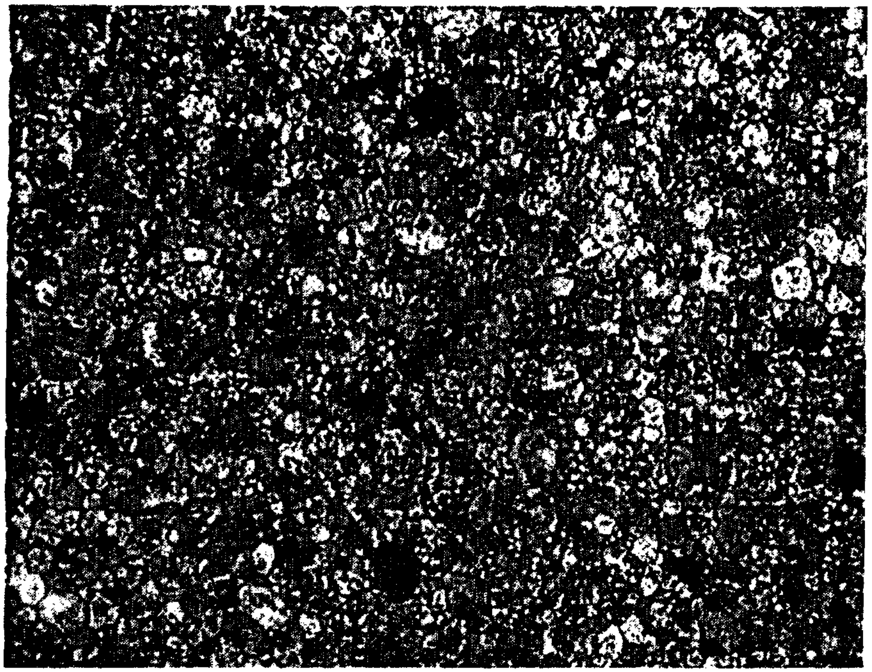

88M855, Fuel etch

(A) Fuel grain structure near edge of interior fuel rod

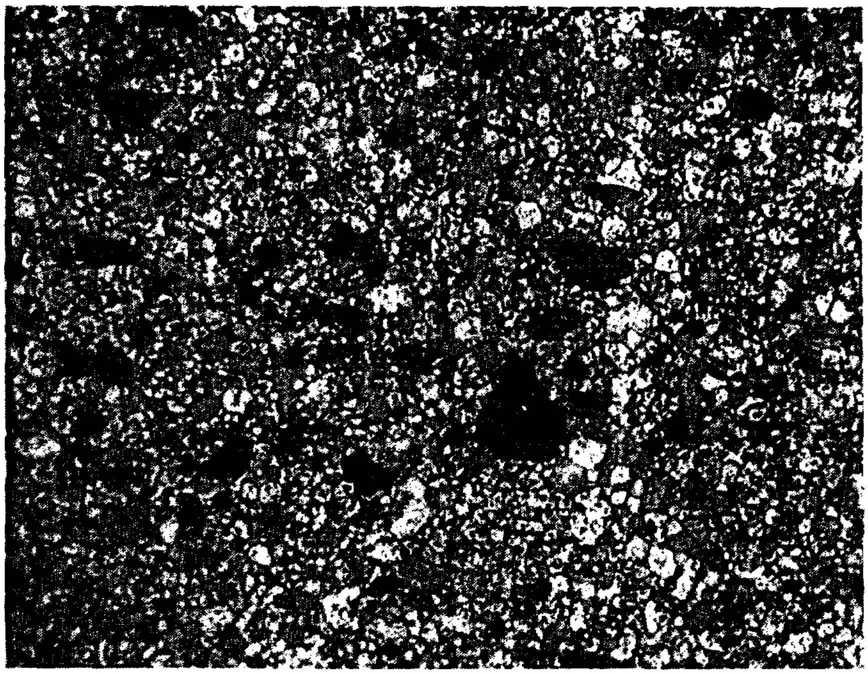

88M856, Fuel etch

(B) Fuel grain structure near center of interior fuel rod

Figure 208. As-fabricated fuel grain structure in interior fuel rod at 0.003 m.

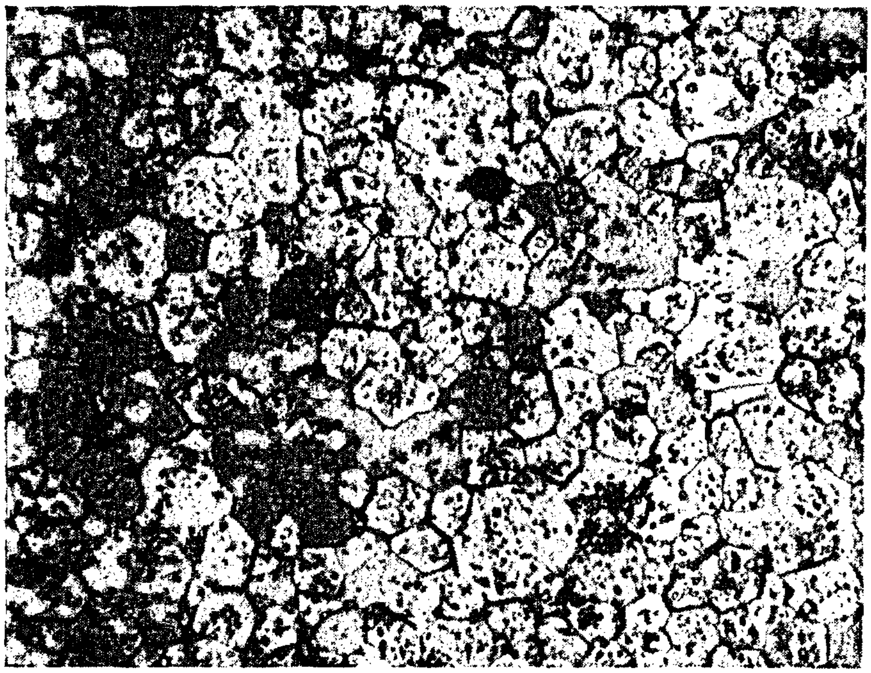

88M66, Fuel etch

20 μm

(A) Fuel grain structure near edge of exterior fuel rod

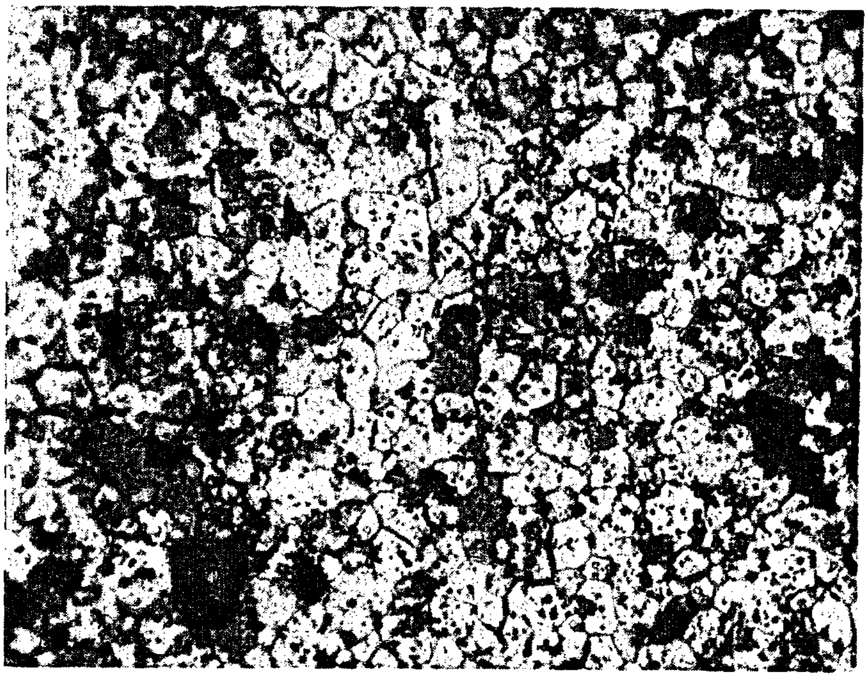

88M67, Fuel etch

20 μm

(B) Fuel grain structure near center of exterior fuel rod

Figure 209. Details of fuel grain structure at 0.03 m.

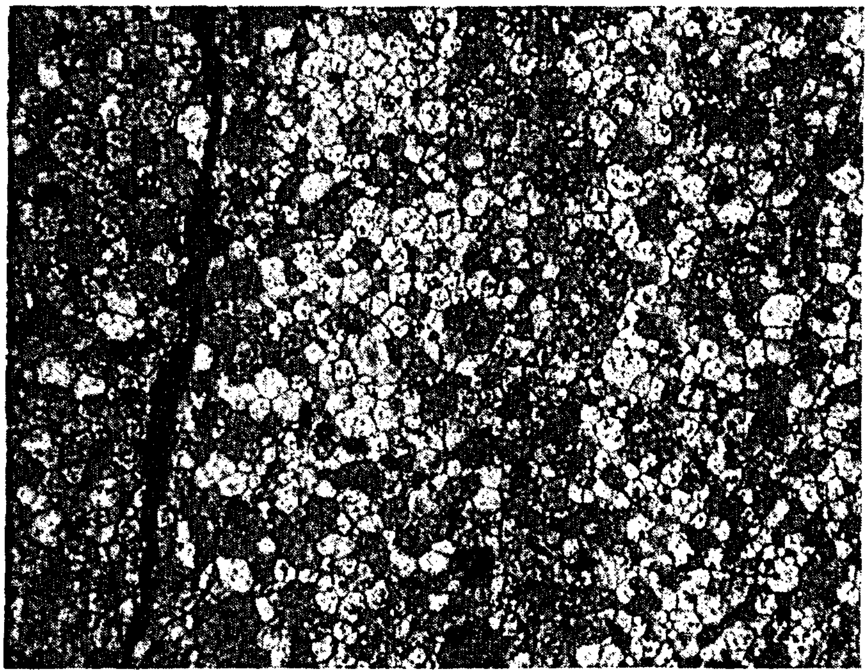

88M1341, Fuel etch

50 μm

(A) Fuel structure near edge of exterior fuel pellet

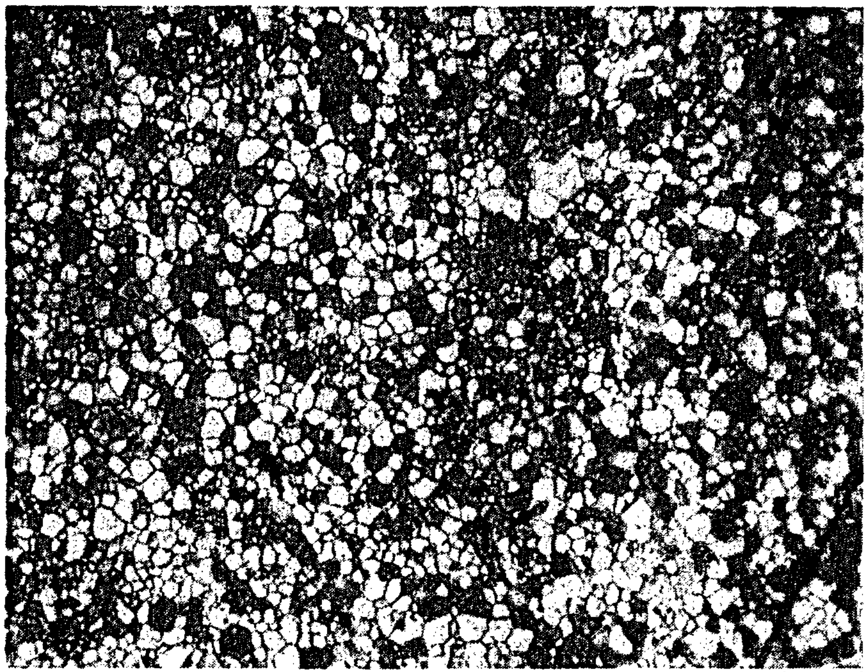

88M1342, Fuel etch

50 μm

(B) Fuel structure near center of exterior fuel pellet

Figure 210. Fuel grain structure at 1.14 m.

grains. This change in fuel morphology probably occurred during steady-state operation (prior to the transient) when the gradient in fuel temperatures would account for higher temperatures in the center of the fuel pellet. This pore migration did not affect the fuel grain size.

As described in Section 4.4, grain growth occurred in the center of some of the fuel pellets. An example is shown in Figure 211. This fuel rod was still intact and unaffected by molten relocating material. This demonstrates that fuel temperatures were sufficient to cause grain growth in the center of some fuel pellets prior to melt relocation. This initial grain growth would be enhanced if high temperature melts subsequently contacted the fuel, as discussed below.

Figure 200 showed the fuel morphology of a fuel pellet, with grain growth in the center, in which a ceramic melt had penetrated the fuel cracks and partially liquefied the fuel. As described in more detail in Section 4.3, melt temperatures in this region were very hot (~3000 K); the ZrO_2 cladding shell on the left side of Figure 200 has melted, while the oxidized cladding on the right side is nearly completely melted. It is apparent that these high temperatures have resulted in pore migration to the grain boundaries, resulting in grain boundary separation in some instances. This is shown in more detail in Figure 212, for the grain growth area near the center of the pellet, and in Figures 213, for an area near a fuel crack on the edge of the pellet. The grain size near the edge of the fuel pellet was as-fabricated (14 μm); however, in the grain growth region, it was nominally 27 μm. The grain boundary separation in the center of the fuel pellet is a result of grain growth and grain boundary coalescence, which has the effect of concentrating the available gas porosity. These results demonstrate that very high temperatures can result in grain boundary separation. In the following subsections, additional factors that may lead to grain boundary separation will be described.

Very large grain growth, leading to columnar grain formations, was observed in the center of some fuel rods. Figures 214, 215, and 216 show

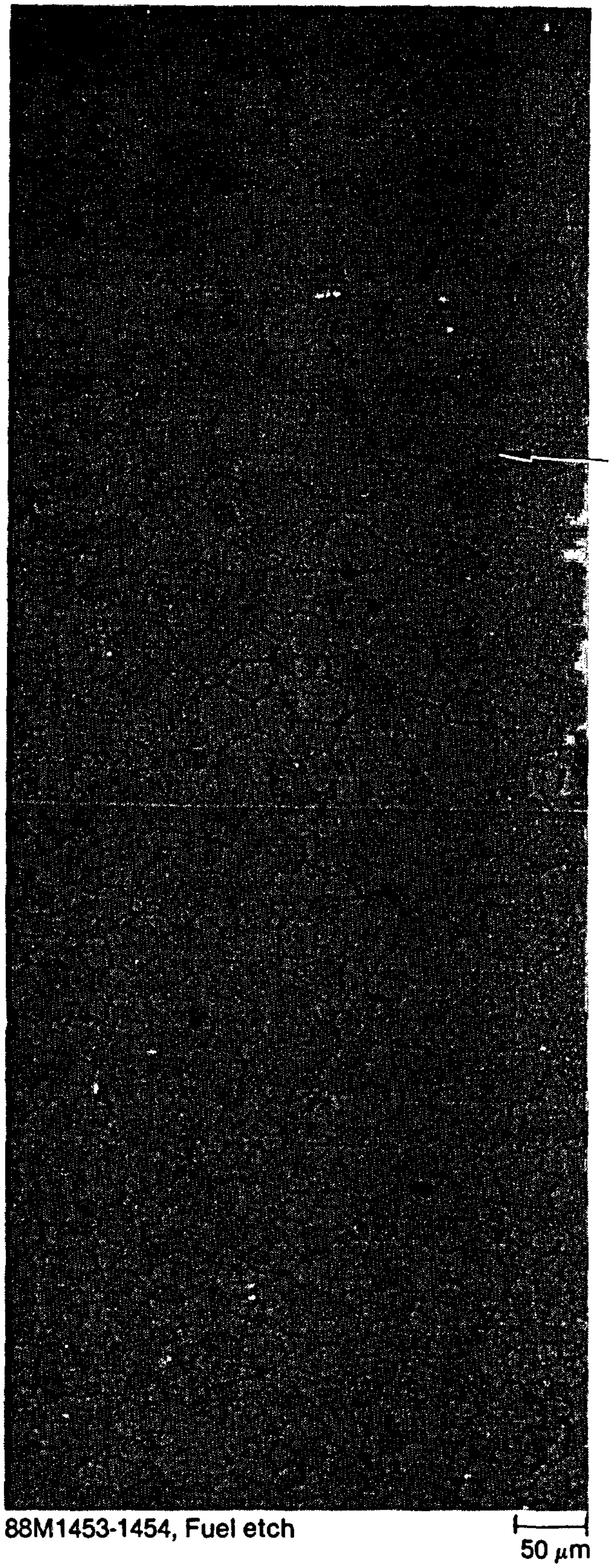

Figure 211. Grain growth in center of fuel pellet at 0.43 m.

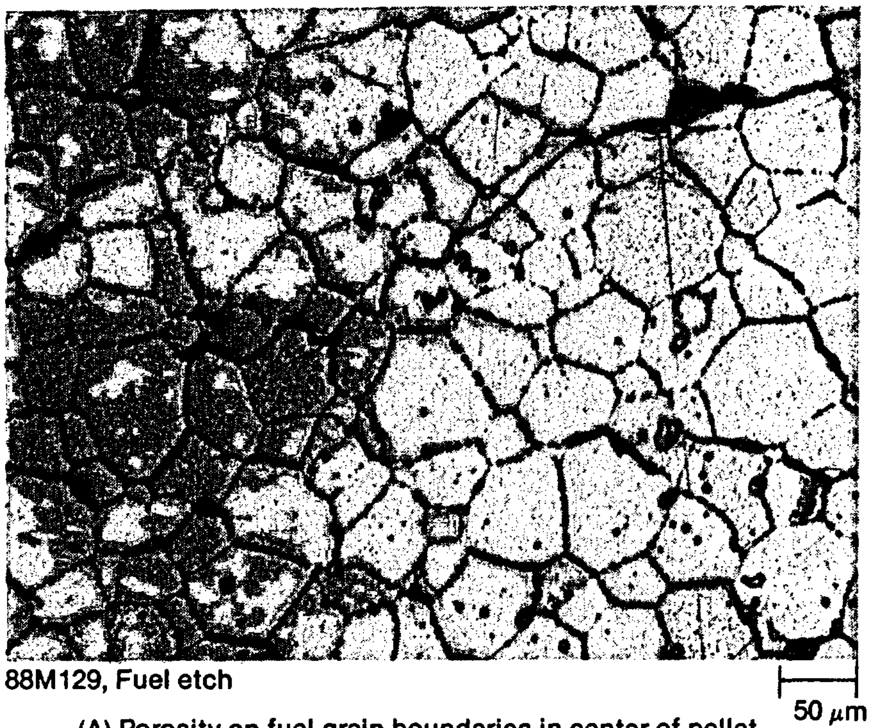

(A) Porosity on fuel grain boundaries in center of pellet

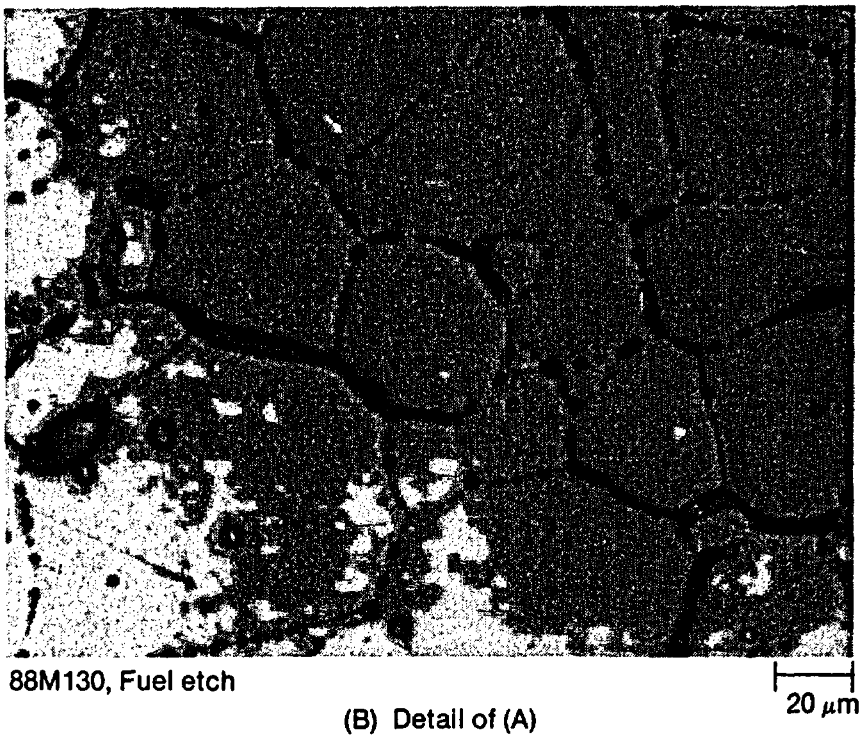

(B) Detail of (A)

Figure 212. Details of grain boundary porosity in center of fuel pellet shown in Figure 200 at 0.66 m.

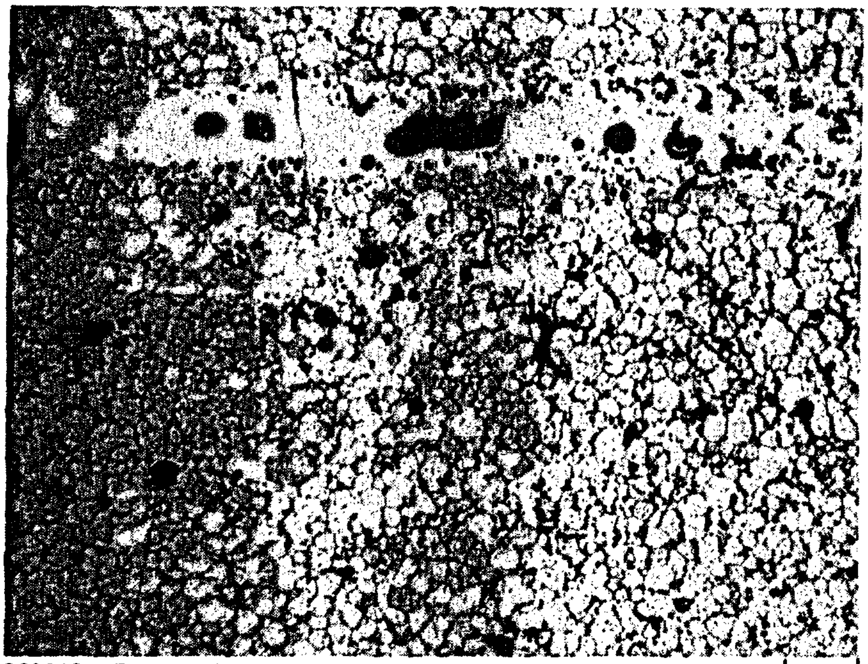

(A) Melt and fuel structure near edge of fuel pellet

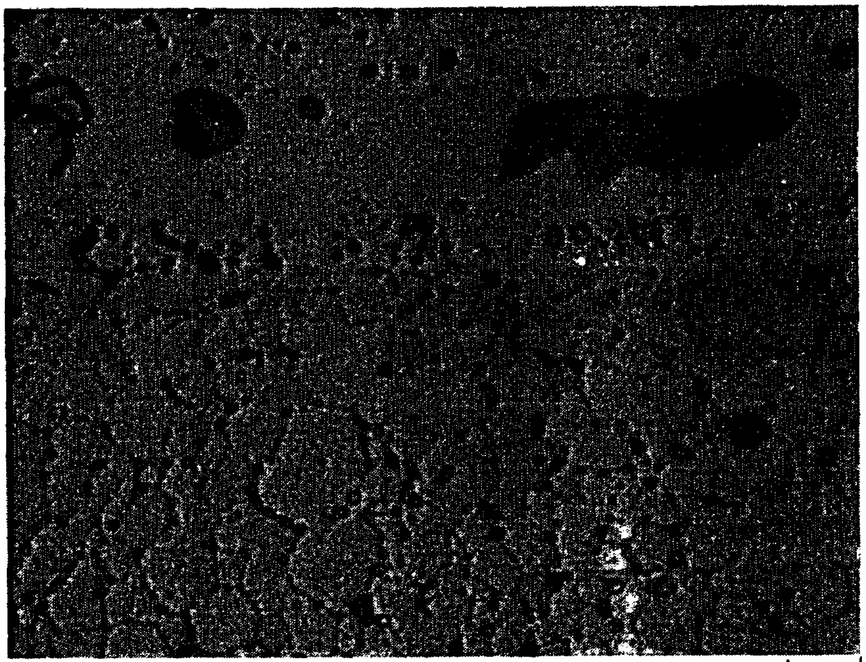

(B) Detail of (A)

Figure 213. Details of grain boundary porosity on edge of fuel in Figure 200 at 0.66 m.

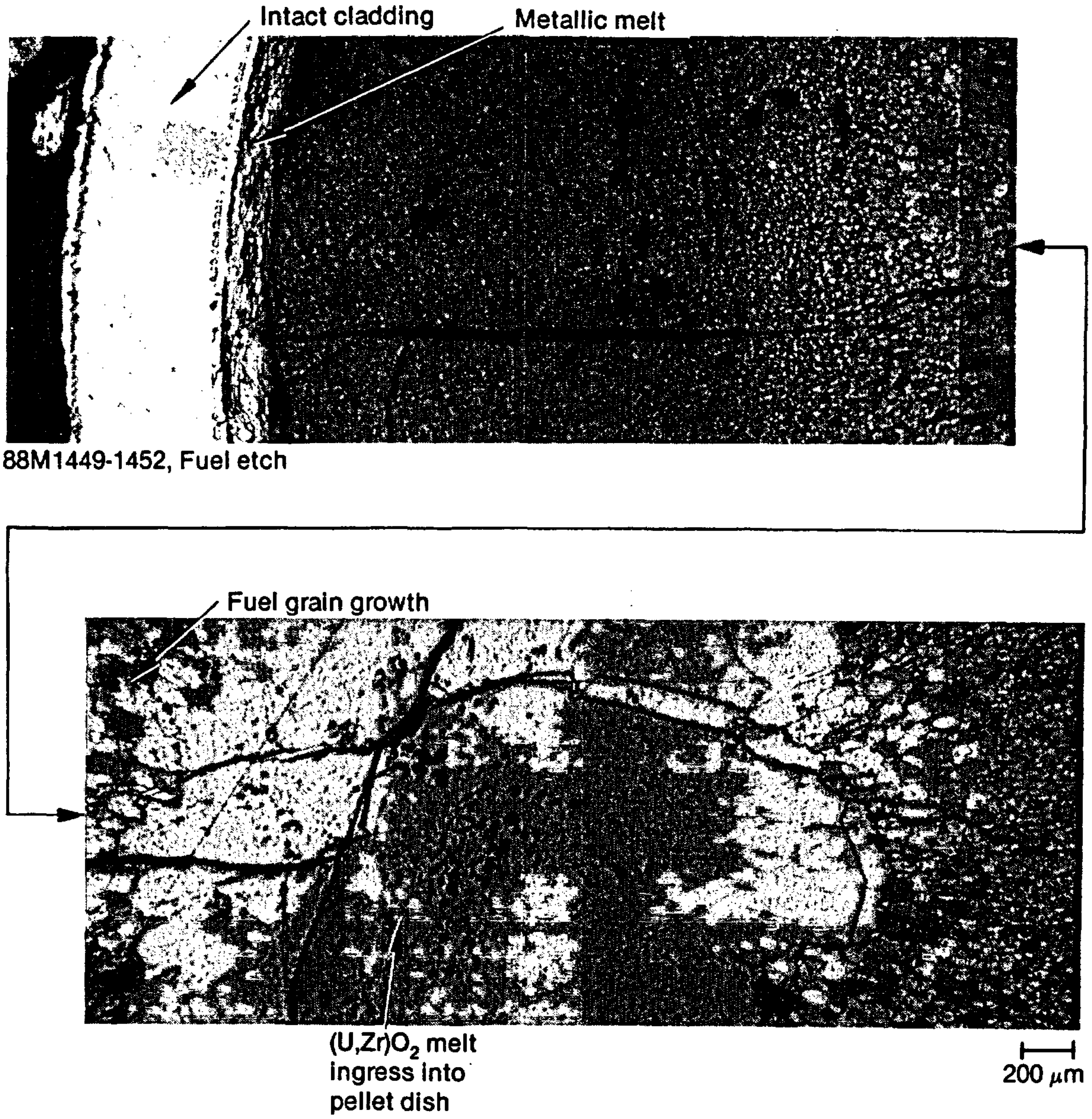

Figure 214. Grain growth and onset of columnar grain structure in center of fuel pellet at 0.43 m.

Figure 215. Columnar grain structure in center of fuel pellet at 0.58 m.

Figure 216. Columnar grain structure in center of fuel pellet at 0.66 m.

this behavior on one fuel rod at several axial locations. This fuel rod was located near the center of the assembly in core position H10 (see Figure 1). It was instrumented with a cladding thermocouple at 0.69 m above the bottom of the instrumented fuel rods. This thermocouple was routed out the top of the fuel rod, so it is not visible in any of these cross sections. It is apparent that at the higher axial positions the columnar grain morphology becomes more pronounced, as a result of increased pore migration towards the center of the fuel pellet. In Figure 216, where the pore migration is most pronounced (a columnar grain structure would be apparent if the fuel were etched as in Figure 214), the fuel pellet is no longer surrounded by cladding. As shown in Figure 217, this fuel pellet was in an area where the ceramic melt melted the ZrO_2 oxidized cladding shells, so temperatures were in excess of 2960 K in this region of the melt. In Figure 215, the ZrO_2 oxidized cladding shell was still present at the 0.58-m elevation; while in Figure 214 at the 0.43-m elevation, the cladding was still intact. These three figures provide a montage of the effects of temperature on pore migration and fuel restructuring in this unusual fuel structure. The area in the center of the fuel pellet in Figure 214 without any grain structure is believed to have been caused by ingress of molten $(U,Zr)O_2$ into a pellet dish. Vickers hardness measurements indicated readings of 882-1018 in this central region; 657-724 in the grain growth region, and 657-734 in an as-fabricated region on the edge of the pellet. Hardness measurements taken in other areas of the ceramic melt indicated comparable hardness readings as those in the center of the fuel pellet in Figure 214.

A columnar grain structure was not routinely observed. (It was limited to only some of the fuel rods in this area of the fuel bundle and was not observed in any other locality of the fuel bundle.) However, another example from another fuel rod at the I elevation (0.66 m) provides some additional information. Figure 218 shows another fuel pellet from the area in which ceramic melt temperatures were hot enough to melt the ZrO_2 oxidized shells. This fuel pellet was from rod F12 (see Figure 1), and its location is also shown in Figure 217. The fuel etch in Figure 218 reveals the extensive grain growth and columnar grain structure in the center of the

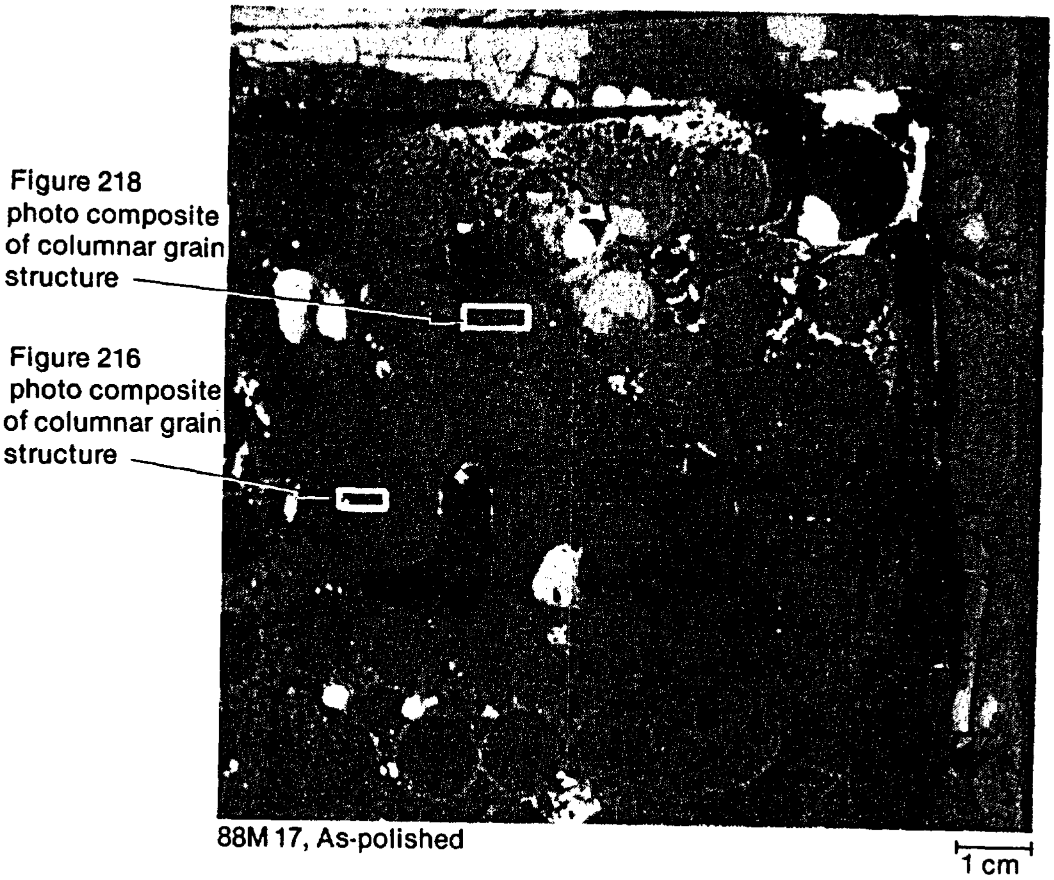

12

Figure 217. Location of fuel rods with columnar grain structure at 0.66 m.

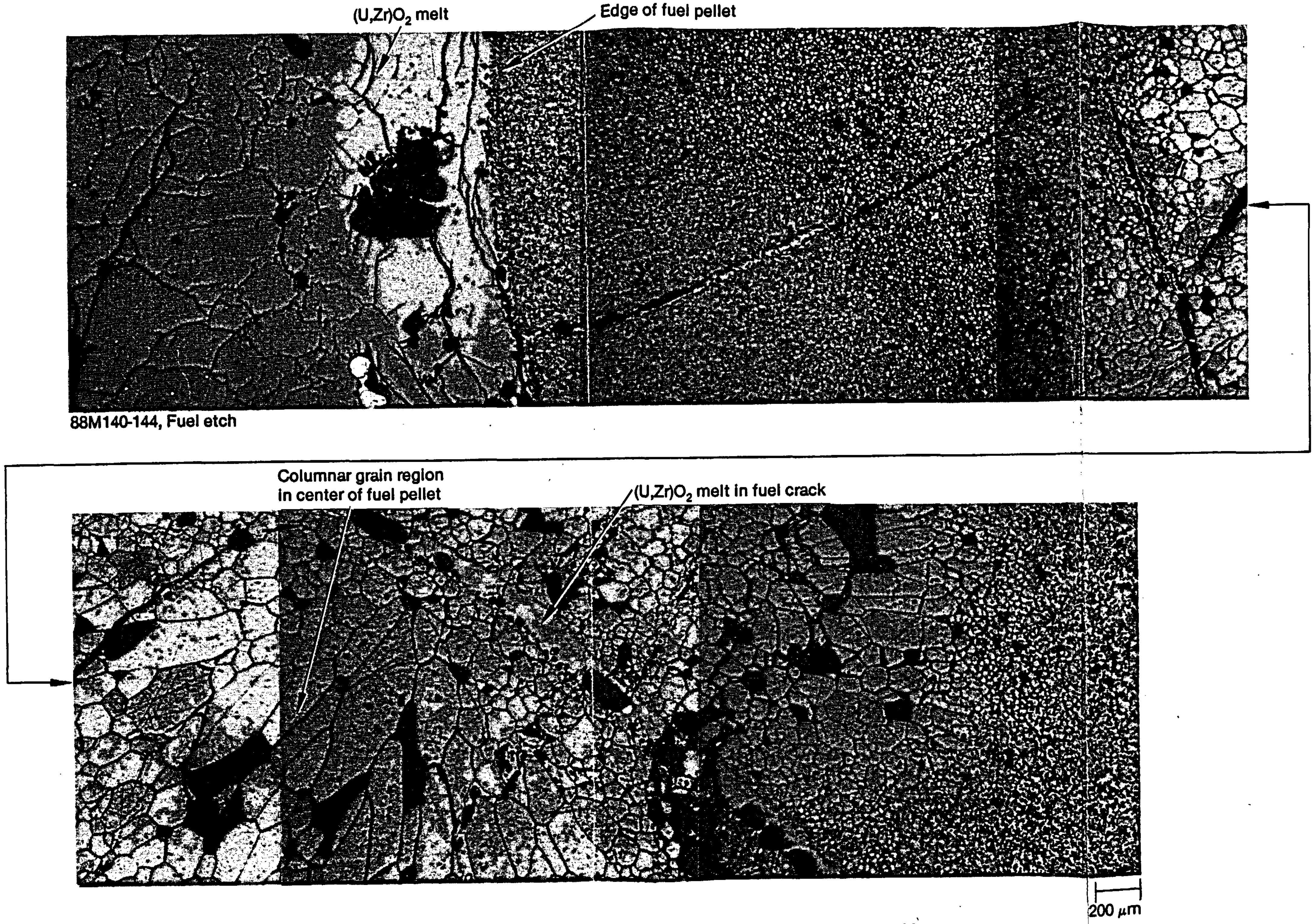

Figure 218. Columnar grain structure in uninstrumented fuel rod at 0.66 m.

pellet. What differentiates this fuel pellet from that shown in Figure 216 is that this fuel rod was uninstrumented; consequently, the formation of the columnar grain structure cannot be attributed to thermocouple effects.

It might be suggested that the columnar grain structure in the center of these fuel pellets is a result of solidification of molten fuel. Solidification of castings can result in a columnar structure very similar to that observed here. However, only during steady-state operation is there a steep temperature gradient that would account for higher temperatures in the center of the pellet; and it can be assumed that fuel temperatures did not approach fuel melting during the fuel conditioning phases prior to the transient. During the transient, the temperature gradient across the fuel becomes very flat. Relocating melt material that surrounded the fuel pellet would heat the fuel pellet from the outer surface and result in a temperature gradient that should be hottest on the outer surface of the fuel. Consequently, it would not be possible to melt the fuel solely in the center of the fuel pellet under the transient test conditions.

The columnar grain structure probably began as an area of grain growth in the center of these fuel pellets. When relocating ceramic melt material later surrounded these fuel pellets, melting the oxidized ZrO_2 cladding shell, this caused the fuel temperature to rise as a result of heat conduction from the melt. The resulting temperature gradient would be expected to have higher temperatures near the outer edge of the fuel or be relatively flat. However, since larger grains were already present in the central region, coalescence of these grain boundaries and enhanced grain growth in the central region could account for the observed behavior.

3.2.9.2 <u>Possible Fuel Reduction by Metallic Melts</u>. It was generally observed that areas of enhanced grain boundary separation were associated with the presence of metallic melts. An example of this is shown in Figure 47, which shows darkened bands in the fuel adjacent to fuel cracks containing metallic melts. These darkened bands can also be observed in many of the cross-sectional photographs, as well as many of the other detailed area pictures from the overall cross sections. Early in the process, these dark bands contain fuel with large amounts of porosity along the grain boundaries; later, the fuel actually separates along these grain boundaries and the darkened bands then correspond to areas of fragmented and/or powdered fuel. An example of this is shown in Figure 29 and, in more detail, in Figure 219. Grain boundary separation and fuel fragmentation are apparent in the areas adjacent to the eutectic metallic melt. Another example of similar behavior at a different elevation is shown in Figure 220. This figure shows in detail how the grain boundary separation area is limited to the area adjacent to the metallic melt in the fuel crack. Other examples of typical fuel behavior near metallic melts are shown in Figures 221, 222, and 223. Figure 224 shows an area of grain boundary separation near the outer edge of the fuel that was in contact with metallic melt between the fuel and intact cladding. Farther inward was an unaffected region of the fuel without any porosity redistribution from as-fabricated conditions, and towards the center of the fuel pellet was an area of grain growth with gas bubbles distributed along the grain boundaries. The fuel restructuring in the center of the pellet was probably due to thermal effects during steady-state operation, whereas the grain boundary separation near the outer edge of the fuel seems to be related to the presence of the metallic melt.

There was evidence that the fuel grain boundary separation observed adjacent to the metallic melts was not just a thermal effect that caused increasing amounts of gasses to diffuse to the grain boundaries. In some instances where ceramic and metallic melts were both in contact with fuel, the grain boundary separation was limited to the areas near the metallic melt. Examples of this phenomenon are shown in Figure 225, 226, and 227. These photographs and the results from the SEM/WDS examinations described below suggest that the presence of the metallic melts uniquely affected the fuel. One possibility is that the Zr-rich metallic melt (the layer of melt adjacent to the fuel in the fuel cracks, see Figures 222 and 223) resulted in a slight reduction of the fuel along the grain boundaries. As shown in Figure G-13 in Appendix G, slightly hypostochiometric fuel can result in the formation of a uranium-rich liquid phase along the fuel grain boundaries at temperatures above approximately 1470 K. The presence of such a liquid film

88M337, Fuel etch

(A) Metallic melt/fuel grain boundary interaction

88M335,336, Fuel etch

(B) Detail of (A)

Figure 219. Grain boundary separation and fuel fragmentation adjacent to metallic melt in fuel crack at 0.22 m.

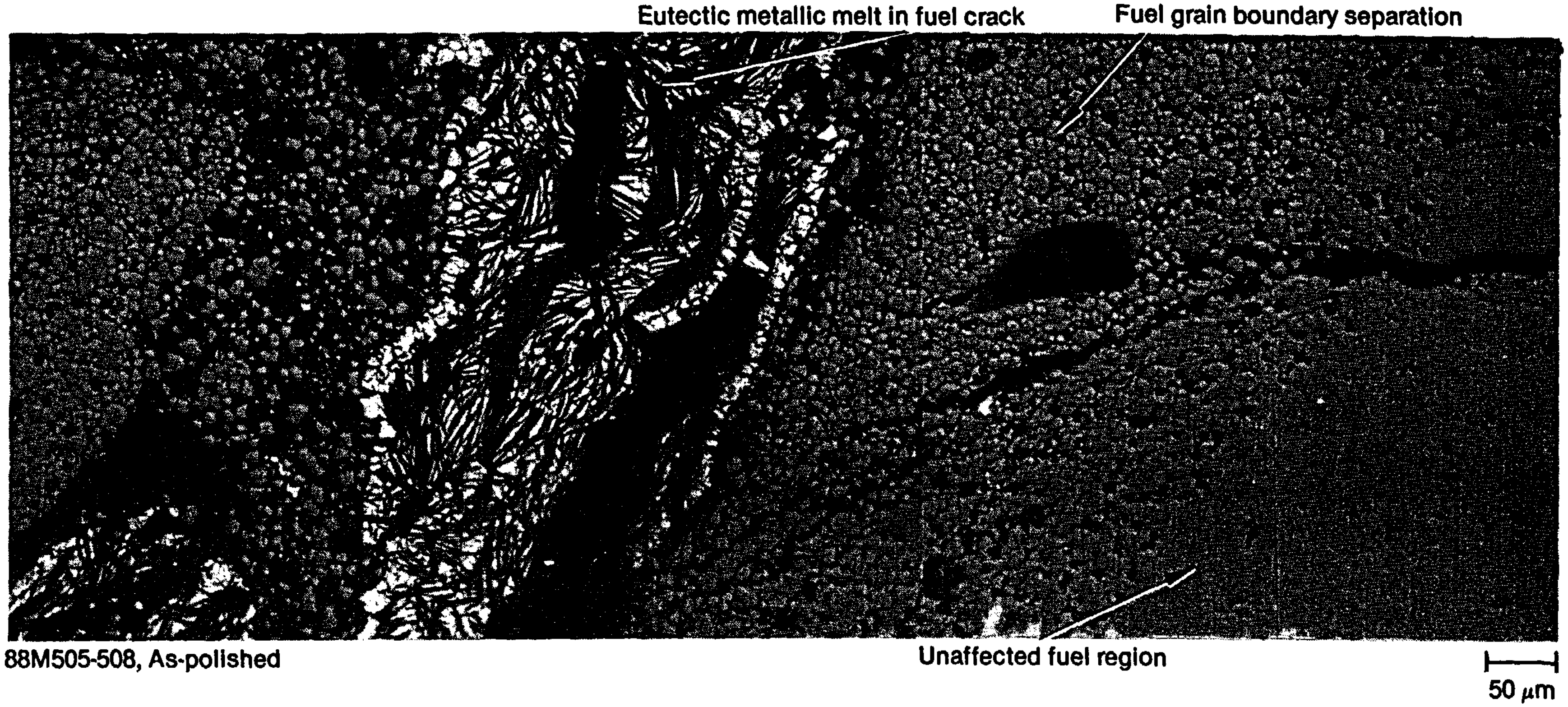

Figure 220. Grain boundary separation and fuel fragmentation adjacent to metallic melt in fuel crack at 0.46 m.

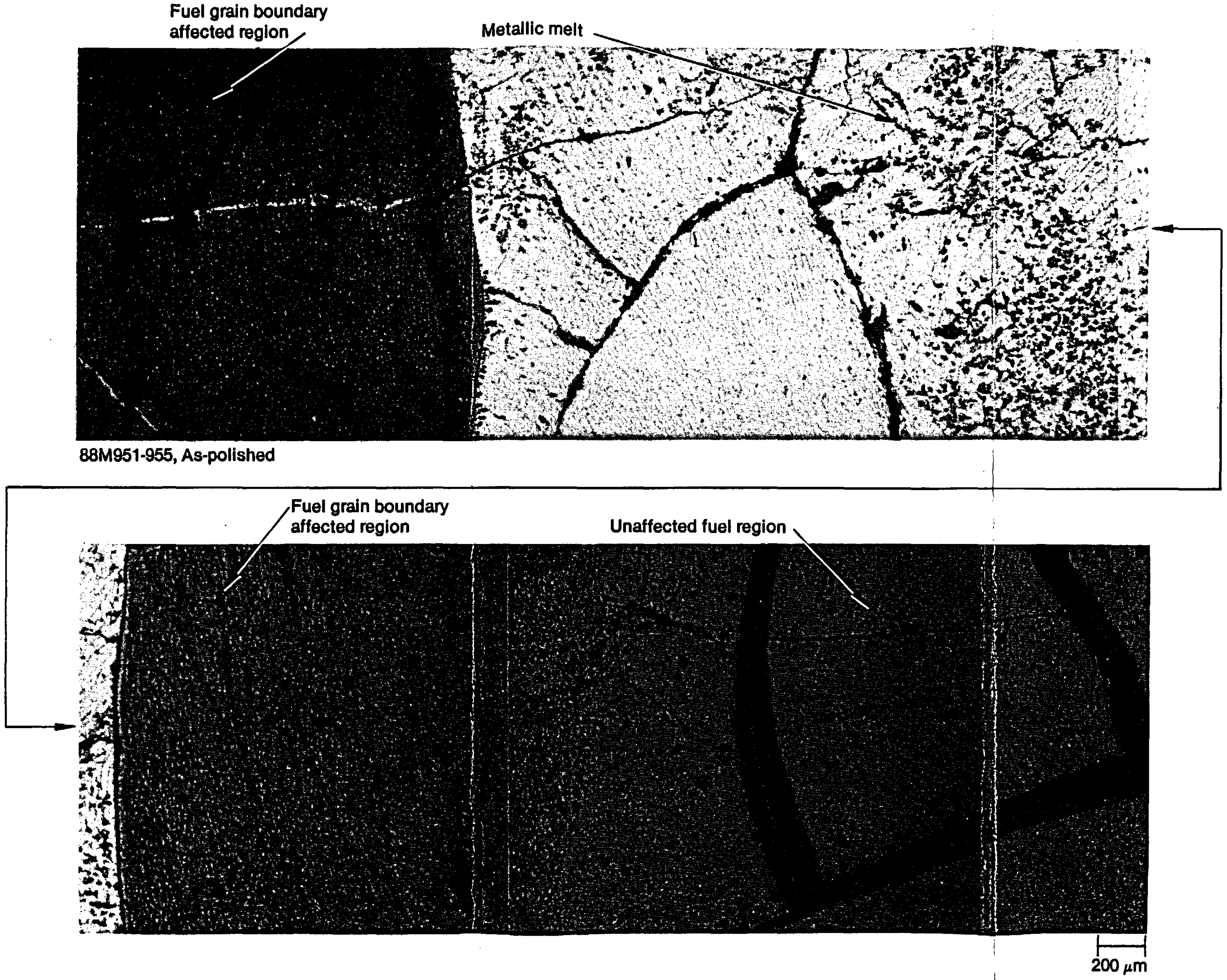

Figure 221. Fuel grain boundary separation adjacent to metallic melt at 1.45 m.

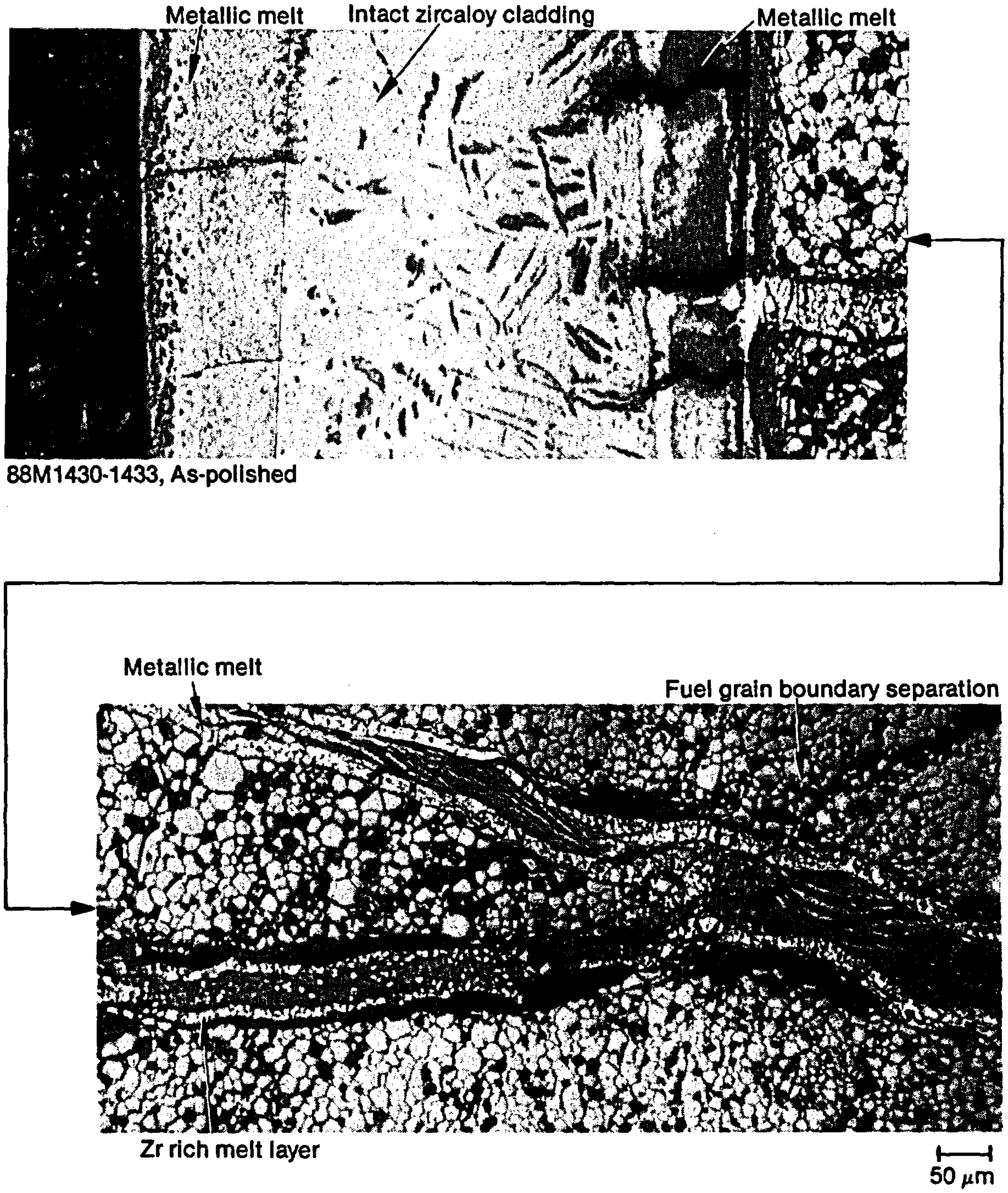

Figure 222. Effect of metallic melt on fuel grain boundary separation at 0.43 m.

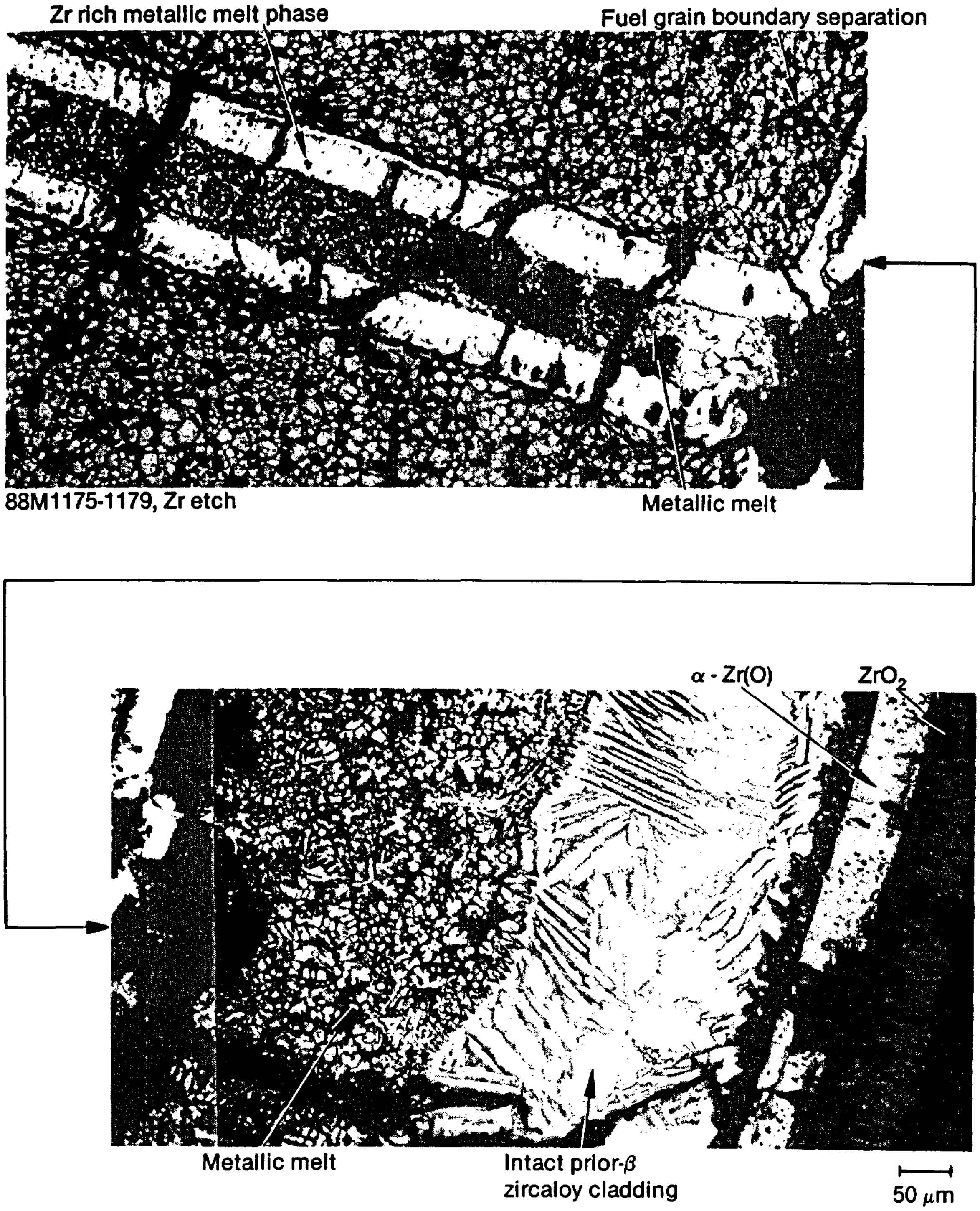

Figure 223. Structure of metallic melts interacting with fuel and zircaloy cladding at 0.58 m.

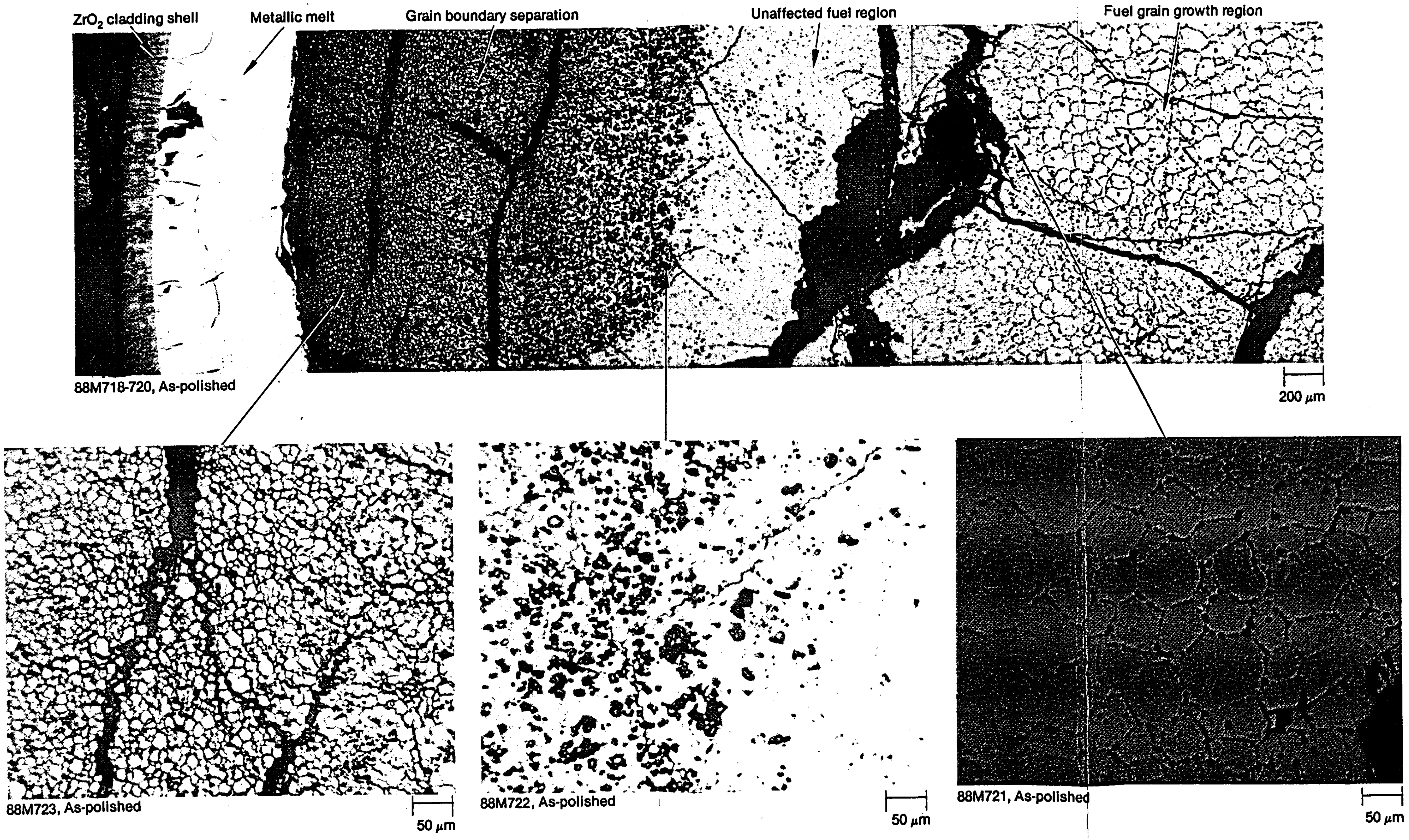

Figure 224. Fuel structural changes in a fuel rod at 0.66 m.

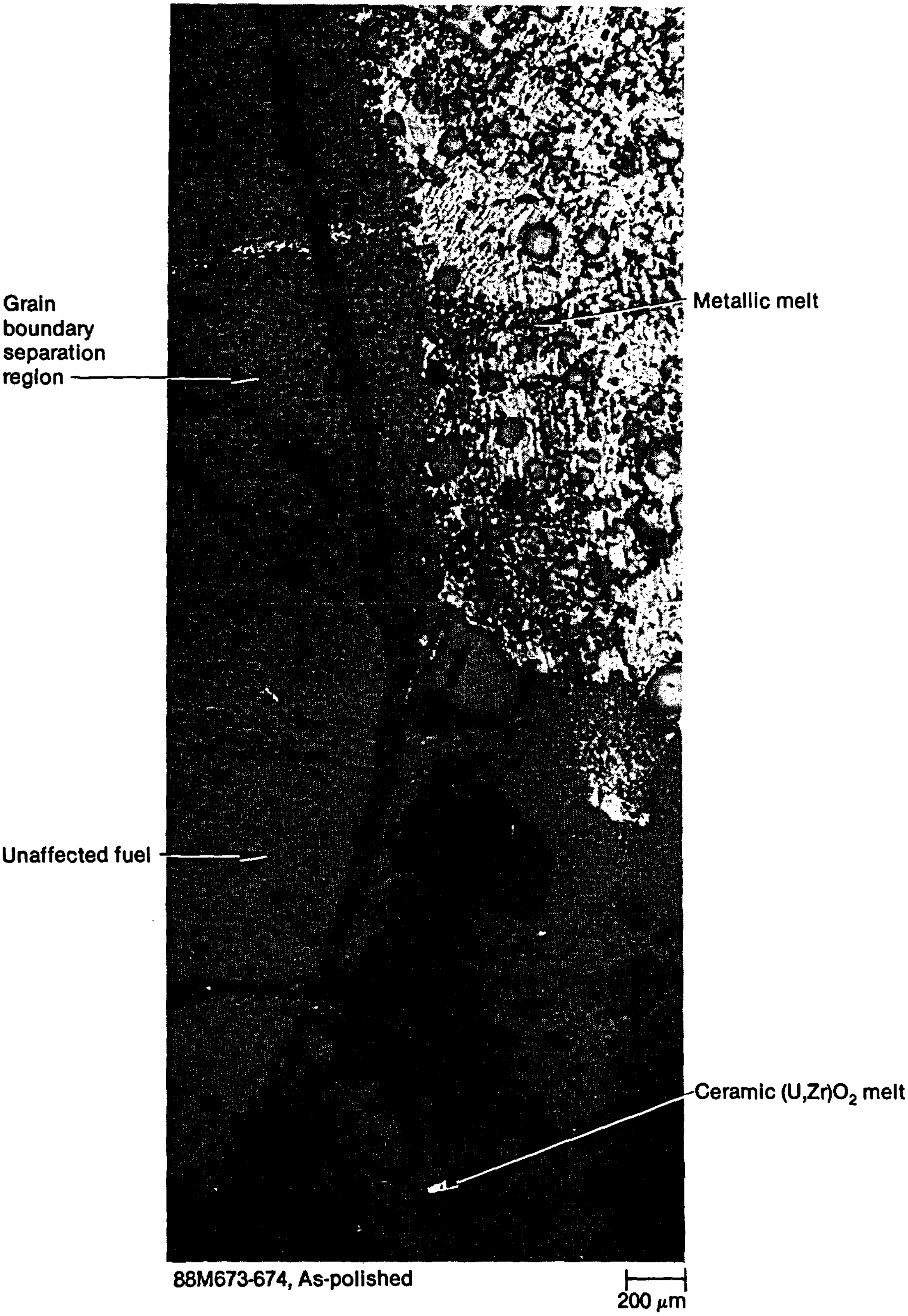

Figure 225. Different fuel structures adjacent to metallic and ceramic melts at 0.66 m.

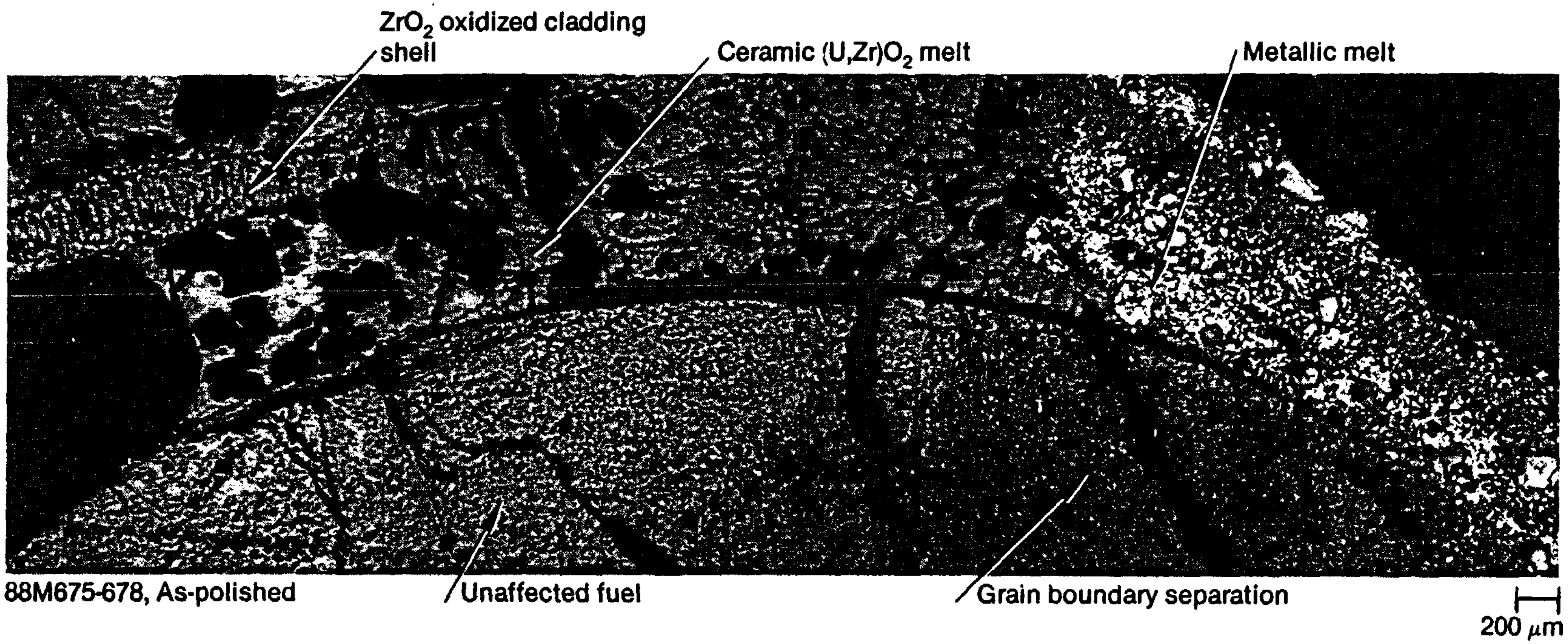

Figure 226. Different effects of metallic and ceramic melts on fuel structure at 0.66 m.

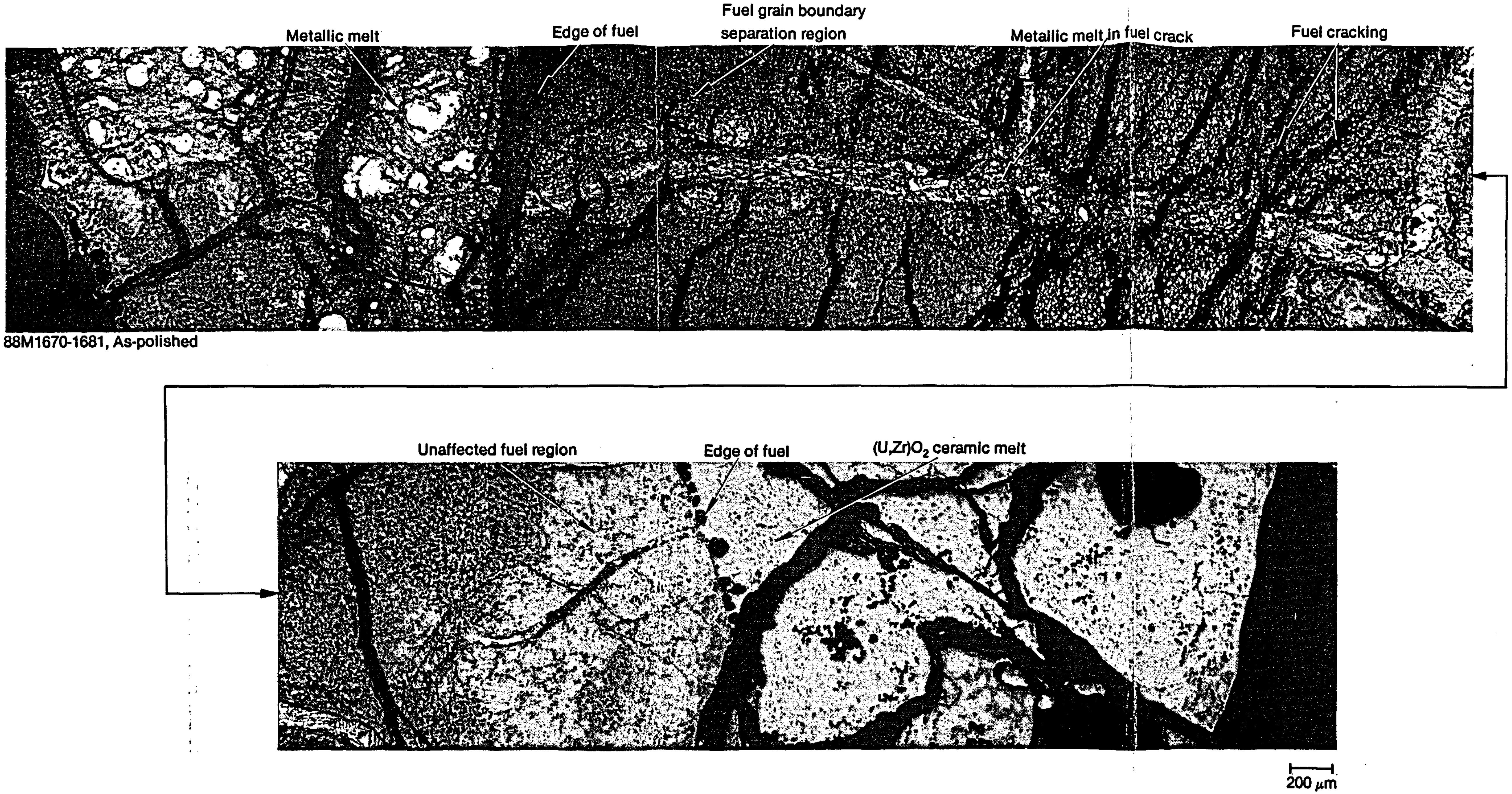

Figure 227. Influence of metallic melt on grain boundary separation and fuel cracking at 0.88 m.

on the grain boundaries could result in grain boundary separation, and similar dissolution and breakup of fuel has been previously observed.[14] In that instance, molten zircaloy contained in a UO_2 crucible resulted in partial disintegration of the crucible.

Several SEM/WDS samples were obtained to investigate areas of grain boundary separation. SEM sample H1-S21 was selected to examine the area shown in Figure 228. This shows an area of grain boundary separation adjacent to a metallic melt in a fuel crack. Only intermittent porosity was present on the grain boundaries farther away from the metallic melt, and still farther away the porosity on the grain boundaries disappears completely. As described in Appendix E for sample H1-S21, no second-phase material was found on the fuel grain boundaries. These examinations confirmed that the melt was indeed metallic (low in oxygen); that the metallic phase lining the edges of the fuel crack was mostly zirconium; and that the metallic melt in the center of the crack contained Zr, Fe, Cr, Ni, Ag, and U. These results are consistent with reduction of the fuel. Any metallic uranium that may have formed on the grain boundaries as a result of this reduction process would have oxidized to UO_2 by the time this sample was prepared and examined and be indistinguishable from the fuel.

As described in Appendix E, similar results were found for SEM/WDS sample G2-S14 (Area 6). No second-phase material was found on the grain boundaries. A zirconium-rich metallic phase was once again segregated along the edges of the melt in the fuel crack, although in this instance the melt in the center of the fuel crack did contain significant amounts of oxidized material. SEM/WDS samples M2-S8 and K1-S23 showed the same type of behavior in typical areas of grain boundary separation, although no dot maps were taken of these areas.

In all these cases, the metallic melt in the fuel cracks did not penetrate into the grain boundary separation regions. This indicates that the metallic melts solidified before the grain boundary separation occurred.

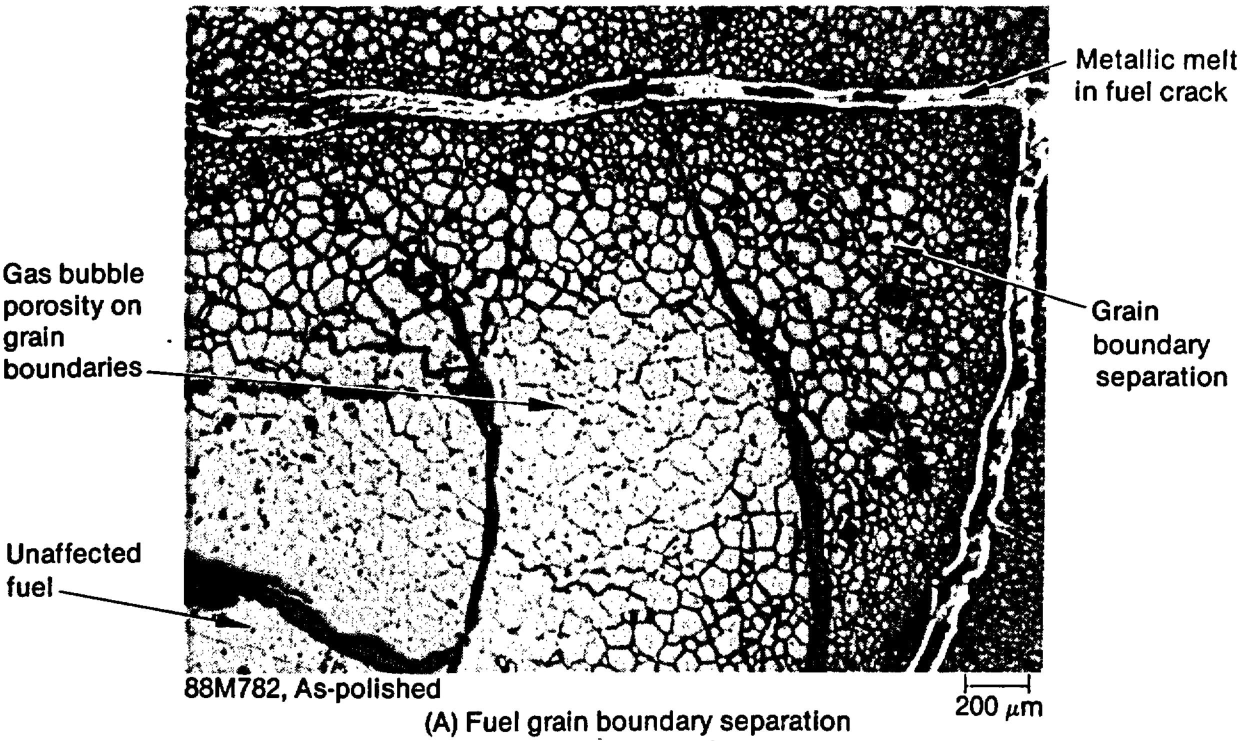

(A) Fuel grain boundary separation near metallic melt in fuel crack

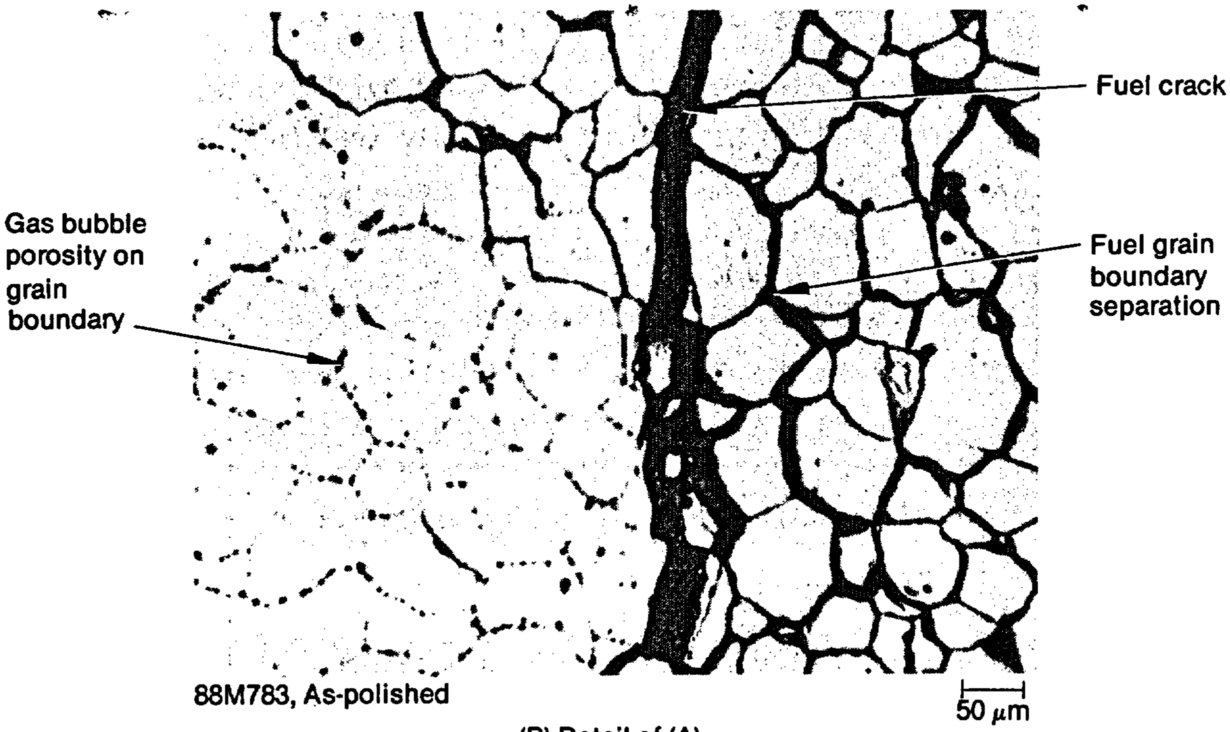

(B) Detail of (A)

Figure 228. Gradient in fuel behavior near a metallic melt in a fuel crack at 0.58 m.

3.2.9.3 Fuel Fragmentation and Powdering. As described in the preceding sections, many factors may have been partially responsible for causing fuel grain boundary separation. These include:

a. Migration of as-fabricated porosity (containing helium gas used to backfill the fuel rods) to the fuel grain boundaries. Outgassing of helium would have been enhanced upon fuel rod failure due to the low pressures in the core; 2.4 MPa (350 psi) helium within an intact fuel rod, compared to pressures of <1.4 MPa (200 psi) in the core;

b. Coalescence of grain boundaries in the grain growth regions, resulting in higher specific concentrations of gas on the remaining grain boundaries;

c. Fission gas release to the grain boundaries;

d. Enhanced diffusion rates due to thermal heating of the fuel by relocating melt material; and

e. Possible reduction of the fuel by metallic melts, which would result in the formation of liquid uranium metal on the grain boundaries of slightly hypostochiometric fuel.

All of these factors would tend to weaken the cohesiveness of the fuel and make it susceptible to grain boundary separation, fragmentation, and powdering.

Fragmentation and powdering (the breakup of the fuel into individual grains) was observed throughout the LP-FP-2 fuel assembly on failed fuel rods that were exposed to water during reflood. It was not observed on intact portions of fuel rods (in the lower portion of the bundle) or fuel rods that were completely surrounded by melt material that prevented fallout of the fuel. However, on fuel rods on the periphery of the melt, or near the exterior edges of the assembly that did not contain significant amounts of melt material, or in the upper portion of the fuel assembly where the cladding had been stripped from the fuel, fuel fragmentation and powdering was observed. This suggests that the thermal shock to the fuel as a result of reflood was a factor in fuel breakup. This is not to say that fuel fragmentation and powdering did not occur prior to reflood. (Fuel grain debris was intermixed with the eutectic metallic melt in the lower blockage region.) The thermal shock from reflood would have caused additional breakup of fuel with weakened grain boundaries. Examples of this fuel fragmentation and powdering are provided in Figures 229, 230, 231, and 232.

Fuel cracking is a normal consequence of fuel irradiation and thermal cycling. Examples of fuel cracking and the resultant fragmentation of unrestrained fuel pellets can be found throughout the photographs of the cross sections. However, the fuel cracking in pellets which were surrounded by a large agglomeration of metallic melt on the K1 cross section (Figure 94) appeared noticeably different. Detailed photographs of a representative fuel pellet from this region were presented in Figure 227, and another representative area is shown in Figure 233. These photographs show large amounts of fuel fracturing, which is in the form of striations which in some cases extend across the entire fuel pellet. This was the only area in the fuel bundle containing this type of agglomerated mass of metallic melt, and it is the only area in the fuel bundle in which this type of fuel cracking was observed. This is further evidence that metallic melts in contact with fuel have an effect on fuel breakup. SEM/WDS sample K1-S23 was obtained to investigate the composition of this metallic melt and its effects on fuel behavior, and the results of those examinations are described in detail in Appendix E. Those examinations indicated complex phases in the metallic melts, (Ag,In) control material penetrating into the fuel, and U-Zr interactions between the fuel and oxidized remains of the zircaloy cladding. Some of these results are further discussed in Section 3.2.11.

3.2.9.4 <u>Fuel Liquefaction and Melting</u>. Areas of fuel with a foamy morphology were observed on the periphery of some fuel pellets in the midcore region and above. Examples of this behavior are shown in Figures 234, 235, and 236. SEM/WDS sample J1-S30 was examined to investigate this

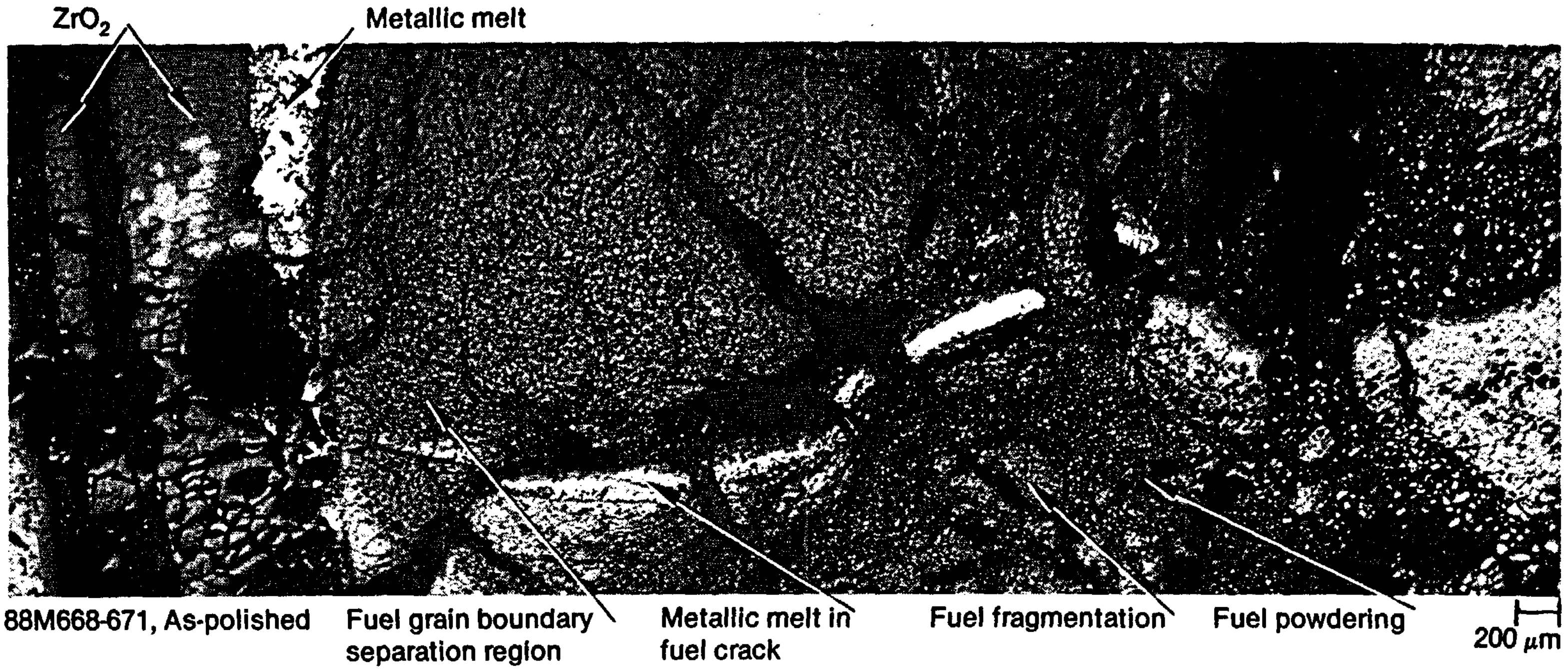

Figure 229. Fuel grain boundary separation, fragmentation, and powdering at 0.66 m.

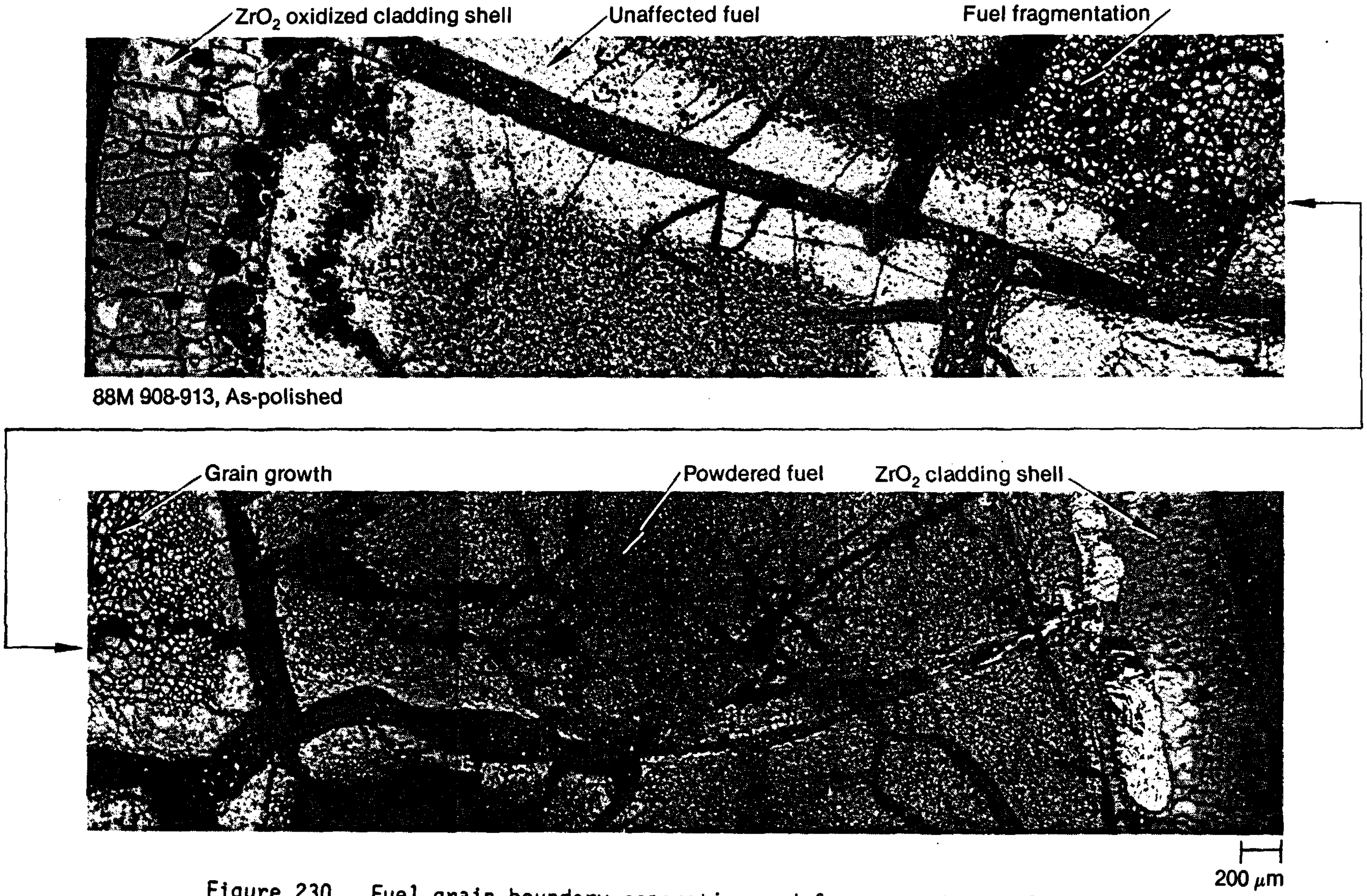

Figure 230. Fuel grain boundary separation and fragmentation at 0.96 m.

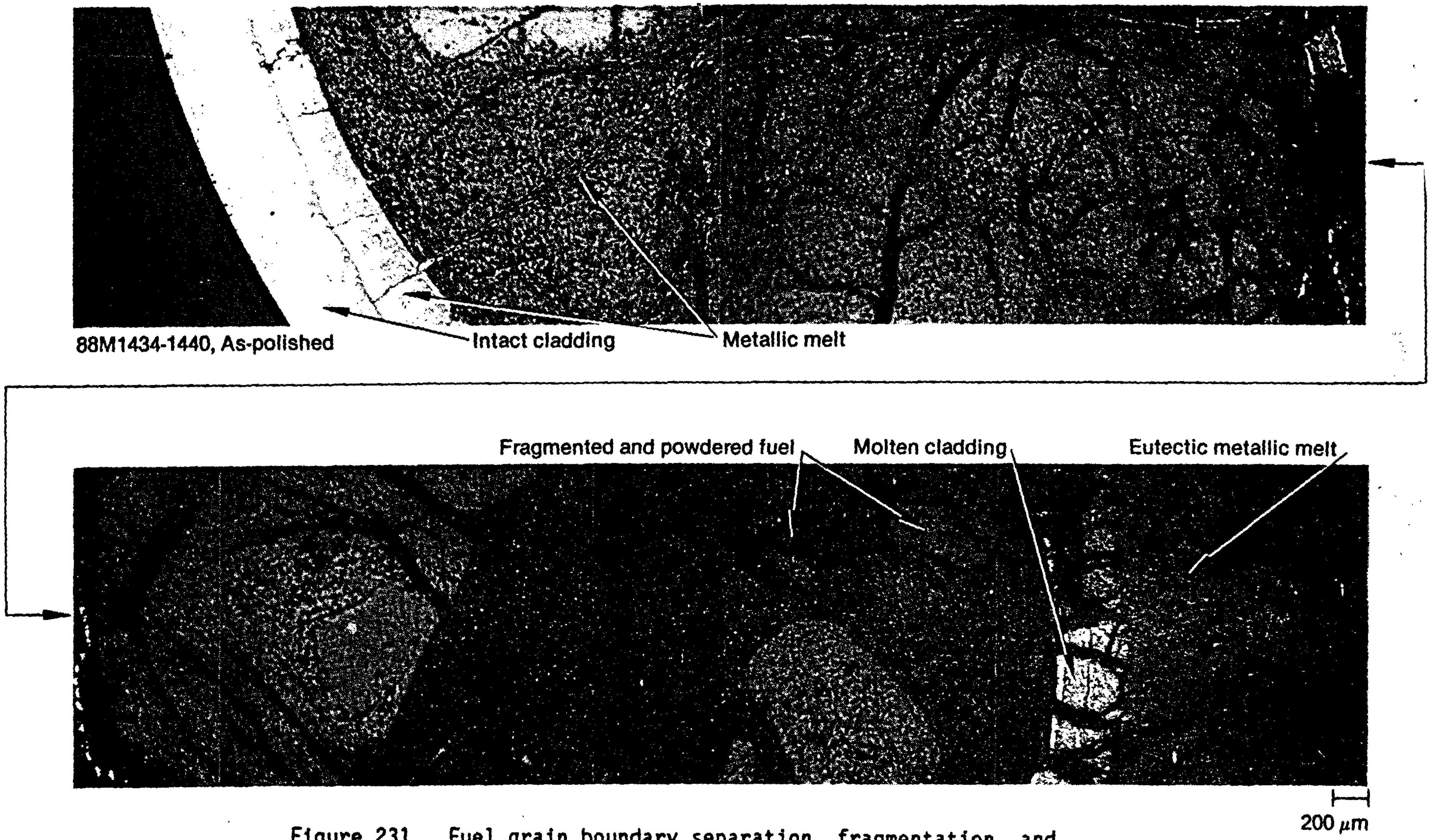

Figure 231. Fuel grain boundary separation, fragmentation, and powdering at 0.43 m.

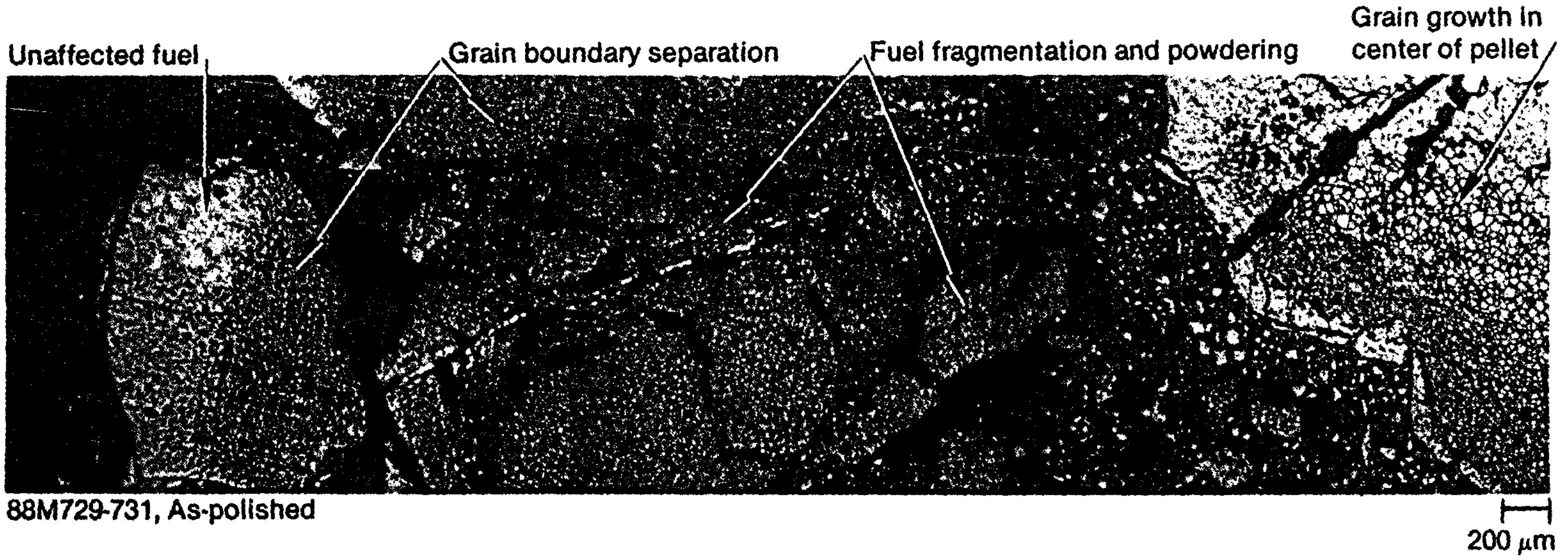

Figure 232. Fuel grain boundary separation, fragmentation, and powdering at 0.66 m.

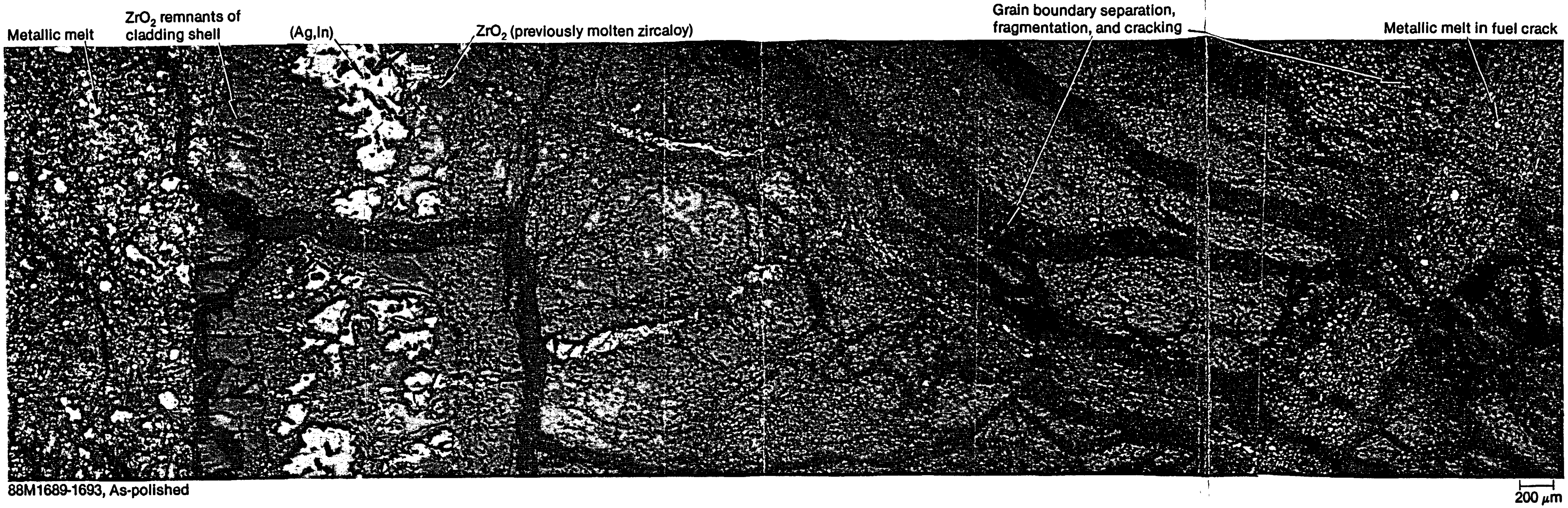

Figure 233. Atypical fuel cracking behavior in fuel pellet surrounded by metallic melt at 0.88 m.

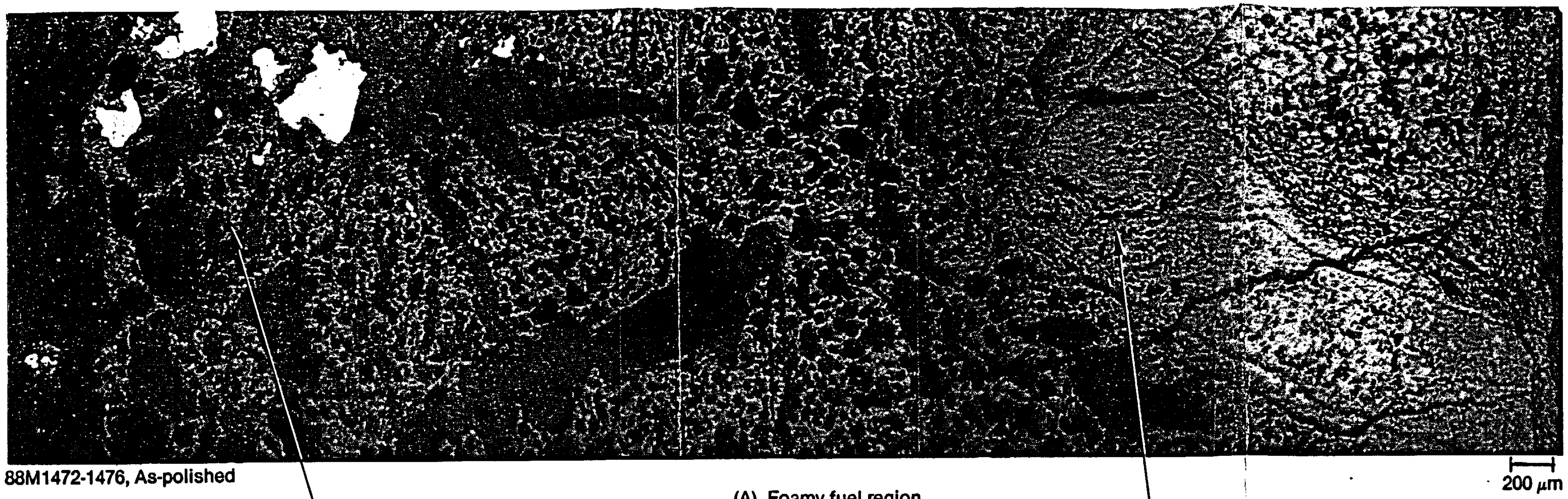

(A) Foamy fuel region

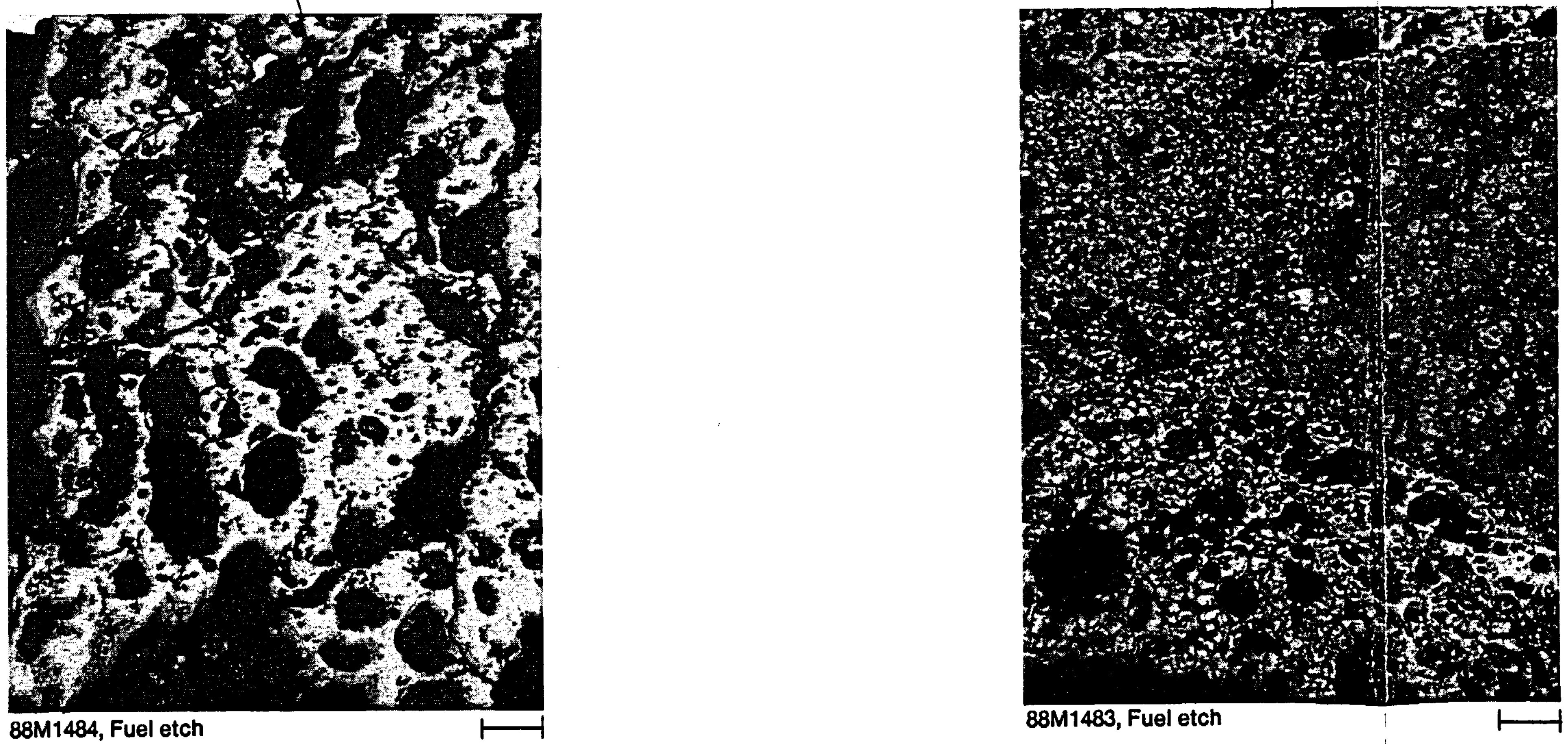

(B) Lack of grain structure in foamy fuel

(C) Grain structure in foamy fuel

Figure 234. Foamy fuel structure at 0.77 m.

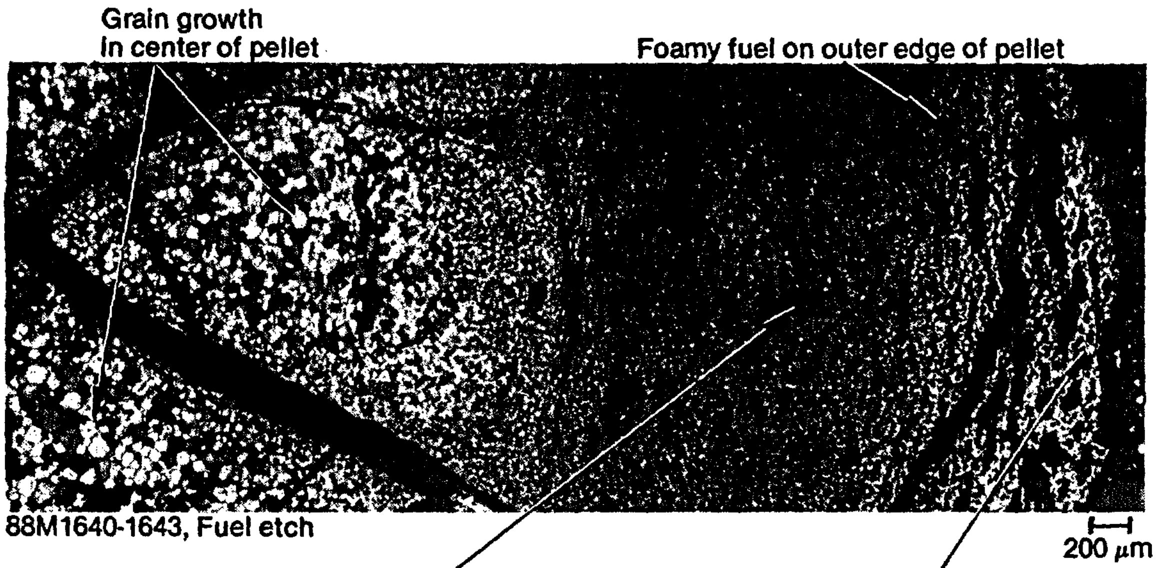

(A) Grain growth and foamy fuel

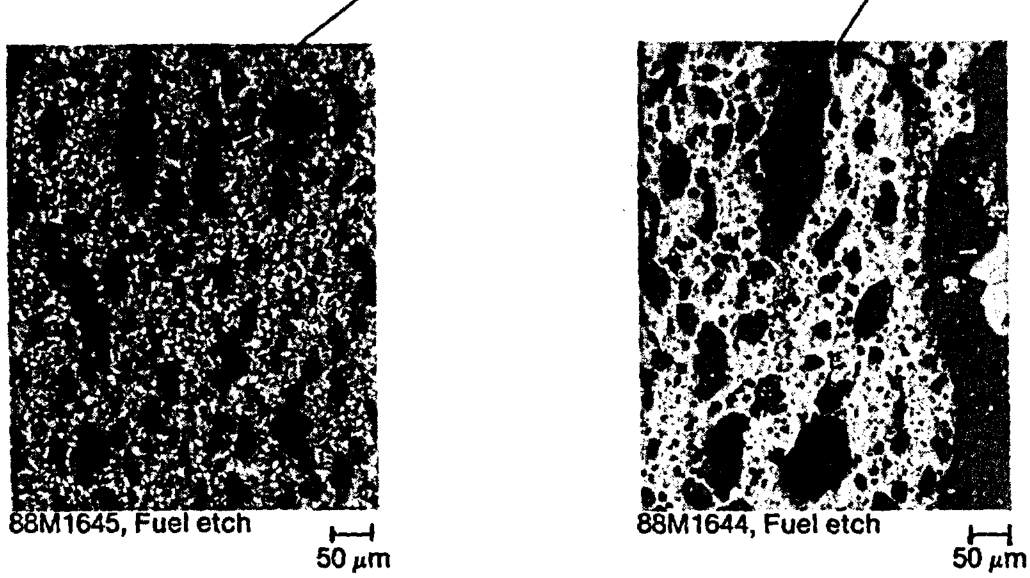

(B) Foamy fuel with grain structure

(C) Foamy fuel without grain structure

Figure 235. Foamy fuel structure on outer periphery of fuel pellet at 0.77 m.

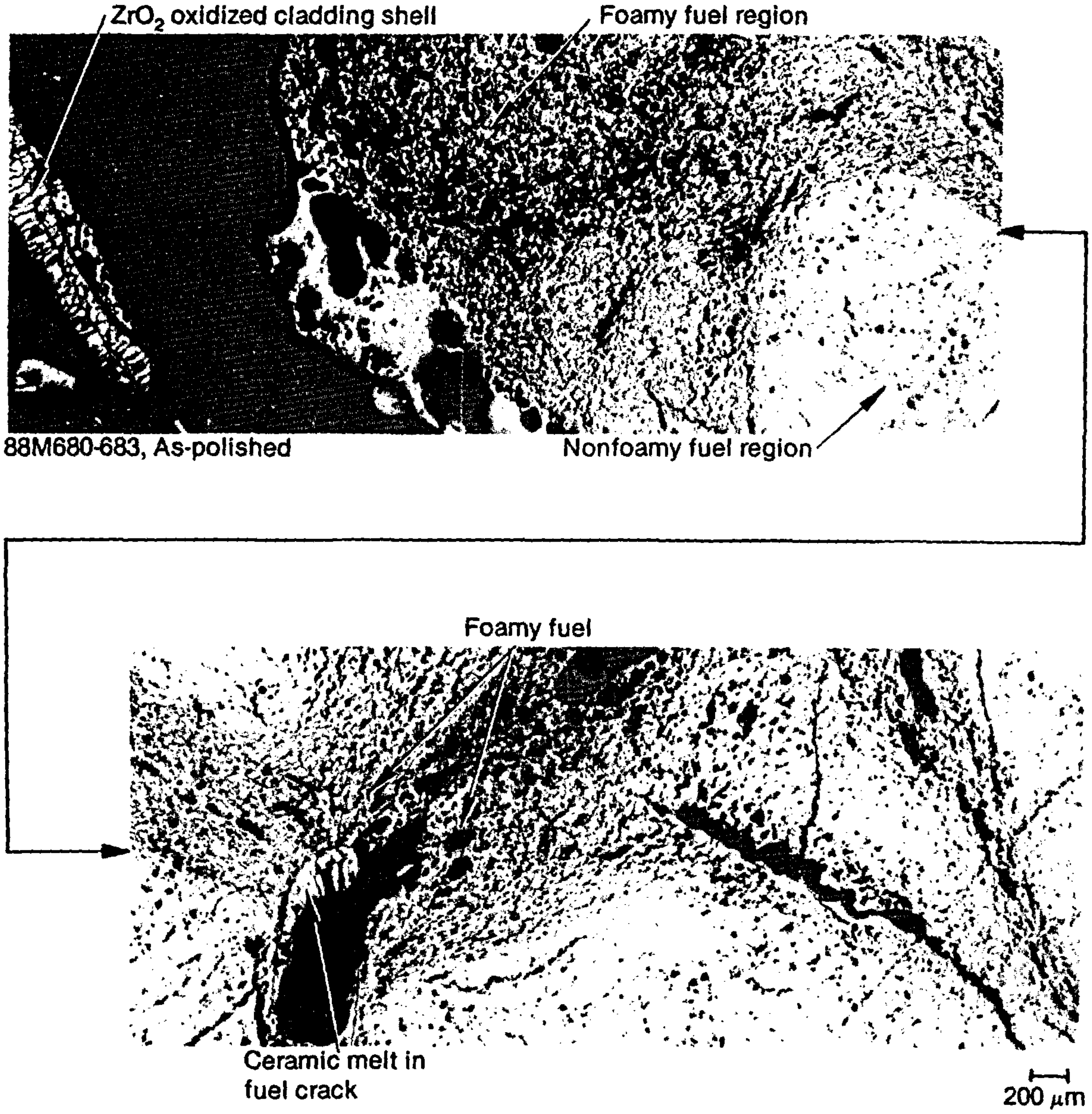

Figure 236. Foamy fuel structure ingress into a fuel pellet at 0.66 m.

behavior. As described in Appendix E, those examinations indicated that an iron-oxide was intermixed with the fuel in the foamy fuel regions. Review of available U-Fe-O phase diagrams[15] indicates that eutectic interactions can take place between these materials, although the data are very limited. However, the data from these postirradiation examinations do indicate that UO_2 can be liquefied by molten iron oxides.

The foamy fuel regions discussed above were no longer surrounded by any molten material. Porous regions were also observed on some fuel pellets that were surrounded by ceramic melt. Examples of these are provided in Figures 237, 238, 239, and 240. SEM/WDS sample K2-S32 was selected to examine this phenomenon; and, as described in Appendix E, these examinations showed that these regions contained areas of porous UO_2, without the presence of iron oxides or significant amounts of zirconium. (The molten $(U,Zr)O_2$ subsequently penetrates into the porous region, but this is after the fact.) This is indicative of temperatures very near fuel melting. Oxidized ZrO_2 cladding shells are also missing from these regions, which would further suggest temperatures in excess of 2960 K. This behavior is observed on many of the fuel pellets in the center of the ceramic upper blockage region.

3.2.10 Material Behavior in the Upper End Box

The bottom face of sample S was through the upper tie plate (1.80 m), while the top face was just above the upper tie plate (1.83 m). These sample elevations were chosen to examine debris noted in this area during visual examinations, and later on the neutron radiographs, and to examine how this debris may have interacted with the stainless steel upper tie plate. A photograph of the debris in the upper end box region is provided in Figure 6.

The photographs of the top and bottom surfaces of sample S are provided in Figures 150-163. These photographs show that major portions of the type 304 stainless steel upper tie plate had melted, particularly in the center of the assembly; that partial liquefaction of the zircaloy guide tube nuts

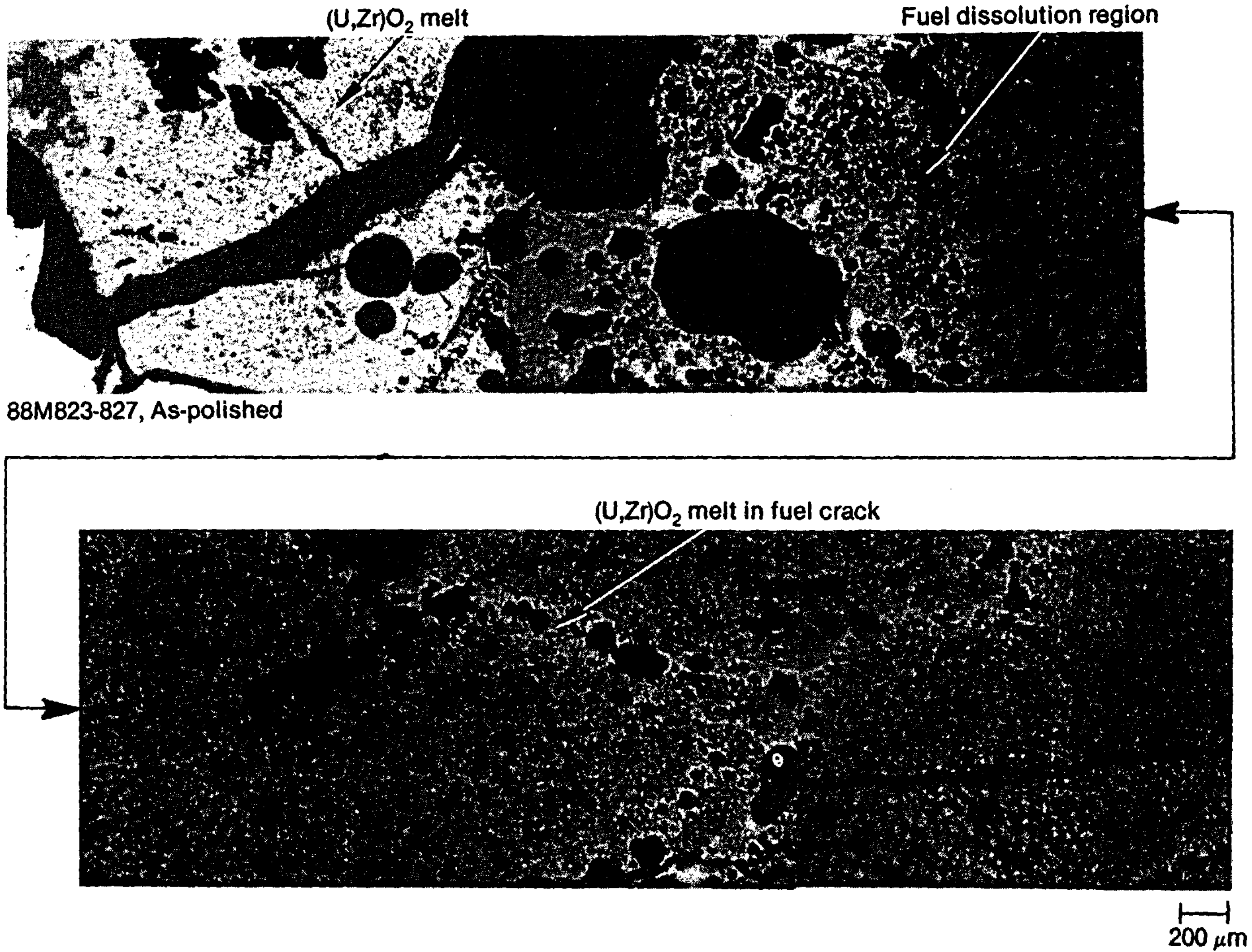

Figure 237. Fuel dissolution in (U,Zr)O$_2$ melt at 0.77 m.

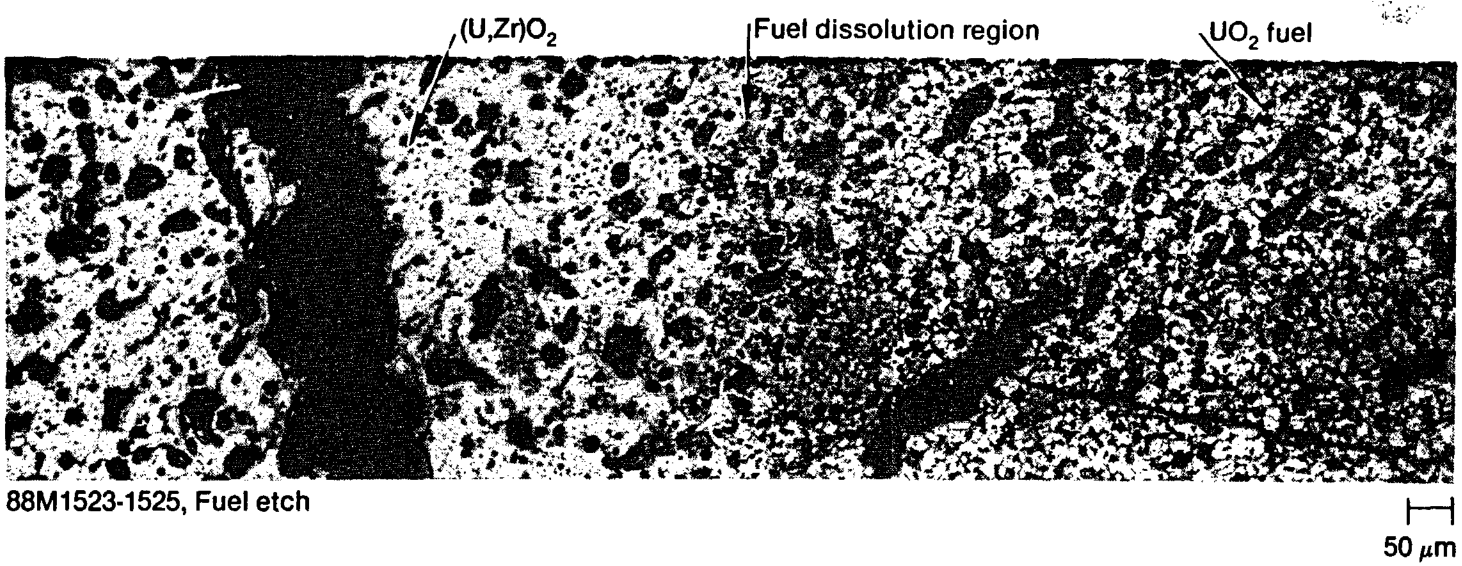

88M1523-1525, Fuel etch

Figure 238. Fuel dissolution in (U,Zr)O$_2$ melt at 1.04 m.

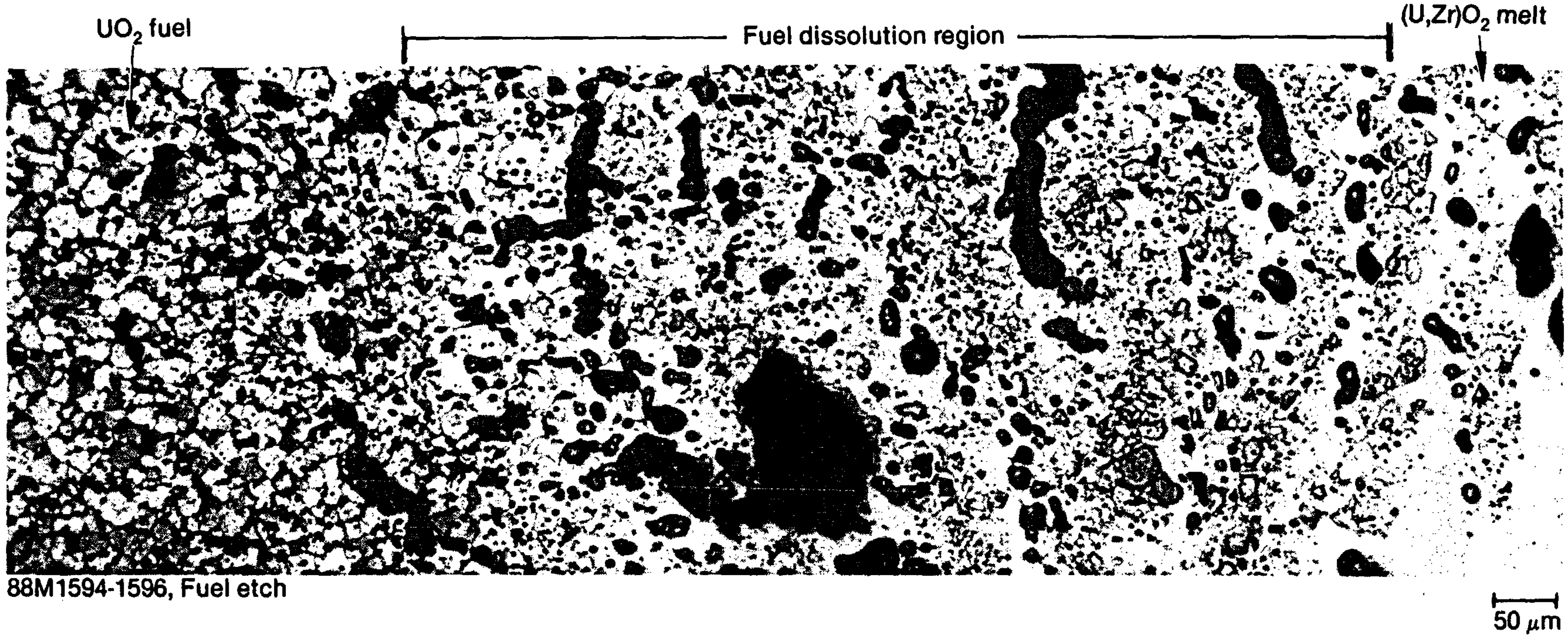

Figure 239. Fuel dissolution in $(U,Zr)O_2$ melt at 0.88 m.

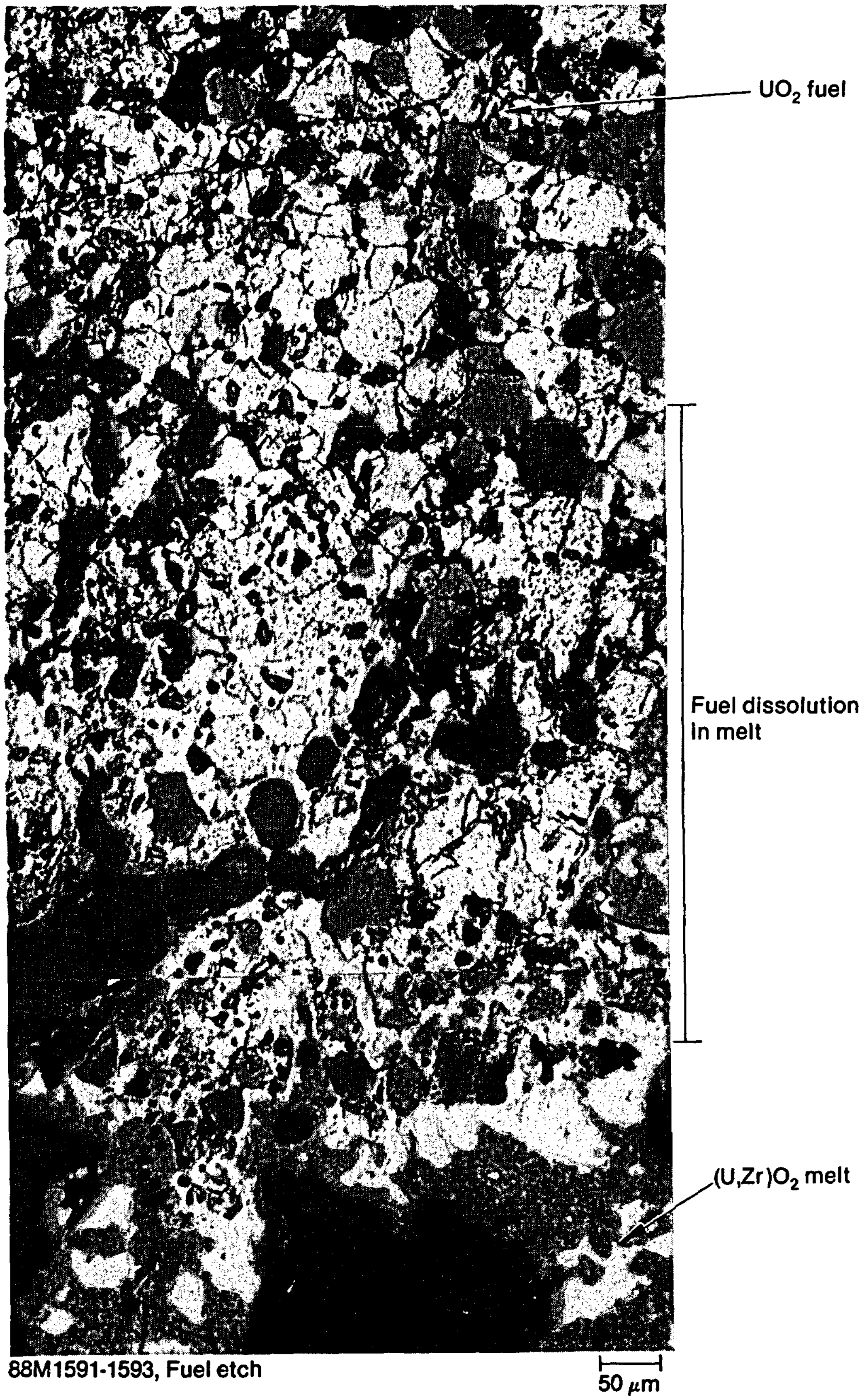

Figure 240. Detail of fuel dissolution shown in Figure 239 at 0.88 m.

above the upper tie plate had occurred; that some fuel pellets had relocated above the upper tie plate; and that a variety of molten phases were present. Figure 155 shows some of the material interactions that occurred around an area of the upper tie plate in which the open flow pattern can still be distinguished, and this area is shown in greater detail in Figure 241. This area was also examined on the SEM as sample S3-S10, and the detailed results are provided in Appendix E. These examinations showed that the metallic melt material in Figure 241 was composed of (U,Zr,O), which interacted with the oxidized remains of the stainless steel upper tie plate. Molten (U,Zr,O) requires temperatures in excess of approximately 2200 K, as shown in Figures G-24 and G-25 in Appendix G.

Figure 242 shows a dendritic melt structure on the edge of a portion of the intact stainless steel upper tie plate. Figure 242B suggests that this is actually a two-phase eutectic melt structure. SEM/WDS sample S3-S26 was selected to examine this area; however, after sample preparation, the structure observed metallographically in Figure 242 was no longer present. As described in Appendix E, only a nickel-oxide layer was found on the edge of the stainless steel. The oxidized melt was examined in Area 2 of SEM/WDS sample S3-S26. These examinations showed that zirconium, uranium, and control materials had relocated upward from the fuel bundle and interacted with the stainless steel. They also confirmed that the molten stainless steel structure was oxidized. Area 3 of sample S3-S26 examined an area similar to that shown in Figure 243 to determine if eutectic melting of the upper portion of the zircaloy guide tubes occurred. This examination indicated Fe, Cr, and Ni were interacting with the zircaloy, with eutectic melt temperatures probably >1300 K.

SEM sample S2-S28 was selected to examine the debris located on top of the upper tie plate. As described in Appendix E, these examinations showed the debris to be mostly small particles of metallic melt, with some fuel particles mixed in.

As described in Section 4.3, thermocouple data from the bottom surface of the upper tie plate indicated that temperatures were <1000 K during the

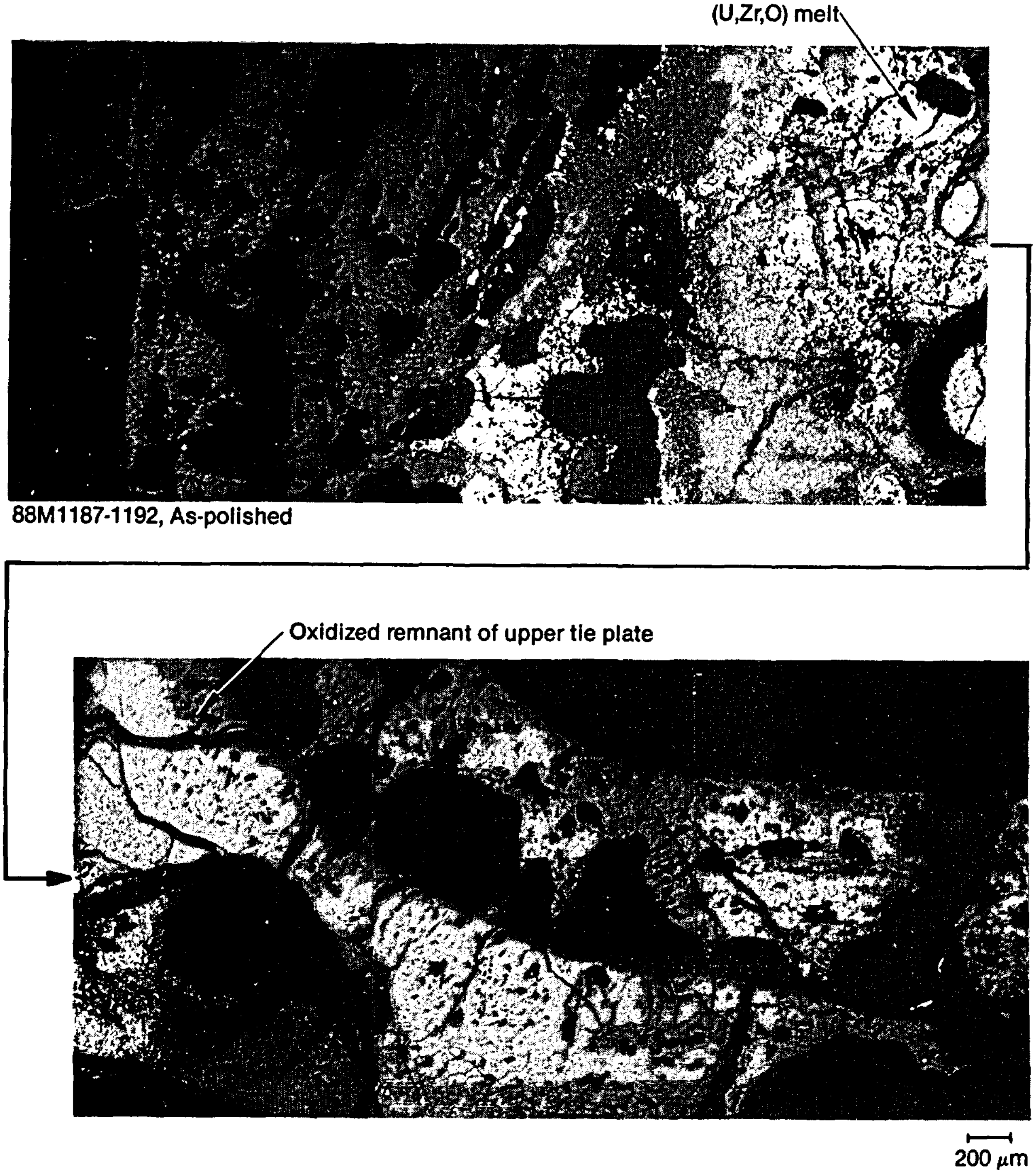

Figure 241. Melt interactions with upper tie plate remnants at 1.80 m.

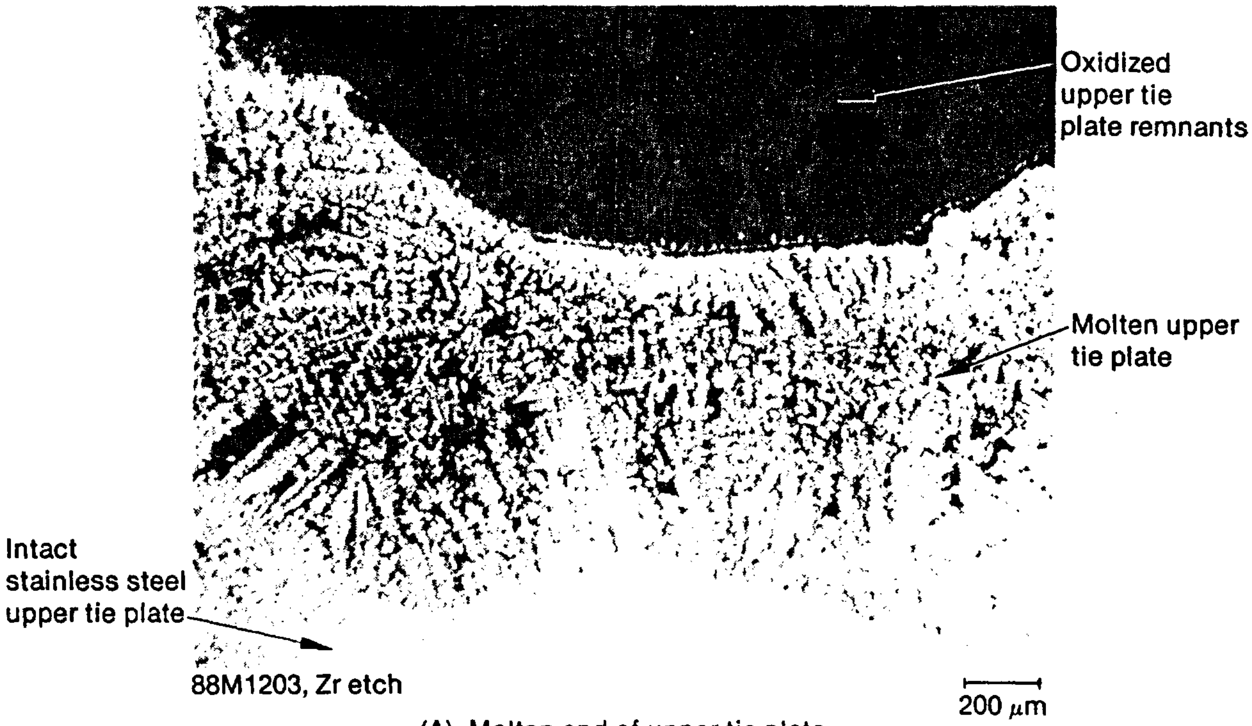

(A) Molten end of upper tie plate

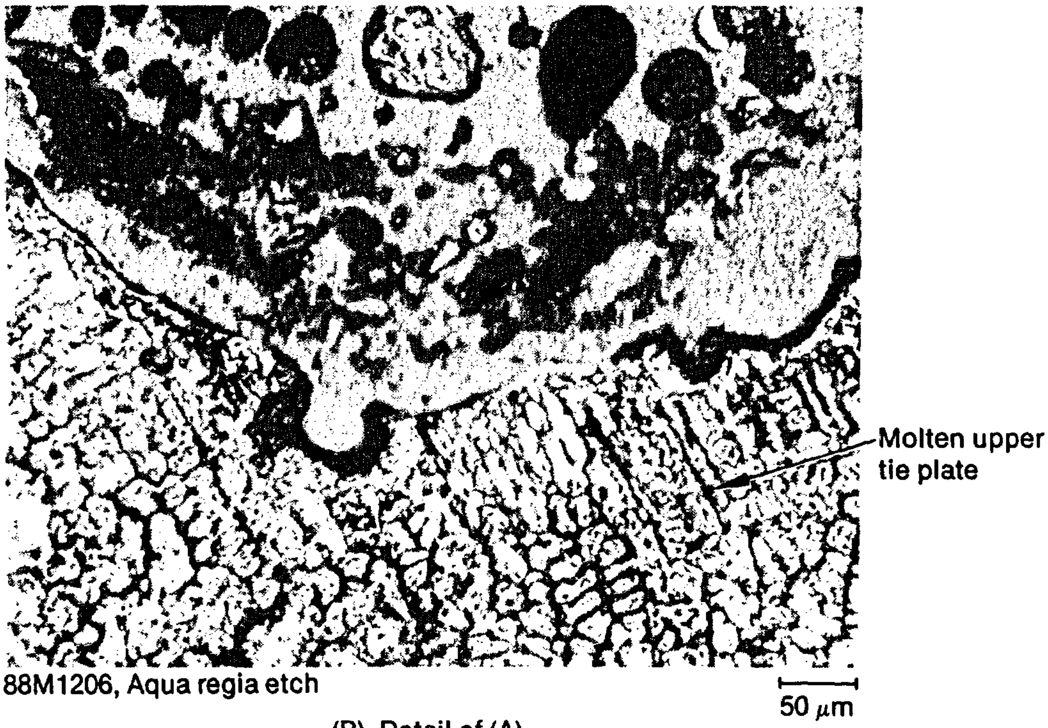

(B) Detail of (A)

Figure 242. Molten end tip of an intact portion of the upper tie plate at 1.80 m.

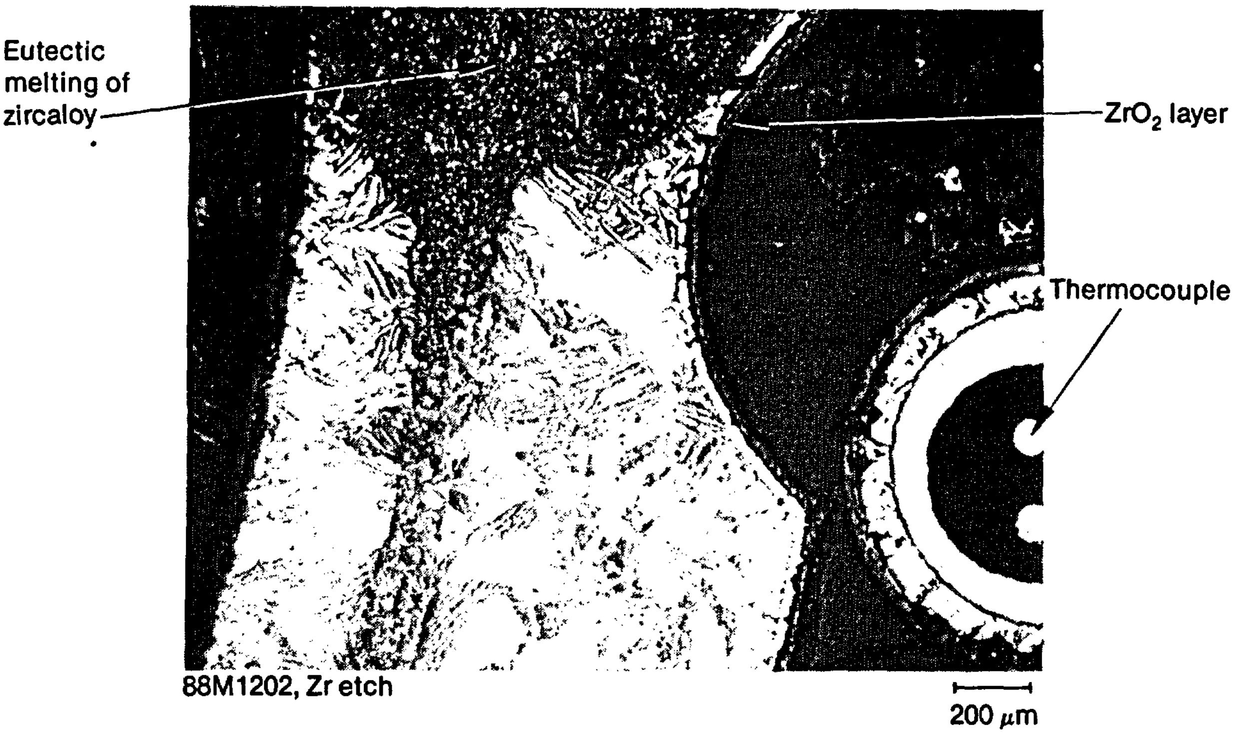

Figure 243. Liquefaction of upper portion of zircaloy guide tubes at 1.80 m.

entire transient; but, following the onset of reflood, there was a temperature excursion in which temperatures exceeded 1700 K. Mass flow rates through the bundle also increased from approximately 13±5 g/s at the end of the transient to about 5 kg/s during reflood. These data indicate that the damage to the upper tie plate, and the relocation of material to this region, had to have occurred during the reflood period. Temperatures were too low during the transient to have caused melting and oxidation of the upper tie plate.

3.2.11 Miscellaneous Material Behavior

Several items of material behavior were observed that could be considered atypical, unusual, or do not fit easily into the other categories already discussed. These miscellaneous items are discussed in this section.

The majority of the $(U,Zr)O_2$ ceramic melts in this experiment were single-phase, amorphous melts (Figure 200). However, at the J elevation (0.77 m), the ceramic melt had a textured appearance. This textured melt is shown in Figure 244 and, in more detail, in Figure 245. This textured melt was not present in a boundary layer adjacent to the fuel. Qualitative SEM/WDS examinations of sample J2-S4 could find no compositional differences between these textured areas and the glassy ceramic melt regions; however, elemental chemical analysis of the one sample from this region (J2-R21) indicated 54 wt.% U and 26 wt.% Zr, which was the greatest U/Zr ratio measured on any of the ceramic melt samples. It is possible that these compositional differences, in conjunction with the fact that the J elevation appears to be the hottest region of the bundle, may have somehow affected the metallographic appearance of the ceramic melt. The porosity distribution in portions of the textured melt regions is reminiscent of fuel structure, which suggests the possibility of a slurry of fuel particles undergoing dissolution in the ceramic melt.

As noted in Section 3.2.9, second-phase material was not found on grain boundaries in areas where fuel grain boundary separation had occurred. An exception to this rule is shown in Figure 246. SEM/WDS sample K1-S22

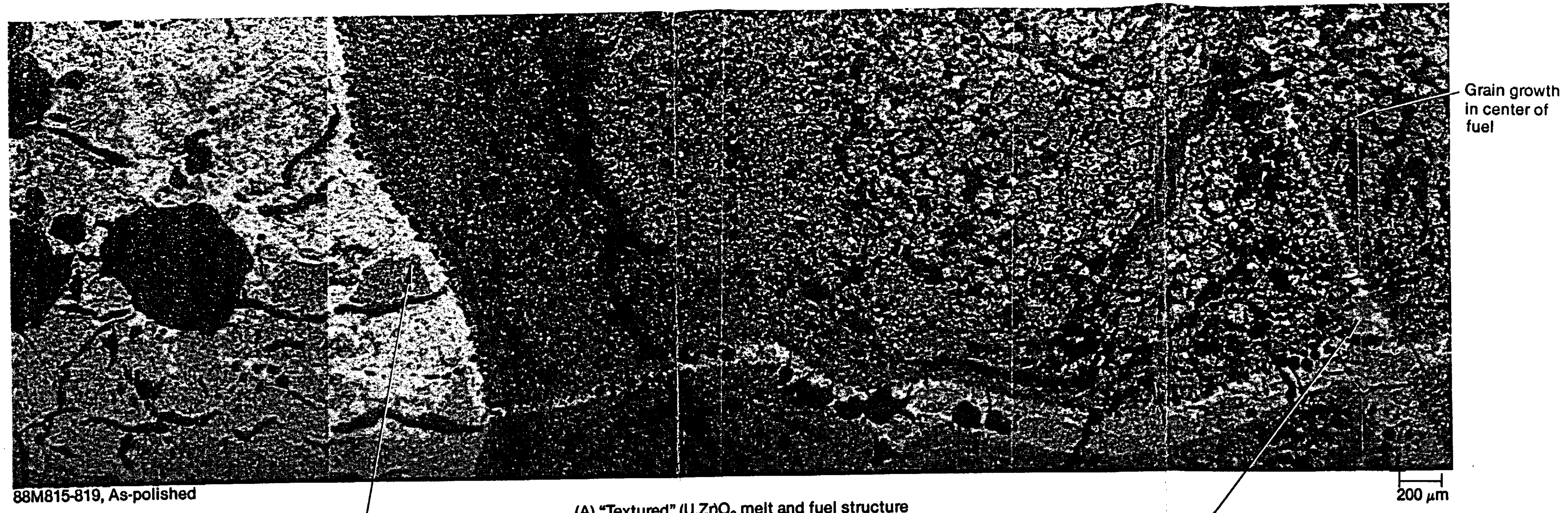

(A) "Textured" $(U,Zr)O_2$ melt and fuel structure

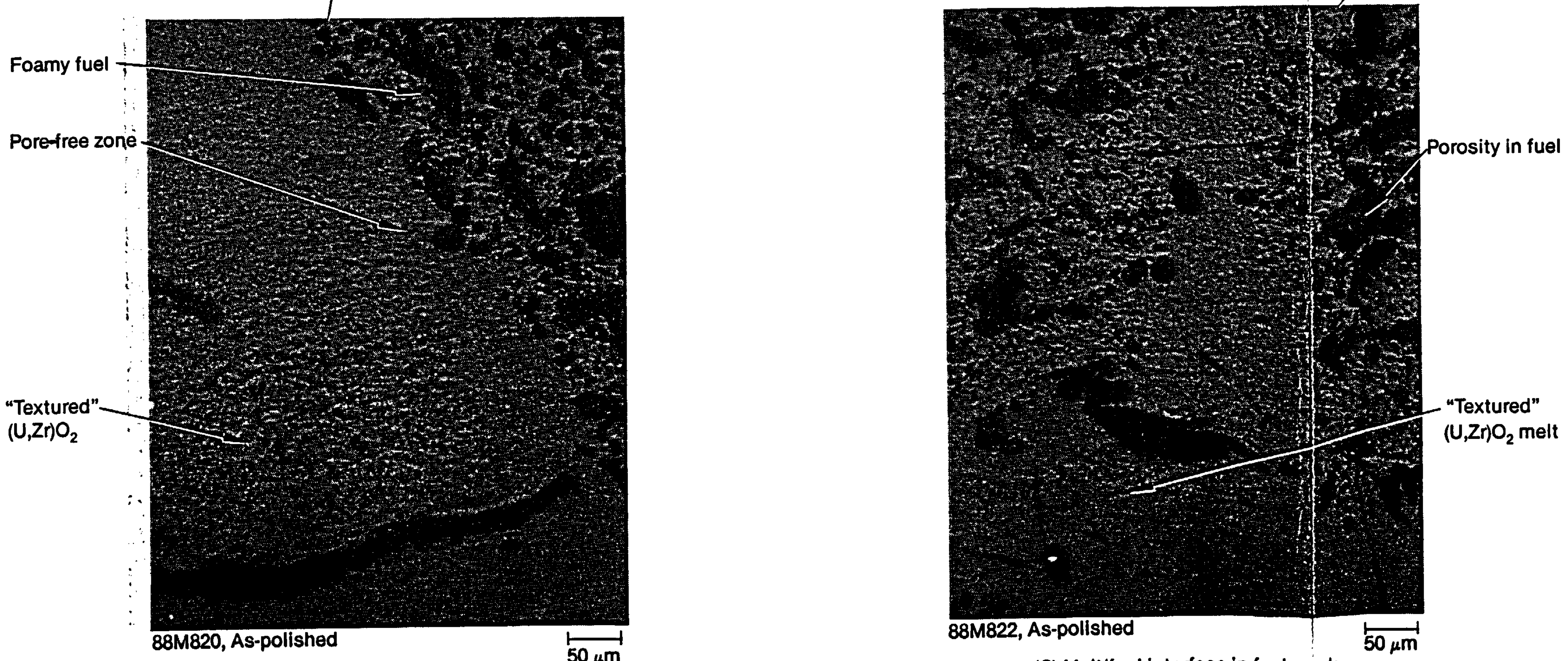

(B) Melt/fuel interface on pellet edge

(C) Melt/fuel interface in fuel crack

Figure 244. "Textured" $(U,Zr)O_2$ melt at 0.77 m.

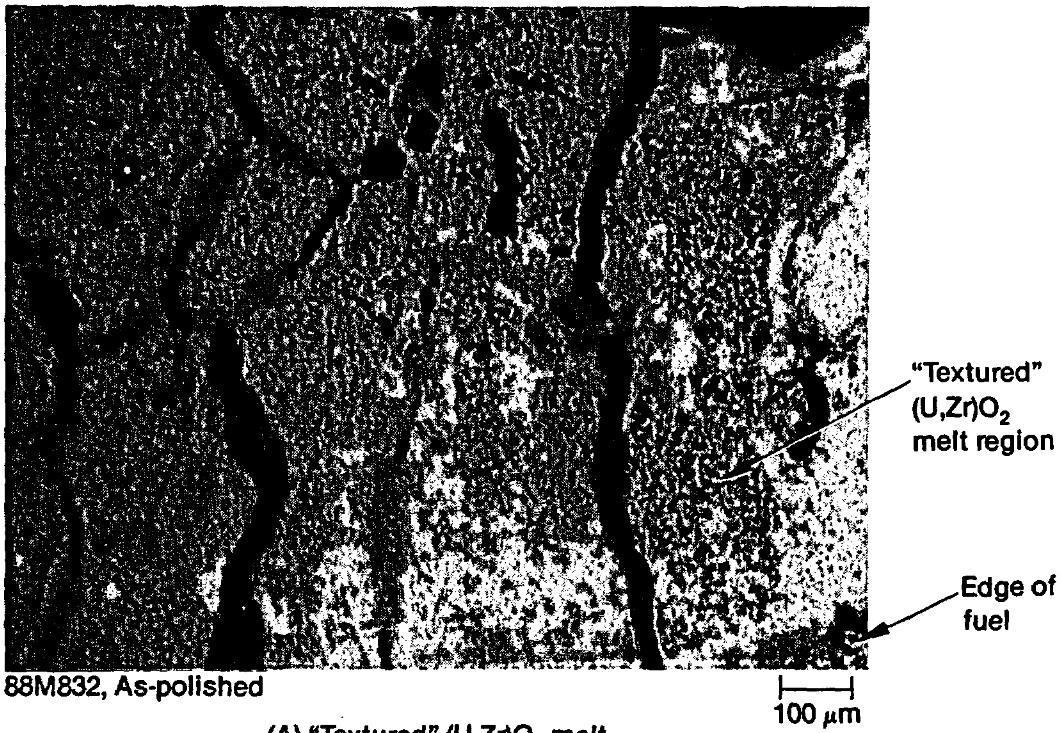

(A) "Textured" (U,Zr)O$_2$ melt

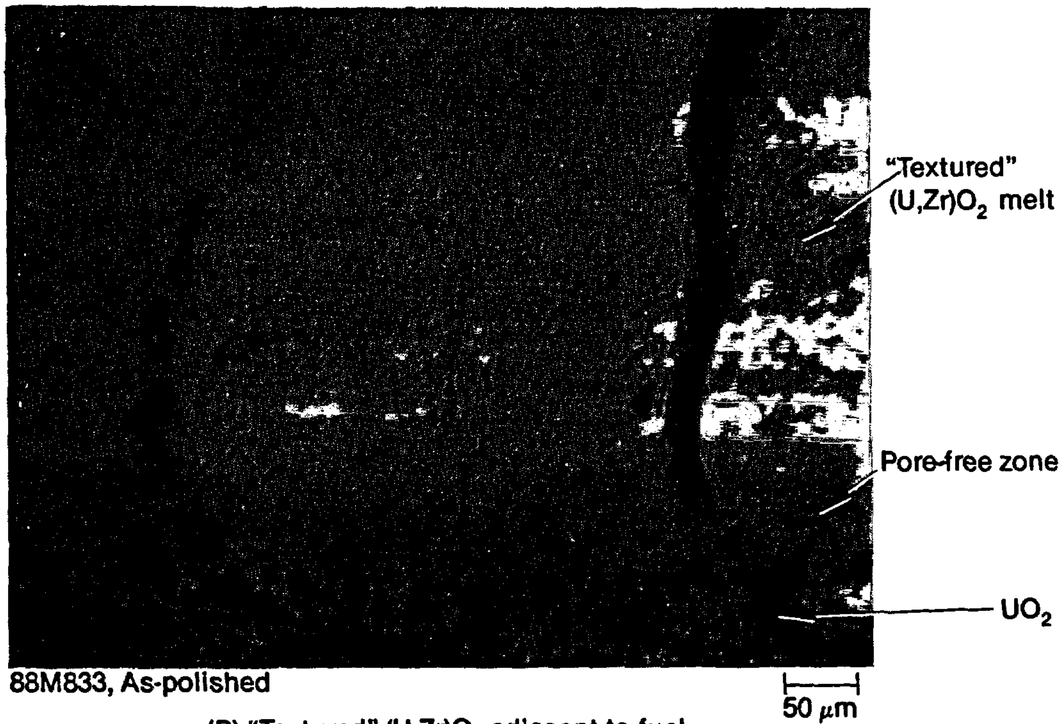

(B) "Textured" (U,Zr)O$_2$ adjacent to fuel

Figure 245. Details of "textured" (U,Zr)O$_2$ melt at 0.77 m.

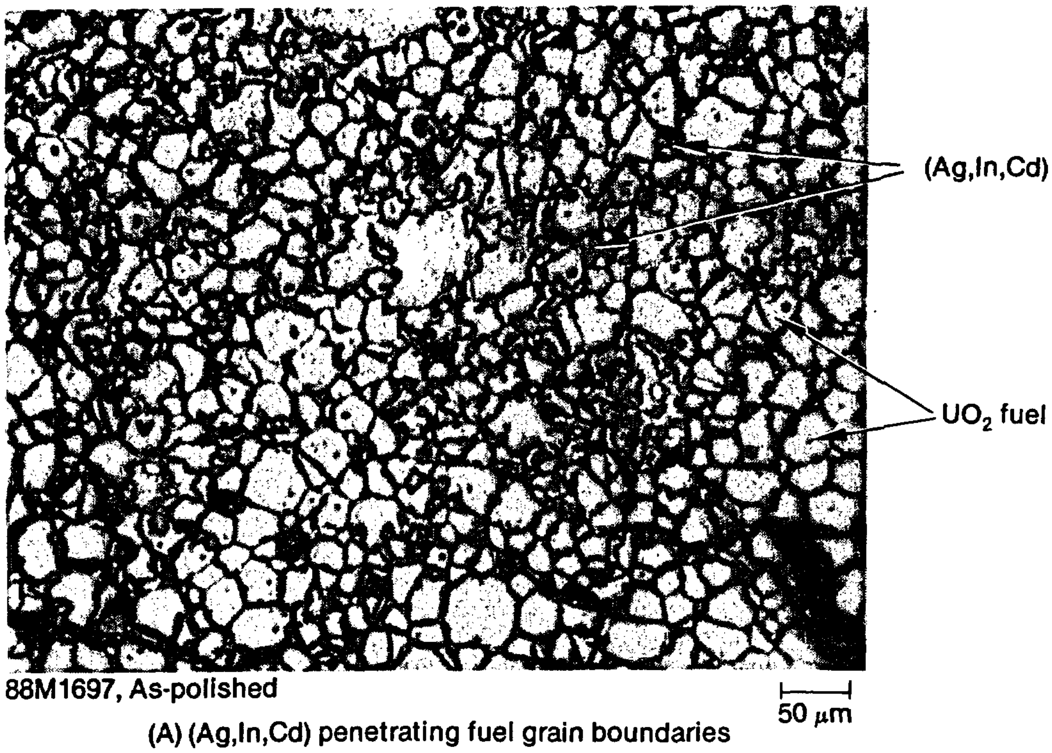

(A) (Ag,In,Cd) penetrating fuel grain boundaries

(B) Detail of (A)

Figure 246. Molten control material along fuel grain boundaries at 0.88 m.

revealed that molten (Ag,In) control rod material was present along fuel grain boundaries in an isolated case. This molten material probably flowed into an area in which fuel grain boundary separation had previously occurred.

Figure 247 shows a very unusual region which appeared, metallographically, to include areas of grain boundary separation with second-phase material present on some of the grain boundaries. The second-phase material on the grain boundaries is shown in more detail in Figure 248. SEM/WDS sample K3-S24 was selected to examine this area, and it revealed that the large grains of material were ZrO_2 and the second-phase material in the grain boundaries was composed of Ta, Fe, Cr, and Ni. The tantalum came from thermocouple sheaths used on the cladding thermocouples.

A dendritic ceramic melt was observed in portions of the R cross section (1.68 m). Photographs of this melt are shown in Figure 249 and 250. SEM/WDS sample R3-S25 indicated the presence of Al, U, O, and some Zr in this melt. The aluminum came from Al_2O_3 spacers on the top of the fuel columns.

Most of the oxidized ZrO_2 cladding shells in the fuel bundle were unaffected by any metallic melts. The only exceptions were at the K cross section (0.88 m), where a large, agglomerated mass of metallic melt had surrounded some of the fuel rods. Photographs of the resultant interactions are provided in Figures 251, 252, and 253. These types of areas were examined on SEM/WDS sample K1-S23; and, as detailed in Appendix E, these examinations indicated the presence of uranium in the oxidized cladding remnants. Stainless steel and control materials in the metallic melt penetrated along the grain boundaries of the oxidized cladding remnants. These metallic melts eventually surrounded the fragments of $(U,Zr)O_2$, dispersing them in the melt, as shown in Figures 251, 252, and 253.

Globules of metallic melt were dispersed throughout the fuel bundle. Below the second spacer grid, these were composed of droplets of molten control material. Above the second spacer grid, these metallic melts were

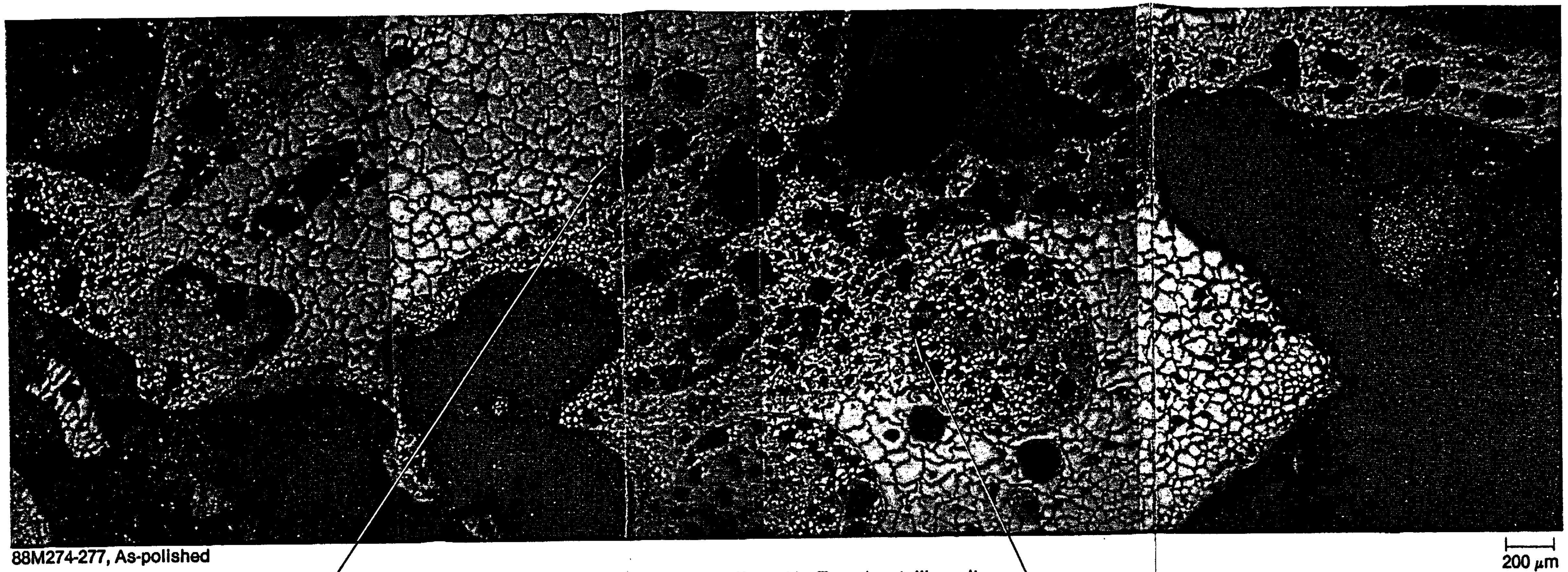

(A) ZrO_2 affected by Ta and metallic melts

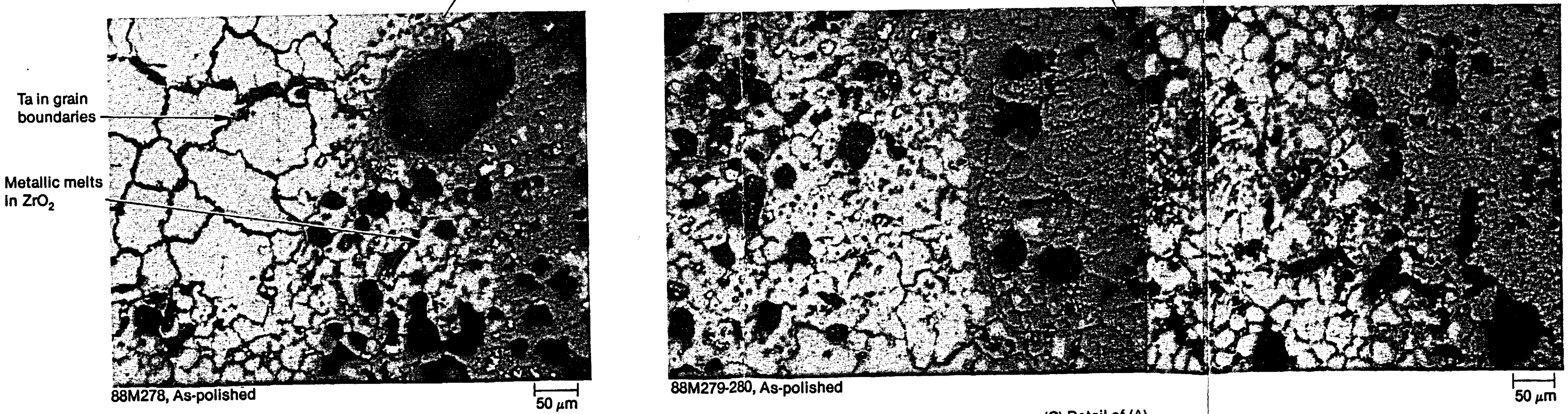

(B) Detail of (A)

(C) Detail of (A)

Figure 247. Tantalum interacting with ZrO_2 at 0.88 m.

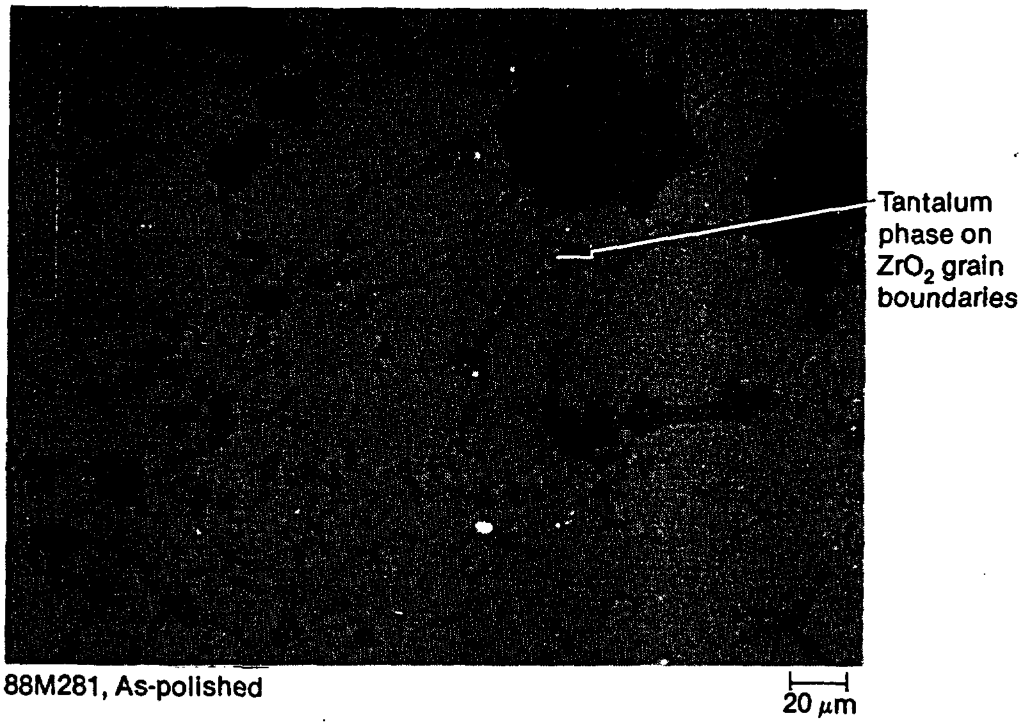

Figure 248. Tantalum-rich second-phase on ZrO_2 grain boundaries at 0.88 m.

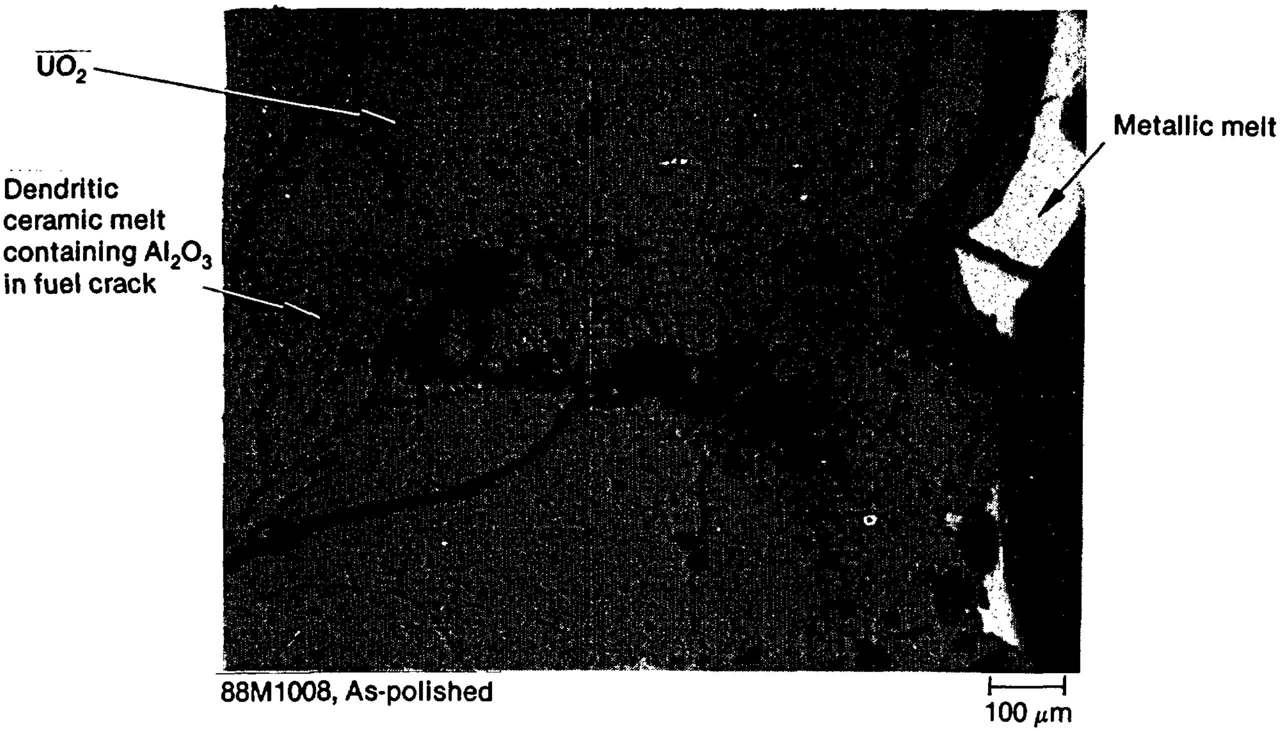

Figure 249. Dendritic ceramic melt containing Al_2O_3 from fuel rod spacers at 1.68 m.

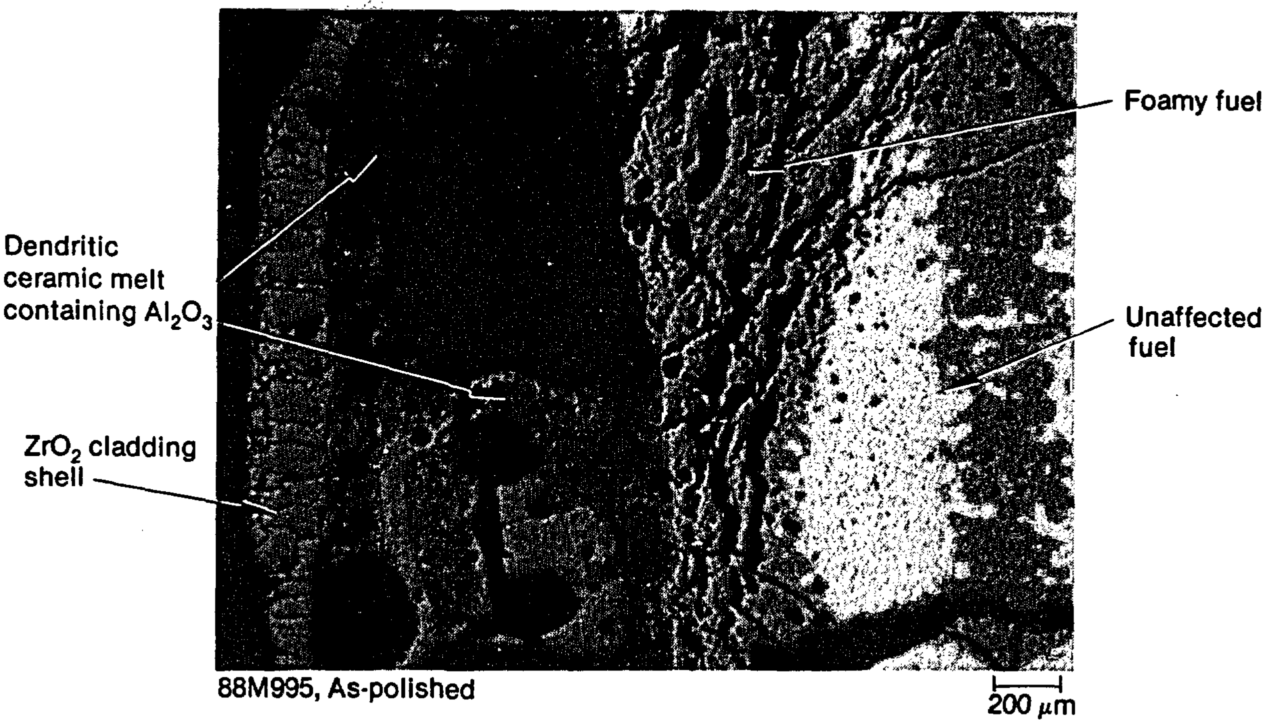

(A) Dendritic ceramic melt and fuel structure

(B) Detail of dendritic melt in (A)

Figure 250. Dendritic ceramic melt containing Al_2O_3 at 1.68 m.

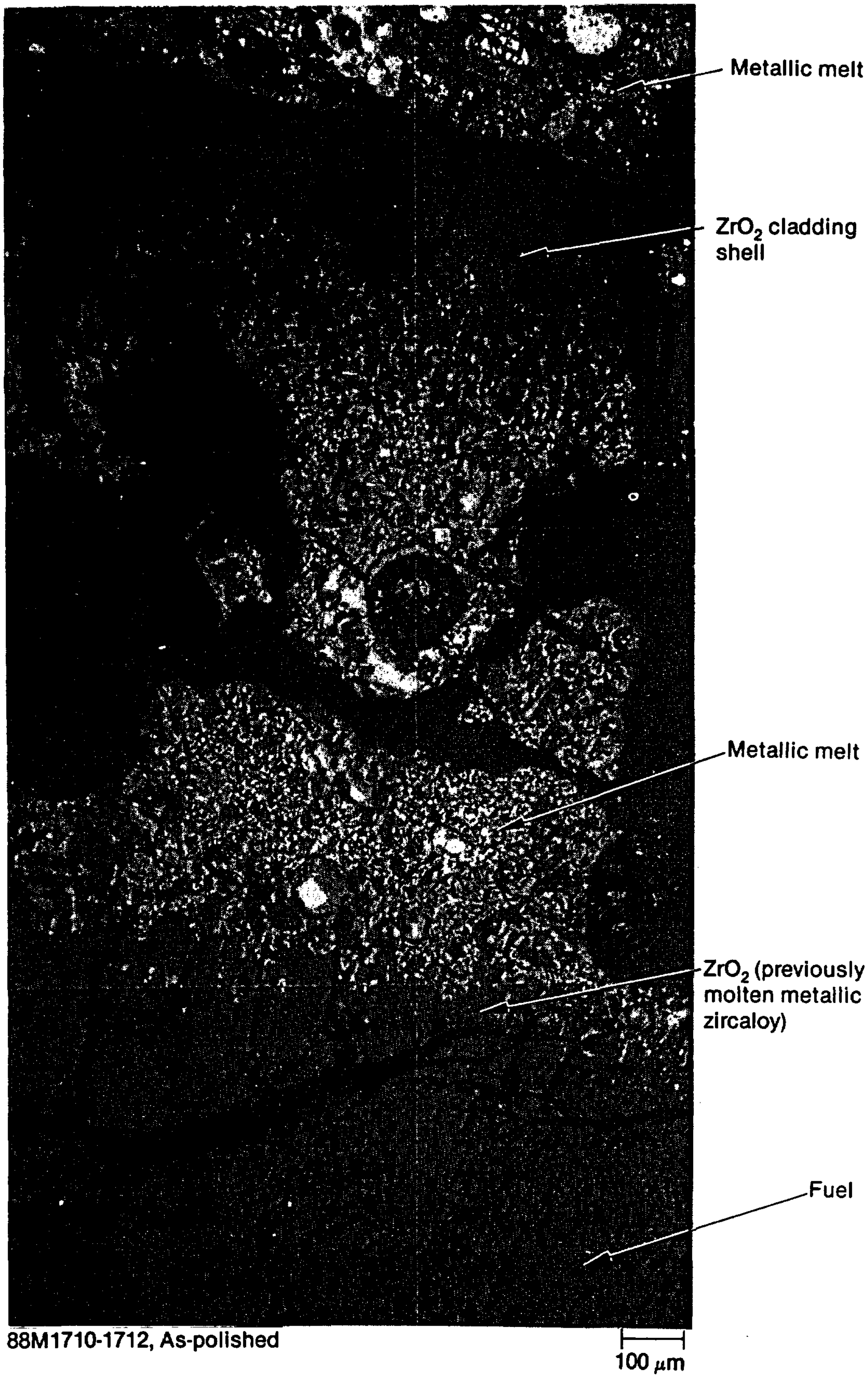

Figure 251. Metallic melt interactions with ZrO$_2$ cladding remnants at 0.88 m.

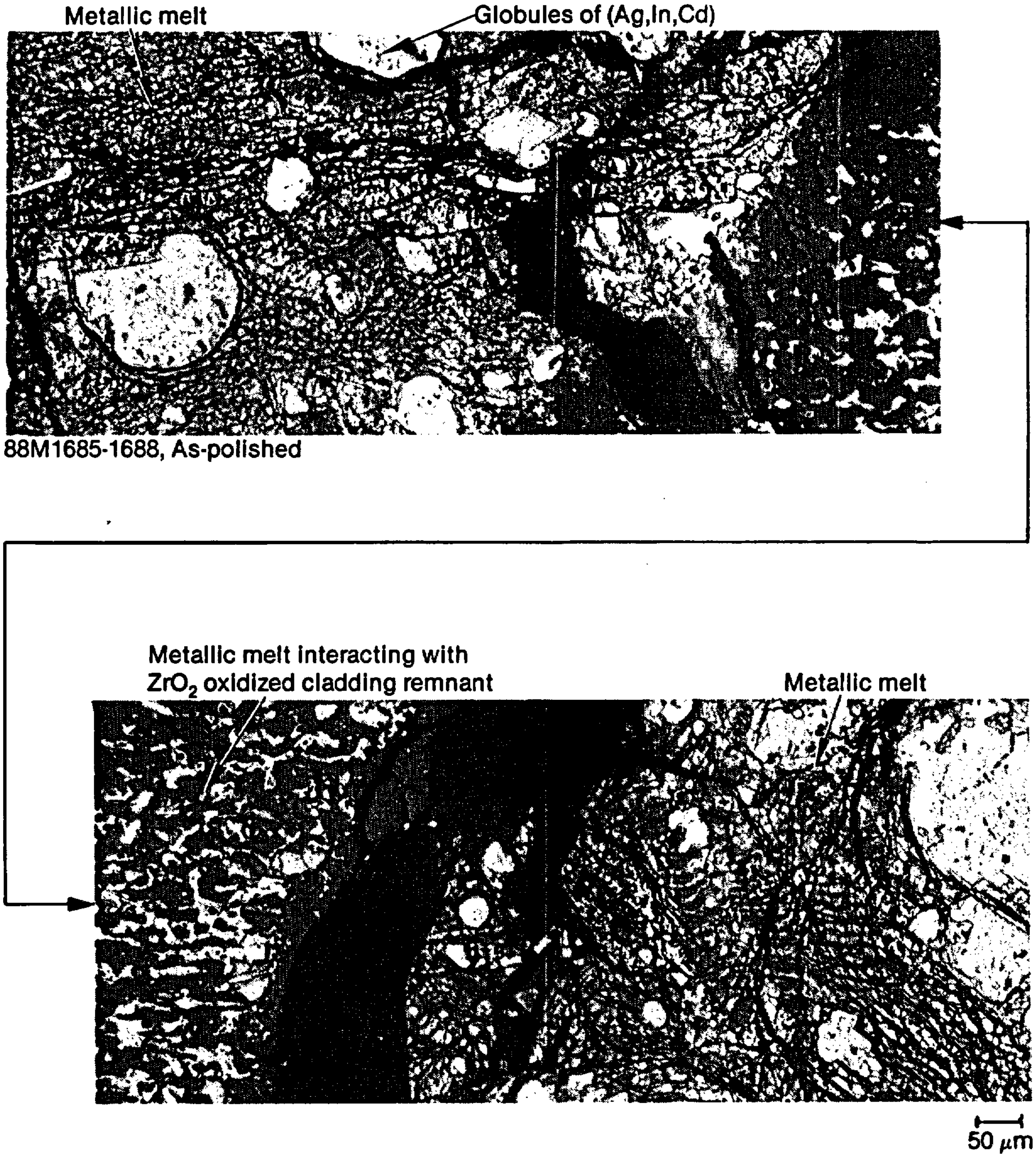

Figure 252. Metallic melt interacting with ZrO_2 cladding remnants at 0.88 m.

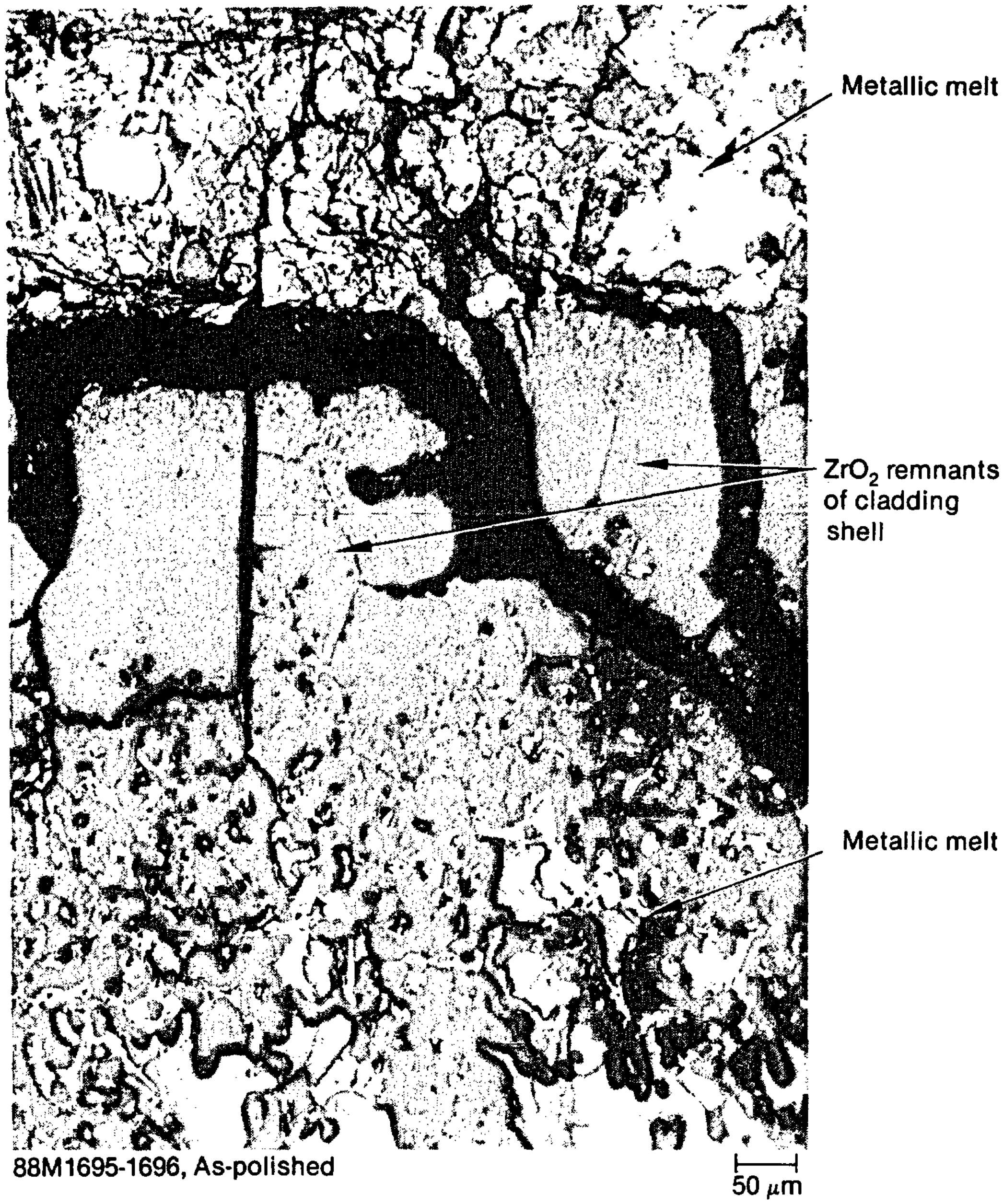

Figure 253. Details of interactions between metallic melts and ZrO_2 cladding remnants at 0.88m.

generally composed of a variety of elements in multiphase mixtures. Some typical examples of these multiphase metallic melts are shown in Figures 254 and 255. SEM/WDS samples I4-S3 and Q3-S9 examined melts similar to these, and the details are provided in Appendix E. Grain boundary separation is apparent in the fuel adjacent to the metallic melt in Figure 255.

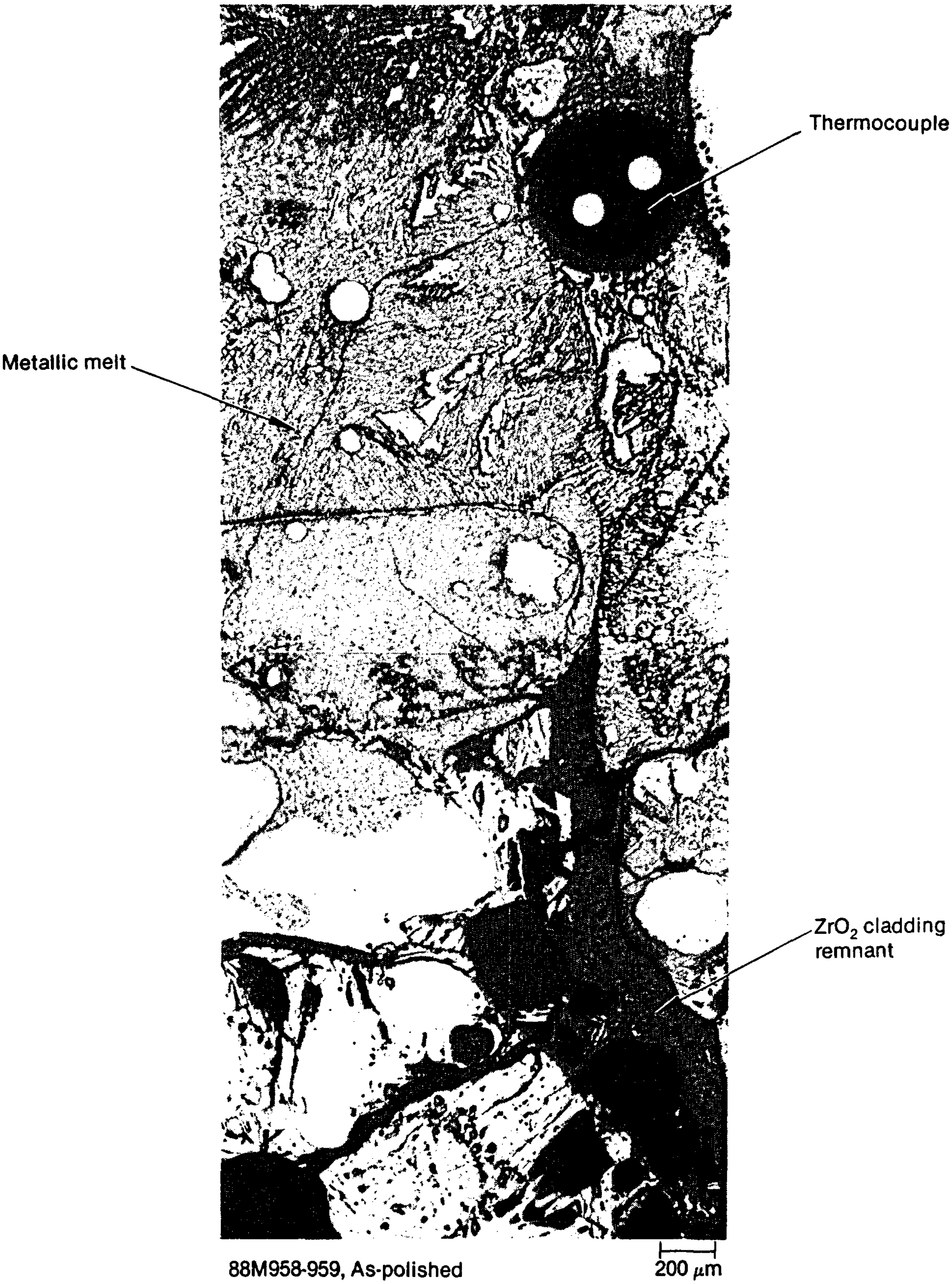

Figure 254. Representative multiphase metallic melt and remnants at 1.45m.

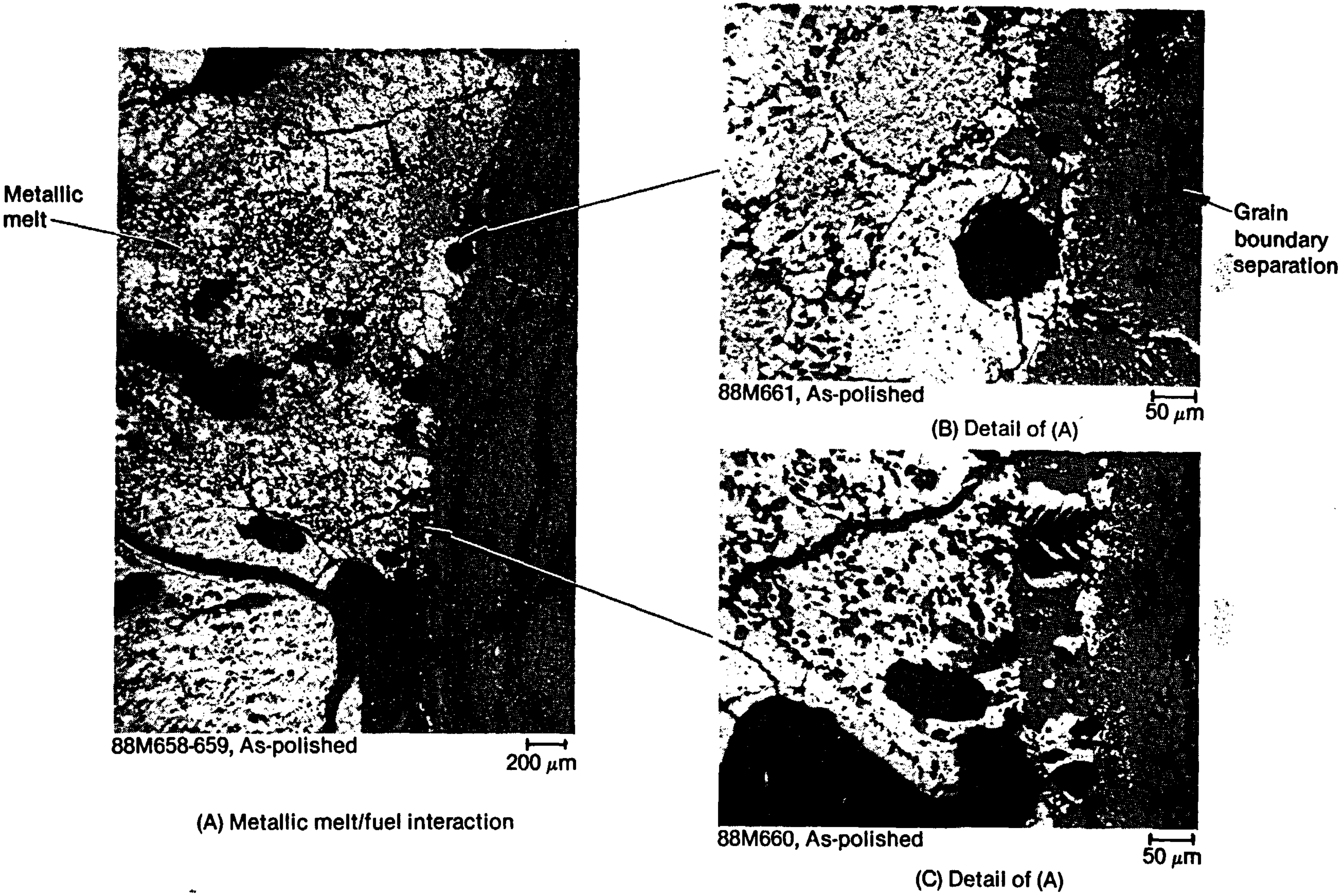

(A) Metallic melt/fuel interaction

(B) Detail of (A)

(C) Detail of (A)

Figure 255. Representative multiphase metallic melt adjacent to fuel pellet at 0.66m.

4. QUANTITATIVE DATA ANALYSES

This section discusses the measurement data and quantitative analyses from the postirradiation examinations of the LP-FP-2 fuel bundle. This includes flow blockage and material redistribution measurements, estimates of the amount of oxidation and hydrogen generation, fuel grain size, and estimates of bundle temperatures. Also included in this section are the results from the radiochemical and elemental analyses of the retained fission product samples.

4.1 Flow Blockage and Material Redistribution

The cross-sectional areas of various types of materials at each metallographic elevation were measured to provide axial distributions, as described in Section 4.1.2. Interpolation of these values provided integral volumes of each category of material as described in Section 4.1.3. Density measurements and elemental analysis of bulk samples taken from representative areas were then used to estimate material compositions in the melt regions and to calculate material balances for uranium and zirconium, as described in Section 4.1.4. These material balances provided an internal consistency check on the material distribution measurements and methodology, as well as providing data on the distribution of uranium and zirconium in the melt regions.

4.1.1 Measurement Techniques and Sources of Error

Where possible, the cross-sectional areas of the bundle constituents were calculated from as-fabricated dimensions. This was generally true for intact portions of the bundle below the second spacer grid. For other areas, an Omnicon image analyzer was used to measure the cross-sectional areas. This image analyzer relies upon the attenuation of a light beam passing through a photograph or piece of paper to calculate the cross-sectional area. Because of the small differences in shading between various materials, and because the shading in one type of material varied across a single photograph due to polishing and lighting factors, it was necessary to trace each component (intact fuel, ceramic melt, metallic melt, etc.) onto its own separate piece of paper and blacken in the area. The image analyzer calculated the fractional area attenuated by the light beam within a known area; and, after correcting for the magnification of the photograph, this provided the cross-sectional area of each material. For very thin components, such as cladding and spacer grids, the area was calculated from length measurements and high-magnification photographs used to measure the component thickness.

In general, very good data were obtained using these methods. However a brief summary of some of the factors that contributed to uncertainties in the data is provided in the following subsections, to discuss the problems which were encountered and some of the steps that were taken to reduce these uncertainties.

4.1.1.1 Human Limitations in Tracing Areas. There were several human limitations in tracing and blackening in the cross-sectional areas, which became more pronounced as the size of the area decreased. For instance, attempts to transfer thin cladding thicknesses to a tracing paper for image analysis resulted in large errors. This problem was very apparent when measurements of the intact zircaloy cladding in the lower region of the bundle indicated values twice that of the known values. This problem was overcome by using a curveimeter to measure the length of zircaloy cladding remnants, in conjunction with the cladding thicknesses, to calculate the cross-sectional areas. Using this method, the measurement results were within 5% of the known values in the intact regions.

Similar problems with accurately tracing the boundary of larger areas was also a factor which contributed to uncertainties in these measurements. The magnitude of the error was inversely related to the size of the overall area. In general, for areas comparable to 1/4 the size of an intact fuel pellet, this error source resulted in uncertainties of <5%. However, in the case of a cracked or fragmented fuel pellet, additional errors were introduced because it was not possible to account for the areas within the cracks. In cases where the fuel pellet was no longer tightly restrained by the cladding, this cracking and fragmentation could lead to a significant overprediction of the amount of fuel present. As discussed in more detail in Section 4.2.1, this was one of the reasons that the uncertainties in the fuel measurements were increased to ±15%.

Another human limitation arose in areas which contained an agglomeration of very small pieces (fuel fragments, melt droplets, cladding remnants). Attempts to draw each and every piece would have put a severe strain on the person performing the work, and large uncertainties would have naturally occurred because of errors in transferring the images. Consequently, in these areas, it was only possible to blacken in the entire area containing these small pieces and then rely upon other data to provide correction factors. Depending upon the situation, this may have involved higher-magnification photographs, SEM/WDS analyses and area fraction measurements, or elemental chemical analyses and density measurements of samples.

Small errors were also introduced in attempting to identify and differentiate all the various materials. The higher-magnification metallographic photographs were relied upon to assist in these determinations where they were available; however, mistakes were undoubtedly made in sometimes confusing a piece of insulation with fuel or melt, for instance. Although unquantifiable, the uncertainties resulting from these errors are considered to be relatively insignificant compared to other sources of error.

4.1.1.2 Errors Resulting from Sample Preparation. A potential source of error was the fact that some of the metallographic samples did not lie flat in the sample tray used to epoxy them in after bundle sectioning. This was caused by material falling out and becoming wedged between the sample and the sample tray and, in the case of the D cross section, was aggravated by warpage of the saw blade, which produced a slightly curved cut. After these cross sections were vacuum-impregnated with epoxy, this resulted in a slight angle of deviation. Polishing of these samples parallel to the final surface therefore resulted in elongated surface features. (This phenomenon is most apparent in some of the longitudinal cross sections presented in Appendix D.) This problem was greatest in the early stages of the bundle sectioning operation when large amounts of the insulation were lost, when loose material in the center of the lower blockage complicated matters, and when problems with saw cut burrs on the bottom of the module made the removal of samples from the work table more difficult. All these problems were either solved or went away of their own accord as the sectioning operation proceeded. However, in the final analysis, the errors associated with this phenomenon were largely negated on these lower cross sections because all the intact material could be calculated based upon as-fabricated dimensions. The impact of this error source on measurements of the relatively large areas of relocated material or open flow in these lower regions of the fuel bundle is also negligible. However, this source of error may have contributed to differences between measured and calculated values in these intact lower regions. This comparison was made as a basis for estimating the overall uncertainties in the measurement techniques.

4.1.1.3 Errors Associated with the Accuracy of the Image Analyzer. The stated accuracy of the image analyzer is ±2%. However, errors introduced by the image transfer process and uncertainties introduced by the machine operator will affect this accuracy. Empirical tests were conducted to assist in evaluating the cumulative error from these sources. A series of circular areas were drawn on a piece of paper using a template. The actual diameter of these areas was then measured, using calipers, and their cross-sectional areas were calculated. In addition, a large square area was also drawn for comparison. Comparisons of the calculated areas with those measured by the image analyzer are provided in Table 3.

These series of measurements provided a basis for estimating the uncertainty in the values obtained from the image analyzer. The differences are indicative of the limitations on the accuracy of the machine itself and the skill of the operator using the machine. They exemplify the fact that larger errors can be expected in measuring very small areas and provide some indications of the magnitude of the error that can be expected for various-sized areas under the best of circumstances. As a point of

TABLE 3. EMPIRICAL EVALUATION OF IMAGE ANALYZER MEASUREMENT UNCERTAINTIES

Caliper Measured Area (mm^2)	Image Analyzer Measured Area (mm^2)	% Difference
3.84	2.23	42
6.82	5.94	13
10.51	8.90	15
15.52	14.09	9
22.13	20.00	10
29.43	28.19	4
2580.60 (square area)	2536.15	2

reference, the cross-sectional area of a fuel pellet is 68 mm^2; and the photograph from which these measurements were made were usually magnified 1.5X or more. The measured area on the photographs would therefore correspond to approximately 153 mm^2. This indicates that errors of ±5% could be expected on material about 1/4 the size of a fuel pellet from these sources. Other problems which have been previously mentioned could add to these uncertainties.

4.1.2 Material Redistribution Data

The axial distributions of various categories of materials are described in this section. The data for the major components are presented graphically in this section, with the tabular data provided in Appendix F.

Because of the measurement techniques involved, it was necessary to define categories of materials that could be easily distinguished from the cross-sectional photographs. In some cases, this resulted in one material being distributed among several different categories. For instance, the UO_2 fuel was distributed among three categories (intact, fragmented, and debris mixed with metallic melt), not to mention the fuel mixed within the ceramic melt. The basic cross-sectional flow blockage measurement data are provided in this section. These data were used in Section 4.1.2 to provide integral volumes of each type of material; and finally, in Section 4.1.3, specific gram quantities of uranium and zirconium in the various regions of the fuel bundle are calculated. The zirconium distribution data were later used to estimate the amount of oxidation and hydrogen generation in the fuel bundle. Material balance calculations in Section 4.1.4 for uranium and zirconium provided an internal consistency check on the material distribution measurements and methodology.

4.1.2.1 Intact Fuel. For these purposes, the term intact fuel refers to fuel pieces of a sufficient size that they could be accurately reproduced using the planimeter techniques previously described. As a general rule, this corresponded to fuel fragments as small as approximately an eighth to a quarter of a fuel pellet. The term intact fuel, as used here, is not meant to infer that the fuel was not cracked or even fragmented; this term is only meant to describe a categorical type of material observed metallographically.

The axial distribution of intact fuel is presented in Figure 256, along with the axial distribution of fuel fragments discussed in the following subsection. At the A-F elevations ($\leq$0.36 m), essentially all the fuel pellets were still contained within the fuel rod cladding and the cross-sectional fuel areas at these elevations were calculated based upon as-fabricated dimensions. These calculations assumed that all the fuel rods that are missing from the C and D elevations (0.12,0.22 m), except for some breached remnants on sample D3, were intact until they fell out after bundle sectioning. The reduction in the amount of intact fuel at the A and B elevations ($\leq$0.03 m) is due to the fact that these lower elevations passed through the bottom end caps of the instrumented fuel rods, not to any loss of fuel material. Fuel rod cladding failure starts to become significant at the G(bottom) elevation (0.43 m), just below the second spacer grid. The amount of intact fuel decreased in the region just above the second spacer grid (0.58 m) due to severe fragmentation of the fuel in this region. From 0.66-0.88 m, many of the fuel rods were surrounded by a large mass of ceramic melt, which held the fuel in place. However, there was some loss of fuel as a result of fuel liquefaction on some rods in the center of the ceramic melt; and fuel relocation occurred on failed fuel rods on the periphery of the assembly. In the upper portion of the bundle, there was an increase in the amount of intact fuel present at 1.20 m due to formation of the debris bed. Above this elevation, the amount of intact fuel decreased, which reflects the fact that the fuel pellets were no longer restrained by intact cladding and were free to relocate.

An uncertainty of ±15% was placed on the measurement data. (Zero uncertainty was assumed at and below 0.36 m, where the values were calculated based upon as-fabricated dimensions.) This estimation was based partially upon a comparison of the amount of intact fuel measured in the region $\leq$0.36 m using planimeter techniques with the calculated values for

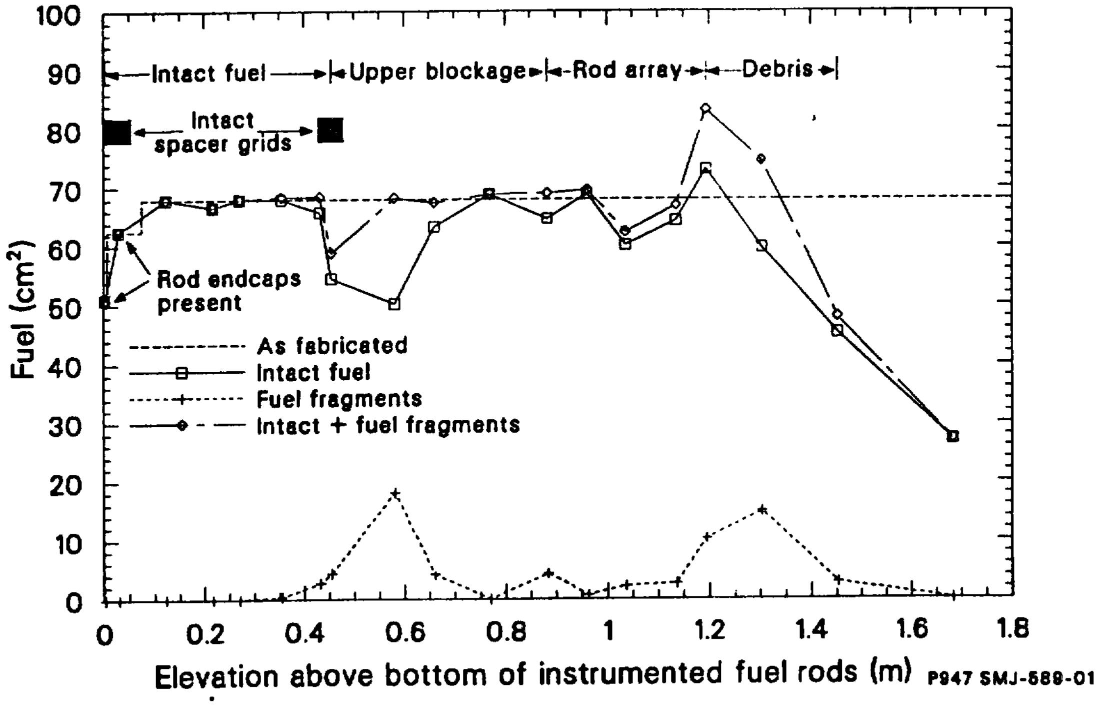

Figure 256. Axial distribution of fuel in the LP-FP-2 fuel module.

this region. This comparison indicated that the measured results were within ±5%. However, as described in Section 4.1.1, there were additional sources of error in measuring the amount of fuel in the upper portion of the bundle, primarily because of fuel cracking and fragmentation. The 15% uncertainty was therefore based upon a lower limit of ±5% under ideal conditions, and rough estimates of the amount of fuel present at the upper elevations. These rough estimates indicated that the measured data were within 15% of reasonable expectations.

4.1.2.2 Fuel Fragments. For these purposes, the term fuel fragments refers to pieces of fuel that were too small to accurately reproduce using manual planimetry techniques. In practice, these particles were generally less than 1/8 to 1/4 of a fuel pellet diameter, and quite often so small that they could not be individually distinguished from the cross-sectional photographs. These particles tended to agglomerate together in masses, with open porosity separating the particles. Visual examinations of the photographs and engineering judgment were used to estimate an average open porosity in these regions of 50%±20%. The measured cross-sectional areas were consequently reduced in half, and the remainder was added to the measured open flow.

The fuel fragment data (corrected for 50% open porosity) are also presented in Figure 256. These fuel fragments are concentrated primarily in two regions, just above the second spacer grid and in the lower portion of the upper debris bed (1.2-1.3 m).

Based upon the empirical accuracy tests described in Section 4.1.1, the uncertainty in the cross-sectional area measurements should generally be within 5%; however, this was increased to 10% to be conservative. The total uncertainty in the nominal values is therefore a combination of this 10% and the 20% uncertainty in the porosity.

4.1.2.3 Zircaloy. This category was divided into three subcategories. The first subcategory included the zircaloy fuel rod cladding, guide tubes, and lock rings surrounding portions of the guide tubes. These rod materials were grouped together because it was not possible to differentiate them after the zircaloy broke into pieces in some regions of the fuel bundle. The second subcategory was the zircaloy inner liner, and the third subcategory was the zircaloy shroud.

Figure 257 shows the axial profile of the zircaloy cladding and the inner liner. All the zircaloy rod components were essentially intact below the second spacer grid. The increase in zircaloy content at 0.03 m is due to the presence of the zircaloy lock rings surrounding the guide tubes at this spacer grid location. At and above the second spacer grid, the zircaloy rod components decreased as a result of fragmentation and melt interactions. The amount of zircaloy remnants was significantly reduced in the upper blockage region, due to melting of the zircaloy from the cladding inner surfaces, as well as complete melting of some of the oxidized cladding remnants. Above the upper blockage region, the amount of remaining zircaloy increased. In this region, much of the rod array was still present and extensive cladding ballooning and rupture had occurred. However, extensive amounts of the zircaloy on the cladding inner surfaces had melted and relocated. In the debris bed region (>1.2 m), only minimal amounts of zircaloy rod remnants remained; and this was limited to the exterior and corner rod positions. All the zircaloy in the central portion of the bundle at these axial elevations relocated either as a melt or as oxidized fragments.

As shown in Figure 257, the zircaloy inner liner was intact at and below the second spacer grid (~0.45 m). Portions of the inner liner have liquefied just above the second spacer grid; and above this elevation, the inner liner was completely gone except for a small remnant in the corner of sample Q3 (1.45 m). It should be noted that at higher magnifications, small remnants of oxidized liner could occasionally be distinguished in the midregion of the fuel bundle. However, these could not generally be distinguished from the cross-sectional photographs and hence are not shown in the axial profiles. These small oxide layers on the inner surface of the liner were probably responsible for retaining molten, unoxidized zircaloy adjacent to the insulation and allowing it to penetrate into the insulation,

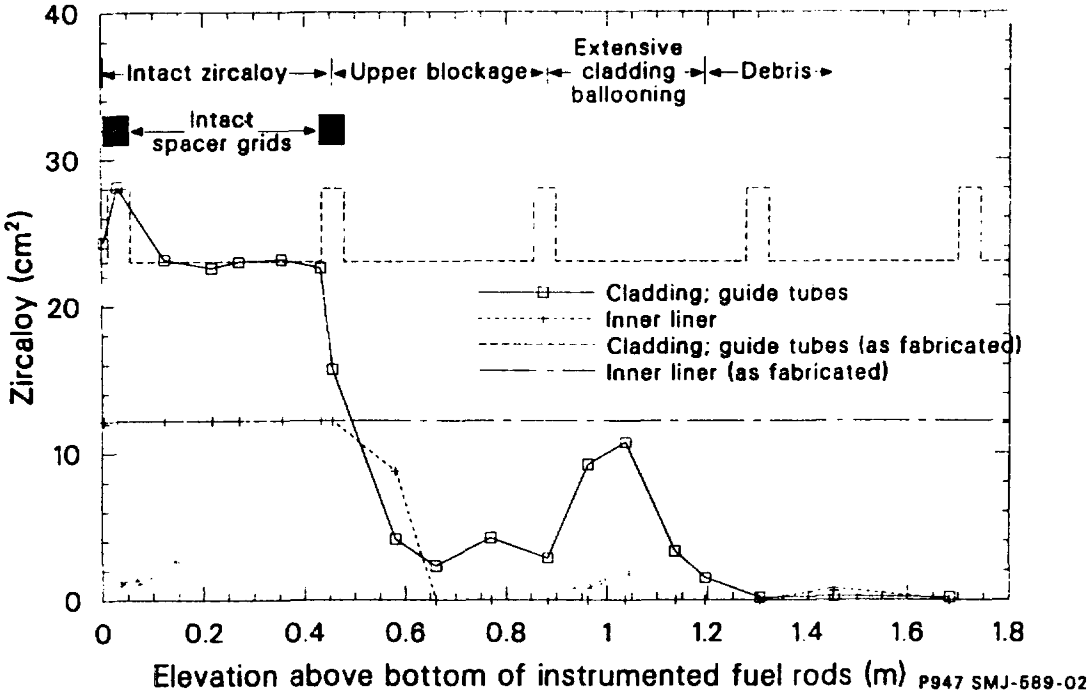

Figure 257. Axial distribution of zircaloy in the LP-FP-2 fuel module.

as described in a later discussion in this section on the insulation behavior.

As described in Section 2.1, following the experiment, the zircaloy shroud was intact except for a small piece in one corner. It is not clear whether this damage occurred during the experiment or whether the damage occurred during handling of the fuel module to remove it from the LOFT reactor and transfer it to the TAN water pit. The damage was first noticed when the module was withdrawn from an underwater storage canister in the TAN water pit for visual examination in January, 1986. To simplify the analysis, it is assumed that the shroud was fully intact at the completion of the experiment. This corresponds to a constant cross-sectional area of 26.8 cm^2, as shown in Appendix F.

As described in Section 4.1.1, a curveimeter was used to measure the length of cladding remnants; and high magnification metallographic photographs were used to accurately determine the cladding thickness. Several cladding thickness photographs were taken at various radial positions at each elevation. This technique was also used to estimate the amount of inner liner remaining at the two elevations where the liner was partially gone. As described in Section 4.1.1, the uncertainty in the curveimeter length measurements was 5%. However, additional uncertainties are associated with the variations in the cladding thickness measurements. These cladding thickness measurements are shown in Table 13 in Section 4.2 as ZrO_2 thicknesses. (The cladding was fully oxidized above the I elevation.) For the cross-sectional areas, the appropriate cladding thickness (exterior, intermediate, or interior radial position) was used to provide the best available estimate. However, to provide some basis for estimating the variation in these cladding thickness measurements, the cladding and guide tube measurements were independently averaged. Both data sets showed an average of 325-333 μm, with 1-sigma variations of 131-133 μm, or 40%. This variation does appear to reasonably approximate the radial and axial variations shown in Table 14; hence, the total uncertainty in the measured cross-sectional cladding areas was estimated as a combination of ±5% in the length and 40% in the thickness.

The uncertainty in the inner liner data was limited to the 5% uncertainty in the measured lengths because the metallography revealed that the thicknesses were generally unaffected; melting of the inner liner was generally only observed at the end tips of the liner remnants.

4.1.2.4 Stainless Steel. The control rod cladding was fabricated from Type 304 stainless steel. The posttest axial distribution is shown in Figure 258, along with the (Ag,In,Cd) control material discussed in the following subsection. The large increase in stainless steel at the bottom elevation (0.003 m) is due to the fact that this cross section passed through the lower end caps of the control rods. The stainless steel control rod cladding was fully intact from the bottom of the rods to just below the second spacer grid (~0.43 m). In the vicinity of the second spacer grid, the stainless steel cladding was partially liquefied; and cladding thickness measurements were used to estimate the amount of remaining stainless steel. Above the second spacer grid, the stainless steel had completely liquefied. Zero uncertainty is assumed for the intact regions, and the effect of uncertainties in the thicknesses in the partially liquefied regions is insignificant.

4.1.2.5 Intact (Ag,In,Cd) Control Material. The category refers to the amount of (Ag,In,Cd) control rod material still contained within the stainless steel cladding. In some instances, this material was molten; but it was constrained by the stainless steel cladding. Droplets of this material, which were observed primarily in the lower portion of the fuel bundle, are accounted for separately in the subsection on metallic melts.

The (Ag,In,Cd) axial distribution is related to the presence of the stainless steel cladding, as shown in Figure 258. The lack of control rod material alloy at the bottom elevation (0.003 m) is due to the fact that this cross section passes through the lower stainless steel end cap of the control rods. Zero uncertainty is associated with these cross-sectional values, since the control rod material was either completely present or completely gone.

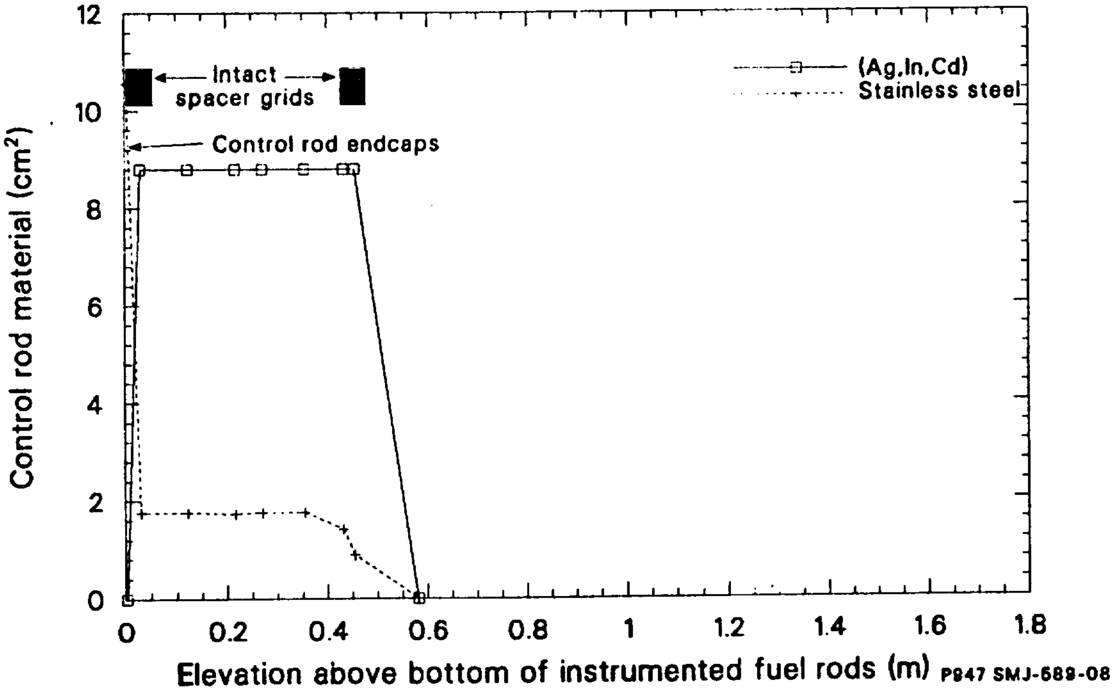

Figure 258. Axial distribution of (Ag,In,Cd) and stainless steel control rod material in the LP-FP-2 fuel module.

4.1.2.6 Spacer Grids. Five Inconel 718 spacer grids were used in the LP-FP-2 fuel module. Following the experiment, only the bottom one was fully intact; and the second highest spacer grid was partially liquefied. A curveimeter was used to measure the grid lengths remaining at the G (top) elevation (0.46 m), and as-fabricated dimensions were used in conjunction with these lengths to determine that 73% of the second spacer grid was still intact, as shown in Appendix F. The spacer grid appears intermittently in the photographs but actually consists of continuous sheets of material. Consequently, the curveimeter measurements assumed a continuous grid except in those areas where it was obvious that gross damage to the grid had occurred. Upper and lower limits of ±5% were established for these values based upon the uncertainties in the curveimeter lengths. The thickness was approximated as being as-fabricated, based upon metallographic results summarized in Section 3.2.1.

4.1.2.7 Neutron Flux Tubes. There were two neutron flux tubes located in the LP-FP-2 fuel module. These tubes were both intact to the second spacer grid, above which first one and then both disappeared. The data are tabulated in Appendix F.

4.1.2.8 Self-Powered Neutron Detector. There was one self-powered neutron detector in the center position of the fuel assembly. This detector was only intact up to the C elevation (0.12 m) near the bottom of the lower blockage region. The data are tabulated in Appendix F.

4.1.2.9 Fuel Rod End Caps. The bottom cross section (0.003 m) passed through the bottom end caps of the instrumented fuel rods. Depending upon whether the thermocouple leads for these rods were routed out the bottom or top of the fuel rod, the cross-sectional geometries of the lower end caps varied. The B cross section (0.03 m) passed through the bottom end caps of instrumented fuel rods that had their thermocouple leads routed through the bottom of the fuel rod, but passed through the fueled region of the uninstrumented fuel rods and the instrumented fuel rods that had their thermocouple leads routed through the top of the rod. A schematic drawing of the axial orientations of the three different types of fuel rods is shown in Figure 3. This accounts for the variations in fuel rod end cap material shown at these elevations in Appendix F. These cross-sectional area data are only included as a bookkeeping device to account for all the material blockage at these lower elevations. It has no other real significance. It should be noted that this stainless steel was excluded from later calculations of integral volumes of stainless steel. Those integral quantities were only based upon the control rod cladding.

4.1.2.10 Insulation. It was necessary to measure the amount of insulation present at each elevation because the inner liner had melted in the upper portion of the fuel bundle and the insulation was able to fall out and relocate into the fueled portion of the bundle.

The insulation region consisted of two adjacent layers of low-density (~20%TD) ZrO_2. The division between these adjacent layers is readily apparent in the cross-sectional photographs. However, during the trimming operation, some of the outer insulation layer was sometimes cut off. Consequently, planimeter measurements were only made of the inner insulation region and any melt/insulation interaction zones. The area of the outer insulation layer was simply calculated and added to the planimeter measurements to obtain the total amount of insulation present at each elevation. The melt/insulation zones were generally limited to the inner insulation region and resulted from molten portions of the inner liner and other metallic melts penetrating into the low-density ZrO_2 insulation.

The data for the intact insulation and the melt/insulation areas are shown in Figure 259. These data show that all the insulation was intact and unaffected by any melt below the second spacer grid (~0.45 m). In the cross-sectional photographs taken at these elevations, the insulation is either completely gone or only fragments remain. This is because the insulation in this region fell out during bundle sectioning and/or handling afterwards. The insulation is known to have been in place prior to fuel bundle sectioning because it can be observed in the neutron radiographs. The assumption that it was unaffected by any melt material is based upon the presence of the intact inner liner at these lower elevations.

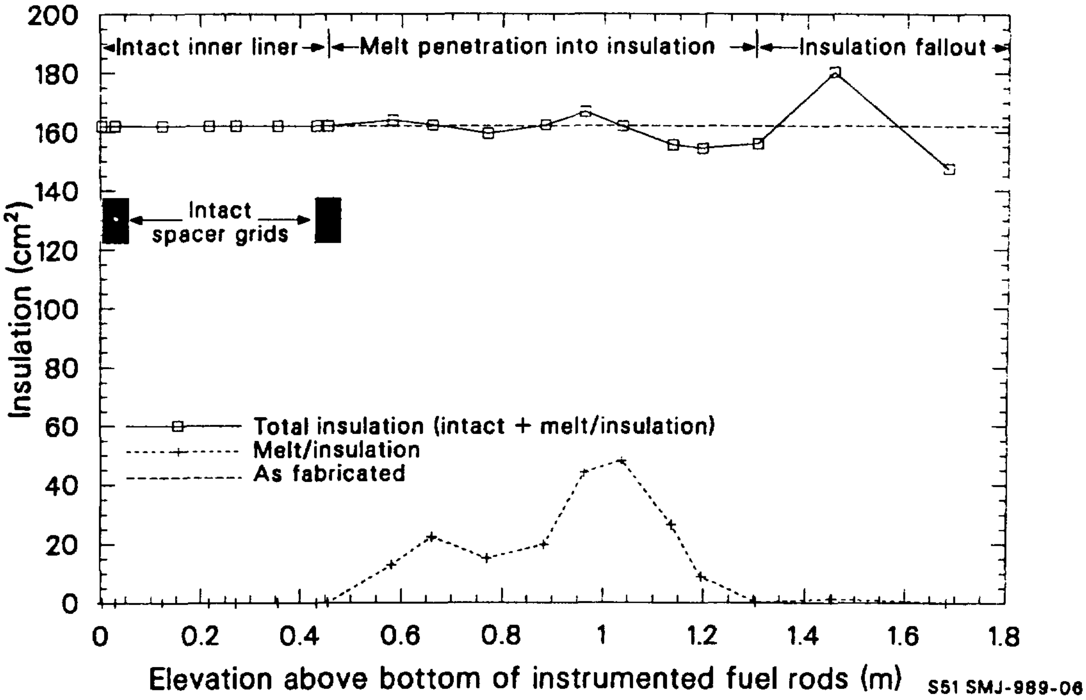

Figure 259. Axial distribution of insulation in the LP-FP-2 fuel module.

Melt penetration into the insulation region occurred throughout the central portion of the fuel bundle, where the inner liner had liquefied. The greatest amount of melt penetration occurred in the region above the upper blockage, and only very minor amounts were observed in the topmost portions of the fuel bundle. One explanation for this distribution may be that the inner surface of the inner liner was oxidized in the central portion of the fuel bundle prior to reaching melting temperatures. This oxide layer would have held molten unoxidized zircaloy adjacent to the insulation when temperatures exceeded 2030 K. This type of behavior is analogous to oxidation of the outer surface of fuel rod cladding observed in this region, with melting of the unoxidized inner surface. Later in the test, when temperatures were sufficient to cause melting of the unoxidized inner liner in the upper portion of the bundle, those melts were not contained and were able to relocate downward without significantly penetrating into the adjacent insulation.

The increase in the amount of insulation above the nominal value at the Q elevation (1.45 m) is due to an accumulation of insulation which relocated from above.

Uncertainty limits of ±15% were estimated for the measured values. Although the measured areas were relatively large, fragmentation of the insulation in the upper bundle made the measurements more difficult. The 15% represents similar uncertainties as were assumed for the intact fuel, with its associated cracking and fragmentation. Zero uncertainty is assumed for the calculated amounts in the outer insulation layer.

4.1.2.11 Ceramic Melt. The majority of the ceramic melt in the LP-FP-2 fuel module was composed of $(U,Zr)O_2$, with relatively small amounts of other bundle constituents mixed in. The exception was near the top of the fuel bundle, where the stainless steel upper tie plate had melted, relocated, and oxidized. The material distribution data for the ceramic melt are shown in Figure 260. This melt is limited to the region above the second spacer grid (~0.45 m), with the greatest accumulation between approximately 0.66-0.88 m.

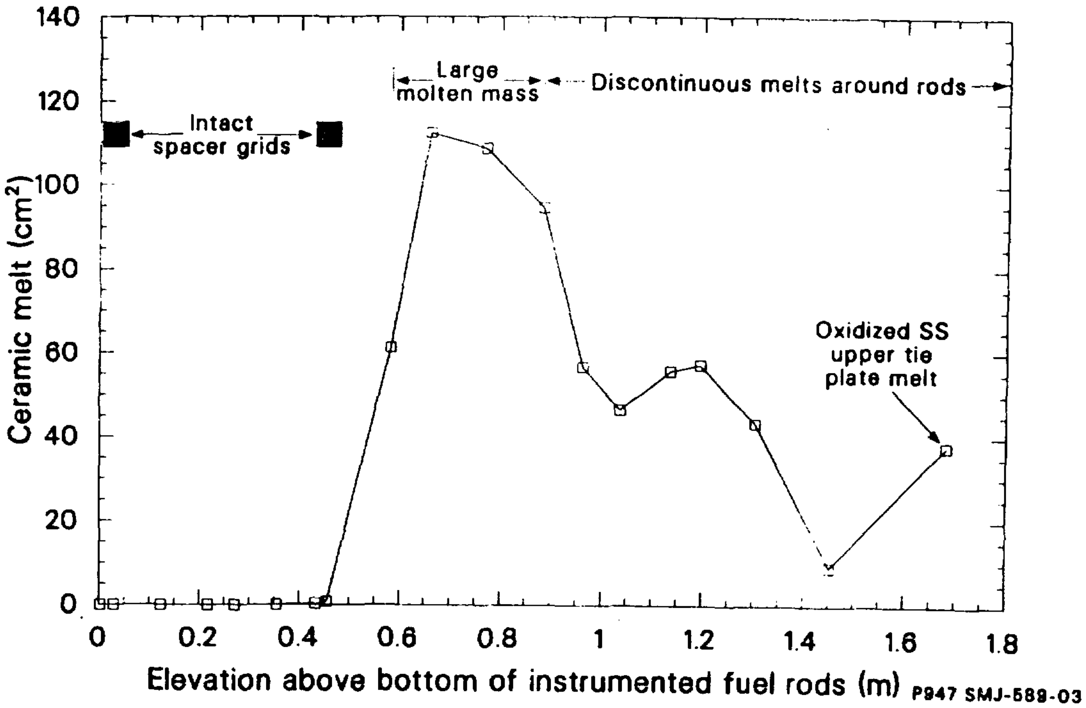

Figure 260. Axial distribution of ceramic melt in the LP-FP-2 fuel module.

The ceramic melt below the L elevation (0.96 m) formed a large solid mass, which completely surrounded much of the remaining fuel rod array. At and above the L elevation (≥0.96 m), the ceramic melt was distributed as isolated melts around some fuel rods, and particularly between fuel pellets and the oxidized cladding outer shells. In the debris bed region where the cladding was completely gone (≥1.14 m), the ceramic melt simply surrounded the fuel pellets.

A 10% uncertainty was placed on the measured data, based upon comparisons of measured and calculated open flow values in the lower portion of the fuel bundle (≤0.36 m). The open flow in these regions was calculated by subtracting all the relocated blockage material from the as-fabricated open flow. Comparisons between these calculated values and measured values using standard planimeter techniques provided an indication of the uncertainties associated with measuring these types of geometries (i.e., open flow or large blockages). This comparison is discussed in more detail in the subsection on open flow.

4.1.2.12 Eutectic Metallic Melt/Fuel Debris. This material was primarily composed of an agglomeration of very small eutectic metallic melt particles (primarily containing Ag, In, Zr, Fe, Cr and Ni), fuel grains and fragments, and small amounts of other assorted fuel bundle debris (cladding remnants, larger metallic melt droplets, and fuel fragments). On a microscopic scale, there was also considerable porosity between the particles. As shown in Figure 261, this material was primarily located in the lower portion of the fuel bundle, just above the first and second spacer grids.

Due to the heterogeneous nature of this material on a microscopic scale, it was impossible to estimate the overall composition from the metallographic results. It was necessary to rely upon elemental analysis and density measurements of bulk samples taken from these regions to estimate the composition. Details of these measurements and analysis are provided in Section 4.5. The porosity within this agglomerated material was not added to the open flow, as was the case with the corrected fuel fragment

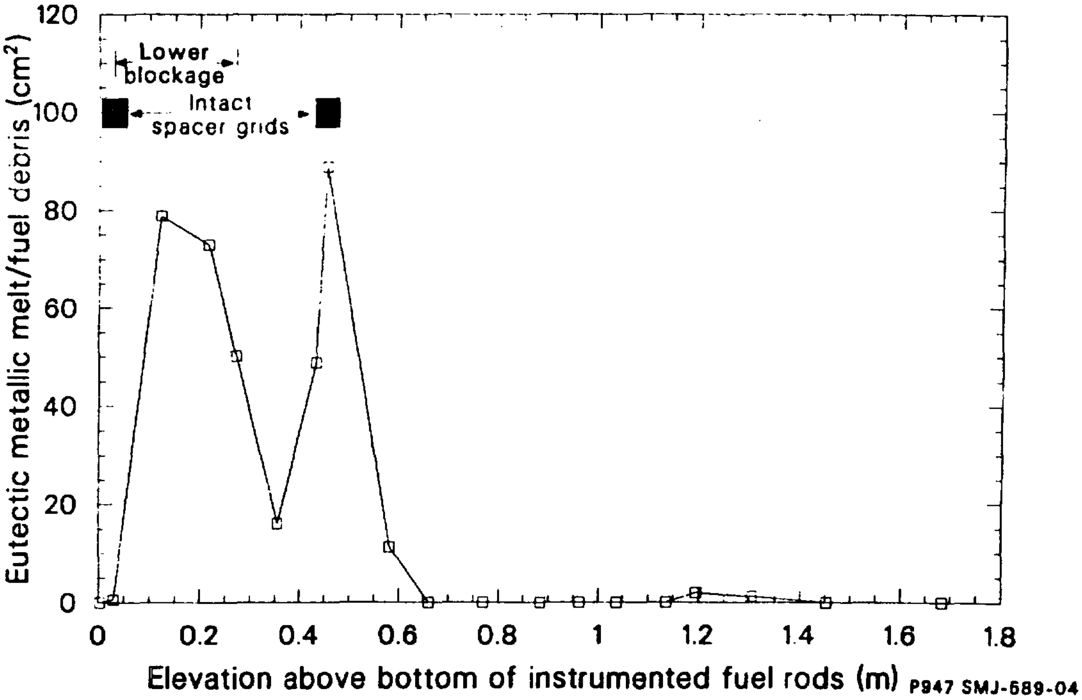

Figure 261. Axial distribution of eutectic metallic melt/fuel debris in the LP-FP-2 fuel module.

data, because this porosity was assumed to be closed. This assumption was based upon the fact that epoxy could not penetrate through this material, as described in Appendix B, which suggests that steam could not easily pass through this material.

Uncertainty limits of 10% were applied to these data, based upon similar considerations as were applied to the ceramic melt and open flow measurements. The uncertainties associated with each of these categories should be similar based upon their similar geometries.

4.1.2.13 Metallic Melts. This category included all metallic melts that were of a sufficient size to be easily distinguished using planimeter techniques. In general, the minimum size was on the order of a quarter of a fuel pellet. These metallic melts consisted of two types--(Ag,In,Cd) control material alloy droplets in the lower regions of the fuel module and multiphase, multiconstituent, metallic melts higher in the fuel bundle.

Most, if not all, the metallic melts at and below the second spacer grid consisted of droplets of (Ag,In,Cd) control rod material alloy. Above this elevation, the majority of the metallic melts consisted of multiphase elemental mixtures. As shown in Figure 262, the amount of these types of metallic melt was relatively small and their distribution was very irregular throughout the fuel bundle. The large increase in metallic melt material near the top of the fuel bundle is due to molten metallic material relocating from the stainless steel upper tie plate and other portions of the upper end box.

These metallic melts tended to be very small; and, based upon the empirical accuracy tests described in Section 4.1.1, uncertainty limits of ±15% were considered appropriate.

4.1.2.14 Debris. In the bottom of some of the empty guide tubes was debris consisting of very small particles of fuel, cladding, and melt materials. It was impossible to accurately differentiate these various materials based upon the cross-sectional photographs; and, since the total

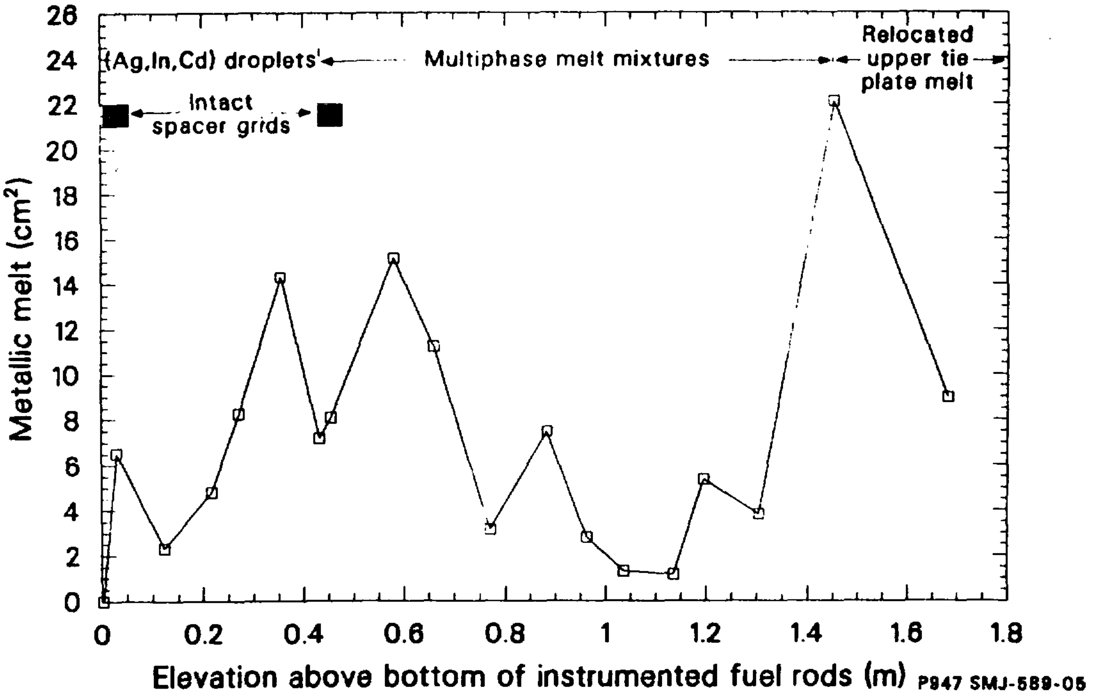

Figure 262. Axial distribution of metallic melt in the LP-FP-2 fuel module.

amount of this material was minimal (~20 cm^3), it was just identified as miscellaneous debris. The only purpose in including this category is a best-effort basis to account for all the blocked flow area in the test. The results are tabulated in Appendix F.

4.1.2.15 Total Blockage. The total blockage for each elevation is shown in Figure 263. These values include the entire fuel bundle cross section, including the insulation and shroud. It was necessary to include the insulation when calculating the total blockage because it varied throughout the bundle, particularly near the top of the bundle where it fell out of some areas and congregated in others. Failure to include it would have, in some instances, given the false impression that blockages were less than they actually were. The shroud was simply added for completeness. For this reason, the open flow axial profile shown in the next subsection probably gives a better perspective of flow conditions through the bundle.

The as-fabricated flow blockage is also shown for comparison in Figure 263, with step increases at the spacer grid locations. It is apparent that a volume expansion occurred within the bundle, which is primarily a result of the porosity contained within the molten regions. As discussed in Section 4.1.2.16, there was a 15% volume expansion in the material within the inner liner, which reduced the overall open flow volume by 11%.

The total blockage profile plotted in Figure 263 shows peaks in the lower blockage region, the upper blockage region, and in the lower portion of the debris bed. The greatest mass accumulation was located through the second spacer grid, which reflects the presence of the spacer grid and the effect it had on impeding material relocation. However, if it is assumed that the cavity within the lower blockage was closed to steam flow, then the flow would be diverted around the lower blockage. Consequently, the greatest flow impedance would be at approximately 0.12 m, as also shown in Figure 263.

4.1.2.16 Open Flow. The measured open flow areas (corrected for 50% porosity in the fuel fragments areas) are shown in Figure 264. It should

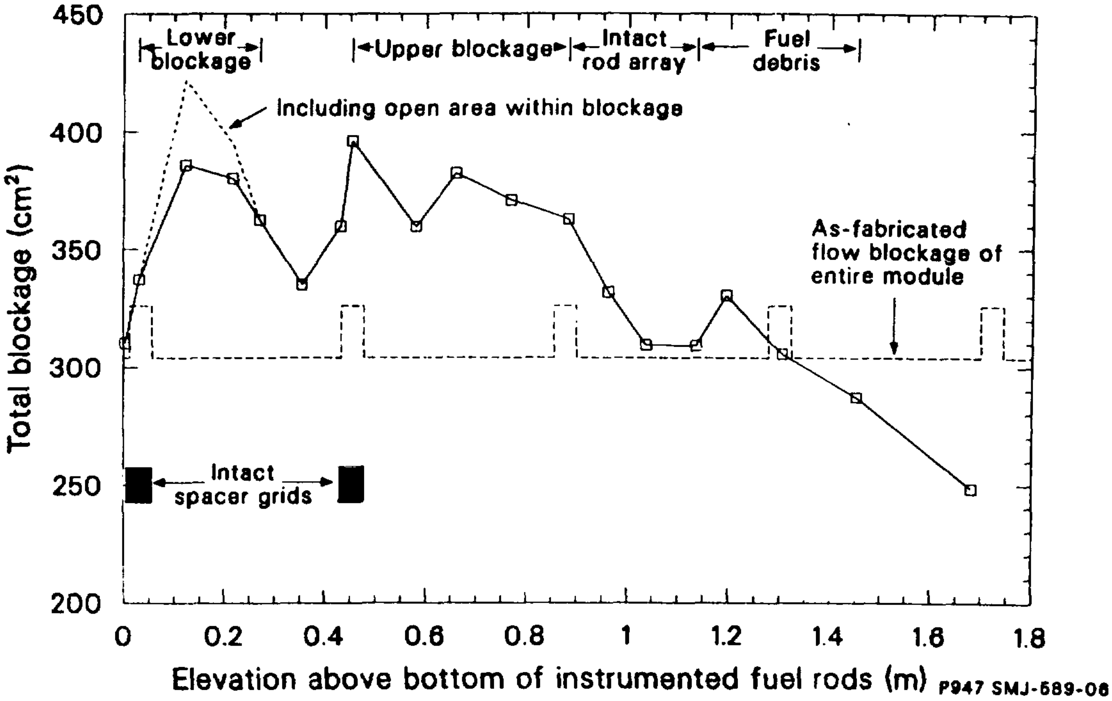

Figure 263. Axial distribution of the total blockage (including insulation and shroud) in the LP-FP-2 fuel module.

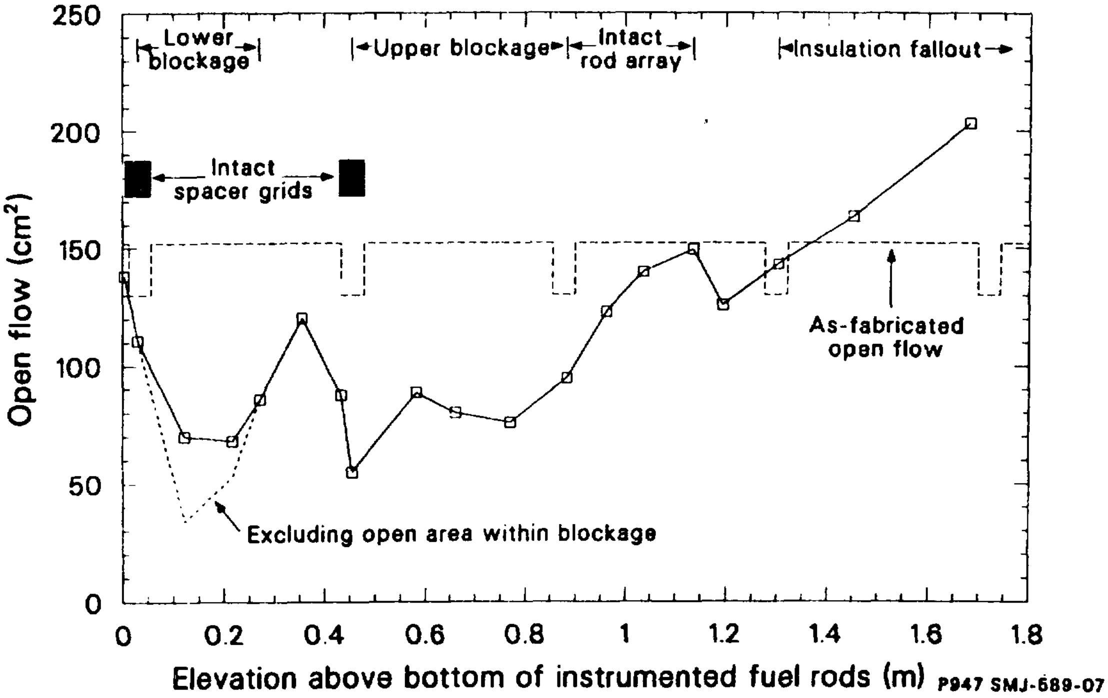

Figure 264. Axial distribution of the measured open flow in the LP-FP-2 fuel module.

be noted that these values are not exactly the same as derived by subtracting the total blockage values in Section 4.1.2.15 from the as-fabricated bundle cross section of 456 cm^2. These open flow values are an independent measurement of the open flow areas, and the comparison between these measured values and those based upon calculating the open flow from the blockage measurements provides an indication of the uncertainties. This is discussed in more detail later in this section.

The measured open flow values in the lower blockage region assume that all the rods passing through the central cavity of this region were present prior to bundle sectioning. The dotted line in Figure 264 further assumes that steam was diverted around the lower blockage and did not have access to the open areas within the central cavity. The flow impedence in this region therefore corresponds to 86% of the area within the inner liner.

Integration of the as-fabricated and posttest open flow measurement data indicates an 11% reduction in the open flow volume (using the solid line data in Figure 264). This corresponds to a 15% volume expansion of the material originally contained within the inner liner. This is the result of porosity within the various melt regions. The reduction in the bundle open flow volume is 12%, if it is assumed that steam was diverted around the lower blockage (using the dotted line in Figure 264).

Uncertainty limits of ±10% were estimated for these areas on the following basis. A rough approximation of the total uncertainty can be made by calculating the open flow as the difference between the total blockage measurements shown in Figure 263 and the as-fabricated bundle dimensions of 456 cm^2. A comparison of these calculated open flow values with the measured open flow values is shown in Figure 265. Only at two cross sections is the difference slightly greater than 10%, and in most instances it is much smaller than 10%. Although errors in the individual component measurements making up the total blockage values would affect this comparison, the fact that the difference is always generally 10% or less does provide some indication of the expected uncertainties. This comparison is strongest in the lower regions of the fuel bundle, where the bundle was

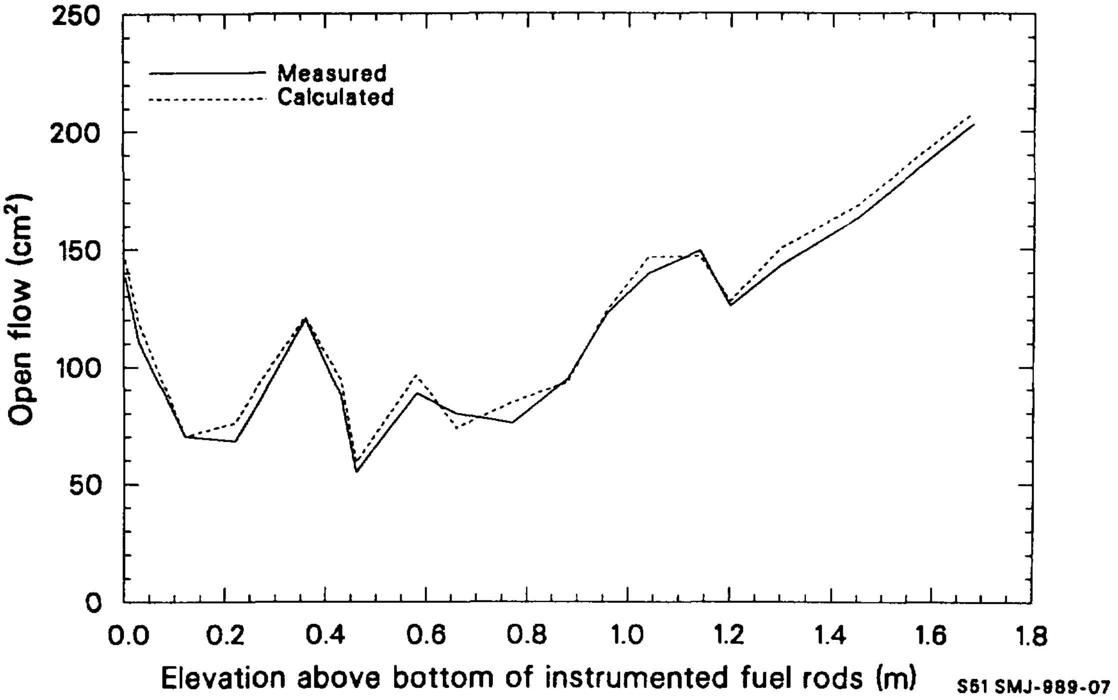

Figure 265. Comparison of measured and calculated open flow values in LP-FP-2.

basically intact and most of the component areas were calculated based upon as-fabricated dimensions. In these instances, measurement errors afffecting the total blockage are limited to only a few components. The best comparisons are at the A (0.003 m), B (0.03 m), and F (0.36 m) elevations, where most of the cross-sectional areas can be calculated and which have large open flow areas. The difference between calculated and measured open flow values in these instances approach the ideal condition of having open flow as the only measured quantity. For these elevations, the difference in the open flow values ranges from 1%-6%.

The magnitude of the estimated uncertainty also appears consistent with the empirical accuracy tests described in 4.1.1. The open flow areas generally had relatively small boundary/surface area ratios, and consequently uncertainty limits within 5% would be expected. Uncertainty limits of ±10% therefore provide a degree of conservatism.

4.1.2.17 Data Uncertainties and Biases. Because of the nature of the measurements, it was not possible to define rigid uncertainties. Instead, the uncertainties in the component measurements had to be estimated based upon empirical accuracy tests, internal consistency checks, and engineering judgment. The basis for estimating these uncertainties for each component have been described in each subsection. By examining the sum of the measured component data, it can be determined whether an overall bias exists in the data and whether all the cross-sectional area are reasonably accounted for.

Figure 266 plots the sum of all the measured data at each cross section against the as-fabricated bundle cross section of 456 cm^2. As tabulated in Appendix F, the resultant deviations were all less than 2%, which confirms that although there may be biases in some of the component data sets in one direction, there must be a corresponding bias in the other direction for other data sets. So, for the individual components, it may only be possible to set upper and lower limits because it is indeterminate whether the values are randomly distributed about a nominal value or whether there is a bias in the data due to the measurement technique. However, it is apparent for the overall flow blockage data that the errors are not all biased in one direction and in fact tend to cancel each other.

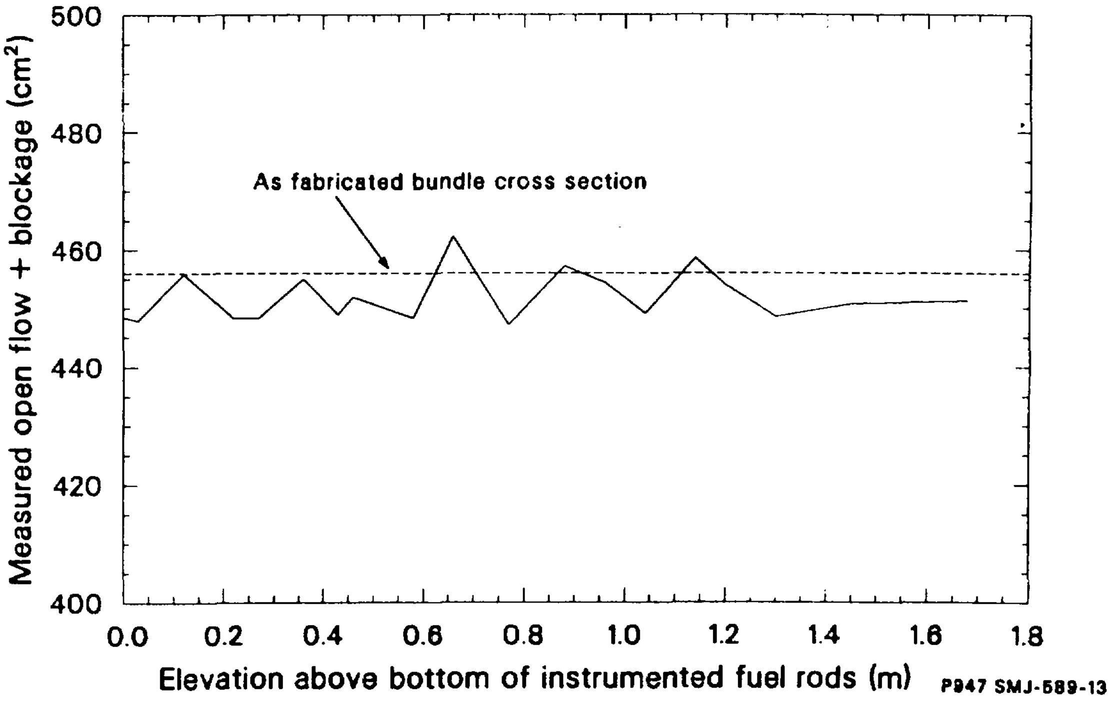

Figure 266. Comparison of the sum of the measured values with the as-fabricated total fuel bundle cross section (including insulation and shroud).

4.1.3 Integral Material Distribution Data

Interpolation of the cross-sectional measurement data provided integral volumes of each of the major categories of material in the bundle. These data are provided in Tables 4 and 5, along with upper and lower limits based upon the uncertainties in the measured data. These limits assumed that all the measurement data for a given component were biased high or low; and, as such, these limits are very conservative.

The integral results indicate that much more zircaloy liquefied than fuel. The results in Table 4 also indicate that approximately 70% of the (Ag,In,Cd) control rod material was released to the fuel bundle either as an aerosol or as molten material. [This is based on the data in Figure 258; additional droplets of (Ag,In, Cd) shown in Figure 262 are accounted for as metallic melts in Table 5.] The insulation results indicate that all the insulation is accountable for, which indicates that very little, if any, was dissolved in the melt regions. This suggests that the relocation of the insulation occurred after the bundle had cooled, perhaps even during subsequent handling of the fuel bundle. The largest volume of melt material was in the ceramic melt region, with large amounts of eutectic metallic melt/fuel debris accumulating in the lower portions of the bundle. Relatively small amounts of metallic melt material were distributed throughout the bundle.

4.1.4 Posttest Mass Balances for Uranium and Zirconium

Core bore samples were obtained from representative regions within the fuel bundle, and elemental analysis was performed on these samples to provide bulk compositional information. Density measurements were also performed on the core bore samples from the ceramic melt and eutectic metallic melt/fuel debris samples to enable estimates to be made of the total amount of material distributed in these regions. This section describes material balance calculations for the major constituents of uranium and zirconium. A mass balance could not be performed for silver because the core bore samples were dissolved in HCl acid, which caused the silver to precipitate out and not be measured accurately. This is discussed

TABLE 4. INTEGRAL VOLUMES OF MATERIAL IN LP-FP-2

Material	Pretest (cm^3)	Lower Limit (cm^3)	Nominal (cm^3)	Upper Limit (cm^3)
Fuel				
Intact		8919 (79%)	10025 (89%)	11133 (99%)
Fuel fragments		495 (4%)	688 (6%)	908 (8%)
Total	11273	9414 (84%)	10713 (95%)	12041 (107%)
Zircaloy				
Cladding	4163	1363 (33%)	1575 (38%)	1806 (43%)
Liner	2207	758 (34%)	767 (35%)	776 (35%)
Control material				
Ag,In,Cd	1475	386 (26%)	442 (30%)	498 (34%)
Stainless steel	319	88 (28%)	88 (28%)	88 (28%)
Spacer grid	366	124 (34%)	126 (34%)	129 (35%)
Insulation				
Intact		25974 (91%)	27251 (95%)	28528 (100%)
Melt/insulation		1495 (5%)	1760 (6%)	2024 (7%)
Total	28595	27469 (96%)	29011 (101%)	30552 (107%)

TABLE 5. INTEGRAL VOLUME OF MELT AND DEBRIS IN LP-FP-2

Material	Lower Limit (cm^3)	Nominal (cm^3)	Upper Limit (cm^3)
Ceramic melt	6070	6744	7418
Metallic melt	1181	1389	1598
Eutectic metallic melt/fuel debris	2517	2796	3076
Miscellaneous debris	10	20	30

in more detail in Section 4.5 and Appendix H. The data were insufficient to attempt to calculate material balances for other elements. These calculations provide data on the distribution of uranium and zirconium in the fuel bundle. The zirconium distribution data were later used to calculate zirconium oxidation and hydrogen generation. The overall mass balances for these elements also provide an internal consistency check on the material distribution measurements and methodology.

4.1.4.1 Material Distribution in the Ceramic Melt. The pertinent compositional and density data from core bore samples in the ceramic melt region are summarized in Table 6. Additional detailed information on these samples is provided in Section 4.5 and Appendix H.

The first step in estimating the amount of uranium and zirconium in the ceramic melt region was to average the compositional and density data for each elevation shown in Table 6. Single values were required to be able to interpolate between the elevations. Upper and lower limits based upon 1 standard deviation were also calculated for the I elevation, but for the other elevations there were insufficient data for such limits. The results are summarized in Table 7.

The uranium and zirconium in the ceramic melt region were calculated by interpolating between the various elevations, using the values in Table 7 along with the volume of ceramic material in each axial node. Upper and lower limits were calculated using the respective limits for the densities, compositions, and volumes of ceramic melt in a given axial node, as shown in Equation (1). (This equation is also used to calculate the uranium and zirconium in the eutectic metallic melt/fuel debris and metallic melt regions as described in Sections 4.1.4.2 and 4.1.4.3.) The I elevation values were used for all the ceramic melt below the midpoint between the I and J elevations; the J data were used from the midpoint between the I and J elevations to the midpoint between the J and K elevations; the K data were used similarly to the J data; and the L data were used for all the ceramic melt above the K-L midpoint. The results of these calculations are shown in Tables 8 and 9, along with other calculated values described in the following sections.

TABLE 6. ELEMENTAL ANALYSIS AND DENSITIES OF CORE BORE SAMPLES IN THE CERAMIC MELT REGION

Sample	U (wt%)	Zr (wt%)	ρ (g/cm^3)
I2-R2	28	12	7.95
I2-R18	44	33	6.30
I2-R1	36	39	6.97
I4-R19	37	36	4.73
J2-R21	54	26	8.38
K1-R6	47	33	6.01
K1-R7	46	29	5.65
L2-R24	43	30	4.95

TABLE 7. VALUES USED TO CALCULATE MATERIAL BALANCE IN CERAMIC MELT

	Lower	Nominal	Upper	Elevation
Uranium (wt%)	29.8	36.3	42.9	I
Zirconium (wt%	17.8	30.0	42.2	I
Density (g/cm^3)	5.1	6.5	7.8	I
Uranium (wt%)	54.0	54.0	54.0	J
Zirconium (wt%	26.0	26.0	26.0	J
Density (g/cm^3)	8.4	8.4	8.4	J
Uranium (wt%)	46.5	46.5	46.5	K
Zirconium (wt%	31.0	31.0	31.0	K
Density (g/cm^3)	5.8	5.8	5.8	K
Uranium (wt%)	43.0	43.0	43.0	L
Zirconium (wt%	30.0	30.0	30.0	L
Density (g/cm^3)	5.0	5.0	5.0	L

TABLE 8. URANIUM MASS BALANCE IN LP-FP-2

Location	Low Estimate (g)	Nominal Estimate (g)	Upper Estimate (g)
Ceramic melt	1.5E4 (14%)[a]	1.8E4 (15%)[a]	2.2E4 (16%)[a]
Eutectic melt/fuel debris	2.1E3 (2%)	2.3E3 (2%)	2.6E3 (2%)
Metallic melt	3.8E2 (0.3%)	9.6E2 (1%)	2.1E3 (2%)
Intact fuel	8.2E4 (79%)	9.2E4 (77%)	1.0E5 (74%)
Fuel fragments	4.5E3 (4%)	6.3E3 (5%)	8.3E3 (6%)
Posttest total	1.0E5	1.2E5	1.4E5
Pretest total	1.0E5	1.0E5	1.0E5
Δ%	0%	20%	40%

---

[a] Percentages are normalized to posttest total.

TABLE 9. ZIRCONIUM MASS BALANCE IN LP-FP-2

Location	Low Estimate (g)	Nominal Estimate (g)	Upper Estimate (g)
Ceramic melt	9.1E3 (28%)[a]	1.2E4 (29%)[a]	1.6E4 (32%)[a]
Eutectic melt/fuel debris	4.9E3 (15%)	5.4E3 (13%)	6.0E3 (12%)
Metallic melt	1.5E3 (5%)	3.0E3 (7%)	5.2E3 (10%)
Melt/insulation	4.1E3 (13%)	5.6E3 (14%)	6.9E3 (14%)
Intact cladding and liner	1.3E4 (40%)	1.5E4 (37%)	1.6E4 (32%)
Posttest total	3.3E4	4.1E4	5.0E4
Pretest total	4.1E4	4.1E4	4.1E4
Δ%	-20%	0%	22%

---

a. Percentages are normalized to posttest total.

$$m = \Delta v \rho W \quad (1)$$

where

m = quantitity of uranium or zirconium (g)

Δ = uncertainty factor in flow blockage area measurements

= 0.9 for lower limit for ceramic melt and eutectic metallic melt/fuel debris

= 0.85 for lower limit for metallic melt droplets

= 1.0 for nominal case

= 1.1 for upper limit for ceramic melt and eutectic metallic melt/fuel debris

= 1.15 for upper limit for metallic melt droplets

v = nominal volume of material in axial node (cm^3)

ρ = appropriate density for lower, nominal, and upper limit conditions (g/cm^3)

W = appropriate weight fraction of uranium or zirconium for lower, nominal, and upper limits

4.1.4.2 <u>Material Distribution in the Eutectic Metallic Melt/Fuel Debris</u>. The pertinent compositional and density data from three locations through the lower blockage are summarized in Table 10. Further details on these samples are provided in Section 4.5 and Appendix H.

Similar interpolation methods were used to calculate the uranium and zirconium in these regions, as were used in the ceramic melt region. The data from the C elevation were used for all the material below the midpoint

TABLE 10. DATA USED TO CALCULATE MATERIAL BALANCES IN EUTECTIC METALLIC MELT/FUEL DEBRIS REGIONS

Sample	U (wt%)	Zr (wt%)	ρ (g/cm^3)
C2-R12	4.9	39.0	5.75
D4-R14	10.0	32.0	5.36
E2-R15	45.0	24.0	6.91

between the C and D elevations; the D elevation data were used from the C-D midpoint to the D-E midpoint. The E elevation was atypical in that it contained many more fuel fragments than other elevations; consequently, the E elevation data were used from the D-E midpoint to the F elevation. It was extended all the way to the F elevation because most of the material in this region was located near the E elevation. At and above the F elevation, the material was more typical of that found at the C and D elevations (less fuel fragments), so an average of the C and D data was used. Upper and lower limits were based upon the 10% estimated uncertainty in measuring the cross-sectional areas of these regions. The data were calculated using Equation (1), and the results are tabulated in Tables 8 and 9.

4.1.4.3 Material Distributions in Metallic Melts. A summary of the elemental analysis of metallic melt droplets is shown in Table 11. In this table, only elements with concentrations >1 wt.% are tabulated; a more detailed description is available in Appendix H. It should be noted that elemental analyses for silver were performed on these and all other samples; however, the measured concentrations are believed to underestimate the actual concentrations. These samples were dissolved in HCl acid, which would have caused silver to precipitate out and not be measured in the ICP analysis. This effect was particularly apparent in the elemental analysis of sample B4-R11, which consisted of a droplet of control rod material alloy. The analysis indicated only 3.7 wt.% silver, with 12.7 wt.% In and 3.8 wt.% Cd, in contrast to the 80:15:5 ratio in the Ag-In-Cd alloy. Similarly, analyses of samples from the lower blockage region indicated very low silver concentrations (<3 wt.%), which were in contrast to metallographic and SEM results that indicated significant amounts of silver were in these regions in the form of Ag-Zr eutectic metallic melts. Consequently, the silver concentrations shown in Table 11 should only be interpreted as providing an indication of the presence of silver. This is discussed in more detail in Section 4.5 and Appendix H. It should be noted that analyses of deposition coupon data from above the LP-FP-2 fuel module indicated that only approximately 20 g of silver had relocated out of the fuel module.[10] This very small amount would be undetectable from the postirradiation examinations of the fuel bundle, even if reliable dissolution processes had been utilized.

TABLE 11. COMPOSITION OF CORE BORES FROM METALLIC MELTS

Sample	Composition (wt%)	Comments
B4-R11	(3.7% Ag)[a], 3.8% Cd, 2.2% Cr, 2.1% Fe, 12.7% In	Droplet of control material in the bottom of the bundle
I4-R3	(6.0% Ag)[a], 6.5% Cr, 15.1% Fe, 11.5 Ni, 11% U, 47% Zr	Multiphase
K1-R23	(2.6% Ag)[a], 1.6% Cr, 3.7% Fe, 2.8% Ni, 4.2% In, 19% U, 33% Zr	Multiphase
Q3-R9	(3.7% Ag)[a], 2.7% Cr, 11.7% Fe, 3.6% Ni, 5% In, 8.2% U, 41% Zr	Multiphase

---

a. Measured silver concentrations underestimate the actual concentration and should only be interpreted as providing an indication of the presence of some silver.

Metallographic observations suggested that the droplets of metallic melt located below the second spacer grid were primarily control material alloy. These droplets had an orange tint when viewed on the metallograph, just as the intact control material alloy did; this was a consequence of the xenon lighting and filters used on the metallograph. In contrast, metallic melts from higher in the fuel bundle were multiphase mixtures with larger concentrations of fuel, zircaloy, and stainless steel. Interpolation of the distribution of metallic melts at and below the second spacer grid indicated 313 cm^3 of control material droplets. Similar interpolations of metallic melt above the second spacer grid indicated a total volume of 1076 cm^3. Estimates of the amount of uranium and zirconium in these multiphase metallic melts were based upon assumed densities of 5, 7, and 9 g/cm^3 (based on density ranges of zircaloy, stainless steel, and control material alloy). Upper and lower limits were based upon these bounding densities and 15% uncertainties in the cross-sectional measurements of the metallic melts. The mass quantities of uranium and zirconium in these metallic melts were calculated using Equation (1), and the results are tabulated in Tables 8 and 9.

4.1.4.4 Material Distribution in Melt/Insulation Regions. Melt penetrated into the low-density ZrO_2 insulation in the central regions of the fuel bundle. As described in Appendix E, sometimes this metallic melt oxidized to form ZrO_2; other times, the metallic melt consisted of unoxidized mixtures of zirconium, stainless steel, and control rod materials. However, it was impossible to accurately determine from the metallography which areas consisted of metallic melts in the insulation and which areas consisted of oxidized melts in the insulation. SEM/WDS analysis of two samples from these melt/insulation regions provided some data to estimate the area fractions of metallic phase within the metallic melt regions. (The remainder of the area within the metallic melt regions was composed of ZrO_2 insulation particles.) Quantitative analysis was also performed in one location to provide some compositional data on the metallic melt. As detailed in Appendix E for samples K1-S31 and M3-S33, these examinations indicated area fractions of metallic phase, contained within the metallic melt regions, ranging from 47-63%. The amount of unoxidized zirconium in the metallic phase, contained within the metallic melt regions, was 77 wt.% at the one point analyzed. The values shown in Table 9 were calculated using Equation (2) and the respective volumes of melt/insulation shown in Table 4. The first term in Equation (2) represents the amount of zirconium in the unoxidized metallic melt regions, whereas the second term represents the amount of zirconium in the oxidized melt regions. In these calculations, the fraction of the measured melt/insulation volume (f_m), which was assumed to contain unoxidized metallic melt, was estimated to range from 25%-75%. The remainder of the melt/insulation volume ($1-f_m$), was assumed to contain oxidized zirconium that had filled the porous regions in the ZrO_2 insulation. (These regions can be seen on SEM/WDS sample K1-S31.) This insulation was nominally 20%TD, so 80% of the theoretical density of ZrO_2 was available for melt penetration.

$$Zr = vf_m f_{mp}(7)(0.77) + v(1 - f_m)(0.8)(5.8)\left(\frac{91.22}{123.22}\right) \tag{2}$$

where

Zr = zirconium in melt insulation region (g)

v = volume of melt/insulation (cm^3)

= 1495 for lower limit

= 1760 for nominal case

= 2024 for upper limit

f_m = fraction of melt/insulation that is metallic melt

= 0.75 for lower limit

= 0.50 for nominal case

= 0.25 for upper limit

f_{mp} = fraction of metallic phase in metallic melt

= 0.47 for lower limit

= 0.55 for nominal case

= 0.63 for upper limit

7 = assumed density of metallic melt in melt/insulation (g/cm^3)

0.77 = weight fraction of zirconium in metallic phase in metallic melt

0.8 = fraction of area within ZrO_2 insulation available for melt penetration

5.8 = theoretical density of ZrO_2 (g/cm^3)

123.22 = molecular weight of ZrO_2 (g/mole)

91.22 = atomic weight of zirconium (g/mole)

4.1.4.5 Calculation of Material Quantities Not in the Melt Regions. The mass quantities of uranium in the intact fuel and fuel fragment categories shown in Table 8 were calculated using Equation (3). The zirconium in the remaining intact portions of the cladding and liner shown in Table 9 were calculated using Equation (4). Upper and lower limits were based upon the corresponding upper and lower volume limits in Table 4. The pretest quantities of these elements were also calculated using these equations and the data in Table 4.

$$U = \frac{v(0.9467)(10.96)(238)}{270} \qquad (3)$$

where

U = uranium in fuel (g)

v = volume of material (cm^3)

0.9467 = as-fabricated fraction of theoretical density of fuel

10.96 = theoretical density of UO_2 (g/cm^3)

238 = atomic weight of uranium (g/mole)

270 = molecular weight of UO_2 (g/mole)

$$Zr = v(6.49)(0.98) \tag{4}$$

where

Zr = zirconium in zircaloy (g)

v = volume of material (cm^3)

6.49 = density of zirconium (g/cm^3)

0.98 = weight fraction of zirconium in zircaloy

4.1.4.6 Material Balance Sums. Tables 8 and 9 show the total mass quantities of uranium and zirconium in each region of the bundle and compare them to preirradiation quantities. For the nominal conditions, the material balance overpredicts the amount of uranium and predicts the amount of zirconium. The overprediction in the uranium mass balance may be partially due to overestimating the amount of fuel present at each metallographic cross section. It is recognized that problems associated with fuel cracking could easily lead to such an overprediction. These data suggest that the lower estimated values for the cross-sectional and integral volumes of intact fuel and fragmented fuel may be more accurate. The good agreement in these material balance calculations indicates that the material distribution measurements and methodology provide a reasonable approximation of the actual conditions.

These data also provide information on the amount of molten uranium and zirconium and the partitioning of these elements among the various melts. Approximately 63 wt.% of the zircaloy was liquefied; however, only about 15 wt.% of the fuel was liquefied. Most of these liquefied materials were located in the ceramic melt region, although significant amounts of zirconium were located in the eutectic metallic melt material in the lower blockage and in the melt that penetrated the insulation. This reflects the dissolution of unoxidized zircaloy by silver to form the lower blockage and the melting of the inner liner. The small amount of fuel in the eutectic metallic melt/fuel debris region consisted of powdered fuel fragments (grain size or slightly larger).

4.2 Oxidation and Hydrogen Generation

The following sections describe the measurement and analyses techniques used to estimate the total oxidation and hydrogen generation in the LP-FP-2 fuel bundle. This includes oxidation of zircaloy, stainless steel, and Inconel components in the fuel bundle. Fuel oxidation did not occur in this test. These results indicate that only a small fraction of the total zircaloy oxidation occurred prior to cladding failure and zircaloy relocation. Most of the oxidized zircaloy is contained in the ceramic melt regions, with significant amounts also in the eutectic metallic melt in the lower blockage region. The oxidation of the stainless steel control rod cladding and upper tie plate and the Inconel spacer grids also contributed significant amounts to the total hydrogen generation in the bundle.

4.2.1 Zircaloy Oxidation

This section describes the data and analyses used to estimate the amount of oxidation and hydrogen generation from the zircaloy cladding and inner liner. Section 4.2.2 describes the oxidation and hydrogen generation from nonzircaloy components, and the total amounts of oxidation and hydrogen generation are discussed in Section 4.2.3.

4.2.1.1 Zircaloy Oxidation Measurement Data. Small oxide layers were present on the zircaloy components below the I elevation (0.66 m). Measurements of these oxide thicknesses were obtained from photomicrographs, and average values are tabulated in Table 12. Very small amounts of oxidized zircaloy were observed on a few rods in the center of the fuel bundle as low as the C elevation (0.12 m). This oxidation is insignificant in terms of the total bundle oxidation, but the spatial location of this oxidation within the cavity of the lower blockage is significant. It indicates that zircaloy oxidation was occurring very low in the bundle prior to the complete relocation of the eutectic metallic melt/fuel debris that formed the lower blockage. As described in more detail in Section 3.2.3, at succeedingly higher elevations the spatial distribution of the zircaloy oxidation increased in thickness and spread radially until complete

TABLE 12. AVERAGE ZIRCALOY OXIDATION THICKNESSES IN PARTIALLY OXIDIZED BUNDLE REGION

					INNER LINER				
	Cladding		Guide Tubes		Inner Surface		Outer Surface		
Elevation	ZrO_2 (μm)	α-Zr(O) (μm)	ZrO_2 (μm)	α-Zr(O) (μm)	ZrO_2 (μm)	α-Zr(O) (μm)	ZrO_2 (μm)	α-Zr(O) (μm)	Comments
A	0	0	0	0	0	0	0	0	--
B	0	0	0	0	0	0	0	0	--
C	Negligible		Negligible		0	0	0	0	$ZrO_2 < 10$ μm on some central rods
D	Negligible		Negligible		0	0	0	0	$ZrO_2 < 30$ μm on some central rods
E	Negligible		Negligible		0	0	0	0	$ZrO_2 < 10$ μm on some central rods
F	Negligible		Negligible		0	0	0	0	$ZrO_2 < 10$ μm on some central rods
G (bott)	15	28	--	--	9	17	17	23	Small oxide layers on all rods
G (top)	17	20	10	13	10	17	10	15	Small oxide layers on all rods
H	230*	**	91	61	58	71	--	--	*ZrO_2 = 66 μm in corners, 225 μm intermediate, 400 interior Average = 230 μm **68 μm α-Zr(O) in corner positions; elsewhere the α-Zr(O) had melted (T >2245 K)

oxidation of the remaining zircaloy was observed at and above the I elevation. During the test, the oxidation of the cladding would have started in the hotter portion of the fuel bundle, probably somewhat above core midplane, and spread radially and axially from that point to produce the posttest oxidation profile.

In regions that were fully oxidized posttest, the unoxidized inner surface of the zircaloy cladding had melted during the experiment, leaving only the fully oxidized outer shell of cladding. (Unoxidized zircaloy melts at 2030 K, whereas alpha-zirconium melts at 2245 K and ZrO_2 melts at 2960 K.) Essentially all of the inner liner had also melted above the I elevation. Oxide thickness measurements at these upper elevations are tabulated in Table 13, using average values for exterior, intermediate, and interior fuel rod positions, as well as average values for the guide tubes and shroud. It was generally found that oxide thicknesses varied significantly as a function of radial position, and this grouping was an attempt to see if a consistent pattern developed axially. However, no such axial pattern was found, which suggests that a nonuniform steam flow distribution existed in the fuel module.

Relocated zircaloy was found in the ceramic melt regions in the upper portions of the fuel bundle and in the eutectic metallic melt in the lower portions of the bundle. It had also penetrated into the insulation where the inner liner had melted. Based upon metallographic observations and SEM/WDS examinations of samples I2-S1, J2-S4, and K1-S6, the ceramic melt was composed of $(U,Zr)O_2$ with small amounts of other bundle constituents mixed in. SEM/WDS analyses of sample C2-S11 from the lower blockage region indicated that the eutectic metallic melt/fuel debris that formed this region was composed primarily of three phases: (Ag,In,Cd) control material; oxidized Zr mixed with Ag and In; and unoxidized Zr mixed with Ag, In, Fe, and Ni. SEM/WDS examinations of samples M3-S33 and K1-S31 indicated that the melt that penetrated the insulation was primarily composed of zirconium and iron, with only some of the zirconium being oxidized. Hence, the zirconium in the ceramic melt was fully oxidized; and the zirconium in the lower blockage region and the zirconium that penetrated into the insulation were partially oxidized.

TABLE 13. AVERAGE ZrO_2 THICKNESS IN FULLY OXIDIZED BUNDLE REGION

	Fuel Rod Cladding Averages								
Elevation	Exterior (μm)	Intermediate (μm)	Interior (μm)	Corner Guide Tube (μm)	Edge Guide Tube (μm)	Intermediate Guide Tube (μm)	Interior Guide Tube (μm)	Shroud Inner Surface (μm)	Shroud Outer Surface (μm)
I	206	237	294	458	--	--	--	--	--
J	312	186	319	--	314	--	--	--	8
K	--	251	188	--	336	--	473	12	12
L	397	414	564	178	204	176	--	4	17
M	288	474	--	462	--	146	408	15	19
N	330	246	--	--	--	506	--	0	24
O	--	628	--	--	--	238	--	4	9
P	--	--	--	--	--	--	--	--	--
Q	--	--	--	--	--	--	--	--	--
R	--	--	--	--	--	--	--	--	--

4.2.1.2 Upper Limit for Zircaloy Oxidation. An upper limit to the zircaloy oxidation in the fuel bundle was established by assuming that all the previously molten zircaloy had fully oxidized. Together with oxide thicknesses measured on intact cladding, this established an upper limit of 1226 g of hydrogen resulting from zircaloy oxidation. This upper limit was later used to estimate the hydrogen generated in the experiment, by subtracting the unoxidized zirconium in the various melt regions. This is described in more detail in sections 4.2.1.3 and 4.2.1.4.

At and below the F elevation (0.36 m), the oxidation was limited to negligible amounts on some of the central rods. For the purposes of these calculations, no zircaloy oxidation was considered to have occurred in this region. Small amounts were observed across the entire assembly at both of the G cross sections (0.43-0.45 m), and significant amounts were measured at the H elevation (0.58 m). The cross-sectional amounts of ZrO_2 were calculated for these elevations using the average oxide thicknesses in Table 12 and curveimeter measurements of the length of the remaining cladding. These cross-sectional areas are tabulated in Table 14, along with the amount of cladding and liner missing from each of these cross sections.

The amount of hydrogen generated as a result of zircaloy oxidation can be calculated based upon the following chemical equation:

$$Zr + 2H_2O \rightarrow ZrO_2 + 2H_2. \qquad (5)$$

This reaction shows that for every mole of Zr or ZrO_2, 2 moles of H_2 will be produced. Based upon this chemical equation, the maximum amount of hydrogen that could be generated in the interval from the G(bottom) to the I elevation, shown in Table 15, can be calculated using Equations (6) and (7). Equation (6) calculates the amount of hydrogen generated from the measured ZrO_2 oxide thicknesses, whereas Equation (7) calculates the hydrogen generated from the zircaloy that melted.

TABLE 14. OXIDIZED AND MOLTEN AMOUNTS OF ZIRCALOY FROM G(BOTTOM) TO I ELEVATIONS

Elevation	Oxidized Cladding + Liner (cm^2)	Molten Cladding + Liner (cm^2)
G_B	0.62	5.47
G_T	0.52	12.42
H	2.82	22.41
I	2.29	32.93

TABLE 15. CALCULATED AMOUNTS OF HYDROGEN GENERATED FROM ZIRCOLOY (G BOTTOM) TO I ELEVATION

Axial Interval	Oxidized Cladding + Liner (g)	Molten Cladding + Liner (g)
G_B-G_T	0.2	5.7
G_T-H	3.9	61.7
H-I	3.8	61.0
Total	7.9	128.4

$$H_2 = \frac{(v)(0.98)(5.8)}{123.22} \left[\frac{2 \text{ moles } H_2}{\text{mole } ZrO_2}\right] \left[\frac{2g}{\text{mole } H_2}\right] \tag{6}$$

where H_2 = hydrogen from oxidized zircaloy (g)

v = volume of oxidized zircaloy (cm^3)

0.98 = weight fraction of Zr in zircaloy

5.8 = density of ZrO_2 (g/cm^3)

123.22 = molecular weight of ZrO_2 (g/mole)

$$H_2 = \frac{(v)(0.98)(6.49)}{91.22} \left[\frac{2 \text{ moles } H_2}{\text{mole Zr}}\right] \left[\frac{2g}{\text{mole } H_2}\right] \tag{7}$$

where H_2 = hydrogen from molten zircaloy (g)

v = volume of zircaloy which melted (cm^3)

0.98 = weight fraction of zirconium in zircaloy

6.49 = density of zirconium (g/cm^3)

91.22 = atomic weight of zirconium (g/mole)

Above the I elevation, all the remaining zircaloy is fully oxidized (except for a negligible amount at the Q elevation). The amount of fuel rod cladding above the I elevation for the uninstrumented and instrumented fuel rods can be calculated based upon Figure 3, and it corresponds to 2215 cm^3. The amount of zircaloy guide tubes from the I elevation to the upper tie plate is 324 cm^3, and the amount of inner liner above the I elevation to the upper tie plate is 1370 cm^3. The total amount of zircaloy above the I elevation is therefore 3909 cm^3. The maximum amount of hydrogen that could be generated by fully oxidizing all the zircaloy above the I elevation can be calculated by inserting 3909 cm^3 into Equation (7). This calculation indicates a total of 1090 g of hydrogen. The upper limit for hydrogen generation as a result of zircaloy oxidation in the LP-FP-2 fuel bundle is therefore the sum of the amounts calculated in Table 15 for the region below the I elevation, plus the amount above the I elevation. This summation gives a maximum upper limit of 1226 g of hydrogen from zircaloy oxidation, which corresponds to 69% oxidation of all the zircaloy in the fuel bundle.

4.2.1.3 Estimation of Unoxidized Molten Zircaloy. The total amount of zirconium in the eutectic metallic melt/fuel debris regions was calculated from the cross-sectional area measurements, density measurements, and elemental analysis of core bore samples taken from these regions. The details are described in Section 4.5. SEM/WDS analysis of sample C2-S11 indicated that some of the zirconium in this region was oxidized, but some of it was unoxidized. It was not possible to extrapolate the quantitative SEM/WDS results from these examinations to estimate the fraction of oxidized zirconium in these region, because it was not possible to determine how much of each phase (containing oxidized and unoxidized zirconium) was present. It was therefore assumed that nominally 50% of the zirconium was oxidized, with upper and lower limits of 75% and 25% of the total zirconium. Using the zirconium content values shown in Table 9 this assumption resulted in nominally 2700 g of zirconium, with lower and upper limits of 1225 and 4500 g, possibly being oxidized (or equivalently unoxidized). This corresponds to a nominal value of 118 g of hydrogen, with lower and upper limits of 54 and 197 g. To estimate the amount of hydrogen generated from zircaloy oxidation in the fuel bundle, these amounts were subtracted from the 1226 g upper limit calculated in Section 4.2.1.2.

SEM/WDS examinations of samples K1-S31 and M3-S33 indicated that some of the zirconium that had penetrated into the insulation was oxidized and some was not. Areas in which the melt was oxidized could not be distinguished from metallic melt areas metallographically, and there were no data to indicate the partitioning ratio. It was therefore assumed that 25%-75% of each category was a reasonable estimate. As described in Section 4.1.3, the total volume of melt/insulation was estimated to nominally be 1760 cm^3, with lower and upper limits of 1495 and 2024 cm^3. Based upon the assumed partitioning, this corresponds to 880 cm^3, with lower and upper limits of 374 and 1518 cm^3 of metallic melt regions that may have been contained in the melt/insulation regions. The estimated amounts of hydrogen that would not have been oxidized in these metallic melt regions were then calculated using Equations (8) through (10). The fractional values used in these equations were based upon the SEM/WDS results, as described in Appendix E. The results of these calculations indicated that for the nominal conditions, 114 g of hydrogen would not have been produced, with lower and upper limits of 42 and 226 g. To estimate the amount of oxidized zirconium in the fuel bundle, these amounts were subtracted from the 1226 g upper limit, as described in Section 4.2.1.4.

$$H_2 = \frac{(1518)(0.63)(0.77)(7)(4)}{91.22} \qquad (8)$$

where

H_2 = upper limit to hydrogen not produced in melt/insulation (g)

1518 = upper limit of metallic melt in melt/insulation (cm^3)

0.63 = upper area fraction of metallic phase in metallic melt

0.77 = weight fraction of zirconium in metallic phase

7 = assumed average density of metallic melt (g/cm^3)

4 = 4 g H_2 per mole zirconium

91.22 = atomic weight of zirconium (g/mole)

$$H_2 = \frac{(880)(0.55)(0.77)(7)(4)}{91.22} \qquad (9)$$

where H_2 = nominal limit to hydrogen not produced in melt/insulation (g)

880 = nominal volume of metallic melt in melt/insulation (cm^3)

0.55 = nominal area fraction of metallic phase in metallic melt

0.77 = weight fraction of zirconium in metallic phase

7 = assumed density of metallic melt (g/cm^3)

4 = 4 g H_2 per mole zirconium

91.22 = atomic weight of zirconium (g/mole)

$$H_2 = \frac{(374)(0.47)(0.77)(7)(4)}{91.22} \qquad (10)$$

where H_2 = lower limit to hydrogen not produced in melt/insulation (g)

326 = lower limit of metallic melt in melt/insulation (cm^3)

0.47 = lower area fraction of metallic phase in metallic melt

0.77 = weight fraction of zirconium in metallic phase

7 = assumed density of metallic melt (g/cm^3)

4 = 4 g H_2 per mole zirconium

91.22 = atomic weight of zirconium (g/mole)

As described in Section 4.1.4, large uncertainties are associated with the amount of zirconium contained in metallic melts throughout the fuel bundle. Based upon the limits shown in Table 9 in Section 4.1.4, 1500-5200 g of zirconium may have been in these metallic melts. Assuming that all the zirconium in these melts was unoxidized, 132 g of hydrogen would not have been produced in the nominal case, with lower and upper limits of 66 and 228 g.

4.2.1.4 Best Estimate of Hydrogen Generation From Zircaloy Oxidation. Subtraction of the unoxidized zirconium in the various melts from the 1226 g upper limit established in Section 4.2.1.2, provided the best estimate of the hydrogen generated solely from zircaloy oxidation. This method was considered to be superior to an alternative method described in Section 4.2.1.5, which was based upon the sum of oxidized zirconium in various regions, because of reduced uncertainties. The advantage of the second method was that it provided data on the distribution of oxidized zirconium.

Table 16 summarizes the calculations, described in detail in Section 4.2.1.3, that were used to provide the best estimate of the amount of hydrogen generated solely from zirconium in the LP-FP-2 fuel bundle. 862 g of hydrogen were nominally estimated, with lower and upper limits of 575 and 1064 g respectively. For the nominal case, this corresponds to 49% of the zirconium in the inner liner, cladding, and guide tubes, with the lower and upper limits corresponding to 32% and 60%. The large uncertainties are due to the conservatism incorporated in minimizing and maximizing these estimates. However, as discussed in Sections 4.2.1.5 and 4.2.3, good agreement between these calculations and two independent methods indicates that there is a high probability that the actual amount of hydrogen generation is near the nominal estimate.

4.2.1.5 Hydrogen Generation Based Upon Sum of Oxidized Zirconium. An alternate method for calculating the amount of zircaloy oxidation in the bundle was performed that has greater uncertainties but does provide information on the distribution of the oxidized zirconium in the various regions of the bundle. This alternate method sums up the oxidized zirconium

TABLE 16. BEST ESTIMATE OF HYDROGEN GENERATION FROM ZIRCALOY

	H_2 (g)		
	Lower	Nominal	Upper
Upper limit from zircaloy oxidation = 1226 g			
Unoxidized Zr in eutectic metallic melt	-197	-118	-54
Unoxidized Zr in melt/insulation	-226	-114	-42
Unoxidized Zr in metallic melts	-228	-132	-66
Total hydrogen from zircaloy oxidation	575	862	1064

in the various regions, as opposed to subtracting the unoxidized zirconium from an upper limit. This information can be used in conjunction with postulated bundle scenarios to provide information on heat generation in the various regions of the bundle at various times during the experiment, and it also provides an independent check on the amount of zircaloy oxidation and hydrogen generation calculated in Section 4.2.1.4.

The amount of zircaloy oxidation resulting from the oxidized ZrO_2 cladding shells can be simply estimated by calculating the volume of these shells. The cross-sectional ZrO_2 areas from G_b-I are listed in Table 14, and the cross-sectional areas of ZrO_2 above the I elevation can be obtained from Tables F-10 through F-19 in Appendix F, since essentially all the zircaloy in these regions was fully oxidized. Interpolation of these values provided a total volume of 339 cm^3 of ZrO_2. Using Equation (11), this corresponds to 63 g of hydrogen. Based upon a 40% possible uncertainty in the average cladding thicknesses and 5% uncertainty in the cladding length measurements, this results in lower and upper limits of 36 and 93 g of hydrogen.

$$H_2 = \frac{(v)(5.8)(4)(0.98)}{123.22} \tag{11}$$

where H_2 = hydrogen generated from oxidized zircaloy cladding (g)

v = volume of ZrO_2 (cm^3)

5.8 = density of ZrO_2 (g/cm^3)

123.22 = molecular weight of ZrO_2 (g/mole)

4 = 4 g H_2 per mole ZrO_2

0.98 = weight fraction of Zr in zircaloy

The amount of oxidized zirconium in the ceramic melt regions can be calculated based upon the mass quantities estimated in Section 4.1.4. These mass quantities were based upon density measurements and elemental analysis of core bore samples from the ceramic melt regions. For these calculations, the amount of zirconium in the upper blockage region was separated from the amount of zirconium calculated to be in the ceramic melts above the upper blockage region. Based upon the density and elemental analysis of core bore sample L2-R24, the lower, nominal, and upper limits of Zr in the ceramic melt above the upper blockage were calculated to be 3996, 4440, and 4884 g. This corresponds to 175, 195, and 214 g of hydrogen. Similar calculations for the Zr in the upper blockage region indicated 225, 327, and 471 g of hydrogen.

In the melt/insulation region, the lower, nominal, and upper limits of hydrogen generation were calculated using Equation (12). These calculations indicated that 133 g of hydrogen may have been produced from zircaloy oxidation in these regions for the nominal conditions, with lower and upper limits of 56 and 229 g, respectively.

$$H_2 = \frac{(v)\left[f_{ZrO_2}\right](5.8)(0.80)(4)}{123.22} \qquad (12)$$

where H_2 = hydrogen generated from oxidation of Zr in melt/insulation region

v = volume of melt/insulation (cm^3)

= 1495 for lower limit

= 1760 for nominal condition

= 2024 for upper limit

f_{ZrO_2} = fraction of melt which is fully oxidized

= 0.25 for lower limit

= 0.50 for nominal condition

= 0.75 for upper limit

5.8 = density of ZrO_2 (g/cm^3)

0.80 = fraction of area within ZrO_2 insulation available for melt penetration. As-fabricated insulation density was nominally 20%TD.

4 = 4 g H_2 per mole ZrO_2

123.22 = molecular weight of ZrO_2 (g/cm^3)

In the eutectic metallic melt regions, the calculations are exactly as were used to estimate the unoxidized zirconium, since it was assumed that the unoxidized limits were 25%-75% and hence the values for the oxidized zirconium are identical. Therefore, the amount of hydrogen produced from these regions was nominally 118 g, with lower and upper limits of 54 and 197 g of hydrogen, respectively.

The estimated amount of hydrogen generated solely from zirconium using this methodology is summarized in Table 17. The total amounts are in very good agreement with the hydrogen estimates displayed in Table 16. The greater limits shown in Table 17 reflect the increased uncertainties associated with calculating the amount of oxidized zirconium in the ceramic melt region in the second method, as opposed to calculating the amount of unoxidized zirconium in the smaller metallic melt regions using the first method. The conservatism incorporated in determining the lower and upper limits in Table 17 is apparent in comparing the upper limit of 1204 g of

TABLE 17. HYDROGEN GENERATION FROM ZIRCALOY OXIDATION IN VARIOUS REGIONS OF LP-FP-2[a]

	LOWER	NOMINAL	UPPER
Oxidized ZrO_2 cladding shells	36	63	93
Eutectic metallic melt	54	118	197
Ceramic melt in large blockage (<0.92m)	225	327	471
Ceramic melt above large blockage (>0.92m)	175	195	214
Melt/insulation	56	133	229
Total from Zirconium	546	836	1204

---

a. These values were calculated using alternate methods than those used to estimate the hydrogen from zircaloy oxidation in Table 16.

hydrogen in this table with the absolute fuel bundle upper limit of 1226 g estimated in Section 4.2.1.2. Since there are significant amounts of unoxidized zirconium in various melt regions, this comparison indicates that the upper and lower limits are indeed very conservative.

The good agreement between the nominal estimates using alternate methods, 862 versus 836 g of hydrogen, is one indication that there is a high probability that the actual value is close to the nominal values. Additional data from independent analyses of samples from the blowdown suppression tank and the primary coolant system also suggest that there is a high probability that the nominal estimates reasonably reflect the actual conditions. This is described in detail in Section 4.2.3.

The results in Table 17 indicate that very little of the zircaloy oxidation was associated with oxidized zircaloy cladding shells. Most of the zircaloy oxidation was associated with previously molten zircaloy in one form or another. The oxidation of the cladding shells had to have occurred relatively early in the test, prior to significant material relocation, because these oxidized shells were surrounded by the melts. It can also be assumed that most of the zirconium in the eutectic metallic melt regions was probably oxidized during the test. This is based upon their position low in the bundle, where they would have been exposed to any steam flow before the rest of the bundle; the probability that they experienced their hottest temperatures as they were relocating to form the lower blockage; and the fact that these would be the first regions quenched by reflood. The data from the melt/insulation regions indicate that a significant amount of the zirconium in these regions was unoxidized. This is probably due to the relatively lower temperatures in these regions of the fuel bundle. These data also indicate that the greatest amount of oxidized zirconium was located in the ceramic melt regions. The partitioning of the zirconium oxidation and hydrogen generation in these various regions provides some valuable information on the possible sequence of bundle events, when these data are compared to measured and calculated hydrogen concentrations in the blowdown suppression tank and the primary coolant system. These comparisons are discussed in detail in Section 4.2.3.

4.2.2 Oxidation of Stainless Steel and Inconel Components

In addition to the zircaloy, major portions of the upper tie plate were molten and oxidized. This can be seen in the cross-sectional photographs of sample S(bottom). This cross section was cut through the middle of the Type 304L stainless steel tie plate. Area fraction measurements indicated that only 69 cm^2 of the upper tie plate were still completely intact and unoxidized out of an original cross section of 185 cm^2. Since this cross section was through the middle of the upper tie plate, it was assumed that this represented nominal conditions. The amount of iron in the molten regions that could have possibly oxidized was estimated using Equation (13), assuming that the iron oxidized to Fe_3O_4.

$$H_2 = \frac{(v)(8)(0.68)}{(55.85)} \left[\frac{4 \text{ moles } H_2}{3 \text{ moles Fe}}\right] \left[\frac{2g}{\text{mole } H_2}\right] \qquad (13)$$

where H_2 = hydrogen generated from oxidation of Fe in stainless steel cladding (g)

v = volume of stainless steel (cm^3)

8 = density of 304L stainless steel (g/cm^3)

0.68 = weight fraction of Fe in 304L stainless steel

55.85 = atomic weight of Fe (g/mole)

This calculation indicated that 77 g of hydrogen could be produced if all this iron oxidized. However, large uncertainties are associated with these calculations, estimated at ± 50%, which results in 77 ± 39 g of hydrogen. Corresponding calculations assuming Fe_2O_3 and FeO resulted in nominal amounts of 86 and 57 g of hydrogen, respectively. So, the estimated amount of hydrogen is relatively insensitive to the assumed oxidation state of the iron. Similar calculations for chromium (19 wt%) were performed using Equation (14) (Chromium oxidizes more easily than iron.). Assuming the same uncertainties as for the iron, these calculations indicated that 26 ± 13 g of hydrogen could have been generated from oxidation of the chromium in the upper tie plate. Total hydrogen generation from the oxidation of the upper tie plate was therefore 103 ± 52 g.

$$H_2 = \frac{(v)(8)(0.19)}{(52)} \left[\frac{3 \text{ moles } H_2}{2 \text{ moles Cr}}\right] \left[\frac{2 \text{ g } H_2}{\text{mole } H_2}\right] \tag{14}$$

where H_2 = hydrogen generated from oxidation of Cr in stainless steel cladding (g)

v = volume of stainless steel (cm^3)

8 = density of 304L stainless steel (g/cm^3)

0.19 = weight fraction of Cr in 304L stainless steel

52 = atomic weight of Cr (g/mole)

The amount of molten stainless steel cladding was 231 cm^3, based upon the values in Table 4. Using the same methodology as for the upper tie plate, up to 80 g of additional hydrogen could have been generated from this source if all the iron and chromium had completely oxidized. However, the metallic melts in the insulation region and elsewhere contained unoxidized iron, which was mixed with other metallics. So, as a first approximation, the amount of hydrogen generated from the oxidation of the molten stainless steel cladding was estimated to be nominally 50%, with lower and upper limits of 25% and 75%, respectively. This corresponds to 40 ± 20 g of additional hydrogen.

Approximately 66% of the Inconel 718 spacer grids melted, as shown in Table 4 in Section 4.1.3. This corresponds to 240 cm^3, or 2040 g of material, based upon a density of 8.5 g/cm^3 for Inconel 718. Similar calculations as those performed for the stainless steel components indicated that 20 ± 11 g of hydrogen may have been generated from the oxidation of the chromium (18.6 wt%) and iron (18.5 wt%) in the molten spacer grids. There was no conclusive evidence of NiO in this experiment (nickel is the primary component of Inconel) based on the SEM/WDS examinations, and NiO is not expected based upon its Gibbs free energy of formation. The presense of metallic tin and indium (see SEM/WDS sample S3-S26 Area 1), which oxidize easier than nickel, also suggests that NiO did not form in this test.

The sum of the contributions from the upper tie plate, molten stainless steel cladding, and Inconel spacer grids, is summarized in Table 18. The total amount from these sources is estimated to be 163 ± 83 g of hydrogen.

4.2.3 Total Hydrogen Generation and Discussion of Results

The best estimate of the total oxidation and hydrogen generation in the LP-FP-2 fuel bundle is the sum of the contributions from the zircaloy components, discussed in Section 4.2.1.4, and the nonzircaloy components, discussed in Section 4.2.2. These data are summarized in Table 19. It indicates that 1025 g of hydrogen were generated in the nominal case, with lower and upper limits of 655 and 1310 g, respectively. This is in excellent agreement with an independent analysis, based upon grab samples from the blowdown suppression tank and calculated amounts in the primary coolant system, which estimated 1024 ± 364 g of hydrogen.[10]

TABLE 18. OXIDATION OF NONZIRCALOY COMPONENTS

	H_2 (g)		
	Lower	Nominal	Upper
Oxidation of SS upper tie plate	51	103	155
Oxidation of molten SS cladding	20	40	60
Oxidation of molten spacer grid	9	20	31
Total hydrogen from nonzircaloy components	80	163	246

TABLE 19. BEST ESTIMATE OF TOTAL HYDROGEN PRODUCTION IN LP-FP2

		H_2 (g)	
	Lower	Nominal	Upper
Upper limit from zircaloy oxidation = 1226 g			
Unoxidized Zr in eutectic metallic melt	-197	-118	-54
Unoxidized Zr in melt/insulation	-226	-114	-42
Unoxidized Zr in metallic melts	-228	-132	-66
Total hydrogren from zircaloy	575	862	1064
Oxidation of SS upper tie plate	51	103	155
Oxidation of molten SS cladding	20	40	60
Oxidation of molten spacer grid	9	20	31
Total hydrogen from nonzircaloy components	80	163	246
Total hydrogen generation in LP-FP-2	655	1025	1310

The amount of hydrogen calculated to be in the blowdown suppression tank, based upon grab samples, was 205 ± 11 g. The amount in the primary coolant system, based upon pressure and temperature measurements and calculated gas compositions, was 819 ± 364 g. These values provide an indication of the amount of hydrogen generated during the transient and the reflood period, because the blowdown suppression tank was isolated just prior to reflood. Although some hydrogen may have been trapped in materials and later released during the reflood period, due to material cracking for instance, these data indicate that most of the hydrogen generation had to have occurred during the reflood period.

The data on the distribution of oxidized zirconium in Section 4.2.1.5 indicated that approximately 181 g of hydrogen were generated from the cladding oxide shells and the oxidized zirconium in the lower blockage. As previously discussed, the oxidation of these components had to have occurred during the transient phase. This agrees very well with the 205 g estimated to be in the blowdown suppression tank, which also must have been generated during the transient portion of the test. Some of the ceramic melt material may have also oxidized during the transient phase. However, as described in the following paragraphs, there is evidence indicating that most of this melt oxidized during the reflood period.

Steam mass flow rates through the fuel bundle were estimated to be 13±5 g/s during the high-temperature portion of the transient (approximately the last 300 s), based on measurements made in the F1 sample line immediately above the reactor core.[10] Conservatively assuming that all this steam was converted to hydrogen, a maximum of only 400 ± 150 g could have been produced during the transient. This indicates that significant amounts of oxidation had to have occurred during the reflood period. During the reflood period, the steam mass flow rates increased to approximately 5 kg/s and it took approximately 10 s to completely cover the core, so there was more than sufficient steam available to account for the oxidation observed posttest. These data suggest that most of the 818 g of hydrogen estimated to have been generated in the ceramic melts, melt/insulation regions, and from nonzircaloy components was produced during the reflood period. The 818 g of hydrogen is also in excellent agreement with the 819 g estimated to be in noncondensible gas bubbles present in the primary coolant system, most of which had to have been generated during the reflood period.

Further evidence that the oxidation of most of the ceramic melt region, the nonzircaloy components, and the melts that penetrated the insulation region had to have occurred during the reflood period is provided from metallographic observations and thermocouple data. As described in Section 3.2.10, the metallographic examinations indicated that extensive melting and oxidation of the stainless steel upper tie plate occurred. As described in Section 4.3, thermocouples on the bottom surface of the upper tie plate indicated that temperatures were less than 1000 K during the entire transient. However, these thermocouples indicated that a rapid temperature excursion occurred during reflood, with temperatures exceeding the 1720-K melting point of the stainless steel. Therefore, the observed melting and oxidation of the upper tie plate could only have occurred during the reflood period. As also described in Section 4.3, fuel centerline thermocouples indicated that a rapid temperature excursion occurred at the 27-in. thermocouple elevation during the reflood period, with some temperatures exceeding 2900 K. Those fuel centerline thermocouples were located on the periphery of the ceramic upper blockage region. These temperature excursions could only have resulted from the rapid and extensive oxidation of zirconium in this region; i.e. the oxidation of most of the material in the ceramic upper blockage region had to have occurred during reflood. Ceramic melts higher in the fuel bundle must have also oxidized during the reflood period because temperatures can be assumed to have been comparable or even less than in the upper blockage region, and the steam would have had to have passed over the zirconium at the lower elevations first. Most of the oxidation of the zirconium melt that penetrated the insulation also probably occurred during the reflood period, when temperatures in these cooler peripheral regions would have increased and large amounts of steam were available. The data are therefore consistent with the hypothesis that most of the ceramic melts, nonzircaloy components, and melt/insulation regions oxidized during the reflood period.

In summary, the 181 g of hydrogen that were nominally estimated to have been generated from the cladding oxide shells and the material in the lower blockage are in good agreement with the 205 ± 11 g of hydrogen measured in the blowdown suppression tank. These values are indicative of the amount of hydrogen generated during the transient portion of the experiment. 818 g of hydrogen were estimated to have been generated from the ceramic melt regions, the melt which penetrated the insulation, and the oxidation of nonzircaloy components. This is in excellent agreement with the 819 g of hydrogen estimated to be in the primary coolant system, which is indicative of the amount of hydrogen generated during the reflood period. Therefore, data from two independent analyses show excellent agreement as to the partitioning of the hydrogen generation between the transient and reflood periods.

Excellent agreement was also found between two alternate methods for estimating the amount of zirconium oxidation and hydrogen generation based upon the postirradiation examination data. These two methods indicated that 836 and 862 g of hydrogen were nominally generated from oxidation of the zirconium. Excellent agreement was also found between independent analyses of the total hydrogen production based upon the postirradiation examination data (1025 g) and the total amount estimated to be in the blowdown suppression tank and primary coolant system (1024 g).

The aforementioned agreement between values calculated by alternate methods and completely independent analyses strongly suggests that the best-estimate nominal values closely reflect the actual conditions. The large uncertainties associated with the individual calculations reflect very conservative upper and lower limits in these individual estimates. However, the good agreement between the various calculations indicates that there is a high probability that the best-estimate nominal values reasonably reflect the actual conditions.

4.3 Fuel Bundle Temperature Estimates

Temperatures within the fuel bundle were estimated based upon metallographic observations of changes in the zircaloy structure and the presence of molten materials and their interaction with other materials. Thermocouple data obtained during the experiment provided information on the axial temperature profile up until failure and shunting of the thermocouples. However, the cladding thermocouples in this experiment generally failed at around 2000-2200 K; and only a limited number of fuel centerline thermocouples were available to provide higher-temperature data (up to 2970 K). Metallographic observations from the postirradiation examinations provide the only data on peak temperatures in many regions of the fuel bundle.

In formulating these temperature estimates, it is important to keep in mind how these data might ultimately be used. The intent of these temperature estimates is to provide data for modelers of this experiment to use in their calculations. These computer models generally must use an average temperature for an entire axial node. Depending upon the nodal distribution, this may encompass several of the metallographic cross sections examined. The appropriate average temperature may also depend upon what the modeler is attempting to model; for fission product release, it may be appropriate to consider an average melt temperature at a given elevation, where inclusion of a lot of lower temperature structural materials or fuel pellets may not be appropriate. In any case, the use of an average temperature for an entire cross section, or even an axial node, ignores large temperature gradients apparent both axially and radially from the postirradiation examinations. There is also obviously a temporal dependence in the temperatures at any given axial or radial location. The temperature estimates provided here were based upon postirradiation examinations of the fuel bundle; and, as such, they are indicative of the peak temperatures. The peak temperatures estimated at the various axial locations could have occurred at different times during the experiment; for instance, there is evidence to suggest that the temperatures near the bottom of the fuel bundle were hottest prior to reflood, whereas in other regions of the bundle there are indications that peak temperatures occurred during reflood. These spatial and temporal dependencies must be recognized when attempting to use these data. It is then up to the needs of the modeler to decide what average temperature to use and to establish the extent of axial nodes.

The axial profile of estimated bundle temperatures in the LP-FP-2 fuel module is presented in Figure 267. Details of the information included in this figure and the basis used to determine this profile are discussed in detail in the succeeding subsections. These subsections describe the estimation of temperatures in four areas of the bundle: (a) elevations A-F (≤ 0.36 m), where the bundle is relatively intact and temperatures can be estimated from changes in the zircaloy microstructure; (b) elevation G(bottom)-G(top) (0.43-0.46 m), where temperatures are estimated based upon material interactions with the spacer grid; (c) elevations H-K (0.58-0.88 m), where large amounts of high-temperature ceramic melt are the overriding influence in estimating bundle temperatures; and (d) elevations L-R (0.96-1.68 m), where very little metallographic information was available for estimating bundle temperatures. Consequently, temperature ranges were based on interpolations between temperatures in the high-temperature ceramic blockage and the upper tie plate. Large uncertainties are associated with the temperatures in this region.

4.3.1 Estimated Temperatures in the Lower Bundle

This region includes the A-F elevations (≤ 0.36 m). The bundle was essentially intact, with relocated eutectic metallic melt/fuel debris surrounding the fuel rod array at the C-E (0.12-0.27 m) elevations. Except for some localized hot spots (as evidenced by localized prior-beta zircaloy structure), the relocated material did not significantly affect the zircaloy cladding temperatures. Average bundle temperatures in this region can therefore be estimated from changes in the zircaloy microstructure. These microstructure changes include zircaloy recrystallization at approximately 920 K and transformation to prior-beta at approximately 1245 K.

Changes in the zircaloy microstructure at these elevations were previously discussed in Section 3.2.3, along with representative

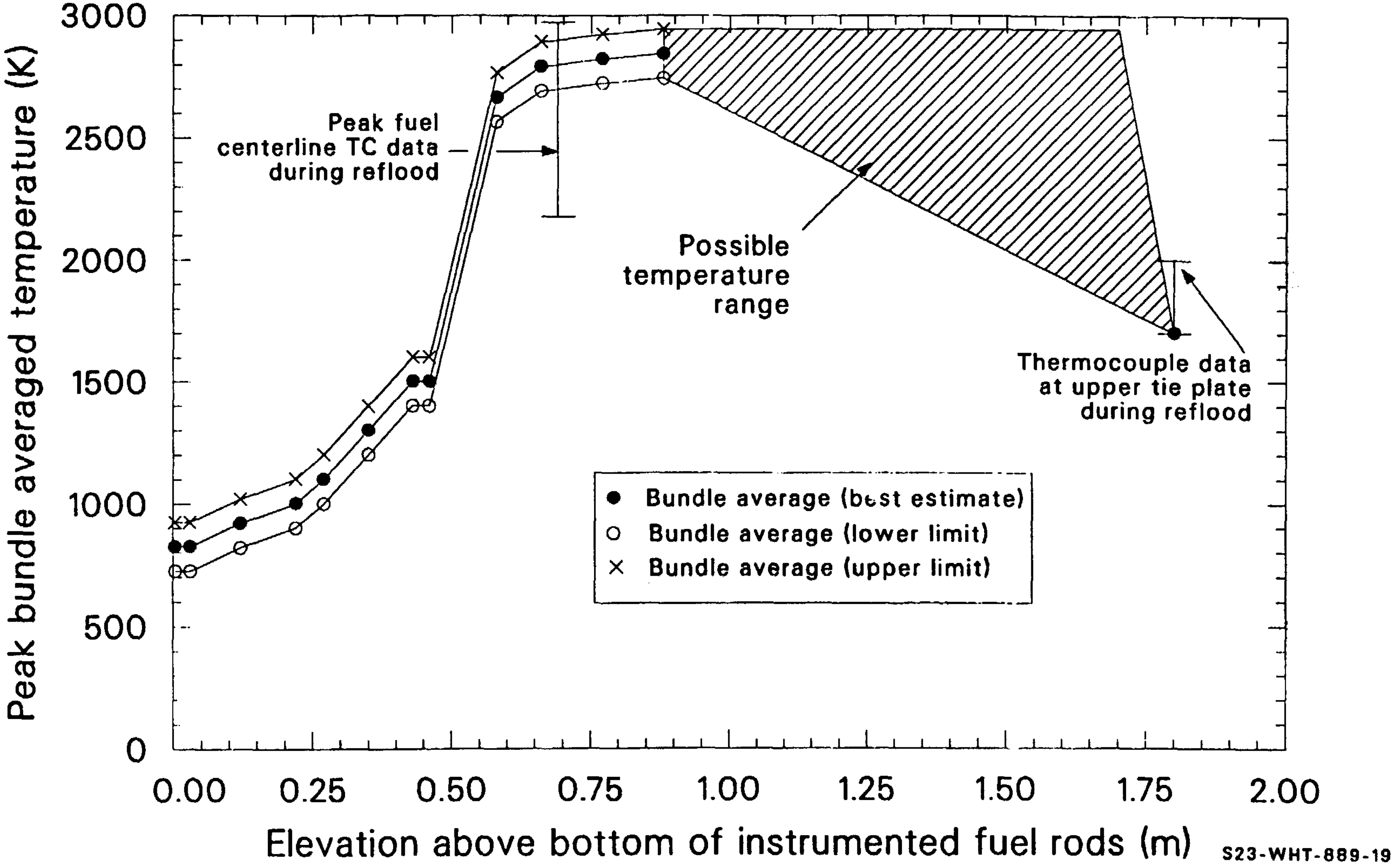

Figure 267. Axial distribution of peak bundle average temperatures in LP-FP-2.

photomicrographs. Consequently, only a brief summary of the pertinent results in estimating temperatures is provided here.

At the A and B elevations (0.003-0.03 m), all of the zircaloy was in the as-fabricated condition. This indicates that cladding temperatures were less than the 920-K recrystallization temperature. There was essentially no relocated material at these locations, and fuel temperatures during the transient were probably not much above cladding temperatures.

At the C elevation (0.12 m), the cladding on some of the central fuel rods recrystallized; however, the cladding towards the outer edge of the assembly (rods surrounded by the eutectic metallic melt/fuel debris) was still in the as-fabricated condition. There were also small areas of prior-beta structure on some of the central fuel rods, which appeared to be associated with small oxidation layers. A bundle average temperature of 920 ± 100 K encompasses the transformation temperature from as-fabricated to recrystallized zircaloy.

At the D elevation (0.22 m), all the cladding was recrystallized, which indicates cladding temperatures in excess of 920 K. Small amounts of prior-beta structure, which were associated with small oxidation layers, were also observed on some of the central fuel rods. Contact between the relocated material and the cladding did not consistently alter the cladding microstructure, which suggests that temperatures of the relocated material were not much above cladding temperatures. These observations suggest a bundle average temperature of approximately 1000 ± 100 K. This agrees with thermocouple measurements taken at the 0.25-m elevation, which indicated cladding temperatures of 910-1100 K.[10] These data also provide a basis for the estimated uncertainty of ± 100 K in bundle average temperatures in these lower intact regions of the fuel bundle.

At the E elevation (0.27 m), most of the fuel rod cladding recrystallized. Prior-beta structure was only observed on some of the interior fuel rods, most notably in the northeast quadrant. (Indications at higher elevations in the bundle also suggest that higher temperatures and greater damage generally occurred in the northeast quadrant.) These fuel rods all had minor amounts of oxidized zircaloy layers associated with the prior-beta structure. Small amounts of relocated material were also present at this elevation; however, they do not appear to have significantly altered the cladding microstructure. None of the (Ag,In,Cd) control rod material contained within its cladding melted, which indicates temperatures were below 1073 K. These observations suggest a bundle average temperature slightly higher than at lower elevations, approximately 1100 ± 100 K.

At the F elevation (0.36 m), all the zircaloy cladding was prior-beta except for on a few rods in the corners of the assembly, which had recrystallized cladding. Small layers of zircaloy oxidation were associated with areas exhibiting prior-beta structure. This indicates that cladding temperatures were in excess of 1245 K over most of the assembly. There was relatively little relocated melt material at this elevation. Most of the (Ag,In,Cd) control material was molten, indicating temperatures in excess of 1073 K; however, in some edge row positions, it was still intact. Bundle average temperatures were slightly higher than those at the E elevation, approximately 1300 ± 100 K.

4.3.2 Estimated Temperatures Near the Second Spacer Grid

Much of the zircaloy cladding in the vicinity of the second spacer grid (0.43-0.46 m) was still intact, although in some areas significant amounts had liquefied as a result of eutectic interactions with molten control rod material. Significant amounts of relocated eutectic metallic melt/fuel debris had accumulated on the second spacer grid. Portions of the spacer grid and stainless steel control rod cladding had liquefied as a result of eutectic interactions with relocating Ag-Zr melts. These data indicate temperatures below the melting point of the type 304 stainless steel and the Inconel 718 spacer grid, both of which melt at approximately 1720-1730 K. The Zr-Fe and Zr-Ni phase diagrams in Appendix G both show eutectic points of 1220-1230 K; however, the stainless steel-zircaloy reaction is believed to proceed very slowly at these temperatures. At temperatures approximately 200 K or more above the eutectic point, the reaction approaches equilibrium in a matter of minutes.[16] Similarly, for the Zr-Ni interactions, an increase of approximately 200 K above the minimum eutectic point would result in a liquid phase over a wide compositional range, as shown in the Zr-Ni phase diagram. These data suggest that a bundle average temperature of approximately 1500 ± 100 K is appropriate for these elevations.

4.3.3 Estimated Temperatures in the Ceramic Melt Region

Extensive amounts of ceramic melt material were present at the H-K elevations (0.58-0.88 m). These ceramic melts were composed of $(U,Zr)O_2$ that was rich in zirconium. Metallic (U,Zr,O) melts that have high zirconium contents can be liquid at temperatures as low as approximately 2200 K (see Appendix G, Figure G-24). Ceramic $(U,Zr)O_2$ melts require temperatures in excess of 2810 K to be in the liquid state (see Appendix G, Figure G-14). To provide a good estimate of bundle temperatures, it is therefore helpful if there is evidence to indicate whether the $(U,Zr)O_2$ observed posttest was a metallic melt, which later oxidized and solidified, or whether it was actually molten as a ceramic. In the case of LP-FP-2, there is evidence suggesting that the relocated material in the upper blockage region was molten as a ceramic and that temperatures approached fuel melting (>3120 K) near the center of this melt region.

Temperatures in the ceramic melt region can be inferred from observations of how this molten material interacted with the fuel and oxidized cladding shells. If fuel melting occurred, then temperatures must have been in excess of 3120 K. If melting of the ZrO_2 oxidized cladding shells occurred, then temperatures must have been in excess of 2960 K. If the melt was molten as ceramic $(U,Zr)O_2$, then temperatures must have been in excess of 2810 K.

Isothermal plots of the four metallographic cross sections through the ceramic melt region were developed based upon the damage criteria mentioned in the previous paragraph. These plots are presented in Figures 268 through 271, and the J cross section (0.77 m) will be discussed as an example. In the middle of the ceramic melt region was an area in which all the oxidized cladding shells and fuel pellets were gone. Surrounding this area was a

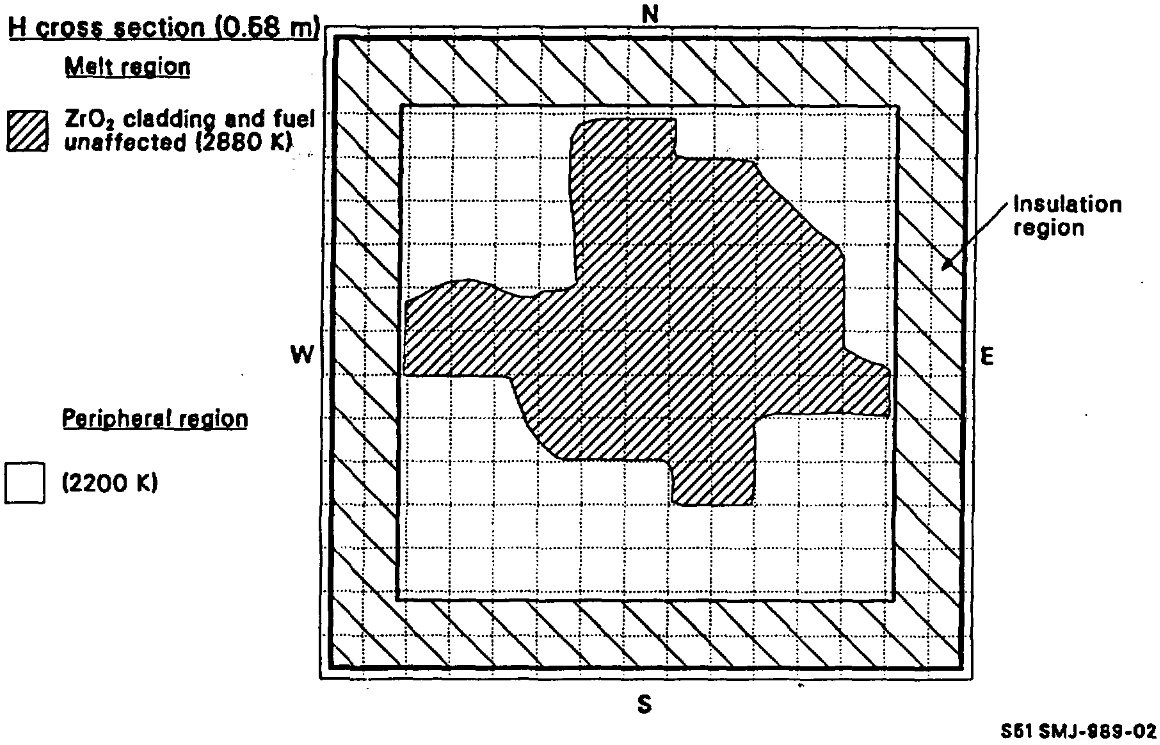

Figure 268. Distribution of damaged areas in the ceramic melt region at 0.58 m.

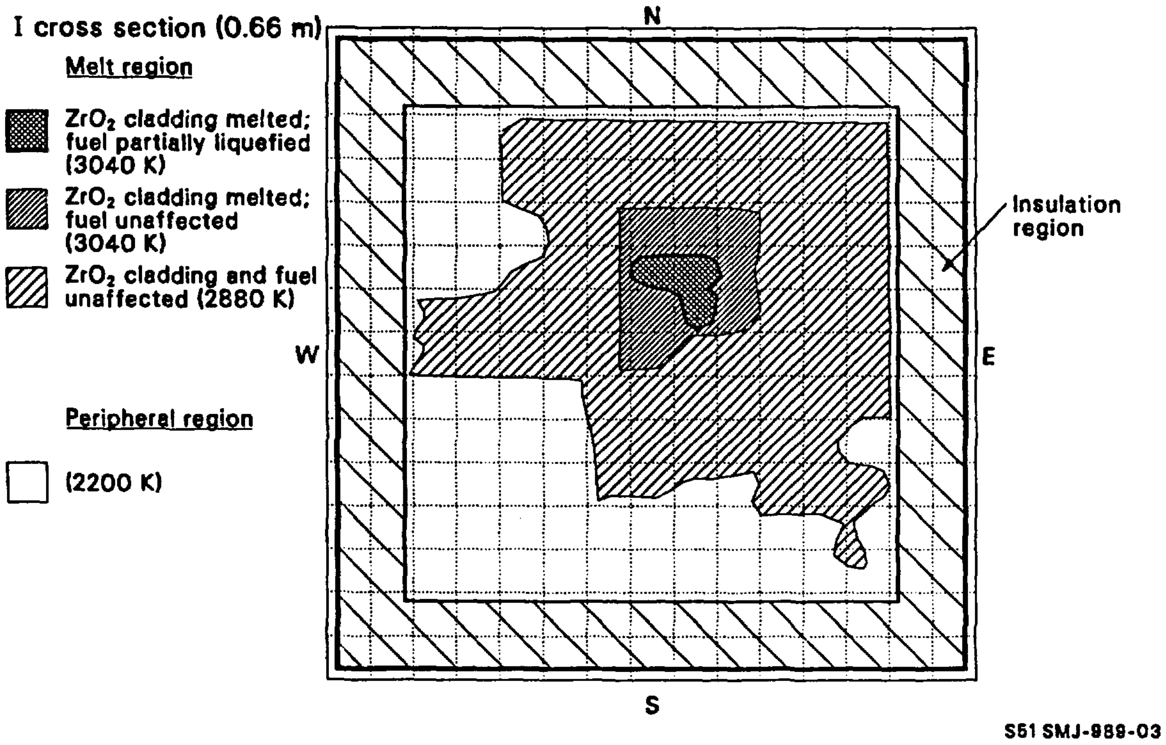

Figure 269. Distribution of damaged areas in the ceramic melt region at 0.66 m.

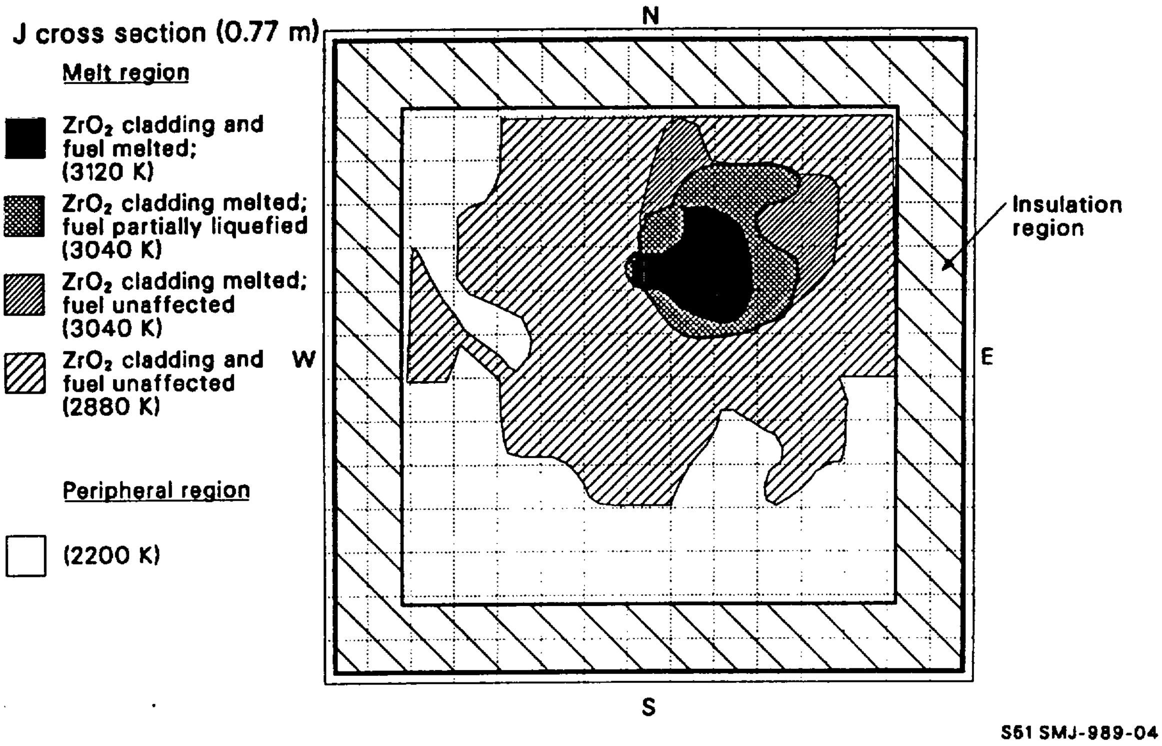

Figure 270. Distribution of damaged areas in the ceramic melt region at 0.77 m.

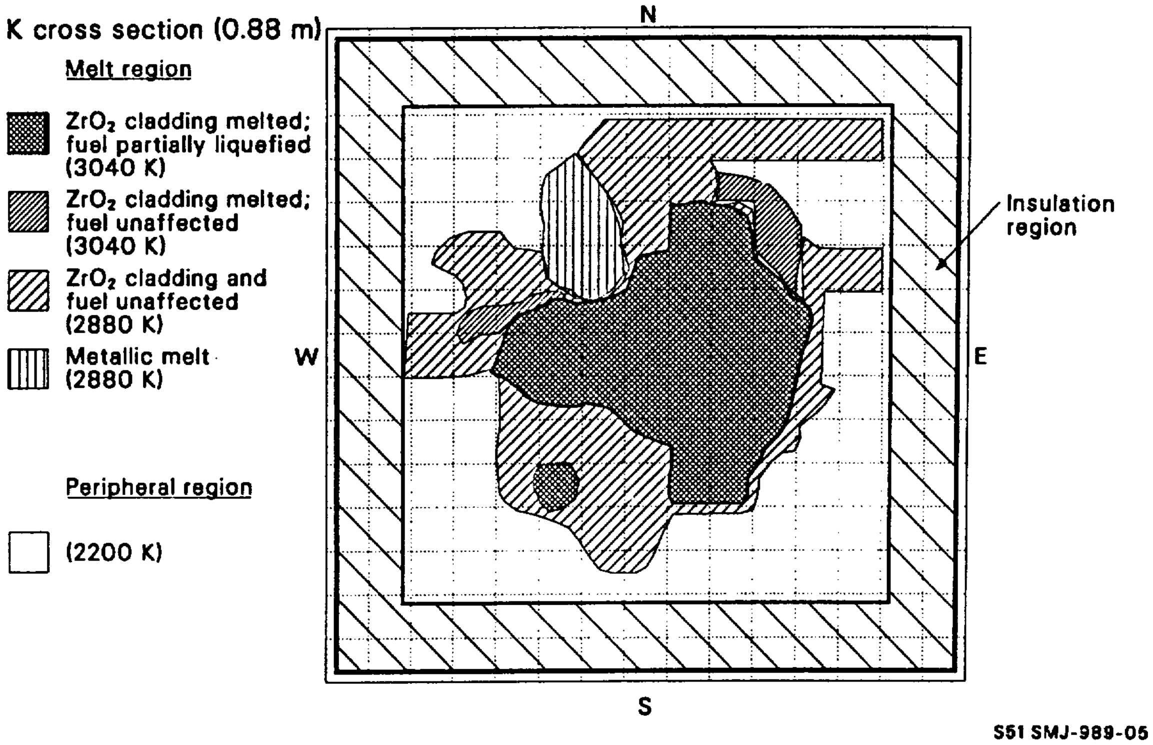

Figure 271. Distribution of damaged areas in the melt regions at 0.88 m.

transition region in which partially liquefied fuel pellet remnants were still present and in which oxidized ZrO_2 cladding shells no longer remained. SEM/WDS examinations of sample K2-S32 revealed a similar area and found porous fuel structures indicative of fuel near melting. This suggests that temperatures in this region were $2960 \text{ K} < T \leq 3120 \text{ K}$ (3040 K average) and that temperatures exceeded fuel melting (3120 K) in the region where the fuel and oxidized cladding were completely gone. Surrounding the region of molten oxidized cladding and partially liquefied fuel was an area in which the fuel pellets appear relatively unaffected; however, oxidized cladding shells were no longer present. This suggests that temperatures in this region were perhaps slightly lower than in the region where the fuel was partially liquefied; however, temperatures were still $2960 < T < 3120$ K (3040 K average). Surrounding this area was a region in which the ceramic melt did not significantly affect either the fuel or the ZrO_2 cladding shells. This indicates that temperatures were certainly less than 2960 K; and, assuming that this was a ceramic $(U,Zr)O_2$ melt, this would establish a lower limit of 2810 K (average temperature of 2880 K). The evidence that supports this assumption is detailed in the following discussion.

In addition to the results from SEM/WDS sample K2-S32, which indicated fuel near melting in the central regions of the upper blockage, thermocouple data also provided indications of extremely hot temperatures on the periphery of the ceramic upper blockage region. Three fuel centerline thermocouples, which have been tested to 2700 K without failing, provided reliable data into the reflood period. These fuel centerline thermocouples were composed of W-Re thermocouple wires insulated with HfO_2 and contained in Re sheaths. The data from these three fuel centerline thermocouples are plotted in Figure 272 up until reflood and in more detail in Figure 273 during the reflood period. Thermocouple TC-5I08-27 was in position I8 (see Figures 1 and 2) near the edge of the ceramic melt region. It indicated peak temperatures prior to reflood of 2313 K at 1782 s. The temperature increased following the onset of reflood; and, at 1792 s, this thermocouple indicated 2382 K just before it finally failed. Thermocouple TC-5M08-27 was in position M8 near the edge of the ceramic melt region, and it indicated a peak temperature of 2220 K at 1782 s. The temperature increased following reflood; and, at 1796 s, this thermocouple indicated 2972 K just before it

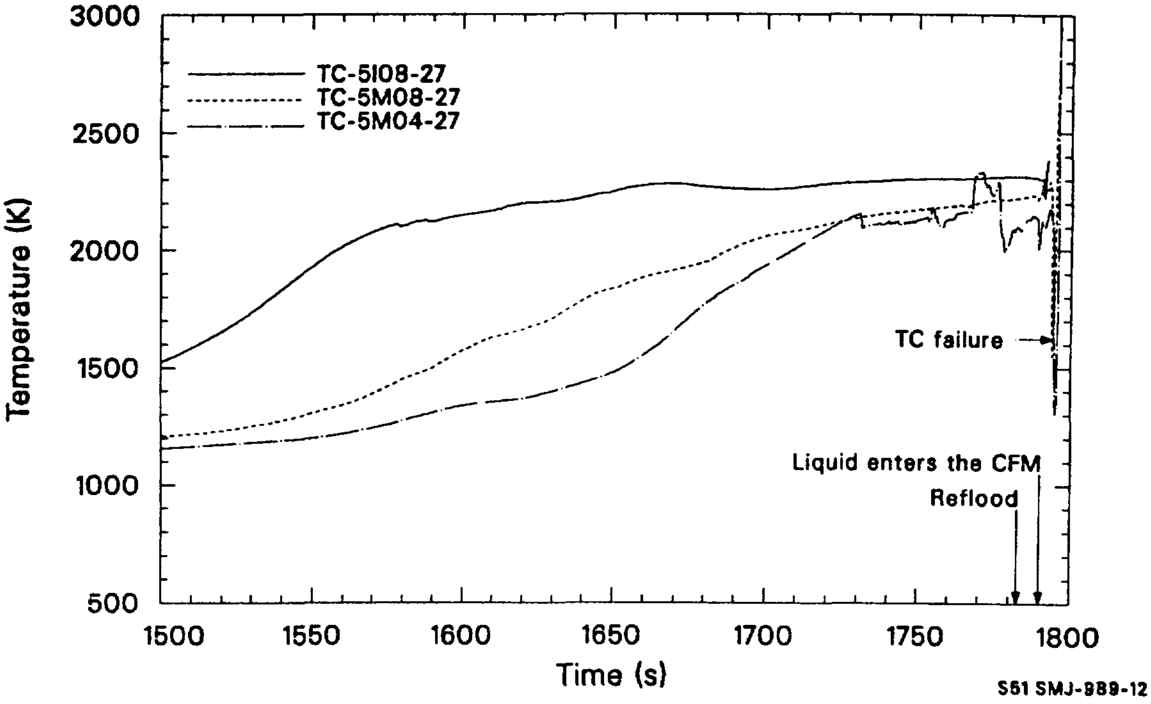

Figure 272. Fuel centerline thermocouple data.

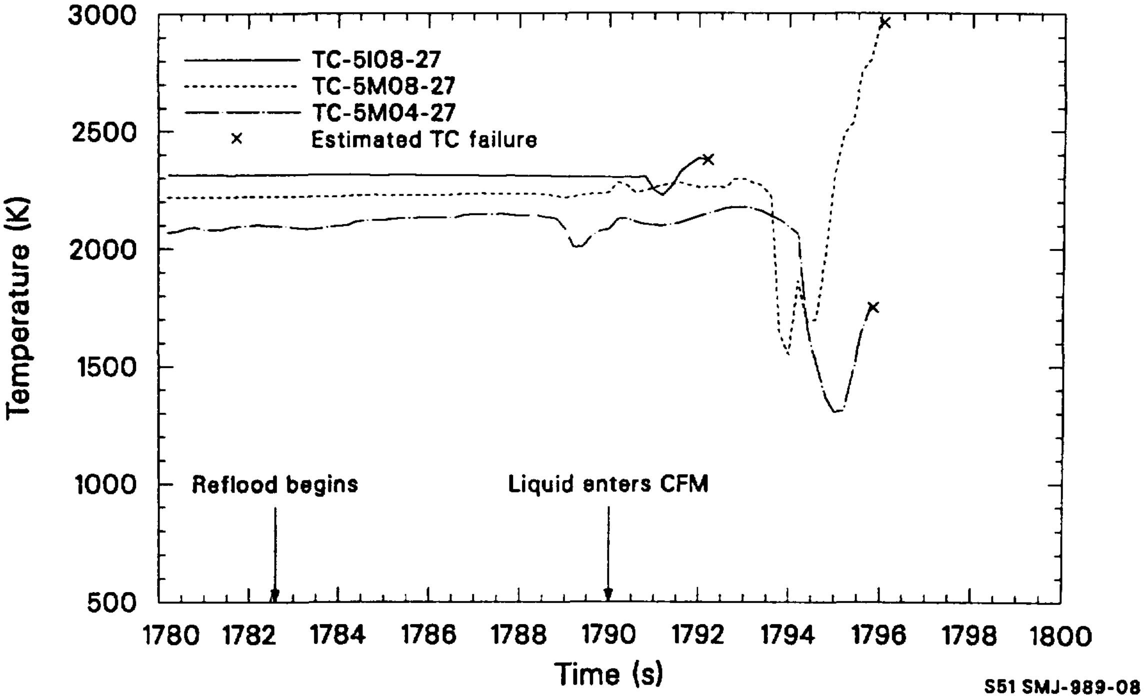

Figure 273. Details of fuel centerline thermocouple data during reflood period.

failed. Thermocouple TC-5M04-27 was located in position M4, in the corner of the assembly well away from the ceramic melt regions; it indicated a peak temperature of 2101 K at 1782 s just prior to reflood. It reached a peak temperature of 2176 K at 1793 s, and then the temperature started to decrease before it failed at 1796 s. These thermocouples provide reliable indications of temperatures on the periphery of the ceramic melt and away from the ceramic melt region, which support the average temperature regimes shown in Figures 268 through 271. They also indicate that the peak temperatures in the ceramic melt region occurred during the reflood period.

Based upon the high temperatures indicated by the fuel centerline thermocouples on the periphery of the ceramic upper blockage region, the SEM/WDS results indicating fuel near melting in the center of the upper blockage, and metallographic observations of the extent of the blockage and the existence of a significant temperature gradient within this blockage, it is reasonable to assume that this mass of material took some time to cool to the saturation temperature after reflood. Indications of this are apparent in the cladding thermocouple data shown in Figure 274. Thermocouple TE-5K11-027 was located in fuel bundle position K11, as shown in Figure 2, which would have been in the northwest quadrant. As shown on sample I1, location K11 at the thermocouple elevation was on the edge of the ceramic melt region. However, this thermocouple was routed upward and would have passed through the melt region on sample J1. Figure 274 shows that this thermocouple measured a rapid temperature increase after 1500 s and that it measured a gradual cooling after reflood. Thermocouple TE-5J07-027 was located in position J07, which corresponds to the periphery of the ceramic melt region at the I-K elevations. In this case, the cooldown takes much longer than measured on cladding thermocouple TE-5K11-027. Although failure and shunting probably occurred on these thermocouples during the transient (cladding thermocouples generally failed around 2000-2200 K, as opposed to the higher-temperature fuel centerline thermocouples), these thermocouples provide trend data suggesting that the ceramic upper blockage did remain hot for up to several hundred seconds following reflood.

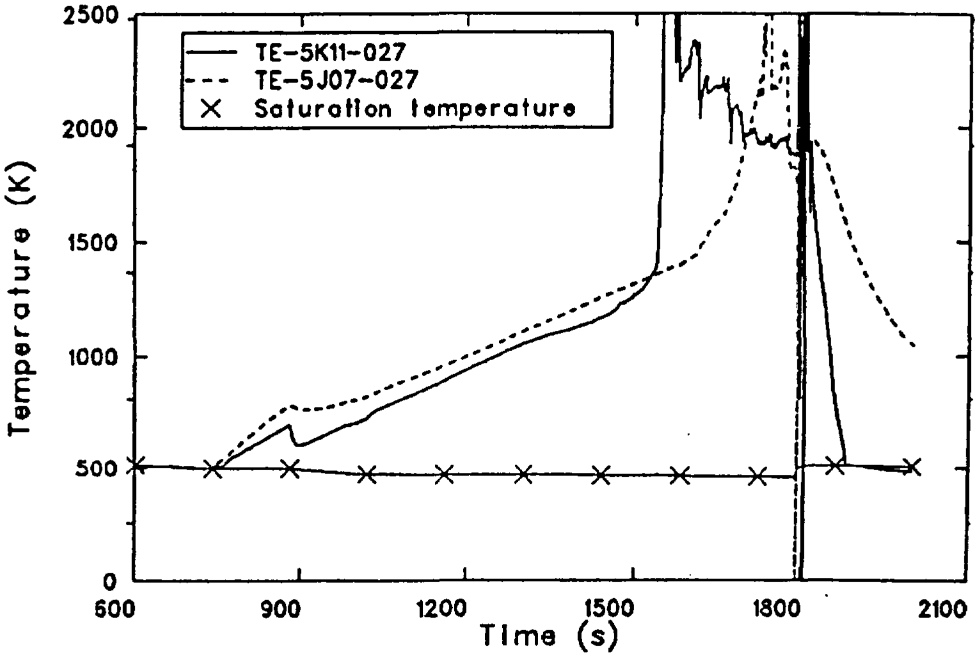

Figure 274. Selected cladding thermocouples showing temperatures above the saturation temperature following reflood.

Additional information from the metallographic examinations also suggests that most of the upper blockage region was composed of molten ceramic material. As has been previously noted, near the central region of the blockage were areas in which the oxidized cladding shells were completely gone but the fuel was unaffected. However, studies have shown that the dissolution of fuel by metallic (U,Zr,O) melts proceeds more rapidly than the dissolution of ZrO_2 by these melts.[14] This suggests that either the melt was $(U,Zr)O_2$, which would only interact thermally with the UO_2 or ZrO_2, or possibly that it was a (U,Zr,O) melt which solidified before it could liquefy the fuel or oxidized cladding. However, if it were (U,Zr,O) that solidified as a metallic and later oxidized at temperatures below 2810 K, then it would be expected that the solidified metallic would have reduced the fuel and oxidized cladding. Reduction of the fuel should have resulted in grain boundary separation and fragmentation, as was observed in other areas of the fuel bundle where metallic melts were located adjacent to fuel (Section 3.2.9.2). However, as described in Sections 3.2.8 and 3.2.9, grain boundary separation was not observed adjacent to the ceramic melts. Extensive fuel cracking was also not observed on fuel pellets surrounded by these ceramic melts, as was the case with fuel pellets surrounded by a large agglomeration of metallic melt at the 0.88-m elevation (Section 3.2.9.3). And, finally, throughout the upper blockage region there were no areas in which the relocated material was not fully oxidized. If it is assumed that this region was formed by metallic melts that quickly oxidized and solidified at the surface of the melts while maintaining temperatures well below 2810 K, then it would be expected that isolated metallic regions would be found somewhere in these regions. However, this is not the case; the $(U,Zr)O_2$ at each elevation is very uniform, which suggests that mixing and oxidation occurred in the molten state. The rapid oxidation of this large mass of material would have resulted in a very large and rapid temperature increase, as was observed during the reflood period.

Very little metallographic evidence was available to form a basis for estimating temperatures in the peripheral regions away from the ceramic blockage region. Fully oxidized cladding shells were all that remained of the cladding. The molten zircaloy that was once contained within these oxide shells had melted and relocated. All that can be definitively stated from the metallographic evidence is that temperatures were above the melting point of unoxidized zircaloy and below the melting point of ZrO_2 (2030 K< T <2960 K). However, a better indication is provided by fuel centerline thermocouple TC-5M04-27, which was located near a corner away from the ceramic melt and which indicated a peak temperature of 2176 K during the reflood period (see Figures 272 and 273).

The fuel bundle average temperatures shown in Figure 267 for these four elevations through the high temperature ceramic melt region were derived by weighting the temperature regions shown in the isothermal plots by the amount of material in each category. In the regions of complete blockage, this was simply the area fractions, as measured from Figures 268 through 271. However, in the peripheral regions, which contained large amounts of open flow, the amount of material in these areas was derived by subtracting the amount of material in the full blockage region from the total cross-sectional blockage within the insulation region, as detailed in Appendix F. The bundle average temperatures therefore represent material-weighted averages, not area-weighted averages. The temperatures assigned to each region were: (a) fuel and ZrO_2 cladding melted: temperatures were somewhat above 3120 K, but an average temperature of 3120 K was used in the calculation; (b) ZrO_2 cladding melted and fuel partially liquefied: $2960 \text{ K} < T \leq 3120 \text{ K}$, an average of 3040 K was used; (c) ZrO_2 cladding melted and fuel unaffected: $2960 \text{ K} < T < 3120 \text{ K}$, an average of 3040 K was used; (d) fuel and ZrO_2 cladding unaffected: $2810 \text{ K} < T \leq 2960 \text{ K}$, an average of 2880 was used; (e) agglomerated metallic melt: temperatures in this region were assumed to be the same as in the regions where the ceramic melt did not affect the fuel or oxidized cladding; (f) peripheral regions away from ceramic blockage: a temperature of 2200 K was used, based upon the fuel centerline thermocouple data from TE-5M04-27.

A sensitivity analysis was performed to help determine the uncertainties associated with the peak bundle average temperatures in these regions. The largest areas of uncertainty were thought to be associated with the peripheral regions of the ceramic melt and the peripheral regions away from the ceramic blockage. For these analyses, a peak bundle average temperature of 2810 K was assigned to the peripheral melt regions (conservatively allowing for the possibility that some of the material near the edges of the blockage may have been metallic melt which oxidized and solidified at temperatures below 2810 K); and uncertainties of ± 100 K were assigned to the average temperatures in the peripheral regions away from the ceramic blockages. The 70-K change in the temperature used for the peripheral regions of the ceramic melt resulted in differences of 32-53 K in the overall bundle average temperatures, while the ± 100-K uncertainties in the peripheral regions away from the blockages only resulted in differences of 15-32 K. It should be noted that the magnitude of these uncertainties is proportional to the amount of each material, and hence the largest uncertainties in the peripheral regions of the ceramic melt are associated with the smallest uncertainties in the outermost region. It is not correct to add the maximums to obtain a maximum uncertainty for a given cross section. Based upon these results, uncertainty limits of ± 100 K on the overall peak bundle average temperatures in these regions were considered adequate to reasonably represent the bundle conditions.

4.3.4 Estimated Temperatures in the Upper Bundle

Temperatures at these elevations were difficult to estimate from the metallographic data because there were very few indicators and the range of possible temperatures was relatively large. At and above the L elevation (0.96 m), there was significantly less prior molten material, essentially all the cladding remnants were completely oxidized, and much of the fuel pellets were in the form of a debris bed. Consequently, temperature ranges in this portion of the bundle were based upon upper and lower bounding interpolations between the temperatures in the ceramic upper blockage region and the upper tie plate. Although the profile can be assumed to be decreasing in this upper region, large uncertainties arise as to the actual shape of the profile, i.e., whether there is a smooth transition in temperatures or whether there is an abrupt change at some point. Some metallographic observations and thermocouple data are presented that provide some insight into the temperatures.

The peak bundle average temperature at the upper tie plate was estimated on a similar basis as was used at the second spacer grid. The stainless steel upper tie plate near the periphery of the fuel module was still intact, whereas the central region had melted and oxidized. Therefore, a peak bundle average temperature of 1700 ± 100 K reasonably brackets this behavior. Four thermocouples were located on the bottom surface of the upper tie plate, and their locations relative to the melted regions are shown in Figure 275. These thermocouples indicated that temperatures were less than 1000 K during the entire transient portion of the experiment, as shown in Figure 276. However, a rapid temperature excursion occurred during the reflood period, as shown in Figure 277, with temperatures exceeding 1700 K prior to failure on the three thermocouples in the melted region. The fourth thermocouple was located in the intact region near the melt/intact transition, and it indicated that temperatures just reached 1700 K. The range in failure temperatures measured by these thermocouples is shown by the bracket in Figure 267.

The lower temperature bound for the upper bundle region, shown in Figure 267, assumes a linear decrease in bundle temperatures from the ceramic melt region to the upper tie plate. The upper temperature bound assumes that the steam passing the high-temperature ceramic melt heats the material in the upper bundle, with a drop-off at the top of the fueled region. Both of these bounds are conservative, but the data are insufficient to attempt to determine a more accurate temperature profile. In the following discussion, some data and observations are presented that provide some insight into the temperatures in this region, but they are very limited.

Cladding thermocouples at the 1.07-m elevation, located near the edge of the fuel assembly, indicated peak temperatures of approximately 2150 K when they failed at approximately 1500 s. At this time, they were experiencing a rapid temperature excursion of approximately 20 K/s. Bundle temperatures certainly exceeded these thermocouple measurements, but it is not possible to say by how much. However, these data do provide an indication of minimum bundle temperatures at a point in time. The cladding

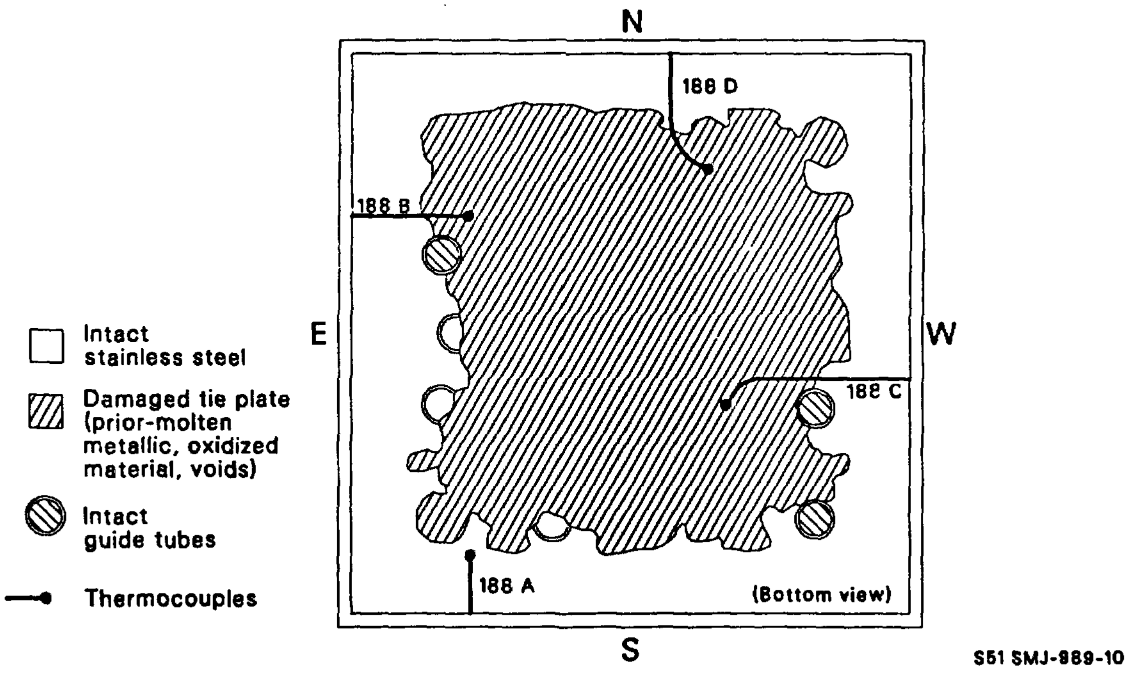

Figure 275. Locations of thermocouples on the bottom surface of the upper tie plate.

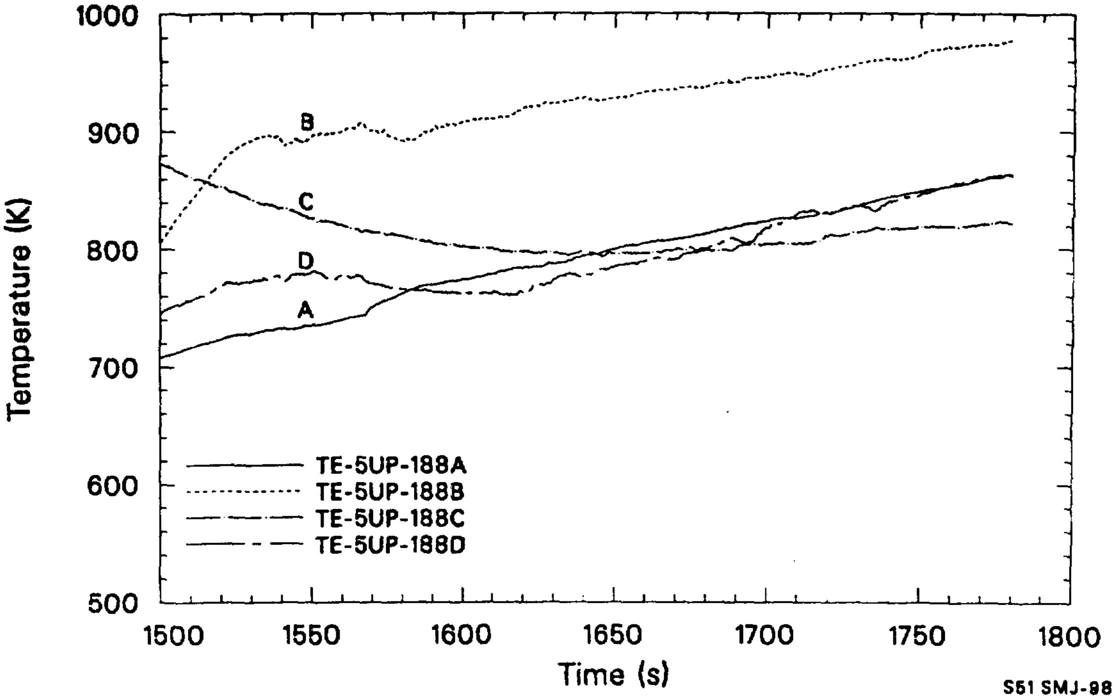

S51 SMJ-989-11

Figure 276. Thermocouple data from the bottom surface of the upper tie plate prior to reflood.

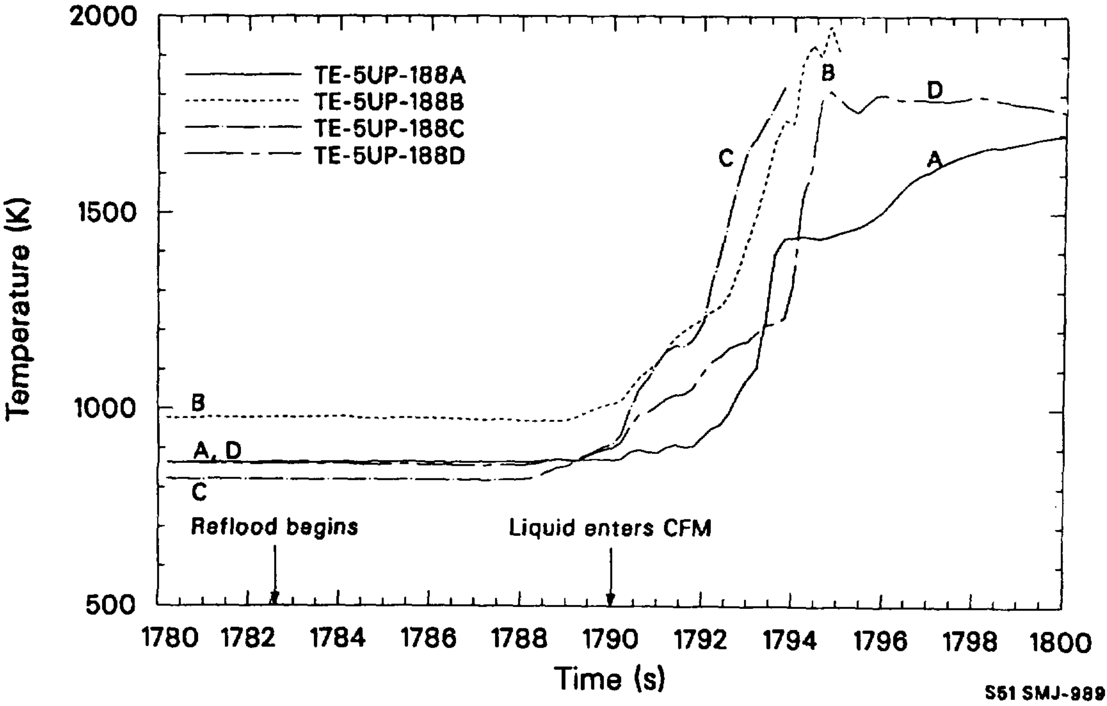

S51 SMJ-989-09

Figure 277. Thermocouple data from the bottom surface of the upper tie plate during reflood.

thermocouple data at the topmost elevation (1.68 m) were limited to fuel rods in the exterior row of the assembly. Thermocouples from this region operated reliably until reflood at 1795 s and indicated peak temperatures of 1369 K. These thermocouples were located 0.12 m below the partially liquefied upper tie plate.

At the L elevation (0.96 m), there were significant amounts of relocated melt material, although quite a bit less than at the H-K elevations (0.58-0.88 m). Some of the central fuel rods no longer have any oxidized cladding shells surrounding them, which may indicate peak temperatures in excess of 2960 K. There is also evidence of fuel liquefaction in some fuel pellets near the center of the assembly. Bundle average temperatures can be assumed to be somewhat less than in the upper blockage region because fuel melting did not occur.

At the M elevation (1.04 m), there was less ceramic melt material than at the L elevation. Oxidized cladding shells surrounded most of the fuel pellets, except for a few rods in the very center of the fuel bundle. Diminished fuel pellet sizes on some of the central fuel rods suggest that some fuel liquefaction occurred. Bundle average temperatures were probably somewhat less than at the L elevation.

4.4 Fuel Grain Size Measurements

Fuel grain size measurements were obtained from photomicrographs taken at the center and edge of fuel pellets located near the center of the fuel bundle and on the periphery of the fuel bundle at every elevation where possible. The grain size was determined using a line intercept method to establish the average fuel grain size.

Measurements taken at the A elevation (0.003 m) were used to establish the as-fabricated grain size. This elevation cut through the lower fuel rod end caps of all 25 of the instrumented fuel rods. Photomicrographs of typical fuel from this region (Figures 206 and 208) show the as-fabricated porosity still contained within the grains. Examination of fuel from the center and edge of fuel pellets located at the center and near the periphery of the fuel assembly showed that all the fuel was similar. Measurements indicated an average fuel grain size of 14 μm at this elevation.

A total of 107 measurements were made in typically representative fuel over the entire axial length of the fuel assembly. These measurements indicated an average grain size of 14 μm, with a 2-sigma standard deviation of ± 4 μm. This is the same as found at the bottom elevation, which indicates that grain growth did not occur in the majority of the fuel. However, grain growth was observed in the center of some of the fuel pellets. This was first observed on some fuel pellets as low as the E elevation (0.27 m) but was most prevalent in the ceramic melt region and above. Thirty measurements were performed to characterize the extent of grain growth in these regions. These measurements indicated an average grain size of 27 μm, with a 2-sigma standard deviation of 17 μm.

4.5 Retained Fission Product and Elemental Analyses

Measurements were made to determine the distribution of core materials and the retention of fission products in the sample materials. The objectives of these analyses were to:

- Determine the distribution of core materials
- Evaluate the retention of fission products in the fuel material
- Determine the effects of fuel morphology and temperature on fission product release
- Evaluate fission product relocation to metallic melts and structural constituents.

4.5.1 Methodology and Quality Assurance

Elemental analyses were performed on the 30 core samples obtained from the LP-FP-2 fuel bundle. The sample locations are shown in Appendix E (Figures E-1 through E-27). The radiochemical analysis methodology was dictated by the hot cell handling requirements necessary to obtain the samples. Discussed below is the order in which the analyses were performed.

Core sections were transported to the chemical laboratories, where 0.20 to 2 g samples were obtained for the radionuclide and chemical analyses. These intact samples were then examined for total uranium content, using delayed neutron analysis and were analyzed by gamma-ray spectrometry to measure the gamma active component. These examinations, although not as accurate as those on the dissolved fractions, were performed to provide quality assurance for the dissolution and subsequent analysis of the samples. Also, duplicate samples were analyzed to assess the heterogeneity of the debris and replicability of the analysis results.

Following this nondestructive examination the samples were individually dissolved using a pyrosulfate fusion technique in a closed system for the retention of volatiles (e.g., ^{129}I). An ^{131}I tracer was added to the intact sample prior to dissolution to determine losses of ^{129}I during the dissolution and subsequent separations. A ^{90}Sr tracer was added to the sample after dissolution, as this radionuclide is not volatile and remains in the dissolved sample. Radiochemical (i.e., gamma spectroscopy and ^{90}Sr) and elemental analyses were performed on the dissolved samples, and ^{129}I analysis was performed on the recovered volatile ^{129}I. All dissolved samples were examined for undissolved material and precipitate formation. Multiple fusions were used when insoluble materials or precipitates were present, and all samples were fully dissolved prior to analysis. The fused material was then dissolved in dilute hydrochloric acid.

The elemental analysis results imply that several samples had relatively large concentrations of Ag that would be expected to precipitate from the hydrochloric acid solution. Therefore, the Ag data are questionable. However, duplicate sample analyses were performed to assess the reproducibility of all results and comparisons were made between the analyses performed on the intact samples (gamma ray spectrometry and uranium content via neutron activation analysis) and the analyses performed on the dissolved samples. These comparisons were performed to assess the uncertainties associated with handling and analysis and to identify problems in the analysis. A comparison between the uranium content data measured by inductively coupled plasma spectroscopy (ICP) and by neutron activation analysis (NAA) is shown in Appendix H. Good agreement is indicated for all samples except those metallic samples where the neutron activation result may have been affected by the presence of silver. Comparisons between the gamma ray spectroscopy measurements on the dissolved and intact samples also indicate good agreement within the uncertainties of the analysis for most samples except those where measurement problems were indicated or for the ^{60}Co data where some deposition or loss may have occurred.

Table 20 lists the comparisons for the three sets of duplicate samples. The results are in good agreement for G2-R16 and J2-R21 which were relatively homogeneous samples; however, the comparisons for J2-R4 indicate that sample heterogeneity can substantially affect the examination results (e.g., ^{129}I and ^{90}Sr). A more detailed discussion of the analytical methods and associated uncertainties is presented in Appendix H.

4.5.2 Elemental Analyses

Elemental analyses were performed by inductively coupled plasma spectroscopy (ICP) for the 27 elements that make up the principal components of the bundle. Table 21 lists the composition of the principal bundle components. The elemental analysis results and the uranium content of the samples, as determined by neutron activation analysis, are listed in Tables H1A through H1D of Appendix H.

The analysis samples represent seven morphology groups: intact fuel, fragmented fuel, foamy fuel/partially liquefied fuel, ceramic melts, eutectic metallic phases with fuel debris, metallic melts, and end box samples. The intact fuel pellet samples would be expected to be homogeneous. The other samples may be relatively heterogeneous, as they are generally mixtures of bundle components.

Examination of Appendix Tables H1A through H1D indicates that uranium and zirconium were measurable in almost all samples, but the structural and instrument materials were measurable primarily only in the metallic or mixed-metallic samples. Comparison of the ICP elemental analysis results for uranium with the uranium measurements performed by neutron activation indicates small differences (<10% and generally <5%) for all but seven samples. All seven samples are partially or fully metallic samples. Six of the seven, C2-R12, D4-R14, I4-R3, K1-R23, Q3-R9, and S3-R10, all indicate higher concentrations of uranium measured by ICP than those measured by neutron activation. These data may indicate that significant amounts of control rod material interferred with the direct neutron assay of the samples. The elemental results show the presence of Ag and In in these

TABLE 20. QUALITY ASSURANCE COMPARISON

		Uranium Content (wt.%)		μCi/g		Intact/Dissolved Gamma Spectroscopy Comparison[c]		
Sample Type	Sample Number	NAA[a]	ICP[b]	^{129}I	^{90}Sr	^{137}Cs[d]	^{144}Ce	^{60}Co
Intact fuel	G2-R16A	87.5	86	3.4 E-4	1090	0.73	0.88	0.86
	G2-R16B	87.4	87	4.4 E-4	1340	0.77	0.94	0.78
Ceramic melt	J2-R21A	54	55	3.3 E-5	686	0.85	0.96	1.05
	J2-R21B	54	53	4.2 E-5	803	0.89	0.89	1.10
Foamy fuel/ partially liquefied fuel	J2-R4A	79	80	5.7 E-5	812	0.93	1.3	0.23
	J2-R4B	78	72	2.6 E-4	1773	0.93	1.1	0.74

---

[a] NAA - Neutron activation analysis with delayed fission neutron counting.

[b] ICP - Elemental analysis using inductively coupled gamma spectroscopy.

[c] Ratio of solid to dissolved material gamma ray analysis results. ^{60}Co and ^{144}Ce based on the ^{144}Pr daughter gamma ray lines are not substantially affected by sample mass attenuation.

[d] ^{137}Cs ratios are less than the actual values (~10%) as the solid sample results are reduced by the mass attenuation of the 661 KeV gamma ray line.

TABLE 21. COMPOSITION OF PRINCIPAL FUEL BUNDLE COMPONENTS

Material	Element	Weight Percent	Material	Element	Weight Percent
UO_2	U-235[a]	9.745	Inconel-718	Ni[a]	51.900
	U-238[a]	78.4		Cr[a]	19.000
	O	11.853		Fe[a]	18.000
				Nb[a]	5.553
Zircaloy-4	Zr[a]	97.907		Mo[a]	3,000
	Sn[a]	1.60		Ti	0.800
	Fe[e]	0.225		Al[a]	0.600
	Cr[a]	0.125		Co	0.470
	O	0.095		Si[a]	0.200
				Mn[a]	0.200
Type 304 stainless steel	Fe[a]	68.635		N	0.130
	Cr[a]	19.000		Cu	0.100
	Ni[a]	9.000			
	Mn[a]	2.000	Ag-In-Cd	Ag[a]	80.0
	Si[a]	1.000		In[a]	15.0
	N	0.130		Cd[a]	5.0
	C	0.080			
			Instrument materials[b]		
			Poison	B[a]	

---

a. Elements for which ICP analysis was performed.

b. Instrument materials for which measurements were performed: rhodium, tungsten, hafnium, tantalum, beryllium, magnesium, aluminum, cobalt, rhenium, yttrium, barium, and titanium.

samples; however, it is difficult to relate control material concentrations directly to the degree of interference. In the seventh anomalous sample (03-R28) the ICP result was less than that measured by neutron activation. 03-R28 was a split sample in which a portion of the sample was removed prior to dissolution. The differences in the analysis results for this sample suggest that the sample was heterogeneous.

A quality assurance check was performed by assuming the expected oxidation state for the major elements in Tables H1A through H1D, and adding the expected oxygen to the sum of all the measured elements. Theoretically, this sum should equal 100%. The results of these calculations are shown in Table 22. Very good agreement was generally found for the intact fuel, fragmented fuel, foamy fuel/partially liquefied fuel, upper end box samples, and ceramic melts, with the exception of sample I2-R2. This sample was unique in that it contained 12% aluminum (from Al_2O_3 spacers at the tops of the fuel stacks), but the cause of the discrepancy in the mass balance for this sample is unclear. Poor agreement was generally found for the eutectic metallic melt/fuel debris and metallic melt samples. The total mass values for the eutectic metallic melt/fuel debris are limits based upon all the Zr being metallic or fully oxidized. (SEM analysis of sample C2-S11 indicated some of the zirconium was metallic and some was oxidized.) For these samples a range is indicated in Table 22. The greatest discrepancy is in sample B4-R11, which was identified from metallographic examinations as a droplet of (Ag,In,Cd) control rod material. As discussed in detail in the following sections, it appears that Ag precipitated out of the HCl acid solution and was not measured during the ICP analysis. Ag should have been present in significant quantities in the eutectic metallic melt samples, based upon the metallographic examinations; and it is also expected to be present in the multiphase metallic melts. The poor agreement in the total mass values for these two categories of materials strongly suggests that Ag was not accurately measured.

The following sections discuss the composition of the seven principal sample types: intact fuel, fragmented fuel, foamy fuel/partially liquefied fuel, ceramic melts, eutectic metallic phases with fuel debris, metallic melts, and upper end box samples. Also discussed are the measured densities for the various sample types.

TABLE 22. ELEMENTAL MASS BALANCE DATA

Sample	Assumed Oxides	Total Mass (wt%)
Intact fuel		
D4-R13	UO_2	99
G2-R16A	UO_2	100
G2-R16B	UO_2	102
I4-R20	UO_2	101
M1-R8	UO_2	103
O3-R27	UO_2	99
Fragmented fuel		
G2-R17	UO_2	95
K1-R22	UO_2	100
L2-R25	UO_2	90
Ceramic melt		
I2-R1	UO_2, ZrO_2	96
I2-R18	UO_2, ZrO_2	94
I2-R2	UO_2, ZrO_2, Al_2O_3	72
I4-R19	UO_2, ZrO_2	95
I4-R21A	UO_2, ZrO_2	100
I4-R21B	UO_2, ZrO_2	95
K1-R6	UO_2, ZrO_2	100
K1-R7	UO_2, ZrO_2	95
L2-R24	UO_2, ZrO_2	95
O2-R26	UO_2, ZrO_2	97
Eutectic metallic melt/fuel debris		
C2-R12	UO_2, (ZrO_2)	59-73
D4-R14	UO_2, (ZrO_2)	57-68
E2-R15	UO_2, (ZrO_2)	86-94
O3-R28D	UO_2, (ZrO_2)	62-65
Metallic melts		
B4-R11	UO_2	26
J4-R3	UO_2	104
K1-R23	UO_2	72
Q3-R9	UO_2	81

TABLE 22. (continued)

Sample	Assumed Oxides	Total Mass (wt%)
Foamy fuel/partially liquefied fuel		
J3-R5	UO_2, ZrO_2	90
J2-R4A	UO_2, ZrO_2	99
J2-R4B	UO_2, ZrO_2	90
End box samples		
S2-R30	UO_2, ZrO_2, Fe_3O_4, Cr_2O_3	101
S2-R10	UO_2, ZrO_2, Fe_3O_4, Cr_2O_3	112

4.5.2.1 Intact Fuel. Intact fuel pellets from five locations were examined - D4-R13, G2-R16A, G2-R16B, I4-R20, M1-R8, and O3-R27 (sample G2-R16 was split into duplicate samples G2-R16A and B). The corresponding sample elevations were: D, 0.22 m; G, 0.43 m; I, 0.66 m; M, 1.04 m; and O, 1.2 m. These fuel samples have an average uranium content of 87.7 wt%, which is within 0.5% of the manufactured composition of 88.1 wt%. The random and systematic uncertainties are on the order of 15% for these data, except where noted in Appendix H.

4.5.2.2 Fragmented Fuel. Three samples of fragmented fuel were examined (G2-R17, K1-R22, and L2-R25), from respective elevations 0.43 m, 0.88 m, and 0.96 m. No duplicate samples were analyzed. As shown in Table H1A, the fragmented fuel samples have uranium as the principal constituent, with an average uranium content of 76 wt% and a range between 73 and 77 wt%. Much of the remaining mass (other than the expected oxygen content of the sample) is Zr (average 5.7 wt%), most of which was melt that penetrated the fragmented fuel. Sample K1-R22 contained significant amounts of control rod and structural metallics (Ag, In, Fe, Cr, Ni, Sn). This is consistent with the metallographic and SEM examinations, which indicated an agglomeration of mixed metallic material surrounding and penetrating the fuel in this region.

Tin apparently concentrated in the metallic melt in sample K1-R22, as the Sn concentrations are several times greater than would be expected for the amount of Zr present. These data suggest that upon melting of the zircaloy, much of the Sn partitioned into the metallic phases. Similar partitioning is also observed in other metallic melt samples (I4-R3, K1-R23, Q3-R9).

4.5.2.3 Foamy Fuel/Partially Liquefied Fuel. Sample J3-R5 was an example of the foamy fuel discussed in Section 3.2.9. The fuel microstructure was characterized by isolated regions of high porosity, typically on the outer surface of a fuel pellet, although it was occasionally observed penetrating into the fuel. SEM examinations of a similar sample of foamy fuel (J1-S30) showed that structural oxides

(Fe,Cr,Ni,O) had penetrated into the fuel in these regions, liquefying the fuel below its melting point. The elemental analysis of retained fission product sample J3-R5 also indicates the presence of Fe, Ni, and Cr, with small amounts of Ag also present.

Sample J2-R4 was a partially liquefied fuel pellet surrounded by $(U,Zr)O_2$ melt in the high-temperature central portion of the upper blockage. This fuel had a porous appearance; however, SEM examinations of a similar sample (K2-S32) indicated that no structural oxides were present, in contrast to foamy fuel sample J1-S30. Similarly, elemental analysis of retained fission product sample J2-R4 indicated no significant concentrations of Fe, Cr, or Ni. The 8% Zr measured in samples J2-R4A and J2-R4B is believed to be from the $(U,Zr)O_2$ ceramic melt that surrounded the fuel pellet and which was included in the core bore (see Figure E-13). These results indicate that the porous structure of some fuel pellets in the central portion of the upper blockage was due to the fuel being very near the 3120-K melting point of the fuel, and not to liquefaction caused by interactions with structural materials.

4.5.2.4 Ceramic Melts. Nine samples of ceramic melt were examined to evaluate differences in composition as a function of core location and morphology. The nine samples are described in Table 23. Table 24 lists the principal constituents of each sample. As indicated in this table, all ceramic melts generally have similar compositions, with U and Zr being the principal components. In all cases but one, uranium is the major component on a weight basis; however, on an atom basis, Zr is generally the principal component by factors of >2:1. Differences in the results from samples at various elevations are discussed below.

o At the I2 core location the uranium content ranges from 28 to 44 wt%, and the Zr content ranges from 12 to 39 wt%. As previously noted, the results for the I2-R2 sample are anomalous. The total accountable mass balance for this sample is only 72%.

TABLE 23. CERAMIC MELT SAMPLES SUMMARY INFORMATION

Sample Identification	Elevation (m)	Sample Description
I2-R2	0.66	Nonporous ceramic melt in a flow channel location.
I2-R18	0.66	Porous ceramic melt in an aerosol sample probe location.
I2-R1	0.66	Porous ceramic melt in a former control rod location.
I4-R19	0.66	Porous ceramic melt in a flow channel near the center of the bundle.
J2-R21	0.77	Porous ceramic melt with a textured appearance in an area of complete fuel liquefaction.
K1-R6	0.88	Nonporous ceramic melt in a flow channel location near the exterior of the bundle.
K1-R7	0.88	Porous ceramic melt in a flow channel near the center of the bundle.
L2-R24	0.96	Porous ceramic melt in an empty guide tube position at the top of the upper blockage region.
O2-R26	1.20	Isolated area of porous ceramic melt between two fuel pellet stacks.

TABLE 24. PRINCIPAL CONSTITUENTS OF CERAMIC MELTS

Sample Identification	Concentration (wt%) U	Concentration (wt%) Zr	Other[a,b]
I2-R1	36	39	Ag(0.6), Cr(0.5), Fe(0.6), Ni(0.4)
I2-R18	44	33	Fe(0.5)
I2-R2	28	12	Ag(0.9), Al(12.0)
I4-R19	37	36	Ag(0.4), Cr(1.2), Fe(1.5), Ni(1.2)
J2-R21A	55	27	Cr(0.6), Fe(0.3), In(0.4)
J2-R21B	53	25	Cr(0.6), Fe(0.3), In(0.4)
K1-R6	47	33	Cr(0.7), Fe(0.5)
K1-R7	46	29	Ag(0.6), Cr(1.1), Fe(1.0), Ni(0.8)
L2-R24	43	30	Cr(1.7), Fe(3.1), Ni(0.7)
O2-R26	75	9.0	--

---

a. Concentrations greater than 0.3 wt%.

b. Measured Ag values may be inaccurate.

- The greatest concentration of uranium in the samples was at the J elevation (0.77 m). The ceramic melt in this region was among the hottest in the bundle, near fuel melting.

- At the K and L core elevations the compositions are similar and indicate a homogeneous melt, with most of the principal constituents present at similar concentrations.

- At the O core elevation there is less Zr than at the other elevations. This is probably a sampling artifact, since this core bore contained a significant portion of an intact fuel pellet in addition to the ceramic melt (see Figure E-22).

4.5.2.5 Eutectic Metallic Phases with Fuel Debris. Four samples of eutectic metallic phases with fuel debris were examined (C2-R12, D4-R14, E2-R15, and 03-R28). The C, D, and E, samples were taken respectively near the bottom, the center, and the top of the lower blockage. The 03 sample was taken from an isolated region in the upper bundle that appeared visually similar to the lower blockage. Table 25 shows the principal constituents in these samples.

The measured Ag values (1%-2.6%) are inconsistent with metallographic observations of the material in the lower blockage, and with the quantitative SEM examinations of sample C2-S11, which indicated silver concentrations of 19-89 wt% in three different phases in the eutectic metallic melt (see Tables E-3 and E-4). This further indicates that the measured Ag data are inaccurate. The possible amount of Ag present, based on the values in Table 22, is shown in parenthesis in Table 25.

Examination of the data in Table 25 indicates increases in the uranium content and decreases in the zirconium content from the bottom to the top of the blockage. This is consistent with metallographic observations of more fuel particulate in the upper portions of this blockage region.

TABLE 25. PRINCIPAL CONSTITUENTS OF EUTECTIC METALLIC PHASES WITH FUEL DEBRIS

Sample Identification	Concentration (wt%) U	Zr	Ag[a]	Other[b]
C2-R12 (bottom of blockage)	4.9	39	2.0 (27-41)	Cd(0.5), Cr(1.5), Ni(3.3), Sn(1.5), In(3.1), Fe(3.3)
D4-R14 (center of blockage)	10	32	1.0 (32-43)	Cd(0.4), Cr(1.7), Ni(3.8), In(2.1), Sn(1.2), Fe(3.1)
E2-R15 (top of blockage)	45	24	2.6 (6-14)	Cr(1.0), Ni(2.2), In(1.5), Sn(1.2), Fe(2.2)
03-R28	42	9	1.2 (35-38)	Cr(0.4), Ni(0.8), In(0.7), Sn(0.7), Fe(1.1)

---

a. Measured Ag data are inaccurate; possible amount of Ag present in each sample based on total quantity of other constituents is presented parenthetically.

b. Concentrations greater than 0.3 wt%.

Tin is present in significant concentrations (1.2%-1.5%) in these samples. The measured Sn/Zr weight ratios in these samples range from 0.04 -0.08 wt%, and are much greater than those in the as-fabricated zircaloy (0.015 wt%). This suggests that the tin is preferentially partitioned to the metallic phase. Similar results were found for the fragmented fuel and metallic melts.

The concentration of Cd in the eutectic melts ranges from 0.5 wt% at the bottom of the blockage to 0.2 wt% at the top of the blockage. Although the Cd/In ratios indicate loss of some cadmium, the retention of any of the relatively volatile cadmium in these regions suggests that these melts were not exposed to high temperatures for any significant period of time. This is consistent with the postulated bundle scenario in Section 5, which indicates that the material in the lower blockage resulted from Ag-Zr melts interacting with structural materials after failure of the control rods at or before 1720 K. As described in Section 4.3, the solidified material in the lower blockage was generally not hot enough to affect the zircaloy microstructure, and temperatures in these regions were generally less than ~1200 K.

4.5.2.6 Metallic Melts. Four samples of other metallic melts were obtained from other locations throughout the bundle (B4-R11, I4-R3, K1-R23, and Q3-R9). The principal results of these examinations are shown in Table 26. As noted previously, several of these samples lost Ag during the analysis. The B4-R11 sample was identified from metallographic observations as a droplet of control rod material that solidified on the lowest spacer grid. The as-fabricated weight ratio of the (Ag,In,Cd) alloy is 80%:15%;5%; however, the measured ratio of 3.7%:12.7%.3.8% in sample B4-R11 indicates the indium and cadmium concentrations are nearly as expected, but that there was a significant reduction in the Ag concentration.

The remaining three samples are multiphase, multiconstituent, metallic melts, with the primary constituent being Zr (average concentration 40 wt%). As discussed in Sections 4.1.2 and 4.1.3, the amount of these multiphase metallic melts in the LP-FP-2 fuel bundle was relatively small.

TABLE 26. PRINCIPAL CONSTITUENTS OF METALLIC MELTS

Sample Identification	Concentration (wt%) U	Zr	Ag[a]	Other[b]
B4-R11	<0.2	0.1	3.7 (74)	In(12.7), Cd(3.8), Cr(2.2), Ni(0.6), Mo(0.4), Fe(2.1)
I4-R3	11	47	6.0 (6)	Al(1.0), Cr(6.5), Ni(1.2), Mn(0.3), Mo(0.5), Sn(2.8), Ti(0.3), Fe(15.1)
K1-R23	19	33	2.6 (28)	Ni(2.9), Cr(1.6), In(4.2), Sn(1.2), Fe(3.7)
Q3-R9	8.2	41	3.7 (19)	Cd(0.7), In(5.0), Cr(2.7), Ni(3.6), Sn(1.7), Fe(11.7)

---

a. Silver data are inaccurate; possible amount of silver present in each sample based on total quantity of other constituents is presented parenthetically.

b. Concentrations greater than 0.3 wt%

4.5.2.7 Samples From the Upper End Box. At the stainless steel upper tie plate, two samples were examined (S2-R30 and S3-R10). In both cases, the samples were primarily Zr (26-50 wt%), with lesser amounts of stainless steel constituents [Fe (8-25 wt%), Cr (5.5-6.5 wt%), and Ni (3.6-5.5 wt%)] and U (9-15 wt%). (Ag,In,Cd) control material was present in small amounts. Fuel and control materials were not originally present at this elevation, so these data indicate that these materials were transported upward from the fuel bundle, either as volatiles or as particulate matter. This is consistent with the metallographic and SEM examinations, which indicated that fuel fragments and molten (U,Zr,O) were present at the upper tie plate, and with deposition coupon data, which indicated aerosol or vapor transport of control materials into the upper plenum region.[9,10]

4.5.3 Density of Core Bore Samples

The measured densities of the core bore samples used to calculate the mass balances of U and Zr in Section 4.1.4 are listed in Table 27. The data for the intact fuel pellets indicate, in general, reductions from the as-fabricated density of 10.38 g/cm^3. The data for the fragmented pellets indicate a range of 6.9 to 9.3 g/cm^3. These reductions from the as-fabricated density may be due to the ingress of metallic melts, or to small amounts of low density (1.2 g/cm^3) epoxy remaining in the open areas within the fragmented fuel or in the dishes in the intact fuel pellets. The eutectic metallic melts/fuel debris samples also have densities less than the expected ranges for the fuel and metals (zircaloy--6.5 g/cm^3; stainless steel--8.0 g/cm^3; (Ag,In,Cd)--10 g/cm^3). This is believed to be due to epoxy being entrapped in the extensive porosity observed metallographically within these samples. The ceramic melts have densities ranging from 4.7 to 8.4 g/cm^3, reflecting variations in concentration and closed porosity within these melts. The effects of entrapped epoxy on these densities should be negligible.

Although the presence of epoxy (e=1.2 g/cm^3) in these samples slightly affected the true sample densities, this effect is negligible compared to other uncertainties associated with estimating the U and Zr mass balances (Section 4.1.4).

TABLE 27. DENSITY OF CORE BORE SAMPLES

Sample Identification	Density (g/cm^3)	Description
Intact pellets		
D4-R13	10.1	Intact fuel pellet
O3-R27	8.9	Intact pellet
R3-R29	10.5	Intact pellet
I4-R20	9.4	Intact fuel pellet
Fragmented fuel		
G2-R17	6.9	Fragmented fuel
K1-R22	9.3	Fragmented fuel pellet with significant penetration of metallic melt
Foamy fuel/partially liquefied fuel		
J2-R4	8.5	Partially liquefied fuel pellet surrounded by $(U,Zr)O_2$
J3-R5	8.3	UO_2-Fe_3O_4 liquefied foamy fuel
Ceramic melts		
I2-R1	7.0	Porous ceramic melt
L2-R24	4.9	Porous ceramic melt
K1-R6	6.0	Nonporous ceramic melt
I2-R2	7.9	Nonporous melt
K1-R7	5.6	Porous ceramic melt
I4-R19	4.7	Porous ceramic melt
I2-R18	6.3	Porous ceramic melt
O2-R26	7.6	Ceramic melt (& fuel pellet)
J2-R21	8.4	Ceramic melt
Eutectic metallic melts/fuel debris		
C2-R12	5.8	Lower blockage metallic melt
O3-R26	7.0	Similar material in upper bundle
D4-R14	5.4	Lower blockage metallic melt
E2-R15	6.9	Lower blockage metallic melt

4.5.4 Radionuclide Fission Product Measurement Data

The radionuclide composition of the LP-FP-2 core samples was determined from the analysis of the 30 samples identified in the previous section. Results of the radiochemical analysis of each sample are listed in Appendix H, Table H2A through H2C. Appendix H also provides a discussion of the uncertainties associated with the analysis results. The associated uncertainty is approximately 30% for all results. To provide information on the characteristic behavior of fission products, the elements have been categorized by volatility as shown in Table 28. In addition, some possible chemical compounds have also been included.

The high-volatility fission product groups (I, II, III, and IV.a) include the noble gasses, halogens, alkali metals, and heavy chalcogens. They are characterized by boiling points less than 1700 K for the elemental forms as well as for the listed oxide compounds. From this group, measurements were performed for ^{129}I and ^{137}Cs.

The medium-volatility fission products are characterized by boiling points less than 3100 K (UO_2 melting). These fission products are from the Group VA metals, alkaline earths, some of the rare earths, and actinides. Radionuclides from these groups for which measurements were made are ^{125}Sb, ^{90}Sr, and ^{154}Eu. The noble metal Ru is also of medium volatility. However, it should be noted that the volatility of these fission products is strongly dependant on the chemical form of the fission product. An example is Ru, which has two highly volatile oxides (i.e., RuO_2 and RuO_4), either of which decompose or boil at less than 400 K.

The low-volatility fission products include elements from the noble metals, the remaining rare earths and actinides, tetravalents, and early transition elements. Generally, the oxides of these elements have low volatilities; however, some (e.g., LaO or CeO) have lower boiling points than do the elements. The only radionuclide from this group that was measurable during the LOFT FP-2 sample examination program was $^{144}Ce/^{144}Pr$.

TABLE 28. CORE MATERIAL VOLATILITY GROUPS

WASH-1400 Group Number	Chemical Group	Element	Boiling[a] Temperature (K)	Vola-tility	Possible Compounds	Boiling[a] Temperature (K)	Vola-tility
I	Noble gases	Kr	120	High	--	--	--
		Xe	166	High	--	--	--
II	Halogens	Br	332	High	CsBr	1573	High
		I[b]	458	High	CsI	1553	High
III	Alkali metals	Rb	973	High	RbI	1573	High
					Rb_2O	--	High
					Rb_2O_2	1284	High
		Cs[b]	963	High	CsI	1553	High
					CsOH	1350[c]	High
					Cs_2O	--	High
					Cs_2O_2	923	High
					Cs_2UO_4	--	--
IV.a	Heavy chalcogens	Se	958	High	SeO_3	453	High
					SeO_2	--	--
		Te	1663	High	TeO_2	--	--
					Te_2O_2	--	--
					FeTe	--	--
					ZrTe	--	--
					SnTe	--	--
IV.b	Group VA metals	Sb[b]	1653	Medium	Sb_2O_3	1323	Medium
V	Alkaline earths	Sr[b]	1639	Medium	SrO[b]	3100	Low
		Ba	1800	Medium	BaH_2	1673	Medium
					BaO[b]	2273	Medium
					BaO_2	1073	High
					$Ba(OH)_2$	1053	High
VI	Rare earths	Eu[b]	--	Medium	Eu_2O_3	--	--
		Sm	2173	Medium	Sm_2O_3	--	--
		Pm	3400	Low	Pm_2O_3	--	--
	Actinides	Am	2873	Medium	AmO_2	--	--
	Noble metals	Pd	2473	Low	PdO	--	--
		Rh	6173	Low	RhO_2	--	--
			(est.)		Rh_2O_3	--	--
		Ru[b]	4423	Medium	RuO_2	--	High
					RuO_4	125	High
		Mo	4780	Low	MoO_2	--	--
					Mo_2O_3	--	--
					MoO_3	--	--
		Tc	--	Low		--	--

TABLE 28. (continued)

WASH-1400 Group Number	Chemical Group	Element	Boiling[a] Temperature (K)	Volatility	Possible Compounds	Boiling[a] Temperature (K)	Volatility
VII	Rare earths	Y	3260	Low	Y_2O_3	--	--
		La	3743	Low	LaO	--	Medium-high
					La_2O_3	4473	Low
		Ce[b]	2690	Low	CeO_2	--	--
					Ce_2O_3	--	--
		Pr	3400	Low	PrO_2	--	--
					Pr_2O_3	--	--
		Nd	3300	Low	Nd_2O_3	--	--
	Actinides	Np	--	Low	NpO_2	--	--
		Pu	3508	Low	PuO_2	--	Low
		Cm	--	Low	CmO_2	--	--
	Tetravalents	Zr[c]	3173 (appr.)	Low	ZrO_2	5273	Low
	Early transition	Nb	~3573	Low	NbO_2	--	Low
					Nb_2O_5	--	--

---

a. Boiling temperature at 1 atm. Data primarily from CRC Handbook of Chemistry and Physics, 56th Edition.

b. Elements for which radionuclide analyses were performed.

c. Zirconium is both a fission product and a structural material.

4.5.5 Radionuclide Comparisons with ORIGEN2

The measured radionuclide concentrations of the core samples were compared with concentrations predicted by the ORIGEN2 code in order to assess retention of radionuclides in the fuel matrix and in the bundle. The ORIGEN2 analysis for the LOFT bundle is documented in Reference 10. The variation in the flux profile (Appendix C) affects the burnup and consequently the production of fission products. The method used to estimate retention is shown below.

$$\frac{\text{Radionuclide concentration } (\mu\text{Ci/g})}{\text{Uranium content (g Uranium/g sample)}} \times \frac{100}{\text{ORIGEN2-predicted radionuclide concentration } (\mu\text{Ci/g U})} = \text{Uranium normalized fission product retention (\%)} \tag{15}$$

The radionuclide concentrations used were from Appendix H, Table H2A-H2C, and the uranium content data were from the ICP analysis data in Table H1A-H1D.

4.5.5.1 Intact Fuel Pellets. Table 29 lists the calculated retention values and their estimated uncertainty (1 sigma) for the intact fuel pellets. Also listed are the estimated peak temperatures of each of the samples as determined from the metallurgical examinations. The uncertainties listed are the propagated measurement uncertainties and the random uncertainty associated with the sample handling and dissolution. The uncertainties associated with ORIGEN2 were not included in this analysis, as they do not affect the relative values.

The ORIGEN2 calculated inventories are core average concentrations. The neutron flux profile at the original core location of the sample affects the fission product concentrations. Samples drawn from the top or bottom of fuel rods, where the flux is depressed will contain less that the core average fission product inventory concentrations. For samples other than melts, which may have mixed materials from several core locations, this flux

TABLE 29. COMPARISON OF MEASURED AND ORIGEN2-CALCULATED FISSION PRODUCT CONCENTRATIONS FOR INTACT FUEL PELLETS

	Radionuclide Retention[a] (%)							
Sample No./ Temperature	^{90}Sr	^{106}Ru	^{125}Sb	^{129}I	^{134}Cs[b]	^{137}Cs	^{144}Ce	^{154}Eu[b]
D4-R13 (~1000 K)	72 ± 22	69 ± 10	69 ± 10	89 ± 32	131 ± 20	79 ± 12	78 ± 12	73 ± 12
G2-R16A (1400-1500 K)	86 ± 26	52 ± 8	103 ± 16	111 ± 40	218 ± 33	117 ± 18	114 ± 17	133 ± 22
G2-R16B (1400-1500 K)	106 ± 32	63 ± 9	104 ± 16	143 ± 51[c]	216 ± 33	116 ± 17	113 ± 17	--[d]
I4-R20 (2600-2900 K)	80 ± 25	114 ± 17	101 ± 15	105 ± 38	246 ± 38	112 ± 17	115 ± 17	--[d]
M1-R8 (2300-2800 K)	73 ± 23	104 ± 16	101 ± 15	67 ± 24	175 ± 27	84 ± 13	105 ± 16	--[d]
O3-R27 (2300-2800 K)	71 ± 22	80 ± 12	77 ± 12	114 ± 42	127 ± 20	76 ± 11	74 ± 11	--[d]

---

a. The ORIGEN2-calculated radionuclide concentrations in μCi/g of uranium for each isotope on July 9, 1985 at 14:00 are: ^{90}Sr, 1440; ^{106}Ru, 3350; ^{125}Sb, 104; ^{129}I, 3.5 E-4; ^{134}Cs, 6.1; ^{137}Cs, 1510; ^{144}Ce, 5030; ^{154}Eu, 0.398.

b. Isotope concentrations are poorly predicted by ORIGEN2.

c. Poor radiochemical yield.

d. Not detected or not measured.

profile dependance can be compensated for approximately by normalizing the retentions to ^{144}Ce, a well predicted burnup indicator that is expected to remain with the fuel even at high temperature. The data in Table 29 indicate that the D4-R13 and O3-R27 samples came from low-burnup regions of the core, as evidenced by the ^{144}Ce retentions of 78 ± 12% and 74 ± 11%. However, the other samples are from burnup locations that are near the core average, as indicated by the uncertainties.

The intact pellet retention data were normalized to the ^{144}Ce content to approximate removal of the burnup dependance of the data and the results are shown in Table 30. Examination of Table 30 indicates very little variation in the retention data at different core locations. Little or no fission product release is expected from intact pellets. For all samples and all isotopes, other than ^{134}Cs and ^{106}Ru, all retention values are within two estimated standard deviations of 100%. ^{134}Cs is poorly predicted by ORIGEN2[10]. The low calculated retention of ^{106}Ru in split samples G2-R16A and B is unexplained.

4.5.5.2 Fragmented Fuel Pellets. Table 31 lists the fission product retentions and estimated peak temperatures for the fragmented fuel samples. This table includes both unnormalized and normalized retentions. These data indicate complete retention of ^{144}Ce, and releases of ^{129}I and ^{137}Cs are noted in the higher temperature samples. The data also indicate loss of ^{90}Sr. However, since the lowest retention is in the lowest temperature specimen, the data appear questionable.

4.5.5.3 Foamy Fuel/Partially Liquefied Fuel. Table 32 lists the fission product retention for sample J3-R5, which was composed of foamy fuel material resulting from iron oxides interacting with the fuel, and samples J2-R4A and J2-R4B, which are partially liquefied fuel samples that were split for examination. Since these samples may contain melt material from other core regions, no ^{144}Ce normalization was done. The results for split samples J2-R4A and J2-R4B indicate large differences in fission product retention in these compositionally similar samples. The temperatures to which sample J3-R5 was exposed are not easily determinable,

TABLE 30. COMPARISON OF MEASURED AND ORIGEN2-CALCULATED FISSION PRODUCT CONCENTRATIONS FOR INTACT FUEL PELLETS (NORMALIZED TO ^{144}Ce CONTENT)

	Radionuclide Retention (%)							
Sample No.	^{90}Sr	^{106}Ru	^{125}Sb	^{129}I	^{134}Cs[a]	^{137}Cs	^{144}Ce	^{154}Eu[a]
D4-R13	92 ± 32	88 ± 19	88 ± 19	114 ± 45	168 ± 36	101 ± 22	100 ± 0	94 ± 21
G2-R16A	75 ± 26	46 ± 10	90 ± 19	98 ± 38	191 ± 41	103 ± 22	100 ± 0	117 ± 26
G2-R16B	93 ± 32	55 ± 12	92 ± 20	126 ± 50[b]	191 ± 41	102 ± 22	100 ± 00	--[c]
I4-R20	70 ± 24	99 ± 21	87 ± 19	90 ± 36	213 ± 46	97 ± 21	100 ± 00	--[c]
M1-R8	70 ± 24	99 ± 21	74 ± 16	64 ± 25	167 ± 36	81 ± 17	100 ± 00	--[c]
O3-R27	96 ± 33	108 ± 23	90 ± 19	155 ± 61	172 ± 37	103 ± 22	100 ± 00	--[c]

---

a. Isotope concentrations are poorly predicted by ORIGEN2.

b. Poor radiochemical yield.

c. Not detected or not measured.

TABLE 31. COMPARISON OF MEASURED AND ORIGEN2-CALCULATED FISSION PRODUCT CONCENTRATIONS FOR FRAGMENTED FUEL PELLETS

	Radionuclide Retention[a]/Normalized to ^{144}Ce (%)							
Sample No./ Temperature	^{90}Sr	^{106}Ru	^{125}Sb	^{129}I	^{134}Cs[b]	^{137}Cs	^{144}Ce	^{154}Eu[b]
G2-R17 (1400-1500 K)	45 ± 14	90 ± 14	115 ± 17	127 ± 46	216 ± 33	112 ± 17	114 ± 17	--c
	39 ± 13	79 ± 14	101 ± 17	111 ± 43	190 ± 41	98 ± 17	100 ± 21	
K1-R22 (2400-2800 K)	85 ± 26	151 ± 23	93 ± 14	47 ± 17	159 ± 24	86 ± 13	120 ± 18	184 ± 30
	71 ± 24	126 ± 27	78 ± 17	39 ± 15	133 ± 28	72 ± 15	100 ± 21	
L2-R25 (2200-2600 K)	72 ± 22	116 ± 18	110 ± 17	63 ± 24	193 ± 29	102 ± 15	122 ± 18	--b
	59 ± 20	95 ± 20	90 ± 19	52 ± 21	158 ± 33	84 ± 18	100 ± 21	

---

a. The ORIGEN2-calculated radionuclide concentrations for each isotope are calculated for July 9, 1985 at 14:00.

b. Isotope concentrations poorly predicted by ORIGEN2.

c. Not measured or below detection limits.

TABLE 32. COMPARISON OF MEASURED AND ORIGEN2-CALCULATED FISSION PRODUCT CONCENTRATIONS FOR FOAMY FUEL/PARTIALLY LIQUEFIED FUEL

	Radionuclide Retention[a] (%)							
Sample No./ Temperature	^{90}Sr	^{106}Ru	^{125}Sb	^{129}I	^{134}Cs[b]	^{137}Cs	^{144}Ce	^{154}Eu[b]
J3-R5 (2200-3100 K)	85 ± 26	93 ± 14	79 ± 12	33 ± 12	80 ± 12	38 ± 6	131 ± 20	242 ± 39
J2-R4A (3000-3100 K)	70 ± 22	80 ± 12	50 ± 8	20 ± 7	54 ± 8	27 ± 4	89 ± 13	131 ± 21
J2-R4B (3000-3100 K)	170 ± 53	25 ± 4	69 ± 10	102 ± 39	72 ± 11	34 ± 5	127 ± 19	193 ± 30

---

a. The ORIGEN2-calculated radionuclide concentrations for each isotope are calculated for July 9, 1985 at 14:00.

b. Isotope concentrations are poorly predicted by ORIGEN2.

and large uncertainties are associated with this sample. The data indicate partial release of the high volatiles and little or no release of the medium and low volatiles.

4.5.5.4 Ceramic Melts. The fission product retentions and peak temperatures for the ceramic melts are listed in Table 33. As noted in Section 4.5.2.4, the compositions of all the melts are relatively similar; however, the fission product retentions vary substantially. The low volatility species (Ce and Eu) are present, with some release indicated near the top of the bundle. However the concentrations of the medium and high volatiles vary considerably, with no discernible correlation with temperature or location. These data suggest that the ceramic melt relocated incoherently, and that fission product release is a complex phenomena dependant on a number of factors, not just simple diffusion as a function of peak temperature. Time at temperature and the material surrounding these small core bore samples are two such factors which could have significantly affected fission product retention.

4.5.5.5 Upper Tie Plate Debris. The fission product concentrations in the samples from the upper end box are shown in Table 34. The data indicate concentrations for both cesium and iodine that are a small fraction of what would be expected based on the amount of fuel transported to the tie plate. There is evidence of loss of the low volatiles ^{144}Ce and ^{154}Eu. However, there were problems with the dissolution of sample S3-R10, in that a number of dissolutions were required to fully dissolve the sample, and there were discrepancies between the intact and dissolved gamma-ray spectrometer data for ^{144}Ce. Consequently, without further substantiation, this result must be considered inconclusive. The anomalously high ^{125}Sb data suggest that deposition of this radionuclide on the upper tie plate surfaces occurred. Examination of the bundle gamma scan data in Appendix C indicates apparent deposition of both ^{125}Sb and ^{129}Te on the upper plenum surfaces.

4.5.5.6 Eutectic Metallic Phases with Fuel Debris. The fission product retention data for the eutectic metallic phase/fuel debris samples are shown in Table 35. The data indicate large variations in the retention

TABLE 33. COMPARISON OF MEASURED AND ORIGEN2-CALCULATED FISSION PRODUCT CONCENTRATIONS FOR CERAMIC MELTS

	Radionuclide Retention[a] (%)							
Sample No./ Temperature	^{90}Sr	^{106}Ru	^{125}Sb	^{129}I	^{134}Cs[b]	^{137}Cs	^{144}Ce	^{154}Eu[b]
I2-R1 (~3000 K)	84 ± 26	5.2 ± .8	24 ± 4	8.5 ± 3.2	24 ± 4	12 ± 2	94 ± 14	183 ± 29
I2-R18 (2800-2900 K)	2.2 ± .7	3.9 ± .6	3.4 ± .5	2.5 ± .9	9.6 ± 1.5	4.9 ± 0.7	81 ± 12	123 ± 19
I2-R2 (~3000 K)	87 ± 27	3.1 ± 0.5	88 ± 13	54 ± 16	90 ± 14	35 ± 5	103 ± 15	182 ± 28
I4-R19 (2800-2900 K)	.09 ± .01	22 ± 3	26 ± 4	18 ± 7	22 ± 3	10 ± 2	86 ± 13	128 ± 25
J2-R21A (>3100 K)	87 ± 27	20 ± 3	29 ± 5	17 ± 7	29 ± 5	14 ± 3	113 ± 17	194 ± 30
J2-R21B (>3100 K)	105 ± 33	14 ± 2	30 ± 5	22 ± 7[c]	38 ± 6	16 ± 4	112 ± 17	202 ± 32
K1-R6 (2800-2900 K)	57 ± 18	.55 ± .09	5.2 ± .8	9.3 ± 3.4	37 ± 6	18 ± 3	78 ± 12	125 ± 19
K1-R7 (~3000 K)	76 ± 24	15 ± 2	14 ± 2	7.1 ± 2.6	22 ± 6	11 ± 3	88 ± 13	162 ± 25
L2-R24 (2400-2900 K)	12 ± 4	3.8 ± .6	2.2 ± .3	1.2 ± .5	5.9 ± .9	3.1 ± .5	63 ± 9.4	--c
O2-R26 (2300-2600 K)	43 ± 13	66 ± 10	48 ± 7	28 ± 10	52 ± 8	52 ± 8	57 ± 8.6	--c

---

a. The ORIGEN2-calculated radionuclide concentrations for each isotope are calculated for July 9, 1985 at 14:00.

b. Isotope concentrations are poorly predicted by ORIGEN2.

c. Poor radiochemical yield

d. Below detection limits.

TABLE 34. COMPARISON OF MEASURED AND ORIGEN2-CALCULATED FISSION PRODUCT CONCENTRATIONS ON THE UPPER TIE PLATE

Sample No./ Temperature	Radionuclide Retention[a] (%)							
	^{90}Sr	^{106}Ru	^{125}Sb	^{129}I	^{134}Cs[b]	^{137}Cs	^{144}Ce	^{154}Eu[b]
S2-R30 (>2000 K)	22 ± 7	22 ± 3	64 ± 10	14 ± 5	7.3 ± 1.9	7.2 ± 1.1	15 ± 2	--c
S3-R10 (>2000 K)	15 ± 5	1.3 ± .2	94 ± 14	13 ± 5	3.3 ± .6	1.9 ± .3	3.5 ± .5	--c

---

a. The ORIGEN2-calculated radionuclide concentrations for each isotope are calculated for July 9, 1985 at 14:00.

b. Isotope concentrations are poorly predicted by ORIGEN2.

c. Below detection limits

TABLE 35. COMPARISON OF MEASURED AND ORIGEN2-CALCULATED FISSION PRODUCT CONCENTRATIONS FOR EUTECTIC METALLIC MELT/FUEL DEBRIS SAMPLES

	Radionuclide Retention (%)							
Sample No./ Temperature	^{90}Sr	^{106}Ru	^{125}Sb	^{129}I	^{134}Cs[b]	^{137}Cs	^{144}Ce	^{154}Eu[b]
C2-R12 (1400-1500 K)	25 ± 8	116 ± 17	910 ± 137	35 ± 12	--[c]	4.7 ± .7	25 ± 4	--[c]
D4-R14B (>1400-1500 K)	52 ± 16	21 ± 3	360 ± 54	231 ± 84[c]	118 ± 18	60 ± 9	73 ± 11	--[c]
E2-R15 (>1400-1500 K)	86 ± 27	21 ± 3	142 ± 21	36 ± 13	199 ± 31	99 ± 15	98 ± 15	--[c]
03-R28 (2300-2600 K)	22 ± 7	52 ± 8	0.6 ± .1	167 ± 61	65 ± 10	59 ± 9	60 ± 9	--[c]

---

a. The ORIGEN2-calculated radionuclide concentrations for each isotope are calculated for July 9, 1985 at 14:00.

b. Isotope concentrations are poorly predicted by ORIGEN2.

c. Below detection limits.

of the cesium and iodine. However, there is evidence of accumulation of ^{125}Sb in the metallic phases in the lower part of the bundle. The data for sample C2-R12 indicate nine times as much ^{125}Sb, as might be expected for the amount of fuel present.

4.5.5.7 Multiphase Metallic Regions. Comparisons with ORIGEN2 were not possible for the multiphase metallic samples, as there was little uranium in these samples, which tends to substantially bias the results. The data listed in Appendix H, Table H2B, indicate very low fission product concentrations in these samples. However, sample K1-R23 did show an accumulation of ^{125}Sb in the metallic phase similar to that observed in the eutectic metallic phases (i.e., ~10 times the amount calculated to be present in the fuel).

4.5.6 Summary of Retained Fission Product Analyses Results

Specific conclusions and observations from these examinations are:

- The fission product comparisons with ORIGEN2 for intact pellets indicate complete retention; however, the code is significantly underpredicting the production of ^{134}Cs.
- Tin apparently concentrated in the metallic melts, as evidenced by Sn/Zr ratios greater than the as-fabricated zircaloy.
- Fuel and control materials were found in the upper end box. This agrees with metallographic and SEM data, which indicate that fuel particulates and molten (U,Zr,O) were transported to the upper end box, and with deposition coupon data, which indicate that control rod materials were transported to the upper plenum by aerosol or vapor transport.
- The upper end box samples showed low retention of all major fission products. This suggests high temperatures or optimum release conditions in the transported fuel material.

- There is evidence of accumulation of ^{125}Sb in the metallic phases in the lower part of the bundle.

- Cesium was generally retained within intact and fragmented fuel pellets. Iodine was retained in the intact fuel pellets; however, significant losses were calculated in fragmented fuel at temperatures of approximately 2200 to 2600 K. Significant losses of both cesium and iodine were measured in foamy fuel/partially liquefied fuel.

- The ceramic melt samples indicate significant loss of cesium and iodine in all cases, ranging from essentially complete release to less than 50% retention. However, fission product release in these melt regions could not be correlated solely to peak temperature. This indicates that other factors (such as time at temperature and surrounding material) affected fission product release.

- The large variations in the fission product data precluded extrapolation to retained bundle inventories.

5. POSTULATED BUNDLE SEQUENCE OF EVENTS

Zircaloy oxidation probably began between the 0.69-m (27-in.) and the 1.07 m (42-in.) thermocouple locations in the hottest regions of the fuel bundle. The thermocouple data indicate that the highest measured temperatures during the transient were at the 1.07-m elevation.[10] The oxidation would have started on the hotter central fuel rods and spread radially and axially. The postirradiation examinations indicate that the lowest extent of this oxidation was limited to very small layers on the central fuel rods at the 0.12-m elevation. The fuel rods at this elevation were surrounded by the material that formed the lower blockage region, which suggests that this oxidation occurred prior to the complete relocation of all the eutectic metallic melt/fuel debris in this region. Above this lowermost extent, the zircaloy oxidation profile spread radially and increased in thickness until full oxidation of all the remaining zircaloy was observed at and above the I elevation (0.66 m).

In the upper portion of the fuel bundle, a significant amount of ZrO_2 oxidized cladding shells remained on essentially all the fuel rods at the 1.04-m elevation. At the next elevation examined, the N cross section at 1.14 m, the oxidized cladding shells were limited to three of the corner positions. No oxidized cladding shells remained in the northeast quadrant, which consistently showed the greatest bundle damage throughout the entire fuel bundle. At the next elevation examined, 1.20 m, even less oxidized cladding shells remained; and these were once again limited to extreme corner positions. Essentially no cladding remnants remained above this elevation, with the exception of small amounts of unoxidized zircaloy liner and cladding in the southwest corner at the 1.45-m elevation. These data suggest that the upper extent to the zircaloy oxidation, prior to massive material relocation, was between the 1.04- and 1.14-m elevations. Following the formation of the lower blockage in the central portion of the bundle, steam flow would have been diverted to the peripheral regions of the bundle; and this may account for the oxidized cladding shells in the corners. The lack of any significant amounts of oxidized cladding shells above the 1.2-m elevation and the presence of unoxidized zircaloy in the southwest corner at the 1.45-m elevation (the opposite corner from the most damaged northeast corner) indicate that oxidation did not occur in these uppermost regions of the fuel bundle prior to zircaloy relocation. Some of the unoxidized zircaloy in this region was liquefied as a result of Ag-Zr eutectic interactions after failure of the control rods occurred at approximately 1500 s. Failure of the stainless steel cladding on the control rods would have occurred by at least 1720 K and may have occurred at temperatures as low as 1400-1500 K if the stainless steel were in contact with the zircaloy guide tubes. The (Ag,In,Cd) would have been molten above 1070 K and, upon cladding failure, would have initially been released as an aerosol, followed by candling as a liquid down the outer surface of the control rods.[17] Silver in contact with zircaloy would begin stripping the zircaloy cladding at temperatures above approximately 1200 K; and up to 67 at.% Zr could be dissolved in the silver melt above 1400 K, as shown in the Ag-Zr phase diagram in Appendix G. The Ag-Zr melt would then have flowed down pass the hotter central regions of the bundle, picking up iron, chromium, and nickel from interactions between the zirconium, stainless steel, and Inconel spacer grids, until it reached the cooler regions in the bottom of the fuel module. There, it solidified to form the lower blockage, ultimately resulting in steam diversion to the periphery of the fuel module. The small amount of ceramic melt in the uppermost region of the fuel bundle probably came from the molten upper tie plate, and from any intact zircaloy cladding that had not oxidized or been stripped away by Ag-Zr interactions.

Zircaloy oxidation resulted in rapid cladding temperature increases. The metallography indicates that the unoxidized inner cladding surface melted at 2030 K and was contained within the oxide shells on the cladding outer surface. As the temperatures increased and the amount of intact zircaloy decreased, the fuel rods ballooned as a result of the internal gas pressure. These fuel rods were prepressurized to 2.4 MPa (350 psi), and pressures in the core were less than 1.4 MPa (200 psi) during the high-temperature portion of the transient. The lowest extent of cladding ballooning can be observed on a few rods at the 0.43-m elevation, just below the second spacer grid. The cladding ballooning becomes more extensive at succeedingly higher elevations, and rod-to-rod contact is observed in many instances. This cladding ballooning led to deformation of the unpressurized guide tubes and deformation between adjacent cladding as a result of contact. In many instances, the oxidized cladding from adjacent fuel rods or guide tubes fused together.

Ultimately, the cladding ballooning led to rupture of the oxidized cladding shells, which then allowed the molten unoxidized zircaloy on the cladding inner surface to be released to the fuel bundle. The molten zircaloy partially liquefied the fuel as it relocated downward and would have oxidized if adequate steam had been available. However, data on the steam mass flow rates through the fuel bundle during the high-temperature portion of the transient, data on the hydrogen release during the experiment, and thermocouple data, all suggest that the majority of the (U,Zr,O) oxidized during the reflood period. Details of the thermal-hydraulic, thermocouple, and hydrogen measurement data are reported elsewhere,[9,10] but a summary of the significant results in regard to the postirradiation examination data is presented below.

The mass flow rates during the high-temperature portion of the transient were very low (~13±5 g/s), as opposed to mass flow rates of approximately 5 kg/s during reflood. The low flow rates during the transient were inadequate to have caused the amount of oxidation observed in the fuel bundle posttest. Only 205±11 g of hydrogen were measured in the blowdown suppression tank, where hydrogen released during the transient should have accumulated. (The blowdown suppression tank was isolated from the system just prior to reflood.) 819±367 additional grams were calculated to be in the primary coolant system, where it could only have ended up as a result of reflood.[10] The total amount of 1024 g of hydrogen is in excellent agreement with the best-estimate amount of 1025 g based upon the postirradiation examinations. The source distribution (calculated using an alternative methodology from that used to obtain the best-estimate value of 1025 g) is also consistent with only the oxidized cladding shells and relocated material in the lower blockage region having oxidized during the transient; approximately 181 g of hydrogen are estimated to have been generated from these sources, with approximately 818 g being generated upon reflood.

The thermocouple data at the upper tie plate indicate that the melting and oxidation of the upper tie plate could only have occurred during reflood when a rapid temperature excursion occurred. The extent of damage to the upper tie plate suggests that comparable liquefaction and oxidation probably occurred in the fuel bundle during the reflood period. The observation of relocated fuel fragments and molten materials to the upper end box also indicates the severity of the reflood phenomenon. The relocation of these materials could only have occurred during the reflood period, when steam mass flow rates increased to approximately 5 kg/s.

Postirradiation examinations indicated that temperatures in the core of the ceramic upper blockage region exceeded fuel melting. This is supported by fuel centerline thermocouple data near the periphery of the ceramic upper blockage region, which indicated temperatures of up to 2970 K during the reflood period prior to thermocouple failure. Trend data from failed cladding thermocouples also suggest that the ceramic upper blockage region remained hot for several hundred seconds after reflood. This behavior could only be due to extensive zircaloy oxidation during the reflood period.

Large releases of hydrogen have been seen in other experiments following reflood. In the Severe Fuel Damage Scoping Test (SFD-ST),[3] the core took several minutes to cool after the onset of reflood and a large hydrogen spike was observed during reflood. Similar behavior was also seen in the CORA-12 test conducted in the Federal Republic of Germany. In that test, on-line mass spectrometers measured a large hydrogen spike following reflood, which was attributed to zircaloy oxidation.[18] The results from the LP-FP-2 experiment further suggest that significant amounts of hydrogen can be generated and released during reflood under the right conditions.

6. SUMMARY AND CONCLUSIONS

The major results and conclusions from the postirradiation examinations of the LP-FP-2 fuel bundle are summarized in this section.

The material relocation and stratification in LP-FP-2 resulted in low-melting-point metallic melts near the bottom of the fuel bundle, a high-temperature $(U,Zr)O_2$ ceramic melt region above this, and a debris bed of fuel pellets near the top of the fuel bundle. This is very similar to the results found in the Severe Fuel Damage 1-4 (SFD 1-4) test,[6] and from examinations of the TMI-2 core.[7,19]

Material interactions between silver and zircaloy resulted in relocation of the zircaloy at temperatures well below the melting point of the zircaloy. These Ag-Zr melts ultimately solidified in the cooler regions of the bundle to form the lower blockage.

The zirconium in the Ag-Zr melts interacted with the stainless steel cladding on the control rods and the Inconel spacer grids to cause liquefaction of these materials well below their melting points. Zr-Fe and Zr-Ni eutectic interactions can both lead to significant liquefaction of stainless steel and Inconel at temperatures above approximately 1400-1500 K.

The lack of oxidized cladding shells in the upper portion of the bundle, and the presence of Ag-Zr melts in the lower portion of the bundle, suggest that silver aerosols may have been responsible for liquefying some of the unoxidized zirconium in the upper portion of the fuel bundle. Aerosol droplets of silver were found in deposition coupons located in the upper structure above the LP-FP-2 fuel bundle.[9,10] Extrapolation of the data from those deposition coupons indicated that very small amounts of silver had left the fuel bundle (~20 g); however, postirradiation examinations of the failed control rods indicated that approximately 70% of the available (Ag,In,Cd) was no longer contained within the control rod cladding. This corresponds to approximately 10 kg of molten control rod material alloy, or about 8 kg of molten silver, which was available to interact with other materials in the bundle.

The greatest damage in the LP-FP-2 fuel bundle was consistently in the northeast quadrant. Large amounts of material had relocated downward from the upper portion of the bundle on the east side, leaving a large open space. Gamma scans of the fuel bundle taken before the fuel bundle was ever laid horizontal indicated that this was the actual condition of the fuel bundle following the test. Neutron radiographs of the fuel bundle taken after the bundle was laid horizontal showed this same configuration, and the metallographic examinations also showed this same distribution. This indicates that there was very little loose material in the fuel bundle, and that the debris bed which formed at the top of the bundle was held together by the small amount of ceramic melt material between the fuel pellets.

The greatest mass accumulation was at the second spacer grid and corresponded to 78% of the area within the inner liner. Assuming that steam was diverted around the lower blockage region and could not penetrate into the cavity within the lower blockage, the greatest flow impedance would be just above the bottom spacer grid; and it corresponded to 86% of the area within the inner liner. This indicates that the spacer grids tended to impede material relocation until, in the case of the upper three spacer grids, they ultimately failed.

Integration of the posttest open flow measurement data indicated that the total volume of open area within the LP-FP-2 fuel module was reduced by 11% as a result of porosity trapped in the melt regions. This corresponds to a 15% volume expansion of the material originally contained within the inner liner.

Fuel grain boundary separation was associated with the presence of metallic melts. This suggests that fuel reduction may have occurred adjacent to these metallic melts, resulting in the formation of a liquid uranium phase along these grain boundaries. The effect was not observed where high-temperature ceramic melts were in contact with the fuel. Fuel fragmentation was also observed in areas that were not surrounded by any melt material, which suggests that the thermal shock associated with reflood may have also contributed to fuel fragmentation. Fission gas and pore migration to the grain boundaries, as well as grain boundary coalescence, would have also contributed to grain boundary separation, fragmentation, and powdering.

Fuel pellets that were surrounded by an agglomeration of metallic melt showed increased amounts of cracking, which took the form of striations through the fuel pellet. This further indicates that metallic melts affected the fuel differently than the high-temperature ceramic melts.

Foamy fuel structures occurred as a result of iron oxides interacting with the fuel and causing liquefaction at temperatures below the melting point of the fuel. The foamy fuel structure that showed this behavior no longer had any melt material surrounding it, and similar structures were found throughout the high-temperature portion of the bundle. However, porous fuel structures were also observed on fuel pellets surrounded by the high-temperature ceramic melt. SEM/WDS examinations of one such fuel pellet definitely indicated that it was not the result of iron oxides or zirconium or any other material interacting with the fuel; it was pure UO_2 very near the melting point. This indicates that peak temperatures near the core of the ceramic upper blockage region exceeded fuel melting (>3120 K).

The grain size for most of the fuel averaged 14 μm. Measurements made on fuel at the very bottom of the fuel bundle, which had not undergone any fuel restructuring, indicated that this was the as-fabricated grain size. Grain growth did occur in the center of some of the fuel pellets in the hotter regions of the fuel bundle. The grain size in these regions averaged 27 μm, with a 2-sigma limit of 17 μm. The relatively large as-fabricated grain size may have been an important factor in the small release of cesium and iodine from intact fuel pellets in this experiment.

Visual examinations of the fuel bundle first identified relocated material in the upper end box of the LP-FP-2 fuel bundle. Subsequent metallographic examinations confirmed that fuel pellet fragments and molten materials had relocated upward and deposited in this region. Metallographic examinations of the upper tie plate structure showed that major portions had melted and oxidized and that the material that had relocated upward had also interacted with the molten structure. Thermocouple data from the bottom surface of this upper tie plate indicated that temperatures were <1000 K at this location all through the transient portion of the experiment, but that temperatures exceeded the 1720-K melting point of the stainless steel during the reflood period. The damage to the upper tie plate could therefore only have occurred during this period. Steam mass flow rates also increased from approximately 13±5 g/s during the high-temperature portion of the transient to approximately 5 kg/s during the reflood period. The high flow rates and temperatures during the reflood period resulted in the relocation and deposition of the fuel fragments and molten materials to the upper end box.

The material redistribution measurements indicated that approximately 63% of the zircaloy cladding and inner liner had liquefied and that approximately 15% of the fuel had liquefied. The greatest amount of molten material was contained in the ceramic melt region, and zirconium was the most abundant element in this region. Large amounts of molten zirconium were also present in various metallic melts.

The best estimate of the hydrogen generated from zircaloy oxidation in the LP-FP-2 fuel bundle was 862 g. This corresponds to 49% of the zircaloy cladding and inner liner. An alternate method for calculating the amount of zircaloy oxidation from the postirradiation examination data indicated 836 g, showing very good agreement between the two methodologies. An additional 163 g of hydrogen was nominally estimated to have been generated from oxidation of the upper tie plate, and molten stainless steel cladding and spacer grids. The best estimate of the total amount of hydrogen generated in the LP-FP-2 fuel module is therefore 1025 g of hydrogen. This is in excellent agreement with measurement data based upon grab samples taken from the blowdown suppression tank, which indicated 205±11 g of hydrogen, and from an estimated amount of 819±364 g in the primary coolant system, for a total amount of 1024 g.[10] Analysis of the postirradiation examination data also indicated that nominally 63 g of hydrogen were generated as a result of oxidation of the cladding shells and 118 g were generated from zircaloy oxidation in the relocated material in the lower portion of the bundle. Oxidation from these sources can be assumed to have occurred during the transient portion of the experiment, and the total of 181 g of hydrogen is in reasonable agreement with the 205±11 g estimated to be in the blowdown suppression tank. This tank was isolated from the system just prior to reflood, so the amount of hydrogen measured in this tank is believed to be indicative of the amount of hydrogen generated during the transient. This suggests that most of the oxidation of the ceramic melt material occurred during the reflood period, and in fact, the steam mass flow rates during the high temperature portion of the transient were inadequate to have caused the amount of oxidation observed posttest. The hydrogen that resulted from the oxidation of the ceramic melt material, the melt which penetrated into the insulation, and the oxidation of the molten stainless steel and Inconel components, totals 818 g based on the postirradiation examination data, which also agrees very well with the 819±364 g estimated to be in the primary coolant system from independent calculations.[10] All the hydrogen generated during reflood would have ended up in the primary coolant system.

Tin apparently was concentrated in the metallic melts, and there was evidence of accumulation of ^{125}Sb in the metallic melt in the lower portion of the fuel bundle.

Cesium was generally retained within intact and fragmented fuel pellets. Iodine was retained in the intact fuel pellets; however, significant losses were calculated in fragmented fuel at temperatures of approximately 2200 to 2600 K. Significant losses of both cesium and iodine were measured in foamy fuel/partially liquefied fuel. The ceramic melt samples indicate significant loss of cesium and iodine in all cases, ranging from essentially complete release to less than 50% retention.

However, fission product release in these melt regions could not be correlated solely to peak temperatures. This indicates that other factors (such as time at temperature and the surrounding material) affected the fission product release.

7. REFERENCES

1. P. R. Davis et al., The Risk Significance of Transient Accidents from PRA Studies, *ANS Topical Meeting on Anticipated and Abnormal Transients in Light Water Reactors, Jackson, WY, September 1983.*

2. *Reactor Safety Study -- An Assessment of Accident Risks in U. S. Commercial Nuclear Power Plants*, WASH-1400, October 1975.

3. A. D. Knipe, S. A. Ploger, D. J. Osetek, *PBF Severe Fuel Damage Scoping Test-Test Results Report*, NUREG/CR-4683, EGG-2413, August 1986.

4. Z. R. Martinson, D. A. Petti, B. A. Cook, *PBF Severe Fuel Damage Test 1-1 Test Results Report*, Volumes 1 and 2, NUREG/CR-4684, EGG-2463, October 1986.

5. Z. R. Martinson et al., *Power Burst Facility (PBF) Severe Fuel Damage Test 1-3 Test Results Report*, NUREG/CR-5354, EGG-2565, to be published.

6. D. A. Petti et al., *Power Burst Facility (PBF) Severe Fuel Damage Test 1-4 Test Results Report*, NUREG/CR-5163, EGG-2542, April 1989.

7. J. M. Broughton, P. Kuan, D. A. Petti, E. L. Tolman, "A Scenario of the TMI-2 Accident," *Nuclear Technology*, August, 1989.

8. J. P. Adams et al., *Quick Look Report on OECD LOFT Experiment LP-FP-2, OECD LOFT-T-3804*, September, 1985.

9. M. L. Carboneau et al., *OECD LOFT Fission Product Experiment LP-FP-2 Data Report*, OECD LOFT-T-3805, May 1987.

10. M. L. Carboneau et al., *Experiment Analysis and Summary Report for OECD LOFT Project Fission Product Experiment LP-FP-2*, OECD LOFT-T-3806, June 1989.

11. D. L. Reeder, *LOFT System and Test Description (5.5-ft Nuclear Core 1 LOCES)*, NUREG/CR-0247, TREE-1208, July 1978.

12. V. T. Berta, *OECD LOFT Project Experiment Specification Document Fission Product Experiment LP-FP-2*, OECD LOFT-T-3802, Revision 1, May 1985.

13. Barry Z. Hyatt, *Metallographic Hydride Standards for LWBR Zircaloy 4 Seed Tubing Based on Out-of-Pile Corrosion Tests*, WAPD-LC(BB)-89, February 1974.

14. P. Hofmann, S. Hagen, G. Schanz, A. Skokan, "Reactor Core Materials Interactions at Very High Temperatures," *Topical Meeting on the TMI-2 Accident Materials Behavior and Plant Recovery Technology, Washington, D.C., October 31-November 4, 1988.*

15. *Phase diagrams for Ceramists, Volume 2*, Figures 2172-2173, 1969.

16. P. Hofmann, private communication, KFK, Federal Republic of Germany, August 1985.

17. D. A. Petti, *Silver-Indium-Cadmium Control Rod Behavior and Aerosol Formation in Severe Reactor Accidents*, NUREG/CR-4876, EGG-2501, April 1987.

18. S. Hagen, private communication, KFK, Federal Republic of Germany, April 1989.

19. D. W. Akers, R. K. McCardell, "Core Materials Inventory and Behavior," *Nuclear Technology*, August 1989.